NASA Contractor Report 177526

An Infrared Sky Model Based on the IRAS Point Source Data

Martin Cohen
Russell Walker
Richard Wainscoat
Kevin Volk
Helen Walker
Deborah Schwartz

CONTRACT NAS2—12515
February 1990

National Aeronautics and
Space Administration

NASA Contractor Report 177526

An Infrared Sky Model Based on the IRAS Point Source Data

Martin Cohen
Russell Walker

Jamieson Science and Engineering, Inc., Scotts Valley, California

Richard Wainscoat
Kevin Volk
Helen Walker
Deborah Schwartz

SETI Institute, Los Altos, California

Prepared for
Ames Research Center
CONTRACT NAS2–12515
February 1990

National Aeronautics and
Space Administration

Ames Research Center
Moffett Field, California 94035

TABLE OF CONTENTS

Summary

We present a detailed model for the infrared point source sky that comprises geometrically and physically realistic representations of the galactic disk, bulge, spheroid, spiral arms (including the 'local arm'), molecular ring, and the extragalactic sky. We represent each of the distinct galactic components by up to 87 types of galactic source, each fully characterized by scale heights, space densities, and absolute magnitudes at BVJHK, 12, and 25 um. Our model has been guided by a parallel Monte Carlo simulation of the Galaxy at 12 um. Our model has been guided by a parallel Monte Carlo simulation of the Galaxy at 12 um. The content of our galactic source table constitutes an excellent match to the 12 um luminosity function in the simulation, as well as the luminosity functions at V and K. We are to produce differential and cumulative infrared source counts for and bandpass lying fully within the IRAS Low Resolution Spectrometer's range (7.7-22.7 um) as well as for IRAS 12 and 25 micron bands. These source counts match the IRAS observations extremely well. In addition, models are given for predicting the density of asteroids to be observed, and the diffuse background radiance of the Zodiacal cloud. The model can be used to predict the character of the point source sky expected for observations from future infrared space experiments (e.g., ISO, SIRTF, LDR).

1.0 INTRODUCTION

Prior to the launch of the Infrared Astronomical Satellite (IRAS) in January of 1983, our knowledge of the infrared celestial background in the 8 to 30 micron region was based largely on ground based measurements of specific celestial objects made through the atmospheric transmission windows and the results of exoatmospheric survey measurements made by the HI STAR, HI HI STAR, SPICE, FIRSEE, and ZIP series of rocket flights by AFGL, and the orbital flight of CMP. The only reliable unbiased survey which covered a significant portion of the infrared sky was the AFGL (HI STAR) survey (Price and Walker,1976). Ninety percent of the sky was covered at 11 and 20 μm to produce a catalog of 1151 sources with 11 μm measurements, and 646 sources with 20 μm measurements. The catalog was complete in the areas surveyed to a limiting flux of 2.3×10^{-16} watts cm^{-2} in a one micron passband at 11 μm, and 1.4×10^{-16} watts $cm^{-2}\mu m^{-1}$ at 20 μm. The high pass filter of the HI STAR sensor electronics emphasized sources of small spatial extent, and attenuated the response from sources of large extent. The bulk of the objects detected were highly luminous giant and supergiant stars with excess infrared flux and bright HII regions. The plane of the galaxy was shown to be narrow and marked by bright extended structure. Only a few extragalactic objects were seen, and only a few members of the highly numerous cool red dwarf stellar population were detected. The AFGL ZIP rocket flights (Murdock and Price, 1985) measured the absolute radiance level of the general diffuse background due to thermal emission from interplanetary grains. Their results show a smoothly varying zodiacal emission, and defined the large scale dependence on celestial coordinate.

These data gave a good understanding of the general character of the diffuse sky, and a fairly complete picture of the distribution of point sources on the sky to a limiting flux of about 2×10^{-16} watts $cm^{-2}\mu m^{-1}$). Models of the sky have of necessity been developed for extrapolation to fainter fluxes. The advent of IRAS has greatly reduced the range necessary for extrapolation, however, as with any new more sensitive survey, IRAS has discovered new infrared phenomena which impact existing sky models.

The purpose of this work was to carry out an IRAS data analysis program of the point source sky. A number of discrete, but related efforts were required to achieve the desired goals. It has been our policy to publish the results of these discrete efforts as soon as they were completed. Thus the results of many intermediate steps have already appeared in the literature or are available in preprint form. With this in mind, the format of the FINAL REPORT is such that the body of the report serves mainly as a series of pointers to the more detailed information contained in the Appendices, which are a compilation of all the published papers and preprints.

1.1 BACKGROUND

The general nature and detailed character of the celestial background constitute the fundamental limit to space based infrared telescope performance. The intensity and spatial structure of both discrete and diffuse components in the background drive engineering trade-offs between sensor aperture, detector size and number, data processing requirements; and define regions of the sky in which the system will experience outages, and/or function at reduced efficiency.

2.0 THE DATA

2.1 IRAS DATA SET

All of the IRAS data products which were released prior to March, 1987 are described in detail in Chapter XII of the IRAS Explanatory Supplement, 1988. With the exception of a re-release of the Zodiacal History File, no additional major data products were available for this study. A brief discussion of the major data products used is included here.

The IRAS Point Source Catalog (PSC) is the base set of data used to develop a model of the star distribution in the Galaxy. The great extent of the data base and its well defined statistics allow one to examine in depth the star distributions in nearly all parts of the galaxy, and confidently develop and test models of galactic structure.

The Cataloged Galaxies and Quasars is a subset of the point source catalog containing 11444 sources associated with previously known galaxies and quasars. It is the basic data set for determining the integrated colors of galaxies of similar morphological type.

The IRAS Reject File is the data set containing all the remaining hours confirmed point sources that for one reason or another failed the various quality and/or confirmation tests necessary to qualify for inclusion in the PSC. This file contains, in addition to spurious sources, real infrared sources that failed weeks confirmation due to their motion across the sky, their infrared variability, or possible extended asymmetries which produce scan dependent detector responses. This is the basic data source for moving objects analysis.

The Small Scale Structure Catalog (SSSC) presents data on sources with spatial scales from 2 to 8 arcmin. The catalog contains data on 16740 sources, the vast majority of which are in or near the galactic plane. These data give an adequate description of the emission from many galaxies, compact H II regions, and planetary nebulae.

The IRAS Asteroid and Comet Survey is the first product to be released from the ADAS processing. It is a catalog of those IRAS detections positionally associated with the numbered asteroids and comets. These are basically the brightest of the asteroid and comet distribution, and this survey is the most complete set of data on the infrared signatures of these small solar system bodies.

To facilitate the analysis of extremely large scale emission features, such as the zodiacal emission, the IRAS survey data were averaged to synthesize a 30"x 32" beam. These data were combined with boresight pointing information averaged over eight seconds of time and written to the Zodiacal Observation History File. We have used this data set to construct a model of the zodiacal emission.

IRAS Additional Observations (AO) were developed to study specific celestial objects, however, execution of the AO gives not only data on the object of interest, but on the surrounding area of the sky as well. The IRAS Serendipitous Survey extracted observations of all the point sources in each field, and enhanced the sensitivity of the measurements by co-adding overlapping fields.

The IRAS Calibrated Reconstructed Detector Data (CRDD) is the equivalent of strip-chart data for each detector. This is the most pristine of the IRAS data bases and can be accessed only at IPAC. We have used these data to perform Power Spectral Density (PSD) analysis of the structured sky.

The IRAS Low Resolution Spectra (LRS) data set is the released database of spectral information in the 7 to 23 μm region for 5425 cataloged point sources scanned by IRAS.

2.2 AUXILIARY DATA SETS

Although strictly an "IRAS data set", the Dutch LRS database of 171,000 extracted low resolution spectra is not currently part of the US public domain IRAS catalogues. However, we were able to arrange its transfer to Ames, along with interrogative data-base software. This proved to be critical to the full spectral definition of the celestial source table with its 87 stellar and nonstellar source types. The much smaller public domain LRS Atlas contains only a few examples of the nonstellar objects that we required, particularly of external galaxies. Only with the LRS database were we able to find sufficient spectra of often faint classes of source to represent each by an adequate LRS spectral shape.

For the characterization of the colors of celestial sources we utilized a wide variety of auxiliary catalogues, notably the

Bright Star Catalog, General Catalogue of Variable Stars, Stephenson's Catalog of Cool Carbon Stars, the Two Micron Sky Survey, the Revised AFGL Sky Survey, the Uppsala General Catalogue of Galaxies, and several small but specific catalogues of HII regions, reflection nebulae, T Tauri stars, Wolf-Rayet stars, and the Strasbourg Catalogue of Planetary Nebulae.

Exactly how each catalogue was used can be determined from the several Appendices that form the main body of this Final Report.

2.3 DATABASE MANAGEMENT TOOLS

The primary tool for querying the IRAS catalogues was the INGRES Relational Database Management software package installed on the VAX cluster at NASA-Ames Research Center's Space Science Division. This provided us with small subsets of IRAS point sources or objects from the Small Spatial Scale catalog that were culled from the primary catalogues by criteria involving galactic coordinate location, fluxes at specific wavelengths, color temperatures, or type of association (stellar, nebulae, extragalactic).

The LRS database arrived with a Dutch interrogation package which proved sufficiently flexible that we were able to modify it for greater efficiency (batch extractions of LRS spectra, 18 at a time, rather than single spectra, interactively).

2.4 SPECIAL ANALYSIS TOOLS

To interpret the global IRAS sky in terms of populations we devised detailed zones for the IRAS color-color planes. These we were able to use to represent the colors of many categories of known celestial population and to search for potential new categories. None were necessary; that is, while IRAS almost certainly must have encountered some objects not yet recognized as distinct from known types of source, these do not occur with sufficient frequency and brightness that we can detect them in our characterization of the two IRAS color planes ([12]-[25], [25]-[60] and [25]-[60], [60]-[100]).

For direct comparison of model predictions with the IRAS sky we broke the sky into many different zones by galactic longitude and latitude. For these we derived source counts (logN,logS) and they provided the crucial tests of both the numerical (Monte Carlo) simulations of the sky and the celestial source-based approach.

Early tests on the LRS database and comparisons of Atlas with database spectra, and of these IRAS spectra with expected energy distributions for real stars suggested that a degree of warping was present in the LRS database (Appendix E).

3.0 RESULTS

3.1 GALACTIC POINT SOURCE MODEL

3.1.1 INFRARED COLORS OF STARS

Several studies finally led us to a full characterization of known celestial sources by their IRAS broadband colors alone. These are found in Appendix A (for standard and normal types of star of all spectral types, subtypes, and luminosity classes); Appendix B (for the infrared-dominant populations of late-type stars, both oxygen- and carbon-rich); Appendix C (where we explore the limitations of classification solely by IRAS colors and attempt to vindicate our own classification scheme by optical spectroscopy of hitherto unknown IRAS sources of late type); Appendix F (a further examination of our classification scheme, this time using the additional information available to us from the entire LRS database which essentially provide completely independent clues to source type); and Appendix D (the full color-color characterization of all relevant types of celestial source).

3.1.2 ANALYSIS OF SOURCE COUNTS

Our final dissection of the sky into galactic coordinate zones involved zones that sampled the galactic plane quite closely, then with increasing coarseness as galactic latitude increased away from the plane. Examples of matches to our model can be found in Appendix G (the Monte Carlo simulations of the sky) and Appendix H (the source-based model that was the final product of our study).

3.1.3 COLOR SYNTHESIS

From the color-color planes we were able to identify occupation zones where known sources of several different types predominantly lie. Consideration of galactic latitude was helpful in disentangling populations with overlapping zones, such as galaxies and reflection nebulae/HII regions. At high latitudes one encounters essentially only external galaxies among the highly colored (red) IRAS populations.

We also explored the necessity to include finite size for some nebulae (reflection and HII) are also found as sources of extended emission in the IRAS Small Spatial Scale Catalog. For galaxies, reflection nebulae, planetaries, and HII regions we examined the dependence of color zones on apparent spatial extent (Appendix D), including galaxies of large spatial extent from the Large Galaxy catalogue issued by IPAC recently. Slight shifts, at most, occur and these are explained in terms of the different beam sizes as a function of IRAS wavelength implicit in the Point Source Catalogue or by the presence of

spatially-extended zones of polycyclic aromatic hydrocarbon molecular emission (which dominantly affects [12]). Likewise, an exploration of the possible consequences for our color-color classification of ignoring the presence emission lines or bands found essentially no distinction between the colors of nebulae with and without such features (Appendix D). Thus, our scheme is viable regardless of whether sources are point-like to IRAS or even rather spatially extended.

3.1.4 GALACTIC STRUCTURE

In order to establish the requisite structure of the Galaxy for our model we carried an initial Monte Carlo study designed to simulate the bulge, spheroid, disk, spiral arms and molecular ring (as well as the isotropic extragalactic sky). This (Appendix G) yielded 12 μm luminosity functions and the geometric parameters and physical dimensions of these several components which were subsequently implemented in the final model.

Full descriptions of the structure we finally adopted can be found in Appendices G and H.

3.1.5 EFFECTS OF CONFUSION

As an infrared telescope scans the sky, the detector base-line fluctuates due to many unresolved point sources crossing the focal plane. If these fluctuations dominate over those due to the intrinsic noise from the detectors the system is said to be confusion noise limited. Confusion noise increases the errors in estimating the position and flux density of a point source, and also reduces the completeness of source counts, simply because confused sources cannot be counted.

It was our goal to determine if source confusion in the large IRAS beam is sufficient to account for the observed roll-off (incompleteness) of the IRAS point source counts near the galactic plane. The details of the study are given in Appendix I with the algorithms and computer code used.

We conclude that a simple model for confusion noise coupled with realistic threshold and confirmation criteria is sufficient to explain the behavior of the IRAS source count data. The observed abrupt roll-offs of the log n vs log f curves are a result of the noise and threshold, and are not indicative of a true decline of the galactic point source population. The criteria used by IRAS to invoke special processing in dense regions are reasonable if somewhat conservative. Thus the regions designated in the PSC as High Source Density regions are a valid indicator of the onset of confusion.

3.1.6 DESCRIPTION OF THE MODEL

Both the Monte Carlo approach (Appendix G) and the source-based approach (Appendix H) are highly complex models, fully described in these Appendices.

3.1.7 MODEL UNCERTAINTY

The characterization of entire populations of IRAS sources by color clearly found that sources are not usually highly confined but have appreciable ranges of color. We mimicked these ranges in terms of Gaussian distributions of colors, for each category of source. Tests implied that the real source populations do conform very closely to Gaussian distributions but potential deviations from Gaussians might affect the final parameters expressed in the celestial source table at the heart of the model.

For nonstandard, user-specified wavebands we used the LRS characterization of different source types. Consequently, the question arises of the validity of the LRS spectral shapes. Our study of the warp of the LRS spectra (Appendix E) resulted in the derivation of a set of mean correction factors at each LRS wavelength that were based on a set of normal stars of intermediate spectral type. However, in a test on larger sample we discovered that stars of type K do not always behave as expected, even after they have been "corrected". This spread in LRS spectral shape may be a consequence of an instrumental effect for which we cannot correct. We did establish that our corrections are probably valid for both blue (stars) and very red (e.g., planetaries) IRAS sources but cannot account for the existence of unpredictable degrees of warping in some stars.

The geometry of the Galaxy implicit in the model is based as far as possible on pre-existing optical, radio, and near-infrared studies as well as on our own Monte Carlo simulations. All these give us some confidence in the locations and physical parameters of the major components. However, the molecular ring presents a problem in that its structure is much less well-determined than is that of the spiral arms. We have tried to base our own model for the ring on star counts at K (2.2 microns) along a tangent direction to the ring but uncertainties still exist. Likewise, the precise locations of the spiral arms in some longitudes are not well-determined; indeed, any planar representation of them must be essentially incorrect given the known warping of the Galactic plane seen in neutral hydrogen. All these effects may conspire to make the matches between model and IRAS data imperfect but, within the limitations of an analytical approach, we can do no better at present.

Quantitative estimates of the associated uncertainties are difficult to make. Generally our fits to the IRAS data are good to within 10-20% in many zones. When we fail more conspicuously it is because there exists some real Galactic feature not accounted for by the idealized representations of bulge, spheroid, disk, arms, and ring. We have made an attempt towards Cygnus, in particular (longitude 70-100 in the galactic plane), to incorporate a physical representation of the local spur that seems to attach to the inner spiral arm (around longitude 50 degrees) and to encompass the solar vicinity. This creates an enhancement of sources in these longitudes not explicable by a simple spiral model. Unfortunately, the precise geometry, location and orientation in space of this spur are ill-determined. Our model fits better with its inclusion than without but we cannot be certain that we have constructed it accurately.

3.1.8 APPLICABILITY AND LIMITATIONS

One does not expect the model to operate in the immediate vicinity of the Galactic center where gradients in population density are changing very rapidly.

Towards Cygnus our representation of the local spur may be imperfect. We have given some details (Appendix H) of those directions in which notable excursions of the IRAS data occur, away from the model's predictions.

3.2 ZODIACAL EMISSION MODEL

The diffuse infrared emission from interplanetary dust grains sets the fundamental lower limit to the photon flux on infrared detectors in the 5 to 30 μm spectral region and, thus determines the ultimate sensitivity of the detection system. The earth is imbedded in the interplanetary medium and, therefore, an earth orbiting infrared sensor will observe the emission in all directions.

Prior to IRAS the surface brightness of the zodiacal emission was believed to be a slowly varying function of viewing coordinate with no components at high spatial frequencies. IRAS changed all this with the discovery of a fine structure consisting of several narrow bands of emission which run nearly continuously around the solar system. These have been suggested to be the result of asteroid collisions in the vicinity of the Main Belt. The intensity of the bands have been observed in the 1/2° x 1/2° synthesized beam of the IRAS Zodiacal History File to be a few percent of the local diffuse component.

At the beginning of our data analysis program several different groups throughout the world were actively developing models to explain both the diffuse and banded components of the zodiacal

emission. It was decided at that time to limit our efforts to coding one of the most promising of the new diffuse emission models, rather than initiate another development. The model chosen was that of J. Good (1988). The final code, discussion, and tests of that model are given in Appendix J, "Zodiacal Emission Code".

At this time there is no model for the banded structure that is sufficiently advanced to permit a predictive code to be written. We, therefore, do not include a model for the zodiacal band structure, however, we will return to this subject when we discuss the moving objects within the solar system.

3.3 SMALL SCALE STRUCTURES MODEL

As detailed in Appendix D, only slight color differences characterize source populations when the colors are based on the IRAS Small Scale Structures Catalog as opposed to the Point Source Catalog. Our model addresses the point source sky expressly, and our representation of populations and their colors is based on the point source characterization. We can see no reason to believe that such an approach misrepresents the sky as seen by IRAS.

3.3.1 INFRARED CIRRUS

The most extensive structure observed in the infrared background is that due to the infrared galactic cirrus discovered by IRAS. The appearance of the cirrus is described by Gautier (1986) as having "long, spider-like filaments, clumps and long arching structures composed of small wisps, filaments and clumps." The structure has all spatial scales down to 2 arcmin, the resolution limit of the IRAS sky flux plates. The angular scale of the cirrus might have structure no finer than 2 arcmin, but this would demand an unexpected coincidence between nature and a machine. There is good reason to expect that the true scale will extend to well below the arcsec level. The emission is seen all over the entire sky and appears to be closely coupled with optical nebulosity and the distribution of atomic hydrogen.

We have analyzed the power spectra of the spatial brightness distribution of several regions containing cirrus clouds. There appears to be some correlation of the slope of the spectrum with galactic latitude. The most reliable measurements were obtained at 100 μm with only very limited success at 12 μm due to the low surface brightness of the cirrus. The details of this work are given in Appendix K, "Celestial Background Structure Definition Study, Final Report, Sub-Contract JSE-88-S-001" and Appendix L, "Celestial Background Structure Analysis".

3.3.2 EXTRAGALACTIC SOURCES

3.3.2.1 SIZE DISTRIBUTION

Appendix D includes a comparison of the spatially-integrated colors of large (nearby) galaxies from full IRAS mapping techniques and their simple Point Source Catalog colors. While the fluxes change appreciably, the colors do not. To this extent the sizes of galaxies do not affect our color table for galaxies.

3.3.2.2 SPATIAL DISTRIBUTION

We have assumed (Appendix H) isotropy of the external galaxy distribution. There may be a slight asymmetry between north and south galactic caps attributable to the contributions of major clusters, such as Virgo, but such clustering is difficult to accommodate analytically in a model such as ours.

3.3.2.3 SOURCE COUNTS

We used the deep IRAS study of the NGC 6543 field by Hacking and Houck in which galaxies and stars have been separated. This deep field provides a good validation of our representation of the extragalactic sky (see Appendix H).

3.3.2.4 DESCRIPTION OF MODEL

The basic tool used was the 60 micron luminosity function and considerable discussion appears in Appendix H on the methods by which we established luminosity functions at 12 and 25 μm, the LRS spectral signature of galaxies, and divided galaxies into different types (normal and starburst, Seyferts, and quasars).

The extragalactic sky is treated through a separate routine in our final model because of its isotropic nature (see Appendix H).

3.3.2.5 MODEL UNCERTAINTY

There appear to be few hard facts relating to the exact luminosity bounds for normal, starburst, and Seyfert galaxies, and for quasars. In Appendix H we detail how we separated galaxies into four populations, each represented by mean and Gaussian distributed colors. Ultimately, the designation of a galaxy is irrelevant to our model; only its appearance (colors, luminosity) to IRAS is important. If optical surveys have misrepresented the frequency of occurrence of Seyferts, or have been unable to determine accurate upper and lower bounds for these galaxies, such uncertainties will be implicit in our model.

3.3.2.6 APPLICABILITY AND LIMITATIONS

Limitations of the model chiefly refer to those regions of the extragalactic sky in which obvious anisotropy exists, for example in clusters and along the so-called "supergalactic equator". We cannot build such enhancements in the space density of galaxies into an analytical model of the sky. Clearly, towards such clumps, the model must be deficient.

3.4 MOVING BODIES MODELS

3.4.1 ASTEROIDS

Several thousand asteroids are known to orbit the Sun in a relatively flat belt concentrated mainly between the orbits of Jupiter and Mars. A few asteroids in highly eccentric orbits cross the orbits of the inner planets, Earth, Venus and Mercury. Physical and dynamical studies lead to the conclusion that the asteroids are a population of small bodies that were probably created and shaped by multiple collisions.

We have developed a simple model, based on the IRAS asteroid observations, to predict the number and density of asteroids that could be observed by a space-borne infrared sensor. The model is quite simple. Given the orbital elements of the asteroid, we compute its position on the sky, its distance from the Sun and Earth, and the phase of its observation. The temperature of the surface of the asteroid is determined by its albedo, emissivity, angle of incident solar irradiance, and distance of the asteroid from the Sun. Integration of the thermal emission from the surface yields the irradiance at the Earth orbiting telescope. The incident flux is then compared with the sensor threshold to determine if the asteroid will be detected.

The details of the model are given in Appendix M.

3.4.2 COMETS AND DEBRIS STREAMS

The large field of view and high sensitivity of the IRAS detectors made the IRAS sensor particularly suitable to detect the faint diffuse thermal emission from cometary dust. As a consequence IRAS discovered seven new comets, recovered five previously known comets, and detected the emissions from an additional 12 periodic comets. These IRAS observations of cometary dust comae represent a quantum jump in the available infrared observations of these objects. These are summarized in Appendix N.

This wealth of new information concerning the infrared phenomenology of comets and their associated debris trails are in only the beginning stages of reduction and analysis. Much work must be accomplished in the future to fully exploit this valuable

resource.

Existing analysis programs are just beginning to give some insight into the complex nature of comet dust production and distribution of the grains around the nucleus, in the tail, and into the extensive debris trail. It would be premature at this time to attempt to develop a model for cometary emission in the infrared.

3.4.3 THE 25 μm SINGLE HCONS

The IRAS sky survey produced a large number of "point sources" that were detected only in the 25 μm band. The presence of the vast majority of these was not confirmed on repeated scans of the sky. This leads one to infer that the detections were either spurious, or of objects with variable brightness and/or celestial coordinate. The purpose of this study was to examine these data, discuss some of the possibilities which have been suggested to explain their origin, and develop the arguments supporting a "most-likely" interpretation of the observations.

We found a significant scan noise component at 25 μm which requires some form of structure or clutter related to the zodiacal background, and lead us to consider the consequences of extended structures in the Zodiacal emission.

The details of this investigation can be found in Appendix O. We conclude that a large fraction of the high quality 25 μm single HCONs are detections of extended structures in the Zodiacal emission. The scale of these features is on the order of 2 arc minutes in ecliptic latitude and may extend from a few arcminutes to 360 degrees in longitude. These features are most likely detections of debris from collisions of asteroids in the inner belt region, possibly related to the Flora family.

The rms scan noise generated by these features is about 3.4×10^5 Jy/sr (1.6×10^{-13} watts cm^{-2} μm^{-1} sr^{-1}) at 25 μm for spatial frequencies within the IRAS passband. This is about 0.3% of the zodiacal radiance at $\beta = 0^0$, $\epsilon = 60^0$. These small scale strucutures could be a significant source of clutter noise for future spaced based infrared telescopes.

4.0 CONCLUSIONS

4.1 GALACTIC STRUCTURE

In order to achieve the best matches of the model to the IRAS observations we have "tailored" parts of the luminosity function of the bulge and molecular ring. The results are good but no observations yet exists to validate our modifications to an otherwise very simplistic treatment of the luminosity

function. Future observations with two- dimensional infrared array cameras, particularly near 2 microns, should assist in the study of bulge and molecular ring, and will provide real constraints on the luminosity functions that we have used. In fact, we altered the first version of our model in response to a comparison of the model at 2 microns with K data towards the molecular ring.

One might iteratively determine in greater detail the physical character of the local spur off the inner spiral arm that envelops the solar neighborhood by adapting our model until it best fits the IRAS data.

The Sky Model matches the observed source counts (log number, log flux) seen by IRAS at essentially all flux density levels and across almost the entire sky. Inflections are often seen in the model predictions for source counts in the vicinity of the IRAS roll-off values. These are clearly related to the exact balance between three galactic components when looking in directions in or very near the galactic plane. These components represent the disk, spiral arms, and molecular ring. Our knowledge of precisely how to construct a good representation of the ring and of the arms is incomplete and comparison solely with IRAS observations cannot help us to refine the modeling of these geometric components.

However, given an increase of an order of magnitude in sensitivity near 12 microns, one can definitely trace the changes in slope of the source counts and use new space-based observations as further constraints on the physical model of the infrared sky. A similar situation arises with the galactic bulge: IRAS source counts clearly dictate the existence of the bulge and imply the character of the bright end of its luminosity function. But IRAS cannot tell us whether the luminosity function continues to mimic that of the disk (always the dominant component in the sky model at wavelengths near 12 microns). In all these cases, having data that run significantly fainter than IRAS will enable us to refine the model representation of the sky and, in particular, to hone our luminosity functions for molecular ring, spiral arms, and bulge. Near 25 microns, these inflections can also be suspected in the source counts at levels again about a factor of 10 below IRAS's detection limits.

4.2 EXTRAGALACTIC ASTRONOMY

Given an increase in sensitivity of 100 over IRAS one could also trace, particularly at 25 microns, the flux levels at which the extragalactic component becomes of comparable surface density in the sky to the galactic; i.e. the points at which the more steeply rising contribution from external galaxy counts intersect the rather flatter counts from the galactic disk. The

galaxies are not expected to be appreciable i.e. to rival the disk source counts) until approximately mag 11.0 at 12 μm, and mag 5.8 at 25 μm, roughly 100 times more sensitive than IRAS at 12 μm, and only about 10 times below IRAS's limit at 25 μm.

It would, therefore, be very helpful to have at least several small areas of the sky surveyed to a threshold much fainter than IRAS in order to improve the current physical model of the point source sky.

5.0 REFERENCES

Gautier, T.M., "Observations of Infrared Cirrus", Proc. First International IRAS Conf., to be published in 1986

Murdock, T. L., and Price, S. D., Astron. J., v 90, no. 2, p 375, 1985

Price, S. D., and Walker, R. G., "The AFGL Four Color Infrared Sky Survey", AFGL-TR-76-0208, 1976

APPENDIX A. "IRAS Colors of Normal Stars"

IRAS[a] COLORS OF NORMAL STARS

MARTIN COHEN
Radio Astronomy Laboratory, University of California, Berkeley, California 94720
and
Jamieson Science and Engineering, Inc., P. O. Box F1, Felton, California 95018

DEBORAH E. SCHWARTZ AND ARATI CHOKSHI
SETI Institute, 101 First Street #410, Los Altos, California 94022

RUSSELL G. WALKER
Jamieson Science and Engineering, Inc., P. O. Box F1, Felton, California 95018
Received 21 November 1986; revised 23 January 1987

ABSTRACT

Using stars from the *Bright Star Catalog*, supplemented by cool dwarf stars from the Gliese catalog, that were detected by *IRAS*, we define empirically the median intrinsic visual-to-infrared color indices for "normal" stars as a function of *IRAS* wavelength (at 12, 25, 60, and 100 μm), spectral type (between O5 and M8), and luminosity class (all classes between I and V). These indices are presented graphically and in tabular form. Anomalously red stars are discussed. Two otherwise undistinguished F giant stars are found with significant excesses at 12 μm. Be stars differ markedly from non-emission B stars in their V-[12] indices due to contamination of the former by free-free emission. Both B and Be stars show large dispersions in V-[25] colors that we associate with the heating of local, but strictly interstellar, dust clouds by some of the non-emission B stars. The derived sequences of stellar colors are closely approximated by either simple blackbody predictions or by model-atmosphere calculations.

I. INTRODUCTION

The *Infrared Astronomical Satellite* (*IRAS*) has provided a wealth of data on stars, both of normal and abnormal types. In order to recognize those stars with unusual long-wavelength infrared properties, it is necessary first to define the infrared colors of "normal" stars; that is, stars without significant infrared emission beyond their photospheric radiation. Our intent in this paper is to provide, in a practical form, visual-to-*IRAS*-wavelength color indices for as many stars, with well-defined spectral types and luminosity classes, as possible. A somewhat similar study has been described recently by Waters, Cote, and Aumann (1987, hereafter referred to as WCA). Although they showed 25, 60, and 100 μm data, their determination of color relations was confined to 12 μm data; excluded, *ab initio*, all supergiants and emission-line stars; and combined data for objects with different luminosity classes. Aumann (1985) restricted his attention solely to objects detected by *IRAS* from the Gliese *Catalog of Nearby Stars* in order to recognize far-infrared excesses like that of Vega (Aumann *et al.* 1984).

In Sec. II we describe our selection of stars and discuss the several ways in which our work differs from that of WCA. Our technique for defining color indices and the corrections that we applied to specific *IRAS* fluxes are discussed in Sec. III. Tables of visual-to-infrared color indices and easily accessible graphical representations of these tables constitute Sec. IV, which also includes a comparison of some of our results with those of WCA. B and Be dwarf stars are distinguished in Sec. V. A very small number of stars not known to be visual or spectroscopic binaries, doubles, or variables showed statistically anomalous colors; these are listed and discussed briefly in Sec. VI. In Sec. VII we compare a representative sequence of our empirical colors with theoretical predictions from both blackbody curves and stellar atmosphere calculations.

II. THE SELECTION OF STARS

We examined all stars from the *Bright Star Catalog* (Hoffleit and Jaschek 1982, hereafter referred to as BSC) associated with sources in the *IRAS Point Source Catalog* (1985, hereafter referred to as PSC) that satisfied the additional constraint of having the highest-quality infrared flux measurements (PSC field "fqual" = 3 at the relevant *IRAS* wavelength). (Inclusion of fluxes from the PSC with poorer flux-quality flags ("fqual" = 2) would significantly increase our scatter in color indices.) To this extent our primary information differs significantly from that of WCA, who used an interim version of the *IRAS* database available only in Holland without fqual flags. WCA did filter out sources whose point-source correlation coefficients were less than 97, but inspection of the PSC shows that this is a far less rigorous selection criterion than "fqual" = 3 (e.g., there exist many sources with a correlation coefficient of 97 or better ["D" through "A"] yet fqual of 2, indicating a flux density of, at best, only moderate quality).

We rejected all stars satisfying at least one of the following criteria: (i) composite spectral types in the BSC; (ii) without explicit luminosity class (e.g., some Ap, Oe, and Be stars); (iii) lacking both $(B-V)$and $(U-B)$ in the BSC; (iv) wide pairs or multiple systems in the BSC with at least two components that could be matched to the same *IRAS* source. Be stars, for example, with luminosity classes were retained, but dwarf stars were later separated from non-emission-line B stars (Sec. V). If the BSC gave an intermediate spectral type, we used the average (e.g., F5–7 became F6). In the case of fractional subtypes, we rounded down (e.g., O9.5 to O9). To obtain the largest samples at each

[a] The *Infrared Astronomical Satellite* was developed and operated by the U. S. National Aeronautics and Space Administration (NASA), the Netherlands Agency for Aerospace Programs (NIVR), and the U. K. Science and Engineering Research Council (SERC).

IRAS wavelength, we required only that a star was detected by *IRAS* in that band.

These several selection criteria resulted in final samples of 4013, 2587, 633, and 124 stellar detections from the BSC alone for use at each of the four bands, respectively. The trends in color indices at 12 and 25 μm were somewhat poorly defined for the coolest class V stars, so we sought, in addition, G, K, and M dwarf stars from the Gliese (1969) catalog that were detected at either 12 or 25 μm, or both. After applying the same criteria as those for our BSC sample, we added 96, 85, and 16 G, K, and M V stars, respectively, at 12 μm, and 25, 30, and 7 at 25 μm. Table I summarizes the composite distribution of all these stars by spectral type at each *IRAS* wavelength.

III. DERIVATION OF COLOR INDICES

The flux densities of sources detected near the constant signal-to-noise detection threshold imposed by the *IRAS* data processing are overestimated. Weak sources were detected when the noise summed favorably with the signal pushing it above the threshold, but were missed when negative excursions caused the signal to be below the threshold and, therefore, not included in the flux average. This well-known threshold effect has been discussed by Beichman (cf. IPAC Newsletters for August and October 1985 and March 1986), and a correction estimated using Gaussian-noise statistics applied to the number of times a source was detected versus the number of times it was scanned. This correction is included in the rerelease of the *IRAS* PSC (version 2.0) and is to be documented in the 1987 version of the *IRAS Explanatory Supplement*. We did not have access to PSC 2.0 until after the conclusion of the present study. Therefore, we chose to calculate the flux-correction factors ourselves, also assuming Gaussian noise, and to apply them as a function of the signal-to-noise ratio (SNR) given in the present *IRAS* PSC. We note that flux correction is a necessity for no more than one star in eight at each wavelength. Our method is described below.

If σ is the rms noise of the detector, let the threshold $= f\sigma$, t = the true SNR of the source $= flux(true)/\sigma$ and tm = measured SNR of the source $= flux(measured)/\sigma$. In the case of Gaussian noise, it is easy to show that the ratio of the observed to true flux density is

$$tm/t = 1 + (B/f)\exp[-(A)^2]/[1 + \mathrm{erf}(A)], \quad (1)$$

where $A = (t - f)/\sqrt{2}$ and $B = \sqrt{(2/\pi)}$.

A look-up table of the correction factor t/tm can be constructed from Eq. (1) by substitution of t and interpolation to the tabulated values of SNR, or by iteration on tm. We adopted the latter scheme and derived the correction factors in Table II with $f = 3.0$ as given in the *IRAS Explanatory Supplement* (1985).

In January 1987 we obtained access to the PSC version 2.0. We have made a comparison between fluxes corrected by our method and those contained within the new PSC. As a representative sample, we have taken the 640 sources detected at 12 μm (before application of the rigorous selection criteria described in Sec. II) that were subject to correction by both our SNR-based technique and the new PSC's flux-based method. Figure 1 presents this comparison. We clearly see that there is no systematic statistical difference between the two sets of corrected fluxes. There is substantial scatter for low values of flux but this is not unexpected since these values correspond to sources with very poor SNR (~ 3). Further, this scatter is quite symmetric about the trend defined by sources with larger fluxes. Formal regression analyses indicate that the best-fit correlation to all the points in Fig. 1 is a line of slope 0.997 ± 0.012 with intercept of -0.004 ± 0.038. A line of slope unity with zero intercept is also plotted in Fig. 1. We therefore conclude that there are no statistically significant differences between median colors defined by our corrections to PSC version 1.0 fluxes and colors that would be based upon PSC 2.0 (especially since flux correction is irrelevant to the vast majority of sources).

Each corrected flux was converted to a magnitude according to the relations on page VI-21 of the *IRAS Explanatory Supplement* (1985). Color correction was then applied under the assumption that each definable *IRAS* color temperature between pairs of adjacent bands was essentially the stellar effective temperature. The correction factors given in Table VI.C.6 of the Supplement were employed. We denote the *IRAS* magnitudes by [12], [25], [60], and [100]. The resulting conversions between magnitude and flux density

TABLE I. Distribution by spectral type of stars detected by *IRAS* and used in our color analysis.

Spectral type	Wavelength			
	12 μm	25 μm	60 μm	100 μm
O	13	5	0	0
B	339	136	57	18
A	438	97	24	7
F	574	113	13	4
G	851	514	40	7
K	1537	1338	192	22
M	458	446	307	66
Total	4210	2649	633	124

TABLE II. Correction factors (multiplicative) applied to low SNR fluxes.

SNR	Factor
3.0	0.661
3.1	0.673
3.2	0.687
3.3	0.701
3.4	0.716
3.5	0.733
3.6	0.751
3.7	0.770
3.8	0.790
3.9	0.812
4.0	0.834
4.1	0.857
4.2	0.879
4.3	0.899
4.4	0.918
4.5	0.935
4.6	0.949
4.7	0.960
4.8	0.970
4.9	0.978
5.0	0.984
5.1	0.988
5.2	0.992
5.3	0.995
5.4	0.997
5.5	0.998
5.6	0.999
5.7	1.000
5.8	1.000
5.9	1.000

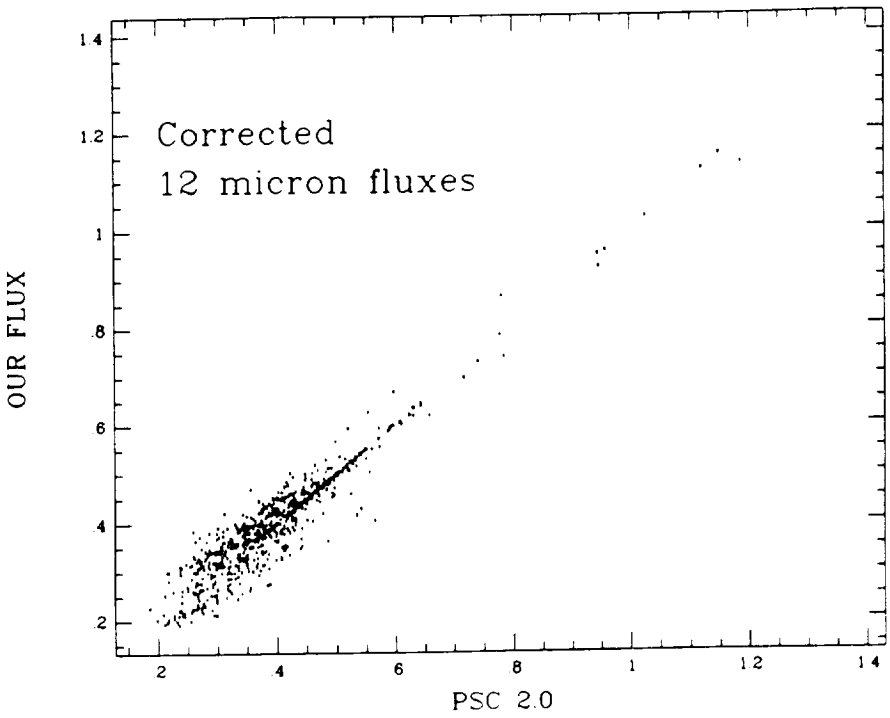

FIG. 1. Comparison between our corrections at 12 μm for flux overestimation in PSC version 1.0 and the fluxes tabulated in the PSC version 2.0 for 640 sources that were corrected by both methods.

were as follows: $[\lambda(i)] = C(i) - 2.5 \log_{10}$ FLUX(i), where $C(i) = 4.03$, 2.44, 0.49, and -0.82, respectively, in the four bands, and FLUX(i) are in Jy.

From the literature (e.g., Allen 1973; Johnson 1966; Panagia 1973; Mihalas and Binney 1981), we culled average sets of intrinsic $(B-V)$ and $(U-B)$ for each well-represented combination of spectral type and luminosity class. We found too few determinations of intrinsic optical colors to define meaningful tables for luminosity classes 0 ("hypergiants"), II ("bright giants"), or IV ("subgiants"). After inspection of a number of stars from each of these classes, we chose to compare hypergiants with class I intrinsic colors; bright giants with class III colors; and subgiants with class V colors. The observed optical colors of each star (from the BSC) were compared with the relevant table of intrinsic colors to determine $E(B-V)$ and $E(U-B)$. We converted these color excesses into extinctions, A_ν, using $A_v = 3.10\ E(B-V)$ and $A_v = 4.72\ E(U-B)$ (corresponding to $R = 3.10$ using a Whitford curve defined by the formula of Miller and Matthews (1972) to represent the extinction law). In the absence of either a $(B-V)$ or a $(U-B)$ in the BSC, we used the estimate based on the other color. If there was a discrepancy between the A_v's of greater than 0.3 mag, we adopted the value corresponding to $E(B-V)$ alone. If this difference was less than or equal to 0.3, we averaged the two estimates. For a few stars, chiefly of type M, we found observed $(U-B)$ colors that were too blue; again, we preferred to use A_v derived from $E(B-V)$ to define V_0, the intrinsic visual magnitude. (Note that WCA chose to correct the optical colors of only the earliest-type stars, O and B, for reddening, although they also excluded all supergiants for which, perhaps, these corrections are most important. We prefer to make these corrections for all stars, since they can also be significant for nonsupergiant, non-early-type objects.) We took the extinctions at all four *IRAS* wavelengths to be zero.

For each star detected by *IRAS* and not already rejected by our several selection criteria, we constructed individual values of V_0-[*IRAS*] and defined the mean color index and standard error of the mean (hereafter referred to as SE), and median index and both lower and upper semi-interquartile ranges of the median (hereafter referred to as SIQT), for each non-empty bin of spectral type and luminosity class. (Hereafter, we shall denote the *intrinsic* color indices merely by V-[λ], dropping the subscript.)

IV. SUMMARIES OF COLOR INDICES

A very small number of stars seemed to have significantly anomalous indices (always too red) for their bins (index $>$ mean $+ 4\sqrt{N} \times$ SE of the mean, or index $>$ median $+ 4\sqrt{N} \times$ upper SIQT, where N is the sample size in the bin). It is statistically legitimate, for normally distributed measurements, which we implicitly assume that we have, to exclude such stars from the tables of color indices. We shall discuss these few stars in Sec. VI. However, if the SE or SIQT values are very small (less than $\sim$0.05 mag), we prefer not to exclude such a star. The median analysis is inherently less affected by such outliers in the color distributions than is the use of averages. We examined the stellar data for all objects that appeared statistically anomalous by either average or median techniques. Virtually all these stars were noted in the BSC as known or suspected variables, optical doubles, spectroscopic binaries, having variable shell or emission-line episodes, or already known from ground-based infrared observations to have circumstellar dust shells. (The latter category includes such objects as 3 Pup, 89 Her, R CrB, and RY Sgr.) These were all treated as explicable peculiarities.

However, since so few stars were genuinely anomalous, we have chosen to summarize our results in the form of tabular and graphical representations of the *unedited* median distributions. It is our belief that these median distributions adequately and honestly represent the data without the necessity for further "editing" on our part. (We do not follow WCA's desire to obtain the smoothest possible subset of the data nor their reliance on means.)

Tables III–XVI represent our median color indices for each *IRAS* wavelength, for the five luminosity classes, I–V,

TABLE III. Median F-[12] colors for class I.

Type	Med.	(SIQT)	Lower	Upper	#
50	− 0.64	—	—	—	1
60	− 1.07	—	—	—	1
80	0.54	—	—	—	1
90	− 0.55	0.15	0.12	0.18	6
100	− 0.65	0.11	0.03	0.19	5
110	− 0.55	0.11	0.06	0.16	6
120	− 0.75	0.03	0.01	0.06	6
130	− 0.31	0.05	0.05	0.05	4
150	− 0.21	0.15	0.09	0.20	5
160	− 0.02	—	—	—	2
180	0.04	0.05	0.05	0.05	4
190	0.26	0.03	0.00	0.07	7
200	0.29	0.11	0.10	0.11	7
210	0.31	0.05	0.05	0.05	4
220	0.38	0.19	0.22	0.16	8
230	0.49	0.08	0.01	0.16	6
250	0.56	0.19	0.33	0.06	3
260	0.56	—	—	—	1
270	0.71	—	—	—	1
280	0.86	0.17	0.30	0.05	3
290	0.94	—	—	—	1
300	0.72	—	—	—	4
310	0.63	—	—	—	1
320	1.06	0.05	0.06	0.04	7
330	1.28	0.32	0.11	0.53	3
340	0.99	—	—	—	1
350	1.11	0.22	0.33	0.11	8
360	1.21	0.17	0.29	0.05	5
370	1.37	0.09	0.12	0.06	10
380	1.31	0.06	0.09	0.04	9
390	1.43	—	—	—	2
400	1.51	0.11	0.04	0.19	13
410	1.80	0.02	0.02	0.02	4
420	1.75	0.08	0.05	0.10	9
430	2.00	0.09	0.10	0.07	9
440	1.94	—	—	—	2
450	2.23	0.11	0.08	0.14	10
460	2.51	0.11	0.18	0.05	5
470	2.21	—	—	—	2
480	2.62	0.04	0.06	0.02	9
490	2.63	—	—	—	1
500	2.89	0.09	0.09	0.09	4
510	2.95	0.07	0.05	0.09	5
520	3.36	0.14	0.19	0.09	8
530	3.46	0.08	0.02	0.14	14
540	3.63	0.10	0.00	0.20	7
550	4.01	0.11	0.09	0.13	3
570	4.18	—	—	—	2
600	5.55	—	—	—	2
610	5.40	0.29	0.36	0.22	7
620	5.48	0.12	0.06	0.18	5
630	3.81	—	—	—	1
650	7.32	—	—	—	1

TABLE IV. Median F-[12] colors for class II.

Type	Med	(SIQT)	Lower	Upper	#
90	− 0.82	—	—	—	1
100	− 1.07	—	—	—	1
110	− 0.87	—	—	—	2
120	− 0.59	—	—	—	2
130	− 0.42	—	—	—	1
150	− 0.38	—	—	—	2
180	0.10	0.39	0.60	0.17	3
190	0.15	—	—	—	1
200	0.15	—	—	—	2
220	0.45	—	—	—	1
230	0.30	—	—	—	1
250	0.64	0.02	0.02	0.02	4
260	0.48	—	—	—	1
300	0.74	—	—	—	4
310	0.78	0.14	0.04	0.24	3
320	0.99	0.03	0.04	0.02	8
340	1.06	—	—	—	1
350	1.17	0.04	0.08	0.00	2
360	1.16	0.12	0.08	0.17	6
370	1.10	—	—	—	1
380	1.44	—	—	—	1
390	1.45	—	—	—	1
410	1.89	—	—	—	1
420	1.97	0.04	0.04	0.03	4
430	2.09	0.06	0.09	0.03	3
450	2.27	0.14	0.24	0.04	15
460	2.13	0.03	0.00	0.07	6
470	2.35	0.12	0.22	0.01	2
480	2.34	0.10	0.08	0.11	35
490	2.30	0.12	0.21	0.04	5
500	2.47	0.19	0.14	0.23	35
510	2.72	0.33	0.15	0.52	25
520	3.03	0.25	0.23	0.28	20
530	3.36	0.13	0.16	0.11	27
540	3.76	0.01	0.01	0.01	4
550	3.71	—	—	—	4
600	4.36	0.21	0.14	0.27	3
610	4.58	0.46	0.08	0.84	6
620	5.06	0.14	0.22	0.07	5
630	5.11	0.58	0.14	1.02	3
640	5.71	0.04	0.04	0.04	4
650	6.55	0.25	0.25	0.25	4

and for each bin of spectral type (a table is reproduced corresponding to each of the meaningful graphical representations in Figs. 2–15). Too few hypergiants were in our sample to define a color grid. All definable lower and upper SIQTs are separately given in these tables, as is the average of lower and upper SIQTs ("(SIQT)"). For distributions without pathologically red objects, our averages reproduce the median analyses within the joint errors. The layout of all these tables is identical. Column (1) gives the spectral type coded as described below; col. (2) is the median for each bin; col. (3) is the average SIQT; cols. (4) and (5) are the lower and upper SIQTs, respectively; col. (5) represents the number of stars in each bin. For bins with only one or two stars, we could not define median color indices; the tables, therefore, give either the individual value for the sole star in that bin or the average index for bins with two stars. In these circumstances, no statistic is substituted for the SIQT ranges. Bins of spectral type, not represented by at least one star in a table, are not listed in that table.

Figures 2–15 represent this tabular information graphi-

TABLE V. Median V-[12] colors for class III

Type	Med.	(SIQT)	Lower	Upper	#
90	− 1.14	—	—	—	1
100	− 1.04	0.12	0.22	0.01	5
110	− 0.94	0.16	0.06	0.26	10
120	− 0.58	0.52	0.24	0.81	11
130	− 0.46	0.46	0.11	0.81	9
140	1.42	—	—	—	2
150	− 0.18	0.67	0.24	1.10	6
160	− 0.46	0.31	0.02	0.59	7
170	− 0.46	0.13	0.10	0.16	8
180	− 0.04	0.37	0.18	0.56	13
190	− 0.06	0.09	0.10	0.08	18
200	− 0.16	0.02	0.02	0.02	4
210	0.17	0.16	0.07	0.25	3
220	0.11	0.12	0.01	0.22	6
230	0.21	0.03	0.04	0.02	5
240	0.36	0.13	0.11	0.15	6
250	0.58	0.13	0.21	0.05	11
270	0.47	0.08	0.09	0.07	13
280	0.55	0.06	0.01	0.12	6
290	0.61	0.10	0.08	0.12	6
300	0.83	0.09	0.11	0.08	18
310	0.84	0.07	0.06	0.07	13
320	0.90	0.05	0.06	0.04	17
330	0.81	0.11	0.09	0.14	8
340	0.97	0.13	0.08	0.19	6
350	1.10	0.05	0.07	0.02	13
360	1.22	0.06	0.02	0.11	7
370	1.16	0.19	0.04	0.34	3
380	1.38	0.14	0.03	0.25	3
390	1.35	—	—	—	1
400	1.67	0.12	0.05	0.18	14
410	1.75	0.38	0.26	0.50	3
420	1.91	0.01	0.01	0.01	7
430	1.74	0.05	0.05	0.05	4
440	1.98	0.05	0.04	0.06	12
450	2.00	0.08	0.08	0.09	44
460	2.08	0.06	0.08	0.05	27
470	2.12	0.10	0.08	0.12	38
480	2.19	0.07	0.07	0.07	251
490	2.28	0.09	0.10	0.08	109
500	2.34	0.09	0.09	0.09	318
510	2.45	0.07	0.08	0.07	222
520	2.58	0.07	0.07	0.06	236
530	2.68	0.07	0.08	0.07	187
540	2.84	0.07	0.06	0.07	132
550	3.04	0.08	0.07	0.09	139
560	3.26	0.03	0.01	0.04	5
570	3.46	0.05	0.08	0.03	17
600	3.95	0.10	0.12	0.09	73
610	4.19	0.14	0.08	0.21	84
620	4.43	0.19	0.13	0.25	87
630	4.91	0.19	0.18	0.19	68
640	5.48	0.26	0.22	0.29	54
650	6.09	0.40	0.39	0.41	17
660	7.67	0.67	0.39	0.96	10
670	9.23	0.70	0.36	1.03	5
680	10.47	—	—	—	2

TABLE VI. Median V-[12] colors for class IV

Type	Med	(SIQT)	Lower	Upper	#
100	− 0.89	0.39	0.19	0.59	6
110	− 0.81	1.41	0.28	2.53	3
120	− 0.68	0.51	0.18	0.84	42
130	− 0.69	0.14	0.09	0.19	14
140	0.25	—	—	—	2
150	− 0.59	0.10	0.00	0.20	5
160	− 0.01	0.64	0.23	1.06	6
170	0.50	0.37	0.54	0.19	5
180	− 0.22	0.48	0.06	0.89	3
190	− 0.08	0.06	0.08	0.04	10
200	− 0.01	0.05	0.04	0.06	8
210	0.05	0.07	0.07	0.07	4
220	0.03	0.09	0.08	0.11	12
230	0.22	0.14	0.11	0.18	19
240	0.34	0.05	0.05	0.05	7
250	0.51	0.07	0.01	0.14	6
260	0.48	—	—	—	2
270	0.63	0.06	0.08	0.03	11
280	0.59	—	—	—	2
290	0.83	0.05	0.06	0.04	2
300	0.71	0.08	0.05	0.11	27
310	0.94	0.05	0.07	0.03	9
320	0.92	0.02	0.01	0.04	12
330	0.96	0.02	0.01	0.03	10
340	1.02	0.06	0.02	0.10	12
350	1.21	0.08	0.13	0.04	14
360	1.21	0.07	0.08	0.06	15
370	1.26	0.09	0.11	0.07	13
380	1.24	0.05	0.04	0.06	9
390	1.28	—	—	—	2
400	1.28	0.02	0.02	0.03	6
420	1.48	0.08	0.16	0.00	7
430	1.15	—	—	—	1
440	1.45	—	—	—	2
450	1.65	0.07	0.04	0.10	11
460	1.89	—	—	—	1
470	1.78	—	—	—	2
480	1.87	0.04	0.04	0.03	13
490	1.83	—	—	—	2
500	1.83	0.06	0.01	0.11	13
510	2.01	0.05	0.03	0.07	9
520	2.03	0.10	0.05	0.14	5
530	2.35	—	—	—	1

cally whenever a meaningful total number of stars is plottable in the diagram. All ordinate scales are identical, and the abscissae are the numerical codifications of spectral type used in Gottlieb's (1978) "SKYMAP" catalog (e.g., O9 = 90, F5 = 350, M8 = 680, etc.) as indicated in our plots too. The error bars in these figures represent both lower and upper SIQTs, hence their asymmetry. For 12 and 25 μm data the samples are meaningfully large at all luminosity classes. By 60 μm the total number of stars supposedly detected is becoming very small, but we present plots for classes I, II, and III to give a sense of the dispersion in colors and to show the emergence of patterns for the late-type stars. At 100 μm, we present likewise only the plot for class III.

It is of interest to compare the colors derived by WCA with our own. Figures 16 and 17 represent such a comparison. For each we have plotted the average of our medians for two adjacent luminosity classes, for all spectral types common to WCA's tabulated averages and our own data, to match WCA's colors for combined luminosity classes (II and III; IV and V). Regression lines for these two figures have slopes slightly greater than unity (1.05 ± 0.05: Fig. 16; 1.12 ± 0.03: Fig. 17) with intercepts of 0.10 ± 0.11 and 0.15 ± 0.15, respectively. Slopes above unity are expected, since average colors will always exceed the median values (stars with colors greatly deviant from the means are invariably too red rather than too blue). With the possible excep-

TABLE VII. Median V-[12] colors for class V.

Type	Med	(SIQT)	Lower	Upper	#
90	0.16	—	—	—	2
100	− 1.17	0.02	0.02	0.02	4
110	− 0.83	0.44	0.21	0.57	5
120	− 0.81	0.29	0.08	0.49	12
130	− 0.67	0.08	0.09	0.07	16
140	− 0.52	0.09	0.17	0.01	5
150	− 0.50	0.08	0.10	0.06	11
160	− 0.14	0.25	0.25	0.25	4
170	0.23	0.17	0.17	0.17	4
180	− 0.12	0.12	0.16	0.08	14
190	− 0.09	0.21	0.08	0.34	28
200	0.01	0.10	0.09	0.10	38
210	0.08	0.10	0.12	0.08	38
220	0.12	0.06	0.07	0.05	56
230	0.20	0.12	0.12	0.12	45
240	0.36	0.10	0.11	0.09	15
250	0.39	0.09	0.08	0.10	29
260	0.48	0.13	0.13	0.13	5
270	0.39	0.09	0.01	0.17	14
280	0.64	0.12	0.03	0.22	10
290	0.63	0.15	0.24	0.06	7
300	0.73	0.08	0.11	0.05	28
310	0.85	0.06	0.06	0.06	16
320	0.93	0.10	0.08	0.13	36
330	1.04	0.12	0.13	0.10	29
340	1.04	0.07	0.07	0.07	25
350	1.10	0.08	0.09	0.07	32
360	1.11	0.07	0.05	0.08	37
370	1.25	0.07	0.07	0.08	32
380	1.27	0.08	0.08	0.08	32
390	1.33	0.16	0.20	0.12	13
400	1.30	0.20	0.30	0.10	37
410	1.45	0.10	0.08	0.13	17
420	1.06	0.24	0.27	0.21	16
430	1.42	0.14	0.09	0.19	10
440	1.31	0.26	0.43	0.09	12
450	1.42	0.19	0.26	0.12	24
460	1.20	0.29	0.04	0.55	5
470	1.57	—	—	—	2
480	1.43	0.31	0.30	0.33	20
490	1.97	0.45	0.22	0.68	3
500	1.68	0.21	0.31	0.11	22
510	1.77	0.22	0.11	0.34	11
520	2.09	0.11	0.15	0.08	8
530	2.29	0.12	0.10	0.13	10
540	2.31	—	—	—	1
550	2.25	0.14	0.06	0.23	12
560	2.77	—	—	—	1
570	2.79	0.13	0.12	0.14	6
580	3.12	—	—	—	1
590	3.54	—	—	—	1
600	3.62	0.12	0.18	0.05	5
610	3.87	0.37	0.45	0.28	3
620	3.83	—	—	—	2
640	4.79	—	—	—	2
650	4.86	—	—	—	2

TABLE VIII. Median V-[25] colors for class I.

Type	Med	(SIQT)	Lower	Upper	#
50	− 0.17	—	—	—	1
90	0.04	0.77	0.30	1.23	3
100	− 0.32	0.97	0.11	1.83	3
110	− 0.44	—	—	—	2
120	− 0.62	—	—	—	1
130	− 0.16	—	—	—	1
150	− 0.09	—	—	—	2
160	0.08	—	—	—	1
180	0.43	0.14	0.21	0.06	3
190	2.43	—	—	—	2
200	1.51	—	—	—	2
210	0.47	0.59	0.28	0.90	3
220	0.47	0.14	0.04	0.23	5
230	0.93	—	—	—	1
250	0.74	0.35	0.61	0.09	3
260	0.99	—	—	—	1
270	0.87	—	—	—	1
280	0.78	—	—	—	2
290	1.43	—	—	—	1
300	0.80	0.05	0.05	0.05	4
320	1.11	3.18	0.20	6.15	3
330	2.55	—	—	—	2
340	1.16	—	—	—	1
350	1.35	0.10	0.06	0.14	5
360	0.91	0.34	0.14	0.54	3
370	1.43	0.01	0.01	0.01	5
380	1.51	0.01	0.01	0.01	4
400	1.63	0.10	0.12	0.08	10
410	1.82	0.11	0.15	0.06	3
420	1.73	0.05	0.04	0.06	8
430	2.01	0.05	0.09	0.00	7
440	2.00	—	—	—	2
450	2.20	0.11	0.03	0.19	8
460	2.57	—	—	—	4
470	2.28	—	—	—	2
480	2.74	0.11	0.12	0.10	8
490	2.67	—	—	—	1
500	2.89	0.15	0.15	0.15	4
510	3.13	0.04	0.01	0.06	8
520	3.52	0.59	0.12	1.06	9
530	3.58	0.07	0.03	0.12	14
540	3.82	0.14	0.12	0.16	6
550	4.14	0.12	0.17	0.08	3
570	4.63	—	—	—	2
600	6.14	—	—	—	2
610	5.39	0.25	0.16	0.35	6
620	5.79	0.12	0.02	0.22	5
630	3.82	—	—	—	1
650	7.54	—	—	—	1

ion of the slight "hook" for the reddest objects in Fig. 17, we ee no substantive difference between WCA's conclusions nd our own for these combined luminosity classes.

V. B AND Be STARS

When we examined the first plots of V-[12] and V-[25] it vas obvious that the scatter in median colors was very large or the B stars with luminosity classes III, IV and V, espe-cially the latter. Therefore we reanalyzed the BSC samples of dwarf stars, separating non-emission B from Be objects. The median trend for the non-emission-line stars in V-[12] is much clearer than for the Be stars. Figure 6, therefore, incorporates the normal B stars' data into the plot for class V. The difference between median colors of Be and non-emission B stars seems to depend weakly on spectral type, ranging from ~ 1.6 for early subtypes to only ~ 0.3 mag for late subtypes (Fig. 18). However, the overall average difference is 1.09 ± 0.20 (SE) mag. The obvious explanation for this excess would be that already established for many Be stars from ground-based measurements (e.g., Allen 1973, 1974; Gehrz, Hackwell, and Jones 1974; Neto and Pacheco 1982; Ashok *et al.* 1984; Goraya and Rautela 1985), namely, opti-

TABLE IX Median V-[25] colors for class II.

Type	Med.	⟨SIQT⟩	Lower	Upper	#
110	−0.80	—	—	—	1
120	−0.60	—	—	—	1
150	−0.19	—	—	—	1
180	1.07	—	—	—	2
230	0.38	—	—	—	1
250	0.91	—	—	—	1
260	0.47	—	—	—	1
300	0.62	—	—	—	2
310	0.76	—	—	—	1
320	1.01	0.12	0.06	0.18	5
350	1.23	—	—	—	2
360	0.98	0.22	0.07	0.37	3
370	1.31	—	—	—	1
390	1.60	—	—	—	1
410	1.82	—	—	—	1
420	2.05	0.02	0.02	0.02	4
430	2.04	—	—	—	2
450	2.30	0.22	0.27	0.18	12
460	2.15	0.05	0.00	0.09	6
470	2.30	0.34	0.15	0.53	6
480	2.40	0.11	0.09	0.12	26
490	2.35	0.14	0.16	0.13	5
500	2.49	0.20	0.10	0.29	31
510	2.80	0.27	0.16	0.38	27
520	3.16	0.25	0.20	0.29	19
530	3.37	0.12	0.10	0.14	27
540	3.78	0.02	0.02	0.02	4
550	3.85	0.02	0.02	0.02	4
570	4.80	—	—	—	1
600	4.39	0.25	0.04	0.45	3
610	4.70	0.43	0.05	0.80	6
620	5.10	0.12	0.17	0.07	5
630	5.22	0.53	0.12	0.94	3
640	5.96	0.02	0.02	0.02	4
650	7.02	0.97	0.38	1.57	5

TABLE X Median V-[25] colors for class III.

Type	Med.	⟨SIQT⟩	Lower	Upper	#
100	−0.65	—	—	—	1
110	−0.98	0.26	0.05	0.47	7
120	1.63	0.33	0.65	0.02	7
130	0.84	0.84	1.29	0.39	3
140	2.35	—	—	—	2
150	1.63	0.95	1.78	0.12	3
160	1.50	0.64	0.64	0.64	4
170	0.98	1.75	1.49	2.02	3
180	0.55	0.52	0.61	0.43	8
190	0.34	0.61	0.20	1.02	6
200	−0.22	—	—	—	2
210	0.34	—	—	—	1
220	0.53	—	—	—	2
230	0.34	—	—	—	2
240	0.88	—	—	—	1
250	0.80	0.14	0.14	0.14	4
270	0.57	0.05	0.05	0.05	8
290	0.74	—	—	—	1
300	1.70	0.64	0.91	0.38	3
310	1.10	—	—	—	1
320	1.05	0.06	0.11	0.02	3
330	0.99	—	—	—	2
340	0.86	—	—	—	2
350	1.14	0.09	0.12	0.07	3
400	1.86	0.09	0.16	0.02	8
410	1.85	0.75	0.50	0.99	3
420	2.05	0.15	0.15	0.15	4
430	2.00	—	—	—	1
440	2.06	0.03	0.04	0.02	9
450	2.10	0.08	0.08	0.08	28
460	2.12	0.11	0.08	0.15	18
470	2.15	0.11	0.10	0.12	27
480	2.23	0.10	0.09	0.10	181
490	2.31	0.10	0.10	0.10	71
500	2.39	0.12	0.12	0.12	251
510	2.53	0.09	0.10	0.09	184
520	2.64	0.09	0.09	0.09	227
530	2.76	0.08	0.09	0.07	184
540	2.90	0.07	0.06	0.09	130
550	3.12	0.07	0.06	0.09	137
560	3.43	0.07	0.11	0.02	5
570	3.49	0.06	0.06	0.06	19
600	4.04	0.10	0.11	0.09	72
610	4.29	0.12	0.10	0.14	83
620	4.54	0.20	0.15	0.24	86
630	5.01	0.19	0.20	0.18	68
640	5.61	0.26	0.25	0.27	55
650	6.07	0.42	0.38	0.45	18
660	7.98	0.93	0.59	1.27	10
670	9.75	0.58	0.22	0.95	5
680	8.28	—	—	—	2

cally thin free-free and bound-free emission from the ionized shell in the Be stars. Although it is known that the same phenomenon occurs in early-type supergiants, its magnitude is much smaller than that shown by the Be stars (Barlow and Cohen 1977), a conclusion supported by the smoothness of our color sequence in V-[12] for class I stars of types O, B, and A (Fig. 2).

What is particularly interesting is to make the same comparison of Be and non-emission B dwarf stars in the V-[25] color indices. We find very little difference in the dispersions of non-emission B and Be objects, and essentially no dependence on spectral subtype for either set of stars (Fig. 19). The Be stars increase their color indices between 12 and 25 μm, yielding a typical value of [12] − [25] of 1.09 ± 0.23. Figure 11, therefore, presents the undifferentiated median data for *all* the B stars.

On the assumption that the free-free continuum is already dominant over the photospheres by 12 μm, one would predict a free-free flux density (F_ν) at 25 μm to be the same as that at 12 μm ($F_\nu \sim$ constant). However, the flux for zero magnitude decreases between 12 and 25 μm by 1.6 mag. Therefore one expects that [12] − [25] would be roughly 1.6. That the observed difference is a little smaller may indicate either that the free-free continuum becomes optically thick in some stars between 12 and 25 μm, or that the photospheric flux is not always a negligible fraction of the total 12 μm emission.

To this extent, the behavior of the Be stars is understandable. What is not immediately obvious is the curious behavior of the non-emission B stars, which on average have [12] − [25] indices of ~1.3. We have isolated the reddest of these stars in V-[25] and find that all are also detected by *IRAS* at 60 μm, with color temperatures between 25 and 60 μm between 85 and 100 K. Optically, almost all of these illuminate reflection nebulae and/or are associated with local obscuration on the NGS Palomar Observatory photographs. We suggest that the sample of non-emission B stars seen at 25 μm includes a normal population (with colors that fit smoothly onto the trend defined by the later-type stars)

TABLE XI Median V-[25] colors for class IV

Type	Med	(SIQT)	Lower	Upper	#
100	− 0.18	1.27	1.05	1.48	3
110	2.49	1.71	3.02	0.39	3
120	1.56	1.36	2.34	0.38	19
130	0.82	0.08	0.08	0.08	4
140	2.05	—	—	—	1
160	2.15	0.21	0.22	0.21	4
170	1.58	0.20	0.20	0.20	4
190	0.00	0.20	0.10	0.30	3
200	0.01	—	—	—	1
210	0.06	—	—	—	1
220	0.14	0.01	0.01	0.01	4
230	0.45	0.01	0.01	0.01	4
240	0.32	—	—	—	2
250	0.97	0.99	0.77	1.21	3
270	3.87	—	—	—	2
280	0.44	—	—	—	1
290	0.62	—	—	—	1
300	0.73	0.02	0.00	0.03	7
320	1.02	0.39	0.06	0.73	3
330	0.88	—	—	—	2
340	1.10	—	—	—	2
350	1.39	0.33	0.35	0.32	3
360	1.31	0.03	0.05	0.00	3
370	1.41	—	—	—	2
380	1.27	—	—	—	2
390	1.33	—	—	—	2
400	0.81	—	—	—	1
420	1.52	—	—	—	1
430	0.88	—	—	—	1
440	1.17	—	—	—	1
450	1.45	—	—	—	2
470	1.51	—	—	—	1
480	2.00	0.09	0.03	0.15	5
490	1.98	—	—	—	1
500	1.34	0.17	0.09	0.25	13
510	2.14	0.04	0.02	0.07	8
520	1.97	—	—	—	3
530	2.67	—	—	—	1

TABLE XII Median V-[25] colors for class V

Type	Med	(SIQT)	Lower	Upper	#
90	3.96	—	—	—	1
100	1.08	—	—	—	2
110	2.75	0.89	0.90	0.88	5
120	− 0.62	1.43	0.13	2.73	5
130	0.87	0.63	0.26	0.99	5
140	2.14	—	—	—	1
150	2.31	—	—	—	1
160	3.36	—	—	—	1
170	1.50	1.17	0.53	1.80	3
180	0.15	0.19	0.19	0.19	4
190	− 0.03	0.18	0.18	0.18	4
200	0.36	0.18	0.21	0.15	7
210	0.21	0.12	0.13	0.11	7
220	0.29	0.31	0.16	0.47	7
230	0.28	0.06	0.04	0.07	7
250	0.50	0.10	0.02	0.17	5
270	0.80	—	—	—	1
290	0.99	—	—	—	1
300	0.94	0.13	0.12	0.14	3
320	0.91	0.10	0.03	0.17	6
330	0.95	—	—	—	1
350	1.28	0.14	0.01	0.26	5
360	1.34	0.09	0.06	0.13	5
370	1.48	0.34	0.02	0.65	3
380	1.70	0.19	0.33	0.05	5
390	1.47	0.48	0.14	0.83	3
400	1.27	0.30	0.31	0.28	14
410	1.63	0.12	0.14	0.09	3
420	1.08	—	—	—	2
430	1.35	—	—	—	2
440	1.32	—	—	—	2
450	1.46	0.12	0.06	0.18	6
460	1.44	—	—	—	2
480	2.03	0.66	0.86	0.45	3
500	1.71	0.15	0.07	0.23	5
510	2.36	2.36	0.19	4.53	3
520	2.17	0.29	0.50	0.08	3
530	2.25	—	—	—	2
540	2.36	—	—	—	1
550	2.46	—	—	—	1
570	3.57	—	—	—	1
600	3.86	—	—	—	2
610	3.79	—	—	—	2
620	4.21	—	—	—	1
640	5.11	—	—	—	1

and a subset of stars with anomalously red V-[25] colors. This subset would include stars that illuminate and excite local clouds of gas and dust, perhaps even clumps of "cirrus." The best way of testing this hypothesis might be to make deep coadded grids of all the relevant *IRAS* data for these few stars and to seek spatially extended components that showed at either 25 or 60 μm, or both.

We feel that the same contamination by free-free excesses affects the V-[25] indices of middle-B giants (Fig. 9). Perhaps the best estimator of normal middle-B III colors would be a smooth interpolation between early-B (B0–1) and late-B (B7–9) indices.

VI. STARS WITH STATISTICALLY ANOMALOUS COLORS

Due to the small number of stellar detections at 60 and 100 μm, the following discussion of anomalous colors relates primarily to 12 and 25 μm. At the longer *IRAS* wavelengths, so few stars are usually found per bin of type and luminosity class, and with such red colors, that probably almost all these are apparent anomalies. We checked their patterns of fquals. Several of these stars had strings of four fqual values that indicate potential confusion of a foreground star with a background pointlike source or a bright spot of "cirrus" (e.g., fquals = 3133 or 1131, etc.). We rejected these long-wavelength sources, since their colors might refer to nonstellar or at least non-BSC objects. The remaining few stars could have genuine anomalies akin to those described by Aumann (1985).

We investigated all stars that have indices greater than the (mean + $4\sqrt{N}\times$SEs) and/or (median + $4\sqrt{N}\times$upper SIQTs) for their bins of spectral type and luminosity class, provided that the samples of stars in these bins were sensibly large.

a) HR 2020

Beta Pic is another nearby star with a Vega-like excess found by *IRAS* (Gillett, Aumann, and Low 1984). It stands out in our analysis as anomalous in V-[25] but not in V-[12], and very red in V-[60].

TABLE XIII. Median *V*-[60] colors for class I.

Type	Med.	(SIQT)	Lower	Upper	#
180	− 3.68	—	—	—	1
190	0.63	—	—	—	1
220	5.12	—	—	—	2
290	6.56	—	—	—	1
300	0.94	—	—	—	1
320	7.68	—	—	—	1
330	4.44	—	—	—	1
350	2.92	—	—	—	2
370	1.34	—	—	—	1
380	2.75	—	—	—	2
400	6.70	2.81	4.80	0.83	3
420	1.98	0.05	0.03	0.07	3
430	1.60	—	—	—	1
450	2.70	—	—	—	1
480	2.49	—	—	—	1
490	2.57	—	—	—	1
500	6.54	—	—	—	1
510	3.13	—	—	—	1
520	4.27	0.38	0.38	0.38	4
530	3.75	0.18	0.31	0.05	7
550	4.08	—	—	—	2
570	4.65	—	—	—	2
600	7.24	—	—	—	1
610	5.70	0.32	0.14	0.50	5
620	5.80	0.47	0.14	0.80	5
650	7.71	—	—	—	1

b) HR 4049

This peculiar hot emission-line star may actually be a protoplanetary nebula, explaining the likely presence of a dust shell around the central object (cf. Lamers *et al.* 1986). Its *V*-[60] is not extreme, however, as would be expected for a planetary nebula.

c) HR 5999

This variable star lies in a dark cloud in a Lupus T association, and within 44″ is HR 6000. The two are often confused. Each is a double and HR 5999 is known to have a dust shell (Smyth, Dean, and Robertson 1979; The *et al.* 1981). The *IRAS* photometry probably refers to all four stars; we therefore dismiss this as nonrepresentative of normal stellar colors.

TABLE XIV. Median *V*-[60] colors for class II.

Type	Med.	(SIQT)	Lower	Upper	#
180	2.44	—	—	—	1
300	2.43	—	—	—	2
350	2.54	—	—	—	1
410	1.81	—	—	—	1
420	2.09	—	—	—	1
450	1.98	—	—	—	2
480	2.18	—	—	—	1
490	2.19	—	—	—	1
500	3.35	1.33	0.80	1.87	3
510	2.57	0.13	0.03	0.23	3
520	3.27	0.04	0.03	0.06	7
530	3.33	0.08	0.10	0.06	12
540	4.10	—	—	—	2
550	3.82	—	—	—	2
600	4.98	—	—	—	1
610	5.17	0.41	0.41	0.41	4
620	5.08	0.05	0.05	0.05	4
630	5.17	—	—	—	2
640	5.89	0.18	0.18	0.18	4
650	7.49	0.78	0.67	0.89	5

TABLE XV. Median *V*-[60] colors for class III.

Type	Med.	(SIQT)	Lower	Upper	#
110	− 0.03	—	—	—	1
120	− 0.36	—	—	—	1
140	− 1.35	—	—	—	1
150	− 1.14	—	—	—	1
160	− 1.15	—	—	—	1
170	2.14	—	—	—	1
180	− 0.03	1.06	1.78	0.34	3
190	0.17	—	—	—	1
230	5.20	—	—	—	1
250	2.24	—	—	—	1
270	1.18	—	—	—	1
300	5.10	—	—	—	1
450	2.26	—	—	—	2
460	4.60	—	—	—	2
470	2.04	—	—	—	1
480	2.16	0.07	0.04	0.09	16
490	2.34	0.87	0.14	1.60	5
500	2.37	0.26	0.11	0.41	14
510	2.56	0.25	0.17	0.34	12
520	2.66	0.12	0.12	0.13	17
530	2.82	0.35	0.18	0.52	28
540	2.92	0.26	0.15	0.38	33
550	3.24	0.22	0.26	0.19	32
560	3.39	0.19	0.04	0.34	5
570	3.46	0.15	0.06	0.23	6
600	4.04	0.10	0.08	0.12	31
610	4.27	0.20	0.12	0.28	37
620	4.54	0.17	0.14	0.20	63
630	4.96	0.20	0.12	0.28	61
640	5.68	0.21	0.22	0.21	50
650	6.24	0.39	0.40	0.39	17
660	7.88	0.90	0.50	1.30	10
670	10.06	0.31	0.31	0.31	4
680	10.72	—	—	—	2

TABLE XVI. Median *V*-[100] colors for class III.

Type	Med.	(SIQT)	Lower	Upper	#
150	5.96	—	—	—	1
170	7.53	—	—	—	1
190	5.62	—	—	—	1
450	7.13	—	—	—	2
460	6.56	—	—	—	1
480	7.78	—	—	—	1
500	7.22	—	—	—	2
510	9.05	2.98	5.83	0.13	3
530	6.89	0.07	0.07	0.07	4
540	5.66	0.92	0.61	1.23	5
550	7.02	2.84	4.10	1.59	3
600	4.92	—	—	—	4
610	4.04	—	—	—	2
620	8.13	1.99	3.98	0.00	3
630	4.92	0.05	0.05	0.05	4
640	5.92	0.96	0.91	1.01	7
650	6.59	0.30	0.16	0.45	8
660	9.10	0.69	1.28	0.09	11
670	9.92	0.22	0.22	0.22	4
680	10.83	—	—	—	2

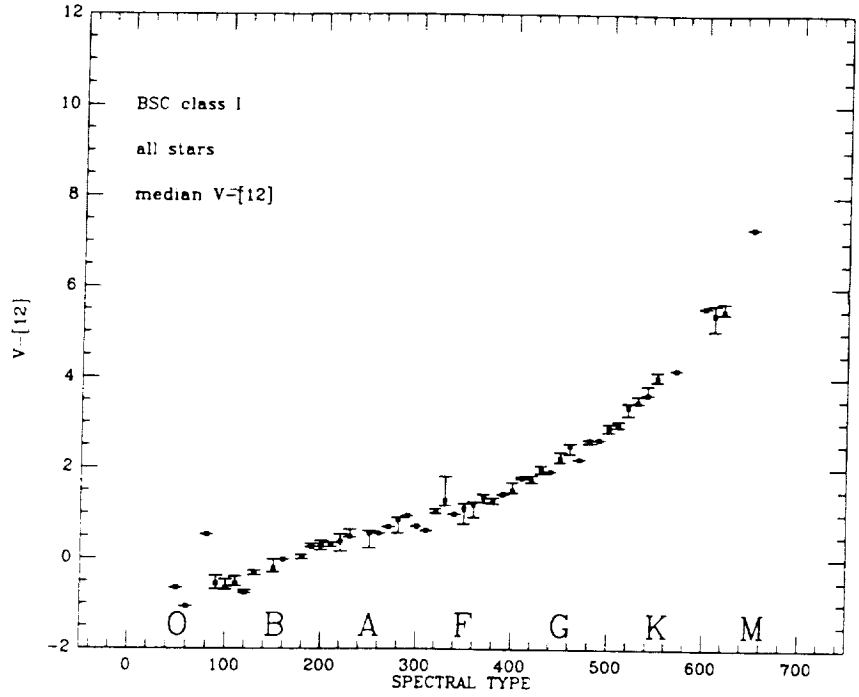

FIG. 2. Median distribution of stellar colors, V-[12], as a function of spectral type for supergiants. Error bars represent both upper and lower SIQTs. The abscissa represents coded spectral type, but letter types are also indicated above the x axis. In this coding, types B0, A0, F0, G0, K0, and M0 are represented by x = 100, 200, 300, 400, 500, and 600, respectively.

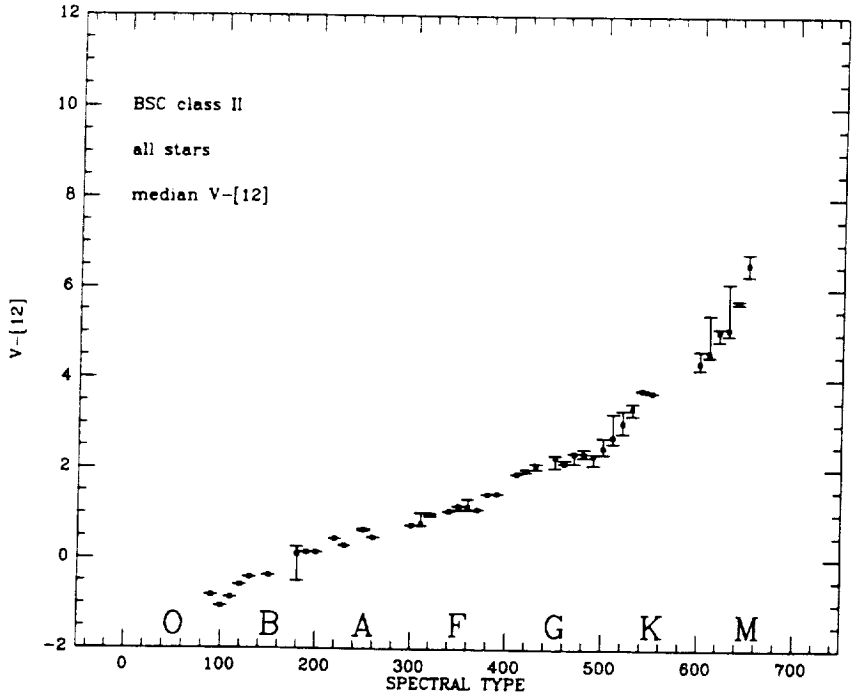

FIG. 3. V-[12], as in Fig. 2, for bright giants.

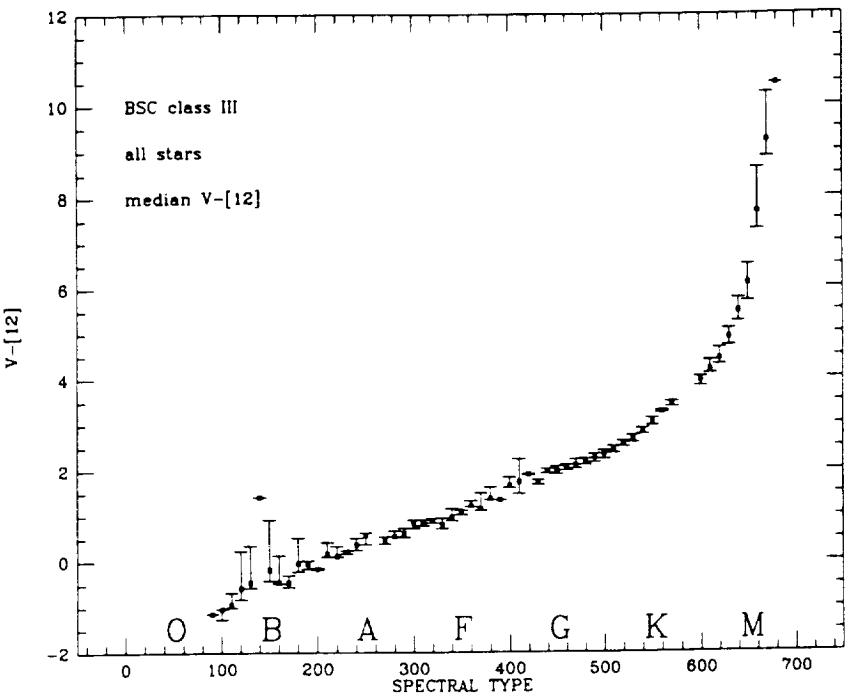

FIG. 4. V-[12], as in Fig. 2, for giants.

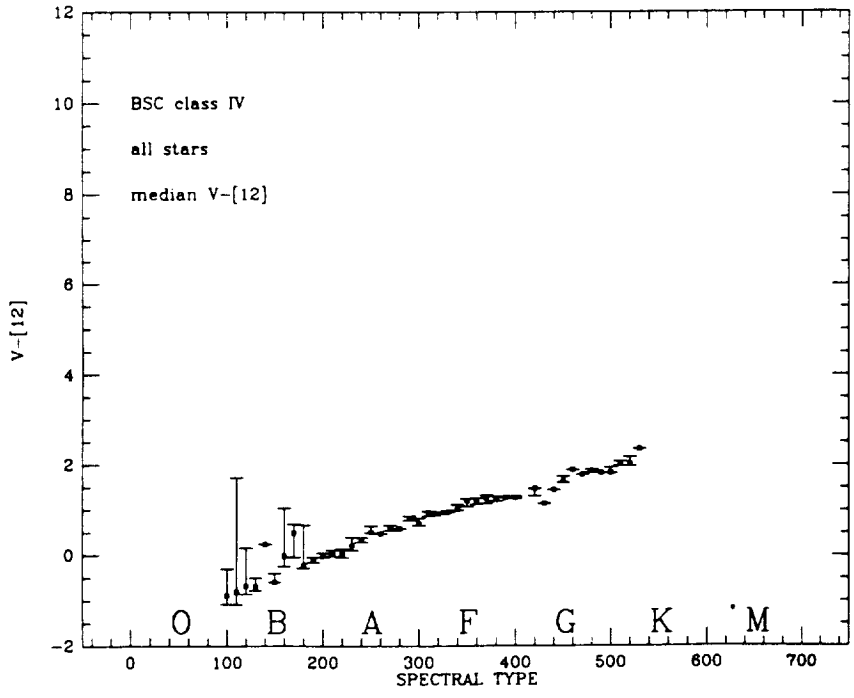

FIG. 5. V-[12], as in Fig. 2, for subgiants.

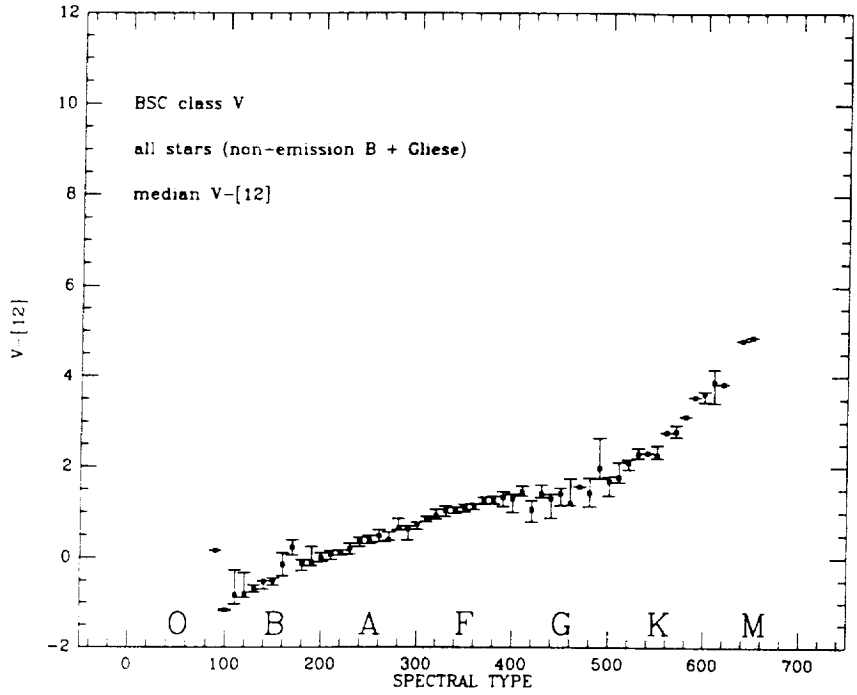

FIG. 6. V-[12], as in Fig. 2, for dwarf stars.

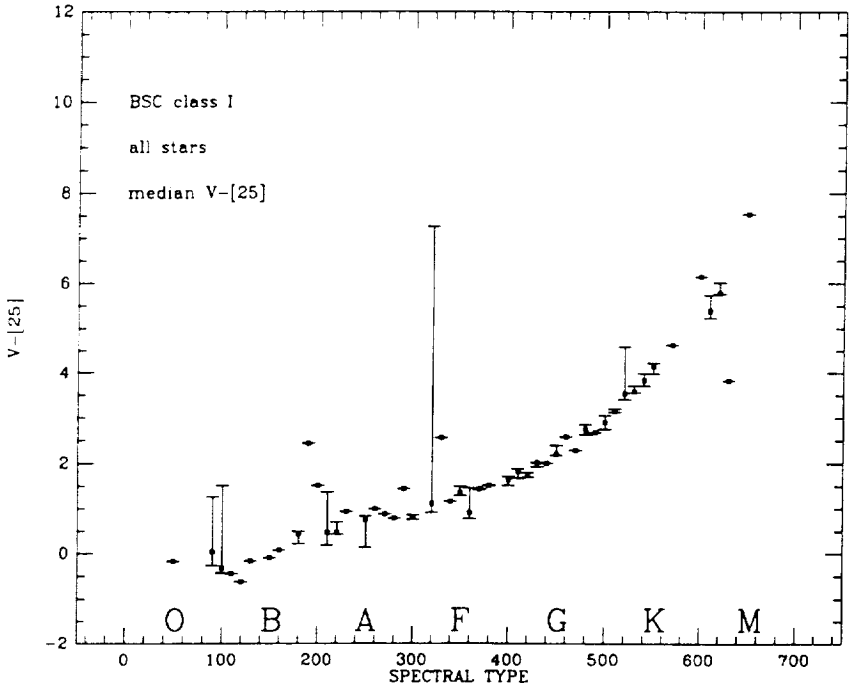

FIG. 7. V-[25], as in Fig. 2, for supergiants.

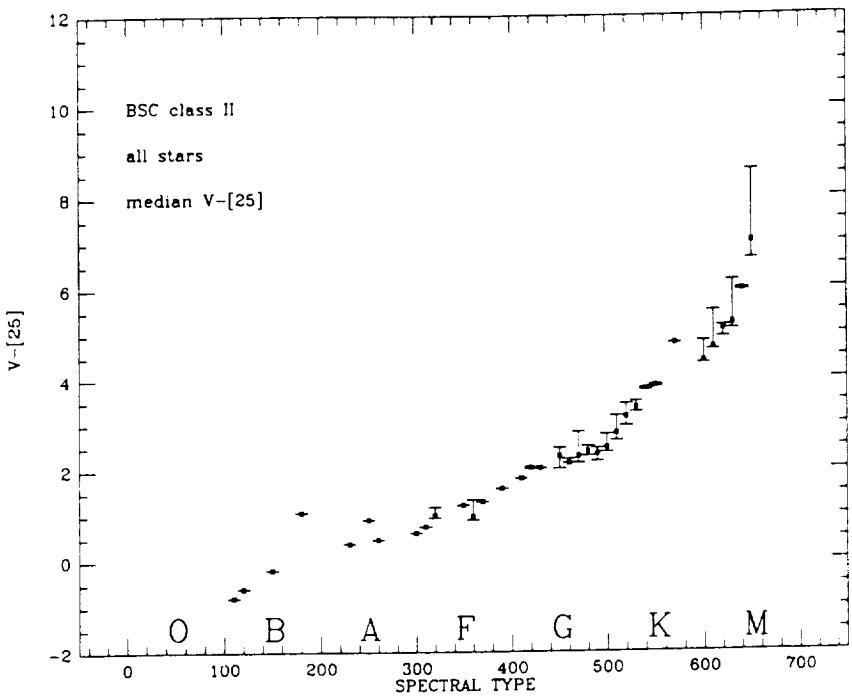

FIG. 8.—V-[25], as in Fig. 2, for bright giants.

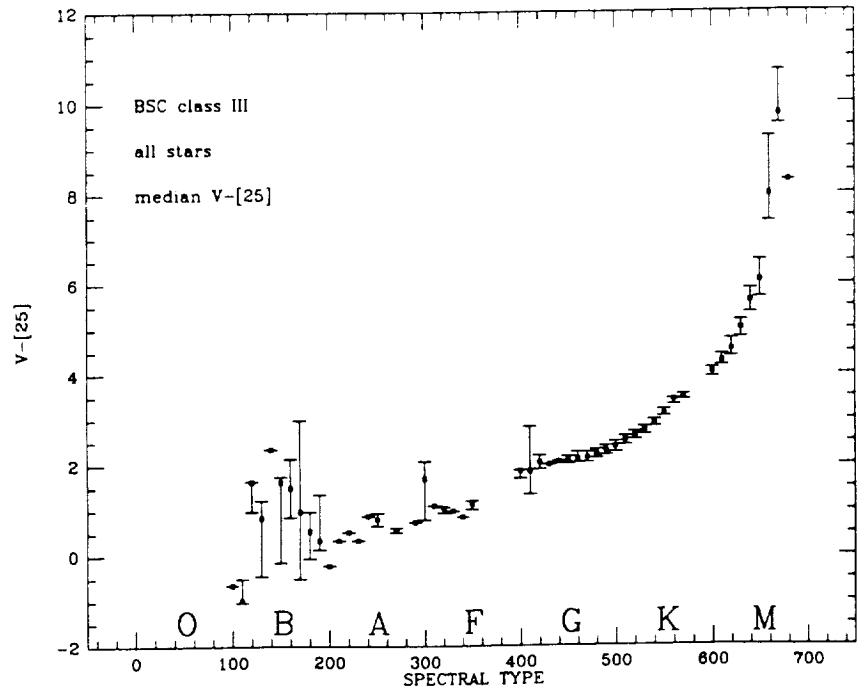

FIG. 9.—V-[25], as in Fig. 2, for giants.

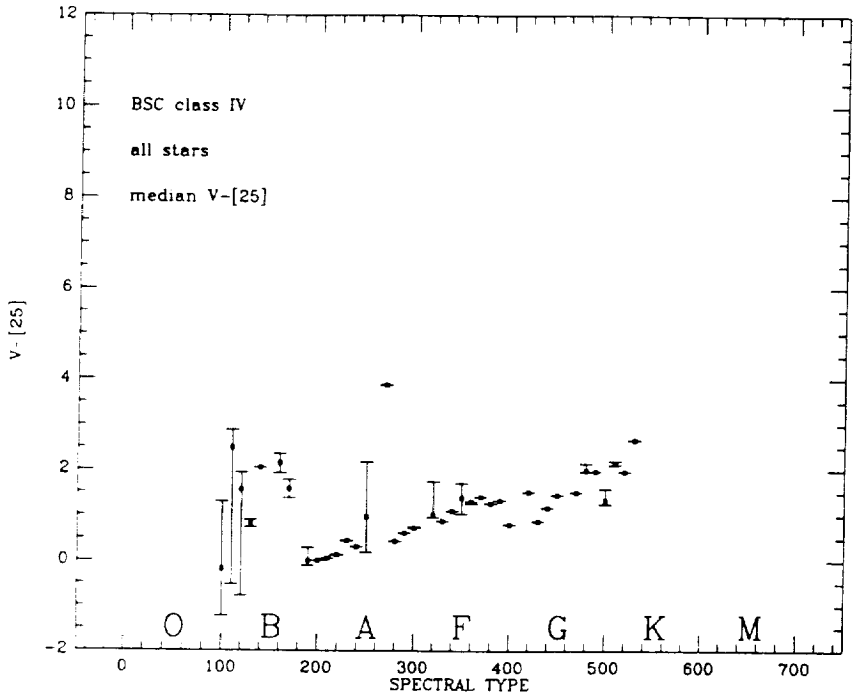

FIG. 10. V-[25], as in Fig. 2, for subgiants.

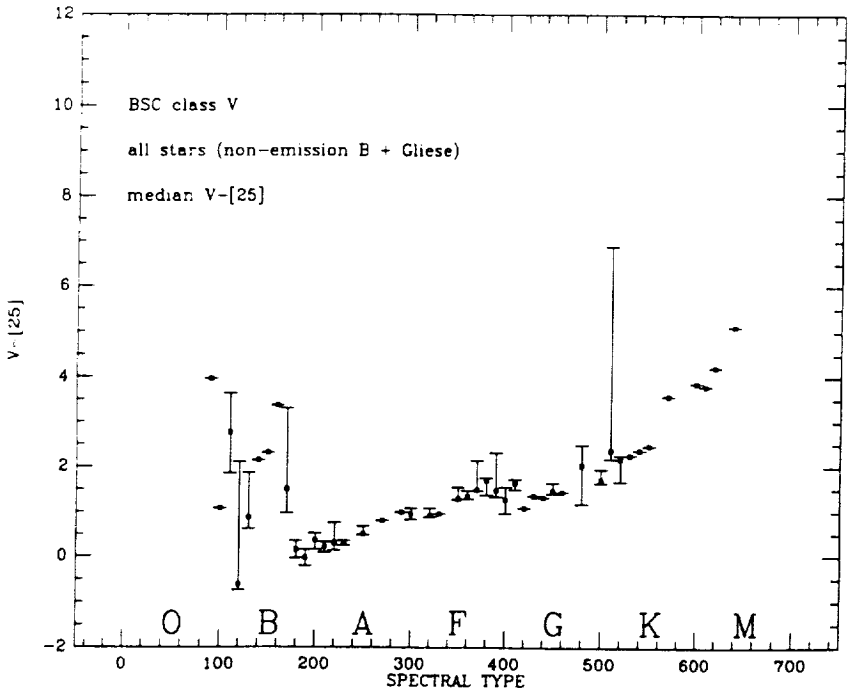

FIG. 11. V-[25], as in Fig. 2, for dwarf stars.

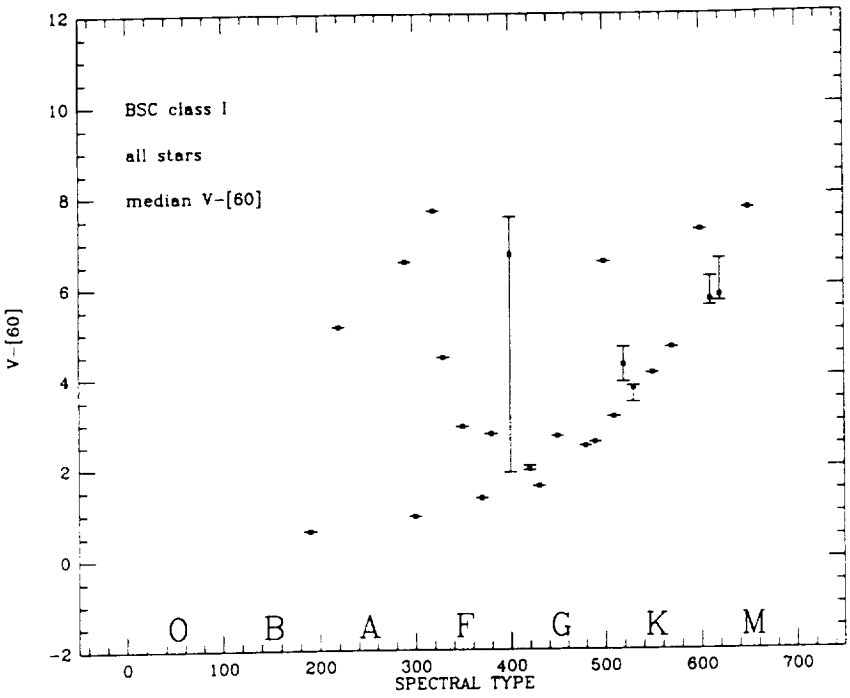

FIG. 12. V-[60], as in Fig. 2, for supergiants.

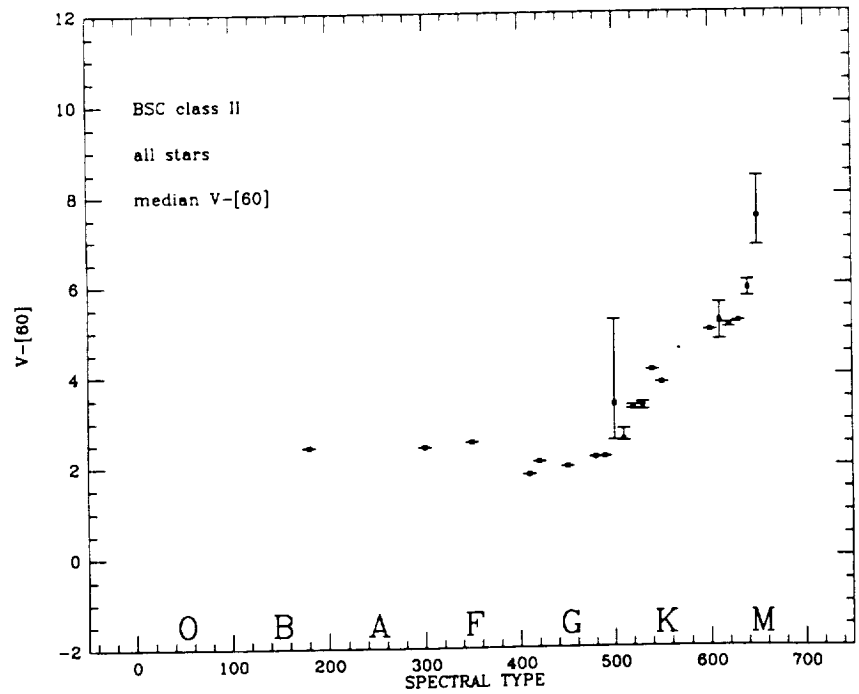

FIG. 13. V-[60], as in Fig. 2, for bright giants.

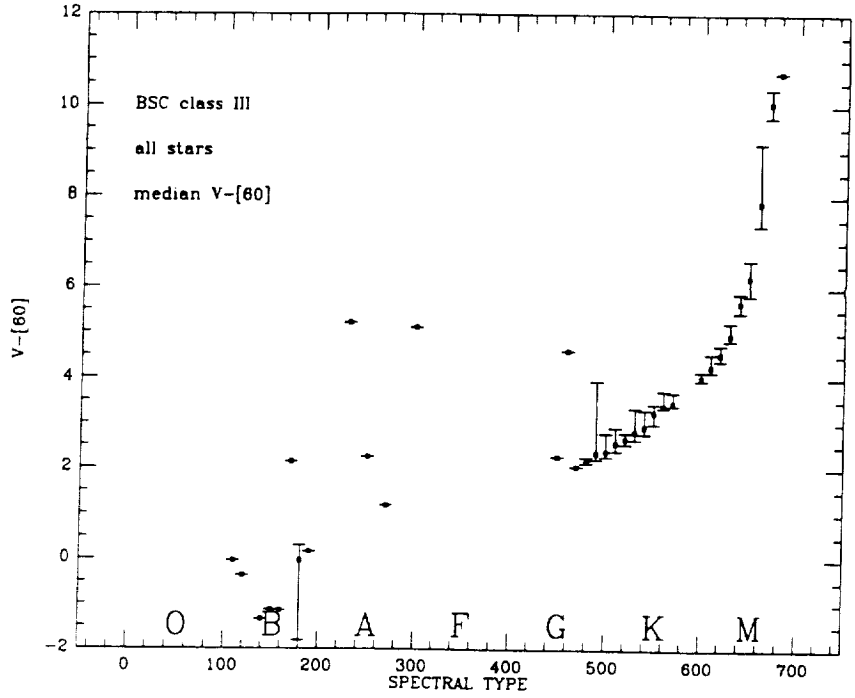

FIG. 14. V-[60], as in Fig. 2, for giants.

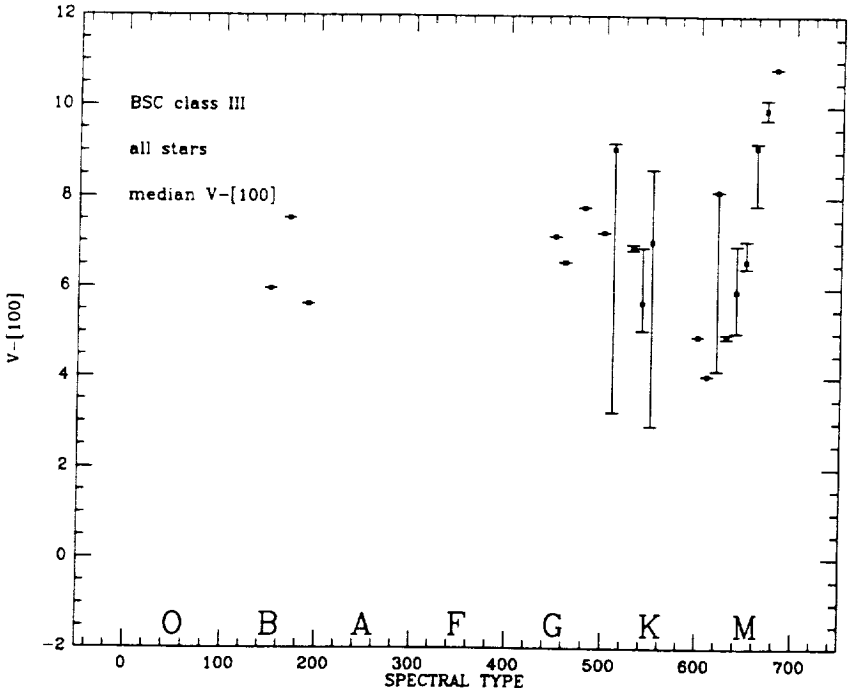

FIG. 15. V-[100], as in Fig. 2, for giants.

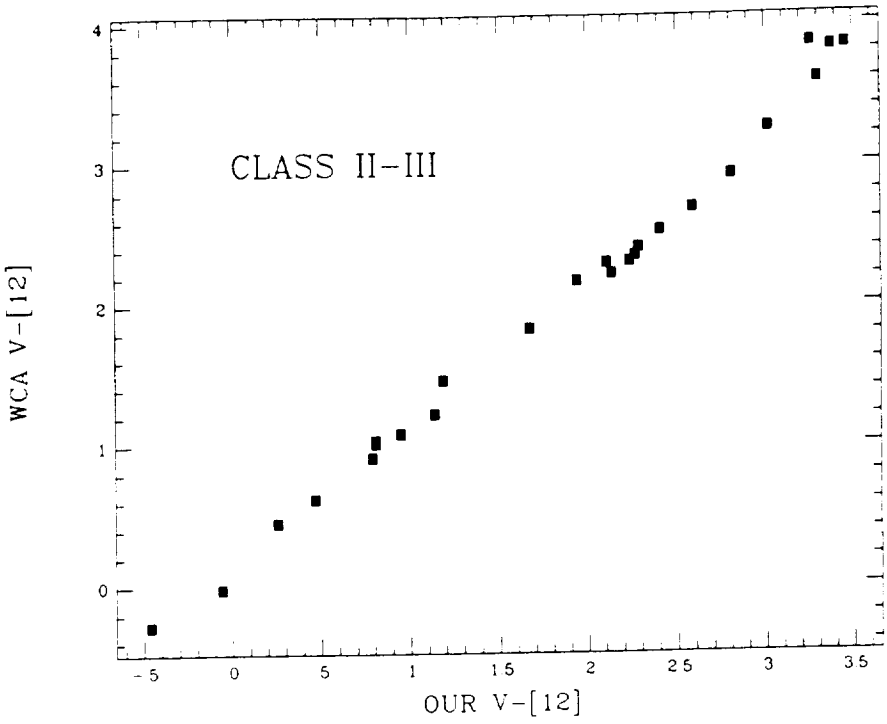

FIG. 16.—A comparison between our median colors averaged over luminosity classes II and III and WCA's average colors.

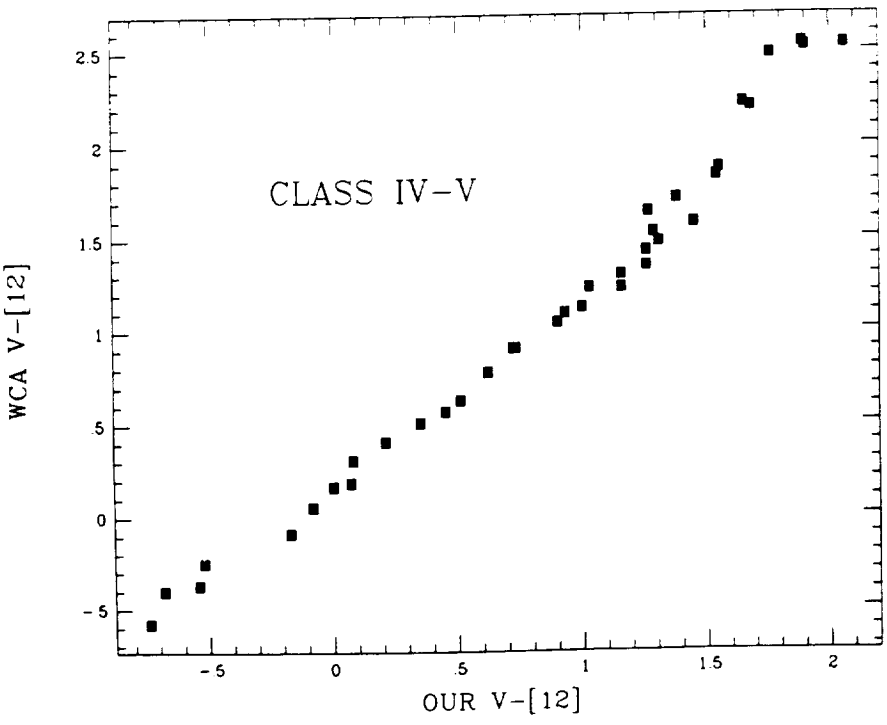

FIG. 17.—As for Fig. 16, but for luminosity classes IV and V combined.

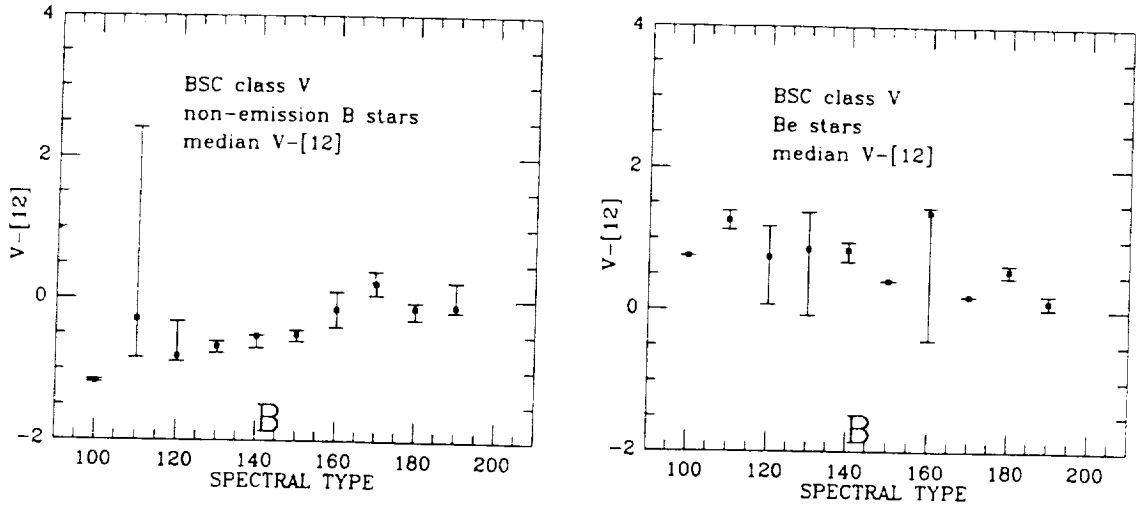

FIG. 18. V-[12] separately for Be and non-emission-line B stars.

d) HR 7001

Vega's anomalous cool dust shell has been discussed in detail by Aumann *et al.* (1984). We can detect no peculiarity at 12 μm and only a marginal one at 25 μm based on our estimates of SIQTs. The anomaly is known to grow with increasing wavelength, but we have too few A0 V stars at 60 μm to recognize this fact.

e) HR 8269 and 9057

We know of no previous discussions of these F giant stars that would imply anomalous infrared free-free gas or thermal dust emission. Both show anomalies at 12 μm only, but the SIQT values for F7 and F8 giants are very small (0.02 and 0.03 mag), so it is possible that the apparent significance of these stars' formal color excesses is purely fortuitous.

VII. DISCUSSION

A comparison of the median color distributions at 12 and 25 μm shows no major differences between the indices of stars between spectral types O, and F to early G, as the luminosity class is varied. However, for stars with types later than G1, the median values separate out with luminosity class at both 12 (Fig. 20) and 25 μm (Fig. 21). Such a pattern is broadly consistent with three expected phenomena: (1) the general offset in effective temperature scales between stars of the same spectral class but different luminosity class; (2) the diminishing value of V magnitudes as estimators of the continuum flux for cooler and cooler stars, where the combination of the Wien portion of the Planck function and the severe mutilation of the spectrum by overlying TiO bandheads leads to an erratic pseudocontinuum; and (3) grain condensation around late-type stars (K and M) in the

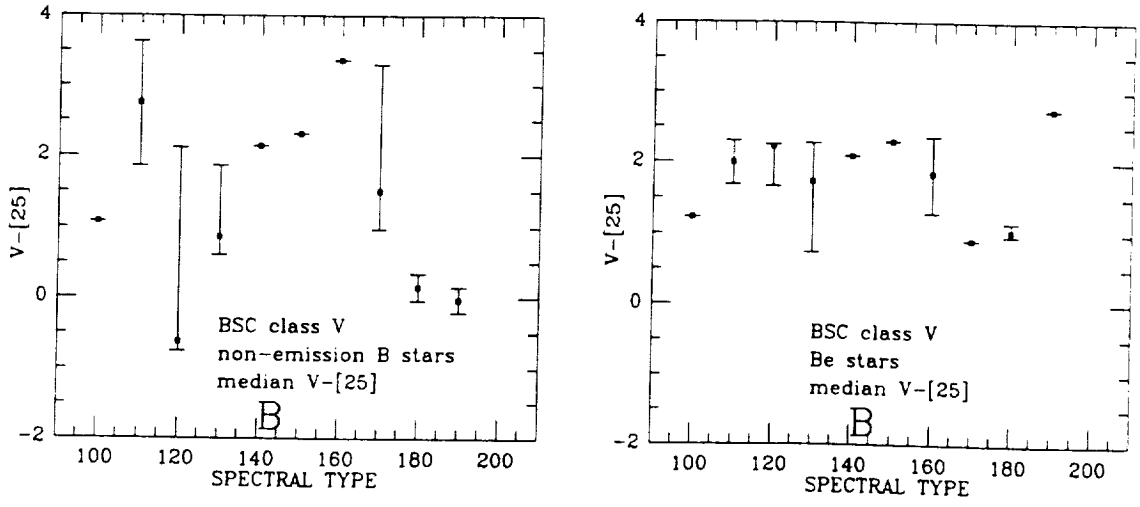

FIG. 19. V-[25] separately for Be and non-emission-line B stars.

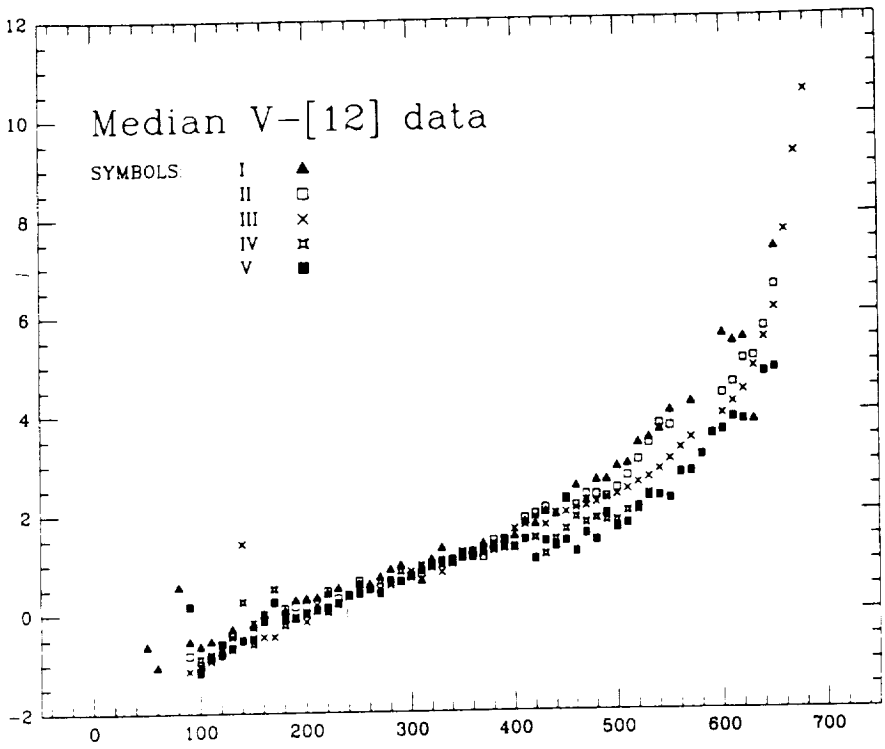

FIG. 20. *V*-[12] sequences for different luminosity classes.

outer parts of cool, radiatively driven stellar winds whose vigor and extent are strong functions of stellar luminosity.

If stars were merely blackbodies corresponding to their effective temperatures, then we could predict the intrinsic indices, V_0-[12], etc. (cf. the Appendix in Barlow and Cohen 1977). We have also compared our color sequences with model-atmosphere calculations published by Kurucz (1979) for O–G stars, interpolating and extrapolating between his two longest wavelength points (10 and 20 μm) to obtain points at 12 and 25 μm, for models with temperatures matched to the stellar effective temperatures (with appropriate values of log g and normal solar abundances). Figure 22 compares Kurucz models and blackbody predictions with a typical color sequence (for giants) at 12 μm. Similar

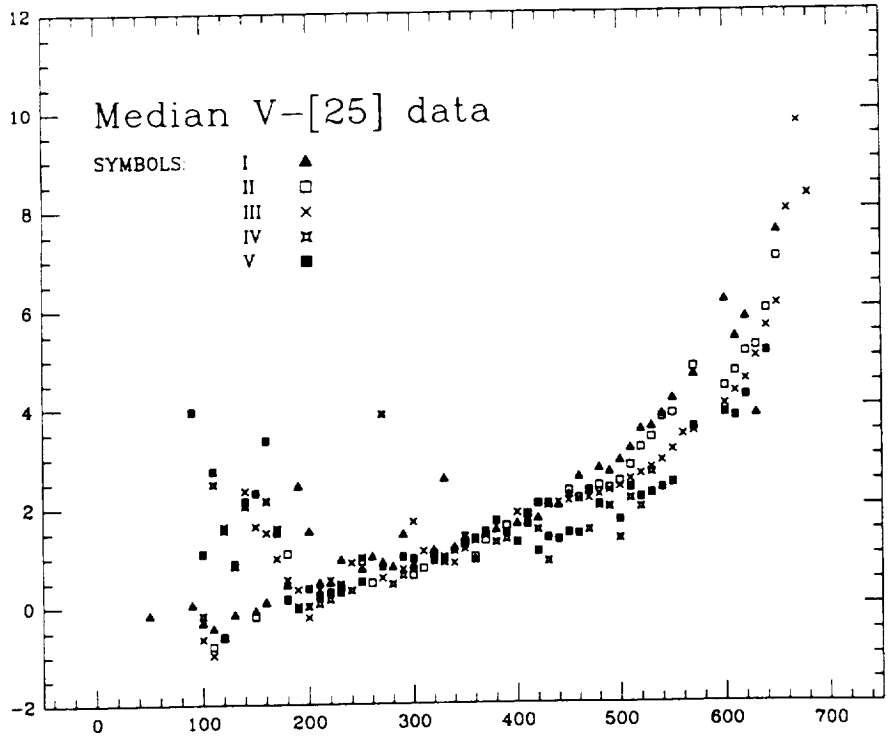

FIG. 21. *V*-[25] sequences for different luminosity classes.

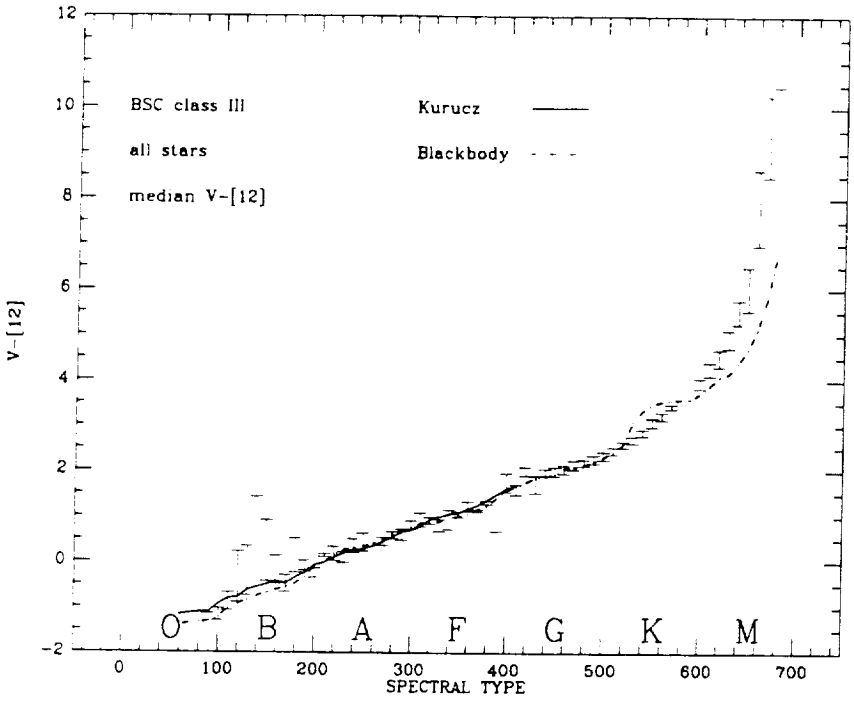

FIG. 22. Comparison between our median colors for giants and the predictions of Kurucz (1979) models (solid line) and of simple blackbodies (dash-dot line).

patterns emerge at 25 μm and for other classes. The model atmospheres fit the observed colors well over their entire range from O to G (the large error bars in the observations of B giants are probably again caused by the inclusion of Be stars: see Sec. V) and blackbodies are a reasonable match to all the observations except for the coolest giants. (Of course, one should not expect a model atmosphere characterized by a single temperature to represent simultaneously both the visible- and infrared-emitting zones of a real star.)

In spite of the improbability of finding cool ($\gtrsim$M4) M giants without dust shells (Gehrz and Woolf 1971), it is gratifying to see that we can define a monotonic sequence of median colors with sensible error bars for stars as late as M7–8. The rapid rise in color indices with lateness of spectral type among the M stars exceeds that predicted simply from the coolness of their photospheres. This may indicate that the further these stars evolve along the giant branch, the faster is their rate of mass loss and consequently their rate of production of dust grains.

At wavelengths as long as 60 and 100 μm, there are very few stars per bin, and the sizable indices observed for most of the earlier-type stars ($<$F) suggest either that none of these stars is without an infrared excess, or that infrared "cirrus" contaminates these supposed stellar colors. It is gratifying to see that the later types can sometimes provide recognizable sequences of color indices at the longest wavelengths, notably the G, K, and M III stars in the V-[60] plot.

M. C. and R. G. W. acknowledge support from an independent research and development program of Jamieson Science and Engineering, Inc., for this study of infrared stellar colors. D. E. S. and A. C. thank the NASA-Ames Research Center, which provides support for *IRAS* studies through the SETI Institute under cooperative agreement NCC 2-407. We are grateful to Gary Villere for *IRAS* database management at NASA-Ames Research Center.

REFERENCES

Allen, C. W. (1973). *Astrophysical Quantities*, third ed. (Athlone, London), p. 206–208.
Allen, D. A. (1973). Mon. Not. R. Astron. Soc. **161**, 145.
Allen, D. A. (1974). Mon. Not. R. Astron. Soc. **168**, 1.
Ashok, N. M., Blatt, H. C., Kulkarni, P. V., and Joshi, S. C. (1984). Mon. Not. R. Astron. Soc. **211**, 471.
Aumann, H. H. (1985). Publ. Astron. Soc. Pac. **97**, 885.
Aumann, H. H., Gillett, F. C., Beichman, C. A., de Jong, T., Houck, J. R., Low, F. J., Neugebauer, G., Walker, R. G., and Wesselius, P. R. (1984). Astrophys. J. Lett. **278**, L23.
Barlow, M. J., and Cohen, M. (1977). Astrophys. J. **213**, 737.
Beichman, C. A., Neugebauer, G., Habing, H. J., Clegg, P. E., and Chester, T. J., editors (1985). *IRAS Astronomical Satellite (IRAS) Catalogs and Atlases. Explanatory Supplement* (U. S. GPO, Washington, DC).
Gehrz, R. D., Hackwell, J. A., and Jones, T. W. (1974). Astrophys. J. **191**, 675.
Gehrz, R. D., and Woolf, N. J. (1971). Astrophys. J. **165**, 285.
Gillett, F. C., Aumann, H. H., and Low, F. J. (1984). Paper presented at "Protostars and Planets II" meeting, Tucson, AZ, January 1984.
Gliese, W. (1969). "Catalog of Nearby Stars", Publ. Astron. Rechen-Institut Heidelberg No. 22.
Goraya, P. S., and Rautela, B. S. (1985). Astrophys. Space Sci. **113**, 373.
Gottlieb, D. M. (1978). Astrophys. J. Suppl. **38**, 287.
Hoffleit, D., and Jaschek, C. (1982). *The Bright Star Catalog*, fourth revised ed. (Yale University Observatory, New Haven).
Johnson, H. L. (1966). Annu. Rev. Astron. Astrophys. **4**, 193.
Kurucz, R. (1979). Astrophys. J. Suppl. **40**, 1.
Lamers, H. J. G. L. M., Waters, L. B. F. M., Garmany, C. D., Perez, M. R.,

and Waelkens, C. (1986). Astron. Astrophys. **154**, L20.
Mihalas, D., and Binney, J. (1981). *Galactic Astronomy*, second ed. (Freeman, San Francisco), p. 106–109.
Miller, J. S., and Matthews, W. G. (1972). Astrophys. J. **171**, 593.
Neto, A. D., and Pacheco, J. A. de F. (1982). Mon. Not. R. Astron. Soc. **198**, 659.
Panagia, N. (1973). Astron. J. **78**, 929.
Smyth, M. J., Dean, J. F., and Robertson, B. S. C. (1979). Mon. Not. R. Astron. Soc. **187**, 29P.
The, P. S., *et al.* (1981). Astron. Astrophys. Suppl. **44**, 451.
Waters, L. B. F. M., Cote, J., and Aumann, H. H. (1987). Astron. Astrophys. **172**, 225 (WCA).

APPENDIX B. "The Classification of Stars from IRAS Colors"

THE CLASSIFICATION OF STARS FROM *IRAS*[a] COLORS

H. J. WALKER
NASA Ames Research Center, MS 245-6, Moffett Field, California 94035
and
SETI Institute, Los Altos, California 94022

M. COHEN
Jamieson Science and Engineering, Inc., P.O. Box F1, Felton, California 95018
and
Radio Astronomy Laboratory, University of California, Berkeley, California 94720
Received 25 November 1987; revised 26 February 1988

ABSTRACT

Three common types of stars were selected from the *IRAS Point Source Catalog*: *IRAS* sources associated with *The Bright Star Catalogue*: sources associated with the *General Catalogue* of *Variable Stars* and having a spectral type M (implying oxygen rich), and sources associated with Stephenson's carbon star catalog. Those stars that had reliable fluxes at 12, 25, and 60 μm were included in the [12] − [25], [25] − [60] diagram, regardless of any other characteristic, e.g., double, binary, shell star, known emission-line star. Similarly, color–color diagrams were made for samples of stars selected from the *IRAS* LRS Atlas, with featureless, O-rich, and C-rich spectra. From the total sample of 4493 stars, it was found that the three types tended to separate in the color–color diagrams, such that O-rich stars were redder in [12] − [25] than the other groups, and C-rich stars were redder in [25] − [60] than the other groups. "Occupation" zones containing around 70% of the stars in each group were defined. The [12] − [25] color of a star was found to be dominated more by its underlying continuum flux between 8 and 20 μm (as determined from LRS spectra) than by silicate or silicon carbide emission features. A group of stars, very red in [12] − [25] and classified as having silicon carbide emission in the *IRAS* LRS Atlas, was found in reality to have silicate emission with mild self-absorption. Of 4300 unassociated *IRAS* point sources with reliable fluxes at 12, 25, and 60 μm, almost 50% are late-type stars, judged from the color–color diagram.

I. INTRODUCTION

We address the problem of spectral classification using only the *IRAS* broadband fluxes. To understand more fully the content of the *IRAS Point Source Catalog*, in particular, to isolate any previously unknown classes of object for further study, we have investigated sources using solely their observed *IRAS* broadband fluxes. If the *IRAS* properties of known stars can be quantified, then previously unknown (and unassociated) *IRAS* sources might be classifiable. Hacking *et al.* (1985), using a sample of 267 stars, defined a zone in the *IRAS* color–color plane where normal stars should be found. They found that carbon-rich (C-rich) stars and oxygen-rich (O-rich) stars occupied separate regions, but their sample was too small to define zones. Zuckerman and Dyck (1986) remarked on the separation of their 136 C-rich and O-rich giant stars, and attributed this to a difference in grain emissivity. Thronson *et al.* (1987) used 619 C-rich stars and 6175 O-rich stars in their work on mass-losing stars, and defined a zone that contains "carbon-rich objects that are relatively unpolluted by oxygen stars". This C-rich zone was, however, completely contained by their defined O-rich zone, so classification from this large sample is not possible. Van der Veen and Habing (1988) defined ten zones in the color–color plane, and investigated the contributions of the different types of star to each zone.

[a] The *Infrared Astronomical Satellite* (*IRAS*) was developed and operated by the National Aeronautics and Space Administration (NASA), the Netherlands Agency for Aerospace Programs (NIVR), and the U.K. Science and Engineering Research Council (SERC).

II. DATA SELECTION

The *IRAS* color–color plane was selected as the diagnostic, and the *IRAS* magnitudes were used because normal stellar photospheres have all their colors close to zero. Three common types of stars were selected from the *IRAS Point Source Catalog*, 2nd ed. (PSC2), based on the associations given in the catalog itself. Those stars that had FQUAL = 3 (showing that the flux was reliable) for fluxes at 12, 25, and 60 μm were included in the [12] − [25], [25] − [60] diagram, regardless of any other characteristic or flag in any catalog; this ignored confusion, variability, and cirrus flags in PSC2. *The Bright Star Catalogue* (Hoffleit and Jaschek 1982) was used to define a set of normal stellar photospheres (referred to as the bright stars group throughout), although no attempt was made to remove from the dataset emission-line stars, binaries, etc., since these were presumed to be a small percentage of the total number. Those stars in the *General Catalogue of Variable Stars* (GCVS) by Kukarkin *et al.* (1970) with spectral type M (implying oxygen rich) were selected; no attempt was made to remove nonvariable stars or binaries from the dataset. Stephenson's carbon star catalog (1973) was used, since it contains those stars observed optically to have carbon enhancement, although it also includes groups such as the hydrogen-deficient R CrB stars. Having extracted the *IRAS* sources associated with these catalogs, they were plotted on the color–color diagram using *IRAS* magnitudes, [25] − [60] against [12] − [25], since in this scheme a normal star will by definition have colors near 0,0. The zero points for the system are taken from the *IRAS* Explanatory Supplement (1985) so that, using the flux densities in Janskys:

$$[12] = 3.63 - 2.5 \cdot \log_{10}(\text{flux}_{12}),$$

$$[25] = 2.07 - 2.5 \cdot \log_{10}(\text{flux}_{25}),$$

$$[60] = 0.19 - 2.5 \cdot \log_{10}(\text{flux}_{60}),$$

$$[100] = -0.92 - 2.5 \cdot \log_{10}(\text{flux}_{100}).$$

It was judged inappropriate to attempt color correction for such diverse groups of stars, potentially involving a wide range of infrared color temperatures. Conversions of the results from this scheme to those using flux ratios are given in an Appendix. (If magnitudes are required, color corrected for normal stellar photospheres, the constants in the above equations should be replaced by 4.03, 2.44, 0.49, and −0.82, from Cohen *et al.* 1987.) The sources selected using these three catalogs are called the optically selected sample in this paper, since catalogs compiled from optical data decided their presence in the sample.

To complement this sample, the stars with *IRAS* LRS spectra (from the *IRAS Atlas of Low-Resolution Spectra* 1986) assumed appropriate to each of the three groups were also extracted and their color–color diagrams created. The LRSCHAR assigned to an *IRAS* LRS spectrum has two parts: the first digit describes the main class of the spectrum, giving its type, the second digit gives the subclass within that type. To provide pairs of mutually exclusive samples, those stars with LRSCHAR = 1 (signifying a featureless spectrum) but not associated with the *Bright Star Catalogue* were selected; those with LRSCHAR = 2 (signifying silicate emission on a continuum declining towards the red) and not associated with the GCVS; also those with LRSCHAR = 4 (signifying silicon carbide emission) and not associated with Stephenson's catalog. In this paper, these sources are the LRS or infrared-selected sample, since presence or absence in any other catalog was not a criterion in the selection (apart from nonassociation with the one specified catalog in each case).

For completeness, the color–color diagrams were made for [25] − [60] against [60] − [100] for those stars with reliable fluxes in all four *IRAS* wavebands. The situation here was less well defined, since flux at 100 μm is not expected for most normal stars.

III RESULTS

When the three groups of optically selected stars are plotted on the [12] − [25], [25] − [60] diagram, a clear separation is seen. By selecting an occupation zone (OZ) to enclose about 70% of the stars in each group (bright, O-rich, C-rich), almost nonoverlapping occupation zones were created; see Fig. 1(d) and Table I. The objects outside the OZs were examined to see if there were reasons for their exclusion. For the bright stars ((Fig. 1(a)), a vertical column of Be and shell stars was discovered with [12] − [25] between about 0.6 and 1.0. There was another vertical column of double stars and spectroscopic binaries, with [12] − [25] around 0.0. Towards the right-hand side of the diagram, at high [12] − [25] and high [25] − [60], were several spectroscopic binaries, stars associated with reflection nebulae, and β Pic, known for its cool dust disk (see Backman *et al.* 1988). The O-rich stars (from the GCVS M star sample) showed a small concentration around 0,0 (see Fig. 1(b)), in addition to their main occupation zone, which reflected the fact that some of the stars (in the Notes section of the GCVS) were judged not to be variable, so it is likely that this whole subgroup has little variability or is constant. Four out of the five redder objects in [25] − [60] are T Tau stars with M spectral type, so they are not genuine members of the O-rich set. Harris *et al.* (1988), for example, give *IRAS* fluxes for 38 known T Tau stars, and these form a group around (2.3,2.1) in the color–color diagram. Two of the reddest objects in [12] − [25] in the C-rich stars' diagram (Fig. 1(c)) are confused in PSC2. For one star, there are two *IRAS* sources close to each other, the carbon star is associated with both sources, and an emission-line star is associated with the source used here. For the other source, there are two *IRAS* sources very close to each other. The third object with high [12] − [25] is V605 Aql, a slow nova. Several of the C-rich stars outside the occupation zone have variable star names, but for most of the stars the only information available is that from Stephenson's catalog. These comments imply that the membership of the defined occupation zones for the optically selected sample is probably much higher than the stated 70%, since the remaining 30% are heavily contaminated by different types of stars.

The procedure was repeated with the LRS-selected sample (see Fig. 2 and Table I), although here it is not possible to investigate the unusual objects outside the defined occupation zones (since they are mostly known only as infrared sources). The OZs appear to be placed in different positions from the optically selected sample, but their relative configuration remains the same, i.e., the O-rich stars are redder in [12] − [25] than the bright stars (or featureless LRS stars), and the C-rich stars are redder in [25] − [60] than the bright stars and O-rich stars. If the criterion of nonassociation with catalogs is dropped, bluer zones in [12] − [25] and [25] − [60] are occupied in the LRS sample, confirming, as expected, that the optical sample is bluer than the infrared-selected sample. The optical sample has, of necessity, a V magnitude associated with each star, and the dust shells must be thin, so [12] − [25] is smaller. The LRS-selected sample is not required to be optically visible and so most of them will have thicker (cooler) dust shells, hence redder [12] − [25].

In the [25] − [60],[60] − [100] diagram, the situation is more complicated, since very few normal stars have any flux at 100 μm. Any star with flux at 100 μm is likely to be intrinsically "odd" (e.g., with a very cool dust shell), or contaminated by cirrus. Figures 3 and 4 (and Table II) show the results for the optically selected sample and the LRS-selected sample. Again, the two samples have occupation zones in slightly different positions (showing that the optical groups are bluer), but the same main conclusions hold, that the O-rich and bright stars have similar colors, and that the C-rich stars are redder in [25] − [60] than the other groups. The [25] − [60] boundaries for the [12] − [25] and [60] − [100] diagrams are different due to the change in sample, but these are reconciled later (see Table IV).

To investigate the potential dependence of the [12] − [25] color on the LRS character, the mean normalized LRS spectra were defined for bins of 0.2 mag in [12] − [25]. The slope of the underlying continuum was measured, ignoring any spectral features. Table III shows, for all three types of spectrum (featureless, O-rich, and C-rich), that the spectral slope gradually flattens as [12] − [25] increases, getting closer to 0.0 than the value of −4.0 expected from the Rayleigh–Jeans tail of the photospheric energy distribution. Not even the strongest observed 10 μm feature affects the [12] − [25] color sufficiently to change the relationship between color and slope, so that

TABLE I. [12] − [25] and [25] − [60] occupation zones defined for groups of stars

	[12] − [25]			[25] − [60]			Number of stars in zone	Number of stars total
Bright Stars	−0.1	→	0.3	−0.3	→	0.3	462	682
O-rich stars	0.3	→	1.1	−0.3	→	0.3	501	711
C-rich stars	0.1	→	0.7	0.1	→	0.9	230	369
LRSCHAR=1	−0.1	→	1.1	−0.3	→	0.3	1006	1395
LRSCHAR=2	0.7	→	1.5	−0.5	→	0.3	753	1005
LRSCHAR=4	0.3	→	1.5	−0.1	→	0.5	252	331
LRSCHAR=3	1.5	→	2.5	0.3	→	1.5	90	155

neither the silicate feature nor the silicon carbide feature dominates the [12] − [25] color. The features do, however, cause serious problems in deriving an accurate value for the slope, so that emission and absorption features must be identified before the continuum slope is measured.

IV. DISCUSSION

The zone given in Table I for the bright stars agrees well with that found by Hacking *et al.* (1985) using a total sample of only 267 stars, although our sample is larger (462 stars in the occupation zone alone). Hacking *et al.* exclude from their sample stars with galactic latitude less than 30°, and sources fainter than 28 Jy at 12 μm ([12] > 0). They find O-rich stars and C-rich stars in the positions of the occupation zones given here, but their sample is too small to define the zones with confidence. We notice, like Hacking *et al.*, a gap between the bright stars and the O-rich stars: this has not been filled in by our larger sample of data. Zuckerman and Dyck (1986) remark on the separation of their samples of 136 C-rich and O-rich stars in the color–color diagrams. They suggest that O-rich and C-rich stars have the same [12] − [25] and [60] − [100] colors, but our work shows that O-rich stars can be found at redder [12] − [25] than C-rich stars. They attribute the separation in [25] − [60] color to a difference in grain emissivity index for C-rich and O-rich stars. The dust-grain emissivity index, according to Zuckerman and Dyck, is 1.1 for C-rich stars and 1.6 for O-rich stars between 25 and 60 μm, and around 1.0 elsewhere for both groups. The C-rich zone defined by Thronson *et al.* (1987) includes some of the C-rich zone defined here, but the zone here is twice as large in [12] − [25] and half as large in [25] − [60]. Thronson *et al.* drew their C-rich zone by eye using a small subset of O-rich stars to avoid overlap, which accounts for the discrepancy. Thronson *et al.* suggested that the difference in position of their C-rich zone when compared to that of Zuckerman and Dyck was caused by their sample being "visually selected stars"; however, our sample is similarly visually selected and agrees more closely with Zuckerman and Dyck. Van der Veen and Habing (1988) show an evolutionary track (in the color–color plane) for a late O-rich star losing mass. The track proceeds initially at a slight angle to the line of constant [25] − [60], and this is probably the cause of the slope in the LRSCHAR = 2 sample (Fig. 2(b)). Hacking *et al.* (1985) noted that the amplitude of variability decreases with increasing wavelength, so that this might also cause the observed slope. The stars in the LRSCHAR = 2 sample were split into two groups with the variability flag VAR (see Explanatory Supplement for details) greater than or less than 0.50, and since both groups showed the same slope, source variability is not the likely cause.

The major problem with the LRS sample was found to be, surprisingly, that the groups were not "pure", i.e., they were contaminated by objects that had the wrong LRS classification. This problem was particularly conspicuous in the LRSCHAR = 1 set, where the redder (in [12] − [25]) spectra had noticeable ripples in the spectrum, showing that silicate emission features (or other absorption features) were present. All the optically selected C-rich stars were examined in detail, since the group was reasonably small (369 stars). If the stars are bright enough to have LRS spectra, they should be classified as either LRSCHAR = 4 (silicon carbide emission) or as LRSCHAR = 1 (featureless), since, for example, the R CrB stars, associated with graphite dust (Walker 1986), have featureless LRS spectra. Willems and de Jong (1988) have produced a list of nine objects which are C-rich with O-rich LRS spectra. Stephenson's catalog lists six of these and they are included in our sample. One of the stars (EU And = CS 3184) has too low a 12 μm flux to be included, but for the five other stars we agree with Willems and de Jong that the LRS spectra of the stars correctly have LRSCHAR = 2. We examined by eye the LRS spectra of 201 C-rich stars in Stephenson's catalog. Of those stars with visible silicon carbide emission, 22% were not classified as LRSCHAR = 4, as expected; most were misclassified as LRSCHAR = 1 (featureless), some were in the LRSCHAR = 2 set, and some in the LRSCHAR = 0 set.

When the reddest (in [12] − [25]) LRSCHAR = 4 set of LRS spectra were studied, it was realized that they did not exhibit silicon carbide emission! The peak around 10 μm (see Fig. 5) was a mildly self-absorbed silicate emission peak, the red wing of which coincided with the expected wavelength of the silicon carbide peak, hence the classification. However, the 18 μm broad emission peak is also visible. From an eyeball inspection of the entire LRSCHAR = 4 dataset, we determined that the effect of the silicate self-absorption commences at [12] − [25] = 1.5, and by [12] − [25] = 1.9 it is the dominant feature in the LRSCHAR = 4 spectra. This red subset acts as a bridge between the LRSCHAR = 2 (silicate emission set) and the LRSCHAR = 3 (the silicate absorption group) 70% occupation zones shown in Fig. 2(d), and the overlap of the OZs is therefore not surprising.

As noted above, none of the infrared-selected samples were "pure," so that the mean LRS spectra for all six sets of stars were examined to see where the OZs merged with each other in [12] − [25]. In the LRSCHAR = 4 set, silicon carbide emission is replaced by mild silicate self-absorption around [12] − [25] = 1.5 to 1.9. In the LRSCHAR = 1 set, spectra showed the presence of weak silicate emission beyond [12] − [25] = 0.3, noted as "ripples" in the spectra. As a consequence, a set of OZs for bright, O-rich and C-rich stars was found, using both the optical and the infrared-selected OZs, shown in Table IV (and shown in Fig. 6(b)). The O-rich sample probably extends to redder values in [12] − [25] than shown by the OZ, since *IRAS* will detect stars not visible in the optical; Fig. 2(b) suggests 2.1 may be the limit in [12] − [25]. Table IV also shows the result of combining the OZ boundaries for the optical and infrared-selected samples in [25] − [60] and [60] − [100]. The zones show the places where these three different types of common star may, most likely, be found, but Figs. 1 and 2

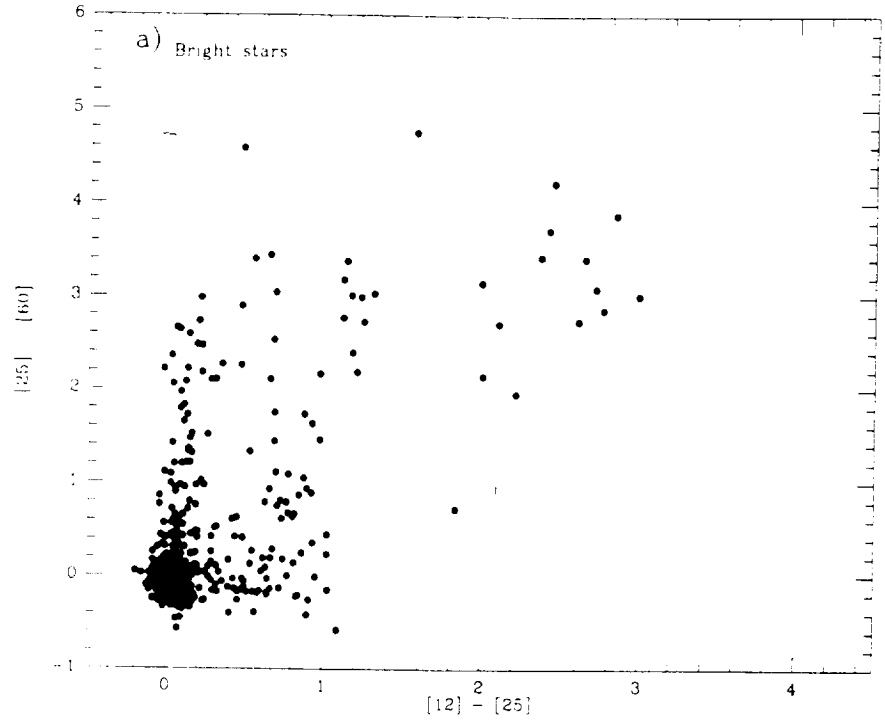

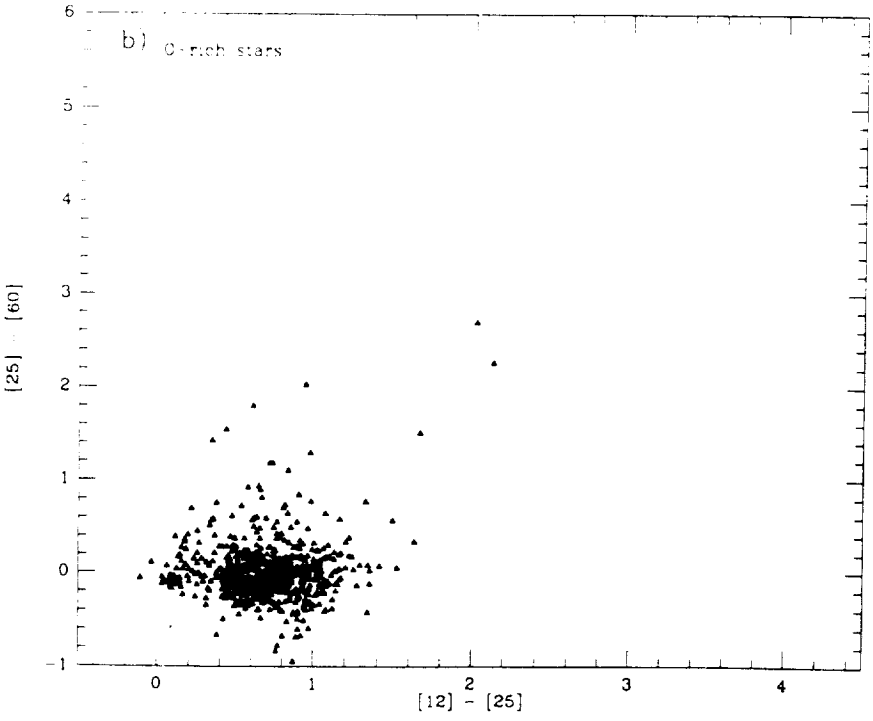

FIG. 1. [25] – [60] plotted against [12] – [25] for (a) bright stars, (b) O-rich stars, (c) C-rich stars, (d) the occupation zones and the blackbody line.

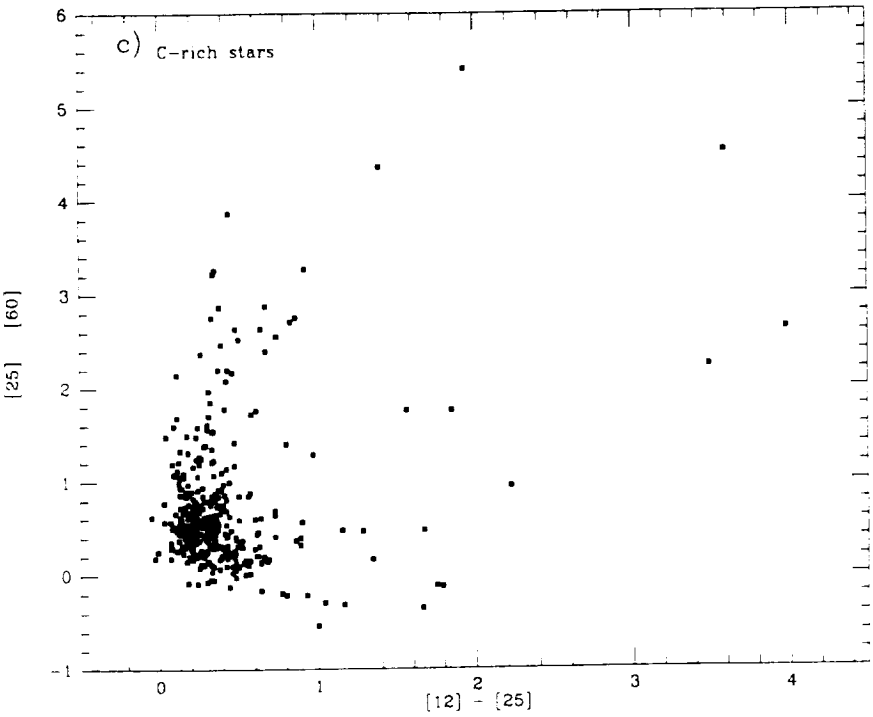

FIG. 1 (continued)

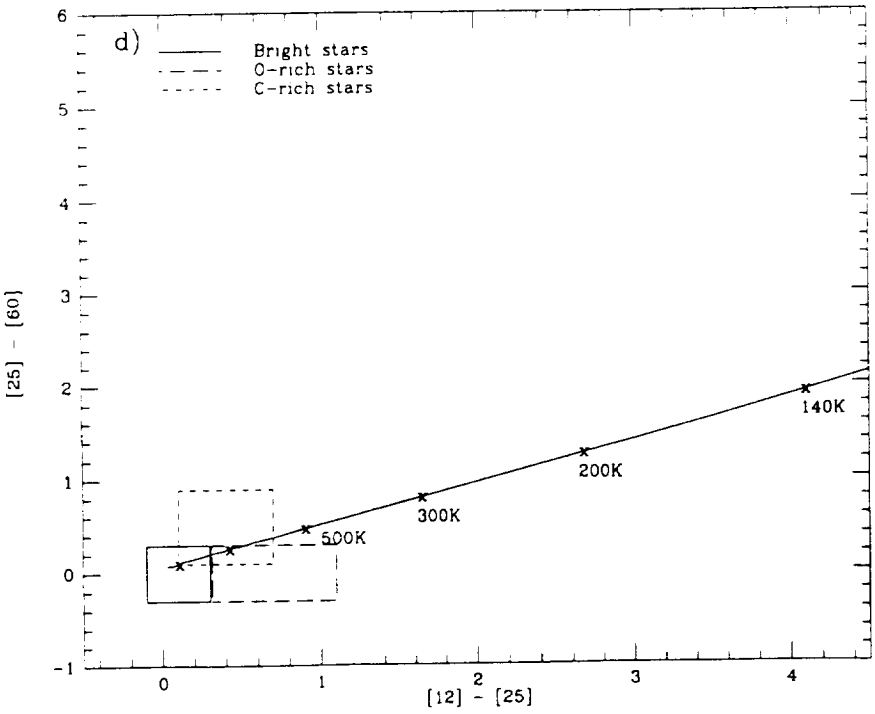

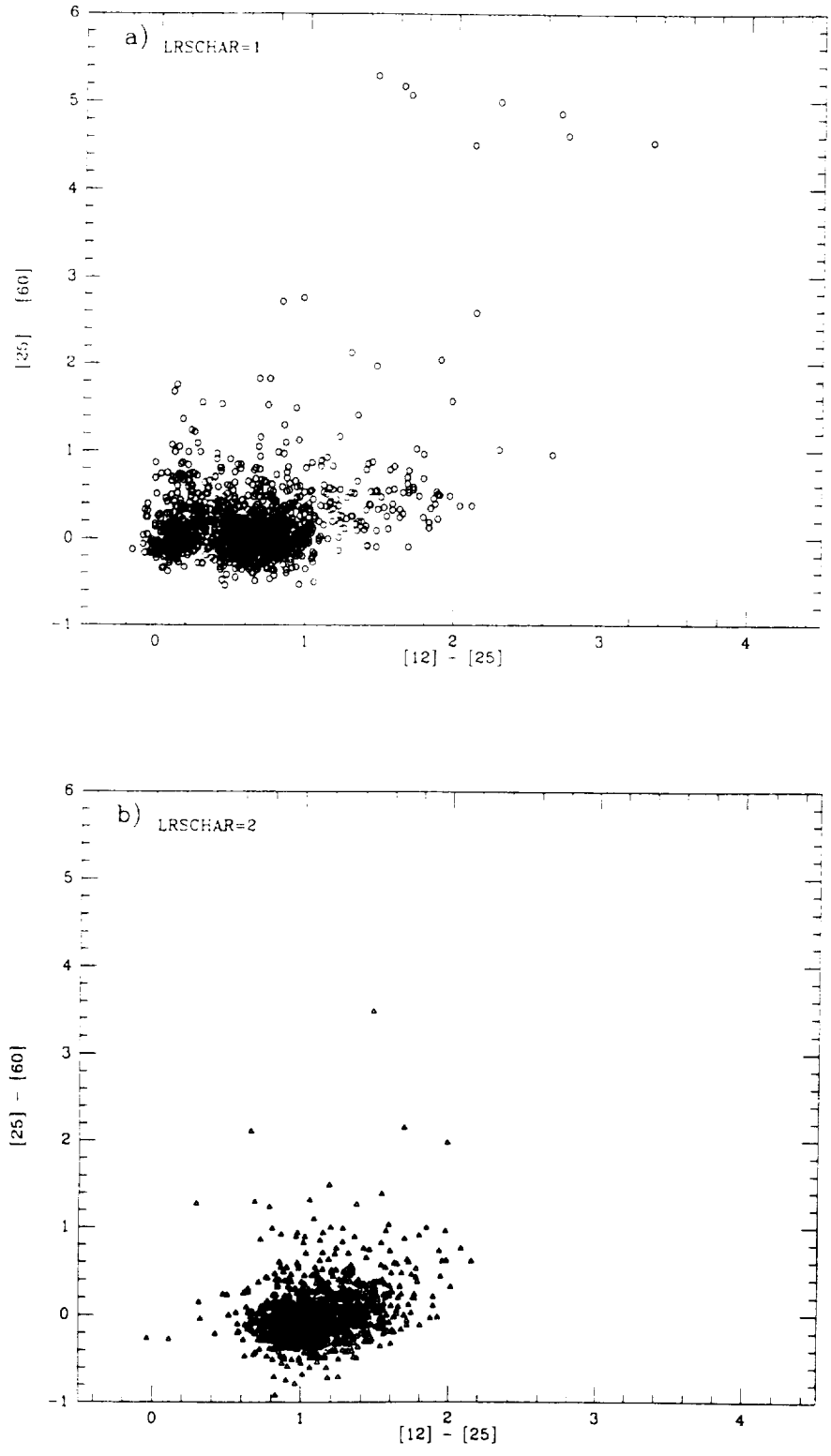

FIG. 2. [25] − [60] plotted against [12] − [25] for (a) featureless spectra (LRSCHAR = 1), (b) O-rich spectra (LRSCHAR = 2), (c) C-rich spectra (LRSCHAR = 4), (d) the occupation zones, including stars with a 10 μm silicate absorption feature (LRSCHAR = 3).

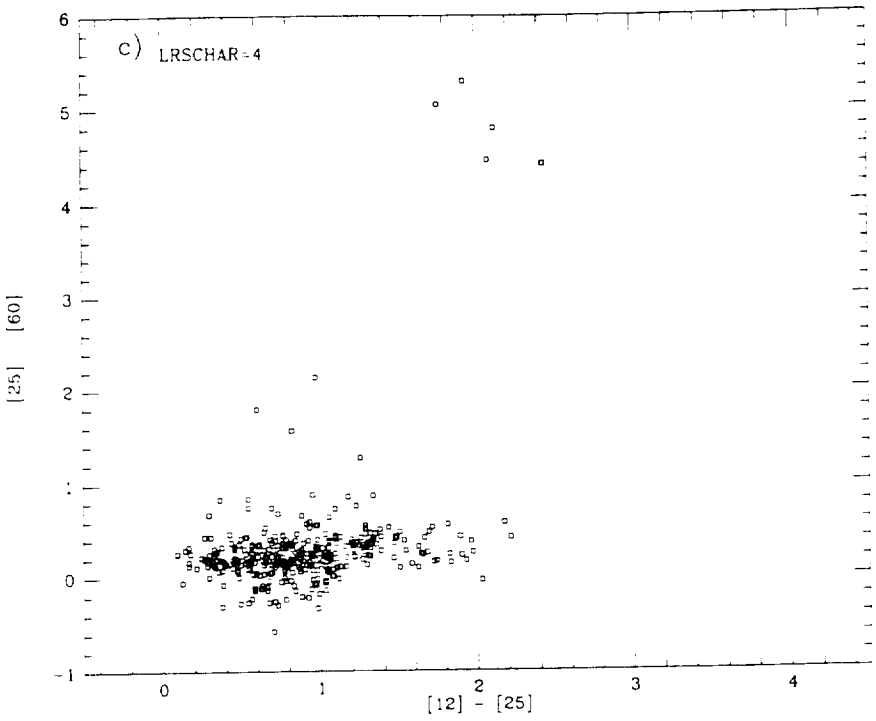

FIG. 2. (continued)

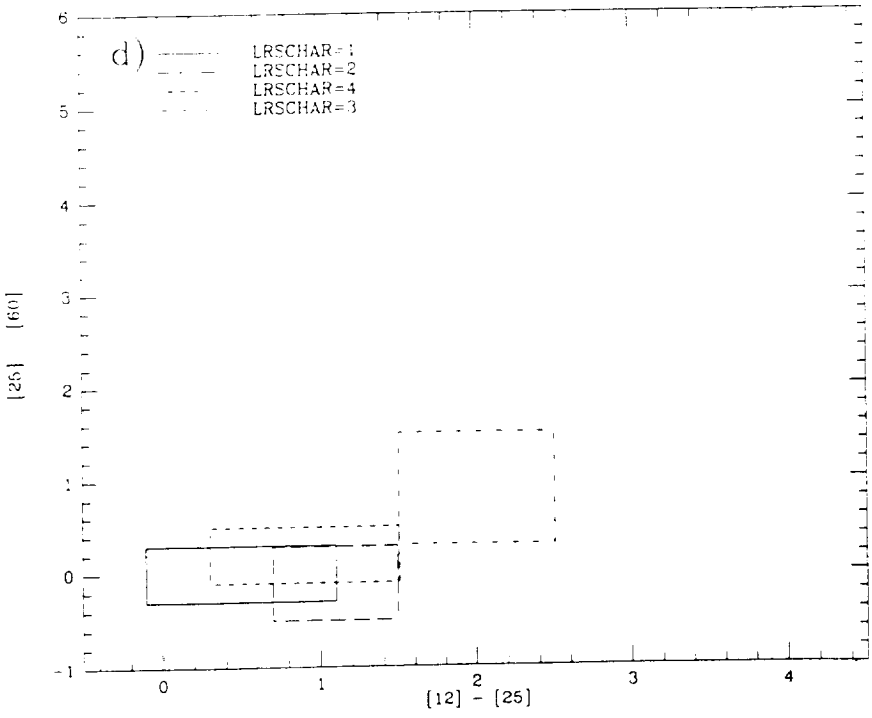

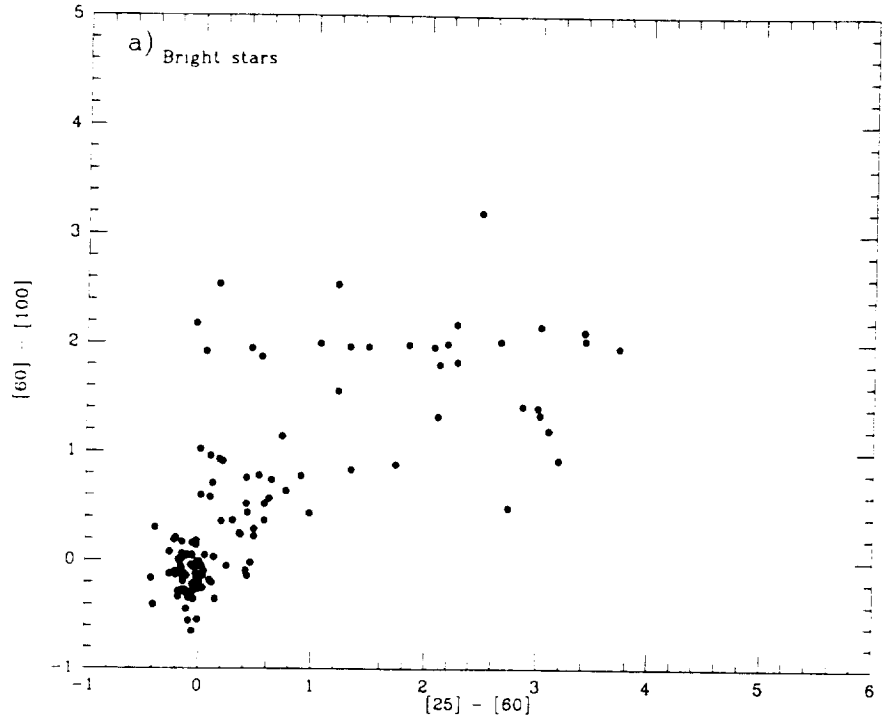

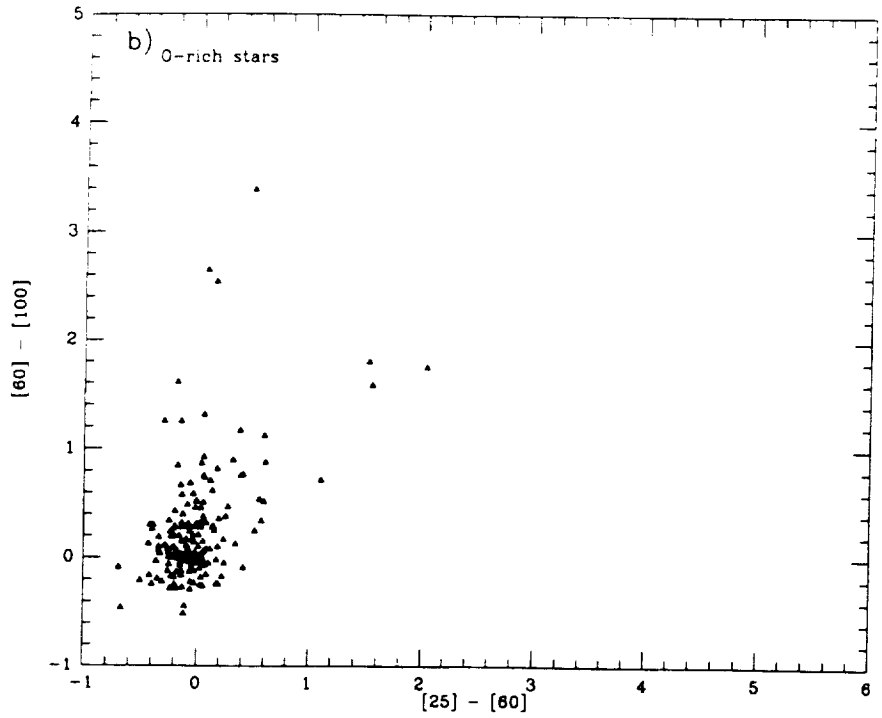

FIG. 3. [60] – [100] plotted against [25] – [60] for (a) bright stars, (b) O-rich stars, (c) C-rich stars, (d) the occupation zones and the blackbody line.

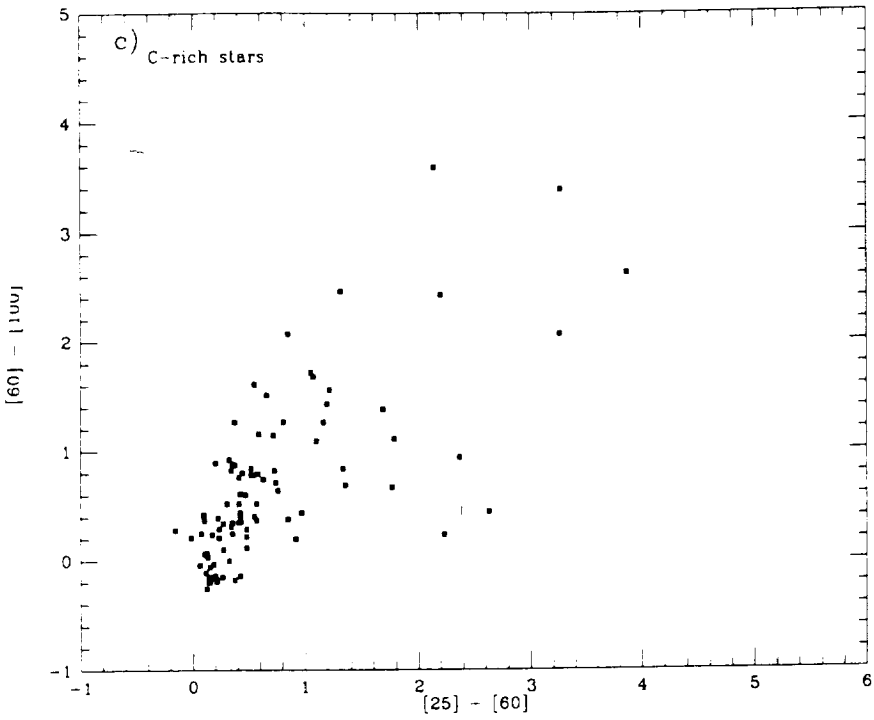

FIG. 3. (continued)

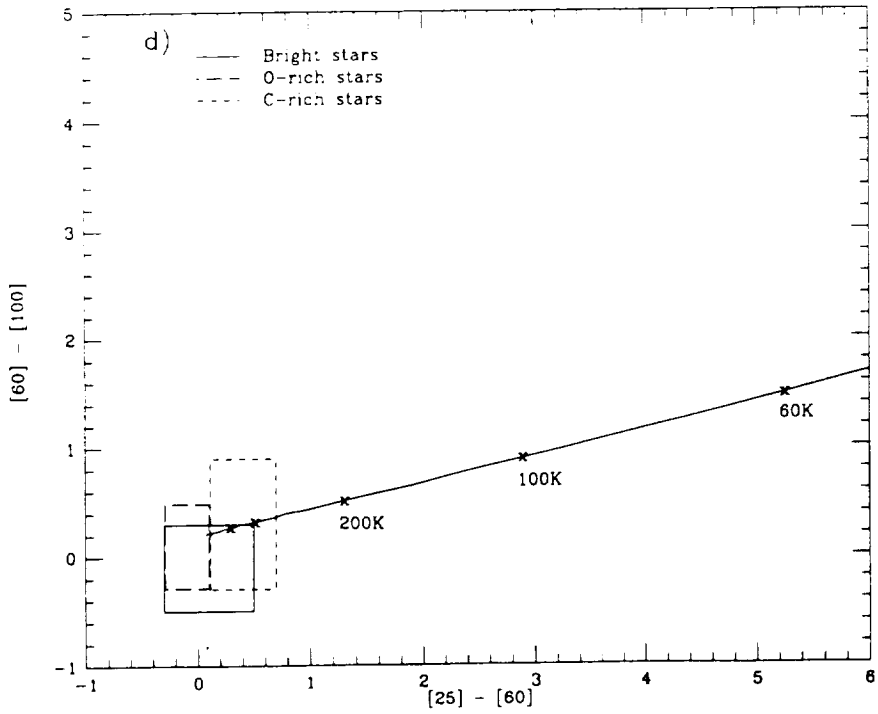

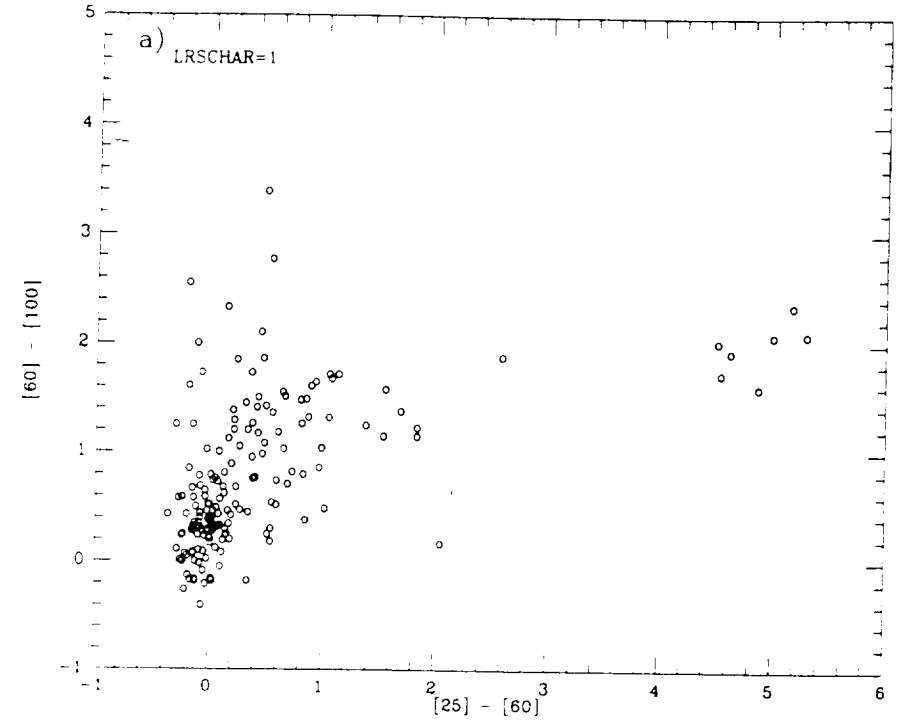

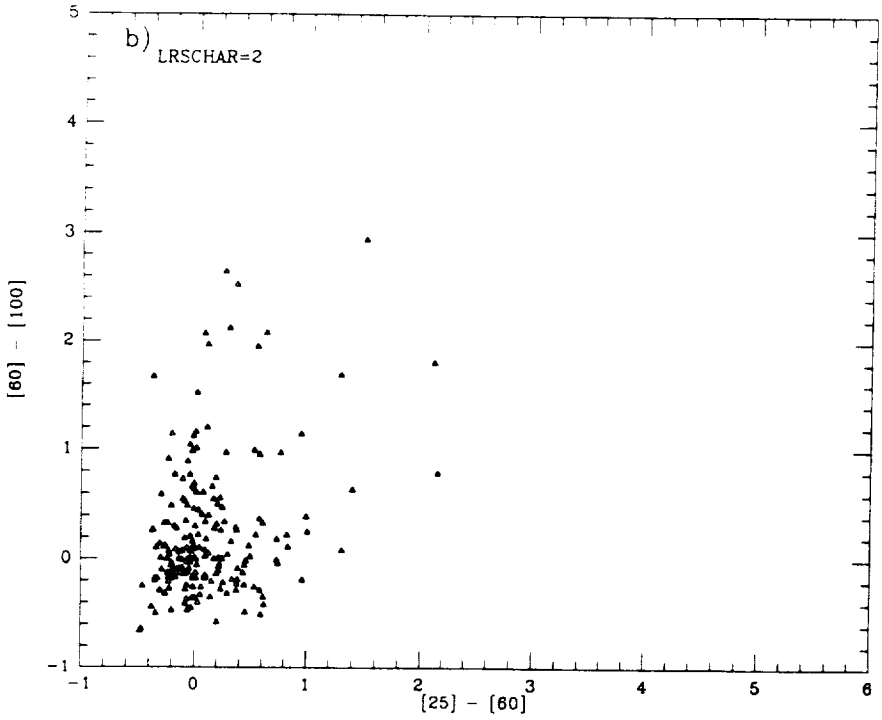

FIG. 4. [60] - [100] plotted against [25] - [60] for (a) featureless spectra (LRSCHAR = 1), (b) O-rich spectra (LRSCHAR = 2), (c) C-rich spectra (LRSCHAR = 4), (d) the occupation zones, including stars with a 10 μm silicate absorption feature (LRSCHAR = 3).

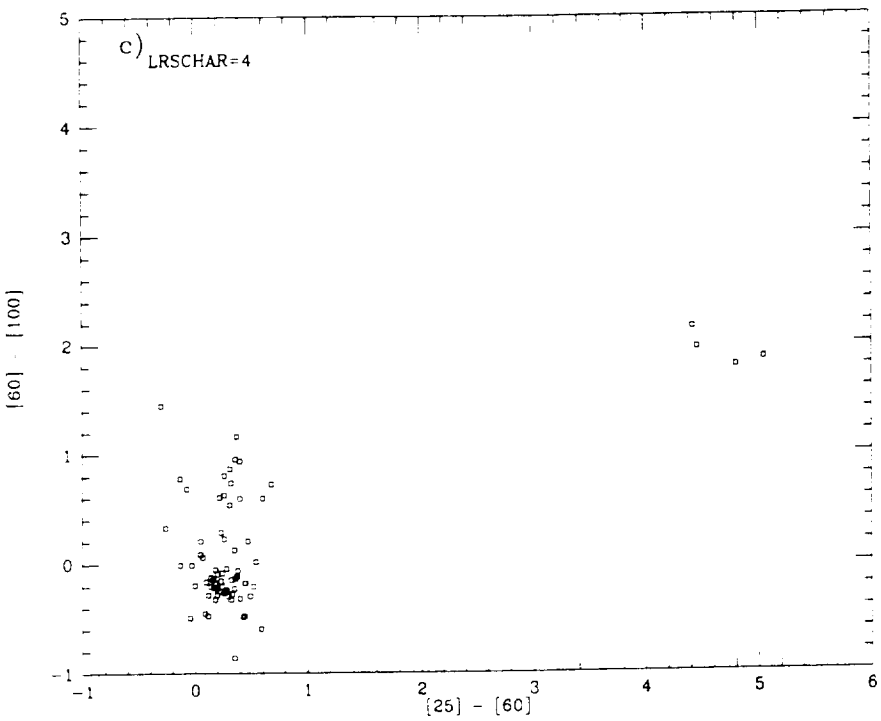

FIG. 4 (continued)

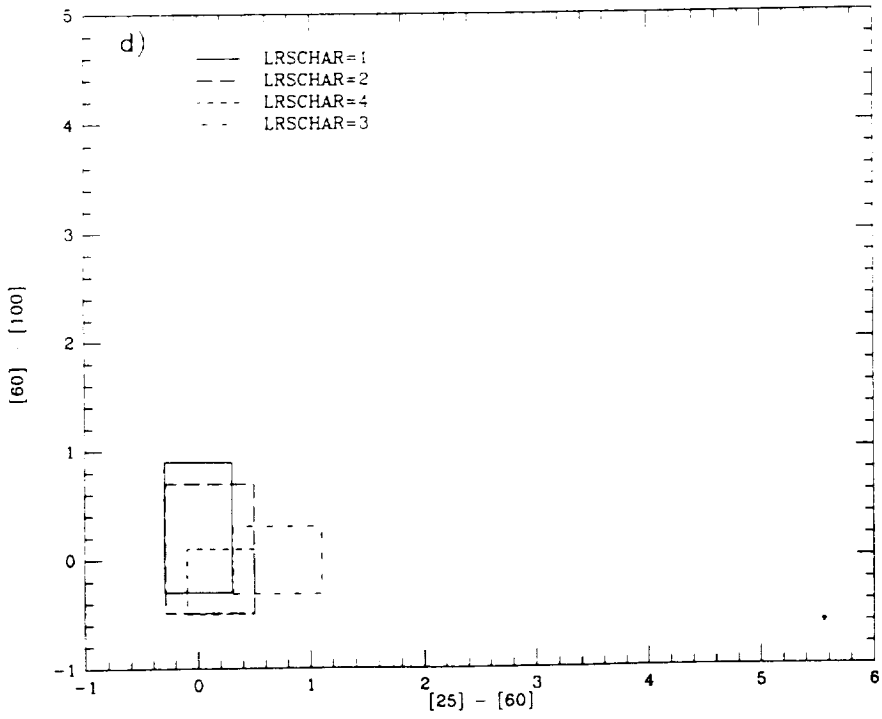

TABLE II. [25] − [60] and [60] − [100] occupation zones defined for groups of stars.

	[25] - [60]			[60] - [100]			Number of stars in zone	Number of stars total
Bright Stars	−0.3	→	0.5	−0.5	→	0.3	68	126
O-rich stars	−0.3	→	0.1	−0.3	→	0.5	113	185
C-rich stars	0.1	→	0.7	−0.3	→	0.9	50	91
LRSCHAR=1	−0.3	→	0.3	−0.3	→	0.9	93	172
LRSCHAR=2	−0.3	→	0.5	−0.5	→	0.7	118	199
LRSCHAR=4	−0.1	→	0.5	−0.5	→	0.1	41	71
LRSCHAR=3	0.3	→	1.1	−0.3	→	0.3	17	38

show that stars were found outside the specified zones. They also show that any star found in the bright-star zone will be a normal star with no dust shell, and the gap in Figs. 1(b) and 2(a) suggests that there is little contamination from other groups in this zone. For sources falling in the O-rich zone, or even to the red in [12] − [25], there is considerable confidence of correct classification (only 10% of the sources in this zone were not expected to be there). Figures 1 and 2 imply that there is overlap between the O-rich zone and the C-rich zone. Figure 6(b) shows that from 0.1 to 0.3 in [25] − [60] there is no separation between O-rich and C-rich stars, but since there are three times as many O-rich stars in the overlap zone as there are C-rich stars, it is more likely that an *IRAS* source found there will be O-rich. As can be seen from Figs. 1 and 2, there are a lot of O-rich stars in the C-rich zone; this effect may be magnified by the disparate sample sizes.

Figure 6(a) shows the color–color diagram of the special subset of 4300 sources in the *IRAS Point Source Catalog* which have good quality fluxes at 12, 25, and 60 μm, no association with other catalogs (see *IRAS* Explanatory Supplement for list) and no LRS Atlas spectrum. Adding the LRSCHAR = 3 zone to the three zones defined here (shown in Fig. 6(b)), and extending the O-rich box to [12] − [25] = 2.1, gives 44% of the unassociated sources in these zones. If the C-rich OZ is extended in [25] − [60] to 1.5, the number of unassociated stars included rises to 47%. The color–color zone of Harris *et al.* (1988), confirmed by data from Cohen *et al.* (1988), for the T Tau stars is also shown in Fig. 6(b). From a study of around 900 sources in the *IRAS Point Source Catalog* with galaxy associations, galaxies mostly have a color of around 2.0 in [12] − [25] and around 4.0 in [25] − [60] (K. M. Volk, private communication). Around 20% of the unassociated sources may be galaxies (or H II regions, since they occupy the same general area of the color–color diagram). Comparison with the zones in Fig. 6(b) shows that there are no large populations of previously unknown types of sources seen by *IRAS* (with reliable fluxes at 12, 25, and 60 μm); 71% of the unassociated sources are now accounted for. Of 766 unassociated sources with reliable fluxes in all four bands, only nine fall in the bright stars/O-rich stars and C-rich stars zones in the [25] − [60], [60] − [100] diagram; 64% fall in the region where galaxies and H II regions are expected. We are in the process of following up sources from the three zones to see if their predicted properties can be confirmed by optical spectroscopy.

IV. CONCLUSIONS

The three major types of stars (bright, O-rich, and C-rich) have a tendency to separate in the *IRAS* color–color diagram, such that almost nonoverlapping zones can be defined for the groups with around 70% of the stars included.

O-rich stars tend to be redder in [12] − [25] than bright stars, and C-rich stars tend to be redder in [25] − [60] than bright and O-rich stars.

The flattening of the underlying continuum slope is the dominant cause of the change in [12] − [25], rather than emission or absorption-feature strengths.

The very reddest in [12] − [25] LRSCHAR = 4 stars are mild silicate self-absorption sources, i.e., O-rich rather than C-rich.

TABLE III. Continuum slopes of mean LRS spectra for [12] − [25] color bins.

Color bin			Bright stars	LRSCHAR =1	O-rich stars	LRSCHAR =2	C-rich stars	LRSCHAR =4
−0.3	→	−0.1	−4.29	−4.06				
−0.1	→	0.1	−4.15	−4.10	−3.94	−4.12	−3.88	
0.1	→	0.3	−3.94	−3.96	−3.88	−3.77	−3.73	−3.63
0.3	→	0.5	−3.27	−3.44	−3.33	−3.62	−3.58	−3.48
0.5	→	0.7	−3.06	−3.38	−3.00	−2.65	−3.27	−3.23
0.7	→	0.9	−2.77	−2.79	−2.73	−2.54	−3.06	−2.92
0.9	→	1.1	−2.67	−2.50	−2.42	−2.13	−2.17	−2.87
1.1	→	1.3		−2.40	−2.10	−1.98		−2.58
1.3	→	1.5		−2.19	−1.58	−1.69		−2.40
1.5	→	1.7		−1.75	−1.33	−1.50	−1.38	−1.63
1.7	→	1.9		−1.67		−1.56		−1.42
1.9	→	2.1		−2.02		−1.77		−1.31
2.1	→	2.3		−1.36		−0.96		−1.19
2.3	→	2.5						
2.5	→	2.7		−0.79				
2.7	→	2.9		−1.08				

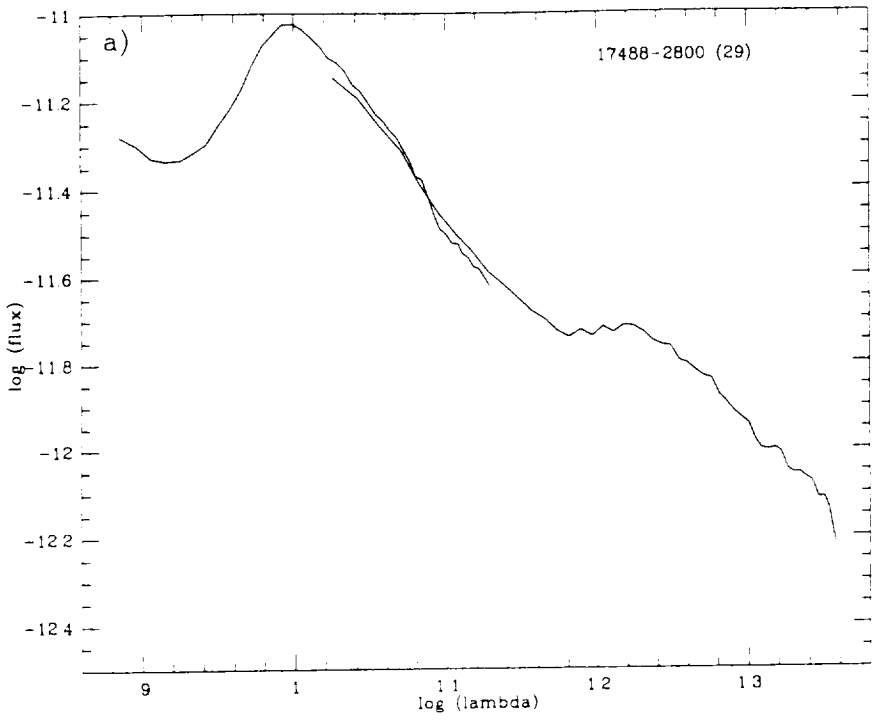

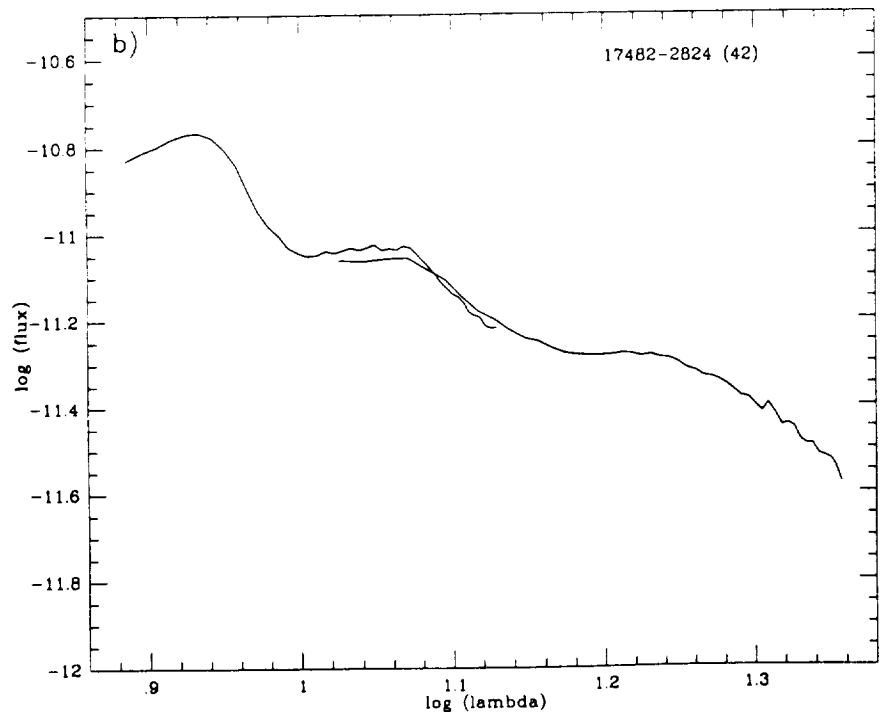

FIG. 5. Examples of LRS spectra for (a) O-rich star (silicate emission), (b) mild self-absorbed silicate star, (c) C-rich star (silicon carbide emission). The ordinate is log $F\lambda$ with flux in W m^{-2} μm^{-1}.

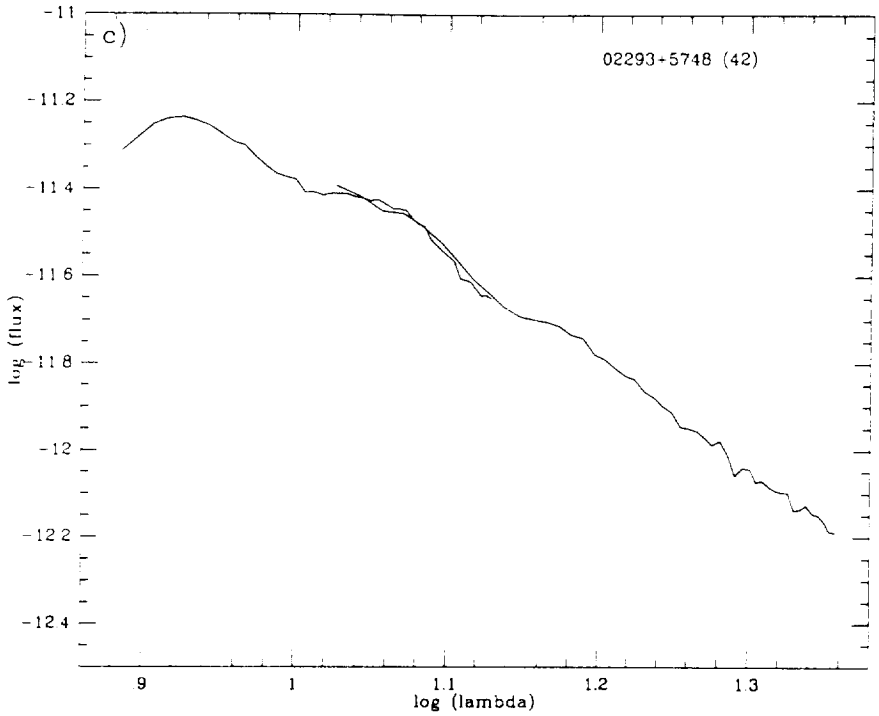

FIG. 5. (continued)

TABLE IV. Combined occupation zones for bright, O-rich and C-rich stars.

	[12] - [25]			[25] - [60]			[60] - [100]		
Bright stars	−0.3	→	0.3	−0.3	→	0.3	−0.5	→	0.5
O-rich stars	0.3	→	1.5	−0.3	→	0.3	−0.5	→	0.5
C-rich stars	0.1	→	1.3	0.1	→	0.9	−0.5	→	0.5

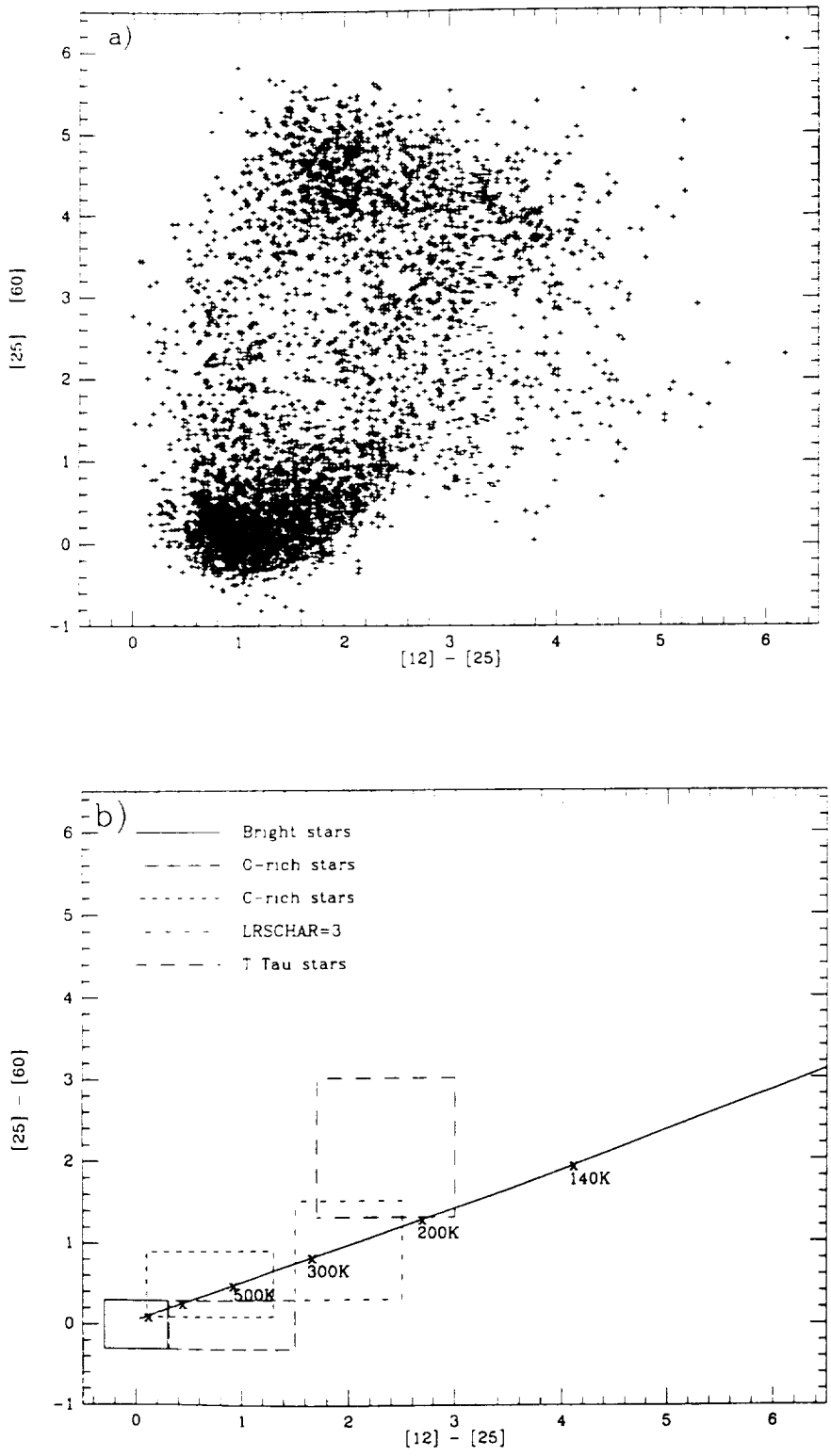

FIG. 6. (a) [12] – [25], [25] – [60] diagram for the 4300 unassociated *IRAS* point sources. (b) the occupation zones as defined from the combined optical and infrared samples, the zone from the LRSCHAR = 3 sample, the T Tau zone from Harris *et al.*, and the blackbody line.

The *IRAS* color–color diagrams can be used to classify *IRAS* stars, and thus indicate the probable nature of unknown *IRAS* sources. Of 4300 unknown, unassociated *IRAS* sources, almost 50% are in or near these zones.

H.J.W. thanks the NASA–Ames Research Center, which provides support for *IRAS* studies through the SETI Institute under cooperative agreement NCC 2-407. This study at Jamieson Science and Engineering, Inc., was supported in part by contract no. NAS 2-12515 with NASA–Ames Research Center. We are grateful to G. Villere for programming support. We thank an anonymous referee for a very careful reading of the paper, and for suggesting a number of improvements.

APPENDIX: THE *IRAS* COLOR ZONES IN FLUX-RATIO TERMS

Flux densities in Janskys:

$$[21] - [25] = 1.56 - 2.5 \times \log (F_{12}/R_{25}),$$
$$[25] - [60] = 1.88 - 2.5 \times \log (F_{25}/F_{60}),$$
$$[60] - [100] = 1.11 - 2.5 \times \log (F_{60}/F_{100}),$$

$$[12] - [25] = 2.36 + 2.5 \times \log (12F_{25}/25\,F_{12}),$$
$$[25] - [60] = 2.83 + 2.5 \times \log (25F_{60}/60\,F_{25}),$$
$$[60] - [100] = 1.66 + 2.5 \times \log [60F_{100}/100\,F_{60}).$$

REFERENCES

Backman, D., Gillett, F., and Witteborn, F. (1988). Preprint
Beichman, C. A., Neugebauer, G., Habing, H. J., Clegg, P. E., and Chester, T. J., editors (1985). *IRAS Catalogs and Atlases, Explanatory Supplement* (U.S. GPO, Washington, DC).
Cohen, M., Emerson, J., and Beichman, C. (1988). Preprint.
Cohen, M., Schwartz, D. E., Chokshi A., and Walker, R. G. (1987). Astron. J. **63**, 1199.
Hacking, P., Neugebauer, G., Emerson, J., Beichman, C., Chester, T., Gillett, F., Habing, H., Helou, G., Houck, J., Olnon, F., Rowan-Robinson, M., Soifer, B. T., and Walker, D. (1986). Publ. Astron. Soc. Pac. **97**, 616.
Harris, S., Clegg, P. E., and Hughes, J. (1988). Preprint.
Hoffleit, D., and Jaschek, C. (1982). *The Bright Star Catalogue*, 4th revised ed. (Yale University Observatory, New Haven).
Joint *IRAS* Science Working Group (1985). *The Point Source Catalog* (U.S. GPO, Washington, DC).
Joint *IRAS* Science Working Group (1986). *IRAS Catalogs and Atlases, Atlas of Low-Resolution Spectra*. Astron. Astrophys. Suppl. **65**, 607 (LRS Catalog).
Kukarkin, B. V., *et al.* (1970). *The General Catalogue of Variable Stars* (Nauka, Moscow).
Stephenson, C. B. (1973). Publ. Warner and Swasey Obs. **1**, No. 4.
Thronson, H. A., Latter, W. B., Black, J. H., Bally, J., and Hacking, P. (1987). Astrophys. J. **322**, 770.
van der Veen, W. E. C. J., and Habing, H. J. (1988). Preprint.
Walker, H. J. (1986). *Hydrogen Deficient Stars and Related Objects*, IAU Colloquium No. 87, edited by K. Hunger, D. Schönberner, and N. K. Rao (Reidel, Dordrecht), p. 407.
Willems, F., and de Jong, T. (1988). Preprint.
Zuckerman, B., and Dyck, H. M. (1986). Astrophys. J. **311**, 345.

APPENDIX C. "IRAS Colors of Carbon Stars: an Optical Spectroscopic Test"

IRAS[1] COLORS OF CARBON STARS: AN OPTICAL SPECTROSCOPIC TEST

MARTIN COHEN

Jamieson Science and Engineering, Inc., and Radio Astronomy Laboratory,

University of California, Berkeley

RICHARD J. WAINSCOAT, HELEN J. WALKER

KEVIN VOLK AND DEBORAH E. SCHWARTZ

NASA Ames Research Center and SETI Institute

[1]The *Infrared Astronomical Satellite* was developed and operated by the U.S. National Aeronautics and Space Administration (NASA), the Netherlands Agency for Aerospace Programs (NIVR), and the U.K. Science and Engineering Research Council (SERC).

ABSTRACT

We have taken optical spectra of 57 photographic counterparts to IRAS sources not previously studied spectroscopically and expected on the basis of their IRAS colors to be M- or C-type stars. Confirmed carbon stars are found only in a restricted range of [12]−[25] index and constitute a striking "vertical" sequence in the 12–25–60 μm color-color diagram. This sequence is in accord with evolutionary models for AGB stars that convert M into C stars by dredge-up, and follow loops in the color-color plane. Optically visible and optically invisible carbon stars occupy different color-color locations consistent with their representations of different evolutionary states in the life of relatively low mass stars.

Subject Headings: stars: carbon — infrared: colors — giants: late-type

I. INTRODUCTION

As part of an ongoing effort to produce an infrared point source sky model we are concerned with the ability to characterize sources solely on the basis of their broadband IRAS colors. In a previous paper (Walker and Cohen 1988) we described our analysis of the IRAS color-color planes in terms of the observed colors of known categories of star. We presented several "occupation zones" such that objects whose colors located them within one of these zones could probably be assigned to a specific category of star. These zones were defined for "normal" stars, oxygen- and carbon-rich giants, and highly-evolved giants suffering significant 10 μm silicate self-absorption.

We emphasized that there can be considerable confusion between oxygen-rich and carbon-rich cool stars if one follows the IRAS Low Resolution Spectrometer (LRS Atlas, IRAS Science Team 1986: hereafter LRS) classification, and that a re-examination of the actual LRS spectra can resolve the difference between a true silicon carbide emission feature and a mildly self-absorbed silicate emission feature. However, M stars can be found even in our restricted occupation zone for carbon stars. The issue of contamination of the regions of the color-color plane where C and M stars lie has also been addressed by Thronson *et al.* (1987, 1988). As a direct test of the degree of this overlap, and in a continuing effort to validate our color-based stellar classification scheme, we have obtained optical spectra of several sets of unassociated IRAS sources with probable optical counterparts, chosen solely on the basis of IRAS broadband colors.

In this paper we discuss the IRAS colors of those stars actually found to be carbon stars from this blind spectroscopic survey of 57 unassociated sources that our color scheme alone would suggest should be late-type stars of type M or C. We report that optically verifiable carbon stars occur only in a narrow slice of [12]$-$[25] color that represents a small fraction of the total range in color index for the

entire carbon star occupation zone. These stars constitute a "vertical sequence" in the ([12]−[25], [25]−[60]) plane, consonant with the distribution of optically known carbon stars (e.g., those from Stephenson's (1973) catalog: cf. Thronson *et al.* 1987). Such a vertical sequence is in accord with an evolutionary scheme in which AGB stars may evolve from type M into type C through the dredge-up of interior material after a thermal pulse; they subsequently follow mass-dependent loops in this color-color plane, approaching zero colors along a steep path, after which mass loss resumes (Willems 1987; van der Veen and Habing 1988; Chan and Kwok 1988). The remainder of the carbon star occupation zone is populated by optically invisible, infrared-bright carbon stars with optically thick circumstellar dust envelopes.

II. SELECTION OF CANDIDATE STARS

Our basic sample of IRAS sources for study was the set of the approximately 4300 unassociated sources (Walker and Cohen 1988), well-detected (FQUAL=3) by IRAS at 12, 25, and 60 μm, that lay within our occupation zones for C and M stars. To keep the demands of source identification manageable, we randomly selected about 15 objects from each of several subsets of sources constrained by [12]−[25] color index as detailed in Table 1. Of these, we restricted our spectra to 46 objects that have plausible optical counterparts either on the NGS-Palomar Observatory Sky Survey or ESO/SERC Southern Sky Survey photographs. A further group of objects was examined because of their colors and probable assignment to M or C star categories on the basis of their IRAS spectral character from the LRS Atlas. Of these, 11 had potential optical counterparts and were studied spectroscopically.

Briefly, our subsets and group labels were as follows. For unassociated objects without LRS Atlas spectra we had: M1, relatively blue O-rich stars; M2, red O-rich; M3, O-rich, unusually red in either [12]−[25] or [25]−[60]; ML, red O-rich, with colors of sources having LRS spectra of type 21–29; C1, C-rich stars; C2, C-

rich, unusually red in [25]−[60]; CL, probable C-rich stars, with colors of sources having LRS spectra of type 41–49. In addition, we defined 2 groups of sources with LRS Atlas spectra: L2, LRS type 24–29 (O-rich sources with silicate emission); and L4, LRS type 43–44 (C-rich sources with silicon carbide emission).

III. THE OBSERVATIONS

For 25 northern sources we took spectra with the Lick Observatory 1 m Nickel telescope using a 500 × 500 TI CCD chip as detector in a Cassegrain spectrograph. Spectra covered the range $\lambda\lambda$4700–7400 with ~11 Å resolution. Even the photographically faintest counterparts were visible with the CCD acquisition and guiding TV on the 1 m telescope. Spectral exposures ranged from 100–900 sec. Table 2 lists each source observed, with its IRAS colors, selection criterion, exposure, and our spectral assignment (M or C). All these sources were studied in the period 1987 December 10–13. Note that all colors cited in this paper follow Walker and Cohen (1988) and are based on non-color-corrected magnitudes.

We observed 32 southern sources in the period 1988 May 9–12 from Siding Spring Observatory with the Australian National University 2.3 m telescope. The instrument was the Double Beam Spectrograph (Rodgers, Conroy and Bloxham 1988) mounted at one of the Nasmyth foci; this spectrograph utilizes a dichroic beamsplitter and separate red and blue optimized optics. We were able to cover the region $\lambda\lambda$3800–8500 in four sections simultaneously, with ~4 Å resolution, using two pairs of fiber-optically coupled photon counting arrays (Rodgers *et al.* 1988); there were small gaps between the two blue arrays and between the two red arrays, but significant overlap between the longest blue and shortest red arrays. When necessary, sources were attenuated to achieve acceptable photon counting rates using "neutral" density filters with known transmission curves.

IV. RESULTS

Spectroscopic discrimination between M and C stars is readily achieved through the presence or absence of TiO, and C_2 and CN absorption bands, respectively (e.g., Yamashita, Nariai, and Norimoto 1976; Stephenson 1973 and references therein). The final columns of Tables 2 and 3 list our assigned types. Figure 1 locates all these sources in the ([12]−[25],[25]−[60]) plane, distinguishing between the four combinations of expected and actual spectral types. The C stars discovered lie in a strikingly narrow range of [12]−[25] (from 0.3 to 0.6). Our occupation zones for normal, M, and C stars also appear in Figure 1 (from Walker and Cohen 1988). For reference, the caption to Figure 1 identifies the colors of well-known representatives for each class whose occupation zone is shown.

It is clear from Figure 1 that there is substantial overlap between the color distributions of C stars and M stars. Even the separation between these types of object in [25]−[60] color index (Zuckerman and Dyck 1986) is insufficient to distinguish C from M stars. Only by optical spectroscopy is it possible to disentangle these two categories of cool star, in the absence of any LRS information (note that, according to Willems and de Jong (1986) and Little-Marenin (1986), even the LRS spectrum is not an infallible guide).

We further note that *all* sources selected as having IRAS colors that seemed to relate them to the LRS silicon carbide emission group and with optical counterparts, are in fact M stars. We cannot, of course, preclude the possibility that these are spurious foreground M stars and that the sources which truly correspond to the IRAS carbon stars are optically invisible. We find that all 10 C stars in the Lick sample and 2 of the 5 C stars in the southern sample show Hα emission, though with varying equivalent widths. In this respect they resemble the very cool carbon stars found as optical counterparts to AFGL sources in a blind survey (Cohen and Kuhi 1977).

Figure 1 is consistent with an evolutionary picture of AGB stars proceeding from M stars, well within the M star occupation zone, and evolving redwards to the silicate self-absorption box (LRSCHAR=31–39: van der Veen and Habing 1988; Walker and Cohen 1988) as mass loss continues. When enough deep interior material has been dredged up, the M star becomes a C star without mass loss, looping relatively rapidly across the color-color plane (from red to blue) and approaching the origin from above (Willems 1987; van der Veen and Habing 1988; Chan and Kwok 1988). After further evolution of these stars through (0,0) toward redder values of [12]−[25], they will again undergo significant mass loss and will rapidly become optically invisible. Such carbon stars may be recognizable, for a while, by their LRS spectra (with the silicon carbide emission feature) or even, when optically too thick for the SiC feature to be seen, through their microwave emission spectra (for example, Zuckerman and Dyck (1986) have argued that a large ratio of CO to HCN 1–0 brightness temperatures can be used as a discriminant between carbon- and oxygen-rich chemistry; one might further strengthen this discriminant by requiring the absence of an LRS silicate feature to exclude oxygen-rich chemistry), but not through optical spectroscopy. This accounts for the dichotomy in attributes of carbon stars in the IRAS color-color plane, and the distinct distributions in the color-color plane of optically known C stars and supposed carbon stars found by radio CO surveys (Figures 1c and 2c of Walker and Cohen 1988). This same duality explains the breadth in [12]−[25] of our carbon star occupation zone.

Volk and Chan (1989) have quantitatively modeled the evolution of AGB objects to carbon stars, and find that it is necessary for low mass stars to make several such loops in order to populate adequately the vertical sequence defined by those optically known carbon stars detected by IRAS. Only the first loop can be caused by the M star to C star transition. In the model, subsequent loops are

caused by an interruption of the mass loss of an initially optically invisible carbon star, which after the maximum [12]−[25] color is attained becomes optically visible and remains visible for most of the duration of the loop.

V. CONCLUSIONS

From a blind survey of 57 IRAS sources expected from broadband colors to be late-type giants and having plausible optical counterparts, we find that our optically detectable carbon stars do not populate the entire C star occupation zone, but are highly confined to the range $0.3 < [12]\text{-}[25] < 0.6$. We attribute this curious distribution to two factors: (i) loops in the color-color plane as M stars evolve into C stars, following temporary disruptions of the mass loss process due to thermal pulses; and (ii) the optical invisibility of C stars induced by the recommencement of mass loss following such a loop and the subsequent generation of optically thick dust envelopes. These latter stars represent objects dominantly unknown optically but characterized by infrared brightness and microwave molecular emission. They are responsible for a dichotomy in these color diagrams of the properties of "carbon stars".

By sharp contrast, the distribution of oxygen-rich stars in the color-color planes is continuous and represents a monotonic evolution from optically visible (e.g., with LRS spectral designations 11–19 or 21–29) to optically invisible (e.g., with LRS spectra of types 31–39) stars.

We, therefore, urge caution in the use of the IRAS color-color planes to classify late-type stars solely from their colors and in the definition of samples of late type stars for analysis. Walker *et al.* (1989) clarify the situation for carbon stars by drawing distinct occupation zones for optically visible and invisible C stars. However, we offer the following practical discriminants. If an unknown IRAS source lies at the left hand side of the Walker and Cohen (1988) carbon star occupation zone, it is probably an optically visible C star with no current mass

loss. If it has $[12]-[25] \gtrsim 0.7$ and (i) possesses any red optical counterpart but lacks an LRS spectrum it is most likely an M star; (ii) possesses a red optical counterpart and has an LRS spectrum with designation 41–47 it is probably a dust-embedded C star, and the optical counterpart is spurious; (iii) has no optical counterpart it is probably a heavily dust-shrouded C star.

Acknowledgements

We thank the NASA Ames Research Center, which provides support for IRAS studies through the SETI Institute under cooperative agreement NCC 2-407. This study at Jamieson Science and Engineering, Inc., was carried out in part under contract number NAS 2-12515 with NASA Ames Research Center. KV acknowledges the support of a postdoctoral scholarship from the Natural Sciences and Engineering Research Council of Canada. We are grateful to G. Villere for programming support.

TABLE 1

DISTRIBUTION OF IRAS SOURCES SELECTED FOR SPECTROSCOPIC STUDY.

Category	[12]−[25]	[25]−[60]	Expectation	Number observed
M1	$0.2 \rightarrow 0.5$	$-0.3 \rightarrow 0.3$	M star	11
M2	$0.9 \rightarrow 1.0$	$-0.1 \rightarrow 0.1$	M star	8
M3	$0.8 \rightarrow 1.0$ or ≥ 1.0	< 0.4 ≤ -0.1	M star	4
ML	$1.0 \rightarrow 1.1$	$-0.2 \rightarrow 0.0$	M star	7
C1	$0.3 \rightarrow 0.6$	$0.5 \rightarrow 0.8$	C star	8
C2	$0.3 \rightarrow 0.6$	> 1.0	C star	1
CL	$0.8 \rightarrow 1.0$	$0.6 \rightarrow 0.7$	C star	7
L2	$0.7 \rightarrow 1.5$	$-0.5 \rightarrow 0.3$	M star/LRS=21-29	7
L4	$0.3 \rightarrow 1.5$	$-0.1 \rightarrow 0.5$	C star/LRS=41-47	4

TABLE 2

NORTHERN IRAS SOURCES OBSERVED

IRAS NAME	[12]−[25]	[25]−[60]	Criterion	Exposure (s)	Spectrum
01583+5508	0.99	−0.13	ML	200	M
02404+2150	1.04	−0.13	ML	300	M
03119+3219	1.05	−0.10	ML	100	M
03513+1801	1.23	0.69	L2	200	M
04130+3918	0.29	0.25	L4	300	C
04184+2008	0.35	0.03	M1	300	M
04427+4951	0.36	0.50	C1	500	C
05013+1128	0.43	0.18	M1	300	C
05184+4208	1.17	−0.42	L2	400	M
05457+4635	0.34	−0.01	M1	500	C
06228−0244	0.92	−0.05	M2	300	M
06558+2853	0.41	0.14	L4	600	C
07239+0044	0.87	0.43	M3	400	M
07368+1209	0.35	1.62	C2	200	C
07497−0321	1.19	−0.24	M3	500	M
07563−0114	1.09	−0.10	M3	400	M
08427+0338	0.39	0.17	M1	600	C
14257−0530	1.79	−0.02	M3	200	M
19411+2400	1.14	0.57	L2	200	M
20101+4123	0.61	0.07	L4	900	C
20459+5015	0.93	−0.01	M2	400	M
21029+4917	1.22	0.13	L2	500	M
21160+5546	0.43	0.38	L4	400	C
22081+3801	1.00	−0.10	ML	500	M
22239+2548	0.34	−0.03	M1	750	C

TABLE 3

SOUTHERN IRAS SOURCES OBSERVED

IRAS NAME	[12]−[25]	[25]−[60]	Criterion	Exposure (s)	Spectrum
05114−7654	0.38	0.45	C1	500	M
07071−3747	0.32	0.52	C1	400	C
07077−4908	0.29	0.16	M1	400	C
07239−3342	0.36	0.17	M1	500	C
07400−1943	0.88	0.56	CL	400	M
07554−0907	0.47	−0.34	M1	400	C
08282−4035	0.87	0.58	CL	400	M
08334−5746	0.83	0.58	CL	400	M
08436−3912	0.71	−0.21	M2	384	M
09464−5538	0.81	0.57	CL	300	?
09595−5131	0.29	0.67	C1	300	M
10076−4703	0.27	0.07	M1	300	M
10596−5413	0.45	0.01	M1	700	C
11031−7120	1.00	−0.12	ML	400	M?
14294−6554	1.03	0.14	ML	348	M
15027−5245	0.35	−0.27	M1	400	M
15053−6023	0.94	0.02	M2	400	M
15115−5110	0.90	0.55	CL	400	M
15237−4113	0.54	0.61	C1	400	?
15548−5452	0.71	−0.01	L2	335	M
15577−7338	0.88	−0.01	M2	465	M
16310−4534	1.18	<0.63	L2	600	M
16450−6104	0.57	0.49	C1	747	M
17050−4123	1.21	0.44	L2	600	M
17252−5012	1.06	−0.11	ML	600	M
17307−4738	0.48	0.69	C1	600	M
17382−5308	0.90	−0.07	M2	600	S
18128−0314	0.93	0.55	CL	480	M
18129−5710	0.96	−0.03	M2	225	M
18539−1939	0.96	0.59	CL	173	M/S?
19037−3912	0.48	0.60	C1	400	M
20298−3405	0.91	−0.04	M2	400	M

References

Chan, S.J., and Kwok, S. 1988, *Ap. J.*, **334**, 362.

Cohen, M., and Kuhi, L.V. 1977, *Pub. A.S.P.*, **89**, 829.

Little-Marenin, I.J. 1986, *Ap. J. (Letters)*, **307**, L15.

Rodgers, A.W., Conroy, P., and Bloxham, G. 1988, *Pub. A.S.P.*, **100**, 626.

Rodgers, A.W., van Harmelen, J., King, D., Conroy, P., and Harding, P. 1988, *Pub. A.S.P.*, **100**, 841.

Stephenson, C.B. 1973, *Publ. Warner and Swasey Obs.*, **1**, No. 4.

Thronson, H.A., Latter, W.B., Black, J.H., Bally, J., and Hacking, P. 1987, *Ap. J.*, **322**, 770.

Thronson, H.A., Latter, W.B., Black, J.H., Bally, J., and Hacking, P. 1988, *Pub. A.S.P.*, **100**, 1446.

van der Veen, W.E.C.J., and Habing, H.J. 1988 *Astr. Ap.*, **194**, 125.

Volk, K., and Chan, S.J. 1989, in preparation.

Walker, H.J, and Cohen, M. 1988, *A.J.*, **95**, 1801.

Walker, H.J., Cohen, M., Volk, K., Wainscoat, R.J., and Schwartz, D.E. 1989, submitted to *A.J.*.

Willems, F.J. 1987, Ph.D. thesis, University of Amsterdam.

Willems, F.J., and de Jong, T. 1986, *Ap. J. (Letters)*, 309, L39.

Yamashita, Y., Nariai, K., and Norimoto, Y. 1976, *An Atlas of Representative Stellar Spectra* (Wiley & Sons: New York).

Zuckerman, B., and Dyck, H.M. 1986, *Ap. J.*, **311**, 345.

FIGURE CAPTION

Fig. 1.—The 12–25–60 μm color-color plane showing the distribution of the IRAS sources observed spectroscopically. Symbols: filled triangles, C star expected, C star found; open triangles, M star expected, C star found; filled circles, M star expected, M star found; open circles, C star expected, M star found. The dashed boxes signify occupation zones from Walker and Cohen (1988) for: 1. stellar photospheres; 2. C stars; 3. M stars; 4. LRSCHAR=31–39 objects (O-rich stars suffering silicate self-absorption). The curve represents the evolution of a star with a mass loss rate of $10^{-5} M_{\odot} \mathrm{yr}^{-1}$ before the loop begins (cf. Volk and Chan 1989). Representative objects have the following colors: 1. α CMa, a normal star, lies at $(0.00, -0.21)$; 2. Y CVn, an optically-catalogued carbon star, at $(0.07, 0.36)$; and IRC+10°216, an infrared carbon star, at $(0.77, 0.36)$; 3. VY CMa, an M-star, at $(1.13, 0.23)$; 4. OH 26.5+0.6, an OH/IR source with silicate absorption, at $(2.17, 1.54)$.

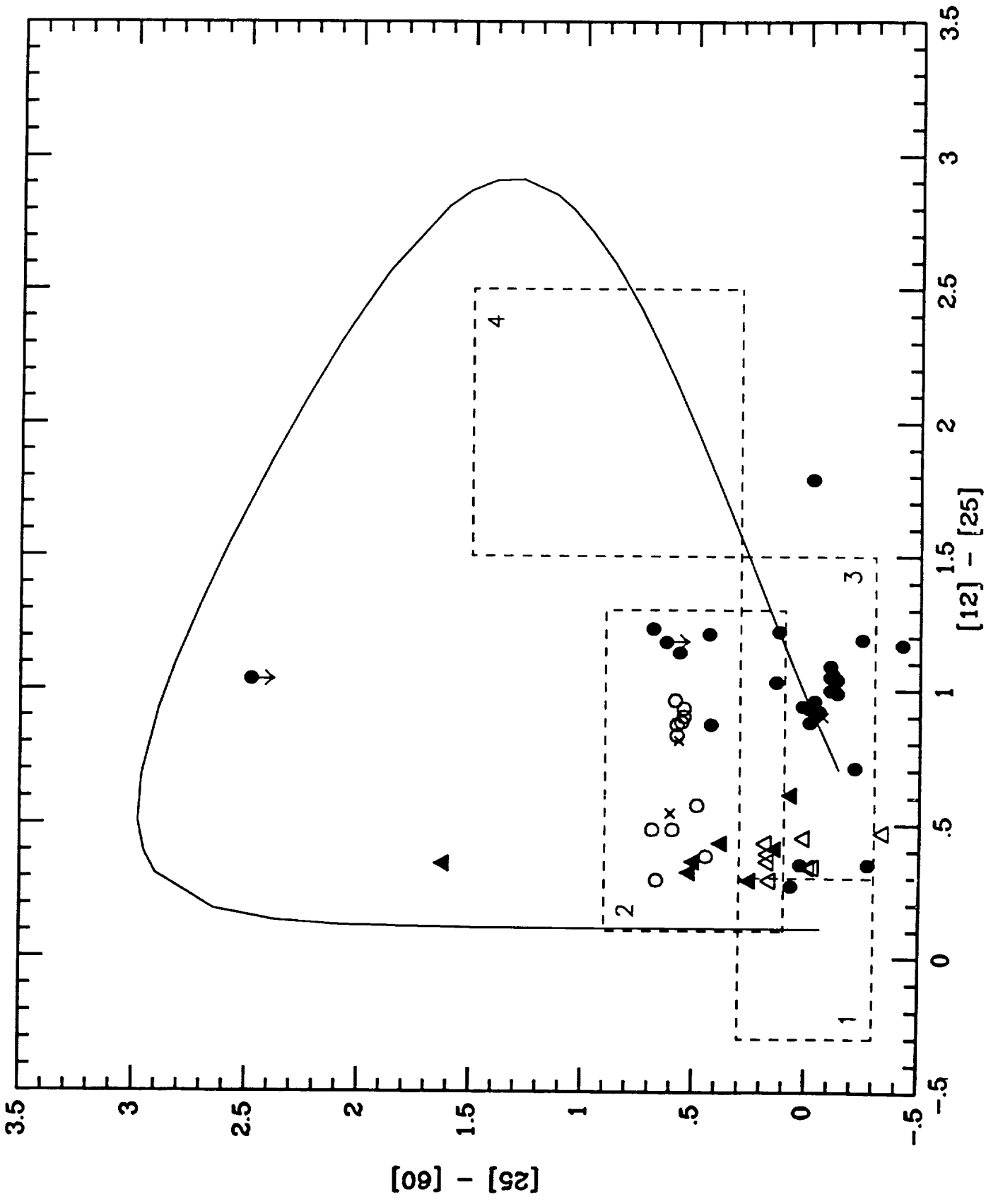
[25] - [60]
[12] - [25]
1
2
3
4

Authors' addresses

MARTIN COHEN: Radio Astronomy Laboratory, 601 Campbell Hall, University of California, Berkeley, CA 94720

DEBORAH E. SCHWARTZ, KEVIN VOLK, RICHARD J. WAINSCOAT, and HELEN J. WALKER: NASA Ames Research Center, Mail Stop 245-6, Moffett Field, CA 94035

APPENDIX D. "A Practical Approach to the Classification of IRAS Sources Using Infrared Colors Alone"

A PRACTICAL APPROACH TO THE CLASSIFICATION OF IRAS SOURCES USING INFRARED COLORS ALONE

HELEN J. WALKER[1]
NASA Ames Research Center, Mail Stop 245-6, Moffett Field, California 94035
and
SETI Institute, 101 First Street #410, Los Altos, California 94022

MARTIN COHEN
Jamieson Science and Engineering, Inc., 5321 Scotts Valley Drive Suite 204, Scotts Valley, California 95066
and
Radio Astronomy Laboratory, University of California, Berkeley, California 94720

KEVIN VOLK, RICHARD J. WAINSCOAT AND DEBORAH E. SCHWARTZ
NASA Ames Research Center, Mail Stop 245-6, Moffett Field, California 94035
and
SETI Institute, 101 First Street #410, Los Altos, California 94022

Received: .....

ABSTRACT

We have defined zones of the IRAS color-color planes in which a variety of different types of known source occur. There is considerable overlap between many of these zones, rendering a unique classification difficult on the basis of IRAS colors alone, although galactic latitude can resolve ambiguities between galactic and extragalactic populations. We have investigated the color dependence of these zones on the presence of spectral emission/absorption features and on the spatial extent of the sources.

[1]Present address: Rutherford Appleton Lab., R68, Chilton, Didcot, Oxon OX11 0QX, England

I. INTRODUCTION

In a previous paper (Walker and Cohen 1988) we described the locations, in the IRAS color-color domains, of "occupation zones" (OZs) for normal stars and for late-type giants, both oxygen-rich and carbon-rich. The definition of these zones was intended to clarify the likely content of the infrared sky as seen by IRAS, as represented by the subset of sources not previously known in other spectral regions: the unassociated IRAS sources, of sufficient flux density to have been detected in at least three IRAS bands in the IRAS Point Source Catalog (1985: hereafter PSC) (see Figs. 1a and 2a). The "unassociated sources" have no counterparts in any of the catalogs searched to find associations (see the IRAS Explanatory Supplement 1985 for list), and they do not have IRAS Low Resolution Spectrometer (hereafter LRS) spectra in the LRS Atlas (1986). Sources in the sample may, however, be associated with sources in the IRAS Serendipitous Survey Catalog (1986), since this is merely a partial survey, slightly deeper than the PSC. There are 4293 totally unassociated sources and 287 sources with associations only with the Serendipitous Survey Catalog.

The color zones provide a practical scheme for the recognition of any populations of previously unknown celestial sources, solely through their IRAS broadband photometry. As a test of our ability to classify sources correctly we have carried out a number of ground-based optical spectroscopic programs in which approximately 300 optical counterparts to unassociated IRAS sources were examined. These spectroscopic studies have very largely vindicated our expectations. However, carbon stars with optical counterparts are much more restricted in the color-color plane than our existing OZ (based on both optically identified carbon stars and IRAS sources with LRS data showing the 11.4μm SiC band in emission) would suggest (Cohen *et al.* 1989a).

Walker and Cohen (1988) estimated that almost half of the 4580 unassociated IRAS sources

locatable in the 12–25–60 μm color-color plane (i.e. having good quality fluxes in these passbands), are late-type stars. A "good quality flux" is one with FQUAL=3 in the tape version of the PSC (or equivalently, a flux density value without either a colon or an L in the printed version: see the IRAS Explanatory Supplement for more information). Our empirical approach to colors has led us to deal exclusively with non-color-corrected color indices, [12] – [25] etc., rather than with flux ratios (see Walker and Cohen (1988) for the definitions of these magnitudes, [12], etc.). Some of our work uses the LRS Atlas (1986) data, since the LRS classification scheme delineates several characteristic types of source in the color-color plane. The Atlas spectra are associated with a 2-digit number, their "class" (see IRAS LRS Atlas) or the parameter LRSCHAR in the tape version of IRAS Catalogs; the first digit being the basic class of the source, the second digit being a subclass. We will refer to LRS=1 sources, which have featureless blackbody spectra in the LRS domain (between 7.7μm and 22.7μm); LRS=2 sources which have the 10μm silicate feature in emission on a blue continuum; LRS=3 sources which have the 10μm silicate feature in absorption; the LRS=4 sources which have an emission feature due to silicon carbide near 11.4μm; the LRS=6 sources which have the 10μm silicate feature in emission on a red continuum (see IRAS LRS Atlas for more information).

Our interest in the development of a color classification scheme is motivated primarily by the demands of a very detailed infrared sky model (Wainscoat *et al.* 1989). This model explicitly incorporates about 90 categories and subclasses of known celestial source, whose contributions are significant within the LRS wavelength regime. Consequently we wish to know if we have omitted any potentially new and "infrared significant" populations of object. We have, therefore, attempted to define meaningful OZs for a much wider variety of sources, mostly non-stellar, to assist in the search for possible new populations and to expand the practical aspects of color-color work. Other studies using the IRAS Point Source Catalog have examined late-type stars specifically (e.g., Zuckerman and Dyck 1986; Thronson *et al.* 1987, 1988), or in combination with the IRAS LRS Atlas (1986) sample

of sources (van der Veen and Habing 1988), or have treated the locations of galaxies in a plethora of different color-color planes (e.g., Helou 1986; Soifer *et al.* 1987). We wish to interrelate the zones for very different classes of object within a common color-color framework.

We shall describe the definition and location of the OZs for planetary and reflection nebulae, HII regions, T Tauri stars, Herbig-Haro Exciting Stars, bipolar nebulae, and galaxies, in both the 12–25–60 μm and 25–60–100 μm planes; present the partitions of these color-color planes into the different zones; examine the dependence of the content of these zones, and of histograms of individual colors for the IRAS sources, on galactic latitude; search for any dependence of the OZs on spatial extent of sources; and assess the probability that IRAS has uncovered new categories of celestial object. The color-color planes do show the presence of extreme examples of known types of source, such as IRAS 09371+1212 (Forveille *et al.* 1987), which may not be included in the OZs. We will conclude that, while one cannot preclude the presence of new categories of source in small numbers, the subset of 4580 unassociated objects (with 12–25–60 μm fluxes) does not involve any conspicuously numerous, hitherto unsuspected, classes of source that are distinguished from known objects by their IRAS colors.

II. COLORS OF KNOWN TYPES OF CELESTIAL SOURCE

The OZs shown in Walker and Cohen (1988) were defined by fitting a box around approximately 70% of each sample of known source, in each of the two color-color planes. In this paper we represent the distribution of sources in each color by a Gaussian, to give a mean and sample standard deviation (sigma). Since a single color (requiring two good quality fluxes instead of three) is used, a larger number of sources can be incorporated in the distribution, giving a more representative estimate of the mean and sigma. The distribution is plotted as a histogram of number per color bin—usually increments of 0.1 magnitude.

If any type of source has two obvious peaks in the distribution, the color-color planes are used to track the two groups through the three colors. The results are given in Table I, and the OZs are displayed in Figures 1b and 2b, for the 12–25–60 μm and 25–60–100 μm planes respectively.

a) Normal stars and cool giants

Walker and Cohen (1988) defined OZs for three types of common stars, the visually normal ('Bright') stars, oxygen-rich and carbon-rich giants. The optically identified carbon-rich stars lie in a different region of the color-color plane to the carbon-rich stars identified on the basis of IRAS LRS spectra (Cohen *et al.* 1989a; also see Walker and Cohen (1988) Figs. 1c and 2c), and the OZ defined by Walker and Cohen reflects the contributions by both the optically and LRS selected samples. The positions of the normal, oxygen-rich and carbon-rich star OZs have been redefined in terms of a mean and sigma, with the carbon stars separated into optically identified and LRS identified samples. The two carbon star samples are poorly fit by a single Gaussian function, in all three IRAS colors, suggesting that there may be more than one grouping of sources in the color-color planes. The normal stars and O-rich giants were combined to give one sample, in all three colors. Only at [12] – [25] were two peaks in the distribution visible, so that Table I reflects a common mean and sigma for the other colors.

b) Reflection nebulae

For samples of reflection nebulae, we extracted those objects from the lists by van den Bergh (1966) and by van den Bergh and Herbst (1975) that were associated with sources in the PSC. Very few reflection nebulae had good quality 60μm and 100μm fluxes, so the [60] – [100] color is poorly defined. The reflection nebulae were split into two groups, a

"blue" set and a "red" set, dominantly distinguished by their [12] − [25] color and their positions in the 12–25–60 μm plane.

c) Planetary nebulae

These were isolated from the PSC by searching for sources with good quality detections and associations with the Strasbourg Catalog of Planetary Nebulae (Acker, Marcout, and Ochsenbein 1981). Some of the IRAS sources were obviously associated with a star rather than with the nebula, since the IRAS colors were near (0,0), and these were discarded. The planetary nebulae tended to scatter along the blackbody line in the color-color plane, but two groups were found in the 12–25–60 μm diagram, a "blue" set (scattered diffusely along the blackbody line) and a "red" set, which were more concentrated and cooler than the "blue" set. These two groups of planetary nebulae were followed through all three color histograms, using the color-color planes as a check. The "blue" set had a redder mean [60] − [100] than the "red" set, although there was a lot of scatter in the distribution of the "blue" set.

d) HII regions

We searched the 120 northern HII regions and 147 southern HII regions covered in the H109α recombination line surveys by Reifenstein *et al.* (1970) and Wilson *et al.* (1970) respectively, for counterparts in the PSC. These surveys have the additional merit of size information (radio diameters in RA and Dec.), as well as distances determined from recombination lines. We extracted the maximal data sets with single IRAS colors. A test was made to see if the size of the HII region (defined from radio continuum data) influenced the colors since the IRAS detectors have different sizes at different wavelengths. No systematic differences were detected between small HII regions (< 2 arcmin), medium size HII regions (2–4 arcmin), and large HII regions (> 4 arcmin) (see Fig. 3).

e) Galaxies

To define single color histograms for extragalactic objects we used several sources. For "normal" and starburst galaxies we used the large redshift survey of IRAS galaxies due to Strauss and Davis (1988); for Seyferts, we adopted Table 1 of Miley, Neugebauer, and Soifer (1985), after converting their spectral indices into our non color-corrected color indices; for quasars, the sample by Neugebauer *et al.* (1986) provided flux densities which we converted into our requisite indices. After eliminating sources with the colors of stars, the [12] – [25] histogram showed two peaks (confirmed as two distinct clusters in the 12–25–60 μm plane) in the joint distribution of the normal and starburst galaxies. We, therefore, give mean colors for "blue" galaxies and "red" galaxies but do not distinugish between normal and starburst types. For [25] – [60] and [60] – [100], however, there was only one peak in the joint distribution, so that a common mean and sigma were found. The color-color plots for quasars were quite well-confined and we simply defined their means and sample standard deviations. For Seyferts we represented our boxes by the medians and "spreads" given by Miley *et al.* (1985). These authors do not record the number of sources contributing to each color.

f) Miscellaneous

The OZs for the T Tauri stars were defined from sources in the lists of Harris, Clegg, and Hughes (1988), and Cohen, Emerson, and Beichman (1989). A set of Herbig-Haro Exciting Stars (HHES in Table I) was selected from Cohen and Schwartz (1987). Table I shows that these stars are widely distributed in each color, so their means and sigmas are poorly defined. We also examined the heterogeneous class of bipolar nebulae (BPN in Table I) using primarily the list due to Calvet and Cohen (1978), but updated to include several of the bipolars studied individually since this older review (e.g., IRAS 09371+1212, Forveille

et al. 1987). This class defines rather scattered distributions in the color-color diagrams, so the formal means and sigmas are tabulated, but the OZs are not plotted. The LRS=3 (sources with silicate absorption at 10μm) and LRS=6 (sources with silicate emission and a red continuum) sets, whose OZs were shown in Walker and Cohen (1988), were also reexamined; their means and sigmas are given in Table I. As can be seen, the [60] – [100] color of the LRS=6 set is effectively not defined, due to the scatter in the histogram and to the very small sample of sources.

A set of Wolf-Rayet stars was also extracted (from van de Hucht *et al.* 1981) and studied, but the sources seen by IRAS represent such a mixture of stellar photospheres, stars with dust shells, and stars with free-free emission that no unique color concentration could be defined for this set. Another potentially distinct type of source is that which appears as a column on the blue edge of [12] – [25] with red [25] – [60] (see Fig. 1a). Some of these sources may belong to the Vega-like sources identified by Aumann (1985) and by Walker and Wolstencroft (1988), and some are undoubtedly stars which underwent mass loss in a previous epoch such as the optically identified carbon stars (Chan and Kwok 1988). Since this domain in the IRAS color-color plane can be occupied by sources with a wide variety of histories, no attempt was made to define an OZ for them. This region corresponds to part of region VIa of van der Veen and Habing (1988).

Figure 1a shows the 4580 unassociated IRAS sources with good quality fluxes at 12μm, 25μm, and 60μm, and Figure 2a shows the subset of these with good quality fluxes at all four IRAS wavelengths, 822 sources. Figures 1b and 2b show the OZs derived from the means and sigmas in Table I, in the two color-color planes. By defining the sides of a rectangular box in a color-color plane each to be 2.78 times the appropriate sigmas and centered on the mean colors, we would enclose 70% of the two-dimensional distribution in our box if the distributions were Gaussian. Actual counts for the smaller subsets of source suggest that all our populations are sensibly Gaussian (70% OZs result for samples

of approximately $\pm 1.5\sigma$ centered on the mean). Therefore, we have plotted $\pm 1.39\sigma$ color-color boxes throughout, with the following few exceptions. The HHES zones and the BPN zones are not plotted due to their high σ and small populations. The LRS=6 set and the blue planetary nebulae set are not plotted on the 25–60–100 μm diagram because their sigmas are very high. These diagrams show that very few unassociated sources lie outside the identified zones. The figures also show that there is considerable overlap between the color zones for various types of source seen by IRAS, so that most unassociated sources with three IRAS fluxes cannot be given a unique classification based solely on IRAS colors.

III. DEPENDENCE OF COLORS ON FEATURE STRENGTH

a) Broad features

Tables II–V show the percentage of sources with LRS spectra of various classes, binned according to the increasing feature strength (based on the LRS subclass, running from 1 to 9 for each LRS class). The sources with LRS=2 show the silicate feature at 10μm in emission, those with LRS=3 have the 10μm feature in absorption. The sources with LRS=4 show silicon carbide in emission. The statements made by Walker and Cohen (1988) concerning the independence of color and feature strength were based primarily on the consistent change in slope of the continuum versus the [12] – [25] color, for all six types of star examined. If the dependence had been driven by feature strength, the featureless 'Bright' stars and LRS=1 sets would have had a different relation of slope versus color from those classes with features. The 10μm silicate feature is the strongest feature in the 12μm IRAS waveband, yet, as Tables II and III show, there is no obvious trend of feature strength (as measured by the LRSCHAR subclass) with [12] – [25] color for stars which show this feature. Van der Veen and Habing (1988) showed that there is a trend of color versus feature strength for the LRS=3 and LRS=4 sets, and this is verified by Tables IV

and V. Walker and Cohen (1988) related the change in color for the LRS=4 set to the continuum slope, so it may be that the feature strength also is related to the continuum slope.

b) Atomic lines and molecular features

The infrared spectra of planetaries, reflection nebulae, and HII regions are often dominated by a combination of atomic fine structure emisson lines and broader molecular features. Once called the "unidentified infrared" bands, these broader features account for an entire spectrum of emissions from 3.3μm to about 13μm, and even beyond, and are usually attributed to polycyclic aromatic hydrocarbons (PAHs; e.g., Cohen *et al.* 1989b). The ubiquity of the PAH bands and their extreme prominence in some nebulae suggests the merit of investigating to what extent their presence might influence the broadband IRAS colors of these three types of nebula. Likewise, the great strength in planetaries of some of the atomic fine structure lines dictates the necessity of the same test for these nebulae.

To this end, Figure 4 presents the 12–25–60 μm color-color plane for two samples of each of three types of nebula, one showing the PAH bands or fine structure lines conspicuously, the other sample without strong features. Neither reflection nebulae nor HII regions show a clear separation in this color-color plane. However, our small test group of planetaries seems to bifurcate into a redder sample with line emission and a bluer sample without. The effects of PAH emission should cause a blueing of the $[12]-[25]$ color index so that this result seems surprising. However, a much larger study of over 100 planetaries with LRS database spectra (Volk and Cohen 1989) indicates that the most common LRS spectral shape among these nebulae has a very red continuum energy distribution, with an obvious 15.6μm [NeIII] emission line. This line will affect the [12] magnitude very little but the [25] substantially. We, therefore, attribute any potential separation in colors for planetary nebulae primarily to the influence of the commonly found, underlying red continua and

secondarily to any long wavelength fine structure lines. Clearly, the effects of these very red continua are capable of overwhelming even the dominantly shorter wavelength PAH emission features. (In reality, the larger set of nebulae used by Volk and Cohen (1989) does not show any clearcut separations although it does suggest a weak tendency for planetaries with PAH emission to be somewhat bluer than those with red continua and fine structure lines.)

IV. GALACTIC LATITUDE DEPENDENCE OF IRAS COLOR SAMPLES

a) Sources detected at 12μm

The reason for the concentration of unassociated sources at [25] – [60] of around 4–5, in Figures 1a and 2a, is not clear. From a direct comparison with our OZs, these very red sources could be either galactic or extragalactic, since the distribution is similar to the galaxy OZs and the reflection nebulae OZs. However, when galactic latitude constraints are applied to the data, the picture becomes much clearer. At $|b| > 30°$ (Fig. 5b) there are few sources: some uncatalogued late-type stars, and some potential galaxy candidates (most of which were serendipitous sources). There are many more unassociated sources with $|b| < 1°$ (Fig. 5a). Some of these must also be uncatalogued late-type stars, often with very thick dust shells (since they occupy the LRS=3 OZ), but most of the sources have the colors of HII regions and reflection nebulae. The requirement of good quality fluxes (FQUAL=3) is too severe for most unassociated normal galaxies to be included in the 12–25–60 μm diagram because they would not have been detected at 12μm. When the set of unassociated sources is located in the 25–60–100 μm plane, with the same galactic latitude constraints, there are far fewer sources due to the additional requirement that the sources must have a fourth good quality flux. The distribution suggests a population of galaxies and reflection nebulae, but no late-type stars, at high galactic latitudes (Fig. 6b).

At low galactic latitudes the distribution suggests a population of reflection nebulae and HII regions, a very plausible disk population (Fig. 6a).

b) Sources not detected at 12μm

Another set of unassociated sources can be extracted from the IRAS Point Source Catalog, the red unassociated sources, which have good quality fluxes at 25μm, 60μm, and 100μm, and only an upper limit for the flux at 12μm. There are 656 sources with no associations, and a further 58 sources with an association only to the IRAS Serendipitous Survey Catalog in this set. Figures 7a and 7b show the color-color plane for the low galactic latitude ($|b| < 1°$) and high galactic latitude ($|b| > 30°$) sets. The high latitude set is slightly bluer in [60] – [100] than the low latitude set; the colors resemble most closely the galaxy OZs, the reflection nebulae OZs, or HII region OZs. Considering the total areas of the sky involved, the high latitude zone should have 29 times as many galaxies as the low latitude zone. We favor the HII regions as the dominant population at low latitudes, since they are seen to great distances, their exciting stars have small scale heights, and PAH emission is less prominent than in reflection nebulae (see Sec. IIIb). There are more sources in the high latitude set of red unassociated sources than with the previous unassociated sample, but the four sets (Figs. 6 and 7) appear very similar to each other, unlike the 12–25–60 μm sets (Fig. 5). Examination of POSS plates for optical counterparts reveals that many of the high latitude red unassociated sources have counterparts that are optically visible galaxies, usually compact and occasionally interacting. Figure 7b highlights the unusual colors of the apparently extremely cool bipolar nebula, IRAS 09371+1212: this object is well isolated from the main concentration (at around 4.9,0.1). The spectrum of this remarkable nebula also shows extremely deep water ice absorptions near 45μm and 70μm (Omont *et al.* 1989) which enhance its [25] – [60] index. This uniqueness may suggest a very short-lived phase, possibly of an intermediate rather than a low mass progenitor.

c) [12] – [25] color histograms

If [12] – [25] alone is used, the changes in color of the IRAS population with galactic latitude can be investigated in more detail. The IRAS point sources with galactic longitude between 30° and 60° (the inner galaxy sample), between 163° and 193° (the outer galaxy sample), and between 275° and 305° (the tangent point sample), and with $|b| \leq 20°$ were examined. These samples included all the associated sources and unassociated sources with good quality fluxes (FQUAL=3) at 12μm and 25μm. The sources were extracted in 1° bands in galactic latitude, and Table VI shows the results, with the number in each color bin expressed as a percentage of the total number extracted in that latitude interval. Percentages were used because there were almost 10 times as many stars at low latitudes in the inner galaxy sample compared to the outer galaxy sample. When $|b| \leq 4°$, the sources tend to peak with [12] – [25] around 0.6 to 1.2, and the distribution has a long tail towards redder [12] – [25]. When $|b| \geq 4°$ there are very few sources with [12] – [25] > 1.4 (see Fig. 8), except at negative latitudes in the outer galaxy sample. These sources in the outer galaxy have the colors, in the 12–25–60 μm plane, of reflection nebulae and T Tauri stars. At the highest latitudes ($|b| > 15$–$20°$) there are usually as many normal stars as late-type giants. The percentages suggest that the colors of the late-type giants become a little bluer in [12] – [25] (from 1.0–1.2 to 0.6–0.8) as the latitude increases, which is consistent with the fact that the AGB phases of higher mass stars are redder and have a smaller scale height than do low mass stars.

V. DEPENDENCE OF COLORS ON SPATIAL EXTENT FOR EXTENDED SOURCES

As mentioned in Sec. IIc, the selected HII regions were investigated to see if the IRAS PSC fluxes had any color dependence on the size of the HII region, and none was found.

In order to check further whether the source size had a significant influence on the IRAS colors, the IRAS Small Scale Structure (SSS) Catalog (1986) was used. The SSS fluxes were extracted (where available) for the HII regions and reflection nebulae used to define the OZs in Sec. II. The IRAS colors derived from the SSS fluxes were found to be slightly bluer in [12] – [25] and [25] – [60], so that the sources tended to cluster towards the lower left corner of the OZ, however the effect was not severe enough to redefine the zones (see Fig. 9). Rice *et al.* (1988) gave IRAS PSC fluxes and 'total flux density measurements' for nearby large galaxies. The color-color diagrams were made for the 28 galaxies in their sample with PSC fluxes at 12μm, and no significant differences were seen between the color-color diagrams using PSC fluxes and those using total flux density colors (see Fig. 10).

Although the color-color zones for both the entire sample of galaxies measured by Rice *et al.* (1988) and our subset of various SSS sources also with PSC measurements do not alter perceptibly when we replace PSC data by data through larger apertures, we can nevertheless see preferential effects on some individual sources. In particular, going from PSC to SSS, or from PSC to total flux density measures for the Rice *et al.* galaxy samples, we do notice a tendency for [25] – [60] to be bluer, and a lesser tendency for [12] – [25] to become bluer. We attribute the longer wavelength blueing to the fact that the PSC beam size is so much smaller at 25μm than at 60μm that the primary effect of including spatially extended flux is to compensate for this differential aperture effect. This naturally enhances [25] compared with [60] and blues this color index. The smaller blueing in [12] – [25] we attribute to the facts that *a*) PAH emission is more noticeable in [12] than in [25] (although there are weak bending modes in the 20μm region too: cf. Cohen *et al.* 1989b), and *b*) PAH emission is preferentially more extended spatially than continuum radiation. This second point is detailed by Cohen *et al.* (1989b) who compared the ratio of IRAS broadband fluxes in the SSS catalog to the PSC for a number of nebulous sources known to have PAH emission (from their 5–8 μm airborne spectra). These ratios clearly showed that 12μm

emission grows faster with aperture when sources are spatially extended than do the 25μm or 60μm fluxes. In particular, when we examine the color-color locations of several nebulae with spatially extended emission (e.g., He 2-77) from Cohen *et al.* (1989b) in comparison with their PSC determined colors we detect the same vectors as noted above in our wider tests using Rice *et al.* and the SSS. These vectors are patently real and explicable even if the occupation zones do not represent their effects through an entire population of sources.

Figure V.A.2 in the Introduction of the IRAS Small Scale Structure Catalog (1986) shows that the sources in that catalog concentrate in the galactic plane; very few sources are found at high latitudes. IRAS SSS sources with quality A or B fluxes, at 12μm, 25μm, and 60μm were extracted, and plotted in the color-color diagram (Fig. 11). The sources cluster at the bluest corner of the blue reflection nebula box, consistent with the galactic distribution.

VI. CONCLUSIONS

1. The 12–25–60 μm plane is dominated by AGB stars and by blue reflection nebulae (probably with PAH emission). The 25–60–100 μm plane is dominated by a combination of reflection nebulae and HII regions.

2. On the basis of our complete set of occupation zones we find little cause to postulate the existence of any major new population of object discovered by IRAS, and well detected in at least three wavebands.

3. These zones show considerable overlap, precluding, in general, any unique classification solely from colors, except for objects lying at the peripheries of some zones (e.g., the blue reflection nebulae zone, and the red planetary nebulae zone). However, a consideration of color and galactic latitude information can clarify an otherwise ambiguous classification.

4. In spite of the suggestion that broadband features determine the colors for LRS=3 and LRS=4 sources, we find no such influence on color for the LRS=2 sample of silicate emitters.

5. Only for red planetary nebulae do we see any hint of a dependence of color on the presence or absence of atomic lines or PAH bands in emission.

6. While small shifts in the colors of individual sources are detectable when total flux measurements are substituted for PSC data, for spatially extended objects, these (i) do not significantly shift the occupation zones defined for these entire populations and (ii) are usually explicable as due to spatially extended PAH emission which dominates the 12μm band, or to differences in detector sizes at different IRAS wavelengths.

7. A detailed model of the sky can greatly aid the classification process, particularly a model that isolates different geometrical, spectral, and physical populations, and keeps track of color information. The present study has been largely in support of just such a model (Wainscoat *et al.* 1989).

We thank the NASA-Ames Research Center, which provides support for IRAS studies through the SETI Institute under cooperative agreement NCC 2-407. MC thanks NASA-Ames for partial support at Berkeley through cooperative agreement NCC 2-142. KV acknowledges support from the National Sciences and Engineering Research Council of Canada. This study at Jamieson Science and Engineering Inc. was supported by an internal research and development program. We are grateful to G. Villere for programming support.

REFERENCES

Acker, A., Marcout, J., and Ochsenbein, F., 1981. Astron. Astrophys. Suppl. 43, 265.

Aumann, H.H., 1985. Publ. Astr. Soc. Pacific 97, 885.

Beichman, C.A., Neugebauer, G., Habing, H.J., Clegg, P.E., and Chester, T.J., editors (1985). IRAS Catalogs and Atlases: "The Explanatory Supplement" (General Printing Office, Washington, D.C.).

Bergh, S. van den, 1966, Astron. J. 71, 990.

Bergh, S. van den, and Herbst, W. 1975, Astron. J. 80, 208.

Calvet, N. and Cohen, M. 1978, Mon. Not. Roy. Astron. Soc. 182, 687.

Chan, S. J., and Kwok, S. 1988, Astrophys. J. 334, 362.

Cohen, M., Emerson, J., and Beichman, C. 1989. Astrophys. J. 339 (in press).

Cohen, M., and Schwartz, R.D., 1987. Astrophys. J. 316, 311.

Cohen, M., Tielens, A. G. G. M., Bregman, J., Witteborn, F. C., Rank, D. M., Allamandola, L. J., Wooden, D. H., and Muizon, M. de 1989b, Astrophys. J., June 1 (in press).

Cohen, M., Wainscoat, R.J., Walker, H.J., Volk, K., and Schwartz, D.E., 1989a. submitted to Astron. J.

Forveille, T., Morris., M., Omont, A., and Likkel, L., 1987. Astron. Astrophys. 176, L13.

Harris, S., Clegg, P.E., and Hughes, J. 1988. Mon. Not. Roy. Astron. Soc. 235, 441.

Helou, G., 1986. Astrophys. J. (Letters), 316, L33.

Hucht, K. A. van der, Conti, P. S., Lundstrom, I., and Stenholm, B. 1981. Astrophys. Space Sci. 28, 287.

Joint IRAS Science Working Group (1985). IRAS Catalogs and Atlases: "The Point Source Catalog" (General Printing Office, Washington, D.C.).

Joint IRAS Science Working Group (1986). IRAS Catalogs and Atlases: "The Serendipitous Survey Catalog (General Printing Office, Washington, D.C.).

Joint IRAS Science Working Group (1986). IRAS Catalogs and Atlases: "The Small Scale Structure Catalog (General Printing Office, Washington, D.C.).

Joint IRAS Science Working Group (1986). IRAS Catalogues and Atlases. Atlas of Low Resolution Spectra. (LRS Catalogue). Astron. Astrophys. Suppl. 65, 607.

Miley, G.K., Neugebauer, G., and Soifer, B.T., 1985. Astrophys. J. 293, L11.

Neugebauer, G., Miley, G.K., Soifer, B.T., and Clegg, P.E., 1986. Astrophys. J. 308, 815.

Omont, A., Moseley, S. H., Forveille, T., Harvey, P. M., and Likkel, L., 1989. in Proc. of 22nd ESLAB Symp., "Infrared Spectroscopy in Astronomy", ed. M. J. Kessler (ESA Publications).

Reifenstein, E. C., Wilson, T. L., Burke, B. F., Mezger, P. G., and Altenhoff, W. J. 1970, Astron. Astrophys., 4, 357.

Rice, W., Lonsdale, C.J., Soifer, B.T., Neugebauer, G., Kopan, E.L., Lloyd, L.A., de Jong, T., and Habing, H.J., 1988. Astrophys. J. Suppl., 68, 91.

Soifer, B.T., Sanders, D. B., Madore, B. F., Neugebauer, G., Danielson, G. E., Elias, J. H., Lonsdale, C. J., and Rice, W. L. 1987, Astrophys. J., 328, 238.

Strauss, M.A., and Davis, M., 1988. IAU symp. No. 130, "Large scale structure in the Universe", eds. J. Audoze and A. Szalay (Dordrecht: Reidel).

Thronson, H.A., Latter, W.B., Black, J.H., Bally, J., and Hacking, P. 1987. Astrophys. J. 322, 770.

Thronson, H.A., Latter, W.B., Black, J.H., Bally, J., and Hacking, P. 1988. Publ. Astron. Soc. Pacific, 100, 1446.

Veen, W.E.C.J. van der, and Habing, H.J., 1988. Astron. Astrophys. 194, 125.

Volk, K., and Cohen, M. 1989, in preparation.

Wainscoat, R.J., *et al.* 1989, in preparation.

Walker, H.J., and Cohen, M., 1988. Astron J. 95, 1801.

Walker, H.J., and Wolstencroft, R.D., 1988. Publ. Astron. Soc. Pacific December (in press).

Wilson, T. L., Mezger, P. G., Gardner, F. F., and Milne, D. K. 1970, Astron. Astrophys. 6, 364.

Zuckerman, B., and Dyck, H.M. (1986). Astrophys. J. 311, 345.

FIGURE CAPTIONS

FIG. 1. [25] – [60] plotted against [12] – [25]: (a) for the unassociated IRAS sources (plus signs) and the serendipitous sources (circles); (b) the occupation zones for the known types of celestial source. The various zones are distinguished by lower case letters in their corners, following the code shown in the final column of Table I. Line types are chosen solely for clarity.

FIG. 2. [60] – [100] plotted against [25] – [60]: (a) for the unassociated IRAS sources (plus signs) and the serendipitous sources (circles); (b) the occupation zones, as for Fig. 1b (note that not all source types have separate zones in this plane: see Table I).

FIG. 3. [25] – [60] plotted against [12] – [25] for HII regions with different diameters: less than 2 arcmin (filled circles), between 2 arcmin and 4 arcmin (open circles), and greater than 4 arcmin (asterisks).

FIG. 4. [25] – [60] plotted against [12] – [25] for nebulae and HII regions with, and without, strong atomic lines or molecular features: HII regions with features (filled squares), HII regions without strong features (open squares); reflection nebulae with features (filled triangles), reflection nebulae without strong features (open triangles); planetary nebulae with features (crosses), planetary nebulae without strong features (plus signs).

FIG. 5. [25] – [60] plotted against [12] – [25] for the unassociated sources (plus signs) and the serendipitous sources (circles) with (a) $|b| < 1°$ (b) $|b| > 30°$.

FIG. 6. [60] – [100] plotted against [25] – [60] for the unassociated sources (plus signs) and the serendipitous sources (circles) with (a) $|b| < 1°$ (b) $|b| > 30°$.

FIG. 7. [60] – [100] plotted against [25] – [60] for the red unassociated sources (crosses) and the red serendipitous sources (squares) with (a) $|b| < 1°$ (b) $|b| > 30°$. The very cool

BPN IRAS 09371+1212 is well isolated from the main concentration (around (4.9,0.1) in Fig. 7b).

FIG. 8. Histograms of number against [12] – [25] color for sources with galactic longitude between 30° and 60°, and with galactic latitude between 1° and 2° (solid lines), or between 10° and 11° (dashed lines). Note that the higher latitude histogram is scaled up by a factor of 10 for easier comparison with the lower latitude plot.

FIG. 9. [25] – [60] plotted against [12] – [25] for PSC and SSS fluxes of HII regions and reflection nebulae: HII regions, PSC fluxes (filled squares), SSS fluxes (open squares); reflection nebulae, PSC fluxes (crosses), SSS fluxes (plus signs).

FIG. 10. (a) [25] – [60] plotted against [12] – [25] for galaxies: PSC fluxes (filled circles), SSS fluxes (open circles). (b) [60] – [100] plotted against [25] – [60] for galaxies as for Fig. 10a.

FIG. 11. [25] – [60] plotted against [12] – [25] for SSS sources: for 12–25–60 μm AAA quality fluxes shown by (stars), AAB by (diamonds), BAA by (circles), ABA by (squares), ABB by (triangles, apices up), BAB by (triangles, apices down), BBA by (crosses), BBB by (plus signs).

TABLE I. Occupation zones for known sources

Source type	[12] − [25]			[25] − [60]			[60] − [100]			Code[a)]
	mean	sigma	#	mean	sigma	#	mean	sigma	#	
Bright stars	0.09	±0.11	(1022)	−0.05	±0.18	(3142)	0.05	±0.29	(509)	a
O-rich stars	0.81	±0.34	(2679)	−0.05	±0.18		0.05	±0.29		b
Opt. C-rich	0.27	±0.12	(308)	0.50	±0.23	(270)	0.40	±0.44	(79)	c
LRS C-rich	0.80	±0.34	(282)	0.24	±0.17	(306)	−0.18	±0.20	(52)	d
HII regions	3.73	±0.32	(42)	4.35	±0.46	(60)	1.72	±0.42	(49)	e
Blue Refl neb	1.84	±0.33	(31)	4.26	±0.80	(22)	2.19	±0.44	(6)	f
Red Refl neb	3.08	±0.53	(35)	3.78	±0.83	(27)	1.56	±0.37	(17)	g
Blue Plan neb	1.93	±0.50	(41)	1.82	±0.77	(41)	1.17	±1.0:	(17)	h
Red Plan neb	3.68	±0.76	(159)	2.20	±0.91	(170)	0.27	±0.31	(102)	i
Blue Galaxies	2.01	±0.32	(202)	4.04	±0.29	(288)	1.81	±0.30	(343)	j
Red Galaxies	2.83	±0.30	(120)	4.04	±0.29		1.81	±0.30		k
Seyferts	2.72	±0.35		3.23	±0.32		1.6	±0.6:		l
Quasars	2.31	±0.44	(49)	2.55	±0.49	(56)	1.56	±0.39	(37)	m
T Tau stars	1.90	±0.27	(43)	2.30	±0.55	(46)	1.50	±0.59	(16)	n
LRS=3	2.07	±0.26	(127)	0.60	±0.37	(140)	−0.23	±0.23	(21)	o
LRS=6	1.33	±0.28	(49)	−0.03	±0.16	(40)	0.24	±1.0:	(14)	p
HHES	2.99	±0.72	(26)	3.11	±0.84	(29)	1.73	±0.77	(28)	...
BPN	2.54	±0.82	(20)	2.84	±1.19	(21)	1.08	±0.78	(19)	...

[a)] "Code" designates the letter by which the occupation zones for each type of source are identified in Figures 1b and 2b.

TABLE II. Percentage of GCVS M stars with LRS=2 in each subclass.

[12] − [25]	1	2	3	4	5	6	7	8	9	#
0.4–0.6	14	29	14	10	5	5	14	10	0	21
0.6–0.8	5	29	15	15	9	5	11	5	5	55
0.8–1.0	5	17	16	17	8	12	5	13	7	76
1.0–1.2	0	5	9	7	16	16	9	16	21	43
1.2–1.4	0	0	22	0	0	0	22	0	56	9

TABLE III. Percentage of all LRS=2 sources (including GCVS M stars) in each subclass.

[12] − [25]	1	2	3	4	5	6	7	8	9	#
0.4–0.6	21	24	17	7	3	3	10	7	7	29
0.6–0.8	5	26	13	11	8	11	7	7	12	129
0.8–1.0	3	10	11	11	10	9	9	11	25	318
1.0–1.2	1	4	5	5	9	12	12	13	40	336
1.2–1.4	0	2	5	5	8	7	16	16	42	231
1.4–1.6	1	2	6	9	17	9	25	6	26	108
1.6–1.8	9	13	13	25	3	13	9	0	16	32
1.8–2.0	25	25	17	25	0	0	0	0	8	12

TABLE IV. Percentage of LRS=3 sources in each subclass.

[12] − [25]	1	2	3	4	5	6	7	8	9	#
0.0–1.6	62	24	11	3	0	0	0	0	0	37
1.6–1.8	47	18	6	12	6	6	0	0	6	17
1.8–2.0	9	45	14	14	9	5	0	0	5	22
2.0–2.2	13	13	19	16	13	9	9	3	6	32
2.2–2.4	0	13	8	4	16	0	8	13	38	24
2.4–3.4	5	10	14	5	5	10	0	5	48	21

TABLE V. Percentage of LRS=4 sources in each subclass.

[12] − [25]	1	2	3	4	5	6	7	8	9	#
0.1–0.3	3	17	15	38	15	6	3	2	0	65
0.3–0.5	0	16	10	32	25	9	6	1	1	79
0.5–0.7	4	13	25	35	15	7	1	0	0	72
0.7–0.9	6	22	46	17	9	0	0	0	0	54
0.9–1.1	7	34	46	13	0	0	0	0	0	68
1.1–1.3	3	61	13	16	6	0	0	0	0	31
1.3–1.5	8	67	17	8	0	0	0	0	0	24
1.5–1.7	13	50	38	0	0	0	0	0	0	8

Table VI. Percentages of sources for latitude degree intervals, ordered by [12] – [25] color bin.

$30° < l < 60°$ positive latitudes

$b°$	0→1	2	3	4	5	6	7	8	9	10	11	12	13	14	15	16	17	18	19	20
total	861	731	585	400	269	217	169	148	101	103	76	72	51	62	46	47	38	43	36	33
−0.4	0	0	0	0	0	0	0	0	0	0	0	0	0	0	0	0	0	0	0	0
−0.2	0	0	0	0	0	1	1	1	1	2	0	0	0	2	0	2	3	0	0	0
0.0	0	1	2	2	1	2	6	5	8	7	12	6	8	16	11	13	21	16	19	18
0.2	1	2	2	5	4	10	8	9	5	6	20	18	12	8	7	21	13	26	25	15
0.4	2	2	4	7	5	3	8	9	8	10	8	13	16	10	9	15	24	12	6	15
0.6	4	8	13	14	16	21	23	18	22	27	18	26	22	15	24	19	18	14	25	9
0.8	10	19	19	20	24	22	25	22	20	22	20	17	24	24	28	13	8	12	11	18
1.0	17	24	22	25	26	20	19	22	12	18	17	13	12	19	13	11	13	14	11	18
1.2	17	20	15	15	13	8	7	11	12	6	3	1	6	5	4	2	0	5	3	3
1.4	14	9	8	5	6	6	2	1	5	0	1	4	0	2	2	2	0	0	0	0
1.6	8	6	5	3	1	2	1	3	3	0	1	1	0	0	0	0	0	0	0	0
1.8	5	2	3	1	1	2	0	0	2	0	0	0	0	0	0	0	0	0	0	0
2.0	4	1	2	1	1	0	1	0	0	0	0	0	0	0	2	0	0	0	0	0
2.2	3	2	1	0	0	1	0	0	1	1	0	0	0	0	0	2	0	0	0	0
2.4	2	1	1	1	0	0	0	0	1	0	0	0	0	0	0	0	0	0	0	0
2.6	2	1	1	0	0	0	0	0	0	0	0	0	0	0	0	0	0	2	0	0
2.8	2	0	0	0	0	0	0	0	0	0	0	0	0	0	0	0	0	0	0	0
3.0	2	0	1	1	0	0	0	0	0	0	0	0	0	0	0	0	0	0	0	0
3.2	2	0	0	0	0	0	0	0	0	0	0	0	0	0	0	0	0	0	0	3
3.4	1	0	1	0	0	0	0	0	0	1	0	0	0	0	0	0	0	0	0	0
3.6	1	0	0	1	0	0	0	0	1	0	0	1	0	0	0	0	0	0	0	0
3.8	1	0	0	0	0	0	0	0	0	0	0	0	0	0	0	0	0	0	0	0
4.0	1	0	0	0	0	0	0	0	0	0	0	0	0	0	0	0	0	0	0	0
4.2	0	0	0	0	0	0	0	0	0	0	0	0	0	0	0	0	0	0	0	0
4.4	1	0	0	0	0	0	0	0	0	0	0	0	0	0	0	0	0	0	0	0
4.6	0	0	0	0	0	0	0	0	0	0	0	0	2	0	0	0	0	0	0	0
4.8	0	0	0	0	0	0	0	0	0	0	0	0	0	0	0	0	0	0	0	0

$30° < l < 60°$ negative latitudes

$b°$	0→1	2	3	4	5	6	7	8	9	10	11	12	13	14	15	16	17	18	19	20
total	841	697	543	348	246	222	165	132	103	93	87	58	63	55	49	40	39	25	31	24
-0.4	0	0	0	0	0	0	0	0	1	0	1	0	0	0	0	0	0	0	0	0
-0.2	0	0	0	0	0	0	1	0	2	0	0	0	2	0	2	0	0	0	0	0
0.0	1	1	2	2	4	4	8	9	4	10	8	10	8	9	12	18	13	16	23	4
0.2	0	2	3	5	6	6	7	11	16	13	15	14	13	11	18	3	18	24	13	8
0.4	1	4	4	3	5	6	7	5	5	13	5	10	5	11	14	8	5	4	13	8
0.6	5	9	16	17	14	19	18	14	16	19	18	16	13	20	8	10	28	24	10	21
0.8	10	21	22	23	25	24	20	24	25	20	28	19	30	20	27	23	21	16	23	42
1.0	16	25	24	25	24	21	22	23	24	16	20	19	21	16	16	23	5	8	10	13
1.2	16	16	13	11	11	14	10	7	5	4	1	3	3	7	0	10	7	4	6	4
1.4	13	9	7	7	4	3	2	3	1	3	2	5	2	2	0	5	0	4	0	0
1.6	10	6	4	2	2	1	2	2	0	0	0	2	3	2	0	3	3	0	3	0
1.8	6	3	2	1	2	1	0	2	1	1	0	0	0	0	0	0	0	0	0	0
2.0	4	2	0	1	0	0	1	0	1	0	0	0	0	0	0	0	0	0	0	0
2.2	3	1	0	0	0	0	0	0	0	0	0	0	0	0	0	0	0	0	0	0
2.4	2	1	0	0	0	0	1	0	0	0	0	2	0	2	0	0	0	0	0	0
2.6	1	0	0	0	0	0	1	0	0	0	1	0	0	0	0	0	0	0	0	0
2.8	2	1	0	0	0	0	0	0	0	0	0	0	0	0	0	0	0	0	0	0
3.0	1	0	0	0	0	0	0	0	0	0	0	0	0	0	0	0	0	0	0	0
3.2	2	0	0	0	0	0	0	0	0	0	0	0	0	0	2	0	0	0	0	0
3.4	2	0	0	0	0	1	0	0	0	0	0	0	0	0	0	0	0	0	0	0
3.6	2	0	0	0	0	0	1	0	0	0	0	0	0	0	0	0	0	0	0	0
3.8	1	0	0	0	0	0	0	0	0	0	0	0	0	0	0	0	0	0	0	0
4.0	1	0	0	0	0	0	1	0	0	0	0	0	0	0	0	0	0	0	0	0
4.2	0	0	0	0	0	0	0	0	0	0	1	0	0	0	0	0	0	0	0	0
4.4	0	0	0	0	0	0	0	0	0	0	0	0	2	0	0	0	0	0	0	0
4.6	0	0	0	0	0	0	0	0	0	0	0	0	0	0	0	0	0	0	0	0
4.8	0	0	0	0	1	0	0	0	0	0	0	0	0	0	0	0	0	0	0	0

$163° < l < 193°$ positive latitudes

$b°$	0→1	2	3	4	5	6	7	8	9	10	11	12	13	14	15	16	17	18	19	20
total	88	61	74	48	69	33	30	29	18	25	32	21	15	17	19	31	25	17	13	16
−0.4	0	0	0	0	0	0	0	0	0	0	0	0	0	0	0	0	0	0	0	0
−0.2	0	2	0	0	0	6	0	0	0	0	6	0	7	12	0	3	0	0	0	0
0.0	10	3	14	4	7	15	27	10	0	12	25	10	13	12	16	23	16	47	23	13
0.2	9	20	20	15	23	9	13	14	22	36	25	19	13	24	11	23	28	35	15	19
0.4	9	18	9	10	9	6	20	7	6	24	9	10	13	18	16	10	16	12	23	19
0.6	14	13	12	19	13	18	20	34	17	12	13	19	27	6	16	13	20	6	15	19
0.8	8	5	9	17	13	9	7	17	22	8	6	29	7	24	21	19	12	0	23	13
1.0	5	11	8	4	6	21	10	14	22	8	6	14	7	6	5	6	4	0	0	6
1.2	3	3	1	6	6	12	0	0	6	0	3	0	13	0	11	0	4	0	0	0
1.4	5	0	1	2	3	0	0	3	0	0	0	0	0	0	5	3	0	0	0	0
1.6	6	2	7	2	3	0	0	0	6	0	0	0	0	0	0	0	0	0	0	0
1.8	5	2	0	4	3	0	0	0	0	0	0	0	0	0	0	0	0	0	0	0
2.0	3	7	3	0	1	0	0	0	0	0	0	0	0	0	0	0	0	0	0	0
2.2	0	5	1	4	3	0	3	0	0	0	0	0	0	0	0	0	0	0	0	0
2.4	6	2	3	4	1	0	0	0	0	0	0	0	0	0	0	0	0	0	0	0
2.6	1	0	3	4	3	0	0	0	0	0	0	0	0	0	0	0	0	0	0	0
2.8	2	2	1	2	1	0	0	0	0	0	3	0	0	0	0	0	0	0	0	6
3.0	2	5	1	0	1	0	0	0	0	0	0	0	0	0	0	0	0	0	0	0
3.2	8	0	0	0	0	3	0	0	0	0	0	0	0	0	0	0	0	0	0	0
3.4	1	0	3	0	0	0	0	0	0	0	0	0	0	0	0	0	0	0	0	0
3.6	1	0	0	2	3	0	0	0	0	0	0	0	0	0	0	0	0	0	0	0
3.8	0	0	1	0	0	0	0	0	0	0	3	0	0	0	0	0	0	0	0	0
4.0	1	0	0	0	0	0	0	0	0	0	0	0	0	0	0	0	0	0	0	6
4.2	1	2	0	0	0	0	0	0	0	0	0	0	0	0	0	0	0	0	0	0
4.4	0	0	1	0	0	0	0	0	0	0	0	0	0	0	0	0	0	0	0	0
4.6	0	0	0	0	0	0	0	0	0	0	0	0	0	0	0	0	0	0	0	0
4.8	0	0	0	0	0	0	0	0	0	0	0	0	0	0	0	0	0	0	0	0

$163° < l < 193°$ negative latitudes

$b°$	0→1	2	3	4	5	6	7	8	9	10	11	12	13	14	15	16	17	18	19	20
total	95	79	59	50	41	35	41	32	44	30	24	24	27	33	24	38	31	17	17	17
-0.4	0	0	0	0	0	0	0	0	0	0	0	0	0	0	0	3	0	0	0	0
-0.2	0	0	2	2	0	0	0	0	2	0	0	0	7	0	0	5	3	0	6	6
0.0	8	8	15	12	20	9	17	6	7	13	21	13	15	9	17	11	6	18	18	24
0.2	12	19	14	6	17	37	15	13	16	17	38	0	19	18	17	18	6	12	29	12
0.4	12	14	14	8	20	9	12	9	14	7	17	17	11	3	8	5	19	6	6	6
0.6	14	10	8	16	20	9	12	9	16	20	17	21	19	15	13	0	6	18	6	18
0.8	4	15	10	10	5	20	27	22	11	7	9	4	11	9	13	8	6	12	18	12
1.0	5	5	8	16	10	14	7	13	9	7	0	8	0	3	4	3	3	6	0	6
1.2	3	3	2	0	5	0	0	9	0	7	0	13	0	0	4	0	0	0	0	0
1.4	1	0	3	4	0	3	0	0	2	3	0	4	7	0	0	0	0	6	0	0
1.6	4	1	0	2	0	0	0	3	5	0	0	8	0	0	0	8	3	6	0	0
1.8	7	3	5	2	0	0	0	3	0	7	0	0	0	12	13	8	10	12	0	6
2.0	7	10	3	2	0	0	2	0	5	0	0	4	0	9	4	8	6	6	0	0
2.2	2	1	0	0	0	0	0	6	2	10	0	0	0	3	0	8	6	0	6	0
2.4	4	3	3	6	2	0	5	3	2	0	0	0	4	3	4	5	0	0	12	0
2.6	3	0	0	2	0	0	0	0	0	0	0	4	4	0	0	3	6	0	0	0
2.8	4	3	3	6	2	0	0	0	2	0	0	4	0	3	0	5	3	0	0	6
3.0	1	0	3	2	0	0	2	3	2	3	0	0	0	3	4	3	3	0	0	0
3.2	3	1	2	2	0	0	0	0	2	0	0	0	4	0	0	0	3	0	0	6
3.4	2	0	2	0	0	0	0	0	2	0	0	0	0	0	0	0	0	0	0	0
3.6	0	3	2	0	0	0	0	0	0	0	0	0	0	3	0	0	6	0	0	0
3.8	1	1	0	0	0	0	0	0	0	0	0	0	0	3	0	0	0	0	0	0
4.0	1	0	0	0	0	0	0	0	0	0	0	0	0	0	0	0	0	0	0	0
4.2	0	1	0	2	0	0	0	0	0	0	0	0	0	3	0	0	0	0	0	0
4.4	0	0	0	0	0	0	0	0	0	0	0	0	0	0	0	0	0	0	0	0
4.6	0	0	0	0	0	0	0	0	0	0	0	0	0	0	0	0	0	0	0	0
4.8	0	0	0	0	0	0	0	0	0	0	0	0	0	0	0	0	0	0	0	0

$275° < l < 305°$ positive latitudes

$b°$	0→1	2	3	4	5	6	7	8	9	10	11	12	13	14	15	16	17	18	19	20
total	510	424	346	218	186	138	118	90	73	64	54	41	42	47	34	34	32	19	19	24
-0.4	0	0	0	0	0	0	1	0	0	0	0	0	0	0	0	0	0	0	0	0
-0.2	0	1	0	0	1	0	3	1	0	2	4	2	5	4	3	0	0	0	0	0
0.0	2	3	4	7	6	4	10	13	10	9	11	7	7	9	15	12	16	26	16	4
0.2	4	8	8	11	9	12	12	20	15	22	15	27	29	34	21	24	19	32	32	21
0.4	5	7	10	7	9	12	9	9	14	9	9	7	7	9	9	15	13	0	0	13
0.6	11	14	14	17	17	15	18	20	21	20	19	10	14	13	15	3	13	32	16	29
0.8	19	20	25	21	23	19	18	19	21	20	9	17	24	13	18	32	22	5	32	21
1.0	19	17	16	17	22	22	14	8	10	14	22	15	5	13	6	6	6	5	5	8
1.2	12	13	11	11	9	7	9	3	4	2	9	5	5	0	6	0	3	0	0	0
1.4	6	6	5	4	1	7	3	4	1	0	0	2	2	0	3	0	3	0	0	0
1.6	4	2	3	3	1	0	1	1	1	0	0	0	0	0	3	6	0	0	0	0
1.8	3	1	1	2	1	1	1	0	1	0	0	0	0	4	0	0	0	0	0	0
2.0	3	2	0	0	0	1	0	0	0	0	0	0	2	0	0	3	3	0	0	0
2.2	3	0	1	0	0	1	0	0	0	2	0	5	0	2	0	0	0	0	0	0
2.4	1	1	0	0	0	0	0	0	0	0	2	0	0	0	3	0	3	0	0	4
2.6	1	0	0	0	1	0	0	0	0	0	0	0	0	0	0	0	0	0	0	0
2.8	2	0	0	0	0	1	0	0	1	0	0	0	0	0	0	0	0	0	0	0
3.0	0	1	0	0	0	0	0	1	0	0	0	0	0	0	0	0	0	0	0	0
3.2	1	1	1	0	0	0	1	0	0	0	0	2	0	0	0	0	0	0	0	0
3.4	1	0	0	0	0	0	0	0	0	0	0	0	0	0	0	0	0	0	0	0
3.6	1	0	0	0	1	0	0	0	0	0	0	0	0	0	0	0	0	0	0	0
3.8	1	0	0	0	0	0	0	0	0	0	0	0	0	0	0	0	0	0	0	0
4.0	0	0	0	0	1	0	0	0	0	0	0	0	0	0	0	0	0	0	0	0
4.2	0	0	0	0	0	0	0	0	0	0	0	0	0	0	0	0	0	0	0	0
4.4	0	0	0	0	0	0	0	0	0	0	0	0	0	0	0	0	0	0	0	0
4.6	0	0	0	0	1	0	0	0	0	0	0	0	0	0	0	0	0	0	0	0
4.8	0	0	0	0	0	0	0	0	1	0	0	0	0	0	0	0	0	0	0	0

$275° < l < 305°$ negative latitudes

$b°$	0→1	2	3	4	5	6	7	8	9	10	11	12	13	14	15	16	17	18	19	20
total	612	577	459	330	261	224	140	144	111	90	77	80	66	59	62	60	42	42	34	35
-0.4	0	0	0	0	0	0	0	0	0	0	0	0	0	0	0	0	0	0	0	0
-0.2	0	0	0	0	0	1	1	0	1	1	1	3	0	2	0	2	5	0	6	9
0.0	1	2	4	5	5	9	9	10	10	10	16	11	15	24	10	15	17	21	24	11
0.2	2	2	3	6	10	12	11	20	17	12	18	14	21	19	21	20	26	24	24	23
0.4	3	5	6	10	8	9	6	10	12	12	3	8	14	14	6	7	10	17	6	11
0.6	8	10	14	18	18	20	19	18	17	19	16	25	18	10	11	8	14	17	9	29
0.8	10	15	20	23	19	20	27	20	15	26	22	16	23	12	18	15	12	7	6	11
1.0	14	18	20	19	21	16	14	17	15	10	17	19	6	10	13	7	10	10	12	6
1.2	15	12	12	8	7	5	5	5	5	2	5	1	0	5	2	3	2	5	3	0
1.4	9	7	5	2	4	2	2	1	1	1	1	3	3	0	0	0	0	0	3	0
1.6	6	5	4	2	2	1	1	1	1	3	0	0	0	0	5	5	0	0	0	0
1.8	5	6	2	1	1	1	1	1	2	2	1	0	0	3	5	3	0	0	0	0
2.0	3	2	1	1	1	0	2	0	0	0	0	0	0	0	2	5	0	0	6	0
2.2	3	3	1	2	0	0	1	0	0	0	0	1	0	0	0	0	0	0	0	0
2.4	3	1	2	0	0	0	1	0	1	0	0	0	0	2	2	3	0	0	0	0
2.6	3	2	1	0	0	0	0	1	2	1	0	0	0	0	0	3	0	0	0	0
2.8	2	2	0	0	0	0	0	0	0	0	0	0	0	0	2	0	5	0	0	0
3.0	2	1	1	1	0	0	0	0	2	0	0	0	0	0	2	0	0	0	3	0
3.2	3	1	0	0	0	0	0	0	0	0	0	0	0	0	0	0	0	0	0	0
3.4	1	1	0	0	0	0	0	0	0	0	0	0	0	0	0	2	0	0	0	0
3.6	1	2	0	0	0	1	1	0	0	0	0	0	0	0	5	2	0	0	0	0
3.8	2	1	0	0	0	0	0	0	0	0	0	0	0	0	0	0	0	0	0	0
4.0	1	1	0	0	0	0	1	0	0	0	0	0	0	0	0	0	0	0	0	0
4.2	1	1	0	1	1	0	0	0	0	0	0	0	0	0	0	0	0	0	0	0
4.4	0	0	0	0	0	0	0	0	0	0	0	0	0	0	0	0	0	0	0	0
4.6	0	0	0	0	0	0	0	0	0	0	0	0	0	0	0	0	0	0	0	0
4.8	0	0	0	0	0	0	0	0	0	0	0	0	0	0	0	0	0	0	0	0

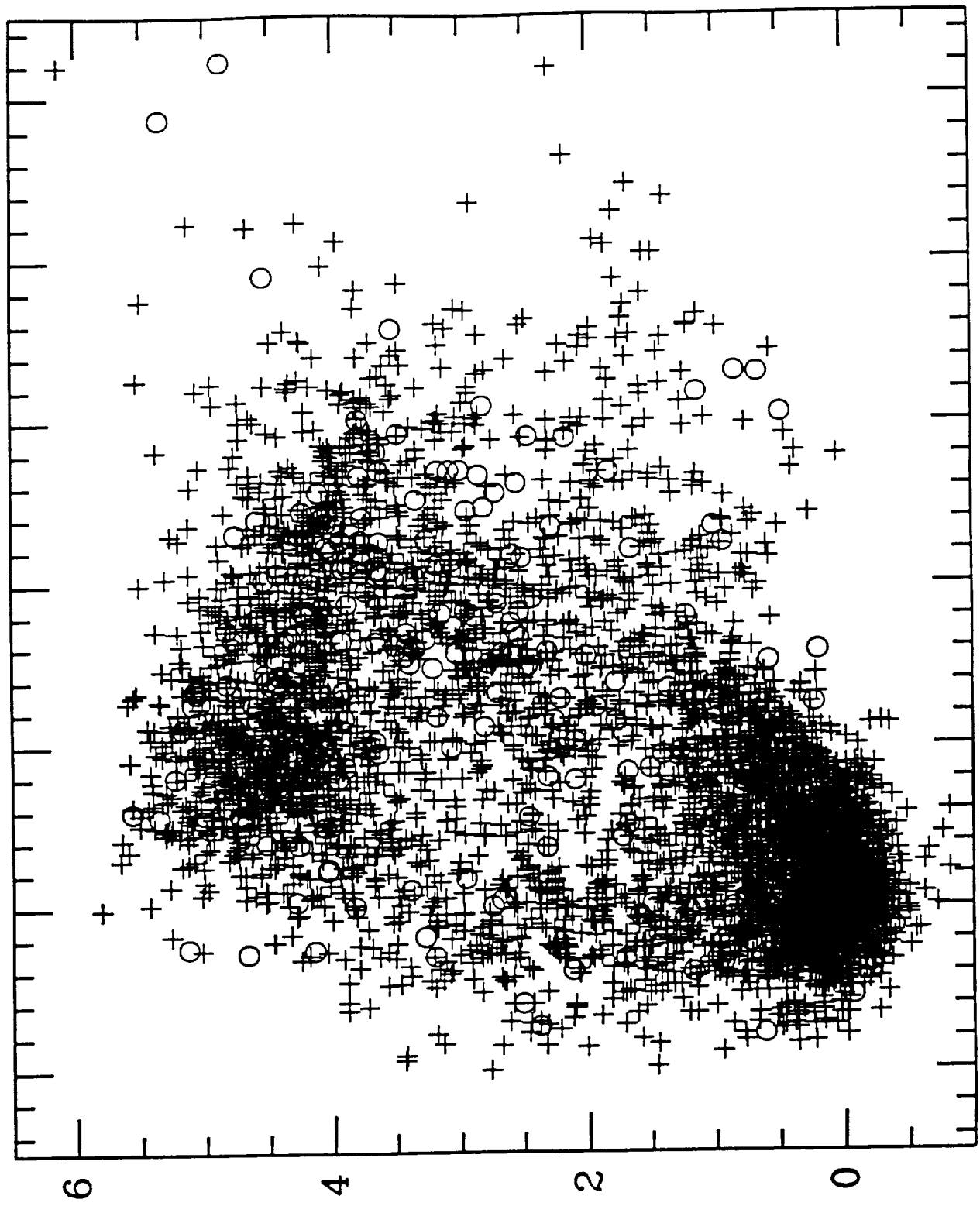

FIG. 1a

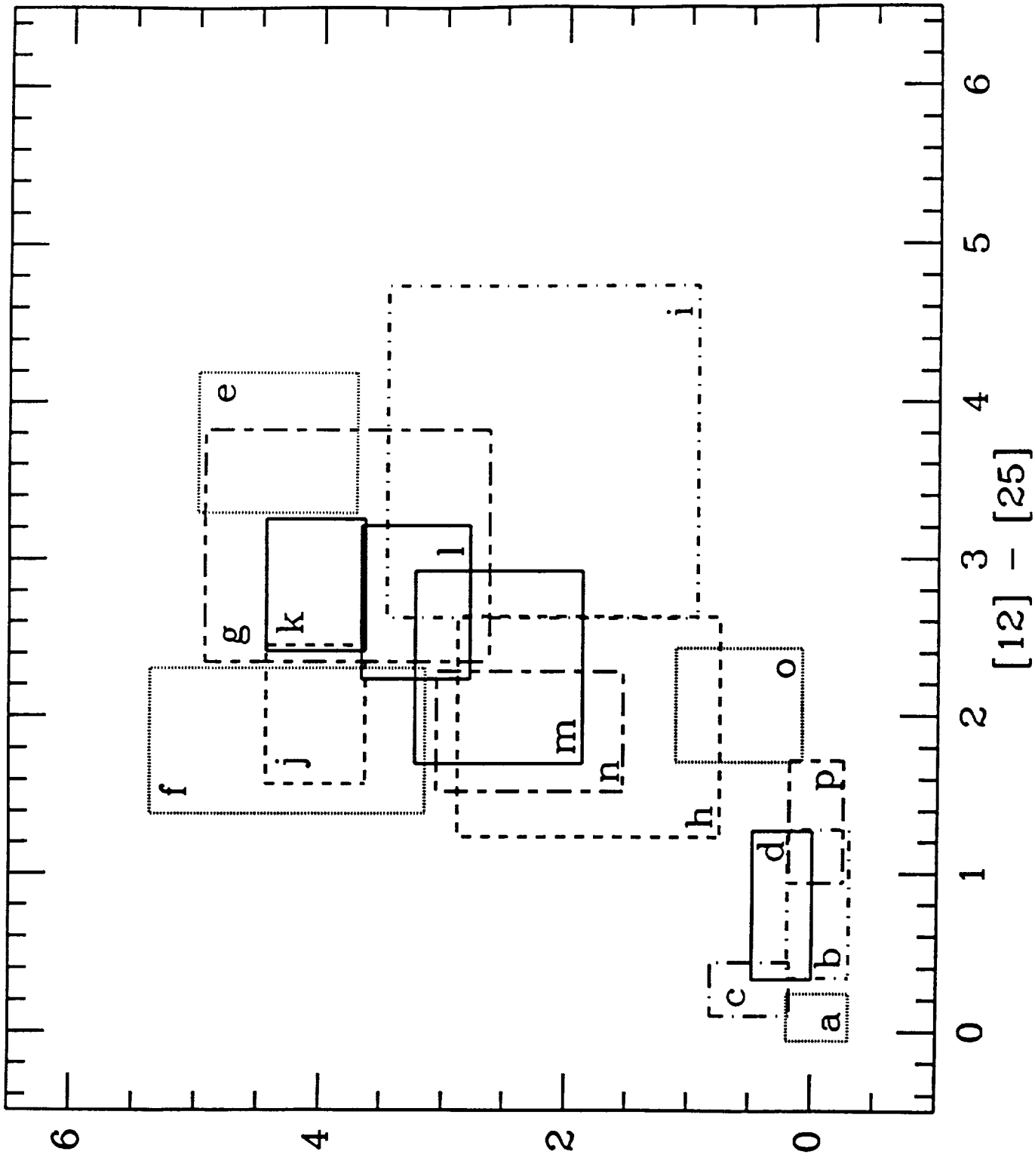

FIG. 1b

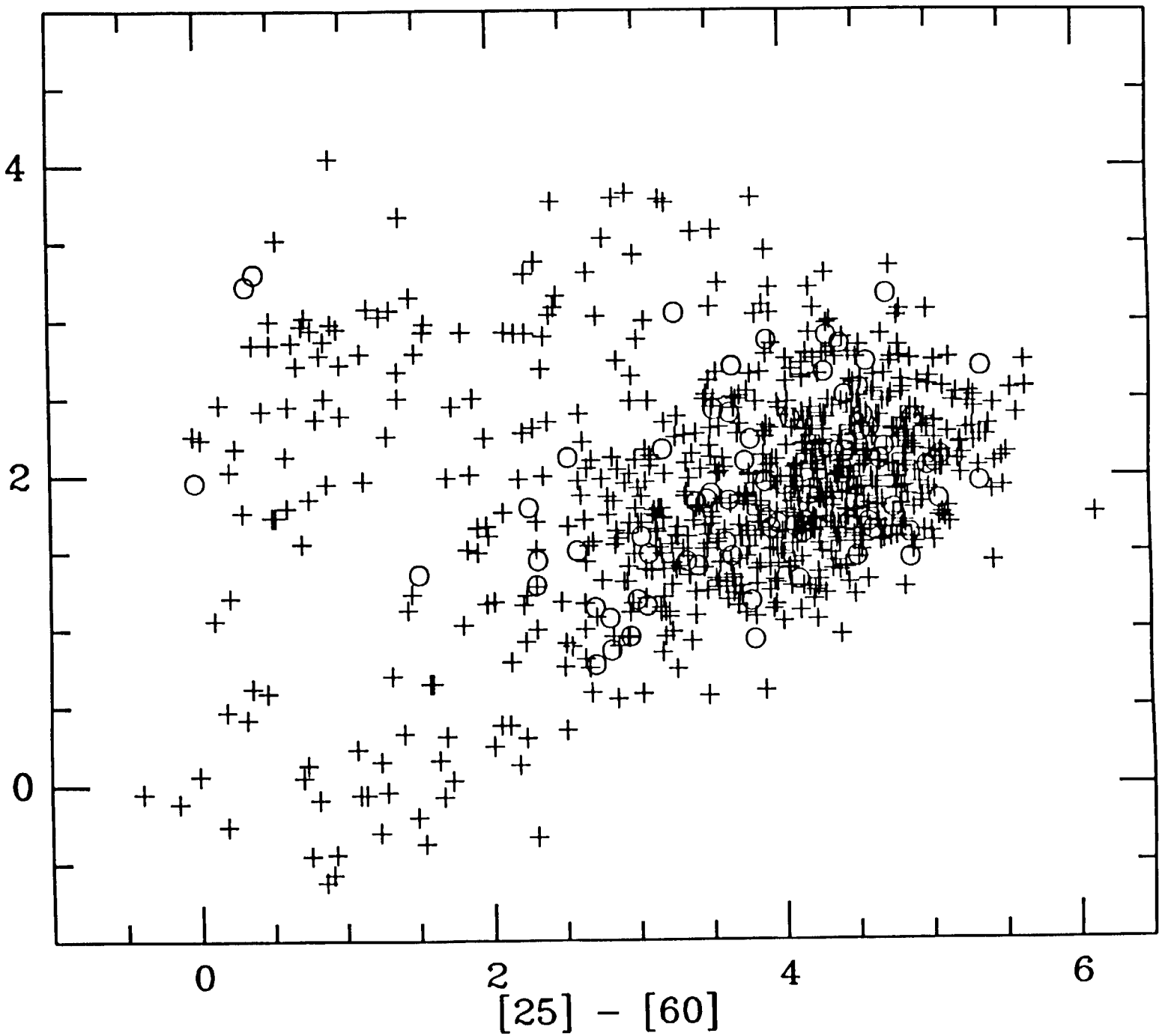

FIG. 2a

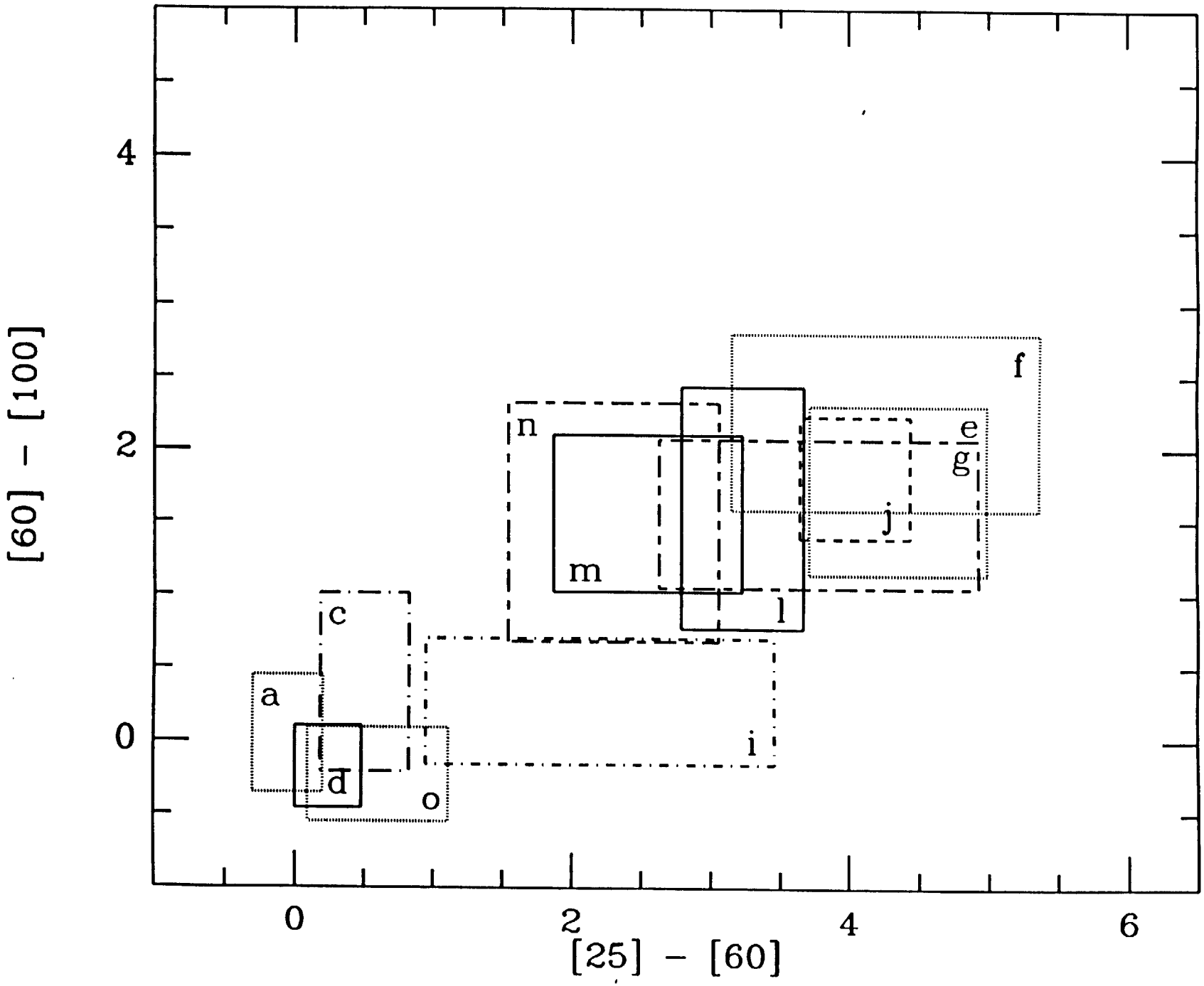

FIG. 2b

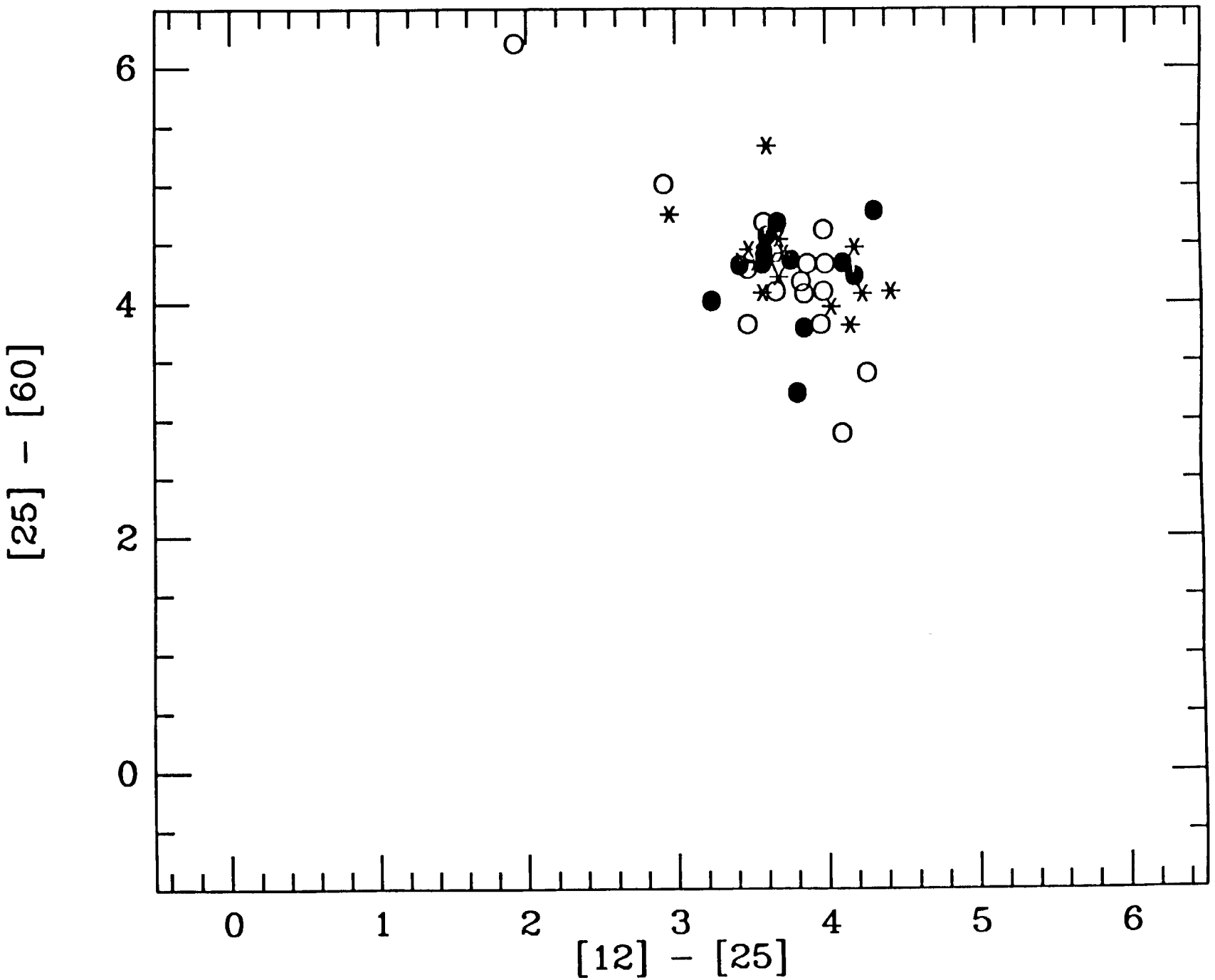

FIG. 3

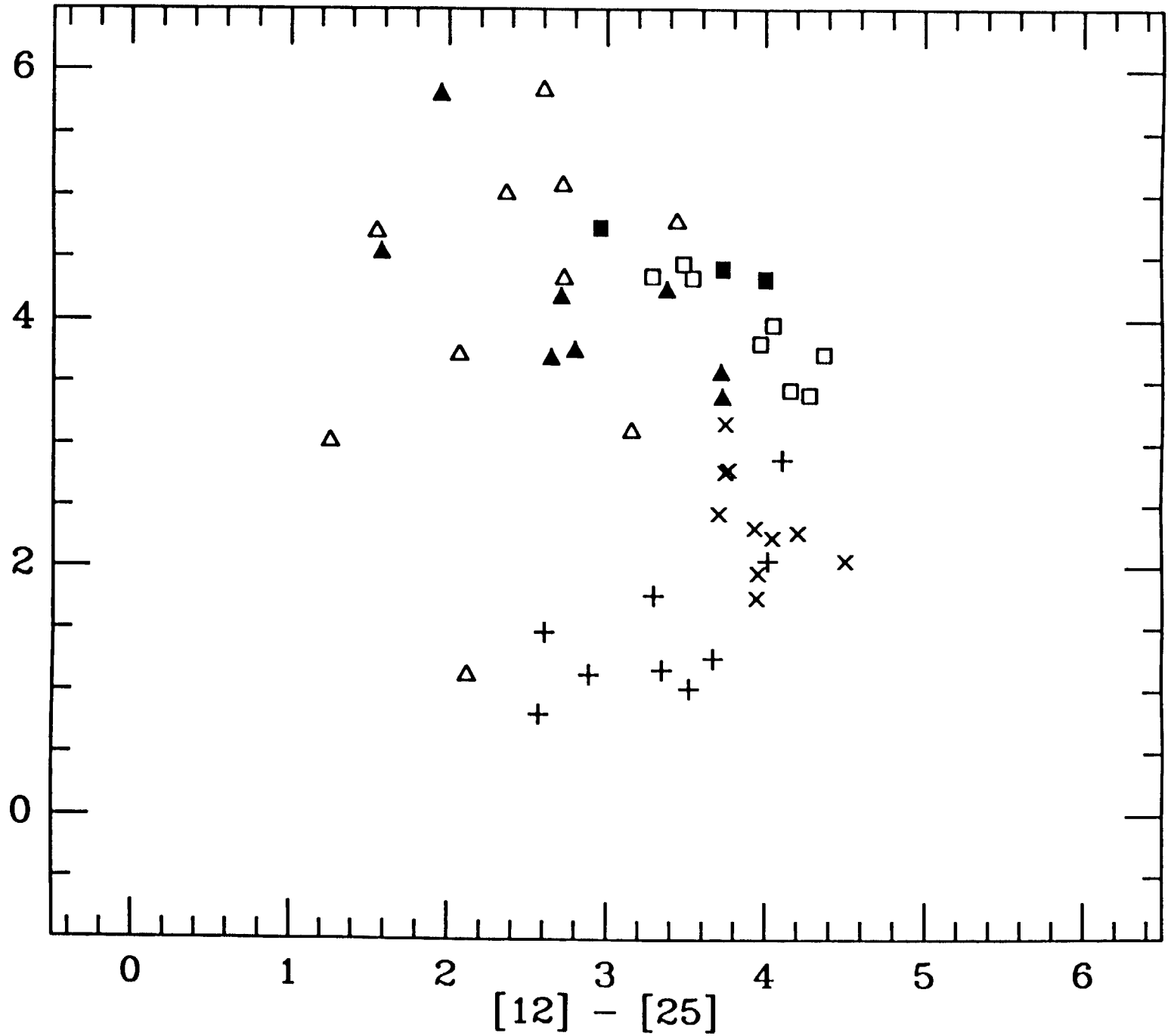

FIG. 4

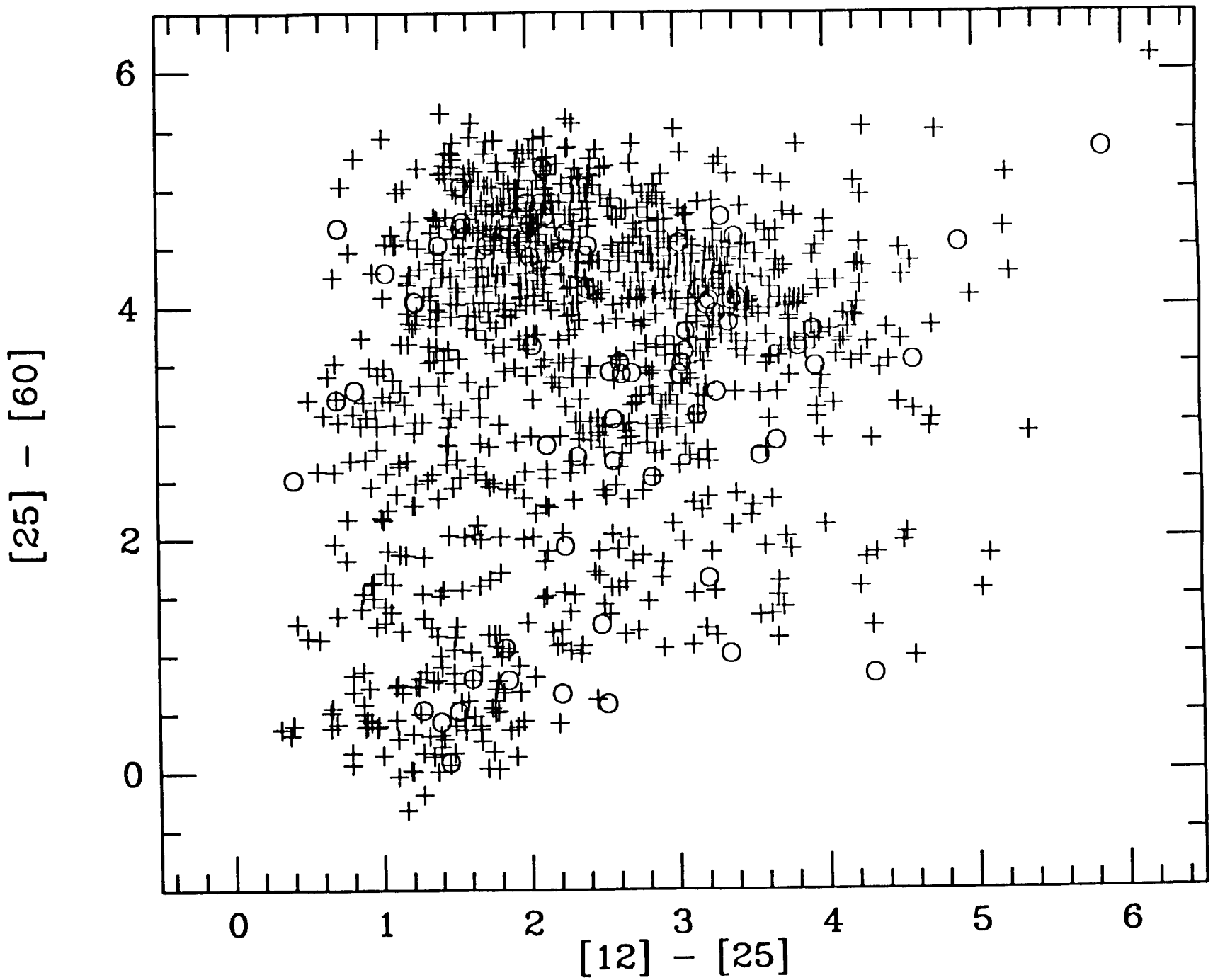

FIG. 5a

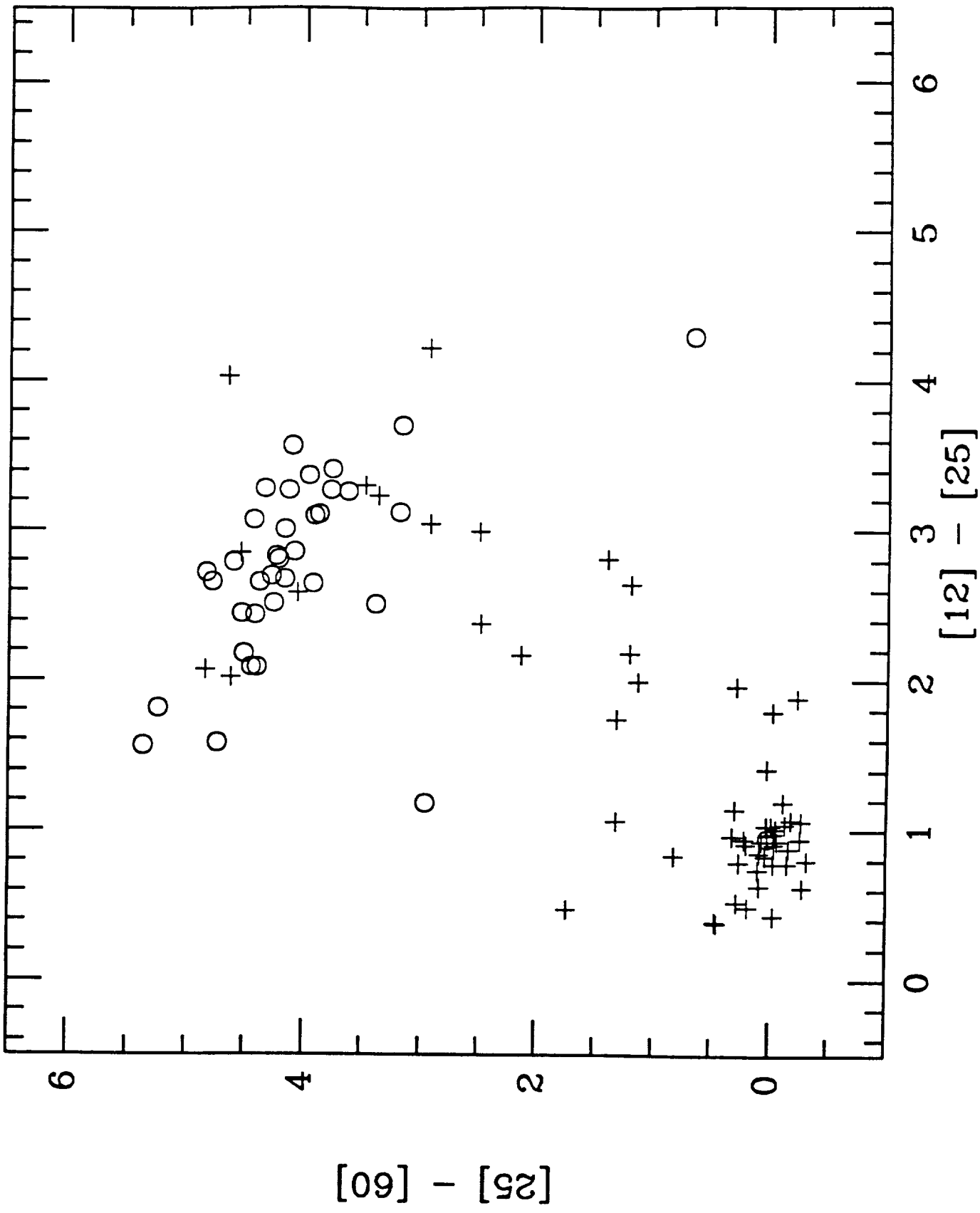

FIG. 5b

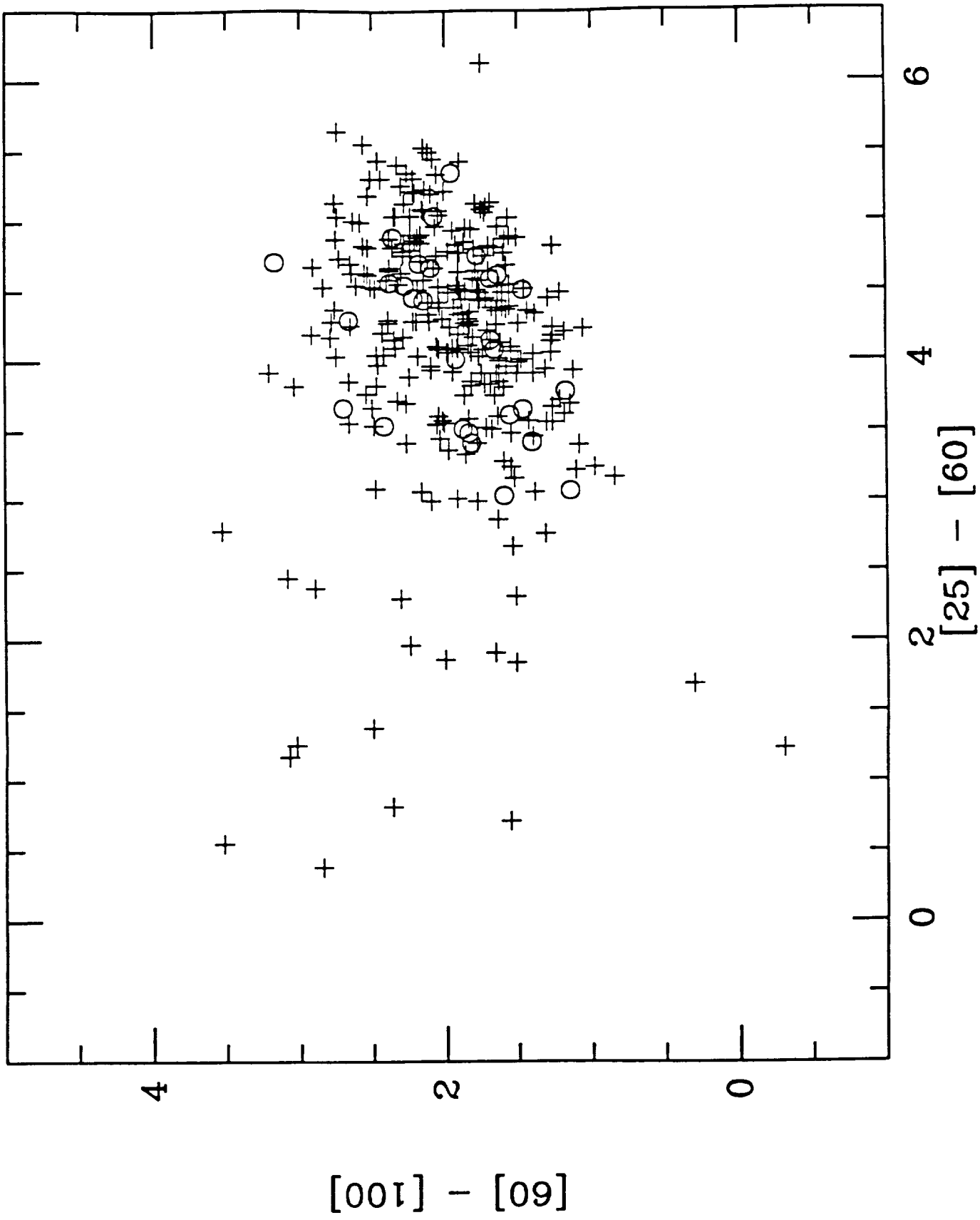

FIG. 6a

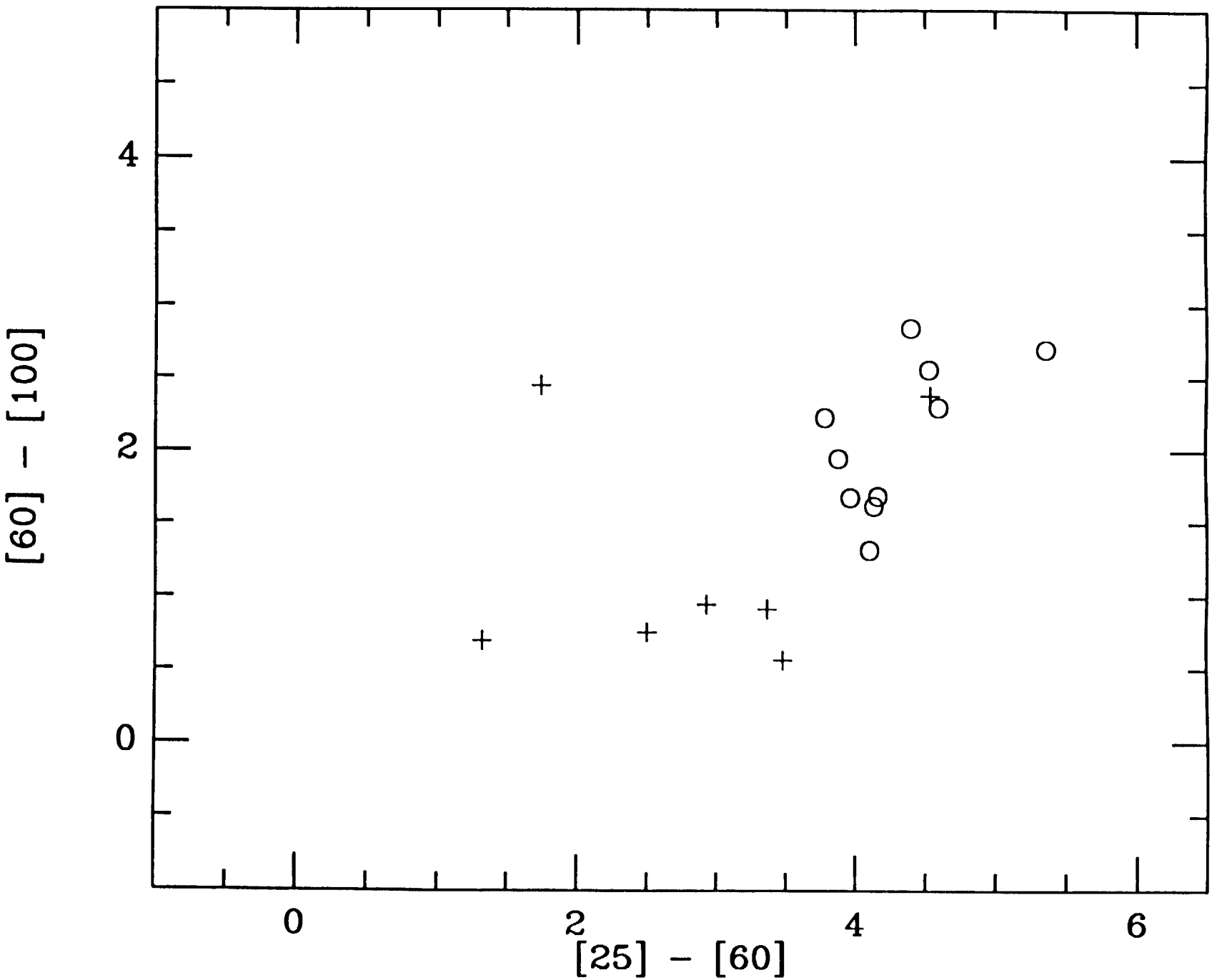

FIG. 6b

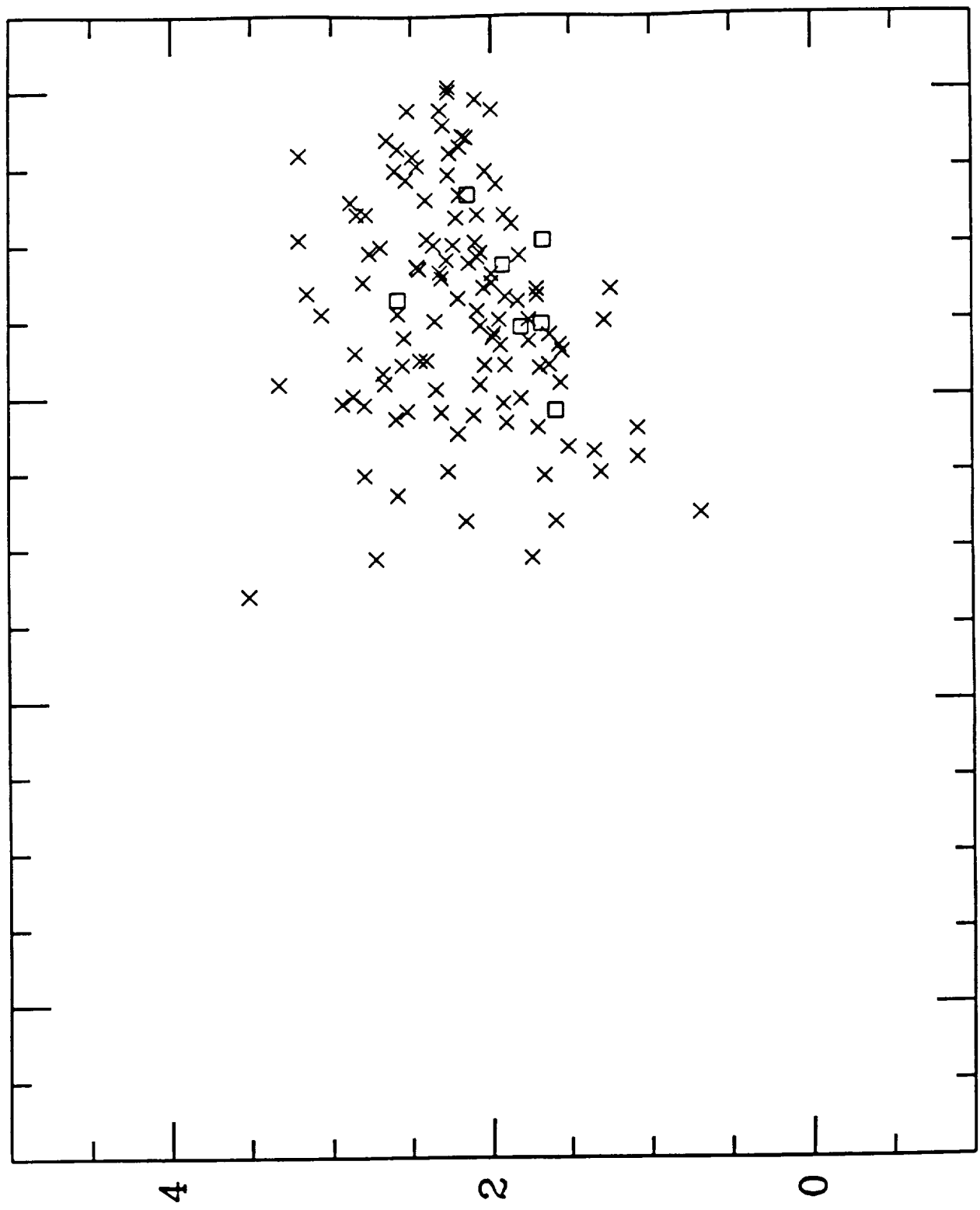

FIG. 7a

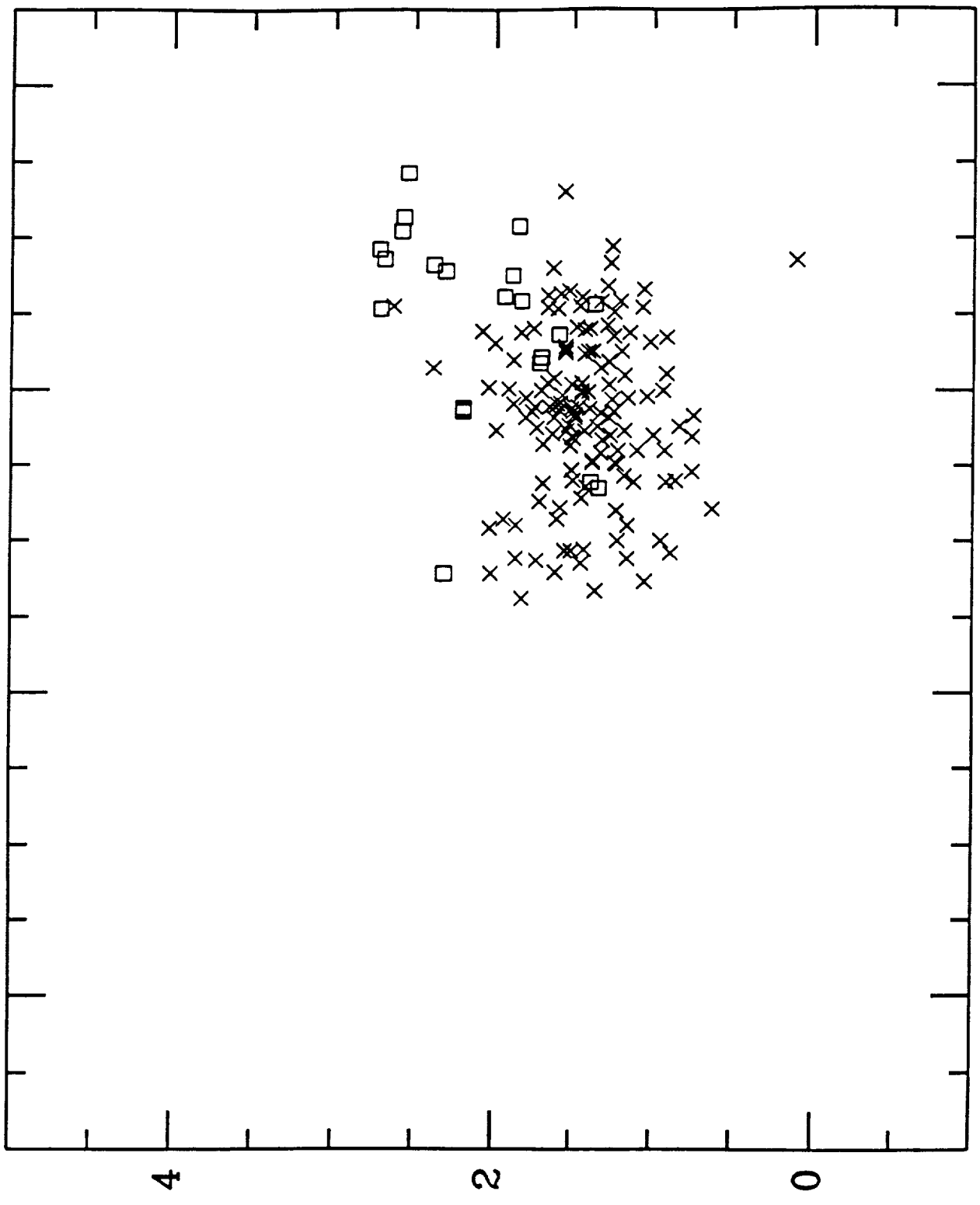

FIG. 7b

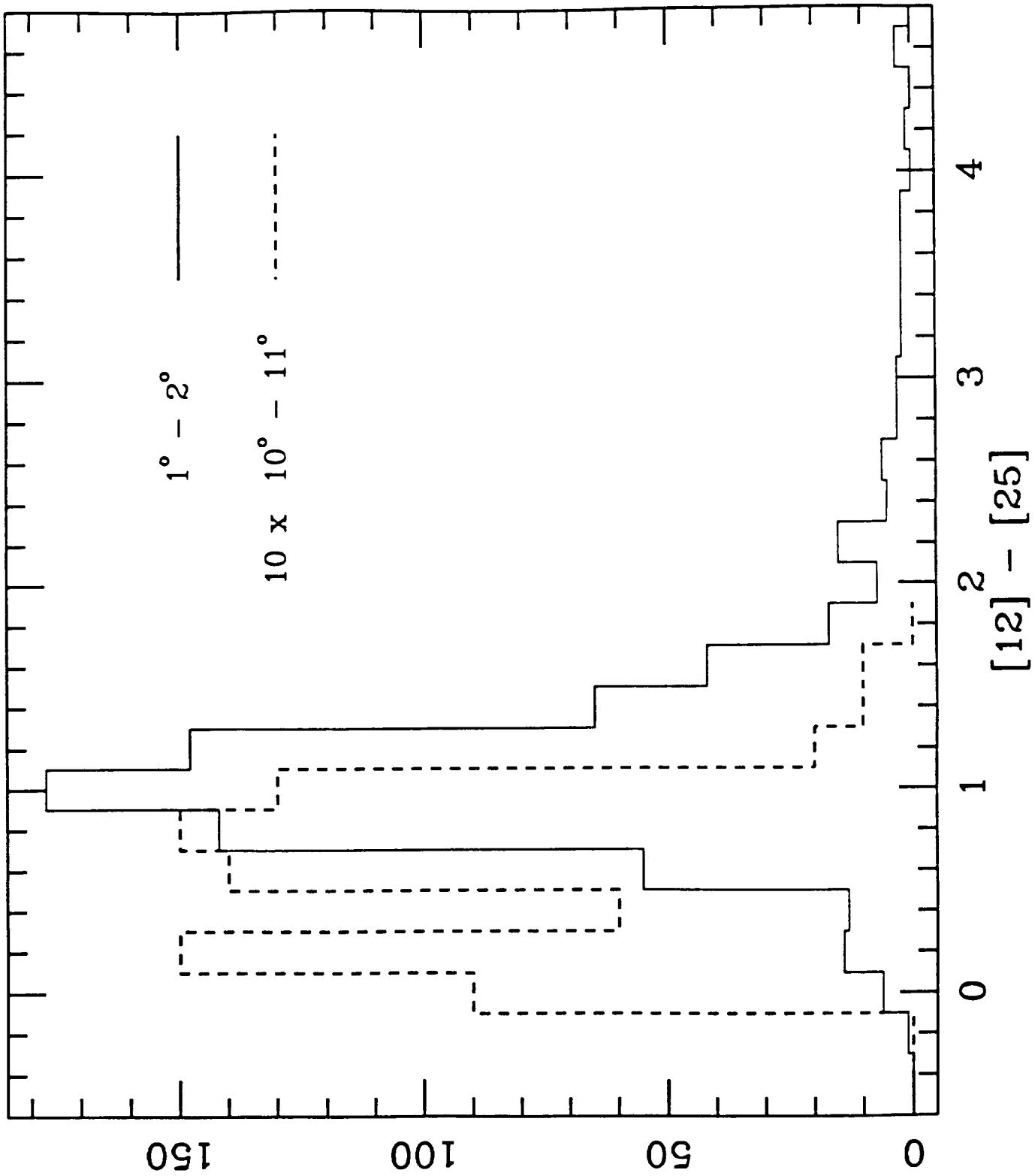

FIG. 8

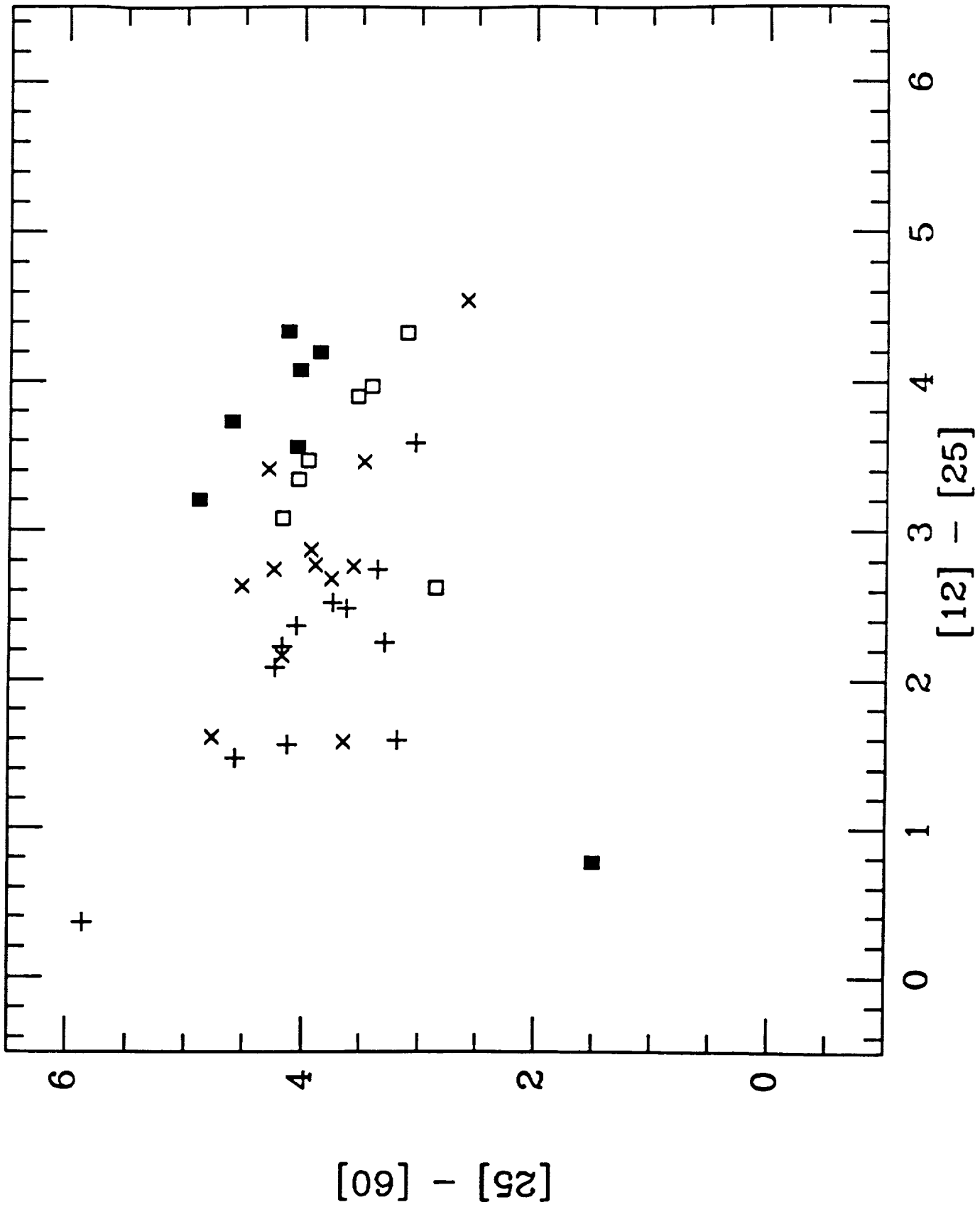

FIG. 9

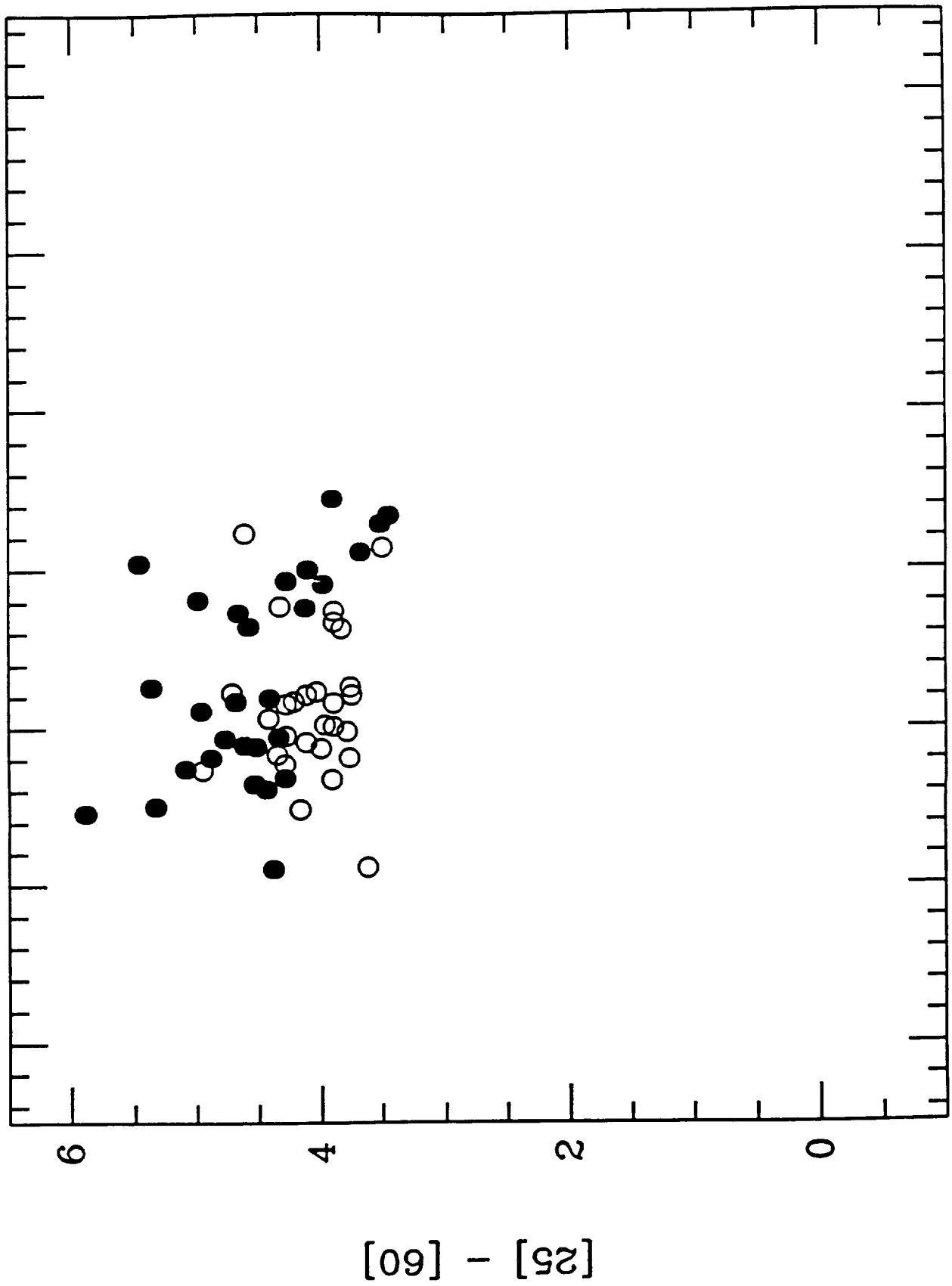

FIG. 10a

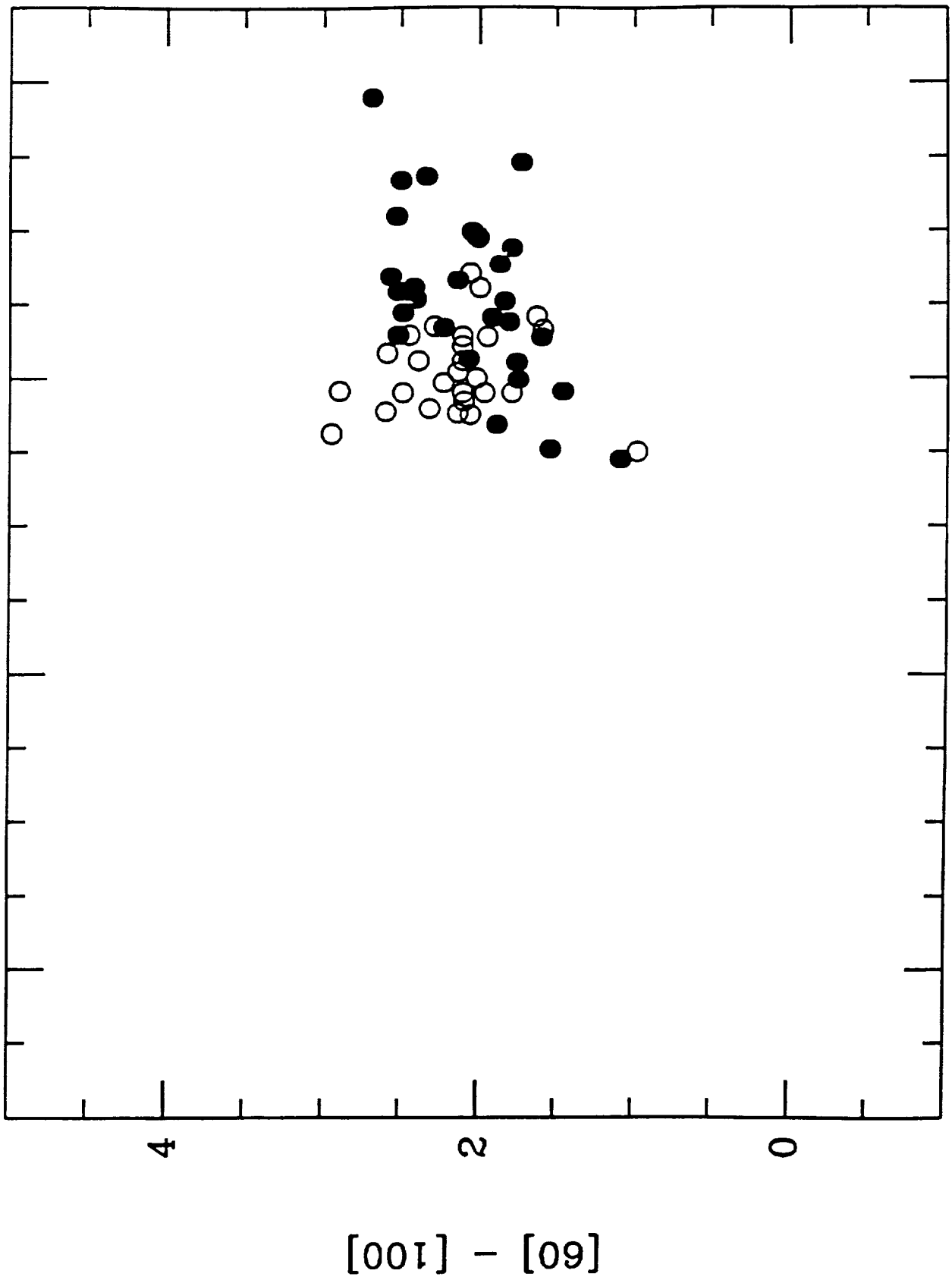

FIG. 10b

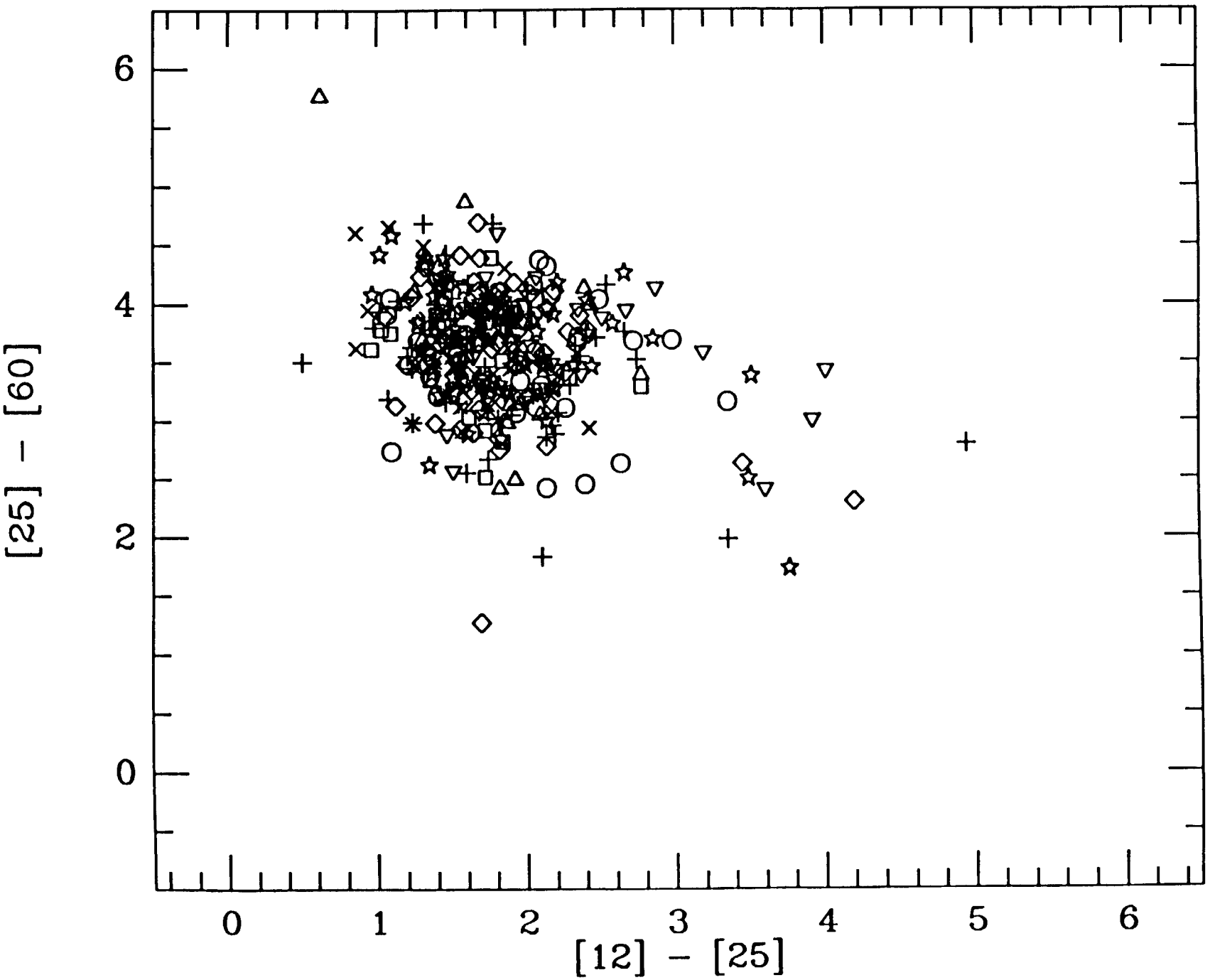

FIG. 11

APPENDIX E. "On the Calibration of the IRAS Low Resolution Spectra"

On The Calibration Of The IRAS Low-Resolution Spectra

Kevin Volk

NASA Ames Research Center, Moffett Field, California 94035

and

SETI Institute, 101 First Street #410, Los Altos, California 94022

Martin Cohen

Jamieson Science and Engineering, Inc., 5321 Scotts Valley Drive, Suite 204,

Scotts Valley, California 95066

and

Radio Astronomy Laboratory, University Of California, Berkeley, California 94720

Abstract

We have investigated the absolute calibration of the IRAS *Catalogue of Low-Resolution Spectra* by comparing blackbodies with the LRS spectra of normal stars. For most stars earlier than K3, the LRS spectra are too blue to fit with blackbodies. We attribute this problem to the substitution of α Tau (K5 III) for α Lyr (A0 V) as the primary calibration standard when it was discovered that α Lyr had circumstellar dust. The LRS data seem to be more reliable for determining spectral shape than for setting photometric levels. Relative correction factors for the individual LRS data points have been derived from a sample of bright, generally early-type, stars with known effective temperatures, radii, and distances. Using these correction factors, color temperatures have been determined for 72 bright normal stars with spectral types from B8 Ia to M7 III. We find that the K-type giants have a wide range of color temperatures from values similar to their effective temperatures (e.g. for α Boo (K1 III)) to values near 2000 K (e.g. for α Tau). There is some indication from the normal stars that the correction factors depend upon the flux density level. A comparison of the corrected spectra of a number of much cooler sources with observations in the literature shows that the corrections apply to sources of all color temperatures.

I. Introduction

In 1983 the *Infrared Astronomical Satellite* (IRAS)[1] surveyed the infrared sky. In addition to photometric observations, IRAS provided low-resolution spectra from about 8 to 23 μm using a slitless spectrometer. The spectra were observed in two sections, a blue section from 8 to 15 μm with resolution $\lambda/\Delta\lambda \sim 40$ and a red section from 13 to 23 μm with resolution ~ 20. The observations were recorded for any source brighter than $\sim$2 Jy at 12 μm or 25 μm. The "better quality" spectra were collected into the IRAS *Atlas of Low-Resolution Spectra* (1986, hereafter the Atlas) which contains the average spectra of 5425 objects. However these spectra are only a small part of the full set of observations. The database of all the spectra extracted from the raw data-stream contains $\sim$170000 individual spectral scans for a total of $\sim$50000 sources. This 'LRS database' contains many good spectra which were not included in the Atlas. Sources were excluded if the individual spectra did not agree well enough to satisfy the criteria for this Atlas, for example if, during the data extraction, the wrong bank of detectors was interrogated so that part of the spectrum was missed. Other sources appear to have had a change in the spectral character between observations, presumably due to real variability. The slitless spectrometer was unsuitable for observing closely spaced sources unless they were oriented perpendicular to the scan direction, because the spectral scans would overlap with a wavelength shift due to the spatial separation of the sources.

While great caution must be exercised in using the LRS database spectra it clearly includes many useful spectra. We discuss the calibration of the LRS spectra based upon a study of "normal" stars observed by IRAS. Corrections must be applied to Atlas or LRS database spectra to give the proper spectral shape. These corrections are probably

[1] The *Infrared Astronomical Satellite* was developed and operated by the U.S. National Aeronautics and Space Administration (NASA), the Netherlands Agency for Aerospace Programs (NIVR), and the U.K. Science and Engineering Research Council (SERC).

the result of the use of α Tau in the place of α Lyr as the primary standard for the flux calibration of the LRS, a substitution that occurred early in the IRAS mission after it was found that α Lyr had an infrared excess. We find that corrections of the order of $\pm 15\%$ must be made to the LRS spectra.

First, we discuss the need for corrections to the LRS spectra based upon the study of a number of normal stars observed by IRAS. Bright stars such as α CMa were found to have spectra that were not consistent with blackbody sources. This effect was generally observed in sources earlier than about K3. In Sec. II we describe an attempt to correct the LRS spectra by changing the blackbody calibration temperature for α Tau, which was assumed to be a 10^4 K blackbody source for the original LRS flux calibration. We find that an anomalously low color temperature must be assumed for α Tau to produce reasonable results for earlier type stars. Section III treats corrections based upon a set of stars with well-determined effective temperatures. These corrections and the resulting color temperatures for $\sim$70 stars with Atlas spectra are discussed in the final section.

II. The LRS Calibration

a) Definition Of The Problem

As part of a project to produce a star-count model for the 8 to 25 μm wavelength range, we have studied the LRS spectra of many types of sources. We required an absolute calibration at each of the individual spectral wavelengths; in effect we considered each point as the result of an observation with a narrow-band filter. This led us to analyze the LRS spectra of ordinary stars, especially those of early spectral type. Our results indicate that the original absolute flux calibration of the LRS data is incorrect.

Each source in the Atlas is assigned a class based upon the presence of features in the spectrum and the spectral index of the continuum. About 40% of the sources are classed as types 10–19, the 'featureless' spectra attributed to stars of spectral classes earlier than

M5. However, many of the 2238 spectra in Atlas classes 10–19 sources are misclassified, in the sense that they are not featureless *photospheric* spectra. In some cases, weak features can be seen in the spectra. For others it is not clear whether there are any features but the spectra are of low spectral index α, defined by

$$F_\lambda \propto 1/\lambda^\alpha,$$

and do not resemble stellar blackbodies. The 943 Atlas sources in classes 10–15, with $\alpha < 3$ where a Rayleigh-Jeans spectrum has a value of 4, are probably all sources with circumstellar material. It is likely that many or all of the 390 class 16 Atlas sources are also not stellar blackbody sources. The 905 Atlas sources of classes 17, 18, and 19 all have associations to stars in the *Smithsonian Astronomical Observatory Catalog* (1966), the *Bright Star Catalogue* (Hoffleit 1982), or the *General Catalogue of Variable Stars* (Kukarkin *et al.* 1970). Most of the sources are ordinary stars with types ranging from late-B to M7. Only a few of these sources have spectral types earlier then K0, fewer still of which are main sequence stars. (There are also a few carbon stars and other sources which are known to have small amounts of circumstellar material with LRS classifications of 17–19.) For a check of the calibration the early-type stars are preferred because (1) the effective temperatures are better determined than for late-type stars and (2) they are less likely to be subject to molecular opacity effects in the infrared. In this paper the term 'early-type stars' refers to stars earlier than K0.

Only a limited number of bright early-type stars are available for calibration of the LRS spectra. Only 4 early-type stars have $F_\nu(12\ \mu m) > 100$ Jy: 05130+4556 = α Aur (G6 III + F9 III), 06228−5240 = α Car (F0 II), 06429−1639 = α CMa (A1 V), and 14359−6037 = α Cen (G2 V + K1 V). To allow an accurate calibration the early-type stars must be bright because the spectrum falls so steeply from 8 to 23 μm. Most of the bright Atlas class 17–19 sources are stars with types K0 III to M5 III. There are only 18 early-type Atlas sources with $F_\nu(12\ \mu m) > 24$ Jy, two of which are variable stars and therefore were excluded from the calibration: 15465+2818 = R CrB (G0 Iep) with a class 15 Atlas

spectrum; and 19132−3336 = RV Tau (G0 Ipe) with a class 16 Atlas spectrum. An oddity of the Atlas classification is that α Cen is assigned to class 21 because of noise in the spectrum near 10 μm. The LRS database does not expand the set of potential calibration sources because no early-type star brighter than 24 Jy at 12 μm, corresponding to V $\lesssim$ 2, is missing from the Atlas.

Our original idea was to use α CMa as a check on the IRAS calibration. It is the brightest star of spectral type near A0 with an Atlas spectrum and shows little sign of an infrared excess similar to that of α Lyr. α CMa does have a small 100 μm excess compared with a 10^4 K blackbody, but that could be due to contamination from infrared cirrus. During our study of α CMa, we became aware of a problem with the LRS calibration. The Atlas spectrum of α CMa is shown in Figure 1 along with a Rayleigh-Jeans function normalized to the data at 12 μm. No blackbody or combination of blackbodies can rise more rapidly than the Rayleigh-Jeans function yet the Atlas spectrum does. Subsequent tests on other early-type stars showed that this effect applied to them too, and even to some early K-type giant stars such as α Boo = 14133+1925 (K1 III).

The discrepancy between the observations and a blackbody is clarified when the spectrum is multiplied by λ^4 to emphasize the temperature dependent part of the blackbody function. Such a plot is shown for α CMa in Figure 2 along with a 10100 K blackbody spectrum, normalized as in Figure 1. On such a plot, an infinite temperature blackbody would give a horizontal line and lower temperature blackbodies would give curves with positive slope. Although the red spectrum of Sirius is noisy, one clearly sees a negative slope. It is impossible to fit a blackbody to the observations. We do not know of an opacity source that would produce this type of effect.

Figure 3 compares the IRAS observations of Sirius and photometry at shorter wavelengths with a blackbody source of the same radius, luminosity, and distance as Sirius. The effective temperature of Sirius was taken as 10100 K (Bell and Dreiling 1981). The observed angular diameter of Sirius, $(5.89 \pm 0.16) \times 10^{-3}$ arcseconds (Hanbury Brown, Davis,

and Allen 1974, corrected for limb-darkening), and the parallax of 0.377 ± 0.004 " (Gliese 1969) were used to fix the blackbody flux densities. Although the blackbody matches the near infrared observations reasonably well, the Atlas spectrum of Sirius is steeper than the blackbody. One also sees a discrepancy between the color-corrected 12 μm flux density from the IRAS *Point Source Catalogue* (1988) and the Atlas 12 μm flux density. From the 12 μm photometric value, 143.1 Jy, and a color correction of 1.45, the predicted F_λ value is 2.05×10^{-12} $Wm^{-2}\mu m^{-1}$, compared with 2.63×10^{-12} $Wm^{-2}\mu m^{-1}$ at 12.026 μm in the LRS spectrum. The Atlas flux density is 30% higher than the photometry implies. Generally the IRAS spectra and photometry agree to within 10% but we have found other examples of significant discrepancies.

We do not understand the cause of this photometric unreliability but we urge that the LRS spectra be used only to determine spectral shape and not to set absolute levels of flux density.

b) LRS Corrections Using α Tau

When we tried to fit a blackbody function to the Atlas spectra for the early-type stars only β Ori = 08121−0815 could be successfully fit. The others behave like α CMa. When we examined the Atlas spectra for later-type bright sources, the best fit for α Tau was for an 8900 K blackbody, although IRAS is not very sensitive to the temperatures above 7000 K. The effective temperature of α Tau is near 3900 K (Di Benedetto and Conti 1983). The most likely explanation for this discrepancy is that, in the original flux calibration of the LRS, α Tau was assumed to radiate as a 10000 K blackbody, in place of α Lyr, because the data reduction system was in place before the satellite was launched. (This assumption is alluded to in the IRAS *Explanatory Supplement* (1988), page IX–6: 'In order to determine the factor for conversion of sample values into flux densities, the observed spectra of α Tau were compared with a black body spectrum of 10000 K.'.)

In our first attempt to correct the spectra, we assumed that α Tau should have an

infrared color temperature of 3600 K blackbody, slightly below its effective temperature. That behaviour of the color temperature is observed in the infrared for the Sun (Peirce and Allen 1977) and α Lyr (Blackwell *et al.* 1983). This correction was not sufficient to match the LRS spectra of the early-type stars to blackbody sources. All the spectra were still too blue, by less than when uncorrected, but by more than the stated LRS uncertainties could explain. By trial and error we found that the color temperature of α Tau had to be reduced to below 2000 K before even remotely reasonable color temperatures were obtained for the early-type stars.

These blackbody fits indicated that in the early K-types there is a change in LRS spectra from a relatively high color temperatures (e.g., the case of α Boo) to a lower color temperature (e.g., α Tau). The early K-type giants divided more or less evenly between these two groups. We do not know why this division exists; perhaps an extended atmosphere or stellar mass loss lowers the color temperature by creating cool circumstellar envelopes. The difference in effective temperature between K0 to K5 is estimated to be no more than 300 K, which makes the dual character of the LRS spectra even more puzzling.

c) Corrections Using Stars Of Known Temperature

Our second attempt to correct the LRS spectra involved 12 stellar systems with well-determined effective temperatures, two of them binaries with relatively bright secondaries. We required: 1) an Atlas spectrum of class 18 (save for α Cen); 2) that the stars be among the brightest of their spectral type observed by IRAS (the late-type stars are much brighter than the early-type stars); and 3) directly determinable radii and effective temperatures. For Vega and Sirius the effective temperatures were taken from model atmosphere fits (Dreiling and Bell 1980; Bell and Dreiling 1981). For the other systems effective temperatures were directly determined from angular diameter measurements (Hanbury Brown, Davis, and Allen 1974; Di Benedetto and Conti 1983; Di Benedetto and Foy 1986) and total flux observations (Blackwell and Shallis 1977). For α Aur the effective temperatures

and radii were taken from Ayres and Linsky (1980) because the components are too close for individual flux observations, while for α Cen the luminosity values from Demarque, Guenther, and van Altena (1986) were combined with the observed radii to derive the effective temperatures of the components. The distances to the systems were taken from the *Catalogue Of Nearby Stars* (Gliese 1969) or from the *Bright Star Catalogue* (Hoffleit 1982). The adopted values are listed in Table 1. For each system, the observations were compared with blackbodies of proper luminosity and radius at the distance of the system (e.g., see Fig. 3, for Sirius). Previously we had assumed that the infrared color temperature should be lower than the effective temperature. However, we abandoned that assumption due to the problems with α Tau and directly compared the LRS observations with the effective temperature blackbodies.

For each system, the ratio of the blackbody flux density and the observed Atlas flux density was calculated for the 93 LRS wavelengths (44 in the blue and 49 in the red). The red part of each LRS spectrum was scaled to match the blue part over the region from 10.6 to 13.4 μm where they overlap. The 93 ratio values were averaged to produce an overall scale factor between the LRS spectrum and the blackbody spectrum, which ranged from 0.78 to 1.33, with mean value 1.08. This range of scale factors is comparable to the range of disagreements between the spectra and the IRAS photometry values for the individual sources. We then normalized the set of ratios at 12 μm to produce a set of relative corrections, the ratio of the observed to the expected flux density, for each spectrum. These are plotted in Figure 4 as a function of wavelength for 11 of the 12 systems (Vega was excluded because of its dust ring, which affects most of the values). Noise is much more evident in the red than in the blue. These corrections divide into two groups. β Ori, α Tau, γ Dra, and μ Gem have correction factors close to 1.0 across the LRS spectrum until noise becomes important. The other 7 systems have correction factors that rise to about 1.15 in the blue part of the spectrum. The two groups are distinct from 7.67 to 11 μm, but not at longer wavelengths.

d) General LRS Corrections

To obtain generally applicable corrections for the LRS we took the mean values for the 7 stars with similar short wavelength corrections. It is possible that β Ori has some contamination of the spectrum due to free-free emission as is commonly observed in B supergiants (Barlow and Cohen 1977) although previous photometric observations have not shown a consistent infrared excess for this star. The other three rejected sources, α Tau, γ Dra, and μ Gem, are all of late spectral type. It is curious that β And, the remaining late-type star we studied, gives corrections very similar to those for the early-type stars. From spectroscopic observations (McClintock *et al.* 1975; Liller 1968) we know that α Boo, α Tau, and β And possess chromospheres, and probably cool circumstellar material (e.g., Kelch *et al.* 1978, for α Tau). Of the three stars, α Tau seems to have the most active chromosphere because there are short-period changes in the circumstellar line profiles. This may be related to the difference in LRS spectral characteristics between α Tau and α Boo.

Our adopted mean correction factors are shown in Figure 5, with uncertainties equal to twice the standard deviation in the mean for each point, and are given in Table 2 along with the LRS wavelengths. Each LRS data value is divided by the corresponding factor from the table to correct the spectrum. The largest factor is 1.14 at 8.576 μm and the smallest is 0.91 at 20.830 μm (excluding the last red point in the spectrum, with a correction of 0.86, where the LRS may suffer from a loss of sensitivity). The uncertainties in the corrections in the red are relatively large but the values decline from 12 μm to $\sim$17 μm and rise slightly from there to the red limit. These values might be improved by a careful examination of the spectra to exclude obviously bad values, but the early-type stars simply do not allow an accurate calibration across the entire wavelength range because of their faintness.

III. Discussion

Using these correction factors, the LRS spectra for 72 sources were fit with blackbodies. The sample of sources included: a) 41 stars of spectral type K0 or later with LRS class 16–19 spectra and $F_\nu(12\ \mu m) > 100$ Jy (hereafter, the bright late-type sources); b) the 18 early-type stars with $F_\nu(12\ \mu m) > 24$ Jy; and c) 13 K-type stars with $F_\nu(12\ \mu m) > 50$ Jy and class 16–19 spectra (hereafter, the faint K-type sources). The faint K-type stars were chosen to examine the transition between sources like α Tau and like α Boo. For each source, a minimum χ^2 criterion was used to find the best-fit temperature. The resulting values are listed in Table 3. For each spectrum the Atlas gives mean signal-to-noise ratios in the red and blue sections. We assumed that the noise was uniform over each section and thereby derived uncertainties from the SNR values for use in the χ^2 calculations. The best fit values do not change much if a simple least-squares fitting is used instead of the weighted χ^2. The temperature ranges given in Table 3 are the formal 95% confidence intervals assuming normal distributions. Table 3 also lists the reduced χ^2 values. It is likely that the assumption of uniform noise in each section artificially increases the χ^2 values by reducing the relative uncertainty assumed for the points with small flux densities, where the noise is larger than average, making the actual noise deviations appear significant. Thus the fits are probably reasonable for reduced χ^2 values of a few. Binary systems (e.g. α Cen) and stars with circumstellar material (e.g. α Her) tend to have very poor fits. The M-type stars nearly always have higher χ^2 values than the early-type stars.

The early-type sources fainter than 50 Jy have temperatures that are systematically too high for the spectral type, with the sole exception of β Ori. The values for the bright late-type stars are much lower than the effective temperatures for stars later than K5. The fainter K-type stars seem to have systematically higher temperatures than the ones in the bright late-type star sample, mimicking the early-type stars.

These results may indicate that there was a non-linearity of response in the LRS

detectors which caused systematic effects in the spectra. It seems that the corrections are too small for the fainter sources, causing systematically high temperature fits. While one might dispute the accuracy of the blackbody fits when applied to noisy spectra, plots of $\lambda^4 F_\lambda$ for some of the fainter early-type stars show that the corrected spectra are bluer than would be expected even allowing for noise in the data. Figure 6 shows the corrected LRS spectrum for α UMi along with the formal best-fit blackbody of 52600 K and a 6500 K blackbody illustrating the difference between the observed and expected spectra. The difference is too small to detect in the red where the data values are very noisy, but shortward of 10 μm there is a significant difference between the observed spectrum and the 6500 K blackbody curve.

The best-fit temperature for α Tau is 2270 K, again significantly lower than the effective temperature. Four of the 9 K-type stars in the bright late-type group have color temperatures of 3000 K or more. The fainter K-type stars also show a split in color temperature although the values are systematically higher than expected. With more K-type stars the dependence of the color temperature upon spectral type becomes blurred (see Fig. 7). The dispersion in color temperature is large from K2 to K5 with no obvious pattern.

Figure 7 shows the best-fit temperatures, T_c, as a function of spectral type, along with the effective temperature curves for main-sequence and giant stars (de Jager and Nieuwenhuijzen 1987). Nine systems with circumstellar dust or free-free emission have very low T_c values. Excluding these, the early-type systems with well determined T_c have values ~10% lower than the expected effective temperatures. The dispersion in T_c is largest for the early K-type stars, where the values are comparatively well determined, but they do not clearly separate into high and low T_c groups. Three of the M-type stars, including β And, have color temperatures which are significantly higher than expected.

We compared the LRS spectra of some stars with stellar atmosphere models, using the MARCS program (Gustafsson, *et al.* 1975). Models were run by Helen Walker for α

Tau and α Car. The model wavelength coverage extends to 12.5 μm. When normalized to the LRS at 12 μm the α Tau model ($\log_{10}(g) = 1.3$, T = 3900 K) agreed well with the LRS data; the α Car model ($\log_{10}(g) = 4.1$, T = 6500 K) did not agree with the LRS spectrum any better than a blackbody of 6500 K. These results are contradictory because if α Tau were correctly flux calibrated the same should be true for α Car. It is possible that the models do not have correct opacities for these wavelengths. If the models are correct our LRS corrections must be color-dependent, applying only to the early-type stars.

We are concerned about the validity of applying our mean correction factors, defined from relatively blue stars, to red and very red LRS spectra. Therefore, we have compared airborne 16–30 μm spectrophotometry (Forrest, Houck, and McCarthy 1981) with our corrected LRS spectra for a variety of red objects. For the cool carbon stars Y Cvn (12427+4542, fit by a 2500 K blackbody), S Cep (21358+7823, 1400 K), V Cyg (20396+4757, 1000 K), CIT 5 (03229+4721, 900 K), IRC+40°540 (23320+4316, 620 K), IRC+10°216 (09452+1330, 600 K), and AFGL 3068 (23166+1655, 350 K), our corrected LRS spectra seem to provide a better match to the 16–30 μm spectral shapes than the uncorrected LRS measurements, although there are certainly some problems with time variability. However, the most critical test derives from even cooler objects such as planetary nebulae. In Figures 8 and 9 we present our corrected LRS spectra for IC 418 (05251−1244, IRAS photometry fit to a 180 K blackbody) and NGC 6573 (18096+0650, 170 K) together with airborne 16–30 μm spectrophotometry (Forrest, Houck, and McCarthy 1981), ground-based 8–13 μm spectrophotometry (Willner *et al.* 1979), and color-corrected IRAS 12 and 25 μm broad-band photometry. Our corrected LRS spectra are in very good agreement with the pre-existing spectrophotometry for these very red sources. (NGC 6572 was observed with apertures significantly larger than the nebular diameter. For IC 418 we scaled the observations to effective beam size 101″ in accordance with the growth of both near-infrared continuum and line flux with aperature (Willner *et al.* 1979). We scaled the 16–30 μm data using to 101″ using the same curve for aperature dependence. All data

sets should, therefore, be comparable to the LRS) Consequently, we suggest that our mean correction factors are applicable even to LRS spectra of very red IRAS objects.

IV. Summary

From our study of the LRS spectra of the brightest infrared stars without circumstellar dust we find that the LRS relative flux calibration is incorrect at the 10–15% level across the spectrum. This problem appears to stem from the use of α Tau as the flux calibration standard in place of α Lyr without allowing for the lower effective temperature. Stars earlier than K0, without circumstellar dust or free-free emission, are bluer than a Rayleigh-Jeans source because α Tau was assigned too high an infrared color temperature in the original LRS calibration.

We compared the spectra of bright early-type stars such as α CMa and α Car with α Tau and found that the color temperature of α Tau must be reduced to $\sim$2000 K in order to alleviate the extreme blueness of the early-type stars. This is true even for stars only slightly earlier than α Tau, such as α Boo. There appears to be a division in the K-type stars observed by the LRS between those with high and with low color temperatures.

To correct the LRS spectra we compared spectra for a set of bright stars, ranging in spectral type from B8 Iae to M0 IIIa, with blackbody sources at the proper effective temperatures. Seven of the 11 systems have a consistent set of correction factors whose mean we have adopted.

Using these corrections, blackbodies have been fit to the LRS spectra of 72 bright stars, either early-type stars or LRS class 17–19 late-type stars. There is some indication that the fainter sources in the group have systematically higher fit temperatures, which may imply a non-linearity in the LRS instrument response. The K-type stars show a wider range of fit temperature than the other spectral types, although we could not clearly isolate groups of 'high temperature' and 'low temperature' K-type stars.

We have so far been unable to recognize any unequivocal color effect in the LRS flux calibration and believe that our correction factors should apply to LRS spectra of all color temperatures.

We are extremely grateful to Dr. Paul Wesselius for providing us with the Groningen LRS database. We thank the NASA-Ames Research Center, which provides support for IRAS studies through the SETI Institute under cooperative agreement NCC 2–407. KV acknowledges support from the Natural Sciences and Engineering Research Council of Canada. MC thanks NASA-Ames for partial support at Berkeley through cooperative agreement NCC 2–142. This study at Jamieson Science and Engineering Inc. was supported by an internal research and development program.

References

Ayres, T. R., and Linsky J. L. (1980), Astrophys. J., **241**, 279.

Barlow, M. J., and Cohen M. (1977). Astrophys. J., **213**, 727.

Beichman, C. A., Neugebauer, G., Habing, H. J., Clegg, P. E., and Chester, T. J., Editors (1988). IRAS Catalogs and Atlases: *The Explanatory Supplement* (General Printing Office: Washington, D.C.).

Bell, R. A., and Dreiling, L. A. (1981). Astrophys. J., **248**, 1031.

Blackwell, D. E., and Shallis, M. J. (1977). Mon. Not. R. Astr. Soc., **180**, 177.

Blackwell, D. E., Legget, S. K., Petford, A. D., Mountain, C. M., and Selby, M. J. (1983). Mon. Not. R. Astr. Soc., **205**, 897.

de Jager, C., and Neiuwenhuijzen, H. (1987). Astron. Astrophys., **177**, 217.

Demarque, P., Guenther, D. B., and van Altena, W. F. (1986). Astrophys. J., **300**, 773.

Di Benedetto, G. P., and Conti, G. (1983). Astrophys. J., **268**, 309.

Di Benedetto, G. P., and Foy, R. (1986). Astron. Asph., **166**, 204.

Dreiling, L. A., and Bell R. A. (1980). Astrophys. J., **241**, 736.

Forrest, W. J., Houck, J. R., and McCarthy, J. F. (1981). Astrophys. J., **248**, 195.

Gliese, W. (1969). *Catalogue of Nearby Stars*, (Verlag: Heidelberg).

Gustafsson, B., Bell, R. A., Eriksson, K., Nordlund, A. (1975). Astron. Astrophys. Supp., **42**, 407.

Hanbury Brown, R., Davis, J., and Allen, L. R. (1974). Mot. Not. R. Astr. Soc., **167**, 121.

Hoffleit, D. (1982). *The Bright Star Catalogue*, (Yale University Observatory: New Haven, Connecticut).

Joint IRAS Science Working Group, (1988). IRAS Catalogues and Atlases. *The Point Source Catalogue*, version 2, (General Printing Office: Washington D.C.).

Joint IRAS Science Working Group, (1986). IRAS Catalogues and Atlases. *Atlas of Low Resolution Spectra.* Astron. Astrophys. Supp., **65**, 607.

Ketch, W. L., Linksy, J. L., Basri, G. S., Chiu, H.-Y., Chang, S.-H., Maran, S. P., and Furenlid, I. (1978). Astrophys. J., **220**, 962.

Kukarkin, B. V., Kholopov, P. N., Efremov, Yu. N., Kukarkina, N. P., Kurochkin, N. E., Medvedeva, G. I., Perova, N. B., Fedorovich, V. P., and Frolov, M. S. (1970). *General Catalogue Of Variable Stars*, Sternberg Institute, Moscow State University.

Liller, W. (1968). Astrophys. J., **151**, 589.

McClintock, W., Linsky, J. L., Henry, R. C., Moos, H. W., and Gerola, H. (1975). Astrophys. J., **202**, 165.

Neugebauer, G. and Leighton, R. B. (1969), *The Two-Micron Sky Survey* NASA Sp-3047 (NASA: Washington D.C.).

Peirce, A. K. and Allen, R. G. (1977). in *The Solar Output And Its Variation*, ed. O. R. White, (Colorado Associated University Press: Boulder), p. 169.

Smithsonian Astrophysical Observatory Star Catalogue (1966). (Washington D.C.: Smithsonian Institution)

Walker, H. J., Cohen, M., Volk, K., Wainscoat, R. J., and Schwartz, D. E. (1989), submitted to Astron. J.

Willner, S. P., Jones, B., Puetter, R. C., Russel, R. W., and Soifer, B. T. (1979). Astrophys. J., **234**, 496.

Figure 1: The Atlas spectrum of α CMa = IRAS 06429−1639 (solid curve) compared with the Rayleigh-Jeans region of a very hot blackbody (dotted curve) normalized to match the observations at 12 μm. The LRS spectrum is distinctly bluer than the Rayleigh-Jeans limit.

Figure 2: Comparison of the Atlas spectrum of α CMa (points) with a 10100 K blackbody spectrum (curve) normalized to match at 12 μm. The F_λ values are multiplied by λ^4 to emphasize the temperature dependent part of the blackbody formula. On this plot an infinite temperature blackbody is a horizontal line and finite temperature blackbody functions have positive slope at all points.

Figure 3: Comparison of the Atlas spectrum (λF_λ) and broad-band photometry for α CMa with a 10100 K blackbody of luminosity 26.75 $L_\odot$ at a distance of 2.67 pc.

Figure 4: Individual correction factors for the 11 systems (see Table 1) from comparison of the LRS spectra to blackbodies. Seven systems yield rising correction factors at the blue end and the remaining 4 systems have nearly constant correction factors across the wavelength range.

Figure 5: The average correction factors, with 2σ uncertainties, from the 7 systems with consistent corrections. The numerical values are given in Table 2.

Figure 6: Comparison of the corrected LRS spectrum of α UMi = IRAS 01490+8901 with a 52600 K blackbody (solid curve; the "best-fit" blackbody temperature from Table 3) and a 6500 K blackbody (dotted curve; the effective temperature) both normalized to match at 12 μm.

Figure 7: The best-fit color temperatures, T_c, for the 72 sources listed in Table 3 as a function of spectral type. Error bars represent the 95% confidence range of fit temperature. Nine systems with circumstellar dust of free-free emission are distinguished by open symbols. The plotted curves are the effective temperature functions for main-sequence (dashed curve) and luminosity class III stars (dotted curve) from de Jager and Neiuwenhuijzen (1987).

Figure 8: Comparison of our corrected LRS spectrum (solid lines) for the planetary nebula IC 418 with ground-based 8–13 μm spectrophotometry (open circles) and airborne 16–30 μm spectrophotometry (crosses) scaled to a common aperature (see text). Filled circles represent color-corrected IRAS broad-band photometry at 12 and 25 μm.

Figure 9: As in Figure 8 for the planetary nebula NGC 6572.

TABLE 1—Parameters For Nearby Stellar LRS Sources

Star Name	Spectral Type	Distance (pc)	Effective Temperature (K)	Stellar Radius ($R_\odot$)	Stellar Luminosity ($L_\odot$)
β Ori	B8 Ia	77	11000 ± 620	21.1 ± 0.4	5860 ± 310
α Lyr	A0 V	8.13 ± 0.32	9650	2.83 ± 0.13	62.66 ± 5.76
α CMa	A1 V	2.67 ± 0.04	10100	1.69 ± 0.05	26.75 ± 1.58
α Car	F0 II	35.7	7460 ± 460	25.4 ± 3.9	1795 ± 71
α CMi	F5 IV	3.508 ± 0.048	6510 ± 220	2.07 ± 0.07	6.96 ± 0.34
α Aur	G8 III	13.33 ± 0.75	5100	11.6	82
	F9 III	13.33 ± 0.75	6000	7.1	59
α Cen	G2 V	1.332 ± 0.008	5700 ± 75	1.23 ± 0.03	1.446
	K1 V	1.332 ± 0.008	4980 ± 80	0.91 ± 0.03	0.46
α Boo	K1 III	10.87 ± 0.58	4294 ± 30	24.6 ± 1.3	186 ± 11
α Tau	K5 III	20.0 ± 2.0	3976 ± 485	43.0 ± 4.4	417 ± 83
α Dra	K5 III	40	3960 ± 270	43.8 ± 6.0	425
β And	M0 IIa	22.2 ± 3.0	3710 ± 64	34.4 ± 4.7	202 ± 2.7
μ Gem	M3 III	50	3570 ± 98	78.4 ± 4.3	899

Table 2—The LRS Correction Factors

Wavelength (μm)	Mean Correction Factor	Standard Deviation In The Mean	Wavelength (μm)	Mean Correction Factor	Standard Deviation In The Mean
7.67	1.054	0.053	12.37	0.979	0.021
7.86	1.074	0.038	12.48	0.953	0.039
8.05	1.123	0.028	12.59	0.979	0.021
8.23	1.129	0.036	12.70	0.988	0.034
8.40	1.131	0.030	12.81	0.963	0.033
8.58	1.137	0.027	12.92	0.958	0.021
8.74	1.120	0.038	13.03	0.978	0.026
8.91	1.111	0.027	13.13	0.957	0.022
9.07	1.104	0.017	13.24	0.933	0.031
9.23	1.105	0.030	13.34	0.945	0.041
9.38	1.086	0.026	13.45	0.942	0.060
9.53	1.077	0.020	10.60	0.963	0.049
9.68	1.074	0.028	10.99	0.980	0.045
9.83	1.058	0.026	11.37	0.984	0.039
9.97	1.053	0.021	11.74	0.996	0.026
10.11	1.052	0.021	12.09	0.978	0.011
10.26	1.045	0.023	12.43	0.981	0.010
10.39	1.031	0.019	12.77	0.969	0.014
10.53	1.031	0.024	13.10	0.983	0.032
10.66	1.017	0.024	13.41	0.970	0.035
10.79	1.023	0.029	13.72	0.963	0.031
10.92	1.023	0.023	14.03	0.963	0.037
11.05	1.013	0.019	14.32	0.977	0.053
11.18	1.023	0.020	14.62	0.959	0.046
11.30	0.998	0.017	14.90	0.955	0.021
11.43	1.010	0.028	15.18	0.952	0.032
11.55	1.004	0.016	15.46	0.955	0.029
11.67	1.018	0.024	15.73	0.942	0.069
11.79	0.997	0.020	15.99	0.969	0.074
11.91	1.003	0.026	16.25	0.972	0.086
12.03	1.000	0.000	16.51	0.944	0.069
12.14	1.002	0.014	16.77	0.913	0.054
12.26	0.977	0.035	17.01	0.939	0.079

Table 2 (continued)

Wavelength (μm)	Mean Correction Factor	Standard Deviation In The Mean	Wavelength (μm)	Mean Correction Factor	Standard Deviation In The Mean
17.26	0.954	0.083	20.39	0.970	0.088
17.50	0.941	0.064	20.60	0.979	0.113
17.74	0.932	0.081	20.80	0.910	0.099
17.98	0.906	0.059	21.00	0.977	0.119
18.21	0.916	0.120	21.20	0.949	0.139
18.44	0.963	0.069	21.40	0.953	0.151
18.67	0.942	0.080	21.60	0.957	0.169
18.89	0.924	0.073	21.79	0.983	0.136
19.11	0.931	0.092	21.98	0.989	0.164
19.33	0.943	0.118	22.17	0.919	0.157
19.55	0.929	0.091	22.36	0.994	0.203
19.76	0.938	0.063	22.55	0.938	0.143
19.98	0.959	0.077	22.74	0.864	0.113
20.19	0.936	0.140			

Table 3—Results Of Blackbody Fits To LRS Spectra

IRAS Name	Star Name	Spectral Type	T_{Best}	T_{min}	T_{max}	χ^2/N	$F_\nu(12\ \mu m)$
01490+8901	α UMi	F7 Ib-II	52600.0	7000.0	53010.0	0.407	25.93
03207+4941	α Per	F5 Ib	12565.0	4500.0	50510.0	0.374	27.39
05121−0815	β Ori	B8 Iae	2205.0	1850.0	2860.0	0.492	41.26
05130+4556	α Aur	G6 III + F9 III	4445.0	3950.0	5110.0	1.180	236.10
06228−5240	α Car	F0 II	5835.0	5150.0	6710.0	0.556	154.80
06408+2510	ϵ Gem	G8 Ib	53225.0	17000.0	53260.0	0.926	40.48
06429−1639	α CMa	A1 V + wd	8870.0	7100.0	12010.0	0.626	143.10
07063−2618	δ CMa	F8 Ia	5725.0	3250.0	34010.0	0.573	35.07
07366+0520	α CMi	F5 IV-V + wd	10300.0	6500.0	32010.0	0.353	79.09
10172+2005	γ Leo	G7 III + K1 III	11305.0	7500.0	27510.0	0.580	85.65
14359−6037	α Cen	G2 V + K1 V	4240.0	3900.0	4710.0	8.217	222.10
15465+2818	R CrB	G0 Iep	665.0	630.0	705.0	0.460	38.86
16232+6137	η Dra	G8 IIIab	8580.0	4000.0	50510.0	0.383	24.94
16280+2135	β Her	G7 IIIa	53245.0	8500.0	53260.0	0.441	24.56
17292+5220	β Dra	G2 Ib-IIa	5945.0	3500.0	50510.0	0.322	25.15
18352+3844	α Lyr	A0 Va	2585.0	2150.0	3360.0	0.936	41.56
19132−3336	RV Tau	G0 Ipe	815.0	790.0	840.0	2.718	77.17
19483+0844	α Aql	A7 V	53245.0	18000.0	53260.0	0.646	32.99
00192−2020	T Cet	M5 IIe	725.0	715.0	735.0	16.243	197.80
01069+3521	β And	M0 IIIa	7460.0	6200.0	9460.0	5.310	286.70
02529+1807	ρ^2 Ari	M6 III	1995.0	1885.0	2120.0	7.769	147.20
02596+0353	β Hor	M1.5 IIIa	2255.0	2170.0	2355.0	14.747	234.70
03019+3838	ρ Peg	M4 II	2245.0	2175.0	2320.0	17.685	308.60
03172−2156	τ^4 Eri	M3.5 IIIa	1510.0	1425.0	1605.0	5.626	162.70
03479−7423	γ Hyi	M2 III	2630.0	2455.0	2830.0	8.278	111.50

Table 3 (continued)

IRAS Name	Star Name	Spectral Type	T_{Best}	T_{min}	T_{max}	χ^2/N	$F_\nu(12\ \mu m)$
03557−1339	γ Eri	M0.5 III	3090.0	2850.0	3410.0	2.098	109.60
04330+1624	α Tau	K5 III	2275.0	2240.0	2310.0	46.691	699.70
05292+1833	CE Tau	M2 Iab-Ib	1580.0	1495.0	1680.0	7.086	145.10
05562+4556	π Aur	M3 II	2105.0	1955.0	2285.0	6.871	107.70
06118+2231	η Gem	M3 III	2040.0	1950.0	2145.0	11.056	190.10
06199+2232	μ Gem	M3 IIIab	2555.0	2465.0	2660.0	35.505	304.50
07153−3700	π Pup	K3 Ib	2320.0	2120.0	2560.0	3.883	130.20
07422+2808	β Gem	K0 IIIb	3895.0	3500.0	4410.0	2.078	124.60
08214−5920	ϵ Car	K3 III + B2 V	1830.0	1795.0	1865.0	30.514	246.00
12148−6741	ϵ Mus	M5 III	2335.0	2240.0	2440.0	22.887	192.40
12283−5650	γ Cru	M3.5 III	2305.0	2275.0	2335.0	282.500	865.40
12530+0340	δ Vir	M3 III	2120.0	1960.0	2305.0	4.518	162.40
13303−0656	S Vir	M7 IIIe	690.0	680.0	700.0	7.398	135.00
13465−3412	V 806 Cen	M5 III	1835.0	1765.0	1915.0	7.154	255.40
14133+1925	α Boo	K1 III	3700.0	3535.0	3880.0	5.498	793.10
14437+1520	HR 5512	M5 IIIab	1445.0	1345.0	1560.0	0.865	106.50
14508+7421	β UMi	K4 III	4355.0	4050.0	4760.0	9.268	160.30
14567+6607	RR UMi	M5 III	2240.0	2115.0	2385.0	8.269	124.50
15011−2505	σ Lib	M3 IIIa	2105.0	1985.0	2250.0	2.239	200.70
16117−0334	δ Oph	M0.5 III	2435.0	2250.0	2650.0	6.067	149.70
16269+4159	30 Her	M6 III	955.0	950.0	960.0	88.324	437.60
16433−6856	α Tra	K2 IIb-IIIa	3020.0	2850.0	3215.0	3.593	144.00
17123+1426	α Her	M5 Ib + G5 III +F2 V	6160.0	6010.0	6350.0	345.855	1515.00
17554+5129	γ Dra	K5 III	2510.0	2425.0	2605.0	17.806	155.10
18142−3646	η Sgr	M3.5 III	2305.0	2155.0	2475.0	4.860	213.70
18359+0847	HD 172171	M6 IIIe + K1 III	605.0	605.0	610.0	13.390	409.00
18527+3650	δ^2 Lyr	M4 II	1745.0	1685.0	1810.0	15.730	155.80

Table 3 (continued)

IRAS Name	Star Name	Spectral Type	T_{Best}	T_{min}	T_{max}	χ^2/N	$F_\nu(12\ \mu m)$
19451+1824	δ Sge	M2 II + A0 V	3445.0	3000.0	4060.0	4.308	101.90
19575−5930	NU Pav	M6 III	1960.0	1890.0	2035.0	22.267	231.40
20356+1805	EU Del	M6 III	1470.0	1435.0	1510.0	23.829	175.20
21243−6943	SX Pav	M5 III	2015.0	1885.0	2160.0	3.813	111.60
21341+4508	W Cyg	M5 IIIae	785.0	775.0	790.0	22.864	349.10
21417+0938	ϵ Peg	K2 Ib	2805.0	2500.0	3260.0	0.842	103.20
22267−4400	δ^2 Gru	M4.5 IIIa	2115.0	1935.0	2335.0	2.042	110.00
23013+2748	3 And	M2.5 II-III	2215.0	2160.0	2280.0	28.500	387.30
00410−1815	β Cet	K0 III	3755.0	2750.0	6360.0	0.592	59.93
02008+4205	γ And	K3 IIb + B8 V + A0 V	3910.0	3400.0	4660.0	1.263	98.55
04537+3305	ι Aur	K3 II	4605.0	3700.0	6260.0	1.057	87.27
05033−2226	ϵ Lep	K5 III	4845.0	3450.0	8510.0	1.053	56.82
09180+3436	α Lyn	K7 IIIab	32410.0	11000.0	50510.0	2.372	86.92
09297−5648	HD 82668	K5 III	3135.0	2800.0	3610.0	3.183	73.10
16454−5857	η Ara	K5 III	5155.0	3250.0	14510.0	0.719	52.18
16544−5554	ζ Ara	K3 III	3310.0	2800.0	4060.0	2.126	82.14
17211−5529	β Ara	K3 Ib-IIa	2095.0	1850.0	2460.0	1.934	62.65
18177−2951	δ Sgr	K3 III	4175.0	3000.0	7010.0	0.374	62.17
19438+1029	γ Agl	K3 II	1485.0	1380.0	1610.0	1.032	76.55
22150−6030	α Tuc	K3 III	6615.0	4600.0	12010.0	1.253	59.29

Table 3—Infrared color temperatures from blackbody fits to the corrected LRS spectra. The best fit temperatures are determined from minimizing χ^2, assuming uniform noise across each spectral section. Column 7 gives the minimum χ^2 per degree of freedom. The temperature ranges are formal 95% confidence intervals. The spectral types are taken from the *Bright Star Catalogue* (Hoffleit, 1982).

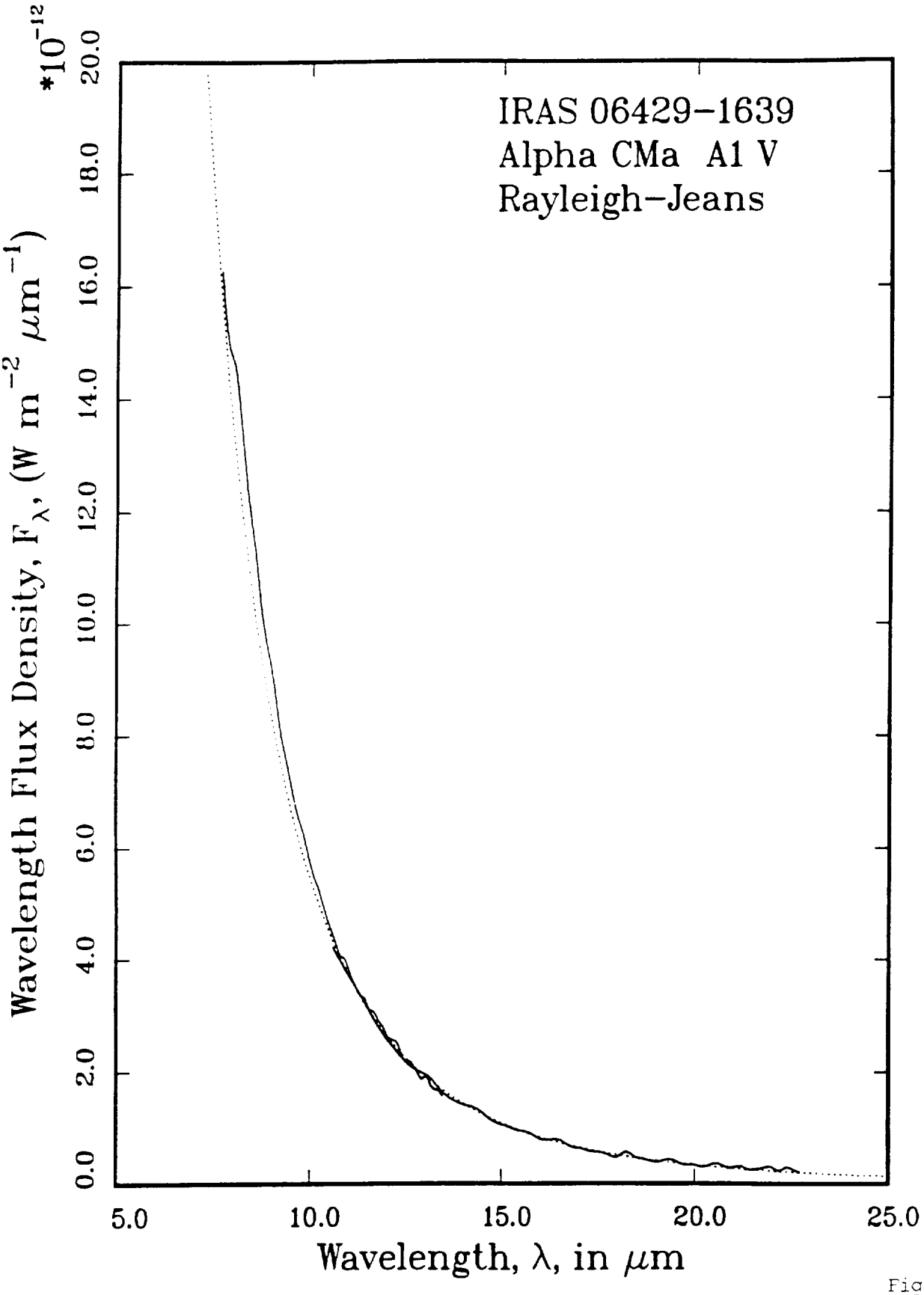
IRAS 06429-1639
Alpha CMa A1 V
Rayleigh-Jeans
Wavelength Flux Density, F_λ, (W m^{-2} μm^{-1})
*10^{-12}
0.0
2.0
4.0
6.0
8.0
10.0
12.0
14.0
16.0
18.0
20.0
5.0
10.0
15.0
20.0
25.0
Wavelength, λ, in μm

Fig. 1

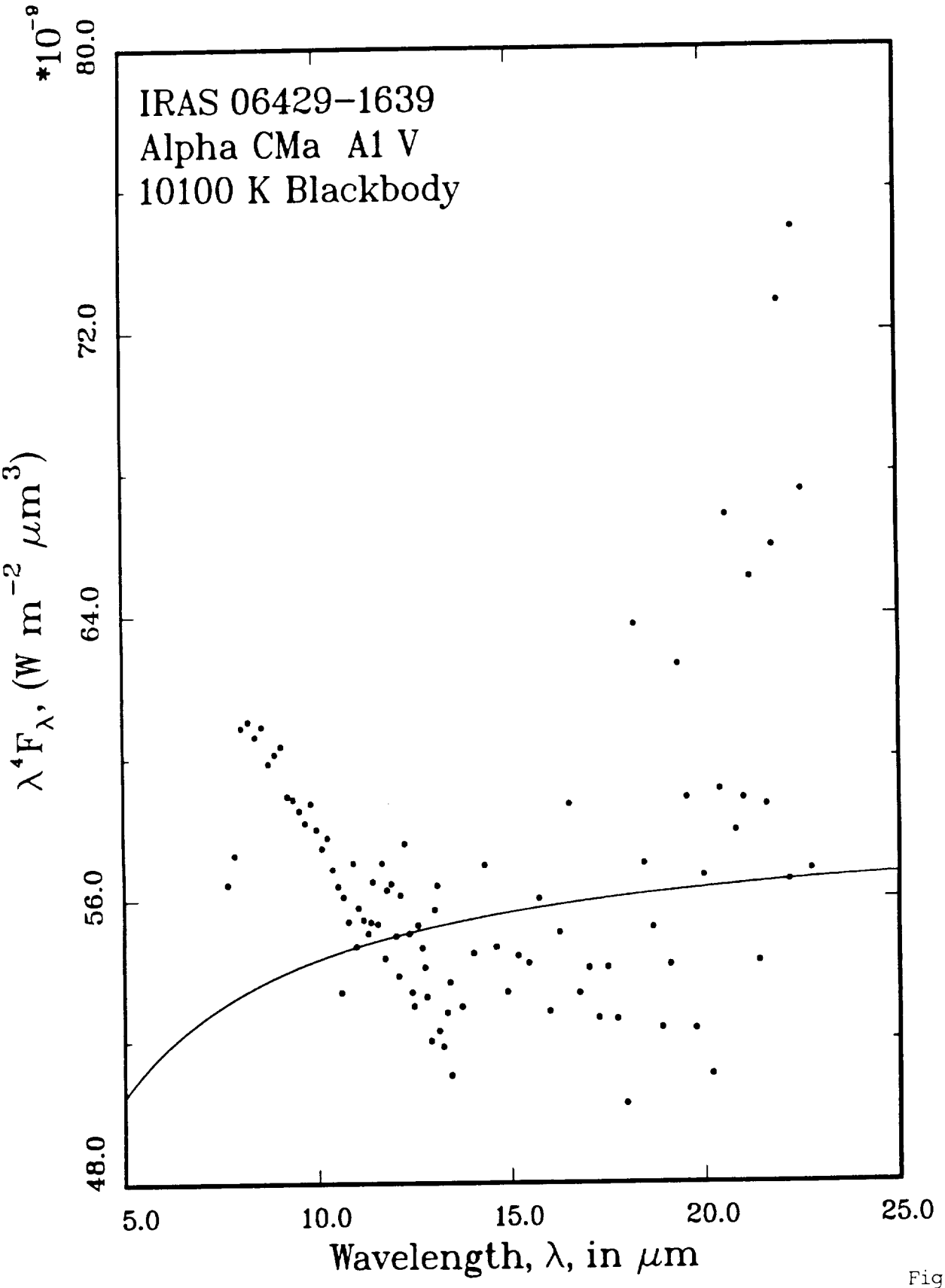
IRAS 06429-1639
Alpha CMa A1 V
10100 K Blackbody
*10^-9
80.0
72.0
64.0
56.0
48.0
λ^4F_λ, (W m^-2 μm^3)
5.0
10.0
15.0
20.0
25.0
Wavelength, λ, in μm

Fig. 2

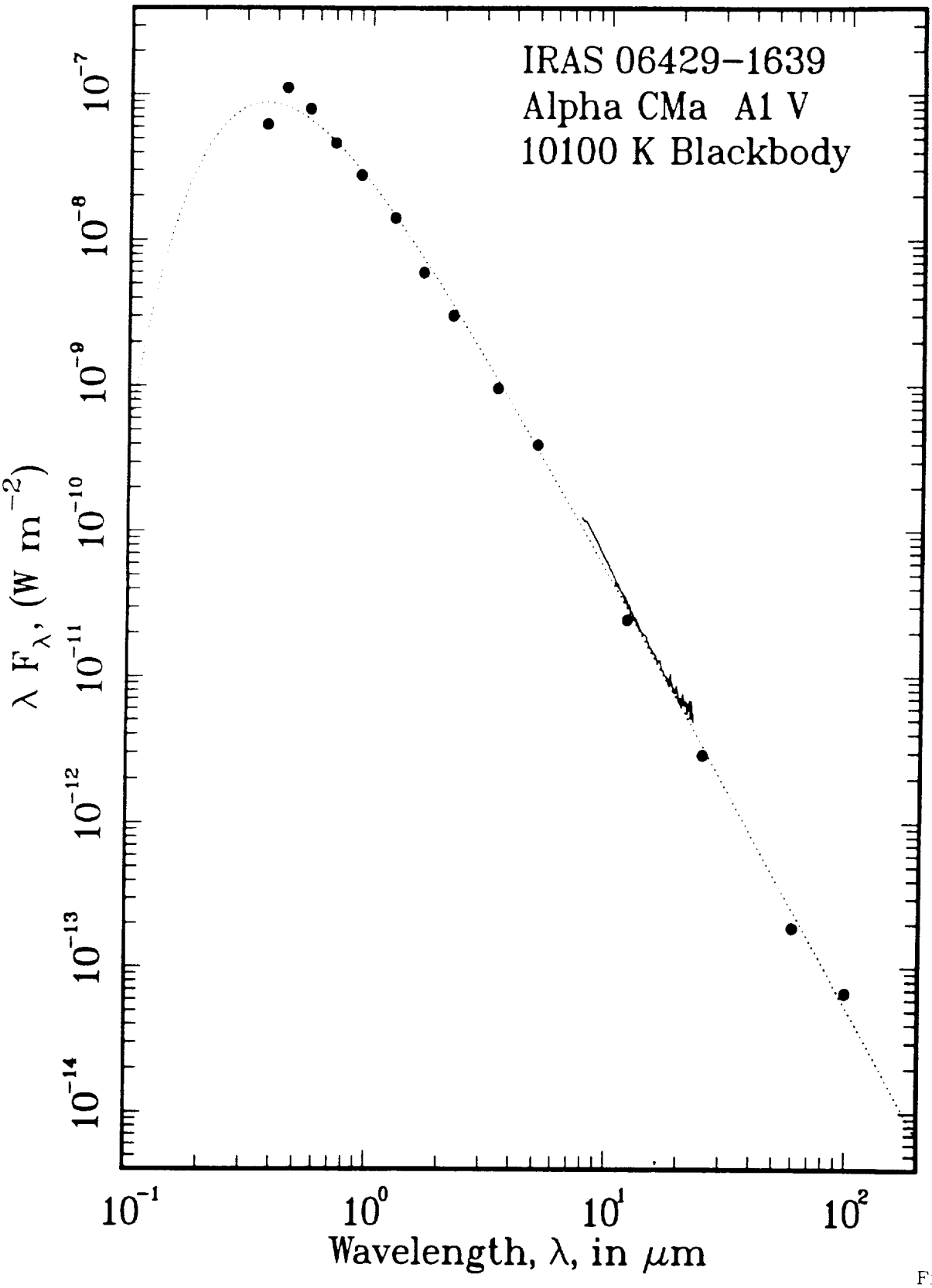
IRAS 06429-1639
Alpha CMa A1 V
10100 K Blackbody
λ F_λ, (W m^-2)
10^-7
10^-8
10^-9
10^-10
10^-11
10^-12
10^-13
10^-14
10^-1
10^0
10^1
10^2
Wavelength, λ, in μm

Fig. 3

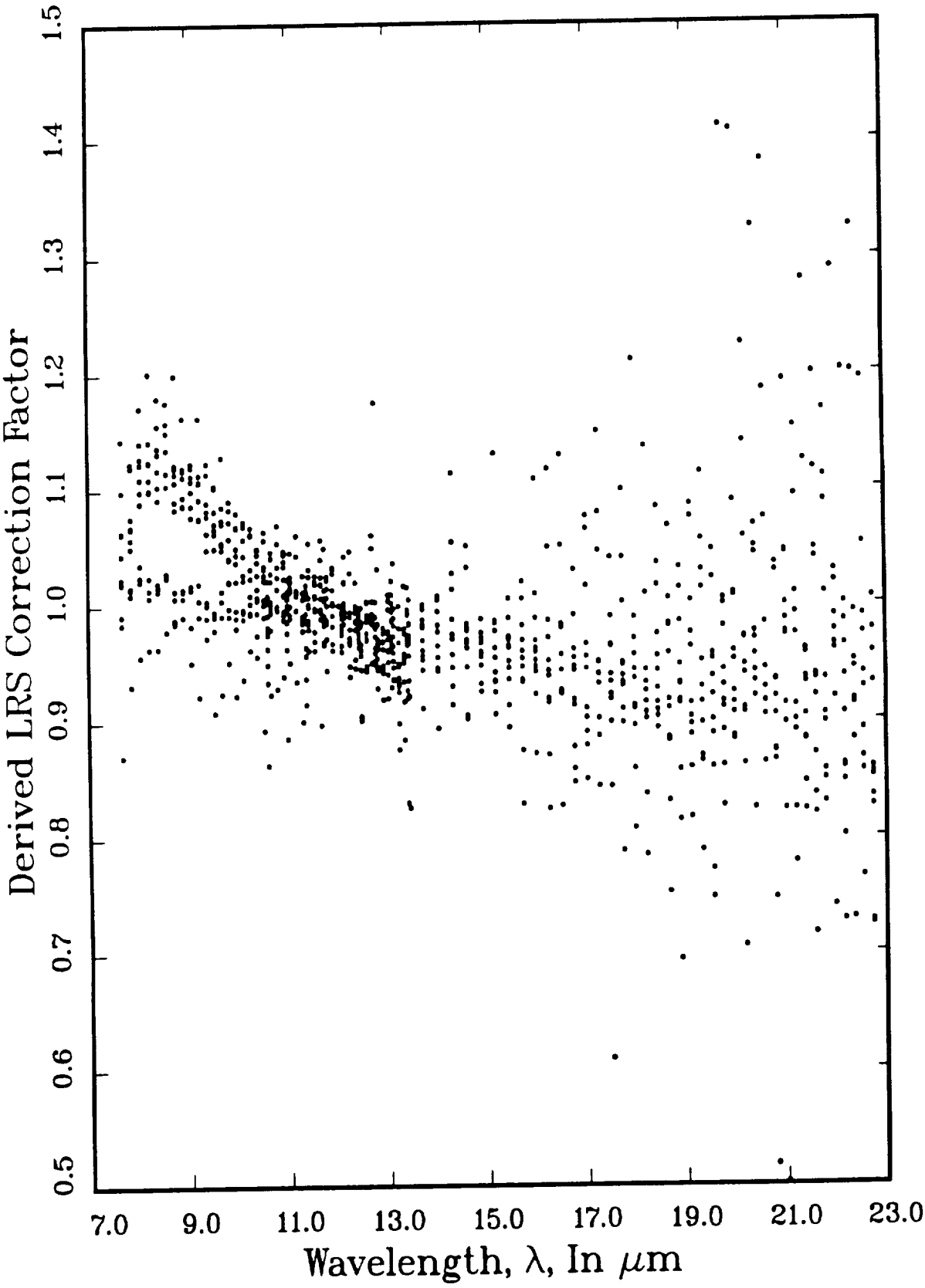
Derived LRS Correction Factor
0.5
0.6
0.7
0.8
0.9
1.0
1.1
1.2
1.3
1.4
1.5
7.0
9.0
11.0
13.0
15.0
17.0
19.0
21.0
23.0
Wavelength, λ, In μm

Fig. 4

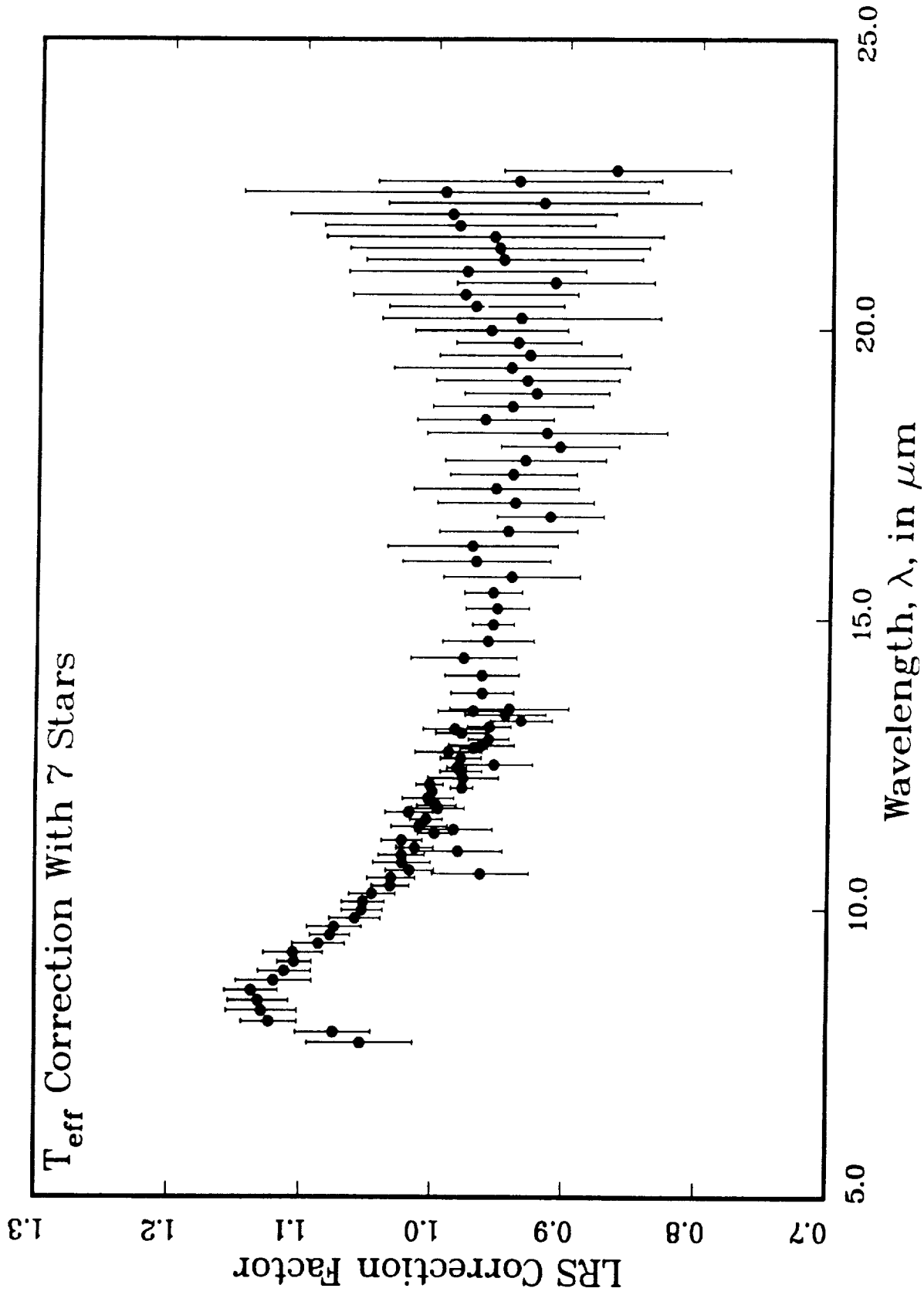
T_{eff} Correction With 7 Stars
LRS Correction Factor
0.7
0.8
0.9
1.0
1.1
1.2
1.3
5.0
10.0
15.0
20.0
25.0
Wavelength, λ, in μm

Fig. 5

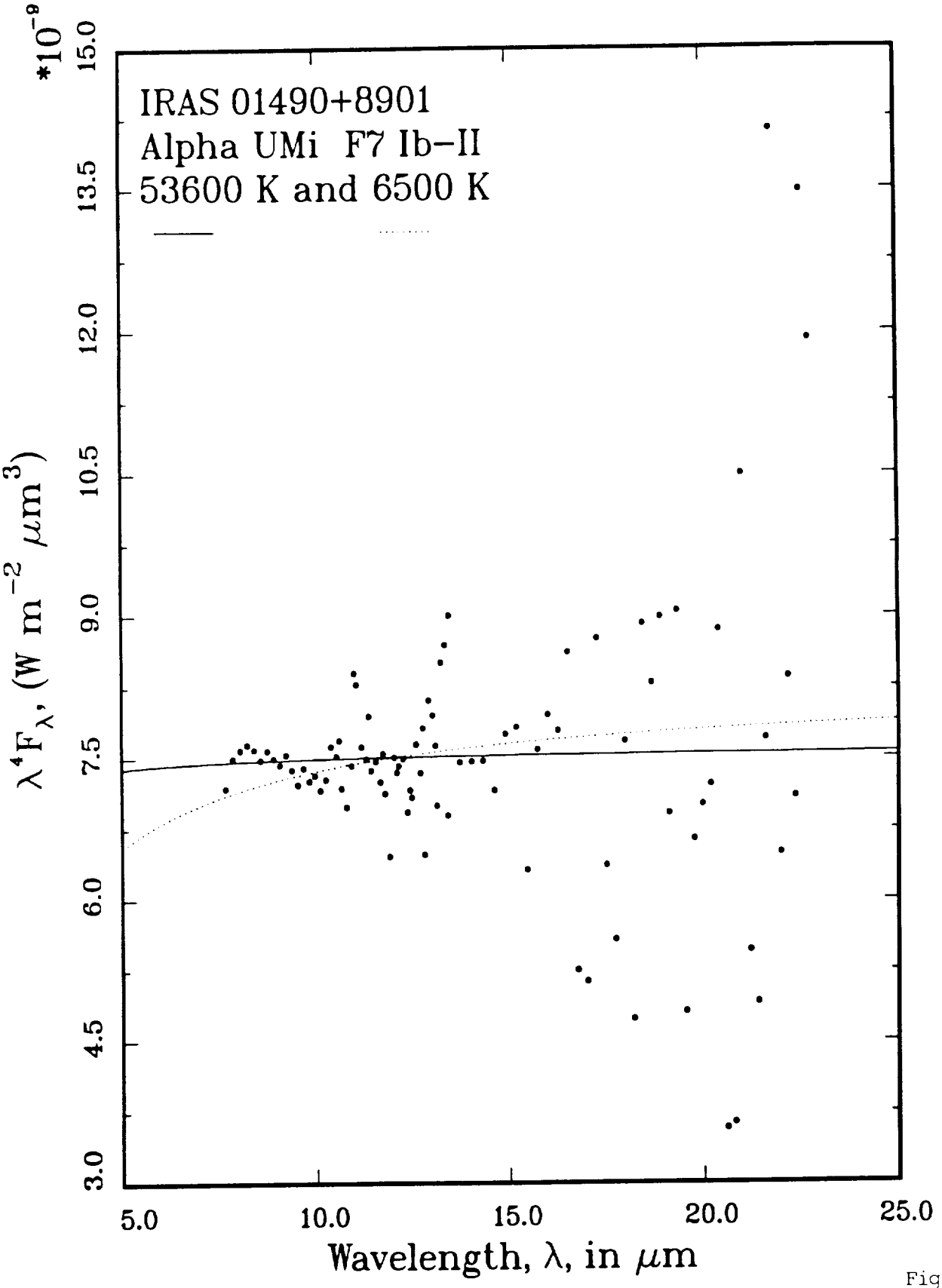
IRAS 01490+8901
Alpha UMi F7 Ib–II
53600 K and 6500 K
*10^-9
15.0
13.5
12.0
10.5
9.0
7.5
6.0
4.5
3.0
λ^4F_λ, (W m^-2 μm^3)
5.0
10.0
15.0
20.0
25.0
Wavelength, λ, in μm

Fig. 6

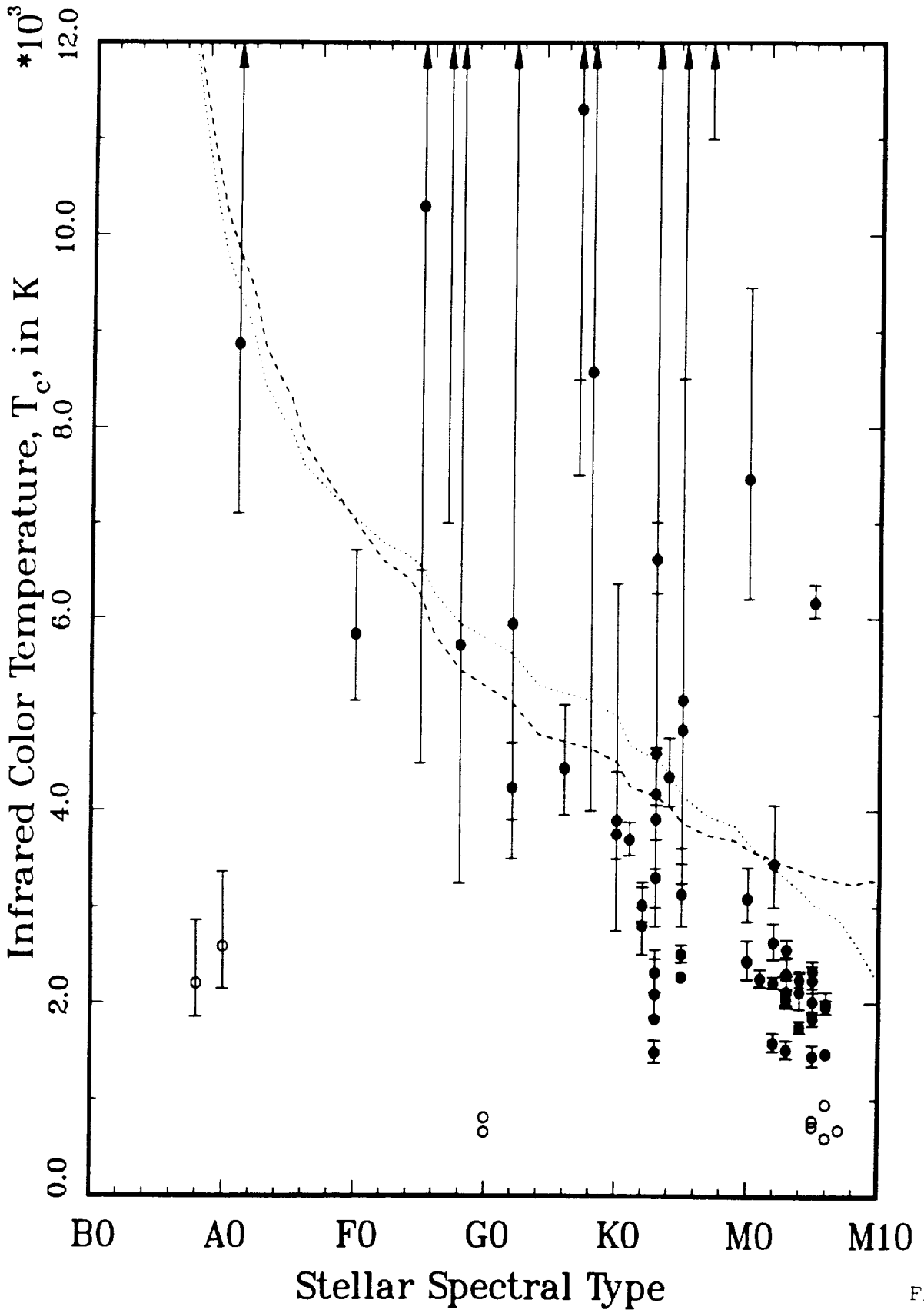
*10^3
12.0
10.0
8.0
6.0
4.0
2.0
0.0
Infrared Color Temperature, T_c, in K
B0
A0
F0
G0
K0
M0
M10
Stellar Spectral Type

Fig. 7

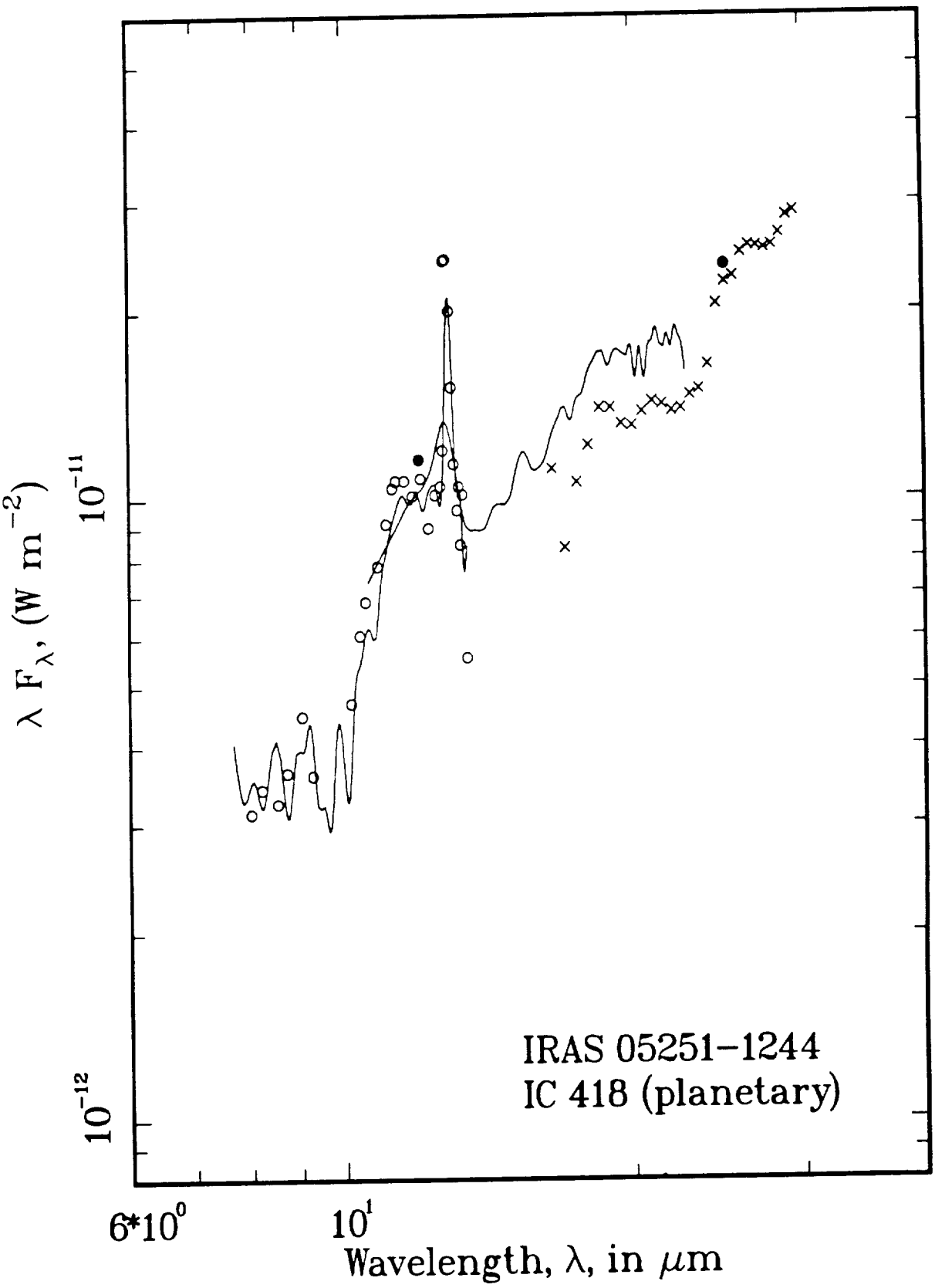
λ F$_\lambda$, (W m^{-2})
10^{-11}
10^{-12}
6*10^0
10^1
Wavelength, λ, in μm
IRAS 05251−1244
IC 418 (planetary)

Fig. 8

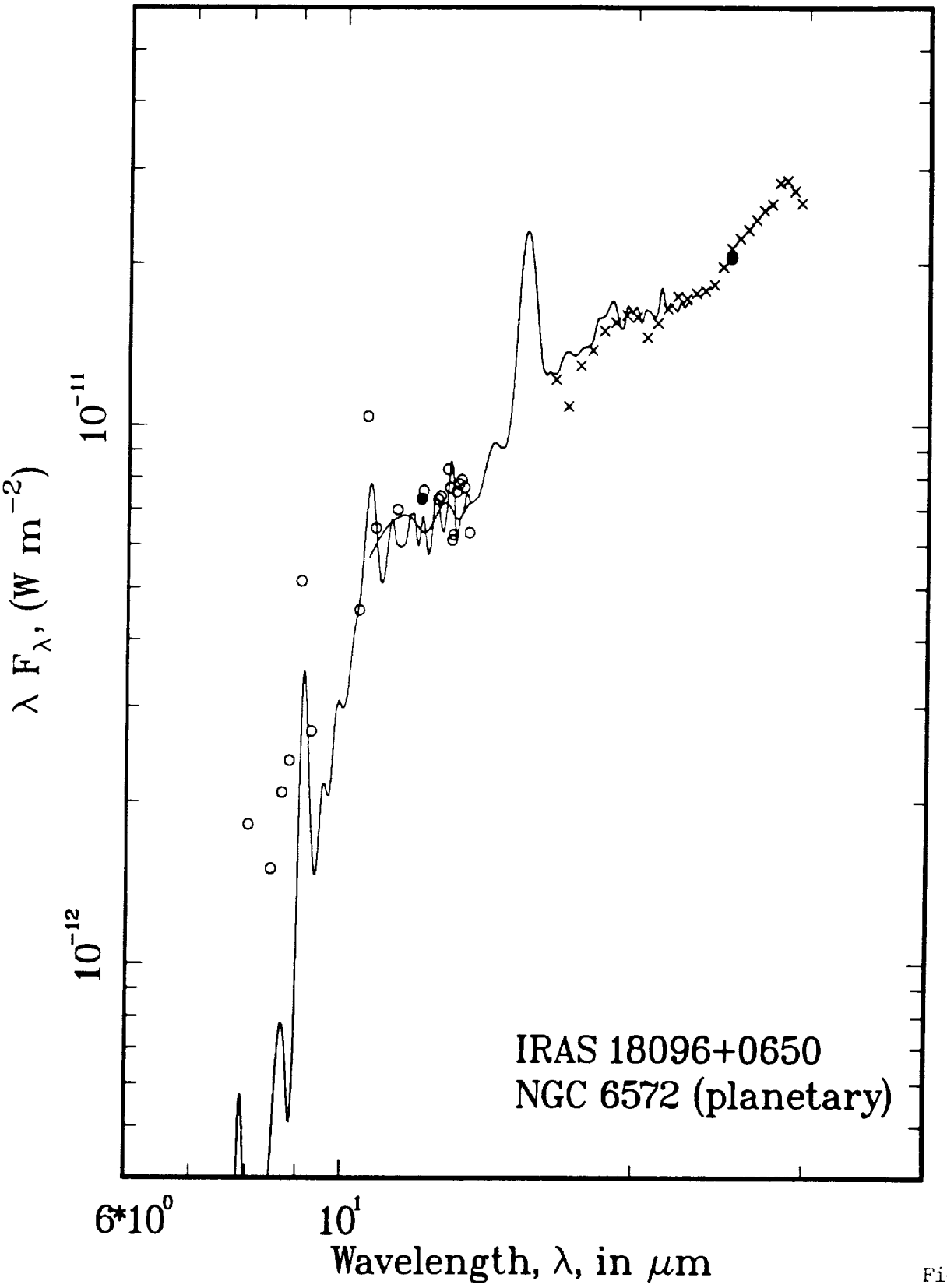
λF_λ, (W m^{-2})
10^{-11}
10^{-12}
IRAS 18096+0650
NGC 6572 (planetary)
$6*10^0$
10^1
Wavelength, λ, in μm

Fig. 9

APPENDIX F. "New LRS Spectra for 356 Bright IRAS Sources"

New LRS Spectra For 356 Bright IRAS Sources

Kevin Volk

NASA Ames Research Center, Moffett Field, California 94035

and

SETI Institute, 101 First Street #410, Los Altos, California 94022

Martin Cohen

Radio Astronomy Laboratory, University Of California, Berkeley, California 94720

and

Jamieson Science And Engineering, Inc., 5321 Scotts Valley Drive, Suite 204,

Scotts Valley, California 95066

Abstract

We present the low resolution spectra of all IRAS point sources with $F_\nu(12\mu m) >$ 40 Jy which were not included in the *Atlas of Low-Resolution Spectra*. These have been classified into 8 groups based upon the spectral morphology. Silicate emission spectra and red continuum spectra associated with HII region sources form ~60% of our sample. All types of spectra in the LRS Atlas are represented in our sample except for emission line sources. The sample is used to test a recent classification scheme for IRAS sources based on broad-band colors. The spectra are consistent with the classifications from the colors in most cases. We also compare our sample with the Atlas.

I. Introduction

In 1983 the *Infrared Astronomical Satellite* (IRAS)[1] surveyed the infrared sky. In addition to photometric observations (the IRAS *Point Source Catalog* version 2 (1989), hereafter the PSC), IRAS provided low-resolution spectra from about 8 to 23 μm using a slitless spectrometer. The spectra were observed in two sections, a blue section from 8 to 15 μm with resolution $\lambda/\Delta\lambda \sim 40$ and a red section from 13 to 23 μm with resolution ~ 20. The observations were recorded for any source brighter than $\sim$2 Jy at 12 μm or 25 μm. The "better quality" spectra were collected into the IRAS *Atlas of Low-Resolution Spectra* (1986, hereafter the Atlas) which contains the average spectra of 5425 objects. However these spectra are only a small part of the full set of observations. The database of all the spectra extracted from the raw data-stream during the IRAS mission contains $\sim$170000 individual spectral scans for a total of $\sim$50000 sources. This 'LRS database' contains many good spectra which were not included in the Atlas. Sources were excluded if the individual spectral scans did not agree well enough to satisfy the criteria for this Atlas, for example if, during the data extraction, the wrong bank of detectors was interrogated so that part of the spectrum was missed. Other sources appear to have had a change in the spectral character between observations, presumably due to real variability. The slitless spectrometer was unsuitable for observing closely spaced sources unless they were oriented perpendicular to the scan direction, because the spectral scans would overlap with a wavelength shift due to the spatial separation of the sources. The LRS database is available in machine-readable form from the Netherlands. In this paper, we present a study of the brightest LRS database 12 μm sources not in the Atlas. We have also used the LRS database to study specific types of source (e.g. planetary nebulae, Volk and Cohen

[1] The *Infrared Astronomical Satellite* was developed and operated by the U.S. National Aeronautics and Space Administration (NASA), the Netherlands Agency for Aerospace Programs (NIVR), and the U.K. Science and Engineering Research Council (SERC).

1989b) using larger samples than are available in the Atlas.

In the PSC there are 1636 sources with $F_\nu(12\ \mu m) > 40$ Jy and a high quality IRAS 12 μm observation. Of these, 316 do not have spectra in the Atlas. An additional 50 sources have only moderate quality 12 μm data of which 40 are not in the Atlas. The 356 'missing' sources include some nearby bright objects such as o Ceti = IRAS 02168−0312 and α Sco = 16263−2619. They also include some very unusual sources such as the Galactic Center complex, 17424−2859, and η Car = 10431−5925. The galactic coordinate distribution of these 356 sources (Fig. 1) shows that most lie near the galactic plane.

We had two main purposes in extracting the LRS database spectra of these sources. First, LRS spectra allow us to test our own classification of the sources based upon their IRAS photometric colors (Walker and Cohen 1988; Cohen *et al.* 1989; Walker *et al.* 1989). Second, we wanted to investigate the quality of the non-Atlas LRS spectra and those factors that might prevent a bright source spectrum from being accepted. The paper is in two parts: the classification of the spectra and the relation of the IRAS colors to the type of source; and a general discussion of the set of spectra.

II. Extraction Of The Spectra

The LRS database consists of the individual LRS spectral scans in order of observation, along with associated header information. To locate a spectrum in the database, the source position is specified and the program extracts all scans with positions within a user-defined search radius to form an average spectrum. We used a search radius of 1′. Sources usually had several individual spectral scans in the LRS database. Typically 3 or 4 are available; a few sources had only one scan while others had more than 10. Sometimes spectra from more than 1 source were extracted within a 1′ radius and the program returned several average spectra for a single position. In these cases, the averages were examined and the best quality spectrum from the position nearest to the source was assumed to be correct.

Any additional spectra found from a search usually had positions distinct from the target source and could be readily rejected. Even when only a single average spectrum was found for a source we did not always use it for classification. If one or more of the scans were poor, because of noise or a detector problem, the average spectrum was often unusual or of poor quality. All such cases were examined, scan by scan, to see if a good-quality scan was available. Often we found perfectly good scans for classification. These individual scans were then substituted for the average in the presentation of the spectra (Figure 2). For 18 sources no good quality spectra were found in the database.

The extracted spectra are presented in Figure 2, ordered by RA. Each plot has the IRAS name and another name, if any is available, at the top and a letter classification in the upper or lower right corner (see Sec. III). The blue part is plotted from 7.67 to 12.81 μm and the red part is plotted from 12.77 to 22.74 μm. Some of the spectra show a decline at the long wavelength end due to a loss of detector sensitivity. We have found that there are problems with the relative calibration of the individual LRS spectral values (Volk and Cohen 1989a) which cause a distortion of the spectrum, but for our morphological classification this is unimportant.

III. The Spectra

The spectra were classified by eye and put into one of nine groups based solely on their appearance. The groups are:

C: 28 spectra with 11 μm SiC emission (equivalent to Atlas classes 40–49), expected to be carbon stars.

S: 23 spectra which are clearly stellar blackbody sources (equivalent to Atlas classes 17–19), expected to be stars with spectral types earlier than M5.

F: 13 featureless spectra that are flatter than a stellar blackbody (equivalent to Atlas classes 10–16), expected to be carbon stars or M-type stars with small amounts of circumstellar dust.

P: 24 spectra with relatively red continua from 13 to 23 μm and a sharp rise at the blue end of the LRS range, usually with the 11.3 μm emission feature which is attributed to PAH molecules (e.g. Cohen, Tielens, and Allamandola 1985). These are equivalent to Atlas class 80 sources. Some of these spectra are very similar to silicate absorption spectra although the abruptness of the rise at 10–11 μm often distinguishes PAH spectra from the silicate absorption spectra. Some of these sources lack a clear 11.3 μm feature and appear to be population I Wolf-Rayet stars of extremely late WC type by comparison with the LRS spectra of Roberts 80 (PSC designation 17590−2337), of type WC 9, RAFGL 2179 (18289−1001), of type WC 10, and RAFGL 2104 (18136−1859) in the Atlas, of type WC 8/9. Group P spectra not assigned to Atlas class 80 would generally be mistakenly assigned to silicate absorption classes 30–39 or 70–79.

A: 21 silicate absorption spectra that are not red enough to be unequivocally due to HII region sources (equivalent to Atlas classes 30–39). It is possible that some of these sources belong to group P, or that some of the group P sources belong in this group.

E: 106 silicate emission feature sources, some of which show superimposed 9.7 μm absorption either in the circumstellar shell (which implies an optical depth of ≥ 2 in the shell at 9.7 μm) or in the interstellar medium. When the 9.7 μm peak is absorbed, the general shape of the spectrum on either side of the feature and beyond 15 μm, where there is still an emission feature at 18 μm, was used to assign the sources to this group. These spectra are equivalent to Atlas classes 20–29, although a few of the sources with peak absorption would have been assigned other LRS classes in the Atlas (e.g. to SiC emission classes; see Walker and Cohen 1988).

H: 94 red continuum sources, some of which show either silicate absorption features or the 11.3 μm PAH feature. These sources should be either planetary nebulae, reflection nebulae, or HII region sources. The LRS Atlas equivalents are of classes 70–79. The vast majority are associated with HII regions.

U: 29 unusual spectra; some flat continuum sources with either no, or unusual, features, and some sources with abnormal silicate emission features. The nature of most of these sources is unknown.

I: 18 noisy or incomplete spectra, including cases where the two parts of the spectrum seem to be copies of each other. When this occurs, the different flux and wavelength calibrations cause the red part to be a magnified, slightly distorted copy of the blue part. Some of these sources can be classified from the blue part of the spectrum but have no useful red scans in the database.

There can be considerable variations of spectral shape within a group. The classifications are not rigorous; no attempt was made to introduce a quantitative classification similar to the Atlas classes. However, the Atlas classes were assigned on the basis of values at a very few points in the spectrum, leading to classification problems when the spectra are noisy at a key wavelength (for example, α Cen = 14359−6047 was assigned to LRS class 21 because of noise near 10 μm), while we consider the entire spectrum. Groups P and A were distinguished by subtle differences in shape that would be difficult to quantify for any automatic classification. It is possible that some of the unusual spectra in the various groups are affected by instrumental problems but we are not able to recognize these effects except for individual glitches in a spectrum (e.g. 00515−6308). A few cases of instrumental problems are noted in Table 1.

During the classification procedure no reference was made to either associations or broad-band IRAS colors. After the groups were created the PSC associations were examined. For 3 of the sources in groups P and A the associations helped us to distinguish between silicate absorption and PAH emission. If the source was associated with an OH maser source it was assumed to have a silicate absorption spectrum. OH maser associations were sought only for group P and group A sources. The division between groups P and A for some of the sources remains problematic. If the features are strong, the difference between a PAH spectrum and a silicate absorption spectrum is obvious, as with group

A sources 18182−1504 and 18216−1311, but in other cases, such as source 18187−1605, there is considerable doubt about the group assignment (see Figure 2).

The sources are listed in Table 1 by group, ordered by RA within each group. The table gives the IRAS name first, the alternative name used on the plot (if any), the spectral group, and a final column giving comments, spectral types, and other associations. The source names are preferentially taken from the *Bright Star Catalogue* (Hoffleit 1982), the *General Catalogue Of Variable Stars* (Kukarkin *et al.* 1970), or the *Smithsonian Astrophysical Observatory Catalog* (1966). If only infrared or radio associations were available, the names from the *Caltech Two-Micron Sky Survey* (Neugebauer and Leighton 1969) were used in preference to others. Save for the OH/IR star identifications, the associations are from the PSC. All associations are solely positional and some are doubtful due to relatively large discrepancies in position. Some absurd associations, such as a strong silicate emission source associated with a radio galaxy, were ignored in assigning identifications but appear in the comments. Source associations with poor positional agreement are followed by a question mark, or two question marks when the agreement is very poor. The spectral types given in Table 1 are, in order of preference, from the *Bright Star Catalogue*, Bidelman (1980), or the *General Catalogue of Variable Stars.*

IV. Source colors

After source classification, the IRAS colors were compared with a set of 'occupation zones' for various types of celestial source seen by IRAS (Walker *et al.* 1989). The resulting color-color diagrams are presented in Figures 3 and 4, although not all of our sources have good IRAS observations beyond 12 μm. When the broadband colors were calculated, color corrections suitable for stellar blackbody sources were applied to the data values, so that a 10^4 K blackbody source has colors near the origin in both forms of the color-color diagram (see the IRAS *Explanatory Supplement* (1988) for a discussion of color corrections; the values used were 1.43, 1.40, 1.315, and 1.09 for 12, 25, 60, and 100 μm). The 12/25/60

color-color diagram (Figures 3a and 3b) shows that most of the groups have internally consistent colors (excluding groups U and I which need not be homogeneous, and group P which includes several distinct types of sources as discussed below). The same is generally true of the 25/60/100 color-color diagram (Figures 4a and 4b).

The locations of the main groups of sources (silicate emission, silicate absorption, carbon stars, the red continuum HII region sources) are all consistent with the corresponding occupation zones. A few of the group E sources have 60 μm excesses which put them above the occupation zone (e.g. η Car), but these lie in the galactic plane and may have infrared cirrus contamination at long wavelengths. There are 5 sources near the blackbody line on the right-hand part of Figure 3a which are likely to be planetary nebulae, although their LRS spectra show no line emission and none are known planetaries. In fact none of our 356 sources has any LRS nebular emission lines, although a number of fainter IRAS sources associated with planetaries do have obvious LRS line spectra (Pottasch *et al.* 1986; Volk and Cohen 1989b).

We now discuss the nature of the sources associated with the various groups of LRS spectra in terms of these color-color planes.

Group C (SiC Emission Sources)—Eight sources in this group lack 60 μm data and another 10 lack 100 μm data. All the sources have good quality 12 μm and 25 μm observations, and those sources without 60 μm data have $[12]-[25]$ values which are similar to the other sources in the group. Carbon stars show two distinct color groups (see Chan and Kwok 1988; Cohen *et al.* 1989)—optically identified carbon stars with small $[12]-[25]$ and usually a 60 μm excess, and carbon stars first identified from infrared or radio molecular line observations which tend to cluster near the blackbody line and have larger $[12]-[25]$ values. Both groups are present in our sample. The sources with 60 μm excesses or with $[12]-[25] < 0.5$ are all optically identified carbon stars (except 17314−3255, which has no optical catalogue association and a 60 μm excess). Three other optical carbon stars are

found near the blackbody line out to $[12]-[25] \approx 0.7$. The group C source found amid the group F sources is an S-type star, 21027+3704 = GR Cyg. It is very surprising that this source shows the SiC emission feature so strongly. The other group C sources, some amid the group E sources and others along the blackbody line, have no optical associations. A number of the sources in Figure 4 show 100 μm excesses and some are near the blackbody line but it is more difficult to separate the optical from the infrared carbon stars in the 25/60/100 diagram (see zones c and d in Figure 4).

Group S (Stellar Blackbodies)—Only one group S source lacks 60 μm data, while 10 more lack 100 μm data. Two sources, 18476−0758 = S Sct and 23438+0312 = TX Psc, have 60 μm excesses and are known carbon stars although the spectra do not show any SiC emission. (For S Sct the spectrum is noisy and could have weak SiC emission; for TX Psc there is no trace of SiC emission). All the other sources have the colors of normal stars and all but one have associations in the *Bright Star Catalogue* with spectral types ranging from K0 III to M7 III. The brightest group S source, 16262−2619A = α Sco, actually has a very weak silicate emission feature. The same is true for 09448+1139 = R Leo. These features were only seen after the associations had been found.

Group F (Featureless Sources)—These sources appear to have intermediate temperature (≈500–1000 K) blackbody spectra, not flat enough to be placed in group U but distinct from group S. Two lack 60 μm data and another three lack 100 μm data. In Figure 3 all but two sources have colors intermediate between those of group S and those of group E. Source 16396−4613 (which has no identification) has a large 60 μm excess. Source 19133−1703 = T Sgr is an S-type star with a mild 60 μm excess. Another source, 07266−0541 (the other unassociated object in this group), has an unusually large $[12]-[25]$ color and a red LRS spectrum that may have a weak SiC or silicate emission feature. Five of the 8 group F objects in Figure 4 have both 100 μm excesses and optical associations,

which is unusual unless the excesses are due to infrared cirrus.

Group P (PAH/Late WC Wolf-Rayet Sources)—It appears that there are 3 distinct sets of PAH sources in this group. First, some of the spectra (16156−5002 and 16506−4512, for example) have a relatively red continuum, although they are not as red as group H sources, and HII region-like colors. The second set has a similar red continuum but weaker 7.6 μm emission (e.g 17028−1004) and smaller [12] − [25] colors. The third set of PAH sources has a blue continuum (e.g. 18216−1617) and much smaller [25] − [60] colors than the others. The latter are difficult to distinguish from group A spectra. Eight group P sources lack 25 or 60 μm data and 6 more lack 100 μm data. There is no box defined for "PAH sources" on either color-color diagram because of the wide variety of objects that show PAH emission. The PAH sources are found in the HII region, reflection nebulae, and LRS class 30 boxes.

The two known and three new potential late-WC Wolf-Rayet stars in group P are generally bluer in [12] − [25] than the PAH sources. Of these only 19288+2923 has a 60 μm flux value and its colors ([12] − [25] = 1.96, [25] − [60] = 0.40) are indistinguishable from the blue continuum PAH sources. It is a questionable late-WC Wolf-Rayet candidate because it may have an 11.3 μm feature, although the spectrum is unusual around 11 μm. The other 4 sources have [12] − [25] values ranging from 1.48 to 0.18. RAFGL 2104 has [12] − [25] in the middle of this range and a similar [25] − [60] to 19288+2923.

Group A (Silicate Absorption Sources)—Four of these sources lack 25 or 60 μm data and another 6 lack 100 μm data. Source 17128−3748 of Group I has no red part but is a silicate absorption source. In some cases the dividing line between group A and group H is somewhat subjective. If the 'continuum' level at 7.7 μm is below the 13 μm level or less than ~75% of the 22 μm level the source is included in group H, even with a very strong silicate absorption feature (e.g. 16330−4725). We find that group A spectra with bluer

continua are less likely to have 60/100 μm data and are under-represented in the color-color plots. The colors of the sources that can be plotted divide almost evenly between low [25] – [60] colors, found near the Atlas class 30 occupation zone, and much larger 60 μm excesses. The slope of the continuum, estimated from 7.8, ~13, and 22 μm, correlates well with the [25] – [60] value; all of the group A sources with continua sloping down from 7.8 to 23 μm (which would be Atlas class 30–39 sources) have [25] – [60] < 2.5 and those with slightly rising continua over this range (which would be LRS class 70-79 sources) have [25] – [60] > 3. Only the bluer sources have OH maser associations; the redder group appear to be HII region sources with surrounding interstellar dust rather than evolved AGB stars. The Atlas class 30 zone does not extend up as far as the bluer continuum sources in Figure 3. The group A sources generally have stronger silicate absorption than most of the Atlas class 30–39 objects.

Group E (Silicate Emission Sources)—The silicate emission sources lack 100 μm data in 75 cases, 60 μm in 33 cases, and 25 μm data in 1 case. The [12] – [25] colors are generally redder than the center of the M-star occupation zone in Figure 3 because the zone was defined using both optically-selected and IRAS-selected stars while our LRS sample is biased to redder objects. IRAS 19486+3247 = HR 7564 has a very weak feature and colors similar to group S sources. The next bluest source, 23173+2600 = W Peg, also has a weak feature. As noted above, two of the group S sources have extremely weak silicate emission which was only recognized after the associations had revealed that they have measurable mass loss.

A number of the sources have 60 or 100 μm excesses. The unassociated source 16372−4614 has the largest 60 μm excess in the group and an unusual rise near the red end of the spectrum, which may indicate that large amounts of low temperature dust are present around the star. In some cases the 60 μm excess is probably due to infrared cirrus emission.

IRAS 16079−5110 is associated with planetary nebula PK 331+0.2, but the spectrum and colors appear normal for a red giant star so the association is probably incorrect. IRAS 16154−4753 has a spectrum which resembles those of several planetary nebulae, including the very young planetary Vy 2–2 = 19219+1947 (which is in the Atlas), but has no 60 or 100 μm data. It has a surprisingly blue [12] − [25] color considering the steep spectral index in the LRS spectrum.

Eleven group E sources have partial absorption of the 10 μm emission feature. These sources have [12] − [25] values ranging from 1.22 to 1.93 with a mean of 1.55. The reddest group E sources overlap with the bluest Atlas class 30–39 sources, consistent with a circumstellar rather than an interstellar origin of the absorption. Some of these sources are bright and would be unusually luminous at 12 μm if they were sufficiently distant to suffer significant interstellar extinction at 12 μm.

In Figure 4 most of the group E sources are in the silicate emission occupation zone. Three sources have very large 100 μm excesses which are probably due to infrared cirrus. The source near the 90 K blackbody point is 10431−5925 = η Car. The unusual colors are probably the result of an ejection of a large amount of material in the late 1800's.

Group H (Red Continuum Sources)—Most of these sources have associations in the Bonn or Parkes radio continuum surveys of the galactic plane, and clearly almost all are sources in HII regions. Most lie in the HII region occupation zones in Figures 3 and 4. Four sources have colors near the blackbody line and may be planetary nebulae although their spectra are not distinctive. IRAS 17424−2859, the galactic center complex, is noteworthy. The IRAS beams are large enough that no single source can be positively identified with the IRAS source; the IRAS beam includes IRS 1, IRS 7 and part of the dust ridge (see Becklin and Neugebauer 1975). IRS 7 is an M-type supergiant star with intrinsic 12 μm emission. IRS 1 a compact HII region of unusual properties (Wolfman, Smith, and Larson 1982) and is the brightest 10 μm source in the complex, so it is the most likely association

for the IRAS source. The LRS spectrum is distinctive because it is heavily reddened by interstellar extinction. Its luminosity over the IRAS wavelength range is of the order of 2×10^6 $L_\odot$ without any correction for the extinction. This source would be extremely bright at 12 μm were it not for the severe extinction; the PSC 12 μm flux density is 1360 Jy. We attempted to de-redden the spectrum using the extinction curve determined by Wainscoat *et al.* (1989) assuming $A_V = 30$ magnitudes; it is likely that the source has intrinsic silicate emission.

Group H spectra show a variety of features in the blue part of the spectrum. Many show strong PAH emission, especially the 7.6 μm feature at the blue edge of the spectrum. A few sources show very strong silicate absorption features at 9.7 and 18 μm probably due to local interstellar material rather than a circumstellar shell (as for group A) or general interstellar extinction . Only a few of the sources (e.g. 17172−3548) have silicate emission features of normal shape. Source 17009−4042 has an unusual feature near 10 μm which may be instrumental in origin. The red part permits unambiguous classification so it was not assigned to group U. The features may influence the colors but we have not studied this possibility.

Group U (Unusual Spectra)—In our entire sample only 29 spectra were classed as unusual. Most do not resemble any common LRS spectral shape. All lie close to the galactic plane. Only 6 were observed at all 4 bands, and 7 others lack only 100 μ data. There are 3 general spectral shapes in the group: sources with a very strong 10 μm emission feature and a very red continuum; sources with a 9 μm emission feature; and sources with flat spectra often showing a feature near 11 μm.

Two sources in group U, 10428 − 5909 = RT Car and 20197 + 3722 = BC Cyg, have what appear to be silicate emission features on very red continua. These spectra are unusual in the strength and the shape of this feature. A number of planetary nebulae or proto-planetary nebulae have Atlas spectra with silicate emission features on a red

continuum, such as 18095+2704 and Vy 2–2 = 19219+0947, but their shape is different from these two group U spectra. Oddly, neither group U source has 25 μm observations. RT Car is classed as a nova-like variable, spectral type M3. BC Cyg is an irregular variable of spectral type M4 Ia. The spectral shapes are consistent in all the scans which argues an instrumental origin.

Four sources, 02036−1027 = UV Cet (type M2), 16488−4407 with no associations, 17377−3211 = BM Sco (type K0), and 17593−2328 = Hen 1560, show a 9 μm emission feature and two show an 18 μm feature. All four sources have very similar [12] − [25] values, near 0.8.

The remaining spectra are heterogeneous, although many show a strange peak near 11 μm on a relatively red continuum. For the latter sources the individual spectral scans agree well with one another. A notable spectrum is that of the unassociated source 18430−0237 which has a strong 11 μm emission feature on a low temperature continuum. This peak resembles the normal 11.4 μm SiC emission feature in shape and width but peaks at 10.9 μm. Most group U sources cluster at intermediate [12] − [25] colors, from 1.5 to 2.5, and do not match any of the occupation zones.

Group I (Noisy/Incomplete Spectra)—In some cases the spectra allow classification even though they are incomplete, usually missing, or having a very bad, red part. Thus 11445+4344 = AZ UMa and 17468−2900 = V758 Sgr are silicate emission sources with normal colors; 17128−3748 is a silicate absorption source with normal colors; and 20141−2128 = RT Cap is an SiC emission feature source with normal colors. Group I sources 16555−4237 and 15411−5352 have strong PAH emission in the blue part of their spectra. When the blue part is missing the classification is more difficult; 17327−3319 is probably a silicate emission feature source, as is clearer when the red part is not truncated at 12.77 μm. Some sources appear to have a copy of the blue part in place of an independent red part (e.g. 15411−5352 = G326.624), possibly because the sources are extended.

It is not clear whether these sources can be reliably classified. Other spectra were too poor to classify; for example, the very bright source 07120 − 4433 = HR 2748 which has no reasonable red or blue scans.

V. Discussion

For 338 of the 356 sources in our sample a reasonable quality LRS spectrum was available in the LRS database. The mean spectra for many of the sources are of very good quality and it is not clear why they were excluded from the Atlas. The sky distribution of the sources indicates that the high source density and background flux levels near the galactic plane contributed to the rejection of the spectra. The sources often showed significant scan-to-scan variations in spectral shape, some of which appear to be instrumental while others are probably intrinsic to the sources. This was particularly noticeable in group H sources. A significant fraction of these sources had unusual average spectra, and individual scans were substituted when they were of better quality.

For the group H sources in particular, some variation in the wavelengths of spectral features was observed. This is illustrated by the spectra of 17430−2848 and 17455−2800. The blue parts appear almost identical but shifted by about 1 μm, and the peaks in the red part before long wavelength roll-off also appear to differ in the same way. The detailed shape of the features in the blue imply strong PAH emission rather than silicate absorption. This shift in wavelength could be caused by a poor estimate of when the source crossed the focal plane, which would be more likely for an extended source such as an HII region. Another source which probably has a shifted spectrum is 18174−1612. This type of variation was sometimes seen in the individual scans for group H sources. There may also be smaller shifts for some objects which are not apparent from casual inspection of the scans.

A few of the LRS database spectra appear to have an incorrect zero level (e.g. 18241−1221). Most spectra with significant numbers of negative values are clearly bad

but others seem to have a normal relative shape even though part of the spectrum is negative. The zero level may be incorrect due to bad baseline values in the raw data scans. This problem may be isolated to a small number of sources, but it casts doubt upon the accuracy of the absolute levels of the spectra presented here and in the Atlas. There are also discrepancies between the absolute flux densities from the LRS spectra and the IRAS broad-band photometry (see Volk and Cohen 1989a).

The 338 classifiable spectra include all of the general classes of Atlas spectra except for emission line sources. The largest group of sources is group E, with 31% of the classifiable sources, followed by H (28%). The remaining 41% includes a small proportion of group F sources (4%) while the remainder are fairly evenly divided between groups U (9%), C (8%), P (7%), S (7%), and A (6%). For comparison, the equivalent proportions in the 5050 Atlas spectra with classes from 10 to 95 are, by number, roughly 34% silicate emission, 26% featureless, 18% stellar, 11% SiC emission, 5% silicate absorption, and the remaining 6% include red continuum spectra, PAH emission spectra, and unusual spectra. These numbers are approximate because our groups do not always match the LRS classes. Group H spectra are over-represented and groups F and S are under-represented in our sample compared with the Atlas. Groups E, A, and C are present in nearly the same proportions as in the Atlas. Emission line sources are absent from our sample, probably because the Atlas requirements were relaxed for such sources.

It is curious that in our sample group S outnumbers group F, when there are significantly more class 10–16 sources than 17–19 sources in the Atlas. The relation between these groups is not clear but it is generally expected that the stellar blackbody sources are the most locally-confined sample of IRAS sources and that, as lower flux thresholds are considered, proportionately less of these sources will be included.

VI. Summary

We have extracted the LRS spectra for all IRAS 12 μm sources brighter than 40 Jy

which were not included in the Atlas. Classifiable spectra were found for 338 of the 356 sources in our sample. The remaining 18 sources have either extremely noisy or incomplete spectra, some of which can be tentatively classified from the available data.

The spectra have been classified manually into nine groups based upon the spectral morphology. By number these groups are: silicate emission spectra (106), red continuum spectra (94), unusual spectra (29), SiC emission spectra (28), spectra with a sharp rise near 8 μm (24), stellar blackbody spectra (23), silicate absorption spectra (21), incomplete or unclassifiable spectra (18), and non-photospheric featureless spectra (13). The spectra with sharp rises near 8 μm include PAH emission sources and a few late-WC Wolf-Rayet stars. The 'unusual' spectra include some peculiar silicate emission sources and some relatively flat spectra with no recognizable features.

These groups were used to test the classification of IRAS sources from the broad-band colors. We compared the distribution of the groups on color-color diagrams with a set of occupation zones for known types of celestial source (Walker *et al.* 1989) on the 12/25/60 and 25/60/100 color-color diagrams. Most groups have colors consistent with the corresponding occupation zones. We find, in common with previous studies, that some groups of sources overlap on the color-color diagrams and, therefore, the nature of some IRAS sources cannot be determined solely from IRAS photometry.

We are extremely grateful to Dr. Paul Wesselius for providing us with the Groningen LRS database. We thank the NASA-Ames Research Center, which provides support for IRAS studies through the SETI Institute under cooperative agreement NCC 2-407. KV acknowledges support from the Natural Sciences and Engineering Research Council of Canada. MC thanks NASA-Ames for partial support at Berkeley through cooperative agreement NCC 2-142. This study at Jamieson Science and Engineering Inc. was supported by an internal research and development program.

References

Becklin, E. E., and Neugebauer, G. (1975). Astrophys. J. Lett., **200**, L71.

Bidelman, W. P. (1980), Publ. Warner and Swasey Obs. **2**, no. 6.

Beichman, C. A., Neugebauer, G., Habing, H. J., Clegg, P. E., and Chester, T. J., Editors (1988). IRAS Catalogs and Atlases: *The Explanatory Supplement* (General Printing Office: Washington, D.C.).

Chan, S. J., and Kwok, S. (1988). Astrophys. J., **344**, 362.

Cohen, M., Tielens, A. G. G. M., and Allamandola, L. J., (1985). Astrophys. J. Lett., **299**, L93.

Cohen, M., Walker, H. J., Volk, K., Wainscoat, R. J., and Schwartz, D. E. (1989), submitted to Astron. J.

Hoffleit, D. (1982). *The Bright Star Catalogue*, (Yale University Observatory: New Haven, Connecticut).

Joint IRAS Science Working Group, (1986). IRAS Catalogues and Atlases. *Atlas of Low Resolution Spectra.* Astron. Astrophys. Supp., **65**, 607.

Joint IRAS Science Working Group, (1989). IRAS Catalogues and Atlases. *The Point Source Catalog*, version 2, (General Printing Office: Washington D.C.).

Kukarkin, B. V., Kholopov, P. N., Efremov, Yu. N., Kukarkina, N. P., Kurochkin, N. E., Medvedeva, G. I., Perova, N. B., Fedorovich, V. P., and Frolov, M. S. (1970). *General Catalogue Of Variable Stars*, Sternberg Institute, Moscow State University.

Neugebauer, G. and Leighton, R. B. (1969). *The Two-Micron Sky Survey* NASA Sp-3047 (NASA: Washington D.C.).

Pottasch, S. R., Preite-Martinez, A., Olnon, F. M., Jing-Er, Mo, and Kingma, S., 1986. *Astron. Astrophys.*, **161**, 363.

Smithsonian Astrophysical Observatory Star Catalogue, 1966. (Smithsonian Institution: Washington D.C.).

Volk, K. and Cohen M. (1989a), submitted to Astron. J.

Volk, K. and Cohen M. (1989b), in preparation.

Walker, H. J. and Cohen, M. (1988). Astron. J., **95**, 1801.

Walker, H. J., Cohen, M., Volk, K., Wainscoat, R. J., and Schwartz, D. E. (1989), submitted to Astron. J.

Wainscoat, R. J., *et al.*, (1989), in preparation.

Wolfman, E. R., Smith, H. A., and Larson, H. P. (1982). Astrophys. J., **258**, 506.

Figure 1. The sky distribution in galactic coordinates of the 356 sources in the sample.

Figure 2. The LRS database spectra of the 356 sources, ordered in RA. For each spectrum the IRAS name and another name (if available) are given above the plot. In the upper or lower right corner we give the group classification letter (see §III).

Figure 3a. The 12/25/60 μm color-color diagram for the sample. Each symbol represents a group: diamonds for group C, open triangles for S, open squares for F, filled squares for P, filled 'up' triangles for A, filled circles for E, filled 'down' triangles for H, open circles for U, and crosses for I. Plus signs on the dotted curve mark blackbody colors for temperatures of 10000 K, 1000 K, 600 K, 400 K, 300 K, 250 K, 200 K, and 150 K , respectively (from left to right). Dashed boxes represent 70% occupation zones for different types of sources (Walker *et al.*, 1989): bright stars (a); oxygen-rich (M-type) stars (b); optical carbon stars (c); infrared carbon stars (d); HII region sources (e); blue reflection nebulae (f); red reflection nebulae (g); planetary nebulae (i); T Tauri stars (n); and LRS class 30–39 sources (o). The associated letters appear in the upper right or lower left corner save for the bright stars zone.

Figure 3b. An enlargement of the lower left part of Figure 3a.

Figure 4a. The 25/60/100 μm color-color diagram for the sample. The symbols and zone letters are as in Figure 3. Blackbody points are plotted for 10000 K, 1000 K, 600 K, 400 K, 300 K, 250 K, 200 K, 150 K, 100 K, 90 K, 80 K, 70 K, and 60 K, as in Figure 3.

Figure 4b. An enlargement of the lower left part of Figure 4a.

Table 1—Bright IRAS Sources Without Atlas Spectra

IRAS Name	Other Name	Group	Additional Associations And Comments
01246−3248	HR 423	C	R Scl, CS 68, type C6 II
04297+2941		C	
06077+2601	TU Gem	C	SAO 78066, CS 461, type N3,C4
06471+0301	SVS 03223	C	IRC+00°131, type C
08088−3243	CS 1081	C	
10350−1307	U Hya	C	CS 1714, type N2,C7
10491−2059	V Hya	C	CS 1766, type N,C7
15477+3943	V CrB	C	CS 2293, SAO 64929, IRC+40°273, type Ne,C6
16081−5042		C	
16373−4732		C	
17092−3905		C	
17314−3255	RAFGL 5354 ?	C	
17446−4048		C	
17512−2548	RAFGL 2023	C	optically invisible
18036−2344	RAFGL 5440	C	
18082−2454		C	
18110−1909		C	
18128−1839		C	
18241−1221		C	LDN 0399 is 9′ away
18288−0837	RAFGL 2178	C	
18356−0951		C	
19285+1808		C	
20180+4744	U Cyg	C	CS 2894, IRC+50°324, type Np,R8
20311+4222	RAFGL 2604	C	
21027+3704	GR Cyg	C	RAFGL 2698, IRC+40°466, type S
21358+7823	S Cep	C	CS 3055, IRC+80°048, RAFGL 2785, type C7,3e
21412+3747	RV Cyg	C	CS 3063, IRC+40°491, RAFGL 2798, type N5,C6
23257+1038	RAFGL 3099	C	3.3 μm absorption implies carbon star

Table 1 (Continued)

IRAS Name	Other Name	Group	Additional Associations And Comments
00254+1736	HR 103	S	TV Psc, type M3 III; noise glitch in spectrum at $\approx$11 μm
00376+5615	HR 168	S	α Cas, type K0 III
00439+1512	HR 211	S	57 Psc, type M4 IIIa
00515−6308	HR 257	S	SAO 248276, type M4 III; glitch at 11.2 μm in one scan
02470+5541	HR 834	S	η Per, type M3 Ib-IIa, spectrum bad for $\lambda > 19.5\mu$m due to nearby source 02470+5536
06597−2751	HR 2646	S	σ CMa, type K7 Ib
09251−0826	HR 3748	S	α Hya, type K3 II-III
09448+1139	HR 3882	S	R Leo, type M8 IIIe
10193+4145	HR 4069	S	μ UMa, type M0 III
11432+0648	HR 4517	S	ν Vir, type M1 IIIab
12526+4728	HR 4909	S	TU Cvn, type M5 III
14427+2717	HR 5506/5	S	ϵ Boo, IRC+30°264, types K0 II-III + A2 V
16262−2619A	HR 6134	S	α Sco, RAFGL 1863, IRC−30°265, types M1.5 Iab + B2.5 V
16501−4258	HR 6257	S	SAO 257359, SVS 08012, type M3 II-III
18476−0758	HR 7089	S	CS 2666, S Sct, type N3,C5
18537+4352	HR 7157	S	R Lyr, IRC+40°334, type M5 III
21402+4532	HR 8298	S	possibly belongs in group 3; IRC+50°392, RAFGL 2794, type M4
22145−8041	HR 8481	S	RAFGL 4288, type M5 III
22274+4726	HR 8572	S	RAFGL 2913, IRC+50°433, type M0 II + B8 V
22396−4708	HR 8636	S	SAO 231258, RAFGL 4292, type M5 III
23077+3329	SAO 73052	S	IRC+30°507, RAFGL 3034, type M7
23142−0759	HR 8850	S	χ Aqr, RAFGL 3058, IRC−10°597, type M3 III
23438+0312	HR 9004	S	TX Psc, CS 3202, RAFGL 3142, IRC+00°532, type C6,2
04157−1837	RS Eri	F	IRC−20°052, RAFGL 563, type M7
04361−6210	HR 1492	F	R Dor, type M8 IIIe
05026+4447	DO 28943	F	IRC+40°111, RAFGL 681, type M5
06067+3125	BU Aur	F	IRC+30°141, RAFGL 883, type M1
07266−0541		F	

Table 1 (Continued)

IRAS Name	Other Name	Group	Additional Associations And Comments
11251+4527	ST UMa	F	SAO 43748, RAFGL 1489, IRC+50°211, type M4 III
11485−1055	RU Crt	F	SAO 156937, RAFGL 1516, IRC−10°258, type M3
16396−4613		F	
16520−4501	RS Sco ?	F	type M5e-M8e
18179−1346	IRC−10°412	F	RAFGL 2127, type M10
19133−1703	T Sgr	E	S star 598, IRC−20°584, type S5/6e
20443+0215	V Aqr	F	DO 6935, IRC+00°491, RAFGL 5541S, type M6e
21115+5953	SAO 33232	F	RAFGL 2725, IRC+60°305, type M2
04269+3510	LKH 101	P	SVS 01618, IRC+40°091, RAFGL 585, type Be
06384+0932	RAFGL 989	P	NGC 2264, apex of fan nebula, type Ae-Be
13086−6231		P	MRSL 305−00/1 is 6′ away
15246−5658		P	individual scans show the PAH feature better than the mean
16153−5016		P	star + HII region spectrum?
16156−5002	G333.245	P	
16385−4635		P	
16399−4601		P	BM 339.0-00.1 ?
16506−4512	G340.778 ?	P	SG 340.8-01.0
16562−3959		P	H II region PAH source, or possibly silicate absorption
17028−1004	PK 10+18.2	P	RAFGL 5334
17240−3449		P	
17331−1618	RAFGL 5359 ?	P	
17380−3031		P	Wolf-Rayet source?
17565−2035		P	
17590−2337	Rob 80	P	IRC−20°417, RAFGL 2048, Wolf-Rayet source, type WC 8-9
18216−1617	RAFGL 2134 ?	P	
18228−1312	Bonn 18.305	P	
18289−1001	RAFGL 2179	P	Wolf-Rayet source, type WC 10
18328−0805		P	

Table 1 (Continued)

IRAS Name	Other Name	Group	Additional Associations And Comments
18340−0839		P	
18405−0448		P	Wolf-Rayet source??
18418−0305		P	
19288+2923		P	Wolf-Rayet source?? If PAH emission, unusual at 11 μm
06056+2131	RAFGL 6366S	A	
06099+1800	RAFGL 896	A	
13395−6153	RAFGL 4176 ?	A	
13481−6124		A	could be an H II region source with PAH emission
15468−5420	OH 327−0.3	A	
16124−5110		A	the colours are typical of H II regions
16522−4322		A	G342.382 is 2′ away, LRS appears normal
16594−4256		A	
17004−4119		A	
17216−3801		A	
17221−3619	G351.467	A	
17411−3154	RAFGL 5379	A	
18018−2426	LKH 115	A	RAFGL 2059, apex of fan nebula, embedded in HII region
18182−1504	OH 16.1−0.3	A	MRSL 016−00/1 is 5′ away
18187−1605		A	
18196−1331	OH 17.6+0.2	A	RAFGL 2136, optically invisible
18327−0715	OH 24.7+0.3	A	
18348−0526	OH 25.6+0.6	A	RAFGL 2205, optically invisible
18445−0238	OH 30.1−0.2	A	
18460−0254	OH 30.1−0.7	A	RAFGL 5535
19010+0526	OH 39.2−0.2	A	
00213+3817	HR 90	E	R And, S star 8, IRC+40°009, RAFGL 59, type S6.5 IIIe
01037+1219	IRC+10°111	E	RAFGL 157; strong absorption of feature
02168−0312	VZ Cet	E	SAO 129835, IRC+00°030, RAFGL 318, type M5e

Table 1 (Continued)

IRAS Name	Other Name	Group	Additional Associations And Comments
02316+6455	SVS 00857	E	IRC+60°092, RAFGL 349, type M9
02427+6247	CQ Cas	E	IRC+60°095, RAFGL 373, type M6
05592−0221	V352 Ori	E	SAO 132754, RAFGL 858, IRC+00°096, type M7ep
08391+0222	RAFGL 1283	E	type M9
08437+0149	EY Hya	E	SAO 117103, IRC+00°179, RAFGL 1288, type M7
10353−1145	FF Hya ?	E	IRC−10°423, RAFGL 1428, type M6
10431−5925	η Car	E	AFGL 4114
11252+1525	AF Leo ?	E	RAFGL 1488, IRC+20°229, AF Leo spectral type M5
12046−0629	RW Vir	E	SAO 138594, IRC−10°263, RAFGL 1535, type M5 III
12344+2720	IRC+30°241	E	RAFGL 1564, type M5
12387−3717		E	
13114−0232	SW Vir	E	RAFGL 1606, SAO 139236, type M7 III
13144−6225	V397 Cen	E	
13436−6220	HR 5171	E	RAFGL 4177, SAO 252488, type K0 Ia-0
13582+3806	SAO 63879	E	SVS 06519, IRC+40°252, RAFGL 4924S, type M8
14047−6113		E	
14086−0730	RAFGL 1686	E	type M9 III
14219+2555	RX Boo	E	SAO 83331, IRC+30°257, RAFGL 1706, type M7e - M8e
14434−5910		E	association to G317.291 is spurious
15502−5424		E	some absorption of feature
15506−5337		E	ID to a radio galaxy presumably is incorrect
15541−5408		E	some absorption of feature
16006−5257		E	strong absorption of feature
16079−5110	PK 331+0.2	E	silicate feature appears normal, unlike other planetary nebulae with silicate emission spectra
16122−5128		E	
16128−5228	W Nor	E	
16154−4753		E	spectrum similar to that of Vy 2−2 = 19219 + 0947, so this source might be a planetary nebula

Table 1 (Continued)

IRAS Name	Other Name	Group	Additional Associations And Comments
16331−4737		E	
16354−4642		E	OB association 66 is in this area
16372−4614		E	strong absorption of feature, has radio source associations
16391−4634		E	strong absorption of feature
16444−4527		E	strong absorption of feature
16450−4448		E	
16557−4531		E	strong absorption of feature
17007−4823		E	
17011−4343		E	
17012−3049		E	
17035−4051		E	
17040−4117		E	
17047−4030		E	
17051−4023		E	
17073−3955		E	
17110−3905		E	
17163−3835		E	
17163−3907	Hen 1379 ?	E	10 μm peak may be slightly absorbed
17215−7114		E	spectrum M3 III + A0 V; unusual LRS spectrum
17261−3348		E	
17281−3400	V483 Sco	E	
17294−4326		E	
17300−2223	IRC−20°368	E	RAFGL 1979, type "late M"
17313−1531		E	
17354−3155	SVS 09327	E	RAFGL 5361, IRC−30°308, type M8
17360−3140	IRC−30°309 ?	E	type M2.4 III + ?
17374−3156	IRC−30°312	E	type M2.6 Ia−
17376−3021		E	

Table 1 (Continued)

IRAS Name	Other Name	Group	Additional Associations And Comments
17454−3024		E	
17501−2656	RAFGL 2019	E	type M8–9, some absorption of feature
17539+1037	IRC+10°340	E	RAFGL 2033, type M6, strong absorption of feature
17560−2637	IRC−30°342	E	RAFGL 5161S, type M8
17599−3653	RAFGL 5430 ?	E	
18004−2148	IRC−20°423	E	type M10
18025−2113	IRC−20°427	E	RAFGL 2062, type M2 (reddened)
18079−1810		E	strong absorption of feature
18090−1853	IRC−20°444	E	RAFGL 2087, type M9
18135−1641	IRC−10°454	E	RAFGL 2103, type M5
18163−1547	IRC−10°463	E	RAFGL 2122, type M6
18225−1152		E	LDN 0406 is 8′ away
18227−1243	RY Sct	E	SAO 161458, RAFGL 5235S, B0ep in eclipsing binary
18246−2216		E	
18248−1229	UY Sct	E	RAFGL 2162, IRC−10°422, type M4 Ia
18252−1229		E	
18262−1133	RAFGL 2168	E	IRC−10°426, type M10, strong absorption of feature
18304−0728	IRC−10°434	E	RAFGL 2185, type M7
18358−0623		E	60 and 100 μm excess, possibly due to cirrus
18373−1835	IRC−20°507	E	RAFGL 5519, type M7
18375−0544	SVS 11180	E	S star 572, IRC−10°450, RAFGL 2223
18383−0542	IRC−40°452	E	RAFGL 2226, type M6
18386−0624	SVS 11201	E	RAFGL 5275S, IRC−10°453
18394−0503	IRC−10°454	E	RAFGL 2229, type M5
18431−0403		E	strong absorption of feature
18455−0200	SVS 11355	E	RAFGL 2254, IRC+00°379, type M6 III
18513+0035	IRC+00°389	E	
18522+0021	SVS 11511	E	RAFGL 5321S, IRC+00°392, type M6

Table 1 (Continued)

IRAS Name	Other Name	Group	Additional Associations And Comments
18539+0026	IRC+00°396	E	type "pec or M(e?)"
18559+0435	DO 5230	E	RAFGL 2288, IRC+00°402, type M2
19371+2855	SVS 12260	E	
19374+0550	EIC 786	E	
19486+3247	HR 7564	E	χ Cyg, S star 625, IRC+20°395, type S7/1.5e
19528+0148		E	PKS 1952+017 is 2′ away
20024+1727		E	
20241+3811	KY Cyg	E	IRC+40°415, RAFGL 2575, type M4
20270+3948	RW Cyg	E	DO 19053, RAFGL 2590, IRC+40°424, type M3 Ia
20276−0455	TZ Aql	E	SAO 144506, RAFGL 2592, IRC+00°477, type M6
20312+4035		E	
20322+4215	IRC+40°434	E	RAFGL 2609, type M4
21565+4132	DL Lac ?	E	
22466+2705	ST Peg	E	SAO 90805, RAFGL 2960, IRC+30°502, type M6 III
23013+3735	CF And	E	SAO 72968, IRC+40°528, RAFGL 3018, type M7, unusual feature
23063−3024	Y Scl	E	SAO 214344, RAFGL 3029, IRC−30°465
23173+2600	W Peg	E	DO 22163, IRC+30°509, RAFGL 3126, type M5
23278+6000	IRC+60°409	E	RAFGL 3109, V582 Cas, type M4, red end affected by 23284+5958
23369+3203	DO 22364	E	RAFGL 3126, IRC+30°515, HS Peg, type M5
23412−1533	HR 8992	E	R Aql, RAFGL 3136, IRC−20°642, type M7 III
02219+6152	RAFGL 326	H	also associated with CED 006C and LDN 1359
02230+6202	RAFGL 328	H	also associated with radio source MH 133.8+01.4
02232+6138	RAFGL 331	H	unusual [25] − [60] and [60] − [100] values
05393−0156	NGC 2024	H	RAFGL 807, same CED and MRSL associations as 05391−0152
08563−4711	VHE 26	H	
08573−4718	G267.943	H	
08576−4334	G265.150	H	
09227−5146	G274.013	H	

Table 1 (Continued)

IRAS Name	Other Name	Group	Additional Associations And Comments
10049−5657	G282.026	H	RAFGL 4101
10295−5746	G285.253	H	
11097−6102	G291.284	H	CED 113C is also associated with this source
12127−6244	G298.868 ?	H	RAFGL 4148 ?
12320−6122	G300.956	H	the association to PK 301+1.1 is spurious
13080−6229	G305.202 ?	H	GS 305.1+00.0
13092−6218	G350.363 ?	H	GM 14
13111−6228	RAFGL 4165	H	G305.551 ?
13471−6120		H	
15061−5806	G320.317 ?	H	GS 320.3−00.2
15061−5814	DTG320.3-0.	H	associations to radio sources seem questionable
15384−5348	G326.441	H	
15408−5356	G326.644	H	same association as 15412 − 5359
15412−5359	G326.644 ??	H	radio source is 4′ away
15492−5426	G327.313 ?	H	GS 327.3−00.5
15507−5359	G327.759	H	
15539−5353	G328.180 ?	H	
16026−5035	G331.354	H	
16083−5154	G331.115 ?	H	
16085−5138		H	MB 1608−51.6 ?
16112−4943	G332.978 ?	H	
16132−5039		H	GS 332.5−00.1 ?
16164−5046		H	MRSL 322−00/1 is 9′ away
16167−5034		H	some radio associations with poor positional agreement
16172−5028		H	some radio associations with poor positional agreement
16177−5018	G333.292 ?	H	
16279−4757		H	colours are typical of planetary nebulae
16330−4725	G337.147 ?	H	GS 337.1−00.2

Table 1 (Continued)

IRAS Name	Other Name	Group	Additional Associations And Comments
16374−4701	G337.949 ?	H	GS 337.9−00.5
16571−4029	G345.231 ?	H	TD 345.2+01.0
17008−4040	G345.945 ?	H	
17009−4042	G345.495 ?	H	unusual feature near 10 μm
17059−4132	G345.425 ?	H	associated with PK 345−0.1, probably spuriously
17136−3617	G350.524 ?	H	
17149−3916	G348.231	H	associated with PK 348−0.1, probably spuriously
17160−3707		H	probably silicate absorption in an H II region
17167−3854	G348.716 ?	H	
17170−3539		H	MRSL 351+00/5 is 4′ away
17171−3542		H	MRSL 351+00/5 is 4′ away
17172−3548		H	S 8 is 9′ away; GM 32 ?
17173−3546		H	GM 32 ? BTD 351.4 + 00.0
17175−3544		H	
17178−3742	G349.840	H	
17197−3552		H	G351.617 is 3′ away
17200−3550	G351.617	H	
17256−3631		H	
17258−3637		H	ADG 351.6−01.2
17271−3309	G354.664	H	
17271−3439	G353.403 ?	H	RAFGL 5345 ?
17392−3008	Bonn 358.605	H	
17423−2855	S 17 ??	H	6′ separation
17424−2859	G359.946	H	the galactic center complex (IRS 1 or IRS 7)
17430−2848	G0.173	H	RAFGL 2004, optically invisible
17455−2800	Bonn 1.130	H	
17574−2403	G5.897 ?	H	RAFGL 2046 ?
17599−2148	G8.134	H	RAFGL 2051

Table 1 (Continued)

IRAS Name	Other Name	Group	Additional Associations And Comments
18006−2422	LKH 108	H	also associated with G5.974 and CED 152A
18060−2005	G10.310	H	RAFGL 4235
18064−2020	Bonn 10.159	H	
18111−1729	Bonn 13.186	H	
18116−1646	Bonn 13.875	H	
18174−1612	G15.033	H	
18248−1158	Bonn 19.068	H	
18288−0207	RAFGL 2177	H	
18314−0720	Bonn 25.384	H	
18355−0650	Bonn 25.382	H	RAFGL 2210
18416−0420	G28.302	H	
18434−0242	G29.947	H	
18449−0158	Bonn 30.776	H	GM 44
18507+0110	Bonn 34.254	H	RAFGL 2271
18576+0341		H	possible planetary nebula based on the colours
18592+0108	G35.191 ?	H	RAFGL 2304 ??
18593+0408	G37.868	H	
19078+0901	Bonn 43.169	H	RAFGL 2334 ?
19110+1045	Bonn 45.066	H	
19120+1103	Bonn 45.451	H	RAFGL 2345 ?
19209+1421	Bonn 49.384	H	GM 50
19213+1424	Bonn 49.486	H	RAFGL 2381
19442+2427	RAFGL 2542 ?	H	S 87 is 2′ away
19446+2505	RAFGL 2455	H	PKS 1944+25.0
20178+4046		H	
20198+3716	V469 Cyg	H	MWC 1015, CS 2896 ?
21413+5442		H	associated spuriously with a radio galaxy
23030+5958	S 156	H	

Table 1 (Continued)

IRAS Name	Other Name	Group	Additional Associations And Comments
23113+6113	S 158	H	CED 209
23116+6111	RAFGL 3048	H	S 158 is 2′ away
02036−1027	UZ Cet	U	SAO 148198, IRC−10°032, RAFGL 297, type M2, 9 μm emission
10428−5909	RT Car	U	SAO 238424, type M3; a nova-like variable
10540−6013	WK−592856	U	
11385−5517	SAO 239288	U	type F2pe (shell)
14068−6111		U	
15452−5459		U	
16441−4506		U	this could be a PAH source with a bad red part
16469−4515		U	
16488−4407		U	emission at 9 μm
17257−3504		U	
17377−3211	BM Sco	U	SAO 209132, IRC+30°313, type K0, 9 μm emission
17380−3015	IRC−30°314	U	
17393−3004	IRC−30°316	U	type M1 (e?)
17444−2902		U	
17516−2525		U	
17583−2201		U	
17593−2328	Hen 1560	U	IRC−20°418, type M3ep, emission feature at 9 μm
18237−1153	LDN 0413?	U	
18250−0351	MWC 297	U	RAFGL 2165, S 62, B[] star
18284−0946	RAFGL 2174	U	S 56 is 3′ away
18352−0655	SVS 11126	U	RAFGL 2162, IRC−10°442,
18363−0607		U	ADG 026.1 − 00.0 ?
18430−0237		U	
18457−0154	RAFGL 5335	U	
18526+0140		U	unusual LRS spectrum
18585−3701	R CrA ?	U	Up 396 − N * 15, type M4

Table 1 (Continued)

IRAS Name	Other Name	Group	Additional Associations And Comments
20197+3722	BC Cyg	U	IRC+40°409, RAFGL 2560, type M4 Ia, H II source colours
20212+3920	MWC 342	U	
20369+5131		U	
05330−0517	NU Ori ?	I	SAO 132328, type B8; also associated with 3 other stars
05391−0152	CED 055p	I	also associated with MRSL 206−16/02
07120−4433	HR 2748	I	L_2 Pup, type M5 IIIe, anomalous [25] − [60] colour
11445+4344	AZ UMa	I	SAO 43889, RAFGL 1511, IRC+40°228, type M6 III, silicate emission source
13125−6223		I	silicate emission, consistently bad red part
15411−5352	G326.624	I	association with PK 326+0.1 is probably incorrect
16374−4608	G338.450 ??	I	
16555−4237	Up 227 − N * 21	I	also G343.490; blue part looks like an H II source spectra
17056−4137		I	all 6 scans are similar
17128−3748		I	would be in class 5 if the spectrum was complete
17327−3319		I	OCL 1021 is 8′ away
17379−3019	RAFGL 5373 ?	I	
17468−2900	V758 Sgr	I	IRC−30°325, RAFGL 2013, type M2, silicate emission source
18176−1617		I	associations all > 5′ away
18184−1623	SAO 161375	I	WK 168625, type B
18219−1311	Bonn 18.197	I	S 53 is 7.5′ away
20141−2128	RT Cap	I	CS 2882, IRC−20°585, RAFGL 2542, type C6,4; good blue part showing 11 μm emission, consistently noisy red part
23118+6110		I	S 158 is 4′ away

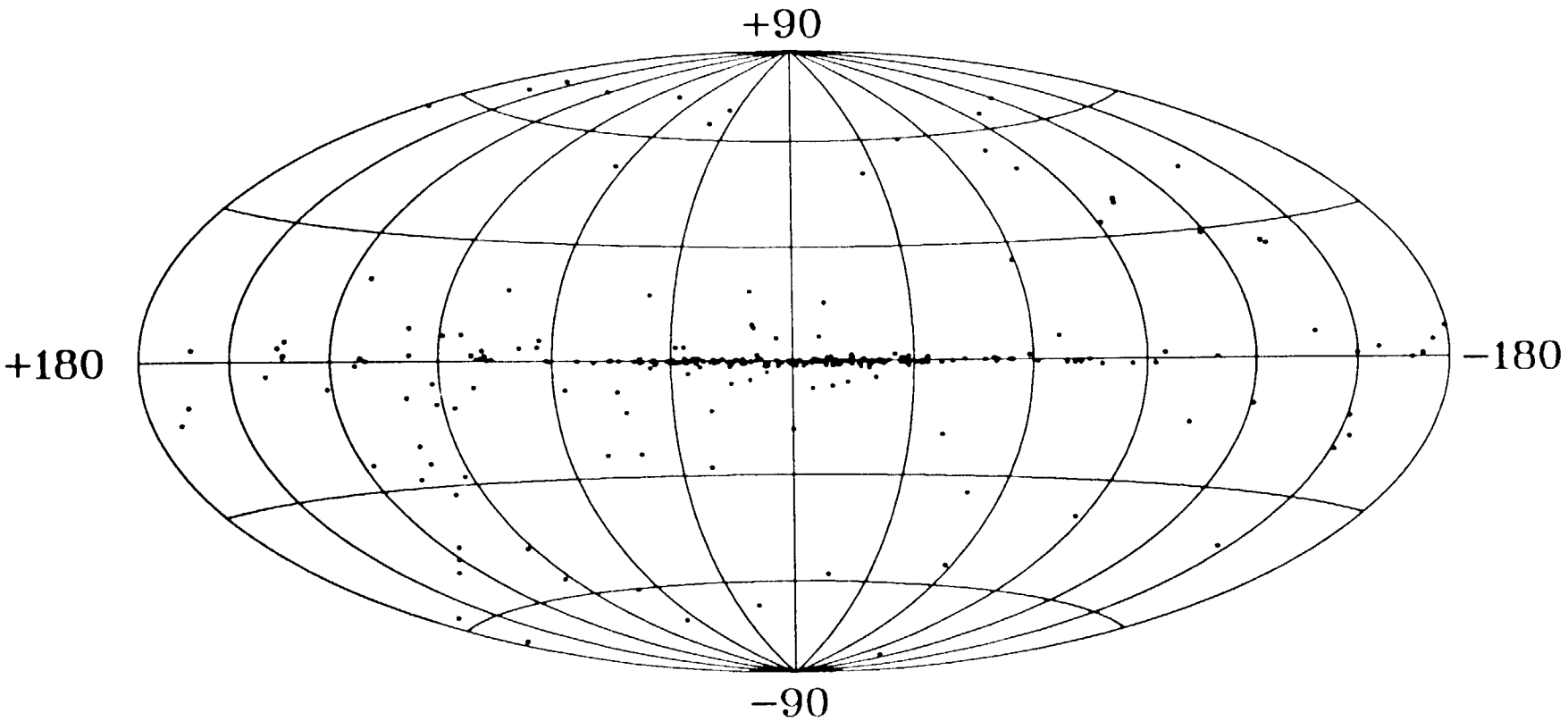

Fig. 1

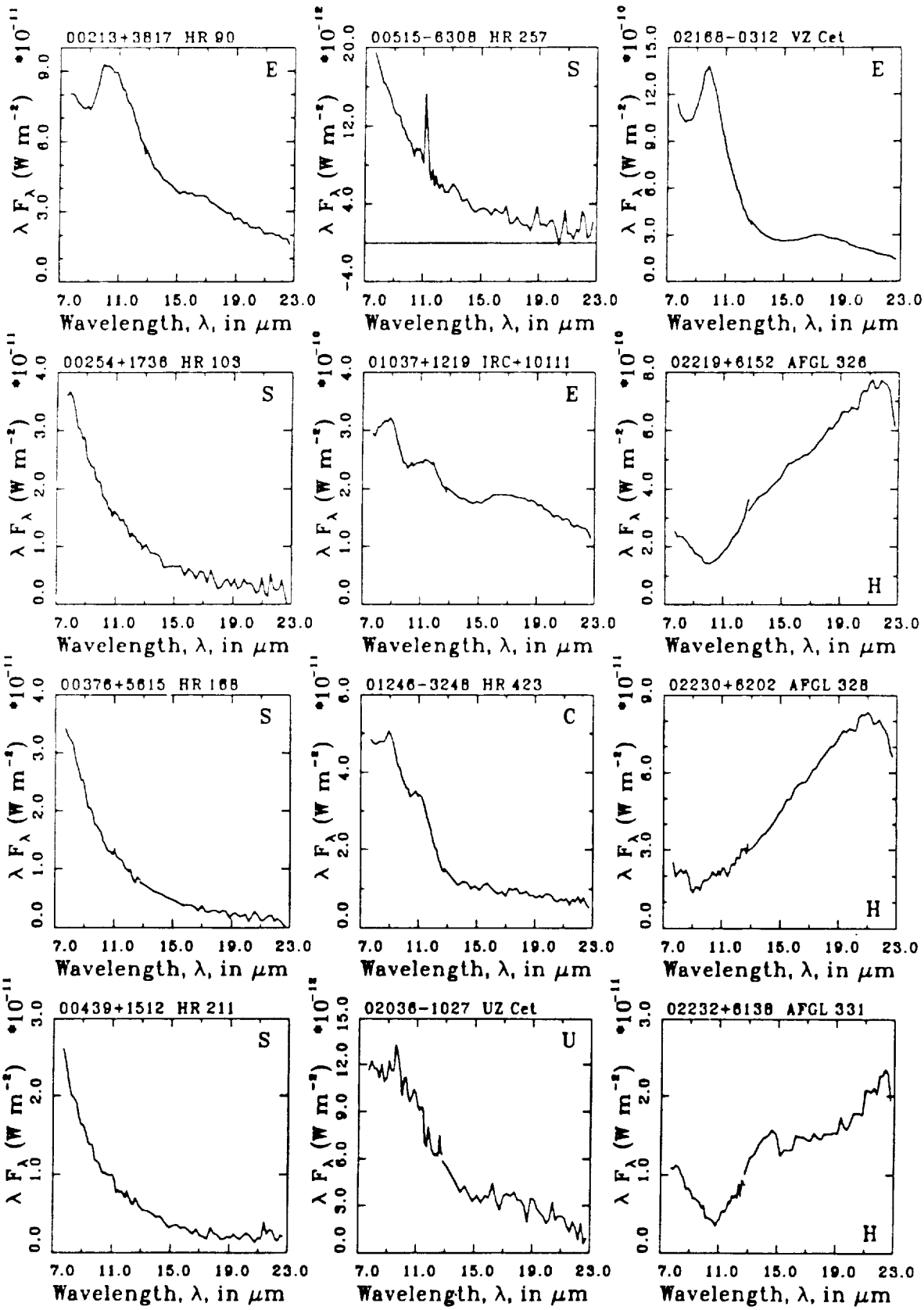
00213+3817 HR 90
E
00515-6308 HR 257
S
02168-0312 VZ Cet
E
00254+1736 HR 103
S
01037+1219 IRC+10111
E
02219+6152 AFGL 326
H
00376+5615 HR 168
S
01246-3248 HR 423
C
02230+6202 AFGL 328
H
00439+1512 HR 211
S
02036-1027 UZ Cet
U
02232+6138 AFGL 331
H
λ F_λ (W m^-2)
Wavelength, λ, in μm
7.0 11.0 15.0 19.0 23.0

Fig. 2, p.1

C3

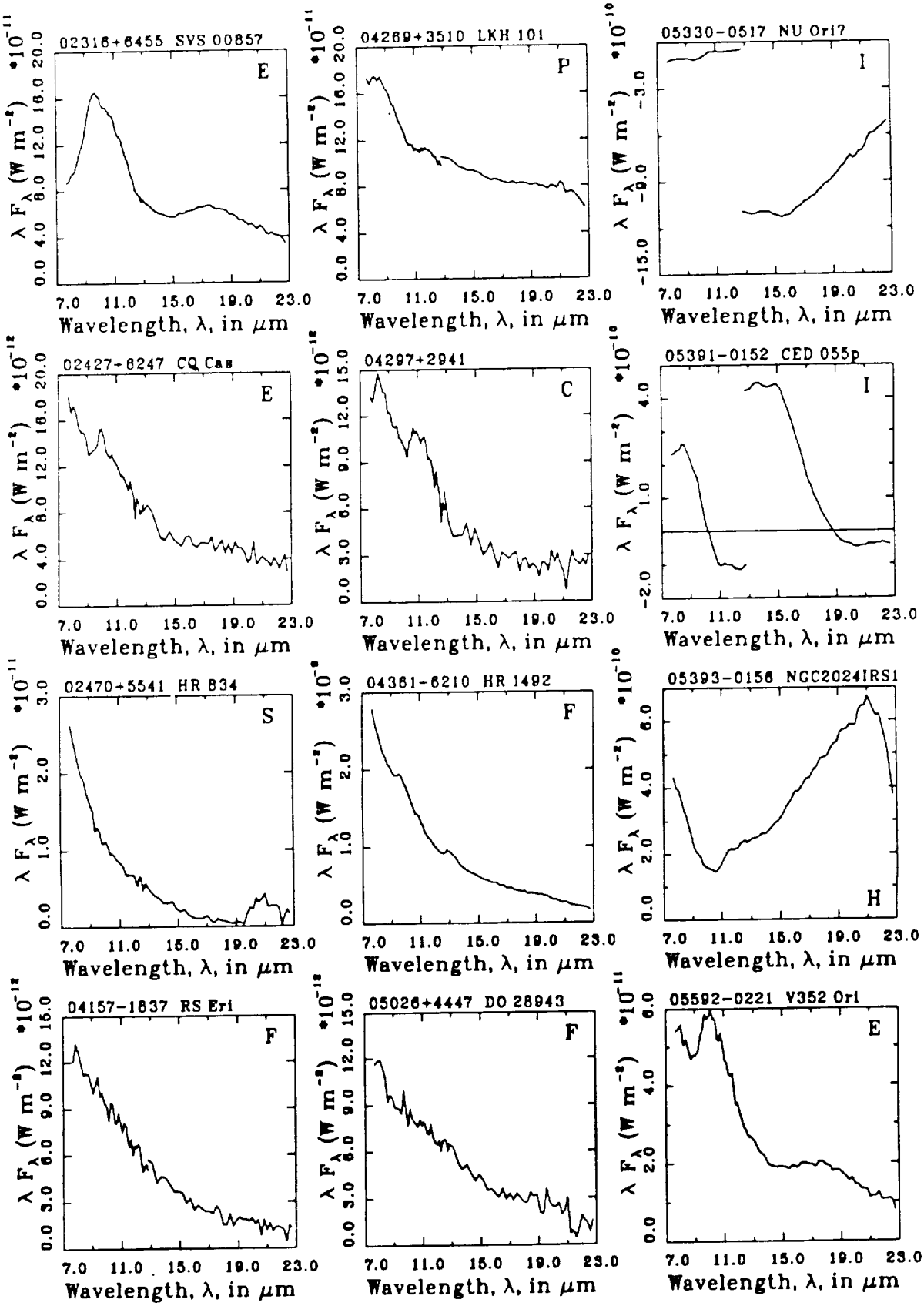
02316+6455 SVS 00857
E
04269+3510 LKH 101
P
05330-0517 NU Ori?
I
02427+6247 CQ Cas
E
04297+2941
C
05391-0152 CED 055p
I
02470+5541 HR 834
S
04361-6210 HR 1492
F
05393-0156 NGC2024IRS1
H
04157-1637 RS Eri
F
05026+4447 DO 28943
F
05592-0221 V352 Ori
E
λ F_λ (W m^-2)
Wavelength, λ, in μm

Fig. 2, p.2

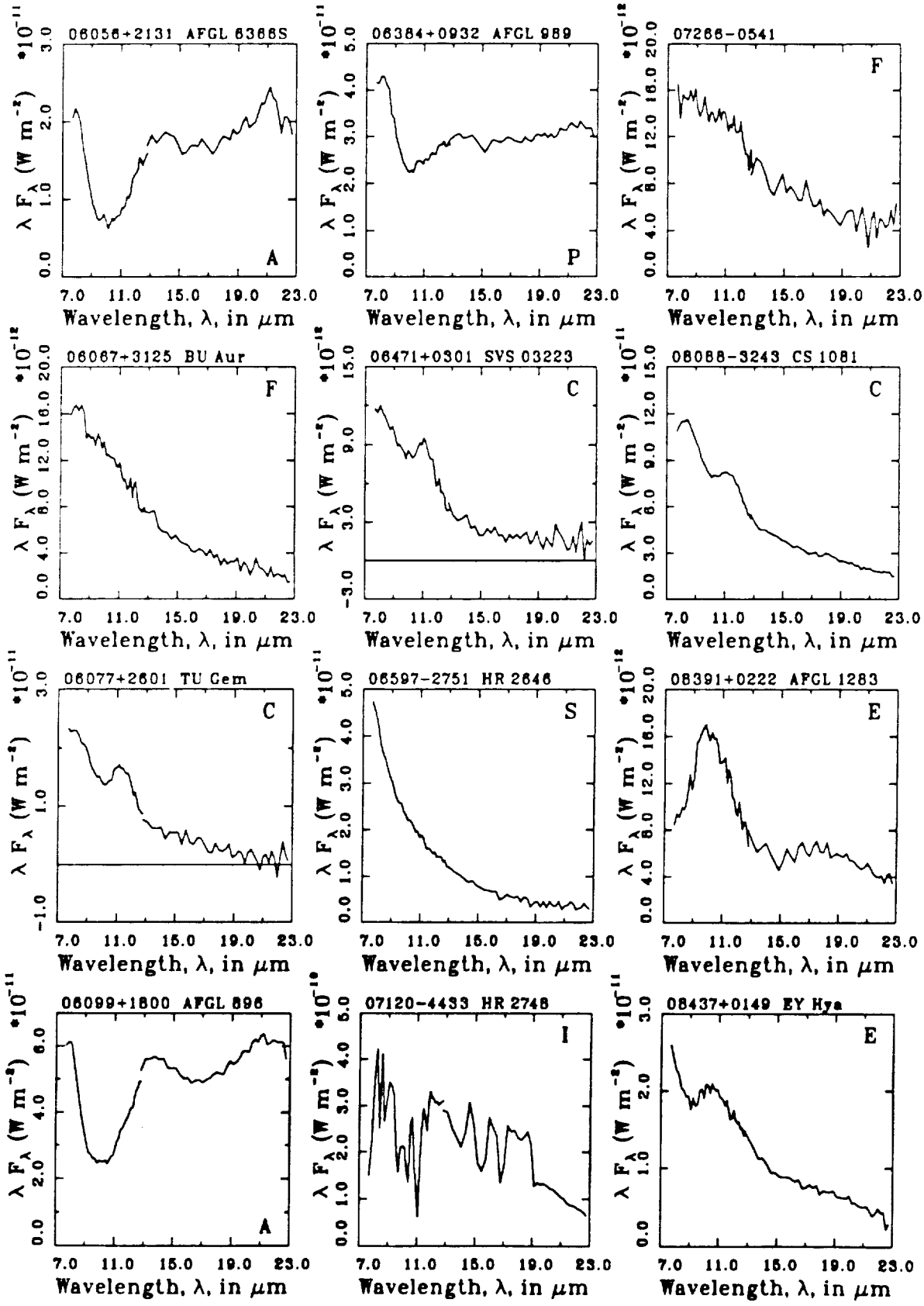
06056+2131 AFGL 6366S
A
06384+0932 AFGL 989
P
07266-0541
F
06067+3125 BU Aur
F
06471+0301 SVS 03223
C
06068-3243 CS 1081
C
06077+2601 TU Gem
C
06597-2751 HR 2646
S
08391+0222 AFGL 1283
E
06099+1800 AFGL 896
A
07120-4433 HR 2748
I
08437+0149 EY Hya
E
λ F_λ (W m^-2)
Wavelength, λ, in μm
7.0 11.0 15.0 19.0 23.0

Fig. 2, p.3

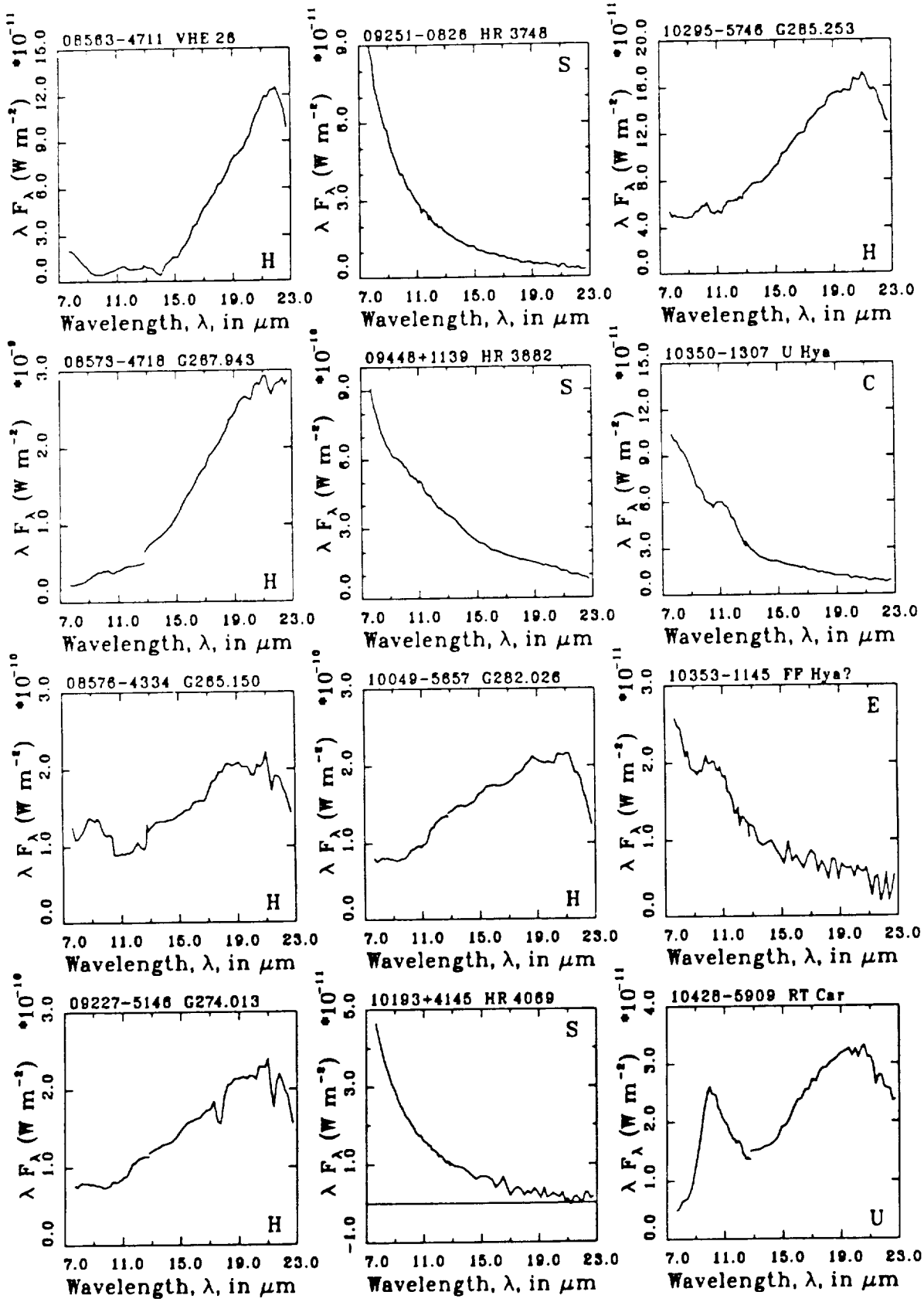
08563-4711 VHE 26
H
09251-0826 HR 3748
S
10295-5746 G285.253
H
08573-4718 G287.943
H
09448+1139 HR 3882
S
10350-1307 U Hya
C
08576-4334 G285.150
H
10049-5657 G282.026
H
10353-1145 FP Hya?
E
09227-5146 G274.013
H
10193+4145 HR 4069
S
10428-5909 RT Car
U
λ F_λ (W m^-2)
Wavelength, λ, in μm

Fig. 2, p.4

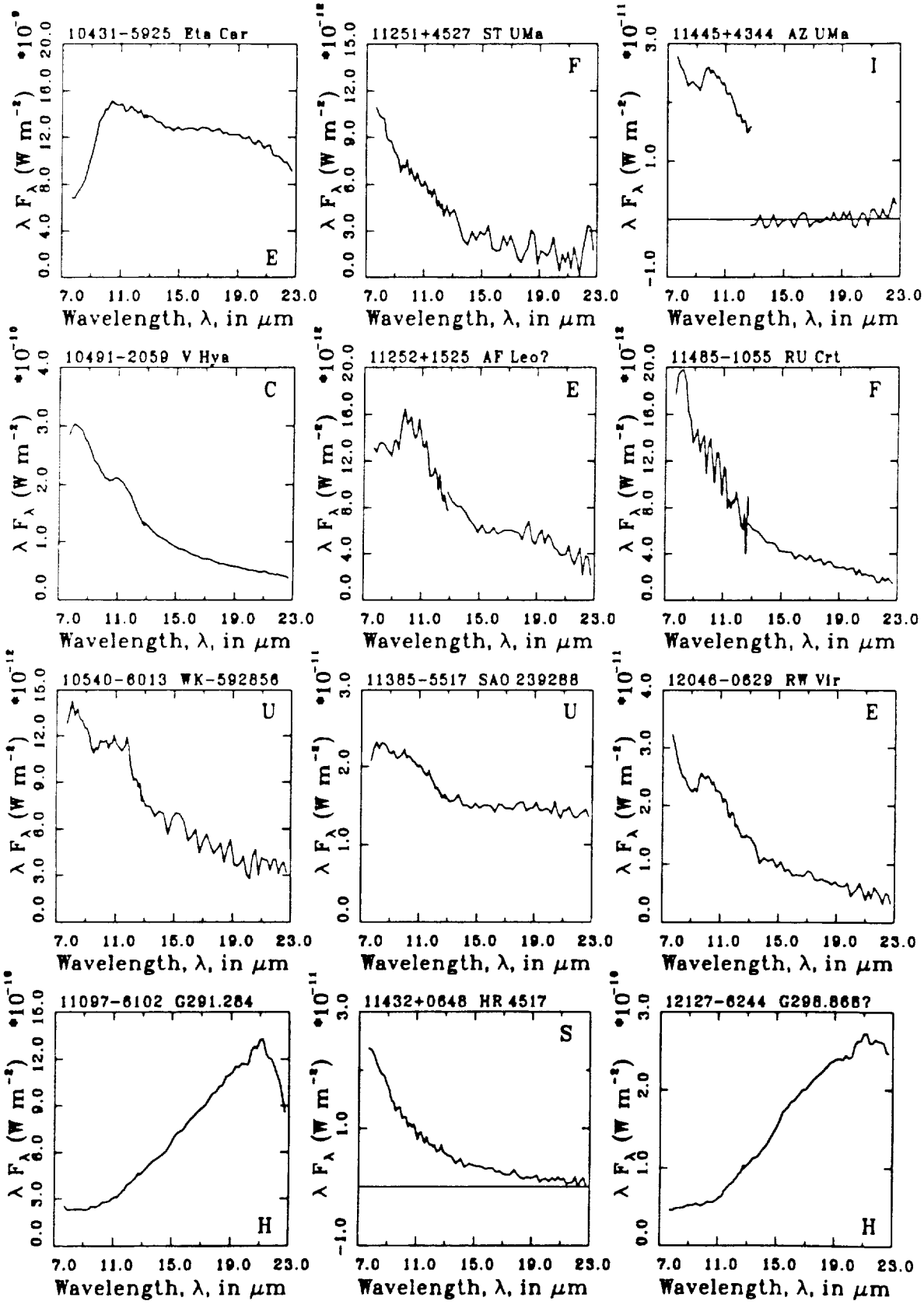
10431-5925 Eta Car
E
11251+4527 ST UMa
F
11445+4344 AZ UMa
I
10491-2059 V Hya
C
11252+1525 AF Leo?
E
11485-1055 RU Crt
F
10540-6013 WK-592856
U
11385-5517 SAO 239288
U
12046-0629 RW Vir
E
11097-6102 G291.284
H
11432+0648 HR 4517
S
12127-6244 G298.868?
H
Wavelength, λ, in μm

Fig. 2, p.5

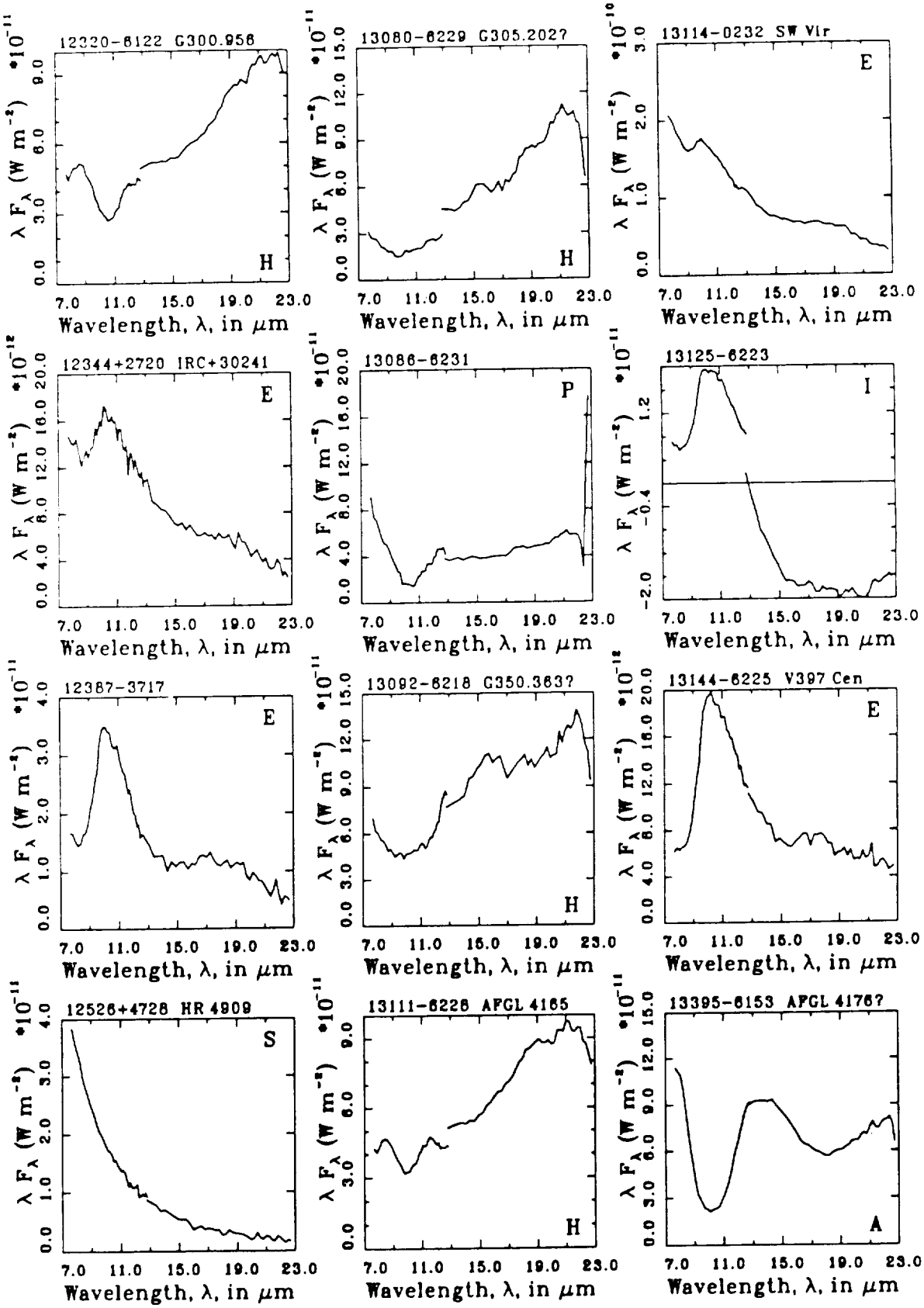
12320-6122 G300.956
13080-6229 G305.202?
13114-0232 SW Vir
12344+2720 IRC+30241
13086-6231
13125-6223
12387-3717
13092-6218 G350.363?
13144-6225 V397 Cen
12526+4728 HR 4909
13111-6228 AFGL 4165
13395-6153 AFGL 4176?
Wavelength, λ, in μm

Fig. 2, p.6

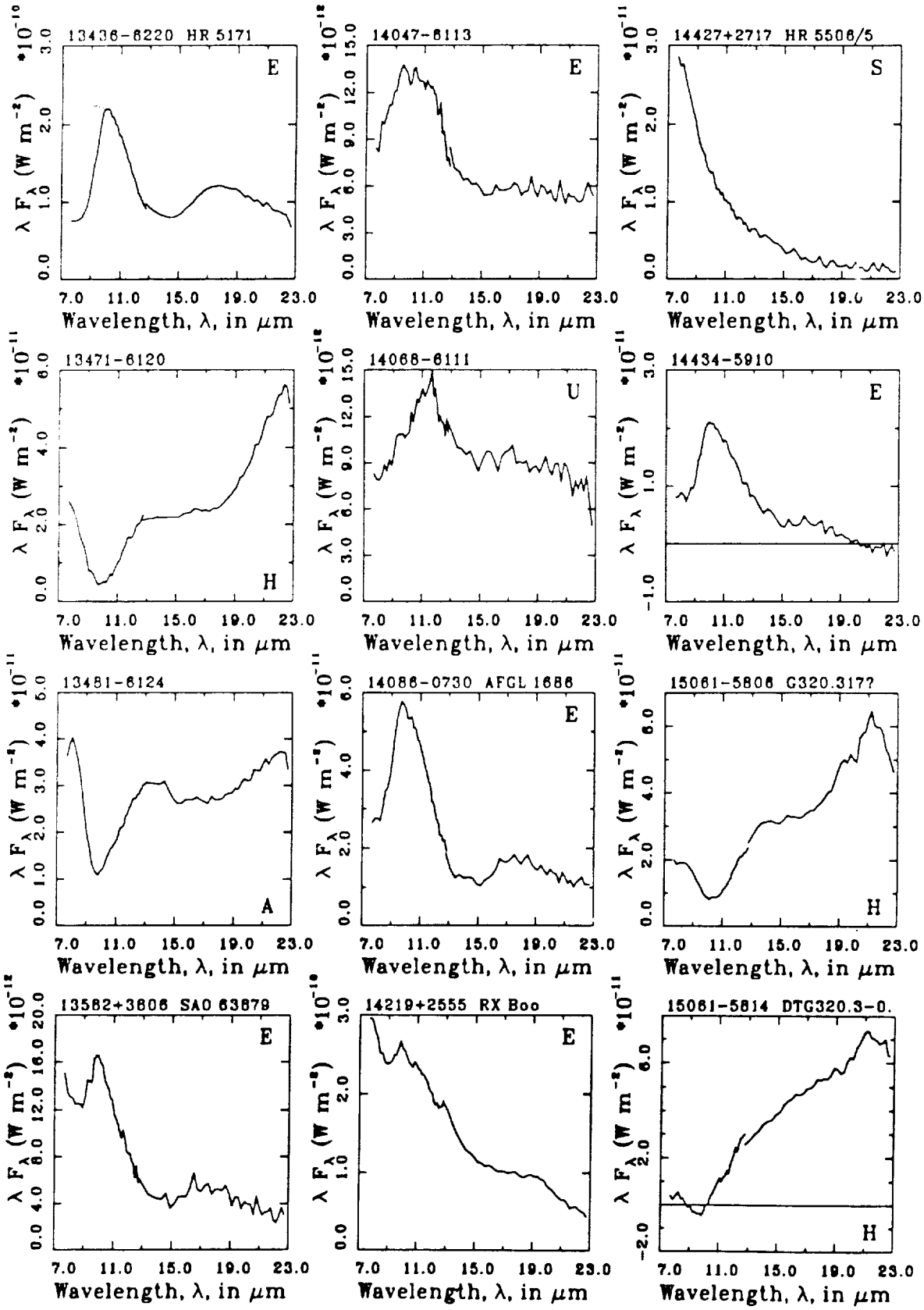
13436-6220 HR 5171
E
14047-6113
E
14427+2717 HR 5506/5
S
13471-6120
H
14068-6111
U
14434-5910
E
13481-6124
A
14086-0730 AFGL 1686
E
15061-5806 G320.317?
H
13562+3606 SAO 63879
E
14219+2555 RX Boo
E
15061-5814 DTG320.3-0.
H
λ F_λ (W m^-2)
Wavelength, λ, in μm

Fig. 2, p.7

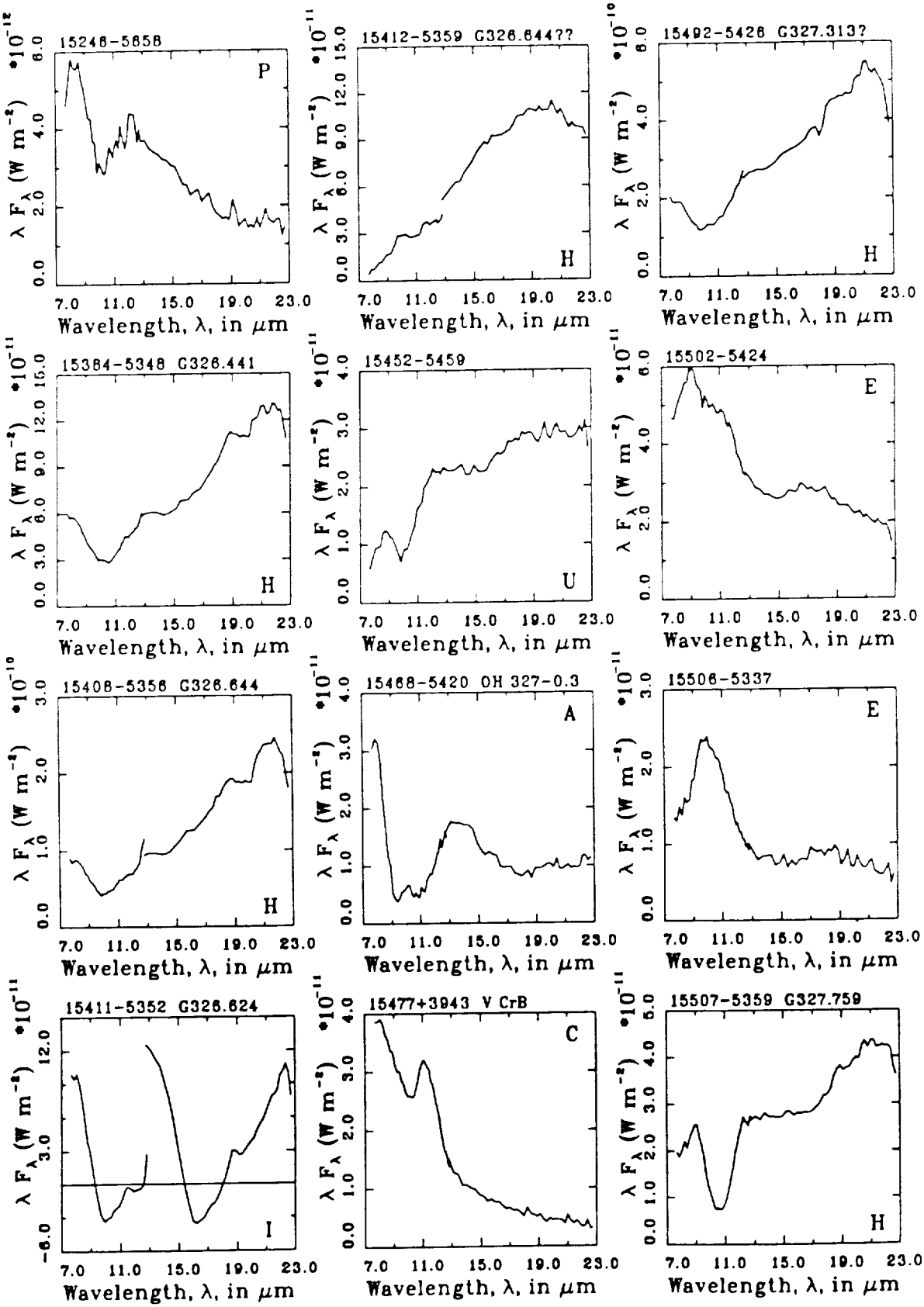
15246-5658
P
15412-5359 G326.644??
H
15492-5426 G327.313?
H
15384-5348 G326.441
H
15452-5459
U
15502-5424
E
15408-5356 G326.644
H
15468-5420 OH 327-0.3
A
15506-5337
E
15411-5352 G326.624
I
15477+3943 V CrB
C
15507-5359 G327.759
H
λ F_λ (W m^-2)
Wavelength, λ, in μm

Fig. 2, p.8

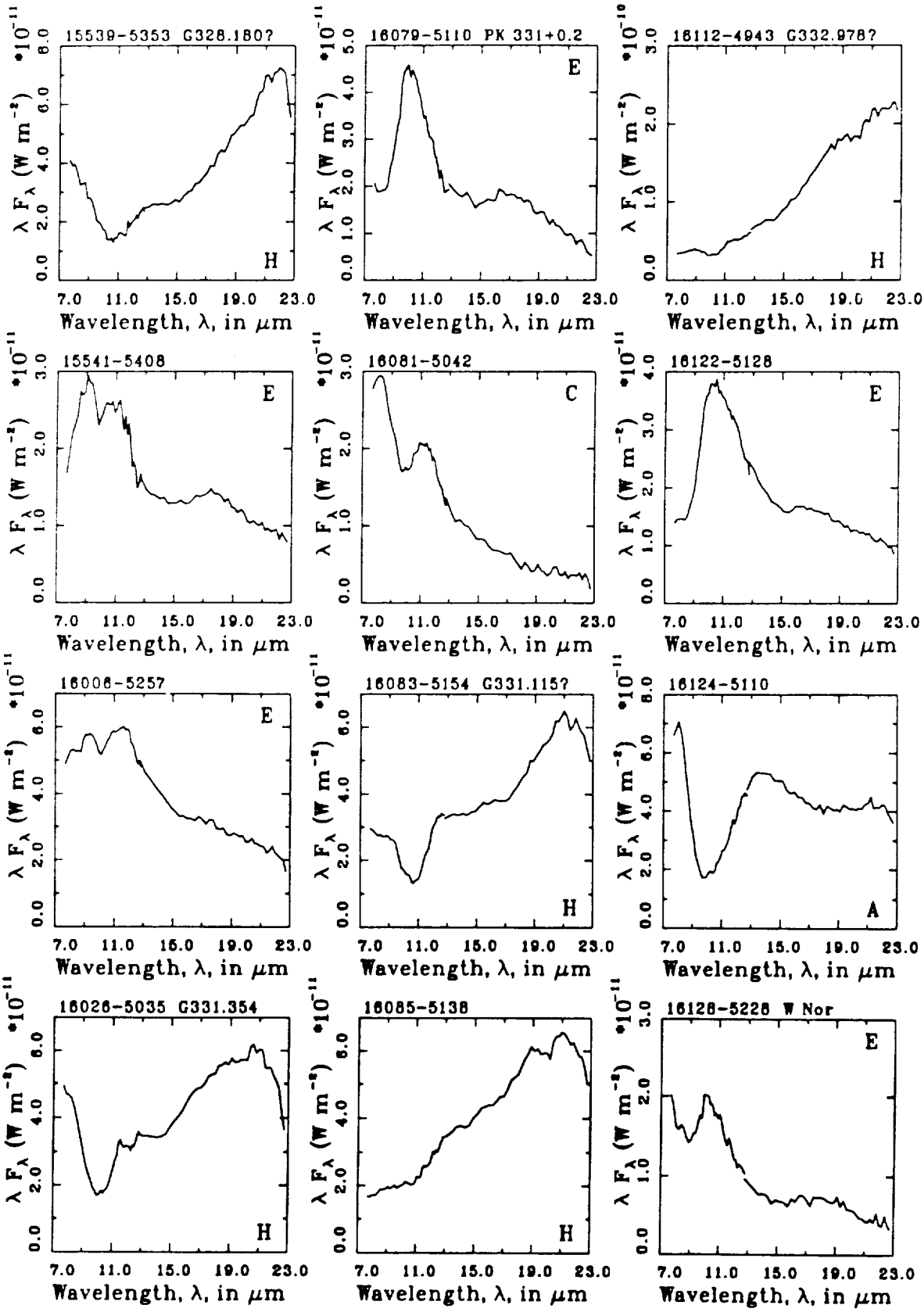
15539-5353 G328.180?
16079-5110 PK 331+0.2
16112-4943 G332.978?
15541-5408
16081-5042
16122-5128
16006-5257
16083-5154 G331.115?
16124-5110
16026-5035 G331.354
16085-5138
16128-5228 W Nor
Wavelength, λ, in μm

Fig. 2, p.9

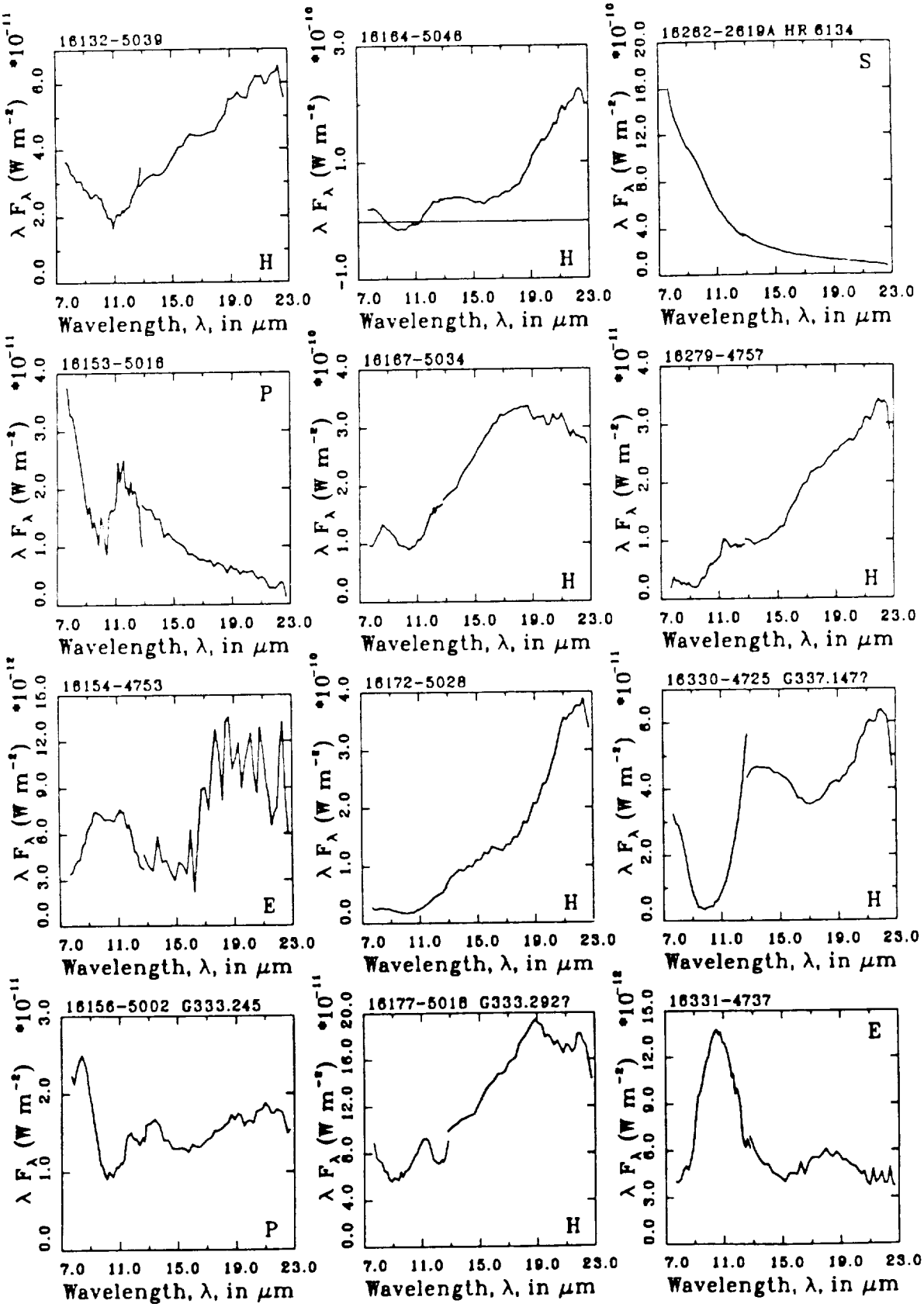
16132-5039
H
16164-5046
H
16282-2619A HR 6134
S
16153-5018
P
16167-5034
H
16279-4757
H
16154-4753
E
16172-5028
H
16330-4725 G337.147?
H
16156-5002 G333.245
P
16177-5018 G333.292?
H
16331-4737
E
λ F_λ (W m^-2)
Wavelength, λ, in μm

Fig. 2, p.10

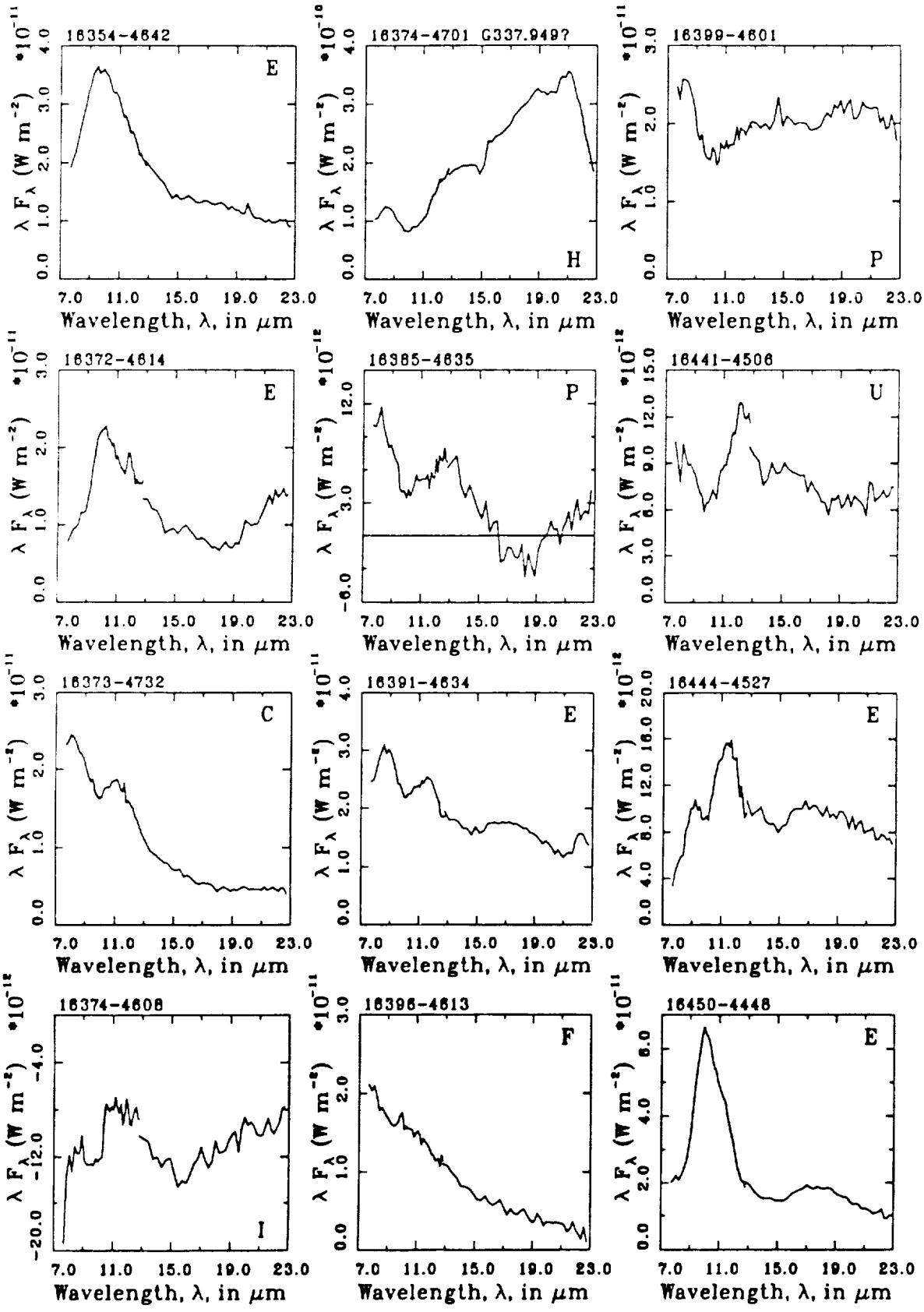
16354-4642
E
16374-4701 G337.949?
H
16399-4601
P
16372-4614
E
16385-4635
P
16441-4506
U
16373-4732
C
16391-4634
E
16444-4527
E
16374-4608
I
16396-4613
F
16450-4448
E
λ F_λ (W m^-2)
Wavelength, λ, in μm

Fig. 2, p.11

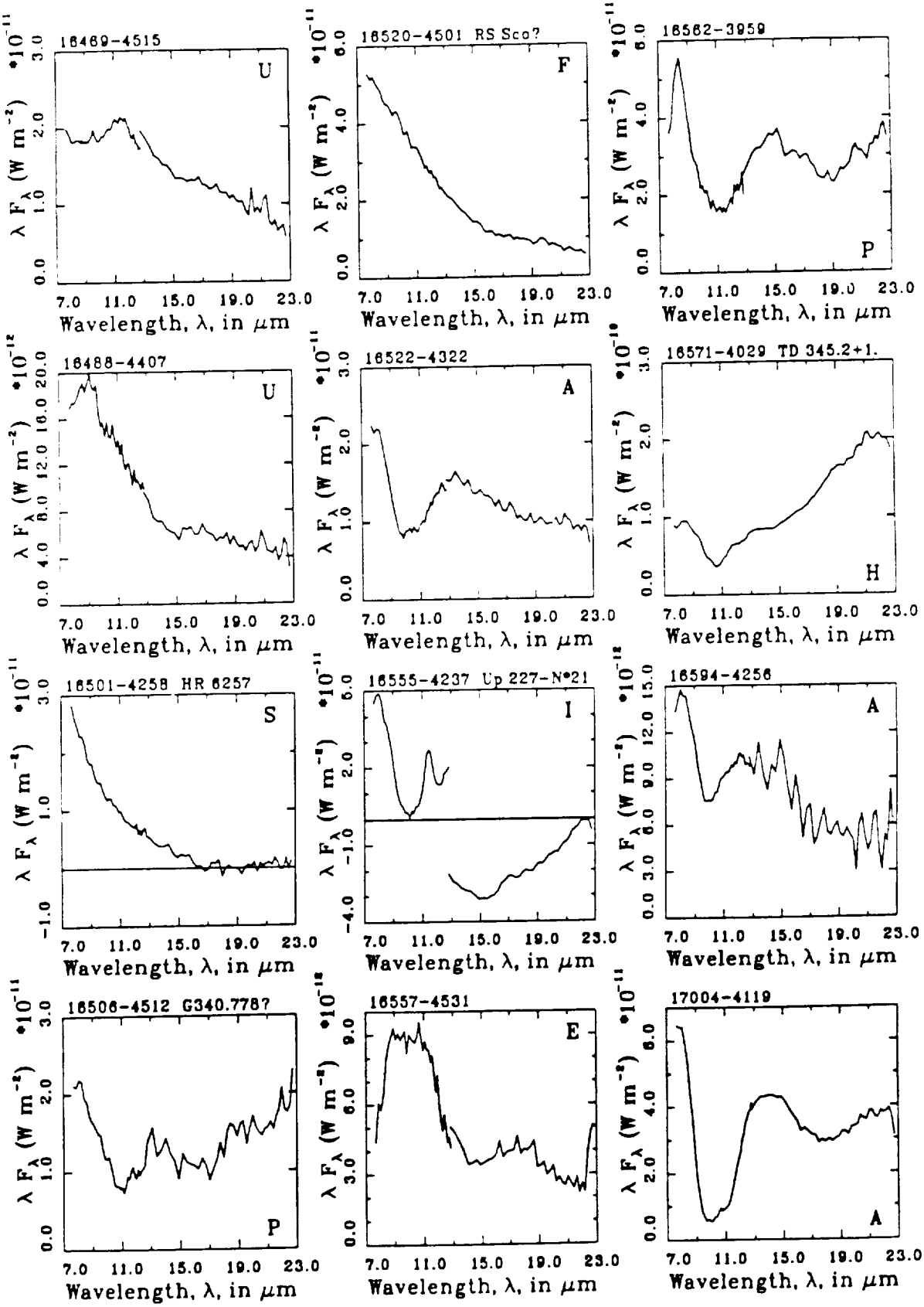
16469-4515
U
16520-4501 RS Sco?
F
16562-3959
P
16488-4407
U
16522-4322
A
16571-4029 TD 345.2+1.
H
16501-4258 HR 6257
S
16555-4237 Up 227-N°21
I
16594-4256
A
16506-4512 G340.7787
P
16557-4531
E
17004-4119
A
λ F_λ (W m^-2)
Wavelength, λ, in μm

Fig. 2, p.12

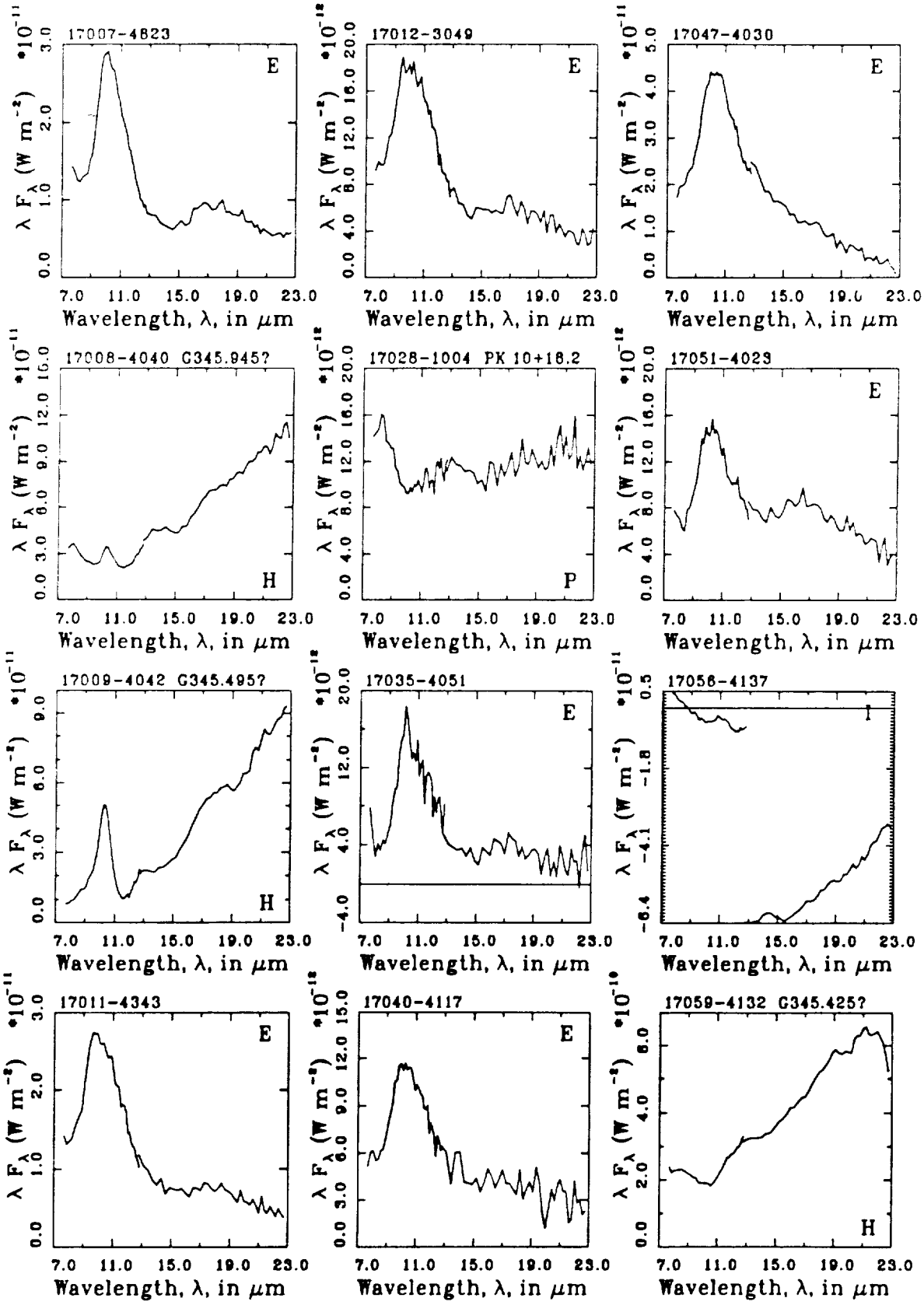
17007-4823
E
17012-3049
E
17047-4030
E
17008-4040 G345.945?
H
17028-1004 PK 10+18.2
P
17051-4029
E
17009-4042 G345.495?
H
17035-4051
E
17056-4137
17011-4343
E
17040-4117
E
17059-4132 G345.425?
H
λ F_λ (W m^-2)
Wavelength, λ, in μm

Fig. 2, p.13

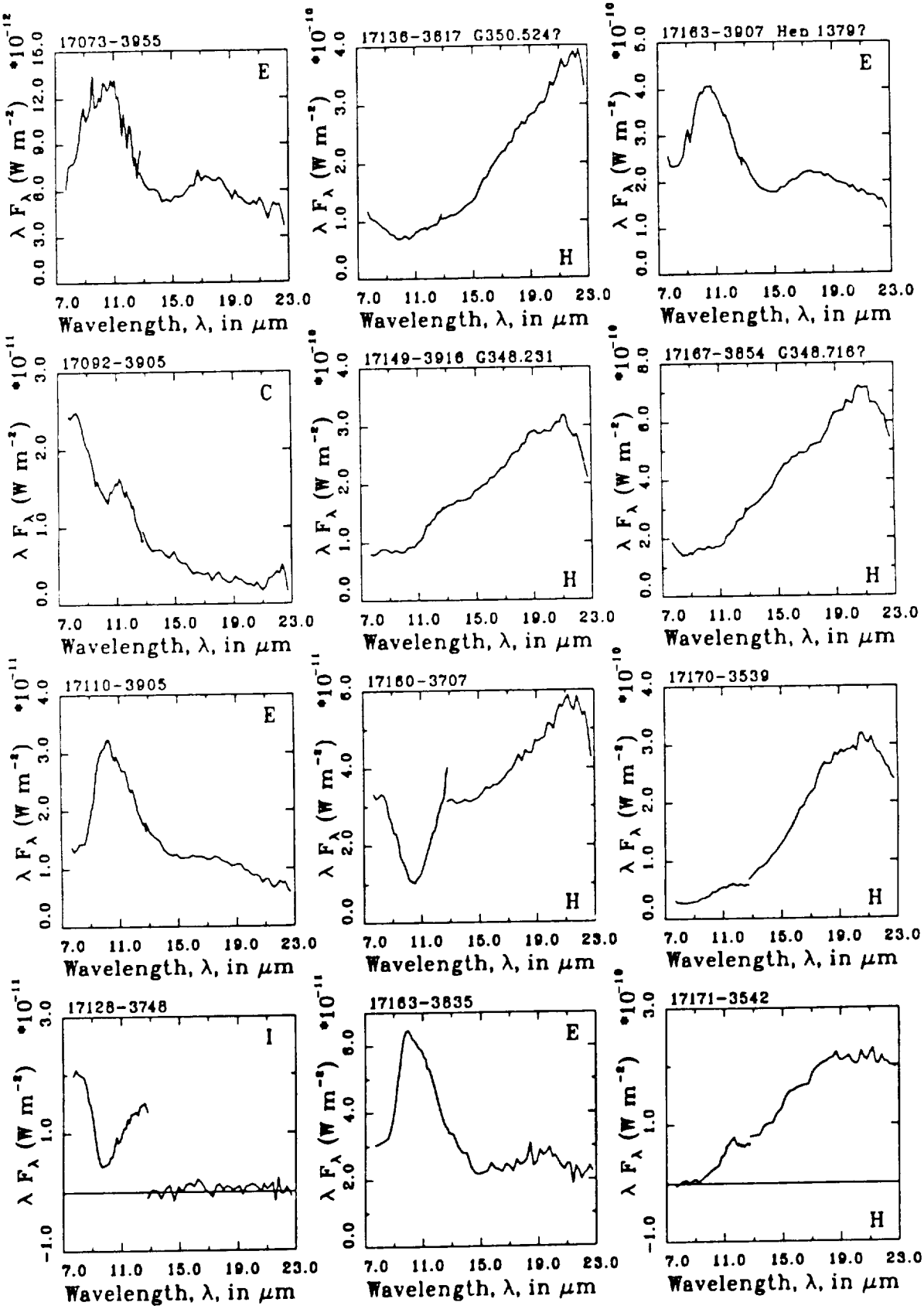
17073-3955
E
17136-3617 G350.524?
H
17163-3907 Hen 13797
E
17092-3905
C
17149-3916 G348.231
H
17167-3854 G348.716?
H
17110-3905
E
17160-3707
H
17170-3539
H
17128-3748
I
17163-3835
E
17171-3542
H
λ F_λ (W m^-2)
Wavelength, λ, in μm
7.0 11.0 15.0 19.0 23.0

Fig. 2, p.14

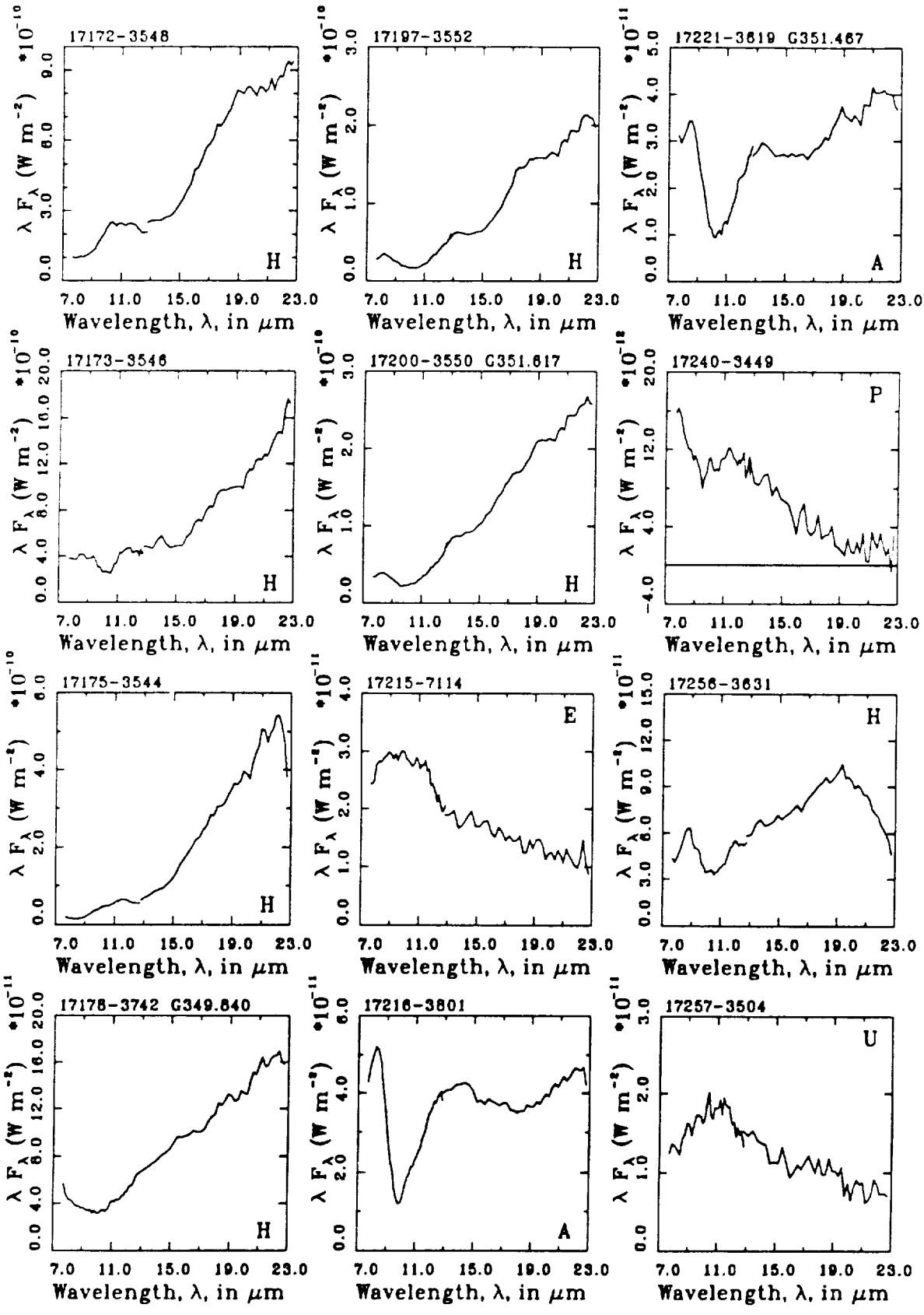
17172-3548
H
17197-3552
H
17221-3619 G351.467
A
17173-3546
H
17200-3550 G351.617
H
17240-3449
P
17175-3544
H
17215-7114
E
17256-3631
H
17178-3742 G349.640
H
17216-3801
A
17257-3504
U
λ F_λ (W m^-2)
Wavelength, λ, in μm
7.0 11.0 15.0 19.0 23.0

Fig. 2, p.15

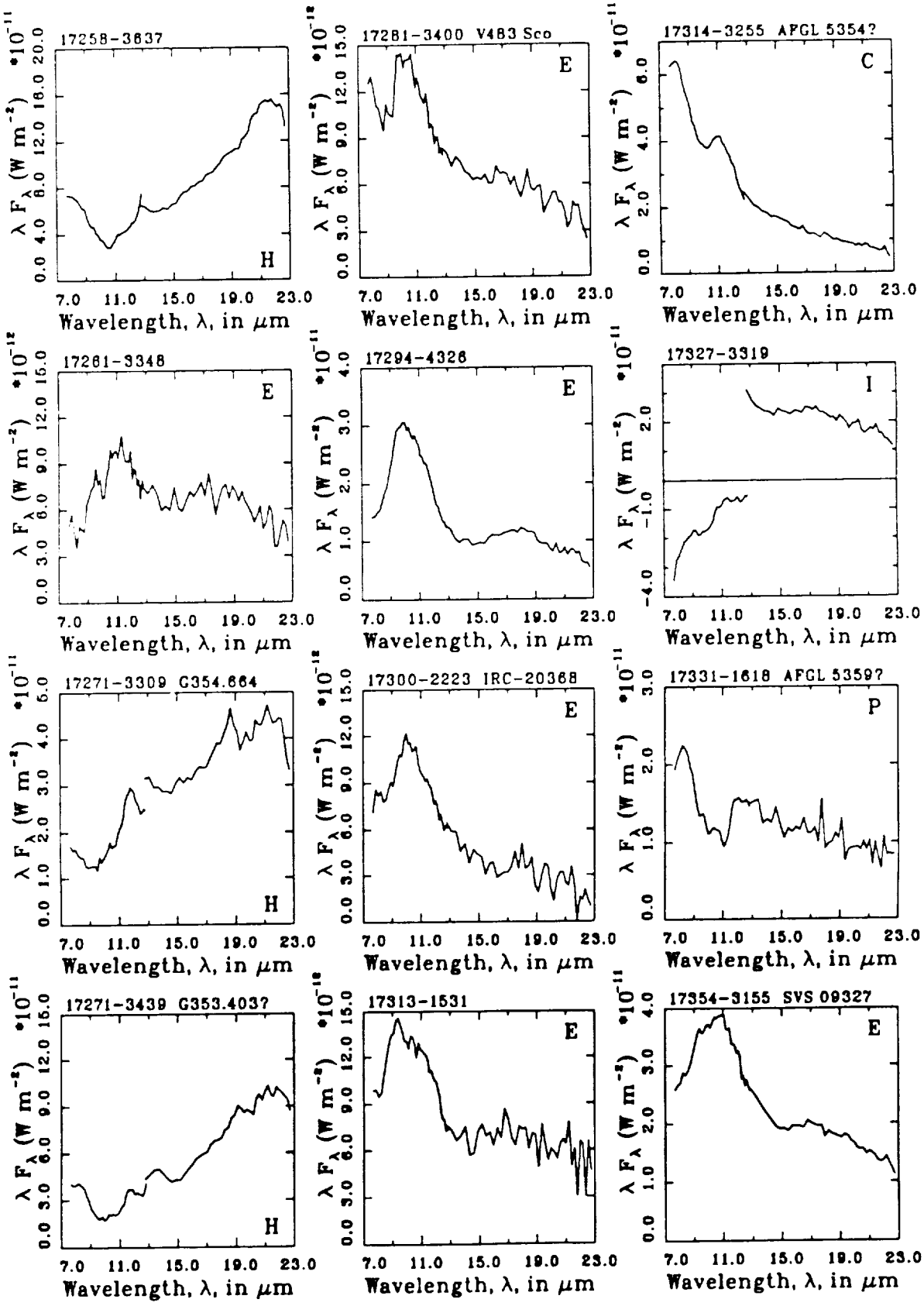
17258-3637
H
17281-3400 V483 Sco
E
17314-3255 AFGL 5354?
C
17281-3348
E
17294-4326
E
17327-3319
I
17271-3309 G354.664
H
17300-2223 IRC-20368
E
17331-1618 AFGL 5359?
P
17271-3439 G353.403?
H
17313-1531
E
17354-3155 SVS 09327
E
λ F_λ (W m^-2)
Wavelength, λ, in μm

Fig. 2, p.16

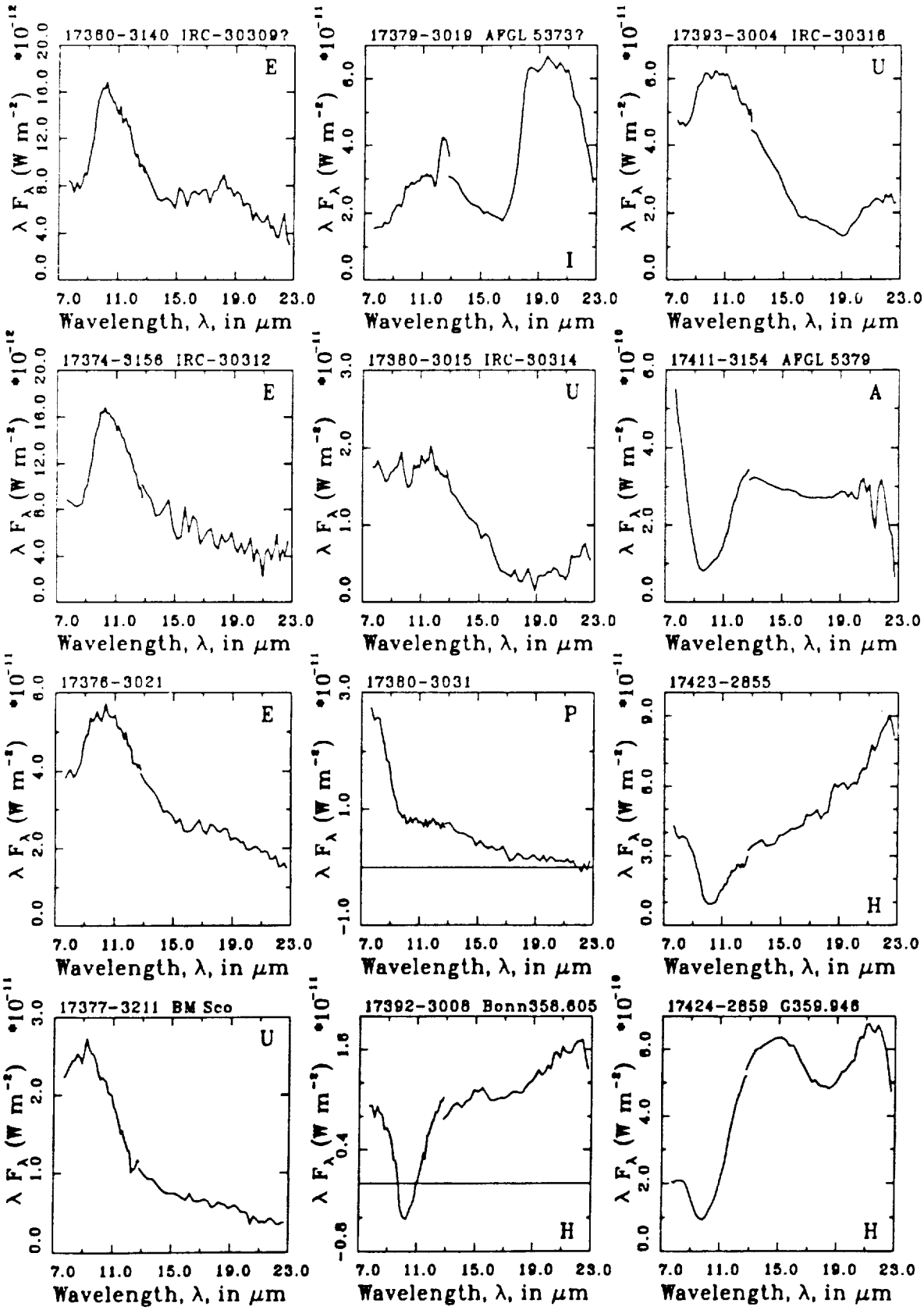
17360-3140 IRC-30309?
E
17379-3019 AFGL 5373?
I
17393-3004 IRC-30316
U
17374-3156 IRC-30312
E
17380-3015 IRC-30314
U
17411-3154 AFGL 5379
A
17376-3021
E
17380-3031
P
17423-2855
H
17377-3211 BM Sco
U
17392-3008 Bonn358.605
H
17424-2859 G359.948
H
λ F_λ (W m^-2)
Wavelength, λ, in μm

Fig. 2, p.17

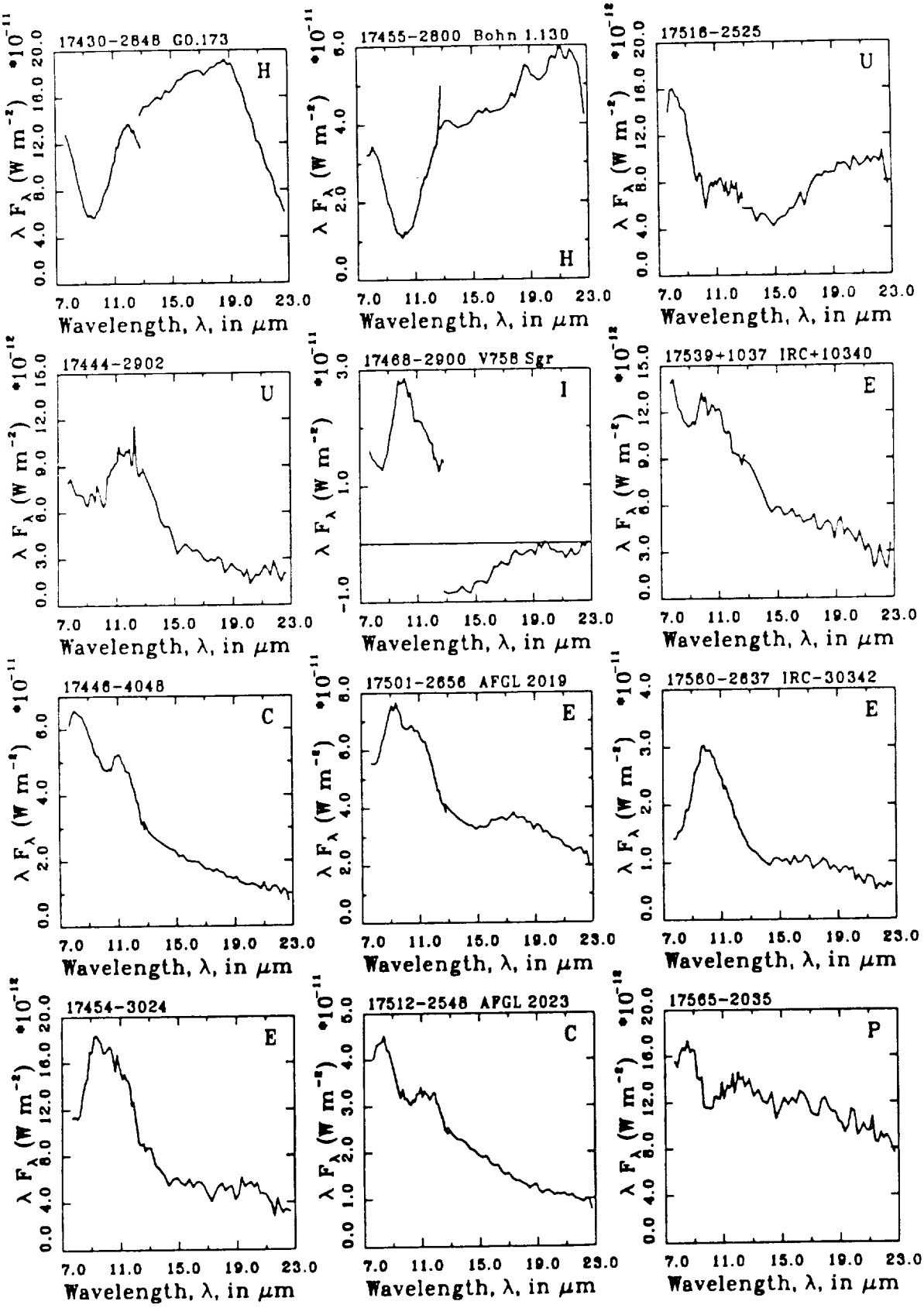
17430-2848 G0.173
H
17455-2800 Bohn 1.130
H
17516-2525
U
17444-2902
U
17468-2900 V758 Sgr
I
17539+1037 IRC+10340
E
17446-4048
C
17501-2656 AFGL 2019
E
17560-2637 IRC-30342
E
17454-3024
E
17512-2548 AFGL 2023
C
17565-2035
P
λ F_λ (W m^-2) *10^-11
λ F_λ (W m^-2) *10^-12
Wavelength, λ, in μm

Fig. 2, p.18

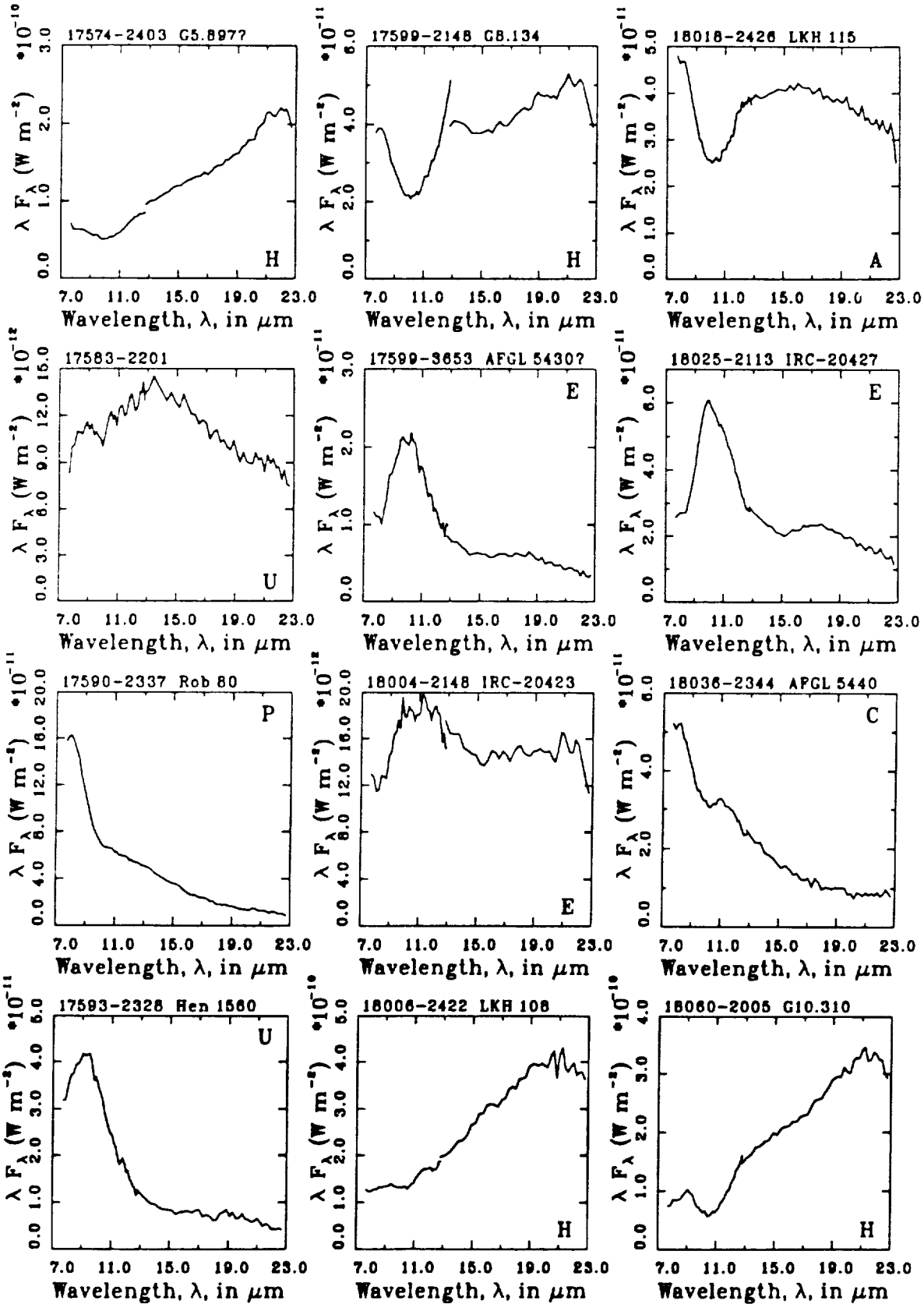
17574-2403 G5.8977
H
17599-2148 G8.134
H
18018-2426 LKH 115
A
17583-2201
U
17599-3653 AFGL 5430?
E
18025-2113 IRC-20427
E
17590-2337 Rob 80
P
18004-2148 IRC-20423
E
18036-2344 AFGL 5440
C
17593-2328 Hen 1560
U
18006-2422 LKH 108
H
18060-2005 G10.310
H
λ F_λ (W m^-2)
Wavelength, λ, in μm

Fig. 2, p.19

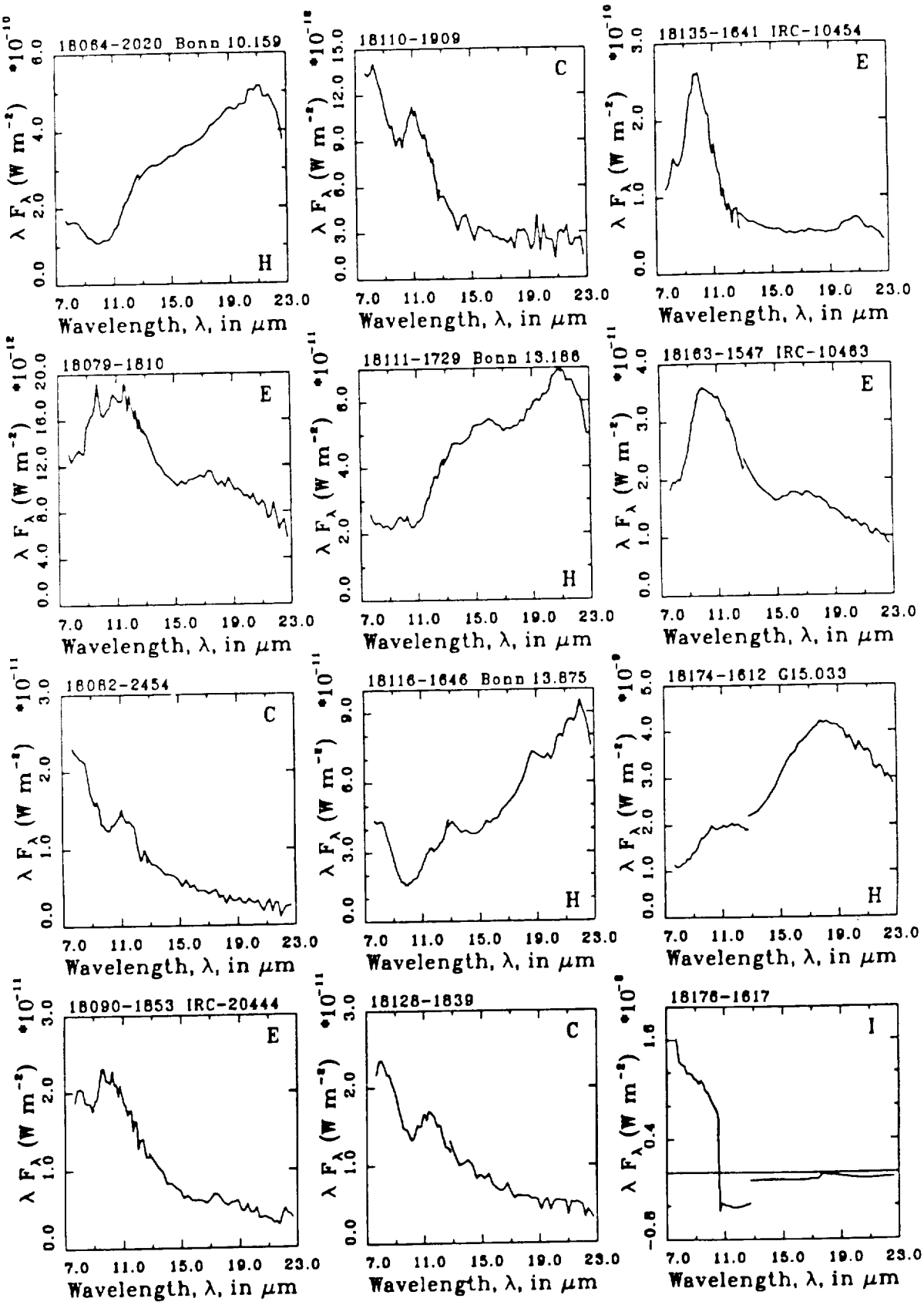
18064-2020 Bonn 10.159
H
18110-1909
C
18135-1641 IRC-10454
E
18079-1810
E
18111-1729 Bonn 13.186
H
18163-1547 IRC-10463
E
18082-2454
C
18116-1646 Bonn 13.875
H
18174-1612 G15.033
H
18090-1853 IRC-20444
E
18128-1839
C
18176-1617
I
Wavelength, λ, in μm

Fig. 2, p.20

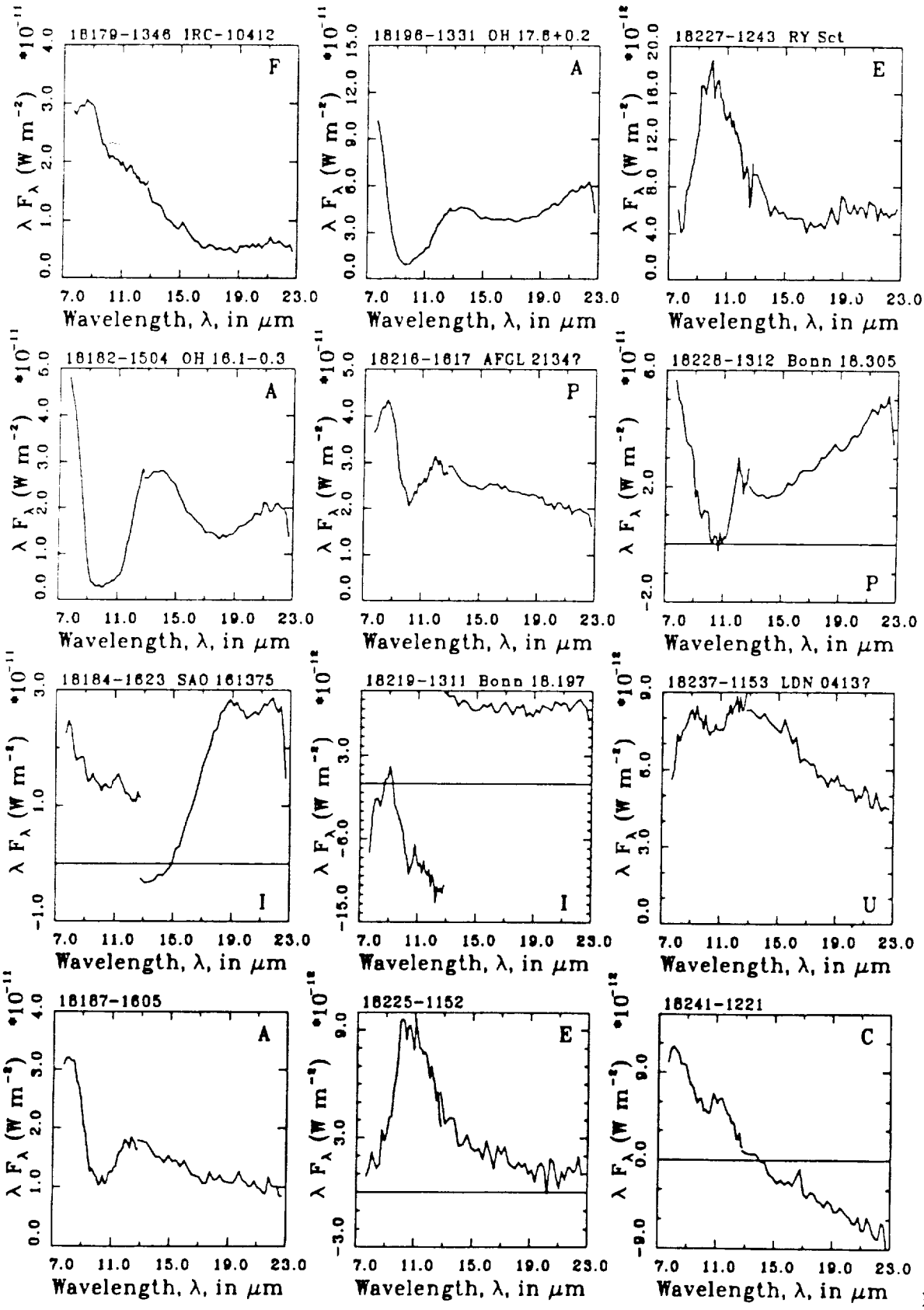
18179-1346 IRC-10412
F
18196-1331 OH 17.6+0.2
A
18227-1243 RY Sct
E
18182-1504 OH 16.1-0.3
A
18216-1617 AFGL 2134?
P
18228-1312 Bonn 18.305
P
18184-1623 SAO 161375
I
18219-1311 Bonn 18.197
I
18237-1153 LDN 0413?
U
18187-1605
A
18225-1152
E
18241-1221
C
λ F_λ (W m^-2)
Wavelength, λ, in μm

Fig. 2, p.21

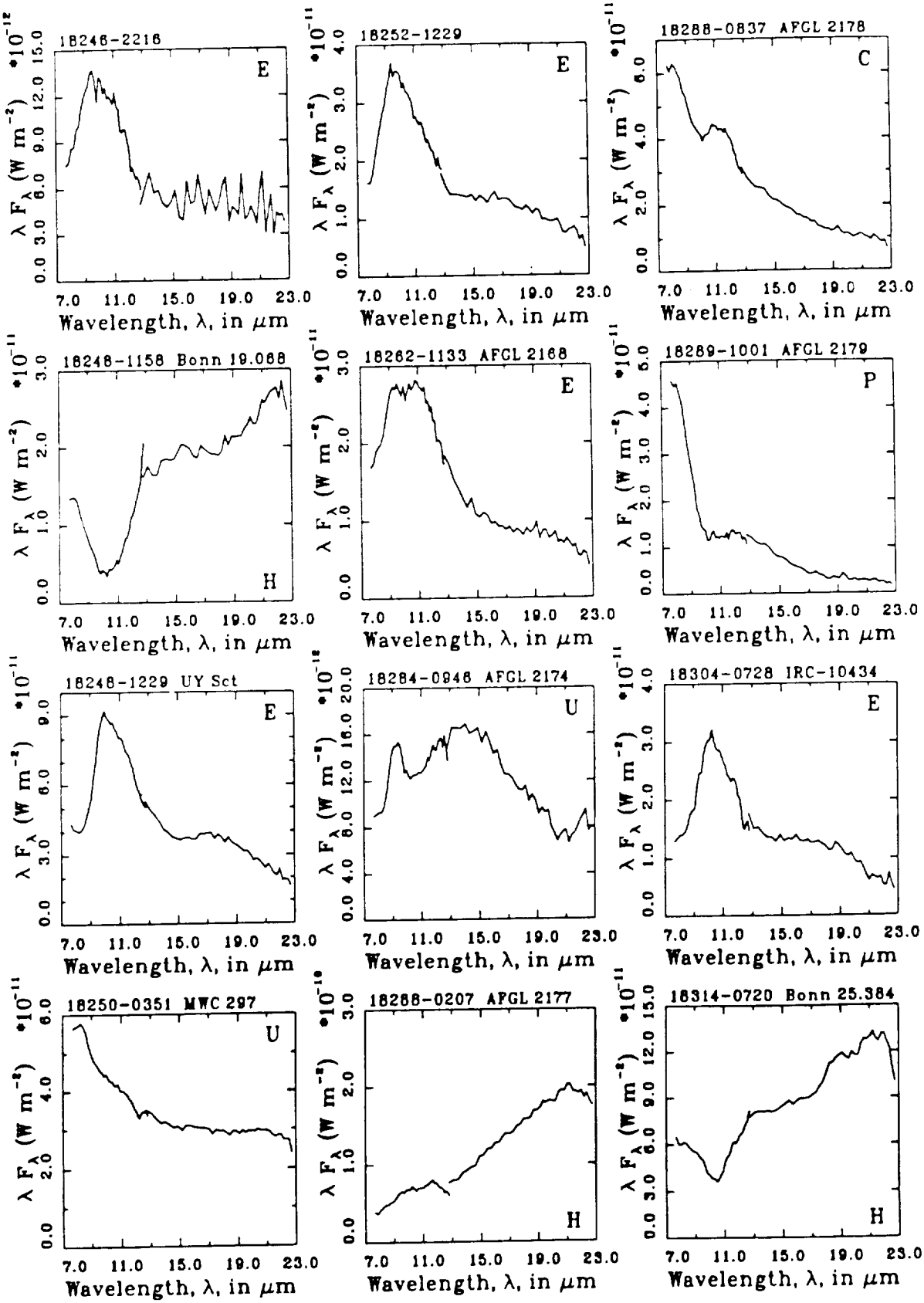
18246-2216
E
18252-1229
E
18288-0837 AFGL 2178
C
18248-1158 Bonn 19.088
H
18262-1133 AFGL 2168
E
18289-1001 AFGL 2179
P
18248-1229 UY Sct
E
18284-0946 AFGL 2174
U
18304-0728 IRC-10434
E
18250-0351 MWC 297
U
18288-0207 AFGL 2177
H
18314-0720 Bonn 25.384
H
λ F_λ (W m^-2)
Wavelength, λ, in μm

Fig. 2, p.22

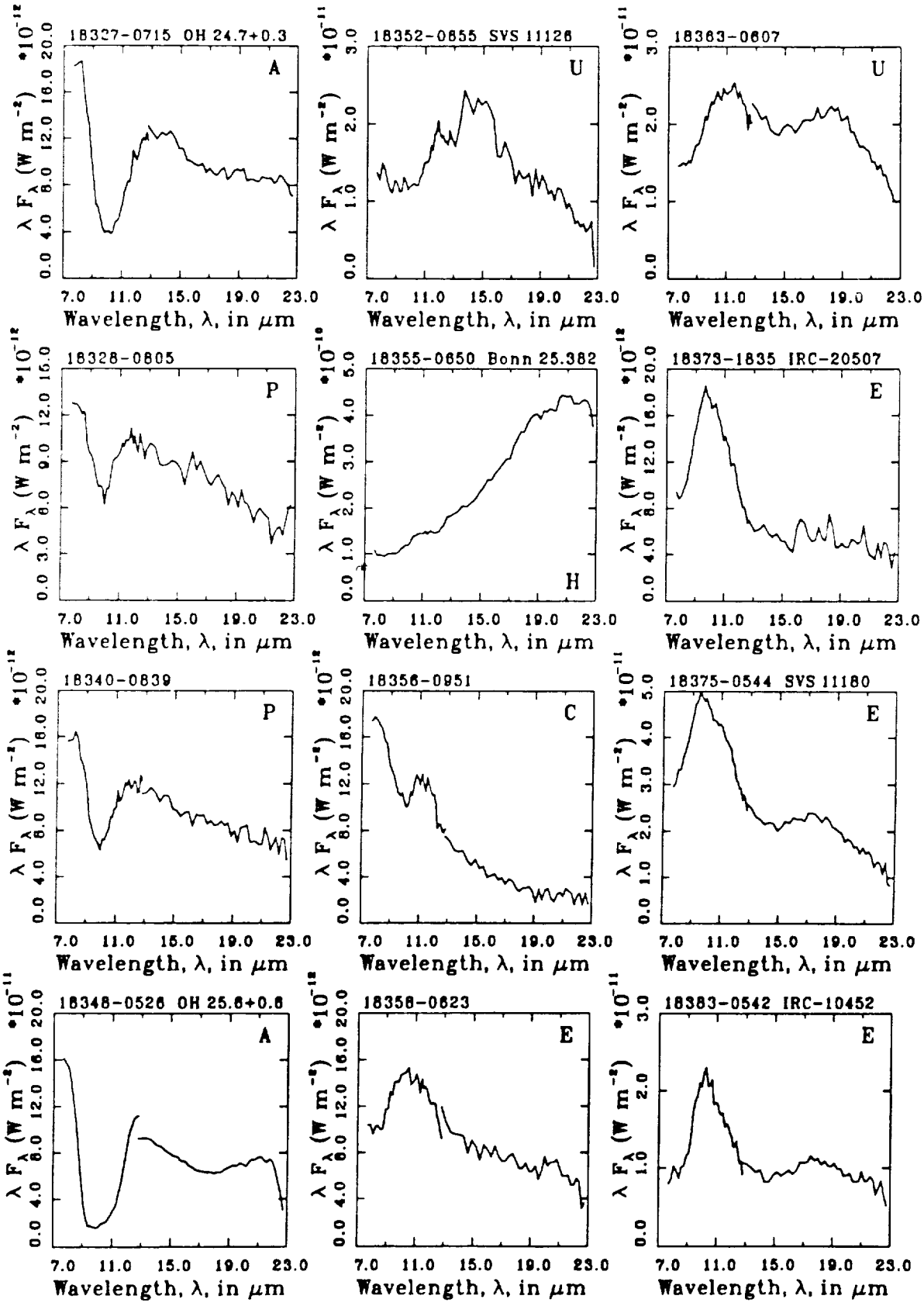
18327-0715 OH 24.7+0.3
A
18352-0855 SVS 11126
U
18363-0607
U
18328-0805
P
18355-0650 Bonn 25.382
H
18373-1835 IRC-20507
E
18340-0839
P
18356-0951
C
18375-0544 SVS 11180
E
18348-0526 OH 25.6+0.6
A
18358-0623
E
18383-0542 IRC-10452
E
λ F_λ (W m^-2)
Wavelength, λ, in μm

Fig. 2, p.23

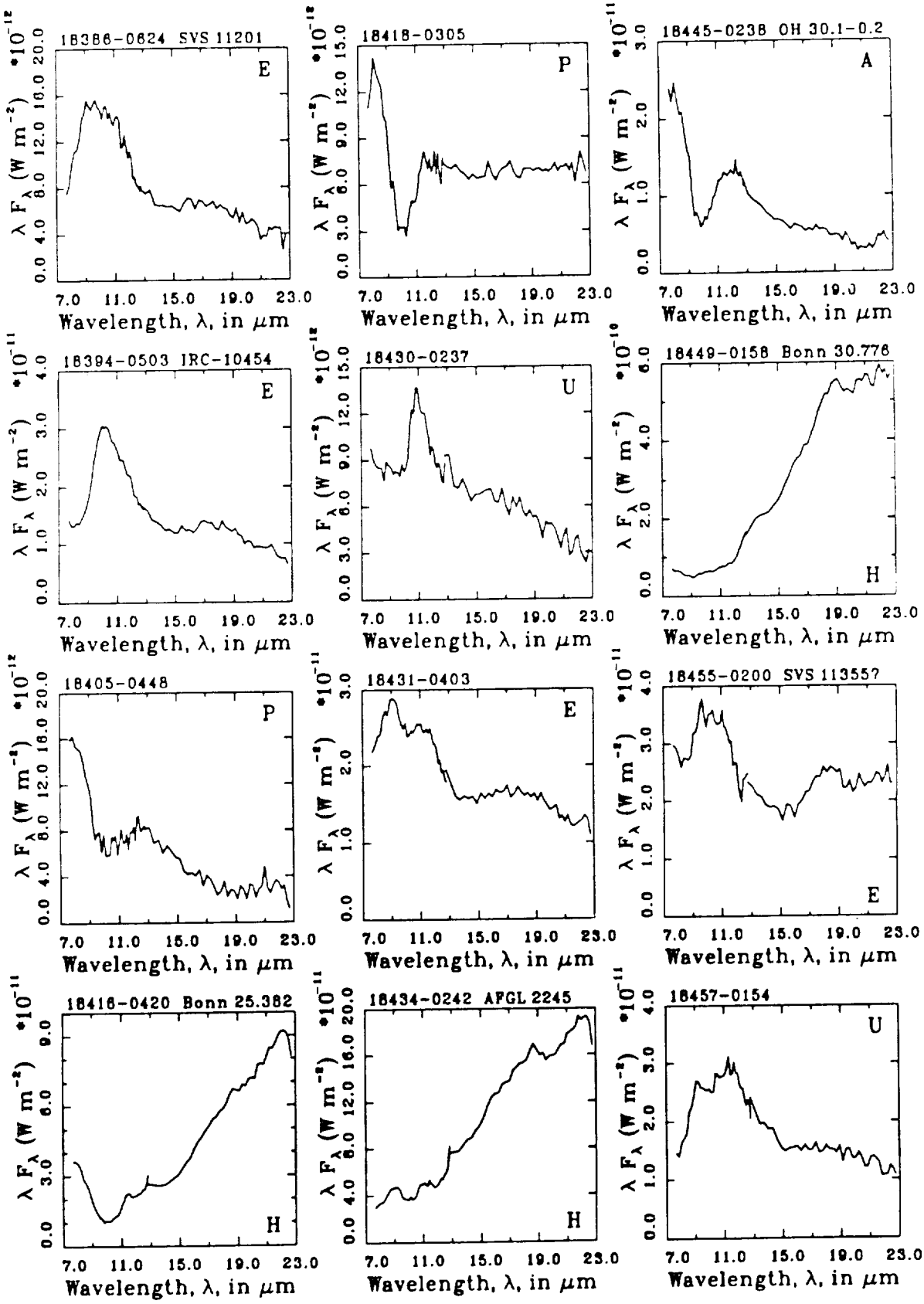
18386-0624 SVS 11201
E
18418-0305
P
18445-0238 OH 30.1-0.2
A
18394-0503 IRC-10454
E
18430-0237
U
18449-0158 Bonn 30.776
H
18405-0448
P
18431-0403
E
18455-0200 SVS 11355?
E
18416-0420 Bonn 25.382
H
18434-0242 AFGL 2245
H
18457-0154
U
λ F_λ (W m^-2)
Wavelength, λ, in μm

Fig. 2, p.24

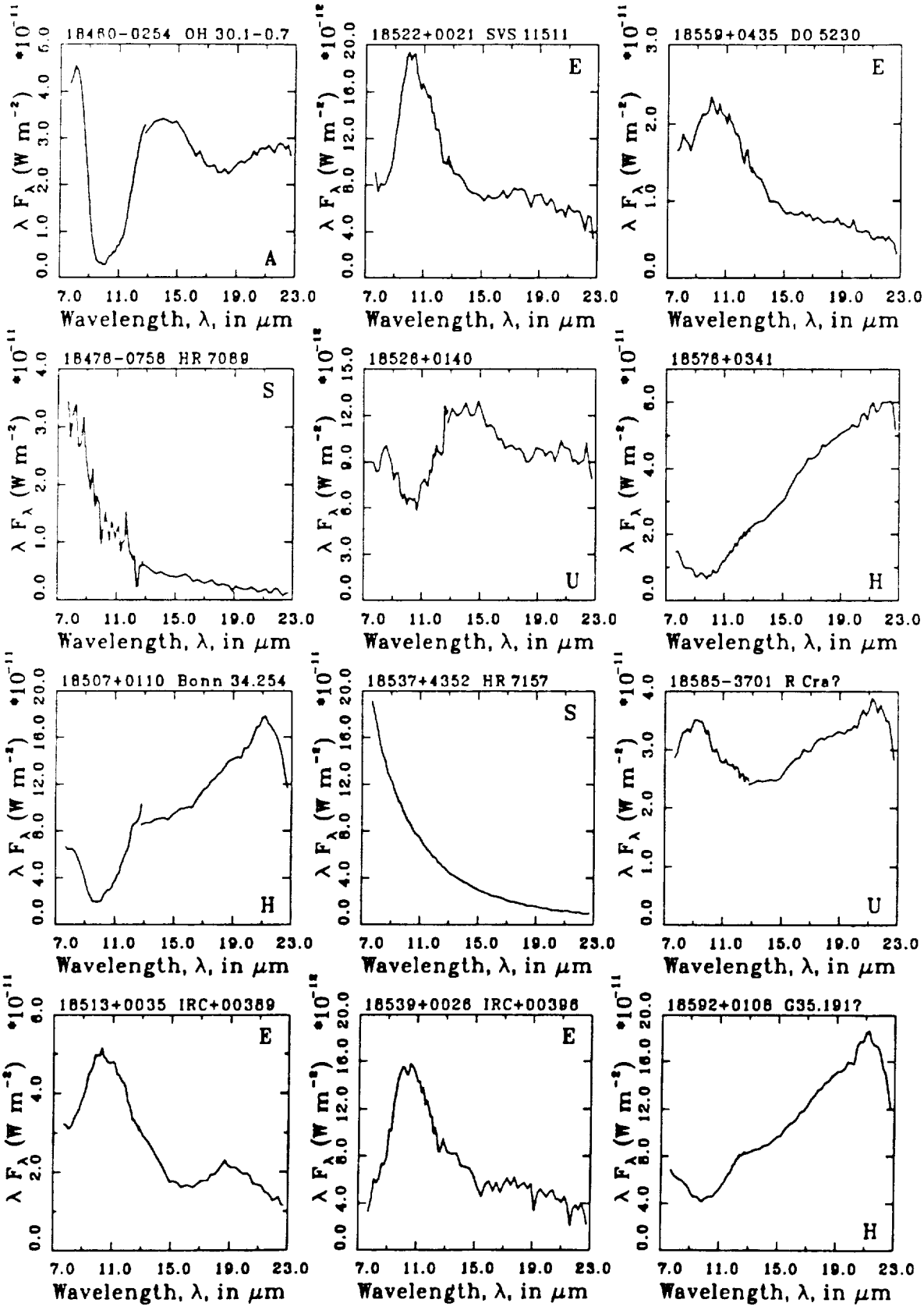
18460-0254 OH 30.1-0.7
A
18522+0021 SVS 11511
E
18559+0435 DO 5230
E
18476-0758 HR 7089
S
18526+0140
U
18576+0341
H
18507+0110 Bonn 34.254
H
18537+4352 HR 7157
S
18585-3701 R Cra?
U
18513+0035 IRC+00389
E
18539+0026 IRC+00396
E
18592+0108 G35.19?
H
λ F_λ (W m^-2) *10^-11
λ F_λ (W m^-2) *10^-12
Wavelength, λ, in μm
7.0 11.0 15.0 19.0 23.0

Fig. 2, p.25

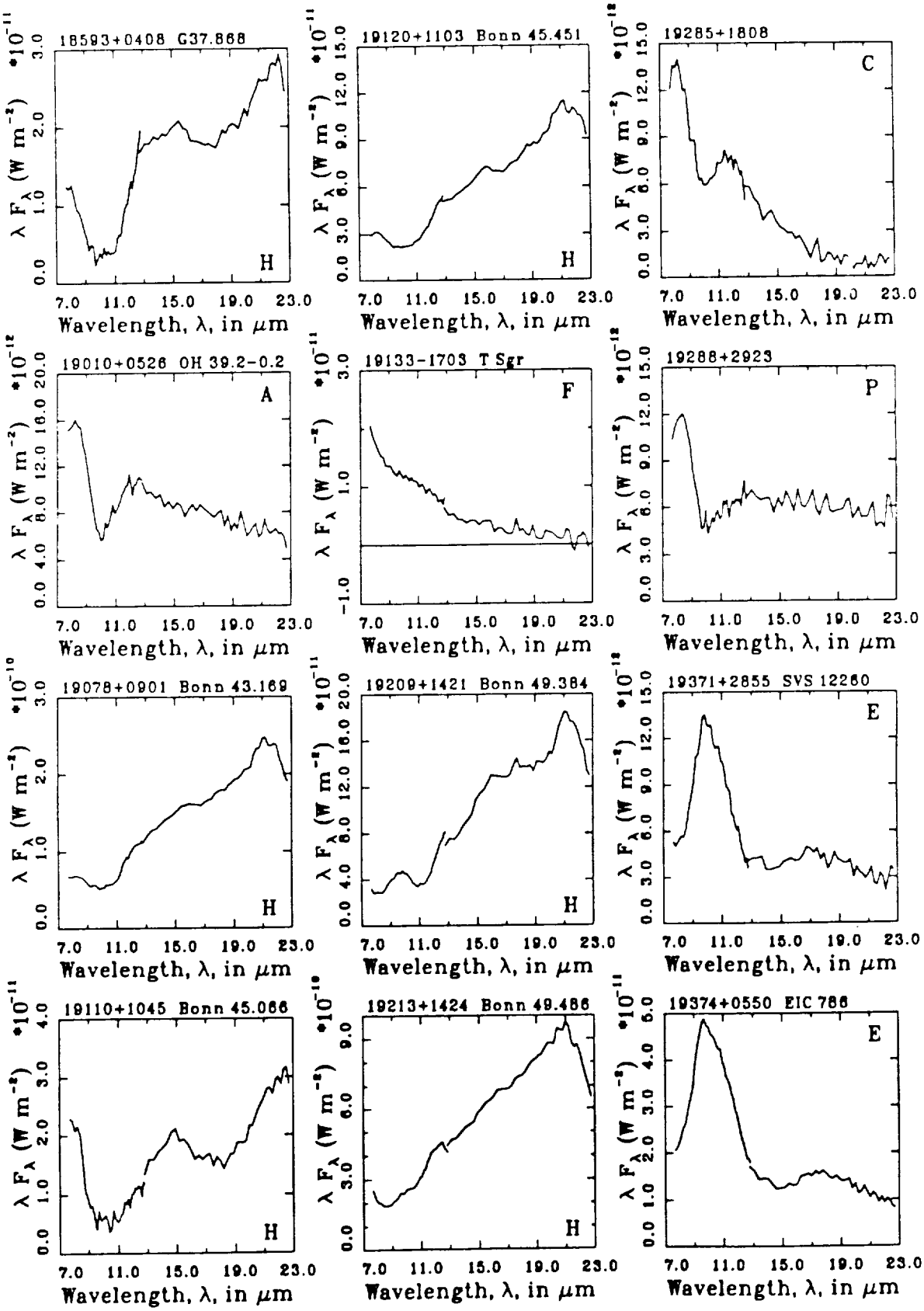
18593+0408 G37.868
19120+1103 Bonn 45.451
19285+1808
19010+0526 OH 39.2-0.2
19133-1703 T Sgr
19288+2923
19078+0901 Bonn 43.169
19209+1421 Bonn 49.384
19371+2855 SVS 12260
19110+1045 Bonn 45.066
19213+1424 Bonn 49.486
19374+0550 EIC 786
λ F_λ (W m^-2)
Wavelength, λ, in μm
H
C
A
F
P
E

Fig. 2, p.26

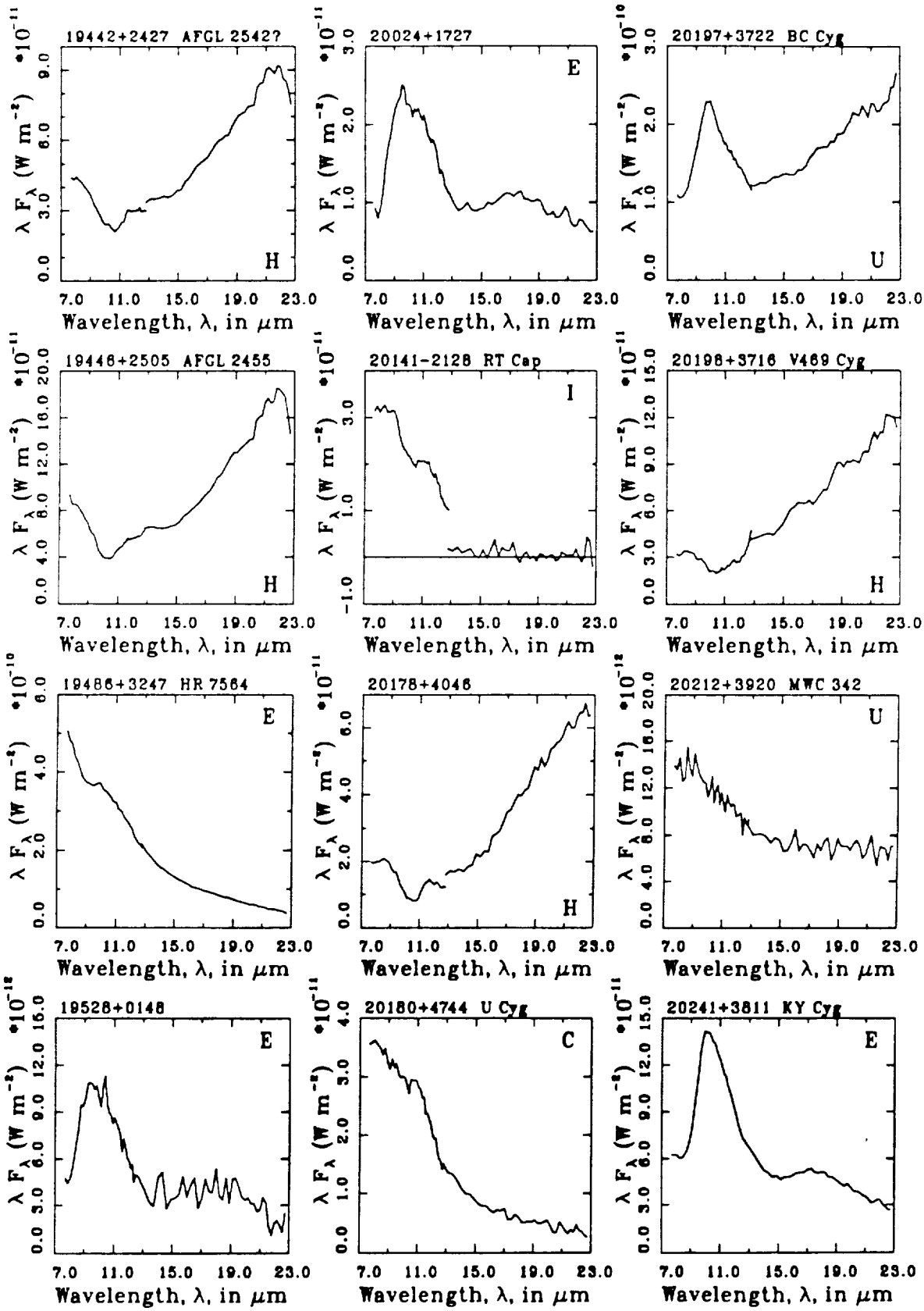
19442+2427 AFGL 2542?
H
20024+1727
E
20197+3722 BC Cyg
U
19446+2505 AFGL 2455
H
20141-2128 RT Cap
I
20196+3716 V469 Cyg
H
19486+3247 HR 7564
E
20178+4046
H
20212+3920 MWC 342
U
19528+0148
E
20180+4744 U Cyg
C
20241+3811 KY Cyg
E
λ F_λ (W m^-2)
Wavelength, λ, in μm
7.0 11.0 15.0 19.0 23.0

Fig. 2, p.27

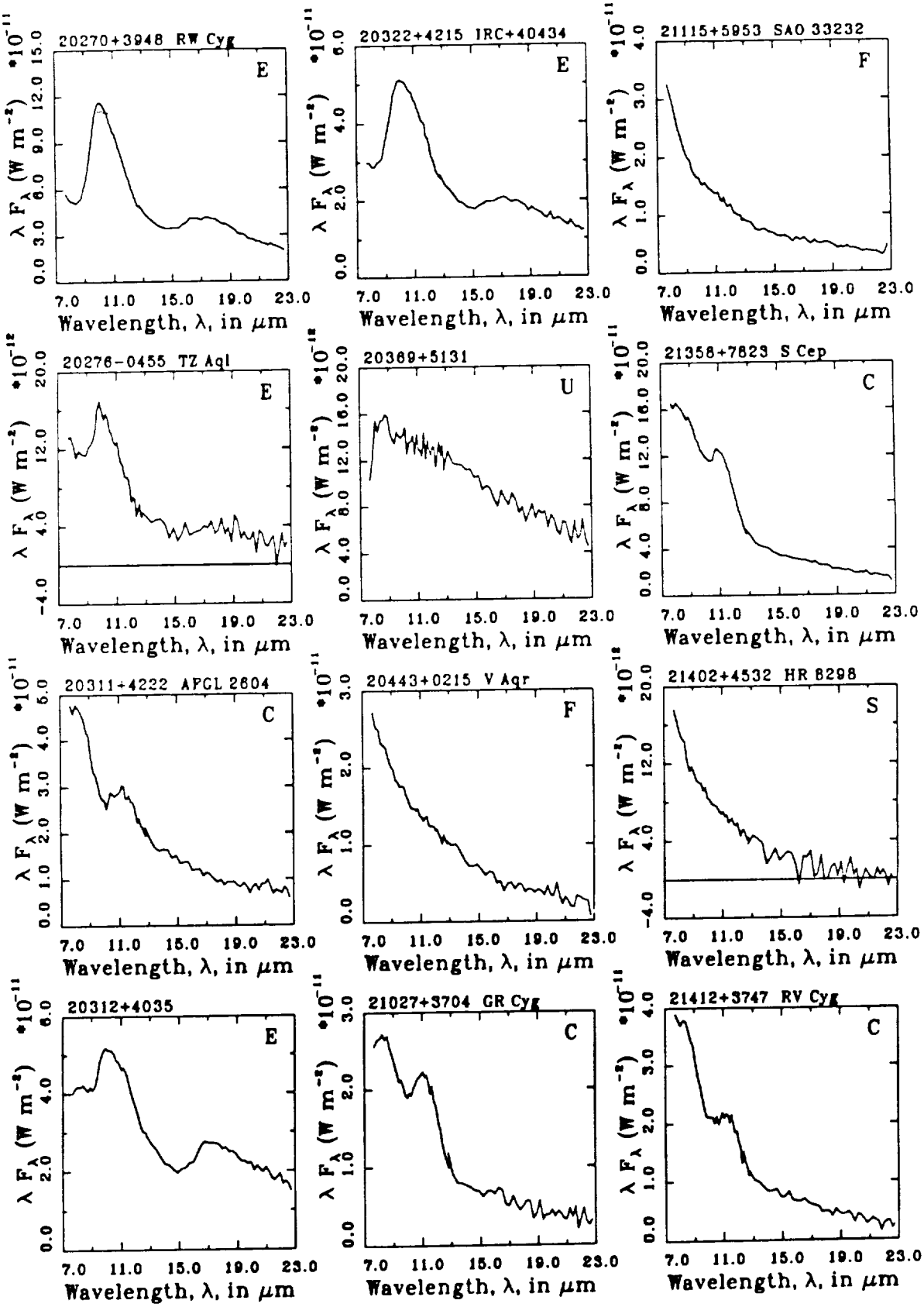
20270+3948 RW Cyg
E
20322+4215 IRC+40434
E
21115+5953 SAO 33232
F
20276-0455 TZ Aql
E
20369+5131
U
21358+7823 S Cep
C
20311+4222 APCL 2604
C
20443+0215 V Aqr
F
21402+4532 HR 8298
S
20312+4035
E
21027+3704 GR Cyg
C
21412+3747 RV Cyg
C
λ F_λ (W m^-2)
Wavelength, λ, in μm

Fig. 2, p.28

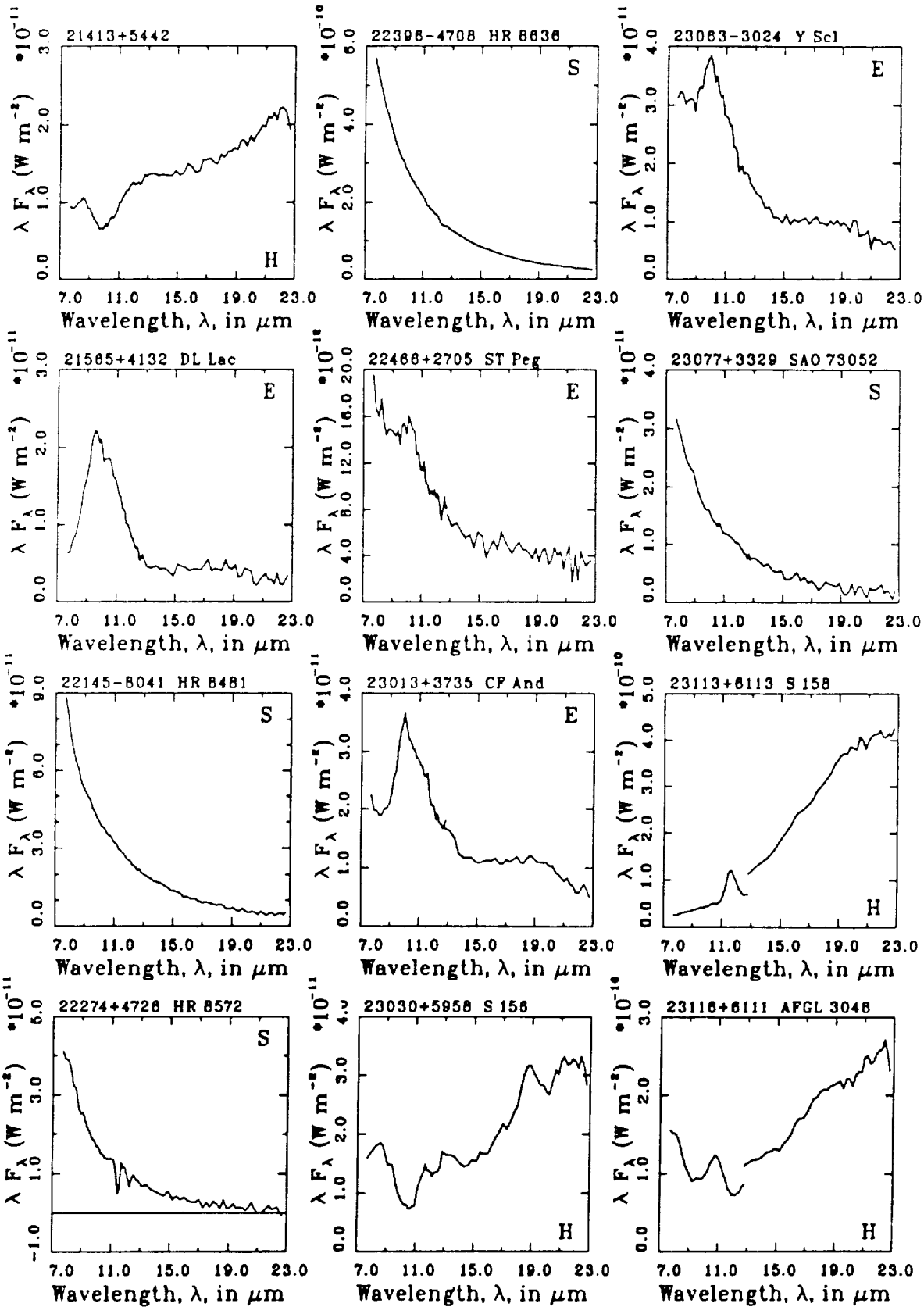
21413+5442
H
22396-4708 HR 8636
S
23063-3024 Y Scl
E
21565+4132 DL Lac
E
22466+2705 ST Peg
E
23077+3329 SAO 73052
S
22145-8041 HR 8481
S
23013+3735 CP And
E
23113+6113 S 158
H
22274+4726 HR 8572
S
23030+5958 S 156
H
23116+6111 AFGL 3048
H
λ F_λ (W m^-2)
Wavelength, λ, in μm

Fig. 2, p.29

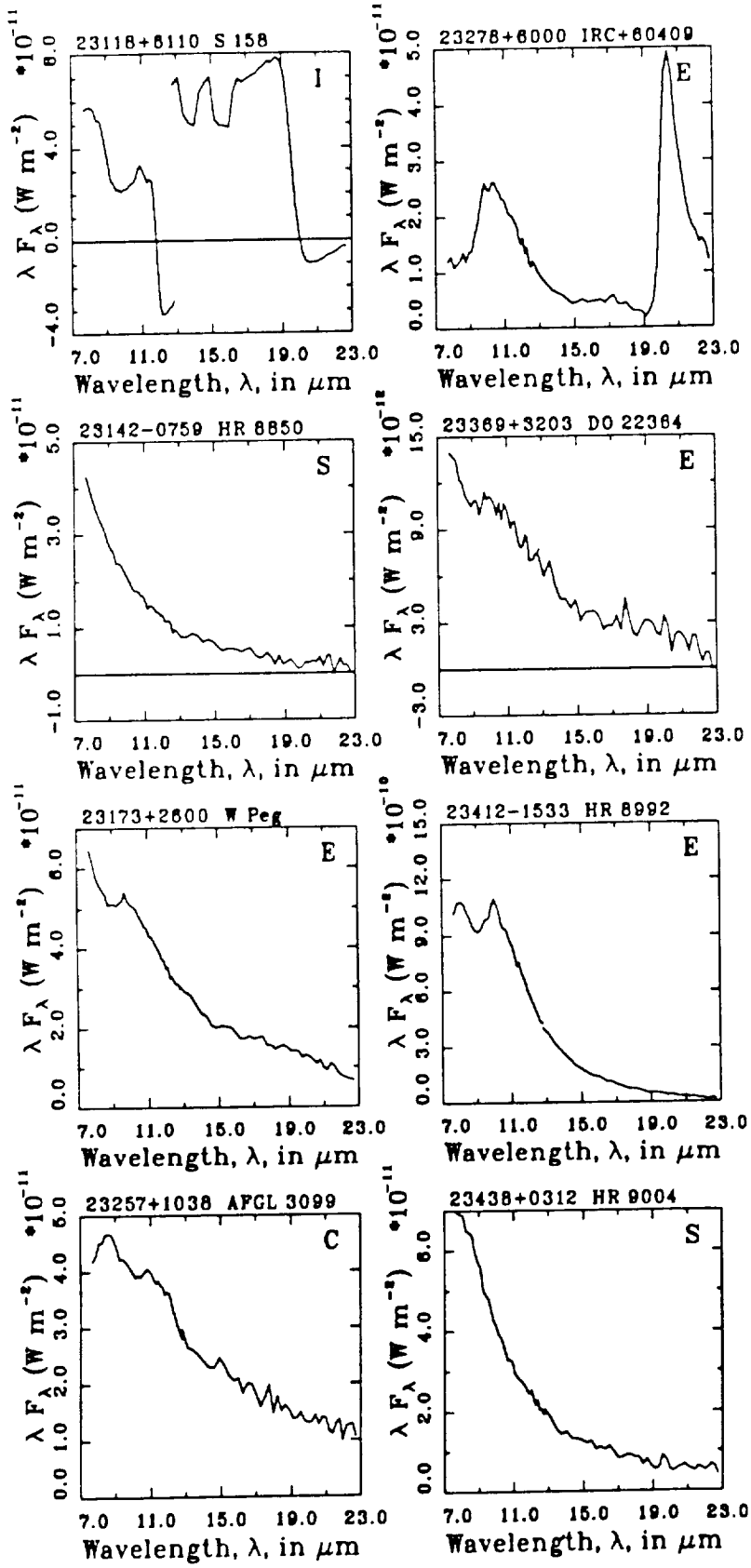
23118+6110 S 158
I
23278+6000 IRC+60409
E
23142-0759 HR 8850
S
23369+3203 DO 22364
E
23173+2600 W Peg
E
23412-1533 HR 8992
E
23257+1038 AFGL 3099
C
23438+0312 HR 9004
S
λ F_λ (W m^-2)
Wavelength, λ, in μm
7.0 11.0 15.0 19.0 23.0

Fig. 2, p.30

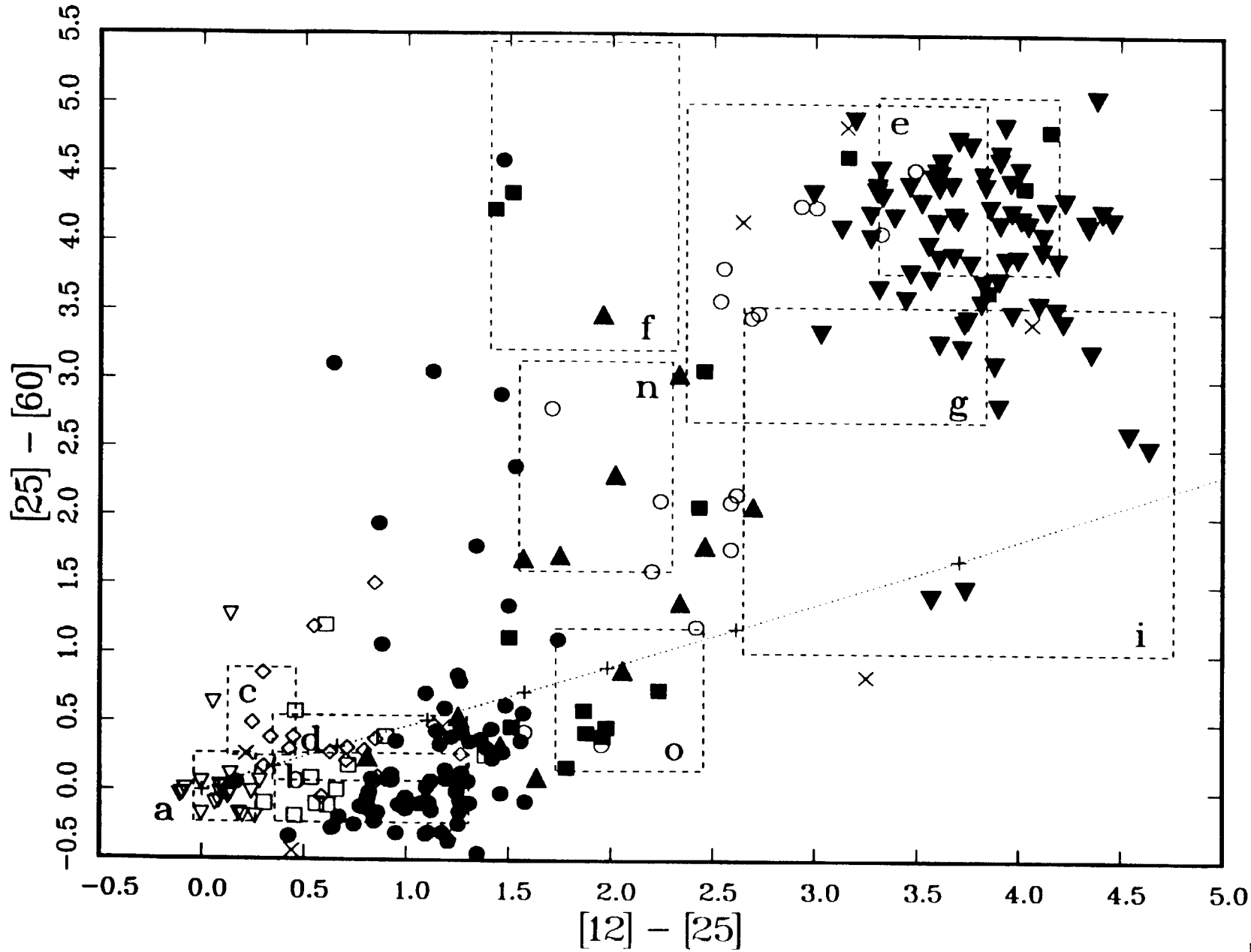

Fig. 3a

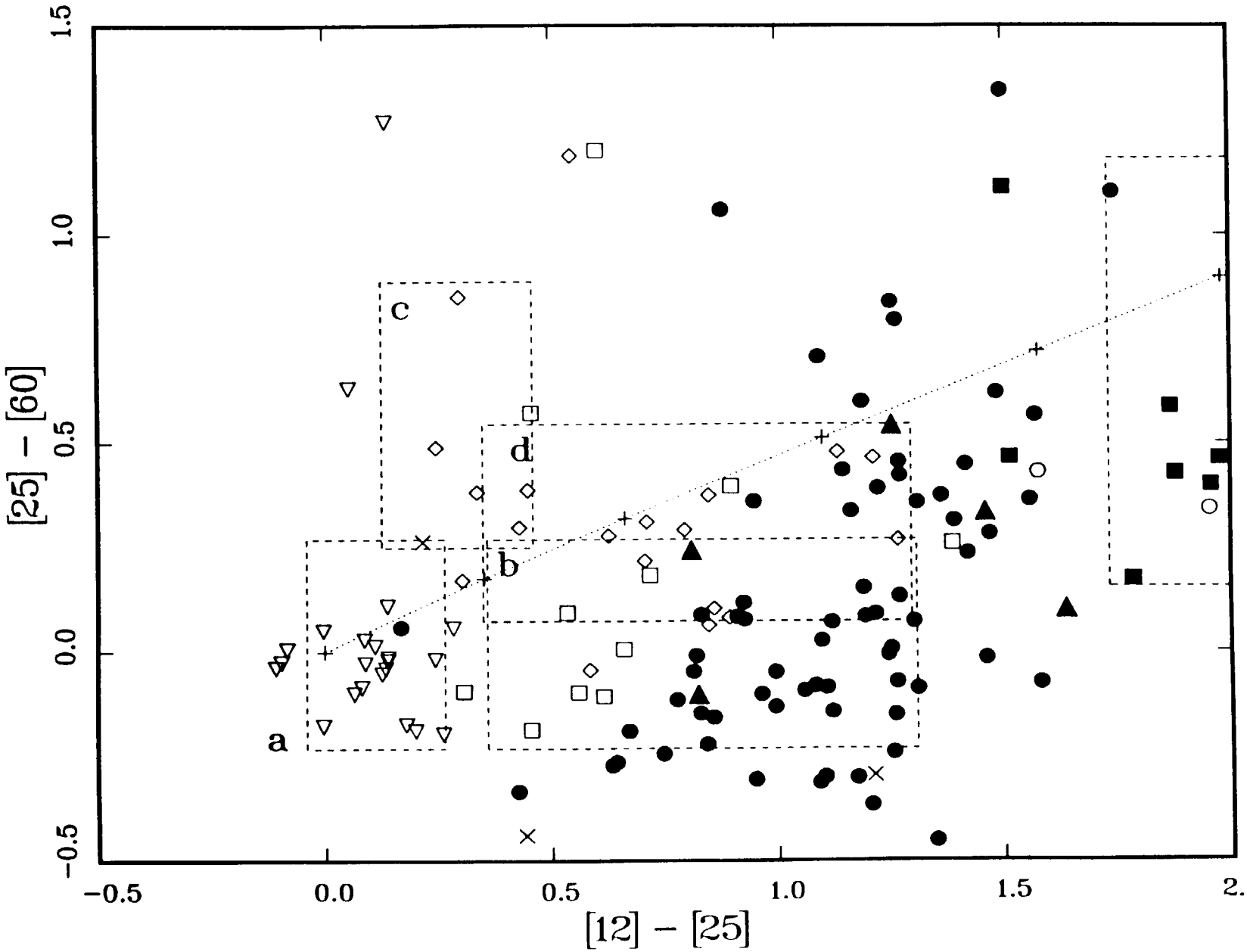

Fig. 3b

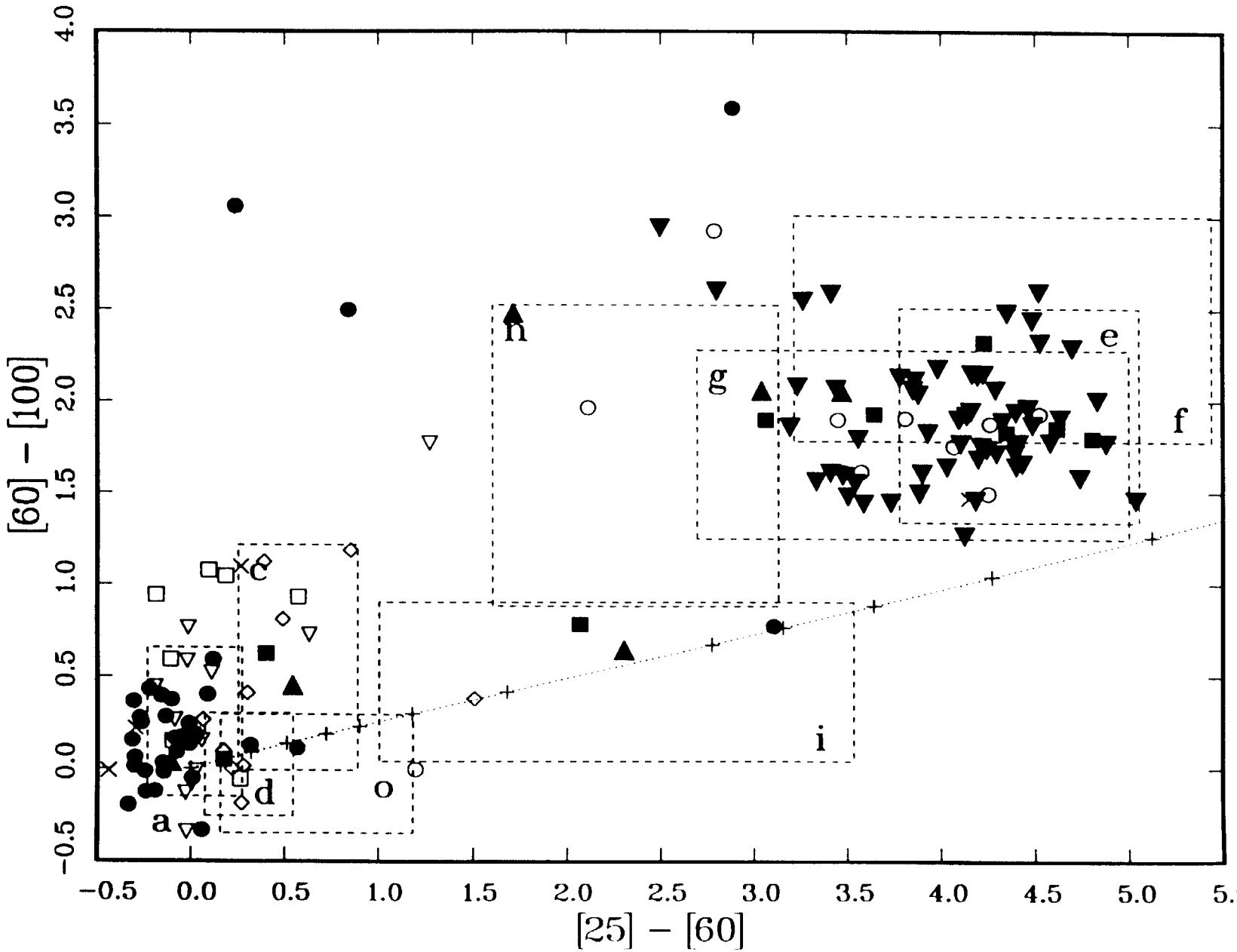

Fig. 4a

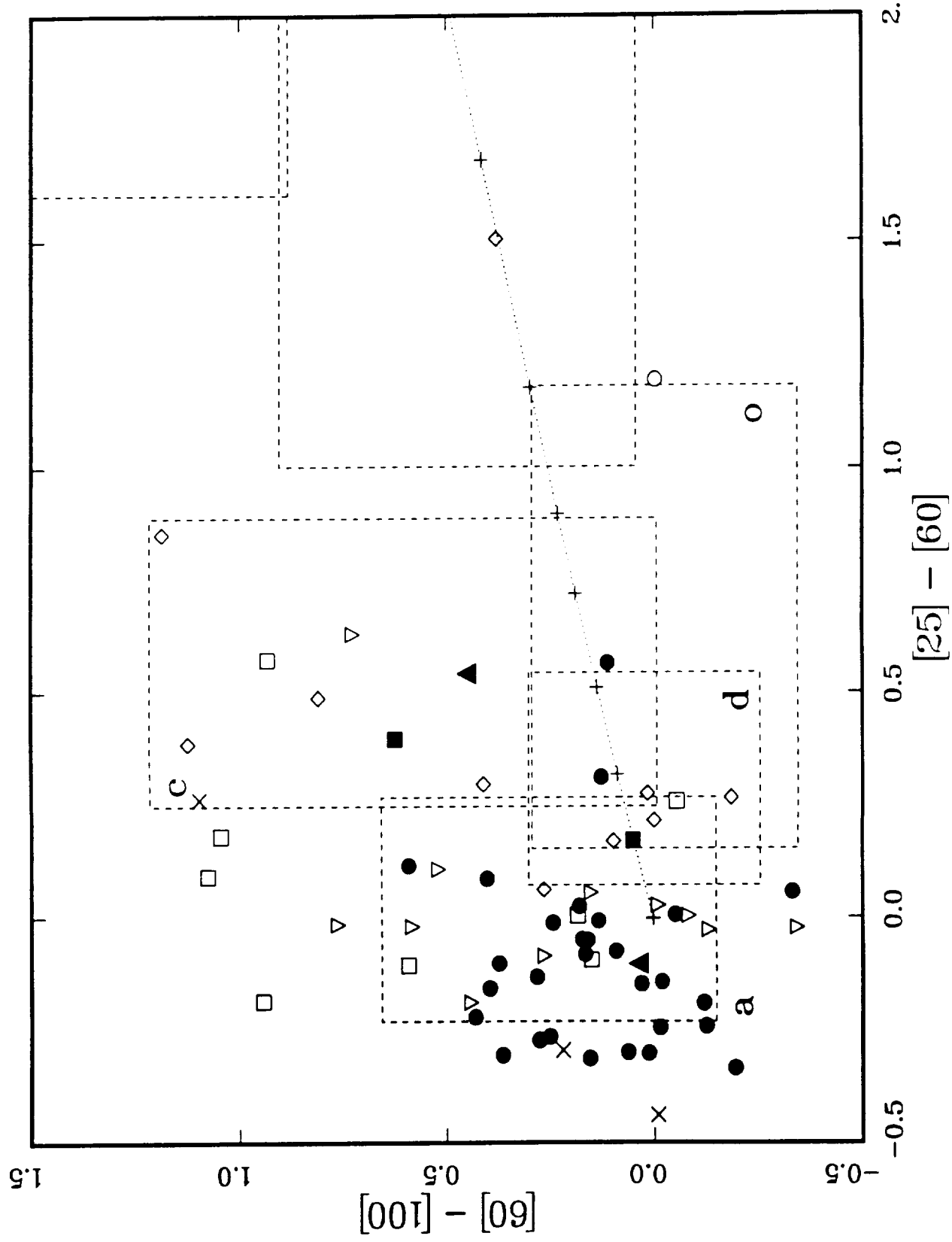

Fig. 4b

APPENDIX G. "Monte Carlo Simulations of the Galaxy at 12 Microns: Implications for Galactic Structure"

Monte Carlo Simulations Of The Galaxy At 12 μm: Implications For Galactic Structure

Kevin Volk and Richard J. Wainscoat

NASA Ames Research Center, Moffett Field, California 94035

and

SETI Institute, 101 First Street #410, Los Altos, California 94022

Martin Cohen

Radio Astronomy Laboratory, University Of California, Berkeley, California, 94720

and

Jamieson Science And Engineering, Inc., 5321 Scotts Valley Drive, Suite 204

Scotts Valley, California 94720

Helen J. Walker, and Deborah E. Schwartz

NASA Ames Research Center, Moffett Field, California 94035

and

SETI Institute, 101 First Street #410, Los Altos, California 94022

Abstract

We present an all-sky star count model at 12 μm based upon the *Infrared Astronomical Satellite* observations that characterizes both the 12 μm luminosity function and the geometrical parameters of the galaxy. Due to the smaller extinction at 12 μm the model could be compared with the IRAS observations at all galactic latitudes. The model includes five components of the galaxy: the bulge, the spheroid, the smooth exponential disk, the molecular ring, and the spiral arms.

We find that the IRAS bulge sources do not follow the de Vaucouleurs $r^{\frac{1}{4}}$ law sky distribution either with a 2.7 kpc effective radius as seen for the globular cluster system or a smaller effective radius as found by Habing (1986). The bulge is well fit by a density function similar to that given by Bahcall (1986) but with normalization radius 2.0 kpc and an axial ratio of 1.6. This suggests that the galactic bulge is not simply the central part of the spheroidal component of the galaxy. Habing's bulge fit can be reproduced by a combination of a Bahcall type bulge and a standard spheroidal component; this implies that Habing's fit is primarily a match to the inner spheroid rather than to the bulge because his analysis is not extended close enough to the galactic center.

We have determined the 12 μm luminosity function from the IRAS observations of the Gliese Catalogue sources (for the low luminosity part) and from comparison of the models with the observed number and sky distribution of bright IRAS sources (which predominantly come from high luminosity 12 μm sources). This luminosity function can be described by the same analytic function as used by Mamon and Soneira (1982), with the parameters $\alpha = 0.36$, $\beta = 0.025$, $\delta = 2/3$, $M^* = 3.0$, and $n^* = 0.0127$ stars mag^{-1} pc^{-3}. For the most luminous 12 μm sources the required luminosity function falls slightly below the values from this analytical approximation.

The model was compared with the IRAS observations in 9 areas of the sky, ranging from the galactic poles to the galactic plane, and with all IRAS 12 μm sources brighter than 2.5 Jy. The distribution of the brighter IRAS sources along the galactic plane required

that the model include sources within the spiral arms and the molecular ring to produce an acceptable fit to the l^{II} distribution. These arm and ring sources appear to be M supergiants and the most massive asymptotic giant branch stars.

Our model fits the observations near the galactic plane in the outer galaxy, although deviations in the total number of sources of the order of 10% occur from area to area. We do not support the conclusion of Habing (1988) that the galactic disk ends just outside the solar circle; we use a galactic disk of 3.5 kpc scale length and maximum radius 15 kpc, and do not require a thick disk component to match the observations. We suggest that Habing's sample includes IRAS sources in the spiral arms but his model for the galactic disk omits this critical component. Alternatively, the small truncation radius may apply only to Habing's color-selected sample and not to all disk sources, perhaps due to gradients in metallicity.

The IRAS data for stars in the two galactic poles show an asymmetry consistent with a solar position about 12 pc north of the galactic plane. A solar offset of more than about 20 pc leads to an asymmetry greater than that observed.

Subject Headings: galaxies: Milky Way — infrared: sources — galaxies: stellar content — galaxies: structure — stars: stellar statistics

I. INTRODUCTION

When the *Infrared Astronomical Satellite* (IRAS)[1] surveyed the sky at wavelengths of 12, 25, 60, and 100 μm it detected stars of late spectral type over a large fraction of the galaxy. At these wavelengths the interstellar extinction is small compared to that at optical wavelengths so sources can be observed out to large distances ($\approx$ 10 kpc). One of the first results to emerge from the survey data was that specific subsets of the observed IRAS sources clearly delineate the disk and the bulge of the galaxy (Habing, 1986). The sources which are observable over such large distances have the properties of evolved stars with circumstellar dust shells, similar to the OH/IR stars and extreme red giant stars which were known from observations at other wavelengths. The circumstellar dust absorbs the stellar radiation and re-emits it in the infrared. As a result, the infrared luminosity is very high for these objects. Another factor in favour of IRAS is that the interstellar extinction is of order 30 times less (in magnitudes) at 12 μm than at V. While optical studies of the galaxy are often severely limited by uncertainties about the extinction and large areas of the galaxy are simply unobservable—so for example supernovae in our galaxy have gone unobserved despite their tremendous luminosity—in the middle infrared we have a relatively clear view of the galaxy. Further, the properties of the sources that can be observed out to large distances by IRAS show that many of them are asymptotic giant branch stars so IRAS gives a new perspective on galactic structure as traced by an evolved population which is dominated by stars of intermediate mass—from about 1.5 $M_\odot$ to 8.0 $M_\odot$. These stars are less massive than the O-type stars that are the traditional optical or radio wavelength spiral tracers. Similar observations are possible in the near infrared, such as at K (2.2 μm). A series of balloon-borne observations have been carried out (Hayakawa *et al.* 1981, Hiromoto *et al.* 1984), at 2.4 microns rather than with the standard K filter,

[1] The *Infrared Astronomical Satellite* was developed and operated by the U.S. National Aeronautics and Space Administration (NASA), the Netherlands Agency for Aerospace Programs (NIVR), and the U.K. Science and Engineering Research Council (SERC).

with beam sizes of 1.7° and 0.4°. The 2.4 μm observations show the galactic bulge, and have similar promise for the study of the galaxy as do the IRAS data. The main limitation of these observations is their low spatial resolution. More recently array cameras have been developed which will provide much more sensitive observations of star counts at K in very small areas but these are not suitable to survey the entire sky. IRAS offers a combination of spatial resolution and all-sky coverage that is not presently available in the near infrared.

One obvious use of the IRAS data is to study the galactic bulge. The difficulty in observing stars in the galactic bulge at optical wavelengths seriously limits our understanding of this fundamental component of our galaxy. Interstellar extinction at optical wavelengths cuts off most of the bulge stars from observation. The Baade windows allow us to get valuable information about a few areas in the outer parts of the bulge. Such studies have shown that the predominant stellar population in these windows is an old, metal-rich population which appears to have [Fe/H] values of up to +1.0 (Frogel and Whitford, 1987). There remains some uncertainty about whether the Baade window sources are typical of the galactic bulge. If the galaxy has a thick disk these stars may be part of that disk rather than of the bulge (Gilmore and Wyse, 1987). It is also not clear how the bulge relates to the spheroid of the galaxy, which for our purposes here may be defined as containing the globular cluster system and the associated old, metal-poor population. The bulge of our galaxy may simply be the central part of the larger spheroid system, or it may be related to the thick disk (if one exists) or it may be an entirely distinct component of the galaxy.

Habing *et al.* (1985), Habing (1986), and Rowan-Robinson and Chester (1987) have looked at the IRAS sources in the bulge and found that they are probably low mass AGB stars. The IRAS source counts as a function of sky position were analyzed in a simple way by Habing (1986). His results indicate that the galactic bulge as seen by IRAS is flattened and has a profile consistent with the de Vaucouleurs $r^{\frac{1}{4}}$ surface brightness formula. The derived scale length on the sky was 5° (700 pc physical scale length for a distance to the

galactic center of 8.5 kpc) in the preliminary analysis (Habing *et al.* 1985) and 0.66° (100 pc for 8.5 kpc to the center) in Habing (1986). In the latter paper a bulge axis ratio of 2.0 was assumed. The bulge scale length is not well determined by these studies but is clearly less than the value of 2.7 kpc which is commonly quoted for the spheroid.

One disturbing aspect of Habing's (1986) analysis is that the fit to the de Vaucouleurs law was based upon the sources more than about 10° from the galactic center. The linear fit to the plot of the source density as a function of $r^{\frac{1}{4}}$ does not match the points closer than 10° from the center. This might result from source confusion since the source density so is high near the galactic center but it seems odd that the plot of the galactic coordinate distribution of the sources in Habing's sample does not show the bulge extending further than 15° from the center. The fit applies over a wide range of angular distance from the center but not where 'the bulge' is conspicuous in the sky distribution plot. Hence his fit may be more indicative of the spheroid at large angular radius than of the bulge itself. If source confusion is causing the deviation of the source density values from the linear fit then Habing's results are a clear indication that the bulge is merely the central parts of the spheroid. Alternatively these bulge stars may not obey a de Vaucouleurs $r^{\frac{1}{4}}$ law. To resolve these questions, and to see whether the bulge axial ratio can be determined from the IRAS data, one must look more carefully at the IRAS bulge sources.

There have already been some attempts to study the structure of the galaxy based upon the IRAS data. Garwood and Jones (1987) present a model for the galactic disk and the bulge based upon the 2.4 μm observations and some IRAS 12 μm data. Their study is difficult to compare with the other studies

since the emphasis is on the 2.4 μm data and the models for comparison with the IRAS data were made by assigning $K - [12]$ colors (hereafter [X] denotes an apparent magnitude at wavelength X microns) to the sources in a 2 μm star count model. The model for the 2 μm sky does not include the sources which are dominant at 12 μm—sources such as OH/IR stars, carbon stars and AGB stars with mass loss—and emphasises cool giant

stars without circumstellar material, which are the majority of the sources seen at 2 μm. Thus there are serious problems in trying to extend the model to 12 μm, as the authors recognised. They deduce a large axial ratio for the bulge, perhaps as large as 4 to 1.

Habing (1988) analyzed the disk as seen from a color selected IRAS subset. His best fit had two separate groups of sources in the disk: a low luminosity, 1 kpc scale height group of sources extending well beyond the solar circle with a 6.5 kpc radial scale length and a higher luminosity, 250 pc scale height group with a 4.5 kpc radial scale length that extends out to 9.5 kpc from the center (assuming the sun to be at 8.5 kpc from the center). Habing tentatively identified the first group of sources with the thick disk. The large scale height component has 20% as many sources as the small scale height component, which is much larger than the value of 2% of all disk stars for the thick disk component which Gilmore and Wyse (1987) derive. The inference that there is an edge to the thin disk at 9.5 kpc, at least for this sample of stars, is also an unexpected result. Both the possible detection of a thick disk by IRAS and the conclusion that the thin disk does not extend very far beyond the solar circle are important results for our understanding of galactic structure. Since Habing's fit was not as good as one would like when measured by the χ^2 value and since the number of sources used in the analysis was relatively small it is important that more analysis be done to see how firm his conclusions are. In any such fit there is uncertainty because one cannot tell if the fit is unique, or whether all the relevant parameter space has been searched.

In this paper an analysis of the IRAS 12 μm sources based upon a Monte Carlo model of the sources in the galaxy will be described. Initially the program was created to analyze the IRAS data for the galactic bulge. It was subsequently expanded to a model for the entire galaxy including the spiral arms, the molecular ring, the disk, the spheroid, and the bulge. The approach is empirical and draws as little as possible upon results at wavelengths other than 12 μm. The program can successfully reproduce many of the features of the observed 12 μm sources over the whole sky. While the model has limitations, it is a much

closer approximation to the real situation than the model presented by Habing and comes to rather different conclusions about what IRAS saw.

Our study of the size and shape of the galactic bulge as seen by IRAS is presented in §II. First the sample of source used in the analysis is discussed, followed by a discussion of two possible descriptions of the stellar density function for the bulge. The general approach used to model the sky distribution of IRAS bulge sources is outlined in §IIc, with some extension to consideration of the infrared luminosity function in §IId. Sections IId and IIe give the results of this part of our study. The specific bulge results are discussed in §IIf.

Expanding the model from a primarily geometrical model concerned with the size and the shape of the bulge to a general 12 μm star-count model poses a number of problems. First, there is the question of the proper luminosity function to use for the disk stars. Second, one must determine what geometrical parameters (scale lengths, scale heights) to use for the disk sources. While a single radial scale length may apply to all types of disk stars, the scale heights vary from one type of star to another. One must incorporate this into the luminosity function. Third, it is necessary to allow for any deviations from the ideal smooth exponential disk such as in the spiral arms. The spheroidal component must also be incorporated into the framework of the model.

Any program trying to model the sky distribution via a Monte Carlo approach is different than the computer models which have been used to study optical star-count data. IRAS detected sources in the top 14 magnitudes at 12 μm but was not uniform in the completeness limit. In the number of sources and the magnitude range that it covers IRAS is analogous to the SAO catalog. Optical star-count model programs such as the Bahcall-Soneira export code (Bahcall and Soneira 1984), are designed to look at small areas of the sky where star counts are available over a much greater range of magnitudes ($-1.41 < m_V \lesssim +23$, Bahcall and Soneira 1984) than is available from IRAS. The aim here is to model the entire sky but not to cover as large a range of magnitudes as would be required in an optical star-count model. Near the galactic plane there were severe

shadowing and confusion effects, which complicate any general analysis of the IRAS data. In looking at the entire sky problems are also introduced by local features, such as the Orion complex, which will not fit into an idealized disk model.

The development of the general galaxy model is discussed in §III. The most critical item that must be determined to produce a model for the IRAS sky at 12 μm is the luminosity function. The determination of a trial luminosity function which served as a starting point for the model is described in §IIIa. In §IIIb the Monte Carlo description of the disk will be discussed. §IIIc describes the IRAS data used with the models The model was compared with all sky sets of IRAS sources down to several limiting flux density values and with all sources in specific areas of the sky chosen to test the various components of the model. Following that, in §IIId, the way that the luminosity function and the local space density are converted into total galactic populations for the Monte Carlo models will be discussed. The model results are presented in §IIIe and discussed in the final section.

II. THE GALACTIC BULGE AS SEEN BY IRAS

a) The data

The full set of IRAS point sources does not clearly show the galactic bulge. The bulge is most clearly seen by selecting a color sub-set of the IRAS Point Source Catalogue version 2 (1988, hereafter the PSC); this reduces the number of nearby disk sources in the sample. Habing (1986) shows how a selection of sources using the ratio $\Re = F_\nu(25\mu\text{m})/F_\nu(12\mu\text{m})$ and $F_\nu(12\mu\text{m})$ yields a sample of sources with a significant bulge component. The bulge is prominent only for $F_\nu(12\mu\text{m}) < 6$ Jy. A few bulge sources may be brighter than this limit but the disk component dominates the brighter samples. $\Re < 0.5$ does not show the bulge; $0.5 < \Re < 2.0$ shows it at lower $F_\nu(12\mu\text{m})$ values for the lower $\Re$ values; $\Re > 2.0$ does not show the bulge, perhaps because the total number of sources has become too small for the shape of the bulge to be obvious.

The range of $\Re$ over which the bulge is observable matches the range of colors expected for evolved red giant stars with mass loss and circumstellar dust shells, but does not extend to the very red colors of HII region sources. This is to be expected because for a purely stellar source (for which $\Re$ is expected to be less than 0.5), only K- or M-type supergiant stars are luminous enough to have been observed by IRAS at distances of several kpc. Sources with $0.5 < \Re < 1.0$ resemble optical Mira variables while those with $1.0 < \Re < 2.0$ resemble the OH/IR stars. A large number of these sources in the direction of the bulge have been discovered to be new OH/IR stars (Hekkert 1989) and, from the OH maser observations, the distances can be determined to eliminate foreground objects. Rowan-Robinson and Chester (1987) have shown that there are more IRAS bulge sources with $\Re < 1.0$ than there are with $\Re > 1.0$ but the contrast between bulge and disk is greater for the redder sample.

Figure 1a presents the sky distribution of the 13428 IRAS sources with $\Re \geq 0.70$ and high or moderate quality fluxes at 12 μm and 25 μm. This sample is similar to the samples used by Habing (1986, 1988) for his analyses of galactic structure. Habing (1986) used the same color range as for Figure 1a but required $0.6 \leq F_\nu(12\mu\text{m}) \leq 6.0$ Jy. Habing (1988) required $0.82 < \Re < 3.8$ and excluded possible planetaries and HII region sources with $F_\nu(60\mu\text{m}) > F_\nu(25\mu\text{m})$.The plot clearly shows the bulge, the disk, the Large Magellanic Cloud ($l^{II} \approx -70°$, $b^{II} \approx -33°$), and the Orion complex ($l^{II} \approx -150°$, $b^{II} \approx -20°$). 219 sources are at $|b^{II}| \geq 30°$ of which 72 are in or near the LMC. Of the other 147 sources, 102 have associations with galaxies, 3 with planetary nebulae, 2 with reflection nebulae or dark clouds, 14 with stars, and 26 have no associations. These associations are based upon the positional match of the IRAS point sources with sources in a set of catalogues as described in the IRAS *Explanatory Supplement* (1988). At $l^{II} \approx 85°$ the sources are interrupted by one of the two large gaps in the IRAS sky coverage. These gaps cover 4% of the sky, extending from the polar regions down to the plane near the tangent points.

Our study of the bulge used the IRAS sources with $1.00 \leq \Re \leq 2.00$ and $0.5 \leq$

$F_\nu(12\mu\mathrm{m}) \leq 6.0$ Jy (Fig. 1b). All sources with high or moderate quality IRAS fluxes at both 12 and 25 μm satisfying these requirements were used unless they had 60 or 100 μm flux densities which indicated that they were HII region sources. Such sources usually have large 100 μm flux densities and are clearly distinct from those with red giant colors. The sample consisted of 3890 sources. This number is reduced to 1160 if only sources with high quality fluxes are used. The number also falls if the IRAS completeness limit, about 1.5 Jy for areas near the plane, is used as the lower flux density limit instead of 0.5 Jy. We found that the sources below the completeness limit helped to define the bulge off the galactic plane; the worst problems with confusion and background emission occur close to the plane. The greatest gain in source number comes from including moderate quality 25 μm flux density data. This sample (Fig. 1b) was used rather than the full sample of red sources (Fig. 1a) because of the higher apparent contrast between disk and bulge. It is necessary to compromise between getting enough sources to define the shape of the bulge and reducing the disk component.

To study the bulge structure, the disk sources must be removed from the sample, at least statistically. Except for HII region sources, it was not possible to remove disk sources explicitly based on the IRAS data alone. To remove the disk stars, we assumed that *a*) the star counts for the disk, as a function of galactic latitude, are the same in the bulge region as they are in a strip of the disk adjacent to the bulge; and *b*) the disk is uniform within 20° galactic longitude of the center. The sources in the zone $15° < l^{II} < 20°$ were assumed to define the disk component. Over this range, the source density declines very quickly away from the galactic plane, but levels off somewhat for $3° < |b^{II}| < 5°$; for $|b^{II}| > 5°$ the source density is zero. For reasons described in §IIe, we assumed that the disk component density fell smoothly to zero at about 3°, and retained the small number of sources at larger $|b^{II}|$, attributing these to bulge or spheroid sources.

We grouped the sources with $|b^{II}| < 14.5°$ and $|l^{II} < 14.5°$ into 1° squares centered on integer values of the coordinates. The resulting 29×29 matrix of values was then corrected

for disk sources by subtracting the estimated number of disk sources per square degree from each column of values. Within 1° of the plane, this resulted in a few small or negative values. This is probably due to an increase in confusion and in shadowing of sources on the plane near the galactic center compared with the 15° to 20° strip. Negative values were set to zero. The area within 2° of the galactic center was ignored in the analysis because of obvious bad values after the subtraction.

The initial plan was to model the 1° square area source counts directly. The corrected values per bin turned out to be small for much of the area under consideration. To avoid severe problems with small number statistics, we decided to express the data in terms of the cumulative l^{II} and b^{II} distributions. The gain in source counts per data bin is accompanied by a loss of detailed shape information in the data. All of the models assumed that the galactic bulge has an ellipsoidal shape of constant axis ratio. This ratio will be denoted by k, defined as ratio of the major-axis to the minor-axis length.

From the histograms of the source counts (Fig. 2b) we found that the bulge can be traced to about $|b^{II}| \approx 9°$. The bulge sources extend beyond the limited l^{II} range chosen for analysis (this was clear when the disk subtraction was performed). The grid was not extended to include these sources for two reasons. We felt that the disk subtraction would become less reliable if a region too far from the center were used to estimate the disk component. Further, because the galactic bulge may be distinct from the spheroid, one must use a sample dominated by the bulge. Too large an area would certainly begin to include the spheroid which might bias the results. The question of the spheroid will be considered further in the discussion (§IIf).

b) Density profiles for the galactic bulge

We required a radial density function for the bulge stars to model the projected sky distribution of IRAS bulge sources. The classical function used for this purpose is the deprojected version of the de Vaucouleurs $r^{\frac{1}{4}}$ law. The observed surface brightness B of

the bulge as a function of effective radius α is assumed to be given by

$$\log_{10}(B(\alpha)/B_e) = -3.33071(\alpha^{\frac{1}{4}} - 1) \tag{1a}$$

where $B_e = B(1)$,

$$\alpha = \sqrt{(l^{II})^2 + k_e^2(b^{II})^2}/a_e, \tag{1b}$$

and where k_e is the axial ratio and a_e the effective angular radius of the bulge. The numerical constant in equation (1a) is chosen so that 50% of the total luminosity is contained within an ellipse of semi-major axis a_e. Young (1976) tabulates the deprojected density function corresponding to this function along with analytic approximations for large and small radii which are often used in place of the tables. The density function is given in terms of an effective radius R_e which corresponds to the angular size a_e. Alternative bulge density functions have been proposed. Bahcall (1986) proposes a bulge density function of the form

$$\rho(x) = \rho_\circ x^{-1.8} e^{-x^3} \tag{2a}$$

where

$$x = \sqrt{R^2 + k_1^2 z^2}/R_1 \tag{2b}$$

is a dimensionless number, $\rho_\circ$ is a normalizing star density, z is the distance from the plane and R is the distance in the plane in cylindrical coordinates (R, θ, z). Equation (2a) has two parameters: the axis ratio of the bulge k_1, and a normalization radius R_1. Hereafter this density profile will be referred to as the Bahcall density profile. At small radii this function matches the variation in star density observed near the galactic center complex at 2 μm (Becklin and Neugebauer, 1968). Bahcall attributes this density function to Oort (1977); Oort did not include the exponential term in the density function. He was concerned only with the region close to the galactic center, and the exponential term produces a rapid decrease in density outside R_1. Both of these possible bulge density functions were used in the analysis of the bulge source sample.

In a Monte Carlo model, the integrated mass as a function of radius is used. The Bahcall density function is integrable in terms of an incomplete gamma function. In the standard notation

$$P(0.4, x^3) = \frac{1}{\Gamma(0.4)} \int_0^{x^3} t^{0.6} \exp(-t) dt \tag{3}$$

defines the incomplete gamma function of order 0.4. $P(0.4, x^3)$ gives the fraction of all bulge sources inside the ellipsoid defined by

$$R^2 + k^2 x^2 \leq x^2 \tag{4}$$

in cylindrical coordinates (R, θ, z). We computed this function using a subroutine from Press *et al.* (1986).

In the model program, the $P(0.4, x^3)$ function actually must be inverted to yield x for given P values, the random variables for each model point in the bulge. Although the density function is singular at $x = 0$, the incomplete gamma function goes smoothly to zero there—this is another advantage of performing the calculation in this manner. The inversion was achieved using a series of trials in x until the P value matched the input random variable to the precision of the calculation. When the x value had been found, the angular position was assigned from two more random variables.

For the de Vaucouleurs function, the numerical integration described by Young (1976) was repeated to produce a table of the fraction of bulge sources as a function of the normalized radius. The results agree with Young's to 4 significant figures at all values of the normalized radius. The table of values was used to associate a radius with every number between 0 and 1 by interpolation. We incremented our table values by 0.0001 in normalized radius very close to the galactic center, and increased this spacing up to $20R_e$ at very large radii. Very few stars fall at very large radii and the gridding is not important for them. The grid was chosen to allot roughly equal numbers of interpolation values to each interval of 0.1 from 0 to 1.

c) The model program

The projected bulge sky distribution using the Bahcall formula was modeled as follows. For each model source the position was initially expressed in coordinates (x, θ, φ) with respect to the galactic center. These coordinates are essentially spherical except that the ellipticity k_1 is applied to the z coordinate. The transformation from ordinary cylindrical coordinates (R, θ, z) is then

$$x = \sqrt{R^2 + k_1^2 z^2}/R_1 \tag{5a}$$

$$\varphi = \arcsin(k_1 z/R_1) \tag{5b}$$

with θ remaining unchanged. For each model point, three random numbers in the interval $(0, 1)$ were chosen. Denoting these numbers as N_1, N_2, and N_3 the equations for obtaining (x, θ, φ) are

$$N_1 = P(0.4, x^3) \tag{6a}$$

$$N_2 = \theta/2\pi \tag{6b}$$

$$N_3 = \varphi/\pi \tag{6c}$$

with all angles in radians. (x, φ) was converted to (R, z) with

$$z = R_1 x \sin\varphi/k_1 \tag{7a}$$

$$R = R_1 x \cos\varphi \tag{7b}$$

for each point. The cylindrical coordinates (R, θ, z) were converted to (d, l^{II}, b^{II}), where d symbolizes the distance from the earth to the source, by simple triangle geometry. Once the sky coordinates (l^{II}, b^{II}) had been calculated for the model sources, the values were binned into 1° square areas exactly as for the data values. Since the models could be run with large numbers of points—typically 2×10^5 per run—the area over which the sky distribution was tabulated was 60° square. All sources falling outside that part of the sky for which the area counts were generated were written to an output file. For the Bahcall function there were very few such sources when $R_1 \leq 2$ kpc. With the same total number

of sources, the de Vaucouleurs function always had significant numbers of sources outside the main grid area. *If R_e was taken as 2.7 kpc the resulting sky distribution was very extended and definitely inconsistent with the data.*

After calculation of the model sky distribution, the l^{II} and b^{II} histograms were compared with the data. The histograms were normalized so that they could be rescaled to whatever total number best matched the data. The total number of IRAS bulge sources was varied for each run to find the best fit as measured by the χ^2 value. The scaling and χ^2 calculation were performed for the l^{II} and b^{II} distributions separately and then simultaneously for both. Comparison of the individual χ^2 values and total numbers suggested where the fit was poor, and how well determined the parameters were.

d) The flux distribution and interstellar extinction

The simulation program calculated $M_{12\mu m}$ values for each of the model sources according to a simple 12 μm luminosity function. To model the IRAS flux values for these sources requires some assumptions about the amount of interstellar extinction along the line of sight to the bulge. Although the extinction is not very great at 12 μm the effect is large enough to be observable over the path to the bulge. In the galactic plane $A_{12\mu m} \approx 0.5$ mag on a path to the bulge. The value is even higher when looking directly at the galactic center, $A_V \approx 30$ mag and $A_{12\mu m} \approx 1$ mag. The latter value applies only to the region very near the galactic center, not for most of the bulge sources.

In order to compare the model flux density distribution with IRAS data, one needs a set of bulge stars as free as possible from contamination by disk sources. Rowan-Robinson and Chester (1987) removed the disk sources statistically using a comparison area to define the flux density distribution. The problem with their approach is that the bulge does not show up well unless a color condition is imposed; the fainter bulge sources will not have 25 μm flux density values and so have no color information. It is difficult to remove the disk component properly under those conditions. Instead, we decided to examine two specific

areas of the bulge having enough sources test the model while avoiding the galactic disk component as much as possible. Two 1° square areas on the sky were chosen, $2° \leq b^{II} \leq 3°$ and $-3° \leq b^{II} \leq -2°$ with $-0.5° \leq l^{II} \leq 0.5°$. All IRAS point sources in these areas with high or moderate quality 12 μm flux densities were taken from the PSC. There were 77 sources in the northern area and 65 sources in the southern area. Most of these sources are not very bright, and have colors consistent with red giant stars with dust shells. There are a few obvious foreground disk sources such as IRAS 17317–2743 which is the OH maser source OH 359.8+2.6. If this source were in the bulge, then its observed flux density of 196 Jy at 12 μm would imply $M_{12\mu m} \approx -17$. While this is possible for a very extreme OH/IR star, it is more likely that this source is much closer than the bulge. Another probable foreground source has IRAS colors similar to those of planetary nebulae and is associated with PK 359–2.3.

Although we cannot estimate the contamination by disk sources, we assumed that the bulk of the faint point sources are indeed in the bulge. Confusion effects must be considered in the entire sample because the number per square degree is above the IRAS confusion threshold of ≈ 45. For the restricted color range used in the sky distribution part of the study, this is a problem only on the plane where the disk contamination prevents much useful analysis; we cannot simulate confusion in our model so we assume that the data set is a random sample from the real source distribution.

It is not clear what value of the extinction, $A_{12\mu m}$, should be used in the model. Rieke and Lebofsky (1985) give a relative value of 0.037 ± 0.006 times A_V for $A_{12\mu m}$ using a narrow-band 12 μm filter. From the tabulated extinction values of Rieke and Lebofsky (1985) and silicate feature profiles based upon IRAS Low Resolution Spectra of sources showing strong silicate absorption, Wainscoat *et al.* (1989) find $A_{12\mu m} = 0.048\ A_V$ for the IRAS 12 μm filter. In the bulge models a value of 0.046 mag kpc^{-1} was used for $A_{12\mu m}$, corresponding to an A_V of 0.95 mag kpc^{-1}. We assumed that $A_{12\mu m}$ is independent of the radial position in the disk.

Another consideration when modeling the bulge is that the dust in the disk has a vertical scale height of about 125 pc (Spitzer, 1976) which must be included in the extinction calculation. If the vertical distribution is strictly Gaussian with a constant half height and there is no radial dependence then the average $A_{12\mu m}$ value along any line of sight can be expressed in terms of the error function. For a line of sight of length d at any b^{II} the mean $A_{12\mu m}$ is given by

$$\langle A_{12\mu m}(d, b^{II})\rangle = \frac{\sqrt{\pi}\mathrm{ERF}(d \sin b^{II}/z_d)}{(d \sin b^{II}/z_d)} A_{12\mu m} \tag{8}$$

where the dust half height is 0.693 z_d. This reduces to the canonical value $A_{12\mu m}$ when $b^{II} = 0$. In the model, the interstellar extinction caused a small but noticeable reduction in the mean flux density per source on the plane. The effect diminishes fairly quickly off the plane.

e) Results of the model.

i) *Sky distribution*

An initial series of models to study the sky distribution using the Bahcall function were run for R_1 values between 1.0 and 2.5 kpc combined with k_1 values between 1.0 and 2.0. The χ^2 values showed that a round bulge was inconsistent with the data for any scale length. Models with k_1 equal to 2.0 were not as good a fit as models with k_1 equal to 1.5. The best fit from this group of models was for $R_1 = 2.0$ kpc, $k_1 = 1.5$. A second set of models were run for values similar to those values. The best fit found was for $k_1 = 1.6$ and $R_1 = 2.0$ kpc. The associated χ^2 values were 26.7 for the l^{II} histogram fit, 47.7 for the b^{II} histogram fit, and 74.3 for the combined fit. The associated probabilities that these χ^2 values are due to statistical fluctuations are 0.427, 0.006, and 0.022 respectively. The number of degrees of freedom is 24 for the individual fits and 48 for the combined fit.

Judging from these values, the l^{II} histogram is well fit by the model but the b^{II} fit is only marginally satisfactory. Thus the overall fit is not as good as might be hoped. Plots

of the model best fit histograms along with the data values are given in Figures 2a and 2b. The plot shows that the b^{II} fit suffers from severe problems near the galactic plane but matches very well for $|b^{II}| \geq 4°$. It is likely that there are still problems with the data near the plane. For example, even assuming that the disk is properly removed there may be completeness problems 2.5° to 3.5° from the plane which cause the inner two data points to fall well below the model predictions. The l^{II} histogram is noisy in the wings where the removal of the plane sources is more critical but is fit better then the b^{II} histogram. It is worth noting that the claim of a shift of 4° in the position of the IRAS bulge with respect to the galactic center by Meurs and Harmon (1988) is not supported by the data used here. Such a displacement would make this type of model fit impossible.

In all the models the b^{II} fit was poorer than the l^{II} fit. A slight improvement in the l^{II} fit was obtained using $R_1 = 1.9$ kpc and $k_1 = 1.5$ but the overall fit is slightly worse than for $R_1 = 2.0$ kpc and $k_1 = 1.6$. The uncertainties in the fit parameters are thus approximately 0.1 kpc and 0.1. Changing these values by more than 0.1 kpc or 0.1 causes a significant decrease in the goodness of fit. There are also small changes in the χ^2 value from run to run with the same input parameters but different random number seed values. These fluctuations are of the same order as the difference between the χ^2 values for the $R_1 = 2.0$ and $k_1 = 1.6$ model and for the $R_1 = 1.9$ and $k_1 = 1.5$ model. Thus the deduced values should be stated as $R_1 = 1.95 \pm 0.10$ kpc and $k_1 = 1.55 \pm 0.10$. However it is not clear that such precision is realistic given the uncertainties in the data. The best fit values are sensitive to exactly how the disk contribution is removed from the data. In an initial stage of our study of the bulge the sky distribution was corrected with the values from the $15° < l^{II} < 20°$ strip without allowing for a small bulge contribution to these values. As a result the early fits that were obtained differed those discussed above. The initial best fit occurred with $k_1 = 1.2$ and $R_1 = 1.4$ kpc. The bulge appeared to be smaller and rounder because the outlying sources were removed by the disk correction. These models did not give satisfactory χ^2 values. Changing the disk correction reduced the χ^2 values

significantly. A better disk correction might allow both of the histograms to be well fit with different parameters.

Some models were also constructed for the de Vaucouleurs $r^{\frac{1}{4}}$ deprojected density profile. These models never produced a good fit to the observed sky distributions, primarily because these models predict a very extended bulge in both l^{II} and b^{II}. Compared to the Bahcall function these models have a sharp decrease in the predicted number of sources within a few degrees of the center and a transition to a slowly declining number of stars per degree interval. This is a grave problem for the b^{II} distribution where the number of sources goes from a fairly large value to zero when the latitude changes from about 4° to about 8°. Even for a small R_e and a large k_e the fit is not satisfactory. An example of a de Vaucouleurs $r^{\frac{1}{4}}$ model compared with the data is shown in Figures 3a and 3b. The model used here has R_e set to 0.75 kpc, 5° on the sky, which is close to the value given by Habing *et al.* (1985). It does not appear that smaller R_e values produce any better results. The predicted histograms are quite different from the data.

The bulge is usually considered to occupy the inner 1 kpc of the galaxy (e.g. Frogel, 1988). We have obtained $R_1 = 2.0$ kpc. In comparing these values it must be remembered that most of the bulge stars are at $r < R_1$ because R_1 defines the scale length of the e^{-x^3} term in the density function. Half of the bulge stars fall within an ellipsoid of semi-major axis $0.525R_1$ and 88% within R_1. Therefore, in our model, most of the bulge stars are found within 1 kpc of the galactic center.

ii) *Flux density distribution*

In order to infer the $M_{12\mu m}$ distribution of the observed IRAS bulge sources the models were run with a 12 μm space density function of the form

$$\log_{10}(\phi(M_{12\mu m})) = \beta + \alpha M_{12\mu m} \tag{9}$$

where α and β are constants. This type of function is what one obtains for the OH/IR stars and also is the high luminosity limit of a function commonly used to parameterize

the ϕ–M_λ relation (see Mamon and Soneira (1982) for a discussion of approximations to the stellar luminosity function as it applies at different wavelengths). In the models, only the relative number of sources as a function of $M_{12\mu m}$ matters because the total number of sources is left as an adjustable parameter. If the range $M_0 \geq M_{12\mu m} \geq M_1$ is taken as the interval for the function ϕ, an integration over $M_{12\mu m}$ gives an expression for the fraction of sources with 12 μm absolute magnitudes between M_0 and $M_{12\mu m}$,

$$f(M_{12\mu m}; \alpha, M_0, M_1) = \frac{\left(1 - 10^{\alpha(M_{12\mu m} - M_0)}\right)}{\left(1 - 10^{\alpha(M_0 - M_1)}\right)}. \tag{10}$$

This equation was used with a random variable, chosen for each source, to assign $M_{12\mu m}$ values to the model sources. Those which fell into the selected areas of the sky were used to construct a model $F_\nu(12\mu m)$ distribution. This distribution was then normalized and compared with the data in the same type of χ^2 analysis as used for the sky distribution.

The result of this analysis was that the de Vaucouleurs $r^{\frac{1}{4}}$ function did not match the observed flux density distribution. All of the bulge models using this density profile predicted both too flat a histogram and that a significant fraction of bright bulge sources should be seen. This is a reflection of the comparatively large range of radii along a line of sight for this density function. The Bahcall density profile results match the data well for an $\alpha \approx -0.4$. The χ^2 values were usually in the range 15 to 20 for 17 degrees of freedom, giving probabilities ranging from 50% to more than 75% that the fit is correct. In part this is due to small number statistics which prevent a stringent test of the model. The α value is not well determined, for with a power law luminosity function most of the observed sources are near the minimum observable luminosity. In these models the minimum $M_{12\mu m}$ was -10.6. Increasing $|\alpha|$ above 0.4 has only a small effect upon the predicted flux density distribution. The models do show that slopes flatter than -0.3 are noticeably worse fits to the data because they produce too many bright sources. It is not clear how steep the slope has to be for a similar poorness of fit. The question of how many foreground disk stars there might be in the sample is also a limitation of the model fit. If the sources brighter than 5 Jy are disk stars then $|\alpha|$ can become large. Figure 4 shows an example of

the fit for the model that matches the sky distribution best. In these small areas off the galactic plane there will be few foreground disk stars. The colors of the sources IRAS saw in these areas support this assumption, for all the sources have the colors of AGB stars of high mass loss rate. So while a few disk sources must be present, they should be a minor part of the sample below 10 Jy at 12 μm. Sources brighter than 10 Jy were excluded assuming that they must be foreground sources, since no color sample shows the bulge if the 12 μm flux density is required to be $>$ 10 Jy. Assuming $\sqrt{N}$ uncertainties the χ^2 value for the model flux density distribution is 14.71 for 17 degrees of freedom. The models also show that the minimum $M_{12\mu m}$ for bulge sources must be near -13, depending upon the exact value of α, if no bulge sources are observed have $F_\nu(12\mu\text{m}) > 6$ Jy. A simple calculation assuming that the front of the bulge is 6.5 kpc away gives a limit of about -12.2 with a color correction included. The models indicate that some sources can be about a magnitude brighter than this without producing too many bright bulge sources.

Although the flux density distribution is not a strong test of the detailed geometry of the bulge, it does support the conclusion, from the sky distribution fit, that the de Vaucouleurs $r^{\frac{1}{4}}$ function does not give a good fit to this set of IRAS sources. To the extent that they trace the shape of the bulge it appears that the bulge is distinct from the spheroid in radial distribution. The $r^{\frac{1}{4}}$ function produces too extended a sky distribution to match the IRAS data. The flux density distribution also implies that the bulge is not very extended along the line of sight. The Bahcall function produces a good fit to the data. It is certain from this analysis that the $r^{\frac{1}{4}}$ law cannot fit the IRAS data for the bulge for $R_e \approx 2.7$ kpc deduced from the globular cluster system. The sources seen by IRAS in the bulge are not simply the central parts of the spheroid population, unless there is some other factor involved (such as metallicity) which affects the observed sources.

f) Discussion of the bulge results

There has been previous evidence that the bulge is not well fit by the $r^{\frac{1}{4}}$ law. At 2

μm, Garwood and Jones (1987) find that the bulge cannot be fit with a de Vaucouleurs $r^{\frac{1}{4}}$ function of a single effective radius if the local ratio of disk stars to spheroid stars is set to 800 to 1 (Schmidt, 1975). For comparison, Bahcall (1986) gives a local star density of 3×10^{-4} pc^{-3} for the spheroid and 0.13 stars pc^{-3} for the disk, a ratio of 433 to 1. From their model Garwood and Jones estimate a local ratio of about 160 to 1 if the spheroid effective radius is 2.7 kpc and the bulge is the central parts of the spheroid. While the value is not well determined, such a high local ratio is difficult to reconcile with other studies. The bulge axial ratio, about 4 to 1, that Garwood and Jones obtain from their analysis also differs from other measurements.

Garwood and Jones (1987) also attempt to analyze the 12 μm IRAS source counts. The comparison IRAS data set that they use does not shown the bulge as clearly as samples used by other studies. They do not describe whether any color corrections were made to the IRAS source magnitudes but it appears that they took all IRAS sources with F_ν(12 μm) > 0.71 Jy, $[12] < +4.4$ (see appendix), in the color range $[12] - [25] < 3.0$. They see the bulge only for $1.0 < [12] - [25] < 2.0$, which is about the same range of colors Habing (1986) used to study the bulge. One problem with the sample Garwood and Jones used is that they did not impose a maximum flux density value for the sample as well as a minimum value thus including more foreground disk sources in the data set. They find that their model does not predict enough sources at 12 μm and that the observations show a much steeper variation of source density with b^{II} than the model predicts. Both of these problems are probably the result of the absence of the most luminous 12 μm sources in their model.

We have found that the bulge as seen by IRAS is well fit by the Bahcall density function with $R_1 = 2.0$ kpc and $k_1 = 1.6$. We were not able to obtain a satisfactory fit using the de Vaucouleurs $r^{\frac{1}{4}}$ deprojected density profile. These results disagree with those of Habing (1986). One important difference between our analysis and Habing's is that we emphasize the sources within 15° of the center for fitting the bulge while in Habing (1986)

(1986) the fit extends over $1.8 \lesssim \theta^{\frac{1}{4}} \lesssim 2.3$ where θ is the angular separation from the center measured in degrees. This corresponds to $10.5° \lesssim l^{II} \lesssim 28.0°$. Habing assumed an ellipticity of 2.0 for his analysis (deduced from the globular cluster distribution). He then divided the sky into elliptical areas to count the sources and calculate the source density. It is possible that the bulge has a different ellipticity than Habing assumed, in which case the elliptical areas will include sources at different 'radii'. This could cause Habing to get a systematically erroneous result. It is not clear whether this effect could be large enough to explain why Habing is able to obtain a reasonable fit with the de Vaucouleurs function when we did not. An additional possibility is that we are not analyzing the same population of stars as Habing did, even though the colours are the same, because of the difference in the area of the sky that is used.

In an attempt to reconcile our results with those of Habing (1986) a model was run using both the Bahcall function with $R_1 = 2.0$ kpc, $k_1 = 1.6$, and a de Vaucouleurs spheroid with $R_e = 2.7$ kpc and $k_e = 2.0$. In addition a disk component was put into the model, with relative numbers 20 : 3.33 : 1 for the disk, the Bahcall function component, and the de Vaucouleurs spheroid. After the model sky positions had been calculated, both sets of sky positions were treated exactly the same way to find the radial number density function: sources with $|b^{II}| < 3°$ were excluded, after which the numbers of sources in elliptical strips 1° wide with axis ratio 2.0 were used to derive source densities for each strip. The results are plotted against the angular separation to the 1/4 power in Figure 5, with the model values normalized to match the data value at the smallest angular separation. Nearly all of the disk sources were excluded by the masking of the plane in both the model and the data sets. The model points closely resemble the data points. Both give small R_e values if a straight line is fit to the points, similar to the values from by Habing (1986). If, however, the inner bulge is masked off as well as the galactic plane, by excluding all sources in an ellipse of axis ratio 1.5 and semi-major axis 15°, both the data and the model show a flattening of the points and the R_e value becomes comparable

to the standard value of 2.7 kpc deduced from the globular cluster system.

III. THE GENERAL GALAXY MODEL

a) The 12 μm luminosity function

Mamon and Soneira (1982) showed that the observed luminosity functions for the *UBVRIJHK* filters can be represented by a function ϕ(M) of the form

$$\phi(M) = \begin{cases} 0 & M > M_d, \\ \phi(M_c) & M_d \geq M \geq M_c, \\ n^* 10^{\beta(M-M^*)}[1 + 10^{-(\alpha-\beta)\delta(M-M^*)}]^{-1/\delta} & M_c > M \geq M_b, \\ 0 & M_b > M, \end{cases} \qquad (11a)$$

which has parameters α, β, δ, n^*, M^*, M_b, M_c, and M_d. This function approaches a simple power law

$$\phi(M) = n^* 10^{\alpha(M-M^*)}, \qquad (11b)$$

for $M < M^*$; for $M > M^*$ the luminosity function flattens out to another power law

$$\phi(M) = n^* 10^{\beta(M-M^*)}, \qquad (11c)$$

and for $M_d > M > M_c$ the luminosity function is set to a constant value. The parameter δ controls the sharpness of the transition between the two power laws. This function provides a good analytic approximation to observed luminosity functions at various wavelengths.

We will assume that the 12 μm luminosity function can also be represented by equation (11a). One way to determine the parameters of this equation for 12 μm is to transform the V luminosity function to 12 μm using the $V - [12]$ colors for all sources which contribute to the V luminosity function. This technique is discussed in detail by Mamon and Soneira (1982). We have transformed the V luminosity function to 12 μm using the $V - [12]$ colors of stars in the *Bright Star Catalogue* (Hoffleit 1982), given by Cohen *et al.* (1987), and the breakdown of the V luminosity function into spectral classes given by Mamon and Soneira. The resulting luminosity function is shown by the dotted curve in Figure 6. It

has parameters $\alpha = 0.52$, $\beta = 0.025$, $\delta = 2/3$, $M^* = 3.0$ and $n^* = 0.0127$ stars mag^{-1} pc^{-3}.

We note that this transformational technique does not properly deal with bright 12 μm sources; there are many very bright 12 μm sources with very faint optical counterparts. IRC+10°216 is a good example of this. It has a $V - [12]$ value of 20–25 mag. Some extreme OH/IR stars probably have even larger color values. Since these sources were not properly identified as parts of the V luminosity function, they were not properly handled in the $V \rightarrow [12]$ transformation. This is also true of sources such as η Car, which are rarer than sources like IRC+10°216, but even more luminous at 12 μm. These sources are very important for an analysis of IRAS observations, because IRAS will have observed a large fraction of them no matter where they are in the galaxy. The transformed 12 μm luminosity function obtained from this technique will therefore be deficient at the brighter $M_{12\mu m}$ values.

An alternative way to derive the luminosity function at 12 μm is to use some complete sample of stars of all types with known distances. The only sample of stars that comes close to satisfying these requirements is the *Catalogue Of Nearby Stars* (Gliese, 1969; Gliese and Jahreiss, 1979); hereafter we will refer to this catalog as the 'Gliese Catalogue'. We describe in detail the derivation of the 12 μm luminosity function from this catalog in the Appendix. This luminosity function is shown by filled circles in Figure 6.

The Gliese sample does not help to define the bright end of the luminosity function. To get an estimate for the bright end, a sample of OH/IR stars was used. Distances can be derived for OH/IR stars either by the phase-lag method (Herman and Habing, 1987) or kinematically. A sample of 136 OH/IR stars with IRAS counterparts and distances was used to determine a space density function by assuming that the galactic disk is a uniform disk of 250 pc scale height and that all OH/IR stars are seen out to the most distant one in any absolute magnitude range. The method is subject to large uncertainties because the OH surveys do not cover the galactic plane uniformly and the sample is probably not

complete for any absolute magnitude value. However, the results should yield lower limits to the space density of OH/IR stars which in turn are a fraction of all stars of a given $M_{12\mu m}$. The resultant luminosity function for OH/IR stars is shown as open circles in Figure 6.

It is clear that the luminosity function derived from the $V \rightarrow [12]$ transformation suffers from a serious lack of high luminosity 12 μm sources. The OH/IR space density values are higher than the transformation would predict when $M_{12\mu m} < -11.5$. Even at modest $M_{12\mu m}$ values, the transformed curve falls below the Gliese Catalogue values.

The solid curve in Figure 6 shows the same luminosity function as that obtained from the $V \rightarrow [12]$ transformation, except with the parameter $\alpha = 0.36$. This new curve matches the bright part of the Gliese values reasonably well and passes above all of the OH/IR star points. Anticipating results to be discussed later, it turns out that the value of α can be directly inferred from IRAS data because the slope of the relation between the number of sources brighter than a limiting magnitude as seen by IRAS, and that magnitude value for an area in the galactic plane, is proportional to α. The solid curve in the figure has the proper slope to match a typical area near the galactic plane observed by IRAS.

At low luminosity there are two points in the Gliese points of Figure 6 which are significantly above the curves. The highest point is solely due to α Cen C. If it is representative of the general disk the space density implied by that point alone is 0.105 stars pc^{-3}. The other anomalously high point is due to 4 IRAS sources with $M_{12\mu m}$ between +7.00 and +7.50 all found within 3.32 pc of the sun. The point between these is due to only 1 source seen by IRAS. It is possible that the luminosity function does not flatten out as our adopted value of β indicates, but instead keeps rising as $M_{12\mu m}$ increases. If so, the total space density would be higher than optical studies indicate, due to large numbers of faint low-mass main sequence stars. At shorter wavelengths, the luminosity functions do not show a rise of that type at low luminosity. The total space density of stars as deduced from the Gliese sample is 0.171 stars pc^{-3}, of which 0.131 stars pc^{-3} is due to

the two points above the curves in Figure 6. The total space density is 0.118 stars pc^{-3} for the solid curve and 0.128 stars pc^{-3} for the dotted curve over the magnitude range in the Figure. The estimated total stellar space density is about 0.13 to 0.14 stars pc^{-3} (Allen 1981) including white dwarf stars which contribute about 10% of the total. The corresponding mass density is ≈ 0.07 $M_\odot$ pc^{-3} from stars and ≈ 0.13 $M_\odot$ pc^{-3} in total.

It is interesting to note that the slope of the luminosity function deduced for the bulge in §II.e.ii was -0.4, the absolute value of which corresponds to the parameter α in equation (11a) since the range of $M_{12\mu m}$ is several magnitudes below M^*. The bulge stars had a cut-off at about -13.5 which is not seen in the OH/IR sample. Radiative transfer models for a star of total luminosity 6000 $L_\odot$, a typical value for a low mass AGB star, show that the $M_{12\mu m}$ value reaches at peak of ≈ -13 at a dust optical depth of about 3 for a 1000 K dust condensation temperature. Presumably the bulge sources are all low mass stars and are unable to reach a higher 12 μm luminosity. The maximum value of $M_{12\mu m}$ is somewhat model-dependent but this supports the idea that the bulge sources are of low mass, as has been discussed by Habing (1986) among others.

b) The Monte Carlo description of the disk

The galactic disk used in the model consists of three separate components which could be adjusted in relative number. In addition to the smooth exponential disk, the model also included sources in the spiral arms and the molecular ring. The need for these components is discussed in §IIIe where the model results are presented. Each of these will now be briefly described.

i) *The smooth exponential disk*

The smooth exponential disk was assumed to have a the density function

$$\rho(r,z) = \begin{cases} \rho_0 \exp[-(R-R_0)/h - |z|/h_z] & R \le R_{\max}, \\ 0 & R > R_{\max}, \end{cases} \qquad (13)$$

where h is the radial scale length, h_z is the vertical scale height, R_0 is the galactocentric distance, ρ_0 is the density in the solar neighborhood, and $R_{\max}$ is the outer radius of

the disk. The disk was assumed to have a constant scale height and scale length for each of a number of ranges of $M_{12\mu m}$. The scale length was usually set to 3.5 kpc (de Vaucouleurs and Pence 1978). We used scale height values ranging from 120 pc to 300 pc depending upon $M_{12\mu m}$. The model program had the capacity to include a thick disk component but it was not needed in the fit. This treatment of the disk is different from that used by Habing (1988). In particular, Habing used the $\mathrm{sech}^2(z/z_0)$ function for the vertical distribution of the disk, rather than $\exp(-|z|/h_z)$, so his scale heights are not directly comparable to the ones used with the exponential form of the distribution. For $|z| \gg h_z$, $\mathrm{sech}^2(z/z_0) \approx 4\exp(-2|z|/z_0)$, so z_0 is equivalent to $2h_z$, but the total surface density differs by a factor of 2 if the two functions are matched far away from the plane. The $\mathrm{sech}^2(z/z_0)$ function is predicted from isothermal relaxation models of the galactic disk while the $\exp(-|z|/h_z)$ function has no theoretical justification, but near-infrared observations of edge-on spiral galaxies show an exponential surface brightness profile to small z (Wainscoat 1989, Wainscoat and van der Kruit 1989). The program included the option of using either form of the z distribution but only the exponential form was used in the models described here.

Values of $R_{\max}$ ranging from 10 kpc to 25 kpc were used. In all cases the galactocentric distance R_0 was assumed to be 8.5 kpc. In most cases, $R_{\max}$ was set to be 15 kpc, and the effect of a smaller disk was determined by removing sources beyond a specified radius from the output files without recalculating the model. The mass of a disk extending to 15 kpc with a 3.5 kpc scale length is 92.7% of that for an 'infinite' disk of the same scale length.

ii) *The spiral arms*

To derive the spiral arm structure, the results of Georgelin and Georgelin (1976) and of Dame *et al.* (1986) were used to trace out the arms. Georgelin and Georgelin trace 4 spiral arms based upon optical and radio observations of large HII region complexes. Two of these spiral arms appear to start in the first quadrant and extend behind the galactic

center to the fourth quadrant receding from the sun. The other two arms are detected coming towards the sun in the first quadrant, one of them being the Sagittarius-Carina arm which can be traced over most of the inner 180° of l^{II} passing ~1 kpc inside the solar position. The arms deduced by Georgelin and Georgelin are surprisingly symmetric about a line through the galactic center perpendicular to our line of sight. They do not state whether this was required in their fitting of the HII region data. The points for equivalent pairs of arms were combined by reflecting them about the galactic center and assuming that the arms are perfectly symmetric. For each of the resulting arms, a least-squares fit to the usual logarithmic spiral function,

$$\theta(R) = \alpha \log(R/R_{\min}) + \theta(R_{\min}) \tag{14}$$

resulted in the following values:

$$\text{Sagittarius} - \text{Carina/NormaArm}: \begin{cases} \alpha = 4.25 \pm 0.26 \\ \theta(R_{\min}) = -0.28 \pm 0.02 \\ R_{\min} = 3.26 \pm 0.49 \text{ kpc} \end{cases}$$

$$\text{Scutum} - \text{Crux/PerseusArm}: \begin{cases} \alpha = 4.89 \pm 0.12 \\ \theta(R_{\min}) = -0.75 \pm 0.02 \\ R_{\min} = 4.77 \pm 0.37 \text{ kpc} \end{cases}$$

with the angles measured in radians from the sun-galactic center line of sight. The uncertainties are 99% confidence intervals from the least-squares fits for α and $R_{\min}$. In the models the nominal values were used because searching for a best match to the IRAS data over a range of parameter values would be very time-consuming. This description of the spiral arms does not include a 'local' spiral arm. If there were a local spiral arm then the galaxy would have unusually closely spaced spiral arms since the Sagittarius arm passes about 1 kpc inside, and the Perseus arm passes roughly 2 kpc outside, the solar circle. It is likely that undue emphasis has been placed on the local tracers because they are nearby and well observed.

To treat the arms in a Monte Carlo simulation we assumed that the stars in the arms have the same radial scale-length as the exponential disk. It was then possible to integrate along the arms to find the relative numbers of stars as a function of the angle θ if the

arms uniformly enhance the disk population over a set width perpendicular to the $\theta(R)$ curve. It was assumed that the arms are 500 pc in width at any point. The integration gave the ratio of the total numbers of sources in the two arms. Any sources to be placed in the arms in the model were assigned to one of the arms by comparing a random number to the relative proportions of the arms. Another random number was used to assign the angle along the arm based upon the distribution of sources within the arm. Finally a third random number was chosen and the position perpendicular to the length of the arm was assigned from the width. The exact width of the arms should not significantly affect the calculation as long as it is much less than one radial scale length.

iii) *The molecular ring*

We also had to include sources in the molecular ring. There is no clear picture of the structure of the molecular ring or of how the stellar content of the disk is changed in the molecular ring. We simply assumed it to have a Gaussian density function along any radial line from the center. The half-width of the Gaussian function was assumed to be 33.3% of the peak radius. The peak radius was set to $0.45R_0 = 3.825$ kpc with $R_0 = 8.5$ kpc. Various papers have somewhat confusing pictures of 'the molecular ring'. For example, what Clemens *et al.* (1988) call the molecular ring seems to correspond to the molecular ring and the part of the Scutum-Crux arm in the first quadrant as pictured in our model. They also comment that the Sagittarius arms appears more ring-like than spiral-like. These differences are probably a matter of interpretation for it is difficult to get a clear picture of the structure of the arms and the ring from inside the disk. Scoville and Sanders (1988) portray the molecular ring as extending from 3 to 7 kpc radius, based upon the same CO survey data for the first quadrant, and do not ascribe anything to spiral arms. If that is the correct interpretation, the molecular ring is not really very ring-like.

In Figure 7 the spiral arms and molecular ring as used in the models are shown along with the position of the sun, as viewed from directly above the galactic center. Clearly it is a highly idealized picture. For any sources thought to be of high initial mass, some of the

sources were put into the spiral arms and the molecular ring as in Figure 7, and some of the sources were put in the exponential disk component. Figure 7 has equal numbers of sources in the ring and in the arms. The arms are followed out for 6 radians from the starting points, which are actually at slightly different angles than those listed following equation (14), to avoid having a double-valued angular variable in the Monte Carlo descriptions of the star distributions while extending out to at least 15 kpc. The 6 radian range for the arms takes them just beyond this value of $R_{\max}$ used in most of the model runs. For the low mass stars, all of the sources in the model were put into the smooth exponential disk because they are not expected to be spiral tracers. The first 13° of each arm has been truncated; since the arms start inside the molecular ring this does not appear to be critical for the models.

Another aspect of the disk model is the question of the solar location with respect to the galactic plane. When modeling the bulge, a small offset from the plane makes no practical difference in the predicted sky distribution. For the disk, this effect is more important. The model was set up so that the point of view could be put anywhere in the galaxy or even outside it entirely. The model sources were placed in the galaxy using a cylindrical coordinate system defined so that the galactic disk is in the (R, θ) plane and the origin is at the galactic center. The model source positions were transformed back to the specified point of observation assuming that the galactic center defines the zero point of both coordinates and that the 'galactic longitude' coordinate spans the long axis of the projected galactic disk. Since the sun is not far from the galactic plane, the effect is to introduce a small rotation into the transformation equations. The sun was first put 20 pc off the galactic plane but that caused too large a difference in the model source counts at the two poles. A value of 12 pc for $z_\odot$ produces a good result. Only a few values of $z_\odot$ were tried in the models so it is not very accurately determined. It probably could not be smaller than 8 pc nor larger than 20 pc. The solar position is north of the galactic plane, defined as the positive z direction in the model.

When the program was run, the luminosity function (shown in Figure 6) was split into an number of sections by $M_{12\mu m}$ and the total galactic population of each part was calculated from the assumed disk parameters. We required that the total local space density of disk stars was 0.14 stars pc^{-3} so there should be 9163 stars within 25 pc and 6244 stars within 22 pc of the sun. The Gliese catalogue lists less than 2000 stars within 22 pc of the sun. Most of those that are missing are probably faint M-type stars. If the sources were bright enough at 12 μm to be observed over at a distance of more than $\approx$ 2 kpc, then the full galactic population was used in the model. For sources with $M_{12\mu m} > -5$ only that section of the galaxy within which the observed IRAS 12 μm flux density would be above 0.1 Jy for the brightest sources in the magnitude range was included in the computation. Thus the models are complete to 0.1 Jy.

A normal galaxy model required the calculation of about 13.3 million source positions and magnitudes to insure that all possible sources with $F_\nu(12\ \mu m) \geq 0.1$ Jy were included. The models were run on a Cray X-MP/48 computer and required about 25 minutes of CPU time per model run. Smaller runs such as that used to produce Figure 7 could be done on a VAX 8600 system, where the program execution was roughly 20 times slower than on the Cray system.

c) Comparison data for the Monte Carlo galaxy model

IRAS detected 158787 sources at 12 μm. The model program is able to simulate all of these sources but the problem of handling the resulting output made this approach impractical. Thus, to test the model, nine specific areas of the sky were chosen for detailed comparison with IRAS. The areas test the parameters of the model in specific ways. The comparison areas are listed in Table 1. The north and south galactic poles were chosen to test the main sequence and local giant stars in the models and, if possible, the contribution of the spheroid to the source counts. In addition, two areas were chosen looking in the galactic plane. An area near the anti-center was chosen to see if any effect of the edge of

the galaxy could be seen. An area in the plane, at $l^{II} \approx 30°$, tests the disk component without going so close to the galactic center that severe problems with completeness and shadowing of sources occur. One area includes part of the bulge and another area looks towards the galactic center at intermediate galactic latitude. The latter area will see some spheroid stars but no bulge stars. The final area chosen for detailed analysis was the area of the IRAS deep survey (Hacking and Houck, 1987). This part of the sky is at the north ecliptic pole and was observed by IRAS every orbit for calibration purposes. It has a 12 μm flux density limit an order of magnitude lower than anywhere else in the sky. The other ecliptic pole is in the direction of the LMC, where the high source density precluded the same type of analysis.

In addition to returning detailed information for these nine areas, the model program returned all sources which had model flux density values above an input minimum. Initially the minimum was set to 90 Jy but, as the model was improved, the value was reduced to 2.5 Jy. IRAS observed 30774 sources with $F_\nu(12\mu\text{m}) \geq 2.5$ Jy. About 70 of these are extra-galactic sources. The number of sources, the brightness distribution, and the sky distribution of these sources all are tests of the model. These bright IRAS sources are mostly optically faint, mass losing stars of high 12 μm luminosity, as is clear from the IRAS colors of the sources and the galactic distribution which is heavily concentrated to the galactic plane. Unless otherwise noted the term 'bright sources' will refer to those IRAS sources brighter than 2.5 Jy at 12 μm.

There are a number of problems in directly comparing the models to the data. Some areas of the sky were not observed by IRAS. About 4% of the sky was not covered in the survey. Most of the gaps in the sky coverage are at high galactic latitude. This directly affects the two galactic pole areas. Using an equal area plot of all sources seen by IRAS at the poles we estimated that 9.9% of the north galactic pole area and 9.6% of the south galactic pole area are missing from the IRAS data set. In those parts of the sky it is reasonable to assume that the sources are uniformly distributed so these percentages give

the correction factors needed to compare the models to the data. It does not appear that any of the other areas listed in Table 1 are affected by the gaps in sky coverage. The bright source samples are affected by the gaps. The loss of sources will be less than 4% since the bright sources cluster to the plane while most of the gap is at high latitude. The gaps reach the galactic plane near the tangent points. No description of the gaps is available in the IRAS *Explanatory Supplement* or other IRAS publications. A project is underway to define the gaps but for these models no correction was attempted except for the two polar areas because a full description of the gaps is needed to do the correction properly.

For areas 1, 2, and 3 in Table 1 there may be problems with source confusion or loss of sources due to shadowing as the scans crossed the galactic plane. These effects are described in the IRAS *Explanatory Supplement* (1988). These are certain to affect area 1. For the other areas near the plane we expect these effects to be smaller than for area 1 because in the anti-center direction the source density is relatively low even near the plane while for area 3, only that part of the region closest to the galactic center has a source density approaching the confusion threshold. Apart from area 1, we expect these effects to be small. For the bright sources there will also be some problems with sources near the plane although for these sources we expect the shadowing to be less of a problem than for the fainter sources because the shadowing effect was caused by problems with the local noise estimation and bright sources should still be above the noise even if it is overestimated. The models actually do predict more sources near the plane than were observed, but we do not have an explicit correction for the confusion and shadowing effects and thus some uncertainty is introduced into the model parameters.

For each area we sought to match both the number and the detailed flux density distribution of the sources. The number of sources with $F_\nu(12\mu\mathrm{m}) \geq F_{\nu 0}$ grows as a power law. When plotted as a cumulative function, $\log_{10}[N(F_\nu(12\mu\mathrm{m}) \geq F_{\nu 0})]$ versus $\log_{10} F_{\nu 0}$, a '$\log N$–$\log S$' plot, there is usually a linear trend. For a uniform disk of identical sources and no extinction the predicted slope is -1.0 when looking in the plane. When sources

over a wide range of luminosity are present in the disk the models predict that the slope will be close to -2.5α when looking in the plane, where α is the parameter from equation (11a). If the flux density threshold is expressed in magnitudes, the slope is just α. Near the galactic plane the slope of the log$N$–log$S$ plots was always near -0.9; this was the basis of our choice of $\alpha = 0.36$ (solid line in Figure 6), replacing the value of 0.52 (dotted line in Figure 6) from the $V \rightarrow [12]$ transformation. This change produced the correct slope in the model log$N$–log$S$ plots for areas in the plane.

d) Local space densities, total galactic disk populations, and interstellar extinction

Having assumed a luminosity function and the parameters of the disk, we then found the total numbers of sources within specific magnitude ranges to run the model. For the brighter sources the model uses the total galactic population. Where only part of the disk is modeled the proper numbers of sources must be assigned to the volume under consideration.

A scale height and radial scale length were assumed for each group of sources in the model. Normally only the scale height changed from group to group. For the brighter sources, some of the sources were assigned to the spiral arms and the molecular ring. To keep the number of free parameters as small as possible, only three values of the scale height were used in the model: 120 pc for the most luminous group of sources, and for main sequence stars with $-5 < M_{12\mu m} < 3$ (stars of spectral type F or earlier); 250 pc for red giant stars with $-13 < M_{12\mu m} < -1$ which include AGB stars with mass loss, stars on the first giant branch, (including K- or M-type giants with little mass loss); and 300 pc for the rest of the main sequence sources. For $-5 < M_{12\mu m} < -1$ there are two groups of stars with different scale heights. Since the optical space density values for the B-type stars is comparable to that for K-giant stars the space density over this range of the luminosity function was initially divided equally between the two scale height values. The scale heights are summarized in Table 2. These scale height values are similar to those

used in the Bahcall-Soneira model (Bahcall, 1986, and the references therein) for the main sequence and disk giant stars. One area in which the model could be improved is in the assigning of better scale height values as a function of $M_{12\mu m}$. At present it is not possible to quantitatively assign specific types of stars to the ranges of $M_{12\mu m}$ so only this crude set of scale heights could be used. For the brighter sources it is likely that there should be 2 or 3 different scale heights since distinct types of stars will be contributing to the population. Aside from the obvious case of the $M_{12\mu m}$ range where the main sequence and the K-type giants overlap it is not clear how the scale heights should be divided among sources of the same $M_{12\mu m}$.

When the models were run we assumed that the total numbers of the red giant stars could be adjusted up or down as needed to match the IRAS data because the luminosity function given in equation (11a) is only an approximation to the actual function; there may be enhancements or deficiencies compared to this function. These factors, which should not be larger than about 3, are free parameters in the fitting of the observed values. The final adopted values of these factors are listed in Table 2. For the main sequence part of the model, the luminosity function was assumed to be well established since the Gliese sample allows the determination of that part of the luminosity function. If there were large numbers of stars with $M_{12\mu m} > +7$ it would not make any significant difference in the models even if the models were extrapolated to $F_\nu(12\mu m) = 0.01$ Jy ($[12] \approx +9$) because these sources could only be seen to a very limited distance.

We assumed that the local space density of stars of all types is 0.14 stars pc^{-3} giving 9163 stars within 25 pc of the sun. For comparison, the Gliese catalogue (Gliese and Jahreiss 1979) listed 1529 systems containing 1890 components with trigonometric parallaxes $\pi \geq 0.045$ arcsec. These systems are 32% of all stars within 22 pc with this total space density. The rest are likely too be faint M-type stars or white dwarf stars that have not yet been discovered or had parallaxes measured. The disk parameters allow calculation of the relative number of stars within 25 pc of the sun. From the luminosity function and

the local star density the local fraction of stars in a magnitude range can be calculated. These two numbers give the total disk population of stars in the magnitude range.

The bulge and the spheroid were assumed to have the same luminosity function as for the disk, except that no bulge sources were allowed to have $M_{12\mu m} < -13.0$. The ratio of disk population to bulge population to spheroid population was kept constant in the models. For the bulge, the ratio was set by matching the observations in area 3 (see Table 1). For the spheroid there is no area where a large fraction of the sources seen by IRAS are spheroid stars so in that case the number ratio was adjusted to obtain a local ratio of about 400–500 disk stars to each spheroid star (Bahcall, 1986). This value is uncertain by at least 25%. For the assumed spheroid effective radius of 2.7 kpc the total number of spheroid stars needed to produce this local ratio of components is 5% of the number of disk sources. If the disk has a total mass of $\approx 7 \times 10^{10}$ $M_\odot$ of which half is due to observable stars then the total spheroid mass is between 1.75 and 3.5×10^9 $M_\odot$, depending upon whether the spheroid has the same fraction of mass in unobservable form as does the disk. This mass range is consistent with the values given in Bahcall (1986).

Table 2 lists the magnitude ranges used in the model calculation, along with the disk parameters and estimated total galactic populations. It also lists the correction factors for the total numbers based upon the best fit to the IRAS sources with $F_\nu(12\mu m) \geq 2.5$ Jy. The largest correction factor is 0.3125 for $-5 > M_{12\mu m} \geq -7$. The lack of sources in this magnitude range is probably due to two effects. First, by $M_{12\mu m} = -5$ the contribution from main sequence stars has declined because only O-type and the brightest B-type stars can attain that magnitude. The early-type giant and supergiant stars may also have magnitudes in this range but they are rare. Second, among the late-type stars only the supergiant K-type stars and luminous M-type stars can achieve such an absolute magnitude but most of the M-type stars will have mass loss and therefore become more luminous than $M_{12\mu m} = -9$. It is therefore not surprising that the 250 pc component contributes less than expected in this range of absolute magnitudes.

A change was made in the handling of interstellar extinction when the program was generalized from modeling the bulge to modeling the whole galaxy. The dust producing the extinction was assumed to have an $\exp(-|z|/h_z)$ density distribution with a scale height of 125 pc, with no radial density dependence. It is more likely that the dust will have a similar radial density distribution to the disk stars; this would introduce many complications since the extinction is probably enhanced in the spiral arms and the molecular ring. Also, the program is explicitly designed to avoid doing integrations along some particular line of sight, as would be required for each source if a radial decline in extinction were assumed. For these reasons the extinction was set at 0.046 mag kpc^{-1} when $z = 0$ over the whole disk. With this simple dust density function the extinction to any source could be calculated from the sky position and distance using an analytic formula.

e) Results of the model

The number of free parameters in the model is quite large. If all of them were going to be varied, there would be 12 free parameters for each of the 9 magnitude intervals. It is clearly impractical to search a parameter space of dimension 108. Most of these potential free parameters were fixed for every run, such as the ratio of disk sources to spheroid sources or the assumed disk radial scale length. Our models began with a total of 8 free parameters: the disk scale length, the disk outer radius, the bulge to disk number ratio, the spheroid to disk number ratio, a maximum bulge star luminosity, and a choice of one of 3 scale heights depending upon which range of $M_{12\mu\mathrm{m}}$ was under consideration. Initially only the first 7 areas in Table 1 were considered along with the number of model sources brighter than 90 Jy. It quickly became apparent that the luminosity function would have to be adjusted since too many sources with $M_{12\mu\mathrm{m}}$ from -1 to -9 were seen at intermediate and high galactic latitude where changing the disk scale length would not be expected to have a strong effect. Thus scale factors were introduced for the brighter sources starting with those in the -1 to -7 range and later extending to those which are more luminous.

Finally when the sample of bright sources was extended down to 2.5 Jy from 90 Jy we found that the spiral arms and the molecular ring are needed to match the observed l^{II} distribution of the sources. We assumed that there would be equal numbers of sources in the ring and in the spiral arms, unless there was some serious problem when that was done, purely to avoid introducing too many additional free parameters. In one magnitude interval model sources were put into the ring but not the spiral arms. Sources were not put into the spiral arms unless the $M_{12\mu m}$ range was appropriate for sources with high main sequence masses. Thus the number of free parameters actively used in the modelling was 17: the 8 listed above; 5 factors for the numbers of sources in the high luminosity part of the luminosity function; and 4 parameters relating to the molecular ring and the spiral arms in those magnitude ranges where IRAS would be able to see the sources out far enough to reach these components. The disk giants and main sequence stars with $M_{12\mu m} > -7$ were not put into the spiral arms or the molecular ring.

Having 17 free parameters in the model is preferable to 108 but is still too large to allow a systematic search of the parameter space. Using these parameters we tried to match the observed numbers of sources in the 9 areas, the total number of sources brighter than 2.5 Jy, the sky distribution of the sources brighter than 2.5 Jy, the local disk to spheroid star number ratio, and the details of the source counts in all of the areas. The models are strongly over-constrained by the data despite the number of free parameters. It is necessary to worry about uniqueness in the fit parameters and how to judge the quality of the fits. The sort of χ^2 tests used by Habing (1988) could be used here, but the amount of data to be matched is much greater; therefore, this was not done. An attempt was made to do that type of parameter fitting for the sub-sample shown in Figure 1a. A grid of disk models having scale heights between 1 kpc and 200 pc, scale lengths from 2.5 to 4.5 kpc, and outer radii from 10 kpc to 25 kpc was made and then a program was created to combine the various models with arbitrary scale factors to fit the observed sky distribution. The sky was divided into 400 areas covering about 100 square degrees each

for this comparison. The models were calculated with a restricted range of luminosities appropriate to the colors. This was done to determine whether a thick disk was needed to fit the data before doing the models of all 12 μm sources. Even with this smaller set of data to match, it turned out that searching the parameter space for the minimum χ^2 values took far longer than running the disk models. Indeed this required far more computer time on the Cray computer than running the full galaxy model. The search was abandoned as requiring too much computer time to complete. In retrospect the disk models used in the search were too simplistic because they did not include any spiral arm or molecular ring contributions and it is not surprising that no good fit could be found.

Rather than try to search the parameter space, the models were built up starting as simply as possible and adding in components when needed. The comparison areas were intended to probe different combinations of all possible components of the galaxy. First the modelling was concentrated on the poles where the main sequence stars and disk giants are observed. These models had only the exponential disk, the bulge, and the spheroid. Once a satisfactory match had been obtained there and at intermediate latitudes our attention was shifted to the galactic plane. For the first phase of the fitting process the sources brighter than 90 Jy were used for comparison with the data. While the number of sources brighter than 90 Jy could be matched the sky distribution was not correctly predicted by the model. The model distribution peaked on the plane close to the galactic center whereas the actual sources show an extended distribution along the galactic plane. Problems were encountered with area 1 because the models always predicted too few sources by a factor of about 2.

When the model was run for comparison with all IRAS sources brighter than 5 Jy rather than 90 Jy, the discrepancy between the model and the data became much worse. Figure 8 shows the predicted histogram of these sources as a function of galactic longitude for sources with $|b^{II}| < 1^\circ$ along with the observed values. The model matches fairly well in the outer galaxy but fits very poorly in the inner galaxy. The model peaks much too

sharply around the galactic center. The 'horns' in the data histogram at $l^{II} \approx \pm 25°$ are in the right place to be due to molecular ring sources. Extensions of the excess in the data to larger longitudes suggest that the sources in spiral arms are also contributing. We assumed that the difference between the model and the data occurs because these components are affecting the observed distribution. The other possibility would be to drastically reduce the radial scale length in the disk. That would cause too few sources to be present beyond the solar circle and would contradict the results of optical determinations of the scale length, so we did not decrease the scale length. After the addition of the new components to the disk the fit to the bright source distribution became much better and *we conclude that the spiral arms and the molecular ring are needed to fit the IRAS observations.* With all the components a good fit was obtained for the areas in the galactic plane as well as at high galactic latitude.

The model judged to be the best fit has the parameters listed in Table 2. The results of the model are given in Figures 9–11. These Figures show the sky counts from the model and from the IRAS data for the 9 areas, plus comparisons of the sky distribution of the sources brighter than 2.5 Jy from the model with the data. In the following paragraphs these results are discussed in the order that the Figures are shown, with comments on how the various constraints shaped the parameter values and some differences between the model results and the data which seem to come from problems in the IRAS data or limitations of what can be built into the models. This particular run gives 9176 ± 59 sources within 25 pc of the sun, 18 of them spheroid stars for a ratio of 510 to 1 in number. The input value was 9163 stars within 25 pc. Within 62.5 pc the disk to spheroid ratio declines because the disk scale heights have some effect. In the larger volume the disk to spheroid ratio is about 440 to 1. IRAS does not provide a good test of the spheroid fraction in the local vicinity. Observations of much fainter sources are needed before quantitative estimates of this ratio can be made.

In order to estimate the uncertainties in the model values, the models were always

run with an excess of stars and then random samples were taken from the resulting model output to bring the numbers down to what was required. This allowed adjustment of the scale factors for the various magnitude ranges listed in Table 2 without having to rerun the full model every time. It also allowed some estimation of the fluctuations in the model numbers. By running 200 samples out of the model files, the means and standard deviations for the quantities could be found. The discrete nature of the models causes some variations in how the model curves look for the brighter sources where the total numbers are still small, so there is some variation in the appearance of the model curves from run to run, although once the number of sources becomes large enough runs with different seed values give the same results. In the discussion of the numbers in the various areas, the means are given with sample standard deviations as the uncertainty values. The numbers of model sources in the plots sometimes deviate from the mean values especially in area 1 and 6 where the total number of sources is small. A breakdown of the contributions to each area and to the bright sources by magnitude range and by component is given in Table 3.

IRAS carried out a flux limited survey, with a flux limit of ~0.2 Jy at 12 μm over most of the sky. The completeness limit is about 2.5 times higher than the flux limit, ~0.5 Jy away from the galactic plane. The data curves in the Figures 9b–9i show a roll-off in the log$N$–log$S$ relation within about a factor of 3 of the flux density limit due to incompleteness. The models are not subject to this since they are certain to include all possible sources brighter than 0.1 Jy. In the plots, the model curves have been terminated at the observed minimum flux density value. Area 1 is the only area that shows no roll-off.

Area 1 (In The Plane, Figure 9a)—This area has 59 sources in one square degree of sky, so it is above the IRAS confusion limit of about 45 sources per square degree. It has an unusually high minimum $F_\nu(12\mu\text{m})$ of 1.499 Jy. The model predicts 73 ± 6 sources over the same range of flux density. It appears that the model has too many sources by about the same factor at all flux densities, which is what we expect if confusion were responsible

for the loss of ~14 sources out of 73 independent of their brightness. The slope of the model points is the same, within expected uncertainties, as that shown in the data. The observed slope is near −0.9, typical of areas on the galactic plane. Areas like this one in the plane sample the most luminous sources. The breakdown by component for the model sources shows that most of them are located in the molecular ring or the spiral arms. If these components were removed the model would not have enough sources in this area by about a factor of 2, unless the disk scale length was made very small. According to the model no bulge or spheroid stars are seen in this area, mainly because it is a small area.

Area 2 (Towards The Anti-Center, Figure 9b)—In many ways the anti-center direction proved to be very difficult to model. As the model stands, there appears to be an excess of sources below about 0.6 Jy compared with the data; above that value the match is very good. One possibility is that the edge of the disk should be closer than the assumed value of 15 kpc to eliminate these excess faint sources, which would support the results found by Habing (1988). This can be directly tested by removing any sources that are too far away from the galactic center from the model output file. When this was done with a maximum radius of 10 kpc, the number of sources predicted to be in this area dropped from 348 to 162 in the specific run used, which is far too small a number of sources. The model curve then falls below the data values by a factor of about 2.4. If the disk edge is moved out to 12 kpc, the model predicts 271 sources in this area and the discrepancy becomes a factor of about 1.4. There is some tendency for the models with smaller disks to predict a steeper slope for this area than in the model plotted in Figure 9b because the bright sources are more likely to come from the high luminosity part of the luminosity function and so be relatively far away. From these results it seems that the edge of the galaxy cannot be much closer than the 15 kpc value assumed here. If a larger radial scale length were assumed, this restriction would be relaxed, but it seems very unlikely that the disk edge could be as close as 10 kpc out from the galactic center based upon these results. It is possible that the small excess of sources comes from our assumed z distribution, which

has a cusp right on the plane rather than a smooth distribution. The spiral arm does not have much of an effect upon this area because the source density has become low so far out from the galactic center.

Area 3 (Towards The Bulge, Figure 9c)—The IRAS observations for this area are unusual in that there is a distinct change in the slope of the star counts. The models suggest that about 60% of the sources in this area are bulge sources and that about 30% of them are exponential disk sources. The roll-off of the data values probably reduces the fraction of bulge sources present since they are more likely to be near the flux density limit than are the disk sources. In this area the model fails to fit the brightest sources although the total number of sources brighter than ~8 Jy in the model is the same, within uncertainties, as that which is observed. We assume that the very bright sources are all foreground disk stars and that the change in slope occurs when the bulge sources begin to contribute to the cumulative number of sources. The model fits well to a flux density of 1 Jy after which there appears to be an extended roll-off in the data.

Area 4 (Intermediate Galactic Latitude, Figure 9d)—Aside from the presence of one very bright source in the area, the model fit to the IRAS data is very good here. The observations begin to suffer incompleteness at about 0.25 Jy. The breakdown of the model sources shows that about 7% of the model sources in this direction come from the spheroid and the rest are from the exponential disk. Most of these sources are relatively nearby; about 10% have $M_{12\mu m} < -9$. Not surprisingly, at higher galactic latitudes the data set is fit better by the model. There are 7 sources in the area which are seen at 12 μm and which are associated with galaxies. An additional five 12 μm sources have colors similar to those galaxies but have no IRAS associations with galaxies. For comparison, there are 139 sources with galaxy associations and 149 possible new galaxies, based upon the IRAS colors, in this area. These are almost all 60 μm sources. The model curve has been adjusted by a factor of $1033/(1033 - 12)$ to simulate the addition of galaxies. The displacement of the points is very small in this case.

Area 5 (North Galactic Pole, Figure 9e)—As noted previously, there are gaps in the coverage near the poles. Galaxies also contribute a significant number of 12 μm sources at the poles. In area 5 there are 612 sources with galaxy associations, out of which 50 are seen at 12 μm. There are also another 170 unassociated sources with the colors of galaxies but none of these were detected at 12 μm. The gap removes 9.9% of the area. The loss of sources from the gap, in fact, almost exactly cancels out the contribution of galaxies in this area, so the model was not scaled nor were the galaxies removed from the data. There are too few galaxies to change the slope of the data. The comparison of the model with the data values shows that the model has a fluctuation above the data for $F_\nu(12\mu\text{m}) \approx 30$ Jy which causes the model points to stay above the data until 3 Jy is reached. This is due to the cumulative plot and does not indicate a serious disagreement between the model and the data over this flux density range. There could be a small effect of having slightly too many bright sources at the poles because the model runs which rise above the data as in Figure 9e are more common than those where the model has a lack of sources near 30 Jy. This effect could be caused by having a slightly incorrect scale height for one of the magnitude intervals. Evidence for this effect is marginal so no adjustments were made to try to correct it.

Area 6 (The Hacking/Houck Area, Figure 9f)—All of the sources that IRAS observed in this area have been identified so it is possible to exclude the galaxies and consider only the stellar sources. The model for this area predicts 60 ± 7 stars compared with 41 observed by IRAS. (The plotted model has only 48 sources due to a statistical fluctuation.) For this area the model completeness limit is much higher than the flux density limit. In Hacking and Houck (1987) it is stated that the 12 μm detections are detector noise limited. They show that the detector noise ranges from 0.001 Jy to 0.010 Jy over the field of the deep survey, with a representative value being about 0.007 Jy. The detections were required to be 5σ detections so the data incompleteness should start at about 0.035 Jy on the average. Allowing for small number statistics and the uncertainties in both the model

and the data the model fits this area reasonably well. This area does not show the same type of roll-off as the other areas. The change in the slope of the data near 0.1 Jy probably indicates the beginning of incompleteness, although this value is significantly higher than the expected completeness level. The models predict that there should be 1 or 2 spheroid stars observed in this area.

Area 7 (South Galactic Pole, Figure 9g)—The sun was located 12 pc north of the galactic plane in the model, resulting in a larger number of model sources in the south pole than in the north pole. There are 20 12 μm sources with galaxy associations; a total of 333 sources have galaxy associations in the entire area. The difference in the number of galaxies seen at the two poles is mainly due to the Virgo cluster. There are 2 other 12 μm sources that could be galaxies based upon the colors, out of a total of 174 potential galaxies. The gap in the south polar cap removes 9.6% of the area. Thus the estimated correction to the number of observed sources is an increase of 6.8% if the gap were not there, and the galaxies were removed. In the plot the model has been scaled down by 6.8% to compare with the data set. The model matches the data very well over most of the plot but there may be a minor problem with the fainter sources since the model curve is slightly above the data values before the roll-off, due to incompleteness below 0.3 Jy. That is a 7% effect at 0.4 Jy. While the observed numbers of sources in the two poles, taken at a flux density limit before the roll-off begins, agree within the expected uncertainties, if the galaxies are removed from the sample there is a larger difference between the two areas because the Virgo cluster is contributing to the north pole area. The models predict about a 20% difference in the number of galactic sources in the poles due to the solar position off the plane. This is what is observed if galaxies are excluded from the data. There is a nearby bright source in this area which has no counterpart in the model, R Aqr = IRAS 23412−1533 (M7 IIIe) with $F_\nu(12\mu\text{m}) = 1577$ Jy.

Area 8 (The Larger Anti-Center Area, Figure 9h)—This area was chosen for study after it became apparent that there were problems in fitting area 2. Area 8 is larger than

area 2 and tests sources further from the plane than does area 2. Figure 9h shows that the model predicts too many sources by ~15% at all flux densities while the shape of the model curve is correct. The statistical uncertainty in the model is probably much smaller than 15%. As with area 2 it does not seem likely that this could be due to having too large a disk. The best way to obtain agreement between the model and the data would be to assume that the disk has a real deficiency of sources in this direction. Optical studies of the local disk have shown that there are local fluctuations in the stellar density within ≈500 pc of the sun. McCuskey (1965) presents plots of the observed surface density of stars of specific types which show several local irregularities. Some of these apparent fluctuations may be due to interstellar absorption; others may be associated with spiral arms in the solar vicinity, but one still is left with a picture of a non-uniform disk, even for comparatively low mass stars.

Area 9 (115° to 140°, Figure 9i)—This final area was chosen to be adjacent to area 8 but still in a direction where the same components of the galaxy would dominate. The model predicts about 8% too few sources in this area rather than 15% too many sources as in area 8. At the bright end there are too few sources compared with the data. The difference in the shapes of the two curves is caused by a group of sources with $F_\nu(12\mu\text{m}) \approx$ 50 Jy in the data, which elevate the cumulative number. About 10 or 12 sources cause a bump in the observed log$N$–log$S$ curve. This suggests a local feature in that part of the sky. A differential plot shows that the model predicts the correct relative distribution of sources except near 50 Jy. Both areas 8 and 9 have contributions from the spiral arms, but as with area 2 the number of sources is relatively small compared with the exponential disk stars.

The Bright Sources: Latitude Distribution, Figure 10—The model predicts a total of 31268 sources with $F_\nu(12\mu\text{m}) \geq 2.5$ Jy compared with 30774 sources actually seen. Some correction must be made for the gaps in the sky coverage, which is a complex problem since no adequate description of these gaps is available. The gaps cover ≈ 4% of the sky,

mostly at high latitude. To get a very rough correction it was assumed that the 4% breaks down into 4.6% of the region with $|b^{II}| \geq 20°$ and 2.9% of the rest of the sky. The gaps come down to the plane near the tangent points. Over the outer galaxy the model has $\approx$60 sources per degree of longitude of which $\approx$13 are at high latitudes. The estimated number of sources lost due to the gaps is $\approx$650 sources. Confusion and shadowing near the plane cause further complications, but we cannot estimate these effects. The model has 494 ± 352 sources more than the data, assuming $\sqrt{N}$ uncertainties in the total numbers, which is consistent with the estimate of sources lost due to the gaps.

The gaps and confusion will have less of an effect upon the relative latitude distributions than upon the total numbers. Figure 10a compares the model latitude histogram with the data for the sources brighter than 2.5 Jy. Figure 10b presents a similar comparison for the sources brighter than 5 Jy. The agreement between the model and the data values is good at high galactic latitudes. Within 10° of the plane there are some differences between the model and the observations. The model peaks more strongly on the plane but has a relative lack of sources from 3° to about 6° from the plane. This may be the result of the scale height changing from 250 pc to 120 pc at $M_{12\mu m} = -13$ rather than changing gradually around this magnitude. The model sample has about 2% of the sources from the spheroid and about 6% from the bulge.

The Bright Sources: Longitude Distribution, Figure 11—To look at the longitude distribution, the bright sources were split into sources within 1° of the plane, sources within 20° of the plane, and the full sample of sources. Figures 11a–d present the longitude histograms for these model samples along with the observed values. In Figure 11a, for the sources with $|b^{II}| < 1°$, the model does not fit all aspects of the actual longitude distribution. The data points show a broader distribution of sources in the inner galaxy which does not peak as sharply as the model does. In the outer galaxy the agreement is satisfactory. The model distribution is strongly affected by the spiral arms and the molecular ring in this latitude range. Figure 11a would be similar to Figure 8 if the

spiral arm and molecular ring sources were transferred to the exponential disk component. Within 25° of the center the model source counts are high enough that we expect there to be confusion effects in the data. This will be particularly true very close to the galactic center. If the range of latitude which is included is increased to 20°, as in Figure 11b, the agreement between the model and the data is much better. In that Figure the data values show an excess of sources relative to the model at about $l^{II} = 50°$, which suggests that the spiral arm representation in the first quadrant is not quite correct. Figures 11c–d give the total longitude distributions for sources brighter than 2.5 and 5 Jy. Figure 11d gives a clearer view of the non-exponential part of the disk. The data values show a broad plateau within ±30° of the galactic center. The model shows a peak near the center, only a small amount of which is due to the bulge (because few model bulge sources are brighter than 5 Jy), and a fairly broad area around that peak due to the arms and the molecular ring. There is an asymmetry in the model distribution because in the first quadrant the spiral arms are observed as they come out from the molecular ring while in the fourth quadrant they are observed as they wind away from the inner disk, which causes their tangent points to be at different places in the two quadrants. Qualitatively this is what is seen in the longitude distribution of all the IRAS point sources: the region of high source number extends further on one side of the galactic center than on the other side. Nevertheless it is clear that the model does not match the extent of the plateau region seen in Figure 11a or 11d. We feel that the description of the spiral arms is probably too simplistic to match the real data. It is also possible that small changes of the parameters listed following equation (14) could change the tangent points of the Sagittarius-Carina/Norma arm enough to match the data values more closely.

The conclusion from these models is that the distribution of the bright sources and of the disk sources seen in the Habing sample shown in Figure 1a is strongly influenced by the Sagittarius-Carina/Norma arm. Habing (1986, 1988) attributes the sky distribution to a simple disk and concludes from the contrast between the inner galaxy and the outer galaxy

that the sun is near the outer edge of the disk. That conclusion appears reasonable from the galactic coordinate distribution of his sample. Here, by contrast, we conclude that the spiral arms and the molecular ring cause the higher density of sources near the plane over most of the inner galaxy. The effect is quite similar to what a disk would produce because the sun is situated close to the Sagittarius-Carina/Norma arm, and so the number of observed sources drops once the tangent points of this arm are passed. The distribution does not look ring-like because of the inner arms and the molecular ring filling in the areas closer to the galactic center. This conclusion is a tentative one and more study will be required to be sure of whether this interpretation is better than that offered by Habing. The results given above for the areas in the outer galaxy also disagree with the idea the we are situated near the edge of the galactic disk. However there is always the problem of uniqueness in the model. Another problem is that the spiral arm description is very idealized and so it is hard to compare it confidently with the data.

The model predicts that most of the bright IRAS sources are intrinsically luminous 12 μm sources. These sources were used to determine the high luminosity part of the luminosity function. The total numbers of sources brighter than thresholds of 2.5, 5, 40, and 90 Jy were used to constrain the total numbers of high luminosity 12μm sources in the galaxy. Trying to match the numbers of sources within 1° and 20° of the plane produces more constraints on the luminous sources. The models suggest that these bright sources predominantly have $M_{12\mu m} < -7$. The 4 groups of model sources from this magnitude interval were subject to 8 conditions to match the total numbers of bright sources as a function of b^{II}, resulting in an over-determined set of conditions from which the scale factors for these groups of sources, given in Table 2, were found. The uncertainties about sky coverage corrections and the shadowing and confusion effects introduce uncertainties in these conditions so no totally consistent set of values could be found. The factors have $\approx$ 10% uncertainty.

The model generally matches the observed number of bright sources within the uncer-

tainties of the data values. The program returned details of all sources with $[12] < +3.023$. The breakdown of the model bright sources by magnitude compared with the IRAS values is given in Table 4. In Table 4 the model values in each interval have been multiplied by a factor 0.98 to allow for the gaps in the coverage. For the brighter sources, with $[12] < 1$, this may be too large a correction because the very bright sources are concentrated more towards the plane and towards the galactic center than are the fainter sources.

If $\sqrt{N}$ uncertainties are assigned to the observed values the χ^2 from the values in Table 4 is 26.82 for the 10 magnitude intervals. There are 4 parameters that were used to produce this match so the number of degrees of freedom is 6. The formal probability of a good fit is $\ll 0.5\%$. This result is, however, sensitive to the gap corrections. If the correction for the gaps in coverage were applied only to the sources above magnitude +2, because they comprise 60% of the sample and would be most affected by the sky gaps (because they tend to be located at higher latitudes), the χ^2 value is reduced to 15.38 and the probability of a good fit becomes about 2%. As is seen from Table 4, the main contribution to the χ^2 value when the correction is applied to all the sources is due to a deficiency of sources in the +2 to 0 magnitude range. It is possible that local galactic features such as the Orion and Cygnus complexes are partially responsible for this. Alternatively, there may still be a problem in the luminosity function used in the model. In view of the uncertainty about confusion, shadowing, and the gaps in the IRAS data set, the bright sources from the model are a fair fit to the data. Further work is needed to see if the discrepancy in the +2 to 0 magnitude range can be removed without large changes in the parameters. For such a study a proper description of the gaps in coverage is needed, as well as some method to simulate the shadowing and confusion problems for sources near the plane.

The specific model run described here lacks sources with $[12] < -6$, like η Car and IRC+10°216. This is just due to small number effects. Other runs of the model produced sources with similar properties to these stars. IRC+10°216 has $M_{12\mu m} \approx -13$ for a distance of $\sim$ 100 pc. In about half of the model runs, a similar source happens to be near

the solar position. The brightest model source in this run had $[12] = -5.91$, at a distance of 1.3 kpc. The model may be lacking a very small number (~ 100) of extremely luminous 12 μm sources like η Car which contribute a few of the $[12] < -5$ sources observed by IRAS. If η Car is at a distance of 2 kpc it has $M_{12\mu m} \approx -17.6$.

f) Discussion of the general sky model

As seen in the previous section, the model produces a fair or good fit to many aspects of the IRAS data using the five components. Areas 3 through 7 show that the model matches the data well at high galactic latitudes. There are areas of the sky where the model components are too simplistic to match the data. The local features of the galactic disk such as Gould's belt and the Orion complex are not included in the description of the disk. For example, a trial run of the model in the direction $l^{II} \approx 90°$ near the galactic plane, roughly towards Cygnus, gave a distinctly steeper log$N$–log$S$ relation than is observed in that area. A differential log$N$–log$S$ analysis showed that the difference was due to a significant number of sources brighter than 10 Jy present in the data set with no counterparts in the model, while the model had the proper number of the fainter sources for this area. In other cases the model would probably fail completely due to the limitations of the spiral arm description. Figure 11 shows areas where the model is deficient in the brighter sources; these areas would probably also have a deficiency of fainter sources. It is possible that the observed discrepancies for areas 8 and 9 are due to local density variations in the disk but more work is needed in the anti-center direction before this conclusion can be given much weight. Possibly other parameters could be used to produce satisfactory fits in all areas. That aspect of the models could be tested if the model could be applied simultaneously at shorter wavelengths and 25 μm as well as at 12 μm because the different wavelengths will highlight different classes of stars. This program deals only with 12 μm data and there presently is no way to identify the sources that contribute to any area of the sky by spectral type or a magnitude other than [12].

One aspect of this work that disagrees with the results of Habing (1988) is that our sky model does not require a thick disk component to match the observations. It appears that we could add a thick disk of relatively low luminosity stars to the model, with some re-adjustment of the parameters, but there is no compelling reason why this should be done based upon our study. A thick disk would contribute to area 4 and area 8. If Habing is correct in concluding that the thin disk ends not far outside the solar circle while the thick disk extends to a much larger radius then the thick disk should be observable in the anti-center direction. Area 4 is a place where a large scale height disk component should be observable. Area 4 was matched well in the model without any component of large scale height. The models for areas 8 and 9 show discrepancies in total number compared with the data but the relative brightness distributions appear to be correct. At present we see no observational evidence for the thick disk from IRAS.

Our results also disagree with Habing's conclusion that the thin disk ends just beyond the solar circle. The type of sources in Habing's sample are equivalent to some of the most luminous 12 μm sources. For these objects we find that their inclusion in the spiral arms and the molecular ring is necessary to match the observed sky distribution. Consequently his result that the disk ends just beyond the solar circle may be the result of how these components appear on the sky. Our position just outside the Sagittarius-Carina spiral arm makes the contribution of the spiral arms and the molecular ring to the sky distribution look similar to the effect of a disk terminating near the solar circle. Habing did not try to fit the total sky distribution of his sample, but looked at selected areas, avoiding the galactic plane. In our model, it was the l^{II} distribution of sources close to the plane that alerted us to the need for the spiral arms and the molecular ring. For areas off the plane these components are less obvious, which may be why Habing did not see any need to include them in his model.

In our model, the disk radial scale length was usually set to $h = 3.5$ kpc, although some tests were made with larger values. This 3.5 kpc value is consistent with some optical

determinations (e.g. de Vaucouleurs and Pence 1978) and with radio observations of HI (Gordon and Burton, 1976) and CO (Knapp, Tremaine and Gunn, 1978). A larger value of $h = 5.5 \pm 1.0$ kpc has been deduced from Pioneer 10 surface photometry observations at $|b^{II}| > 20°$ (van der Kruit 1985). It is possible that our model would fit the observations just as well with a larger value of the radial scale length; although at this time we do not know whether this is the case.

Another limitation of the present model is that no allowance has been made for the problems of confusion, incomplete sky coverage, and shadowing in the IRAS data. An improvement in the fit to the bright sources could be obtained only if some method of allowing for these effects became available. Of the 9 test areas only the two areas in the poles were affected by the gaps in sky coverage, and in those cases it was reasonable to assume that the sources are uniformly distributed so a correction for the gap could be made. For the areas where the gaps in coverage reach into the galactic plane, no such simple correction is possible because of the gradient of source density.

In the future we hope to extend the star count model by including color information for the sources, which would allow the direct study of the sample that Habing used in his analysis. A color based study would give a much better idea of how our models relate to Habing's. A more detailed model fit to his sample might alleviate the need for a small outer radius to the galactic disk. It is possible that this specific subset of IRAS sources has a different maximum radius than the general disk. Such an effect could be produced by a metallicity gradient in the disk, because the sample used by Habing (1988) consists of sources with thick dust envelopes; as heavy element abundances decline it becomes more difficult for sources to have thick circumstellar dust shells.

IV. CONCLUSIONS

In this paper we have presented the results of a star count model specific to the IRAS 12 μm data. The model seeks to characterize both the geometrical parameters of

the galaxy and the 12 μm luminosity function. The model began with an analysis of the galactic bulge as seen by IRAS since it is a component of the galaxy which is difficult to study at optical wavelengths due to interstellar extinction. Subsequently the model program was expanded to include other components of the galaxy so IRAS observations at 12 μm could be analyzed for any area of the sky. Due to the small interstellar extinction in the middle infrared, the star count model could be compared with the observations right down to the galactic plane, in contrast to the optical star count studies which are made at relatively high galactic latitude to avoid problems with extinction. The model is an all sky simulation program rather than a program that looks deeply at a small area of the sky.

Our main conclusions are the following:

1) The sky distribution of a color-selected sample of IRAS bulge sources is well fit by a density function given by Bahcall (1986) with normalization radius $R_1 = 1.95 \pm 0.10$ kpc and axis ratio $k_1 = 1.55 \pm 0.10$. It also matches the flux density distribution of sources in a bulge test area. The distribution cannot be well fit by a de Vaucouleurs $r^{\frac{1}{4}}$ law, either with a 2.7 kpc effective radius as is deduced from the globular cluster system or with a smaller value similar to that found by Habing (1986). The $r^{\frac{1}{4}}$ law does not fit the flux density distribution of IRAS sources in the test area. These results suggest that the bulge as seen by IRAS is not simply the inner parts of the spheroid component.

2) A model with both the Bahcall type bulge and a standard de Vaucouleurs spheroid can reproduce the results of Habing (1986), who fitted a de Vaucouleurs function of small effective radius to the IRAS 'bulge' sources. It appears that Habing's fit is a match to the inner spheroid rather than the bulge because he did not extend his analysis close enough to the galactic center.

3) For the brighter IRAS sources, a fit to the l^{II} distribution near the galactic plane requires that the model have spiral arm and molecular ring components. The molecular ring sources were assumed to have a Gaussian radial distribution peaking at $0.45R_0$ and

of half-width $0.15R_0$. The spiral arms were approximated by a fit to the data of Georgelin and Georgelin (1976). The sources in these components seen by IRAS appear to be massive AGB stars and M-type supergiants, which contribute many of the most luminous 12 μm sources.

4) There is a small north/south asymmetry in the IRAS 12 μm sources (when the extragalactic sources are removed from the sample) which is fit well if the sun is positioned about 12 pc north of the galactic plane. A model assuming a solar offset of 20 pc predicts an asymmetry greater than that observed.

5) We have determined the 12 μm stellar luminosity function. Using the analytical representation given by Mamon and Soneira (1982) to describe the luminosity function (see equation 11a) the parameters are $\alpha = 0.36$, $\beta = 0.025$, $\delta = 2/3$, $M^* = 3.0$ and $n^* = 0.0127$ stars mag^{-1} pc^{-3}. For the most luminous 12 μm sources the required luminosity function falls slightly below the values from the analytic representation. (Correction factors are given in Table 2 as a function of $M_{12\mu m}$.)

6) The model is able to fit the observations near the galactic plane in the outer galaxy, although deviations in the total number of sources of the order of 10% occur from area to area, with the galactic disk extending out to 15 kpc galactocentric distance and a 3.5 kpc radial scale length. This differs from the results of Habing (1988) who deduced that the disk ends just beyond the solar circle. In our model no satisfactory fit was found for a maximum radius within ~5 kpc of the solar circle.

7) The model is able to fit the IRAS observations without any need for a thick disk component. This does not rule out the presence a thick disk in our galaxy but it is not obviously required by the general IRAS star counts.

In the future we hope to improve the model by including color information and thereby relating the 12 μm sources to specific types of objects in the galaxy.

Acknowledgements

We thank the NASA Ames Research Center, which provides support for IRAS studies through the SETI Institute under cooperative agreement NCC 2-407. This study at Jamieson Science and Engineering, Inc., was supported in part by contract no. NAS 2-12515 with NASA Ames Research Center. K.V. acknowledges the award of a Natural Sciences and Engineering Research Council of Canada Postdoctoral Fellowship.

APPENDIX

IRAS observations of stars in the Gliese Catalogue: The 12 μm luminosity function

The Gliese catalogue attempts to list all stars within 22 pc of the sun. However, there are still stars within this volume being discovered today, especially from observations of faint, high proper-motion stars. The main problem with using this catalogue to determine a luminosity function is that the most luminous sources are not represented. There are also incompleteness effects which are a complex function of the absolute magnitude of the stars under consideration because many of the Gliese Catalogue sources are too faint to have been seen by IRAS.

A search of the PSC resulted in the selection of 638 sources from the Gliese Catalogue with good quality 12 μm flux densities. Most of these sources are at relatively high galactic latitude and there should be no ambiguity in the identification of the IRAS source with the Gliese Catalogue source. In some cases the associations are to stars in a multiple system which IRAS was unable to resolve. Usually it is clear that only one Gliese star is bright enough to have been observed by IRAS. The 638 associations represent about one third of the systems in the Gliese Catalogue. As a check that these sources are indeed the nearby sources, Figure 12 shows the color/magnitude diagram for 630 of the 638 sources for which an accurately determined distance was available. The 8 that were excluded are sources where either no trigonometric parallax was found in the Gliese Catalogue, so that a spectroscopic parallax was the only available distance estimate, or sources where the trigonometric parallax disagrees significantly with the distance found from photometric or spectroscopic observations. (The trigonometric parallax values were assumed to be the best values for determining the distance to the sources.) The Figure is a form of the Hertzsprung-Russell diagram. The 12 μm magnitudes are color corrected assuming that the sources have a 4000 K blackbody spectrum. The conversion from PSC flux density to

[12] is then

$$[12] = 4.018 - 2.5 \log_{10}(F_\nu(12\mu\mathrm{m})). \quad (12)$$

For IRAS the difference in color corrections between 10000 K and 2000 K is very small so no adjustment was made for the different types of stars. Approximate mean colors for various spectral types are shown in the Figure. The bluest source present is α Gru = IRAS 22051−4712, of spectral type B5 V. Most of the sources lie along the main sequence, the horizontal width of which gives some indication of the scatter in $V - [12]$ color with spectral type. This scatter is probably due to inaccuracies in the distances, uncertainties in the [12] values, and the complications caused by binary systems with stars of significantly different effective temperatures. The dominant sources are of G- to middle K-type. Main sequence stars later than K5 are too faint for IRAS to observe out to the limiting radius of the Gliese catalogue, while the earlier spectral types have such a low space density that they are poorly represented. At $V - [12] \approx 2.5$, there is a split in the distribution, where the late G- and early K-type sub-giant and giant stars with larger M_V values break away from the main sequence. All these stars have about the same $V - [12]$ value because the range of effective temperature is not very large and they have no circumstellar dust. The 7 sources with $M_V < 4.0$ and $V - [12] > 3.5$ or $M_V < 0.2$ are all bright giants. These sources define the late-type giant sequence in the diagram. Starting from the left the sources are α Aur = 05134+4556 (G5 III + G0 III), α Ari = 02043+2313 (K2 III), α Boo = 14133+1925 (K1 III), α Tau = 04330+1624 (K5 III), β And = 01069+3521 (M0 IIIe), HR 5603 = 15011−2505 (M3.5 III), and HR 4949 = 13039+2253 (M5 III). These stars do not have high mass-loss rates. They have IRAS colors and LRS spectra consistent with stellar blackbody sources and have no sign of any circumstellar dust.

There is at least one case where the IRAS source is a background object: 02138+4244 has an association with G134–22 which is a carbon white dwarf star of $m_V = +16.23$ and a nominal [12] of +3.78. A few other sources appear to have $V - [12]$ colors which are somewhat larger than normal and might also be cases where a background source has been

associated with the Gliese star. There are two sources with $M_V \approx +8$ that are a magnitude or more redder than the main group. Both of the sources, 01583+6139 = DM+61°366 and 11442+2718 = DM+27°2055, are associated with main sequence K-type stars and may be background sources even though the color excess is small compared to that of 02138+4244.

The Gliese sample can be used to create an observed space density function by examining ranges of $M_{12\mu m}$ and finding the number of sources and the distance to which these sources have been observed. For the M-dwarf stars the limit of IRAS detections is much less than 22 pc. For example α Cen C, with $M_{12\mu m} = +8.3$ was just barely detected by IRAS at a distance of 1.3 pc. The star with the lowest $M_{12\mu m}$ in the sample is α Tau with a value of -4.62 at a distance of 20 pc. The luminosity function derived from the Gliese catalogue is shown by filled circles in Figure 6.

REFERENCES

Allen, C. W. 1981, *Astrophysical Quantities*, (London: Athlone Press).

Bahcall, J. N. 1986, *Ann.Rev.Astron.Astrophys.*, **24**, 577.

Bahcall, J. N., and Soneira, R. M. 1984, *Ap. J. Supp.*, **55**, 67.

Becklin, E. E., and Neugebauer, G. 1968, *Ap. J.*, **151**, 145.

Clemens, B. P., Sanders, D. B., and Scoville, N. Z. 1988, *Ap. J.*, **327**, 139.

Dame, T. M., Elmegreen, S. G., Cohen, R. S., and Thaddeus, P. 1986, *Ap. J.*, **305**, 892.

de Vaucouleurs, G. 1977, *A.J.*, **82**, 456.

de Vaucouleurs, G., and Pence, W. D. 1978, *A.J.*, **83**, 1163.

Frogel, J. A., and Whitford, A. E. 1987, *Ap. J.*, **320**, 199.

Frogel, J. A. 1988, *Ann.Rev.Astron.Astrophys.*, **26**, 51.

Garwood, R., and Jones, T. J. 1987, *Pub. A.S.P.*, **99**, 453, 1987.

Georgelin, Y. M., and Georgelin, Y. P. 1976, *Astr. Ap.*, **49**, 57.

Gilmore, G., and Wyse, R. F. G. 1987, in *The Galaxy*, ed. G. Gilmore and B. Carswell, (Dordrecht: D.Reidel), p. 247.

Gordon, M. A., and Burton, W. B. 1976, *Ap. J.*, **208**, 346.

Habing, H., Olnon, F. M., Chester, T., Gillett, F., Rowan-Robinson, M., and Neugebauer, G. 1985, *Astr. Ap.*, **152**, L1.

Habing, H. 1986, in *Light On Dark Matter*, ed. F. P. Israel (Dordrecht: D.Reidel), p. 329.

Habing, H. 1988, *Astr. Ap.*, **200**, 40.

Hacking, P., and Houck, J. R. 1987, *Ap. J. Supp.*, **63**, 311.

Hayakawa, S., Matsumoto, T., Murakami, H., Uyama, K., Thomas, J., and Yamagami, T. 1981, *Astr. Ap.*, **100**, 116.

Herman, J., and Habing, H. 1987, in *Late Stages Of Stellar Evolution*, ed. S. Kwok and S. R. Pottasch, (Dordrecht: D.Reidel), p. 55.

Hiromoto, N., Maihara, T., Mizutani, K., Takami, H., Shibai, H., and Okuda, H. 1984, *Astr.Ap.*, **139**, 309.

Hoffleit, D. 1982, *The Bright Star Catalogue*, (New Haven, Connecticut: Yale University).

IRAS *Explanatory Supplement* 1988, ed. C. A. Beichman, H. J. Habing, P. E. Clegg, and T. J. Chester, (Pasadena, California: JPL)

Joint IRAS Science Working Group, 1988, IRAS Catalogues and Atlases. *The Point Source Catalogue*, version 2, (General Printing Office: Washington D.C.).

Knapp, G. R., Tremaine, S. D., and Gunn, J. E. 1978, *A.J.*, **83**, 1585.

Mamon, G. A., and Soneira, R. M. 1982, *Ap. J.*, **255**, 181.

McCuskey, S. W. 1965, in *Galactic Structure*, ed. A. Blaaw and M. Schmidt, (Chicago: University of Chicago Press), p. 1.

Meurs, E. J. A., and Harmon, R. T. 1988, *Astr. Ap.*, **206**, 53.

Oort, J. H. 1977, *Ann.Rev.Astr.Astrophys.*, **15**, 195.

Press, W. H., Flannery, B. P., Teukolsky, S. A., and Vetterling, W. T. 1986, *Numerical Recipes*, (Cambridge: Cambridge University Press).

Rowan-Robinson, M., and Chester, T. 1987, *Ap. J.*, **313**, 413.

Scoville, N. Z., and Sanders, D. B. 1987, in *Interstellar Processes*, ed. D.J.Hollenbach and H.A.Thronson, (Dordrecht: D.Reidel), p. 21.

Spitzer, L. 1976, *Physical Processes In The Interstellar Medium*, (New York: Wiley).

van der Kruit, P. C. 1986, *Astr.Ap.*, **157**, 230.

Wainscoat, R. J. 1989, in preparation.

Wainscoat, R. J. and von der Kruit, P. C. 1989, in preparation.

Wainscoat, R. J. *et al.* 1989, in preparation.

Young, P. A. 1976, *A.J.*, **81**, 807.

Table 1—Comparison Areas For The Monte Carlo Models

Area Number	l^{II} Range	b^{II} Range	Area (Square Degrees)	Number of 12 μm Sources	Minimum $F_\nu(12\ \mu m)$ In Jansky
1	+29.0° to +30.0°	−0.5° to +0.5°	1.00	59	1.499
2	+170.0° to +180.0°	−1.5° to +1.5°	30.00	197	0.242
3	−0.5° to +5.0°	−5.0° to −3.0°	10.97	515	0.474
4	+0.0° to +30.0°	−45.0° to −20.0°	627.54	1033	0.235
5	−180.0° to +180.0°	+70.0° to +90.0°	1243.93	576	0.217
6	+95.153° to +98.846°	+29.66° to +30.34°	4.34	41	0.011
7	−180.0° to +180.0°	−70.0° to −90.0°	1243.93	618	0.226
8	+150.0° to +175.0°	−4.0° to +4.0°	199.83	1246	0.221
9	+115.0° to +140.0°	−4.0° to +4.0°	199.83	2167	0.188

For each area all IRAS sources with good or fair 12 μm flux density values were included in the comparison set. For area 6, the area of the north ecliptic pole scanned hundreds of times by IRAS, the data is from Hacking and Houck (1987) rather than the IRAS *Point Source Catalog* (1988). It that case the sky area observed was defined in equatorial coordinates rather than galactic coordinates, so the limits given in the table for the model program are not the real boundaries. Area 6 covers the same amount of sky and is centered at the same point as the area for which Hacking and Houck present data values. At this galactic latitude the shape should not make any difference in the results.

Table 2—Summary Of The Galaxy Model Parameters

Range Of 12 μm Magnitude	Z Scale Height h_z (pc)	Fraction Of Disk Stars Within 25 pc	Fractional Space Density In Magnitude Range	Nominal Disk Population	Adopted Disk Population	Fraction Value For Magnitude Range
−13 to −17	120	2.94×10^{-7}	1.80×10^{-7}	5605	2556	0.4560
−11 to −13	250	1.47×10^{-7}	7.92×10^{-7}	49300	24050	0.4879
−9 to −11	250	1.47×10^{-7}	4.15×10^{-6}	2.87×10^{5}	1.41×10^{5}	0.5462
−7 to −9	250	1.47×10^{-7}	2.17×10^{-5}	1.35×10^{6}	6.98×10^{5}	0.5163
−5 to −7	250	1.47×10^{-7}	1.13×10^{-4}	7.04×10^{6}	2.20×10^{6}	0.3125
−1 to −5	250	1.47×10^{-7}	1.70×10^{-3}	1.06×10^{8}	3.31×10^{7}	0.3125
−1 to −5	120	2.94×10^{-7}	1.70×10^{-3}	5.30×10^{7}	5.30×10^{7}	1.0000
+3 to −1	120	2.94×10^{-7}	5.25×10^{-2}	1.64×10^{9}	1.64×10^{9}	1.0000
+7 to +3	300	1.24×10^{-7}	2.28×10^{-1}	1.69×10^{10}	1.69×10^{10}	1.0000
+11 to +7	300	1.24×10^{-7}	3.45×10^{-1}	2.56×10^{10}	2.56×10^{10}	1.0000
+15 to +11	300	1.24×10^{-7}	2.75×10^{-1}	2.75×10^{10}	1.69×10^{10}	1.0000

Disk radial scale length, h = 3.5 kpc; R_{max} = 15 kpc.
Galactocentric distance R_0 = 8.5 kpc, solar offset $z_\odot$ = 12 pc.
Total disk star population = 7.17×10^{10} stars, which implies a total disk mass of about 7×10^{10} $M_\odot$.
The limiting distances for the model calculations were 2.012 kpc for $-5 < M_{12\mu m} < -1$, 0.319 kpc for $-1 < M_{12\mu m} < +3$, and 0.0505 kpc for $+3 < M_{12\mu m} < +15$.

The bulge population was assumed to be 23% of the disk population for $M_{12\mu m} > -13$. The bulge parameters are those discussed in §IIe, R_1 = 2.0 kpc and k_1 = 1.6. The spheroid was assigned 5% as many sources as the disk, giving a local ratio of 517 : 1 disk to spheroid sources. The spheroid has R_e = 2.7 kpc and k_e = 2.0.

Table 3—Breakdown Of The Model Results

Range of Absolute Magnitude	Area 1	Area 2	Area 3	Area 4	Area 5	Area 6	Area 7	Area 8	Area 9	$F_\nu \geq 2.5$ Jy
$-13 > M_{12\mu m} > -17$	13	1	3	1	0	0	0	3	10	2518
$-11 > M_{12\mu m} > -13$	30	11	227	10	5	0	2	45	98	10698
$-9 > M_{12\mu m} > -11$	26	42	680	62	12	0	14	224	529	7463
$-7 > M_{12\mu m} > -9$	3	117	116	136	34	1	24	725	1094	4703
$-5 > M_{12\mu m} > -7$	0	68	27	254	68	2	79	491	633	2295
$-1 > M_{12\mu m} > -5$ ($h_z = 250$ pc)	0	22	7	248	207	17	236	164	221	843
$-1 > M_{12\mu m} > -5$ ($h_z = 120$ pc)	0	59	13	369	182	10	222	465	663	2164
$+3 > M_{12\mu m} > -1$	0	13	4	243	295	28	373	108	133	570
$+15 > M_{12\mu m} > +3$	0	1	0	5	17	2	22	3	5	14
Total	73	334	1076	1328	820	60	972	2228	3386	31268
Uncertainty	±6	±13	±21	±22	±16	±7	±20	±31	±40	±177
Exponential Disk	26	329	325	1228	791	58	945	2181	3158	20462
Spheroid	0	0	50	100	29	2	27	4	10	645
Bulge	0	0	626	0	0	0	0	0	0	1986
Spiral Arms	17	5	13	0	0	0	0	44	213	4812
Molecular Ring	30	0	62	0	0	0	0	0	0	5363

Note: The values given in the upper part of the table are the means of a series of 200 sets of values. The numbers for the galactic components in the lower part of the table are for the set of values which most closely matched the mean values given in the upper part of the table.

Table 3 - Breakdown Of The Model Results (Continued)

	$F_\nu(12\ \mu m) \geq 90$ Jy	$F_\nu(12\ \mu m) \geq 2.5$ Jy			$F_\nu(12\ \mu m) \geq 5$ Jy		
		All Sources	$\|b^{II}\| < 20°$	$\|b^{II}\| < 1°$	All Sources	$\|b^{II}\| < 20°$	$\|b^{II}\| < 1°$
$-13 > M_{12\mu m} > -17$	278	2518	2504	1710	2040	2028	1305
$-11 > M_{12\mu m} > -13$	165	10698	10573	3932	5026	4929	1584
$-9 > M_{12\mu m} > -11$	112	7463	7092	1650	3371	3067	546
$-7 > M_{12\mu m} > -9$	62	4703	3583	344	2177	1470	120
$-5 > M_{12\mu m} > -7$	19	2295	1249	78	963	463	28
$-1 > M_{12\mu m} > -5$	7	843	368	24	347	153	9
($h_z = 250$ pc)							
$-1 > M_{12\mu m} > -5$	17	2164	1164	67	910	483	27
($h_z = 120$ pc)							
$+3 > M_{12\mu m} > -1$	2	570	221	6	194	79	0
$+15 > M_{12\mu m} > +3$	0	14	5	1	5	1	0
Total	662	31268	26699	7812	15033	12628	3619
Data Values	671	30774	26466	7097	15168	12897	3459
Exponential Disk	393	20462	16081	3132	9722	7421	1351
Spheroid	10	645	470	80	308	216	30
Bulge	0	1986	1986	542	448	448	97
Spiral Arms	181	4812	4799	2118	2826	2814	1155
Molecular Ring	78	3363	3363	1940	1729	1729	986

Table 4—Magnitude Breakdown Of The Bright Sources

[12] Range	Model Number N_m	Observed Number N_o	$(N_m - N_o)/\sqrt{N_o}$	χ^2
+3.023 to +2.0	19355	19083	1.969	3.877
+2.0 to +1.0	7052	7330	−3.247	10.543
+1.0 to +0.0	2609	2749	−2.670	7.130
+0.0 to −1.0	1063	1044	0.588	0.346
−1.0 to −2.0	379	380	−0.051	0.003
−2.0 to −3.0	127	132	−0.435	0.189
−3.0 to −4.0	42	39	0.480	0.231
−4.0 to −5.0	12	9	1.000	1.000
−5.0 to −6.0	3	6	−1.225	1.500
−6.0 to −8.0	0	2	−1.414	2.000
total				26.819

FIG. 1A.—A color selected sample of 13428 IRAS sources similar to that used by Habing (1986, 1988) to analyze the structure of the disk and the bulge of our galaxy. This colour range predominantly selects evolved asymptotic giant branch stars. The plot is an equal-area projection in galactic coordinates. The sample clearly shows stars in the galactic bulge. Sources in this color range at high galactic latitudes are usually galaxies, although some are spheroid stars. The Large Magellanic Cloud ($l^{II} \approx -70°$, $b^{II} \approx -33°$) and the Orion complex ($l^{II} \approx -150°$, $b^{II} \approx -20°$) are also prominent in the plot. The small latitude extent of the disk component indicates that these sources are generally distant and therefore luminous at 12 μm and 25μm.

FIG. 1B—As in Fig. 1a for the color selected sample that we used to study the bulge, a sub-set of the sources in Fig. 1a.

FIG. 2a.—Results of the fit to the galactic bulge sources using the Bahcall density function (eq. [1]). The histogram gives the scaled model longitude values. The filled circles are the data values for 1° strips excluding the inner 3 values where confusion and shadowing effects make the data unreliable. The model predicts a total of 1067 bulge sources in the sample color range.

FIG. 2b.—As in Fig. 2a but for the scaled model latitude histogram. The model predicts 1221 bulge sources of these colors. The fit is good at higher latitudes but fails nearer the galactic plane. There may be a north/south asymmetry in the sample latitude distribution, perhaps reflecting the solar position north of the galactic plane.

FIG. 3a.—Model latitude distribution for a de Vaucouleurs $r^{\frac{1}{4}}$ law with $r_e = 750$ pc or 5° on the sky and a round bulge. The histogram shows the predicted values for the best available fit. The $r^{\frac{1}{4}}$ function peaks too sharply at the center and has too extended a sky distribution. If an ellipticity of 2.0 is assumed the latitude fit becomes worse because the model is even more sharply peaked.

FIG. 3b.—The model longitude distribution for a de Vaucouleurs $r^{\frac{1}{4}}$ law with $r_e = 750$ pc or 5° on the sky. The histogram shows the predicted values for the best available fit. As with the latitude distribution, the model peaks too sharply at the center and has too extended a sky distribution to match the observations. This model is for a round bulge.

FIG. 4.—Comparison of the model flux density histogram for the areas $2° \leq b^{II} \leq 3°$ and $-3° \leq b^{II} \leq -2°$ with $-0.5° \leq l^{II} \leq 0.5°$ with the observed values (filled circles) for the best fit bulge model.

FIG. 5.—Comparison of a model which has a bulge with the best fit parameters given in §IIe, a standard de Vaucouleurs spheroid of 2.7 kpc effective radius and ellipticity 2.0, and a galactic disk component of 3.5 kpc radial scale length and 250 pc scale height with the data set shown in Fig. 1a. The model has source number ratios 1 to 3.33 to 20 for the spheroid, the bulge and the disk components. The model points (×) are normalized to match the data values (•) at the innermost point.

FIG. 6.—The 12 μm luminosity function as derived from various methods. The filled circles show the luminosity function derived from the Gliese catalogue sample in Fig. 12. The open circles show the space density values derived from the OH/IR stars with kinematic or phase-lag distances. These points are poorly determined because of the non-uniformity of the various OH maser observations but should represent lower limits for the luminosity function because the OH/IR stars represent only part of all the luminous 12 μm sources. Also shown is the transformed $V \rightarrow [12]$ luminosity function (dotted curve) fit to the function given in eq. (11a) with parameters $M^* = +3.0$, $\alpha = 0.52$, $\beta = 0.025$, $\delta = 2/3$ and $n^* = 0.0127$ stars mag^{-1} pc^{-3} assumed to apply over all $M_{12\mu m}$. This curve falls well below both the Gliese catalogue points at higher luminosity and the most luminous OH/IR star values. The solid curve has the same parameters as the dotted curve except that $\alpha = 0.36$ which fits both the Gliese catalogue values and the IRAS observations

near the galactic plane. Aside from small adjustments to the high luminosity part of the function this curve was used in the Monte Carlo models.

FIG. 7.—Illustration of the spiral arm and molecular ring components of the model projected onto the galactic plane. The open circle marks the position of the sun, 8.5 kpc from the galactic center. The plot has equal numbers of sources in the arms and the molecular ring. The description of the spiral arms is given in eq. (14). The arms are assumed to be 500 pc wide at any θ.

FIG. 8.—The histogram shows the longitude distribution of all IRAS sources with $F_\nu(12\mu\text{m}) \geq 5.0$ Jy within 1° of the plane. The filled circles are the model points for a pure exponential disk of 3.5 kpc scale length. This figure should be compared with Fig. 11a where the spiral arms and the molecular ring have been added to the model.

FIG. 9a.—Comparison of the model star count cumulative distribution to the observed values for area 1 (see Table 1 for the limits of the comparison areas). The data values are the filled circles. The model points are not plotted explicitly but are connected by lines.

FIG. 9b.—As in Fig. 9a, but for area 2.

FIG. 9c.—As in Fig. 9a, but for area 3.

FIG. 9d.—As in Fig. 9a, but for area 4.

FIG. 9e.—As in Fig. 9a, but for area 5.

FIG. 9f.—As in Fig. 9a, but for area 6.

FIG. 9g.—As in Fig. 9a, but for area 7.

FIG. 9h.—As in Fig. 9a, but for area 8.

FIG. 9i.—As in Fig. 9a, but for area 9.

FIG. 10a.—Comparison of the latitude distribution of sources brighter than 2.5 Jy at 12 μm seen by IRAS with the model prediction. The model is the histogram while the filled circles are the data points. No correction has been made for losses of observed sources due to the sky gaps.

FIG. 10b.—As in Fig. 10a, but for sources brighter than 5.0 Jy.

FIG. 11a.—This is the same as Fig. 8 but with the additional disk structure put into the model. All sources brighter than 5.0 Jy within 1° of the plane are shown for the model (filled circles) and the data (the histogram). The agreement is much better than in Fig. 8. The excess of model sources in the range $-30° < l^{II} < +5°$ may be due to confusion in the IRAS data or it may indicate that the model is too idealized in the treatment of either the molecular ring component or the interstellar extinction.

FIG. 11b.—As in Fig. 11a but for sources within 20° of the plane. In the range $+50° < l^{II} < +90°$ there is an excess of observed sources compared with the model which shows that the spiral arm is not properly represented near the sun in the first galactic quadrant.

FIG. 11c.—The galactic longitude distribution of all sources brighter than 2.5 Jy at 12 μm in the model (histogram) and the data (filled circles). The data values are matched well in the outer galaxy but there are some discrepancies in the inner galaxy, particularly at $b^{II} \approx \pm 60°$, which indicate that the real galaxy has a more complex spiral arm structure than the models assume. The model also shows a strong peak at the center which the data does not show, presumably due to confusion.

FIG. 11d.—As in Fig. 11c, but for sources brighter than 5 Jy.

FIG. 12.—The color-magnitude diagram based upon V and [12] for the Gliese catalogue sources observed by IRAS at 12 μm. The two isolated sources with $M_V \approx +8.0$ are

probably cases where a background object has been associated with the Gliese catalogue star. One point which is not shown falls far to the right of the others and is certainly a bad association. The vertical lines mark the approximate mean colors for sources of the spectral type given just to the right of the line, save for the line furthest to the left for the A0 stars.

Authors' addresses

Deborah E. Schwartz, Kevin Volk, Richard J. Wainscoat, and Helen J. Walker: NASA Ames Research Center, Mail Stop N245-6, Moffett Field, California, 94035.

Martin Cohen: Radio Astronomy Laboratory, 601 Campbell Hall, University of California, Berkeley, California, 94720.

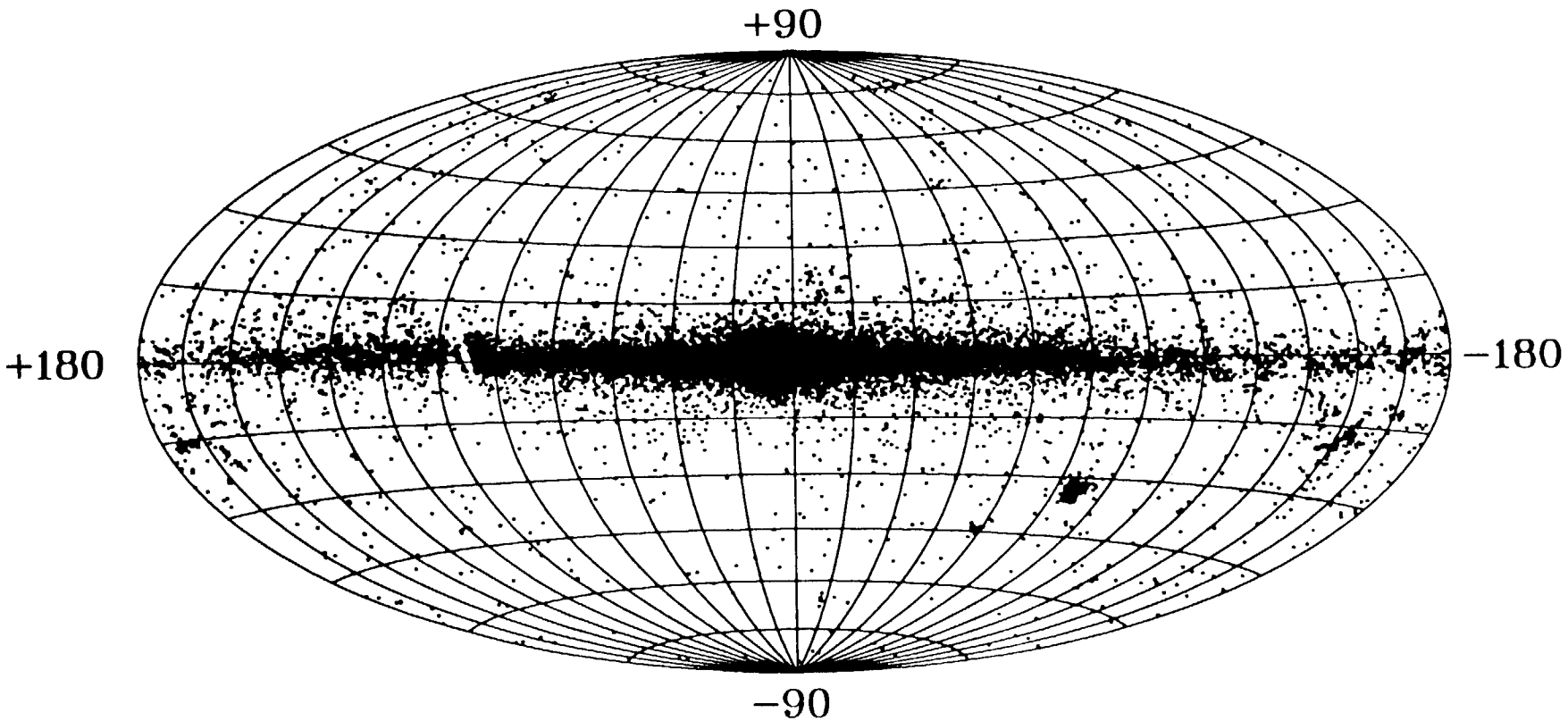

Fig. 1a

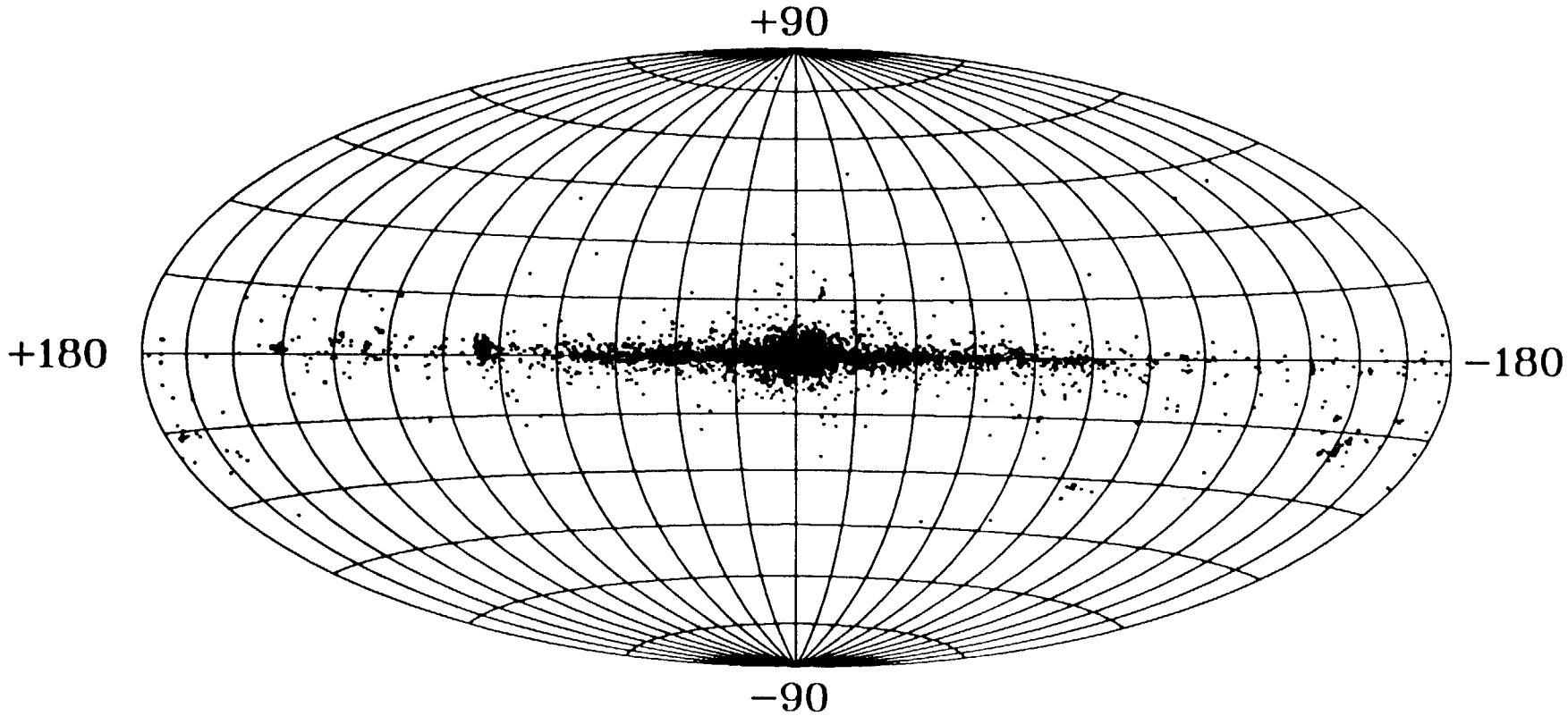

Fig. 1b

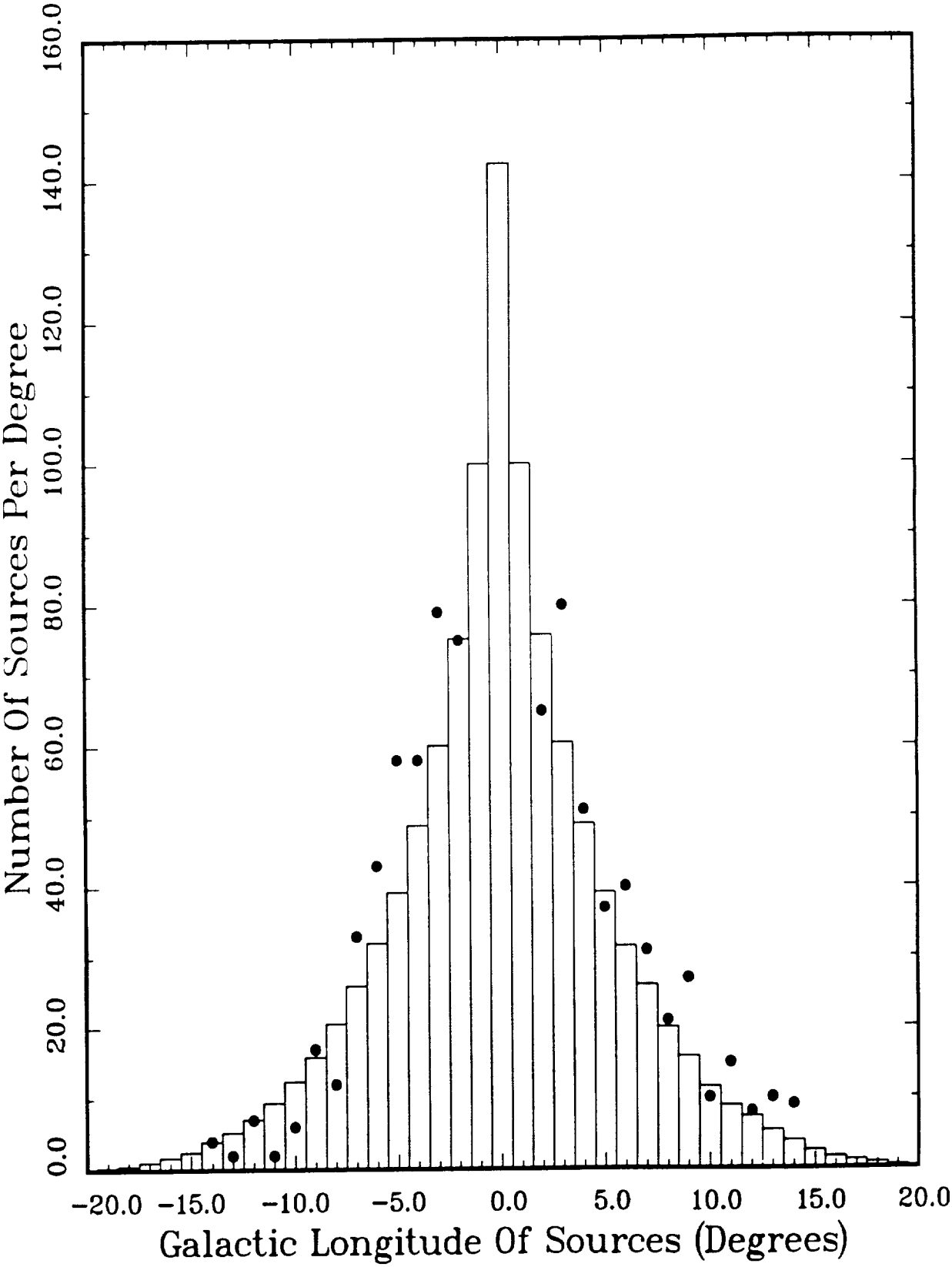
Number Of Sources Per Degree
0.0
20.0
40.0
60.0
80.0
100.0
120.0
140.0
160.0
-20.0
-15.0
-10.0
-5.0
0.0
5.0
10.0
15.0
20.0
Galactic Longitude Of Sources (Degrees)

Fig. 2a

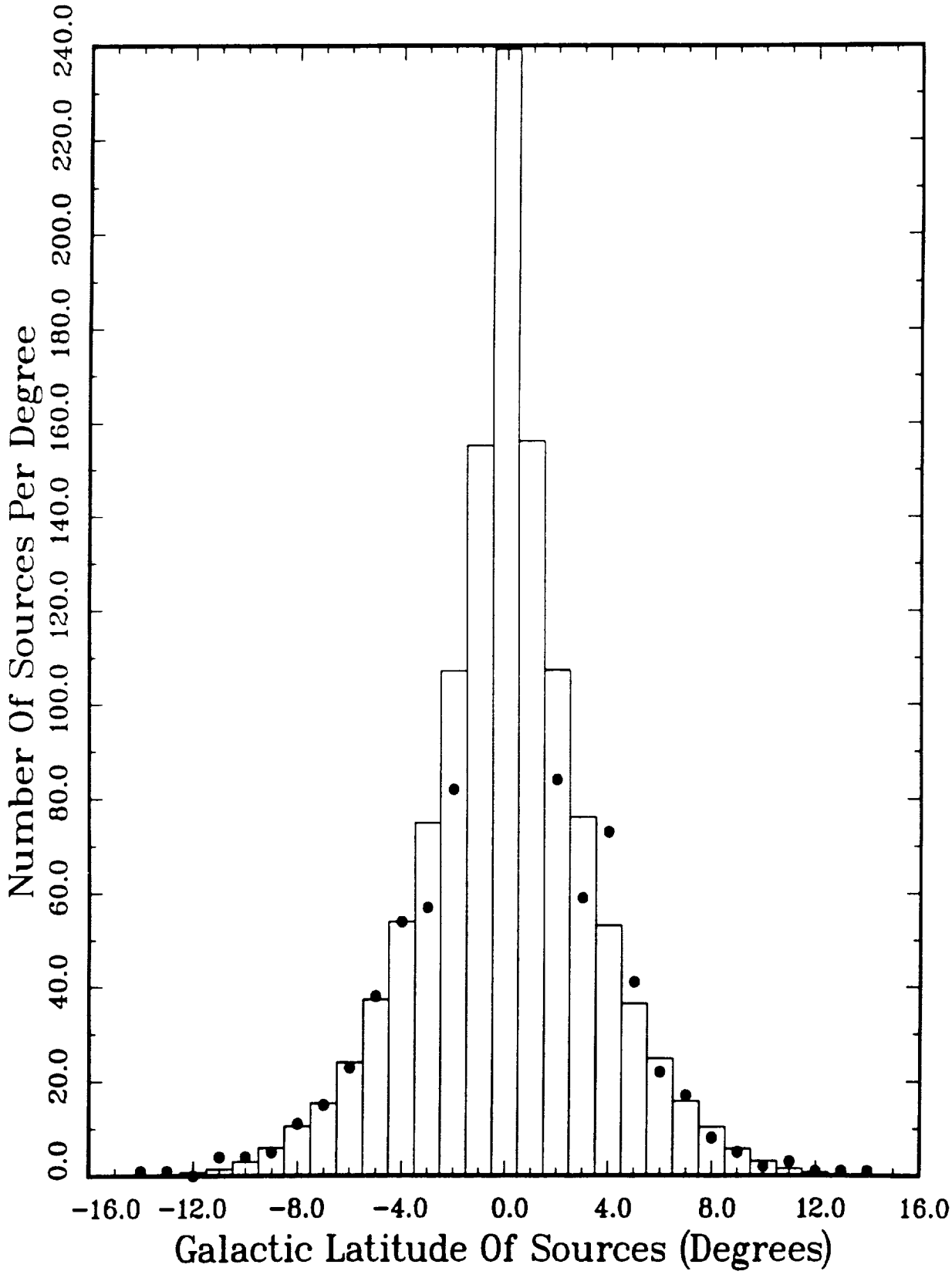
Number Of Sources Per Degree
0.0
20.0
40.0
60.0
80.0
100.0
120.0
140.0
160.0
180.0
200.0
220.0
240.0
-16.0
-12.0
-8.0
-4.0
0.0
4.0
8.0
12.0
16.0
Galactic Latitude Of Sources (Degrees)

Fig. 2b

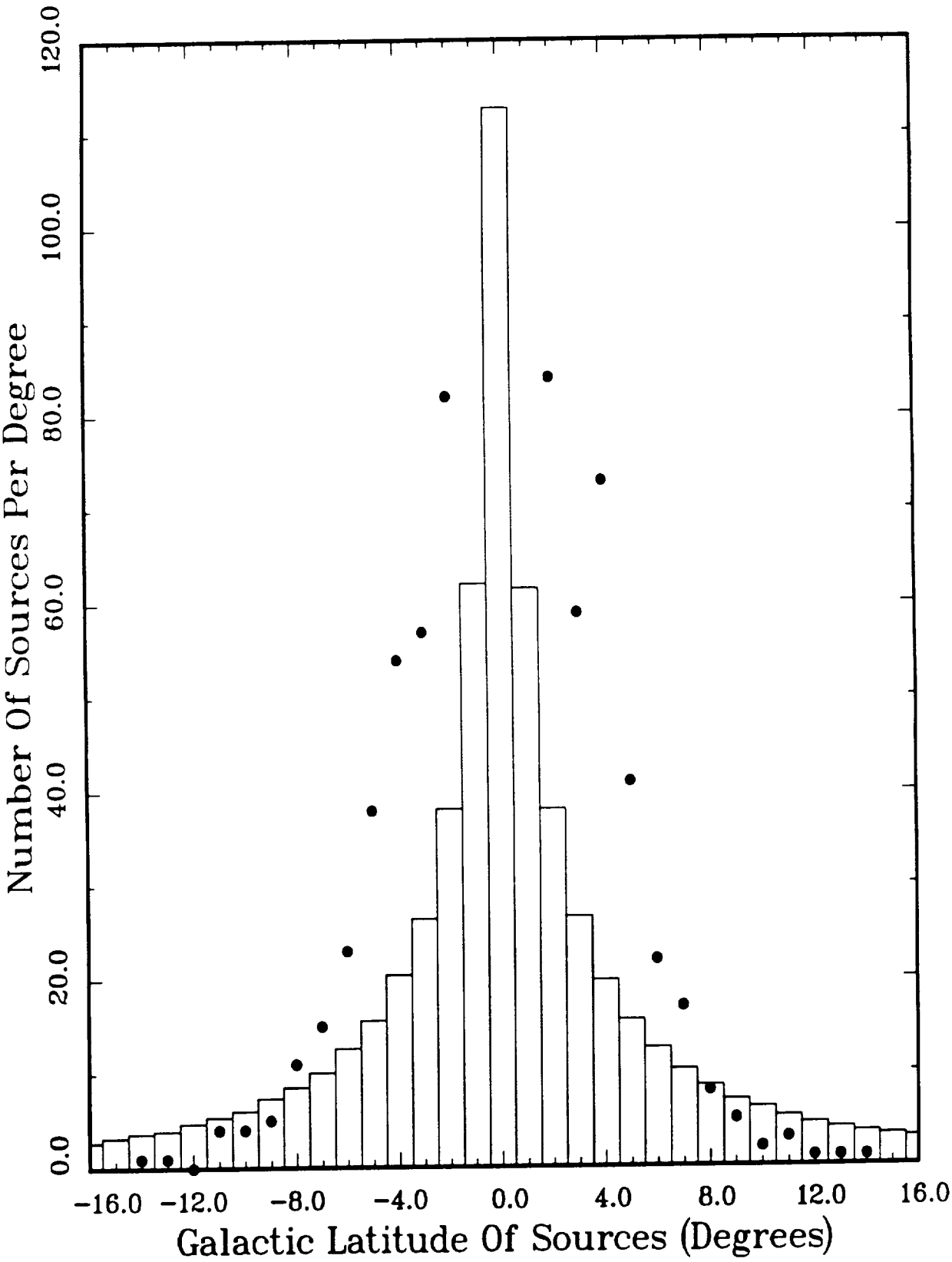
Number Of Sources Per Degree
0.0
20.0
40.0
60.0
80.0
100.0
120.0
-16.0
-12.0
-8.0
-4.0
0.0
4.0
8.0
12.0
16.0
Galactic Latitude Of Sources (Degrees)

Fig. 3a

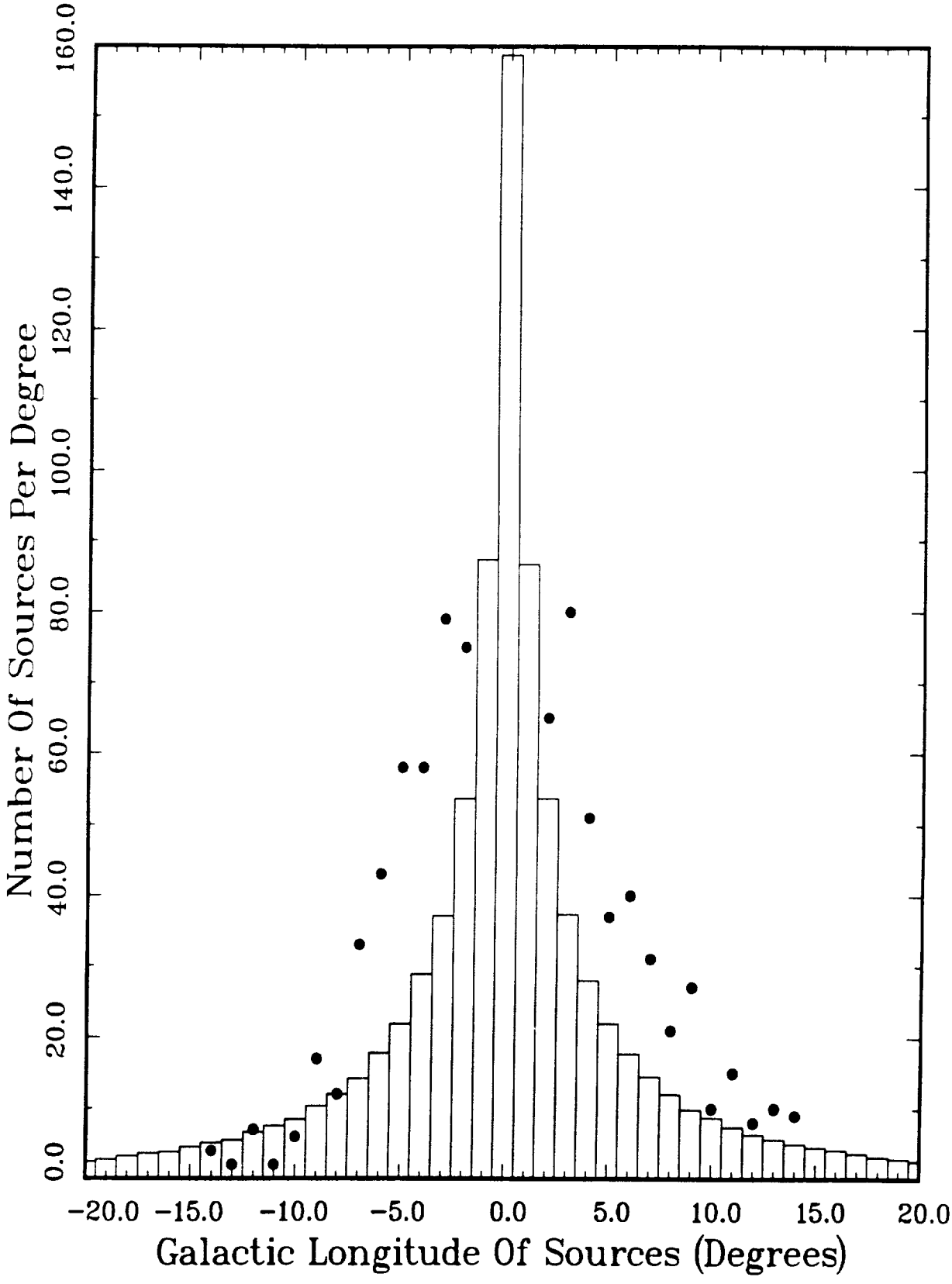
Number Of Sources Per Degree
0.0
20.0
40.0
60.0
80.0
100.0
120.0
140.0
160.0
-20.0
-15.0
-10.0
-5.0
0.0
5.0
10.0
15.0
20.0
Galactic Longitude Of Sources (Degrees)

Fig. 3b

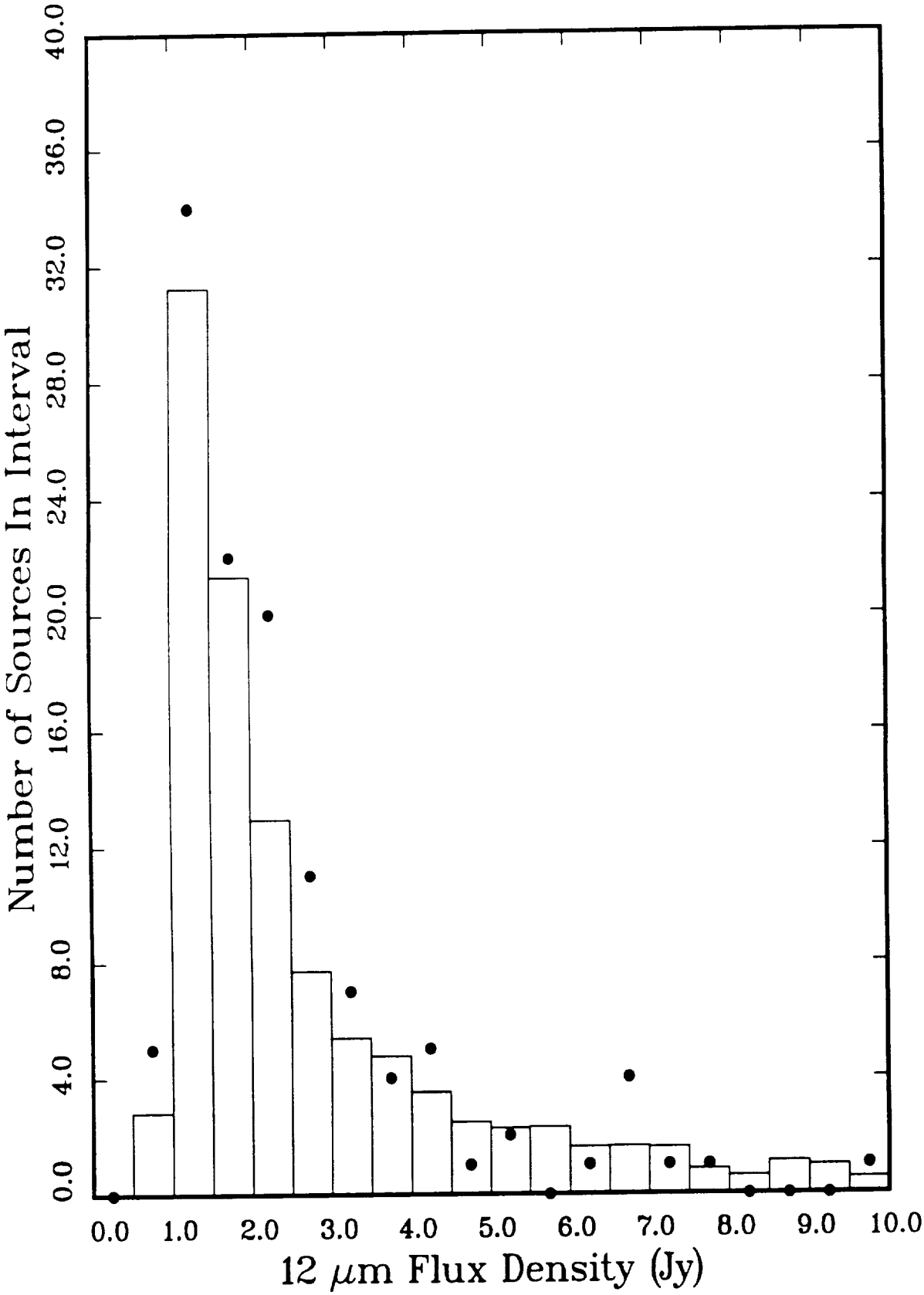
Number of Sources In Interval
0.0
4.0
8.0
12.0
16.0
20.0
24.0
28.0
32.0
36.0
40.0
0.0
1.0
2.0
3.0
4.0
5.0
6.0
7.0
8.0
9.0
10.0
12 μm Flux Density (Jy)

Fig. 4

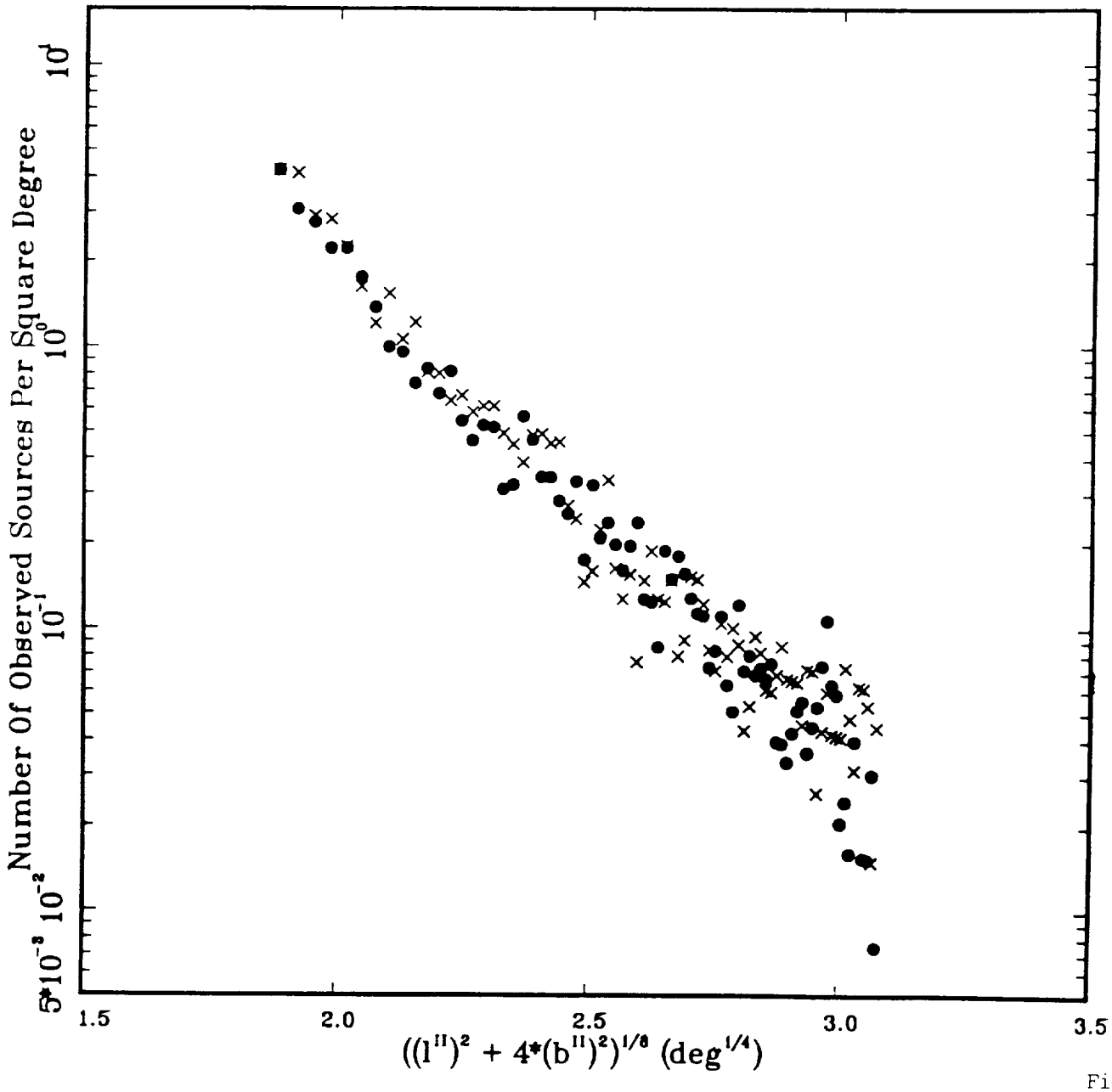
Number Of Observed Sources Per Square Degree
5*10⁻³
10⁻²
10⁻¹
10⁰
10¹
1.5
2.0
2.5
3.0
3.5
((l^II)² + 4*(b^II)²)^1/8 (deg^1/4)

Fig. 5

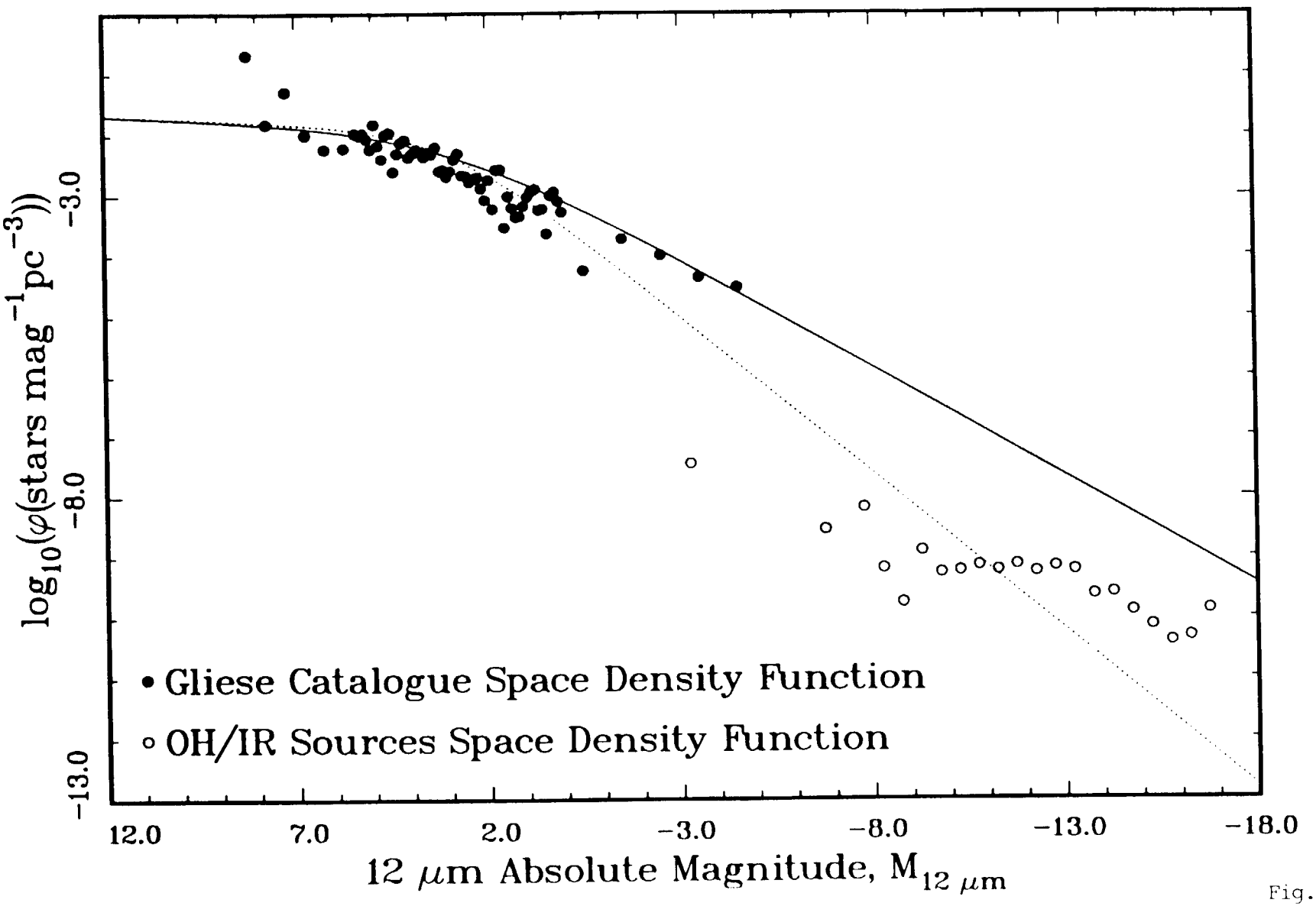
$\log_{10}(\varphi(\text{stars mag}^{-1}\text{pc}^{-3}))$
-3.0
-8.0
-13.0
• Gliese Catalogue Space Density Function
◦ OH/IR Sources Space Density Function
12.0
7.0
2.0
-3.0
-8.0
-13.0
-18.0
12 μm Absolute Magnitude, $M_{12\ \mu m}$

Fig. 6

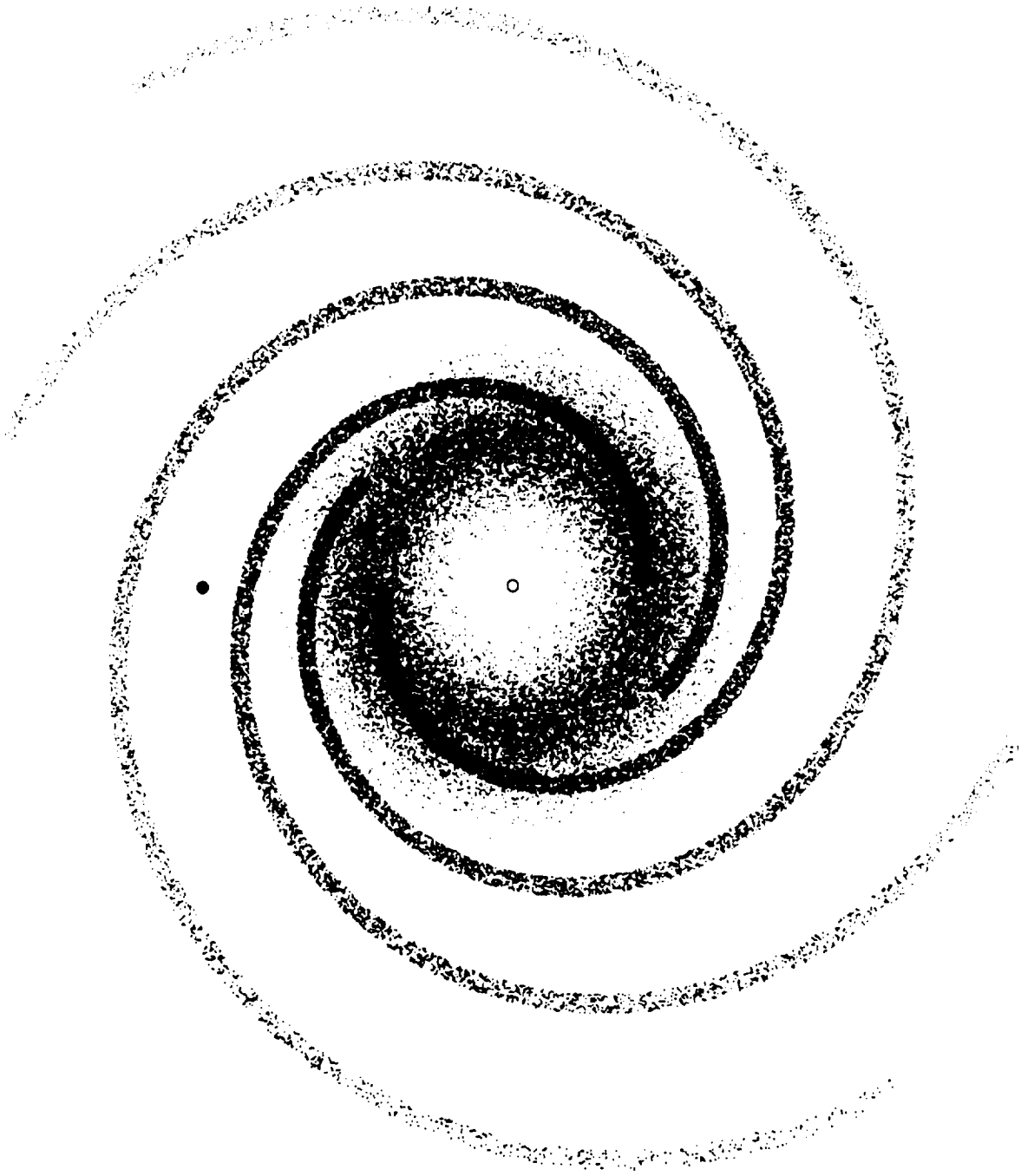

Fig. 7

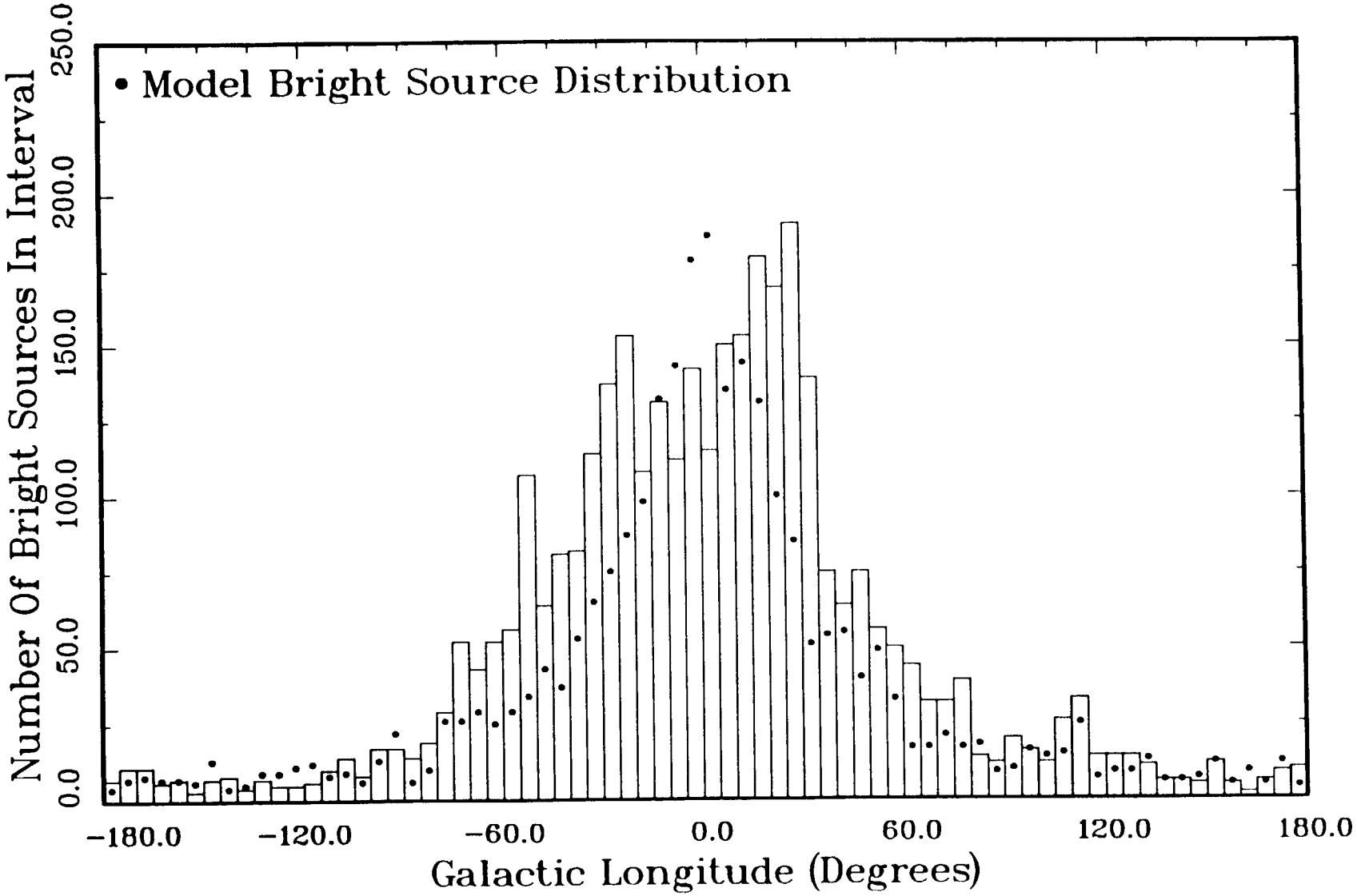
• Model Bright Source Distribution
Number Of Bright Sources In Interval
0.0
50.0
100.0
150.0
200.0
250.0
-180.0
-120.0
-60.0
0.0
60.0
120.0
180.0
Galactic Longitude (Degrees)

Fig. 8

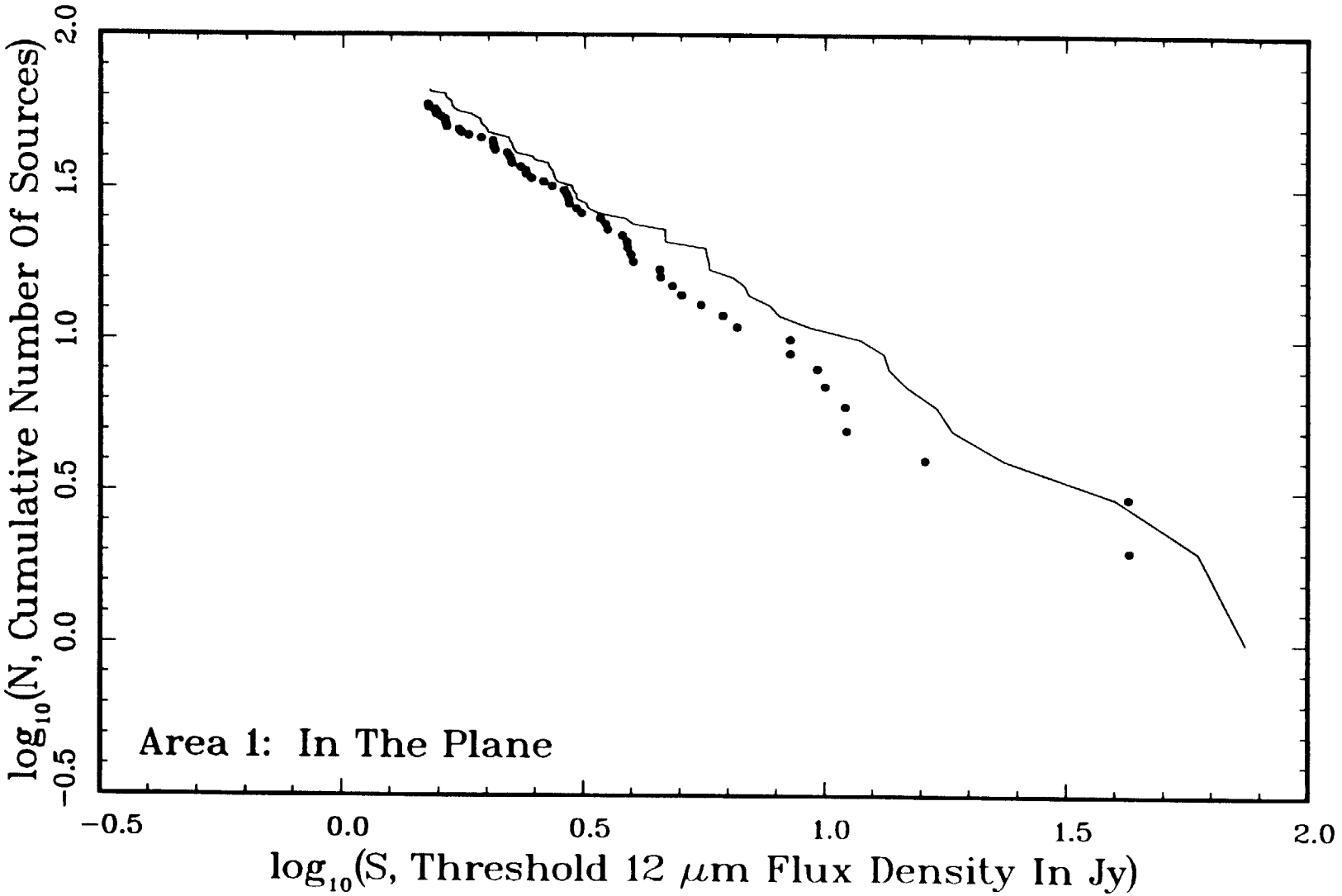
Area 1: In The Plane
log10(N, Cumulative Number Of Sources)
log10(S, Threshold 12 μm Flux Density In Jy)
−0.5
0.0
0.5
1.0
1.5
2.0

Fig. 9a

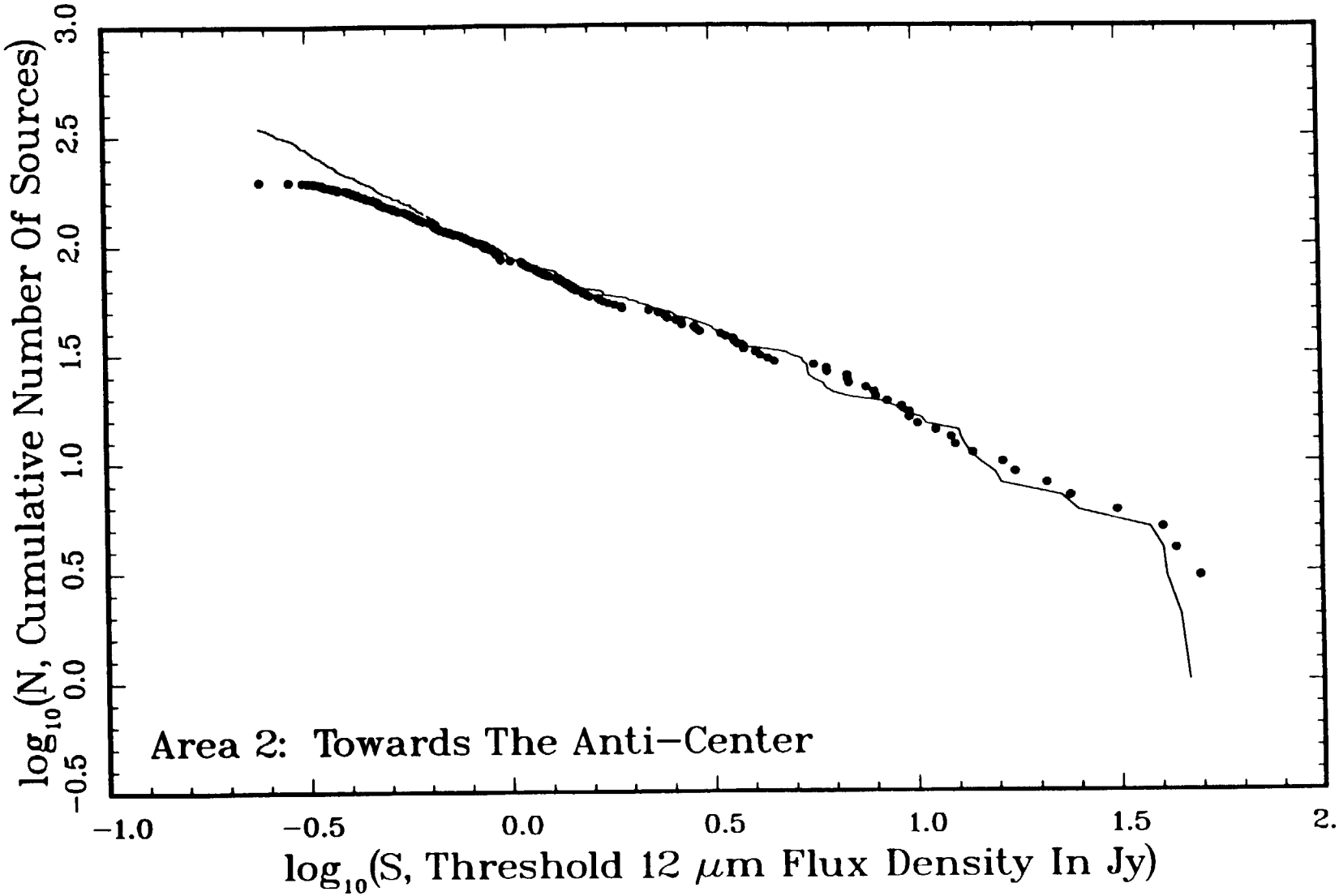
Area 2: Towards The Anti-Center
log10(N, Cumulative Number Of Sources)
log10(S, Threshold 12 μm Flux Density In Jy)
−0.5
0.0
0.5
1.0
1.5
2.0
2.5
3.0
−1.0
−0.5
0.0
0.5
1.0
1.5
2.0

Fig. 9b

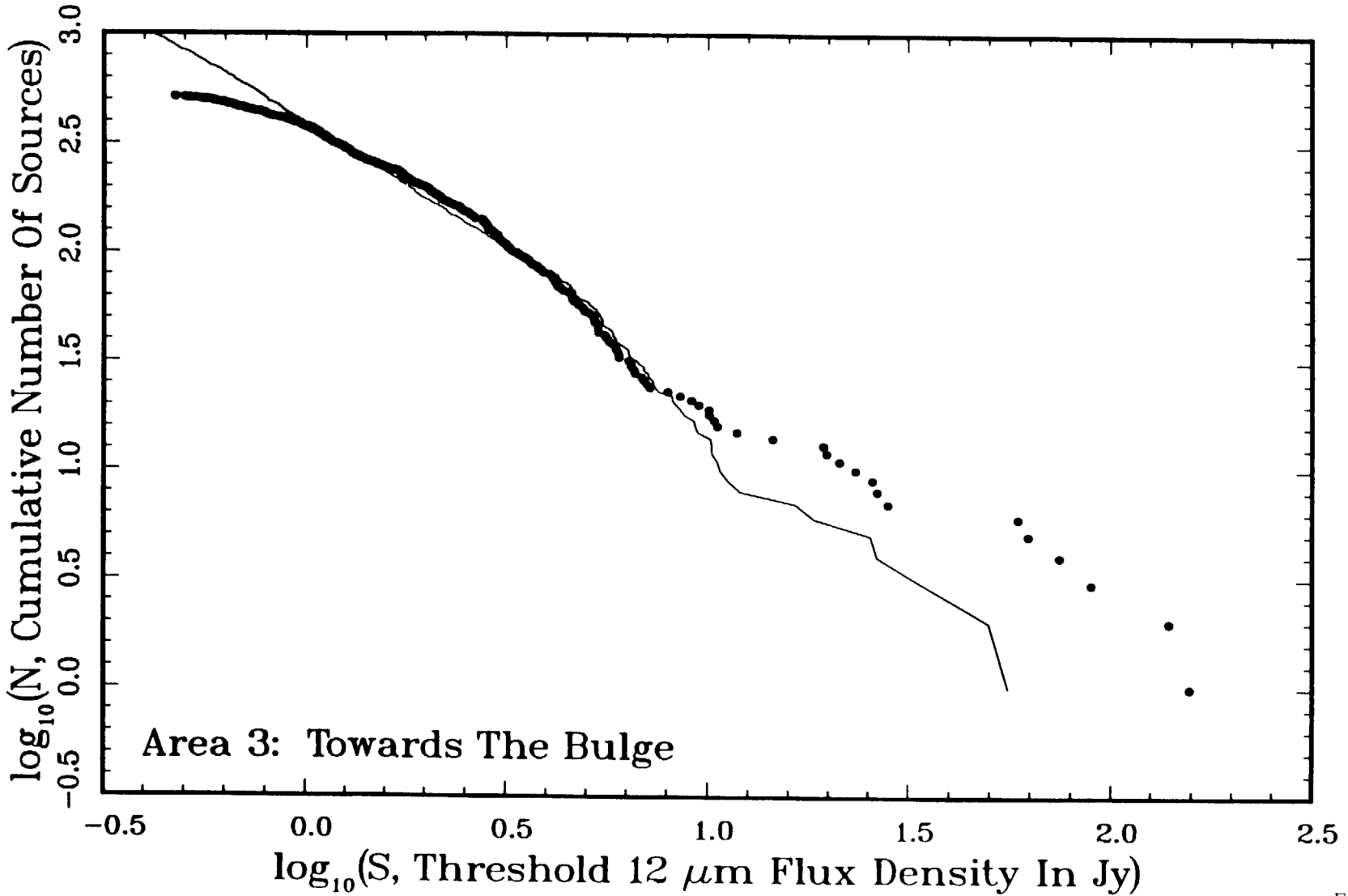
Area 3: Towards The Bulge
log10(N, Cumulative Number Of Sources)
log10(S, Threshold 12 μm Flux Density In Jy)
−0.5
0.0
0.5
1.0
1.5
2.0
2.5
3.0

Fig. 9c

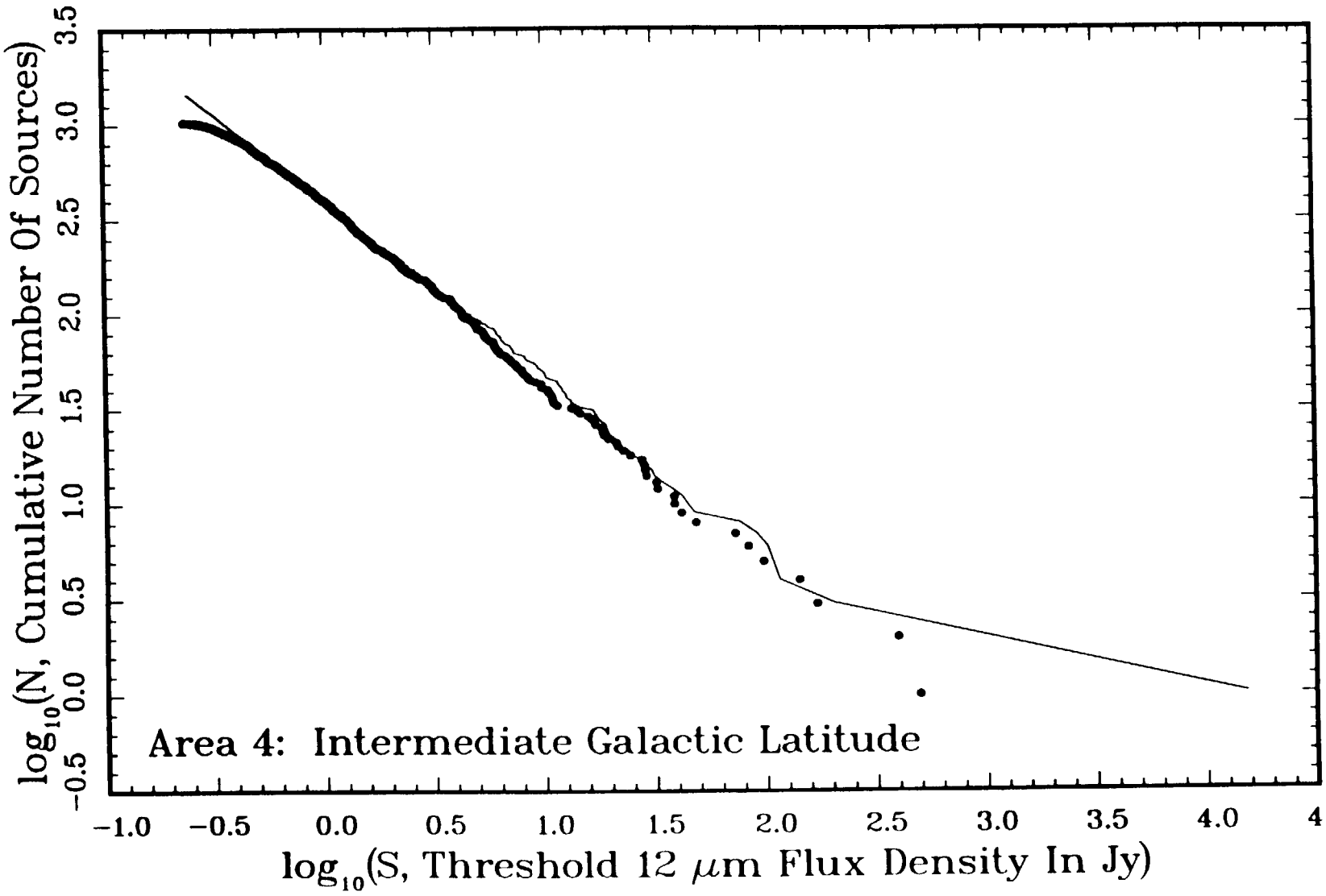
Area 4: Intermediate Galactic Latitude
log10(N, Cumulative Number Of Sources)
log10(S, Threshold 12 μm Flux Density In Jy)
−0.5
0.0
0.5
1.0
1.5
2.0
2.5
3.0
3.5
−1.0
−0.5
0.0
0.5
1.0
1.5
2.0
2.5
3.0
3.5
4.0
4.5

Fig. 9d

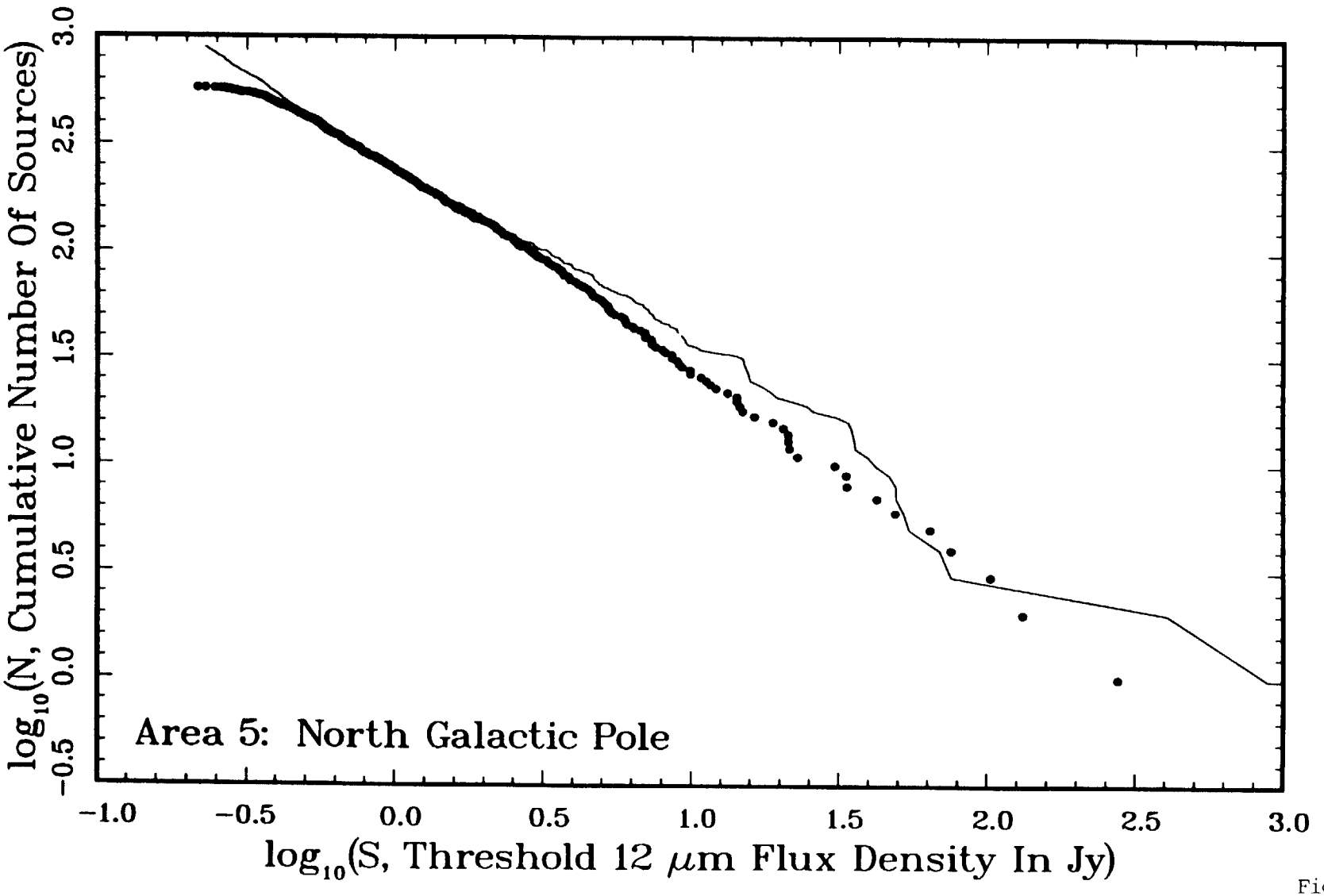
Area 5: North Galactic Pole
log10(N, Cumulative Number Of Sources)
log10(S, Threshold 12 μm Flux Density In Jy)
−0.5
0.0
0.5
1.0
1.5
2.0
2.5
3.0
−1.0
−0.5
0.0
0.5
1.0
1.5
2.0
2.5
3.0

Fig. 9e

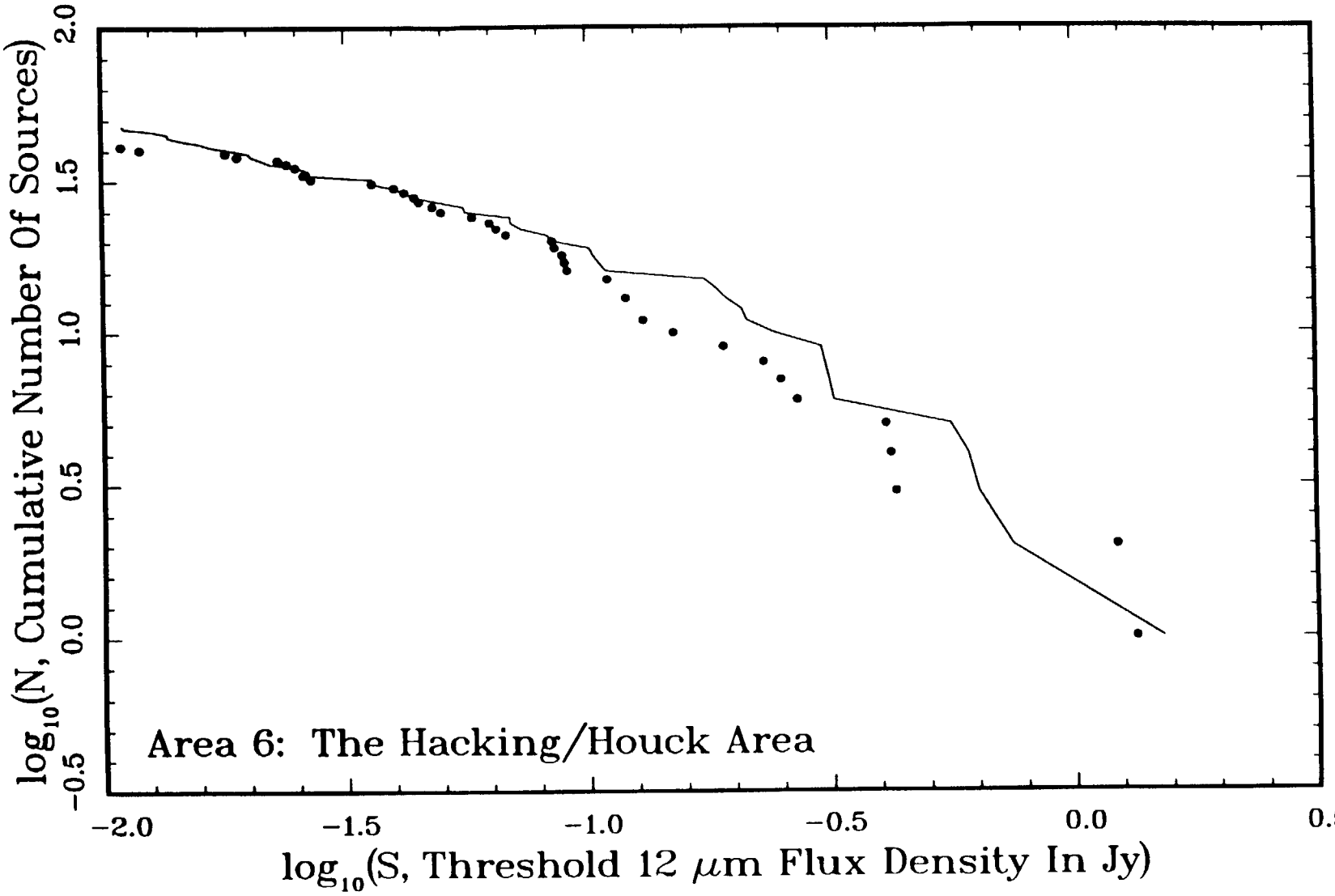
Area 6: The Hacking/Houck Area
log10(N, Cumulative Number Of Sources)
log10(S, Threshold 12 μm Flux Density In Jy)
2.0
1.5
1.0
0.5
0.0
−0.5
−2.0
−1.5
−1.0
−0.5
0.0
0.5

Fig. 9f

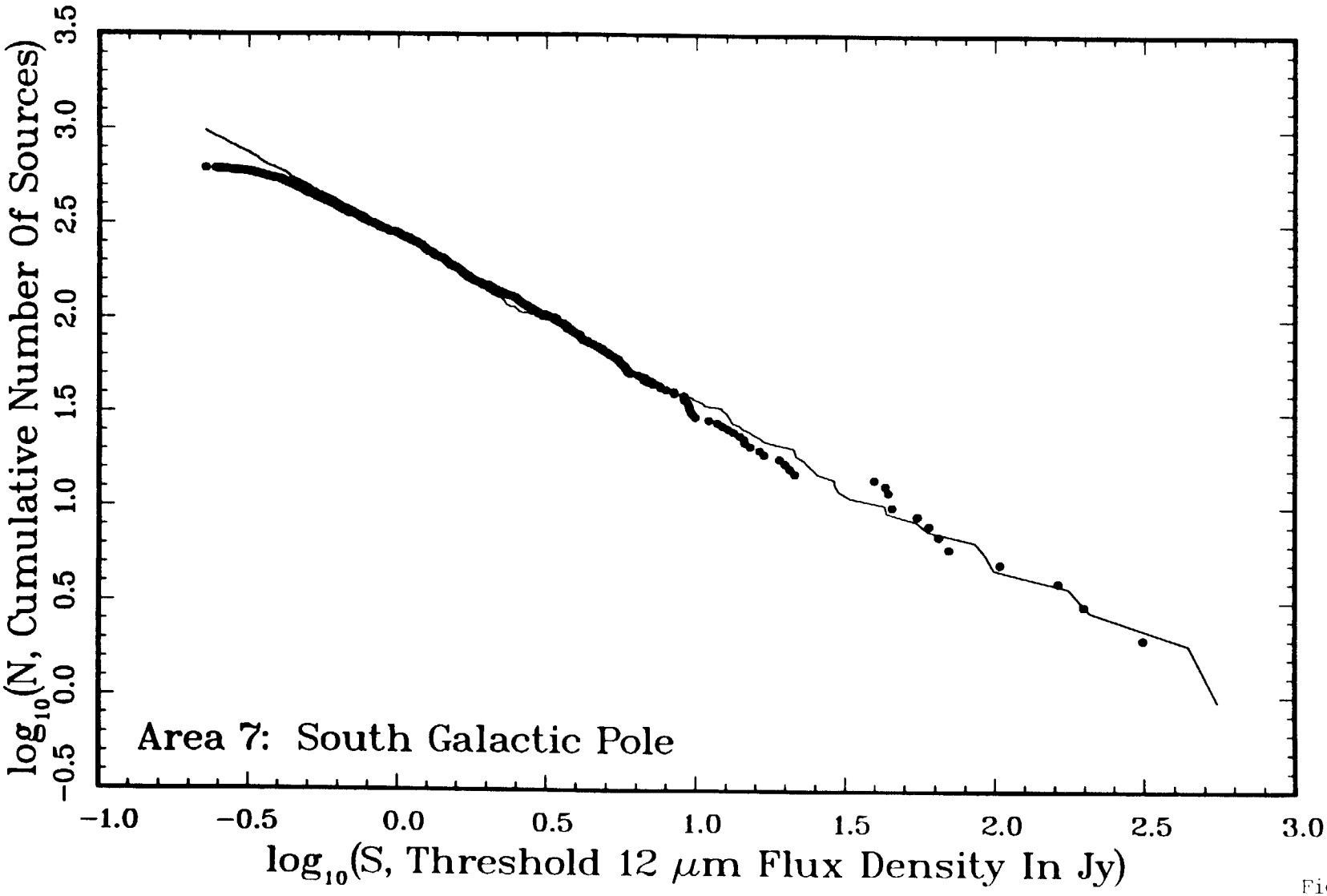
Area 7: South Galactic Pole
log10(N, Cumulative Number Of Sources)
log10(S, Threshold 12 μm Flux Density In Jy)
−0.5
0.0
0.5
1.0
1.5
2.0
2.5
3.0
3.5
−1.0
−0.5
0.0
0.5
1.0
1.5
2.0
2.5
3.0

Fig. 9q

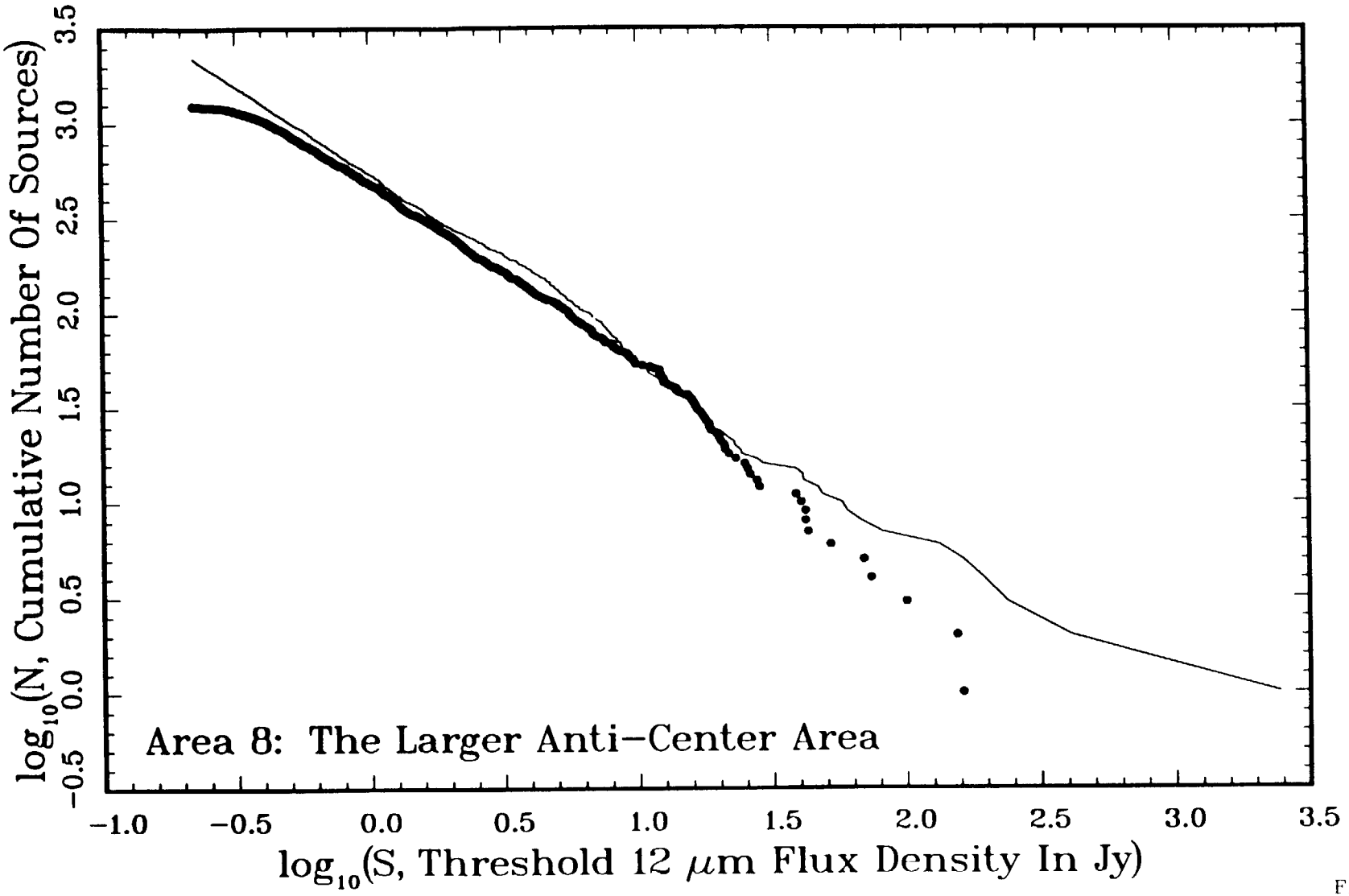
Area 8: The Larger Anti−Center Area
log10(N, Cumulative Number Of Sources)
log10(S, Threshold 12 μm Flux Density In Jy)
−0.5
0.0
0.5
1.0
1.5
2.0
2.5
3.0
3.5
−1.0
−0.5
0.0
0.5
1.0
1.5
2.0
2.5
3.0
3.5

Fig. 9h

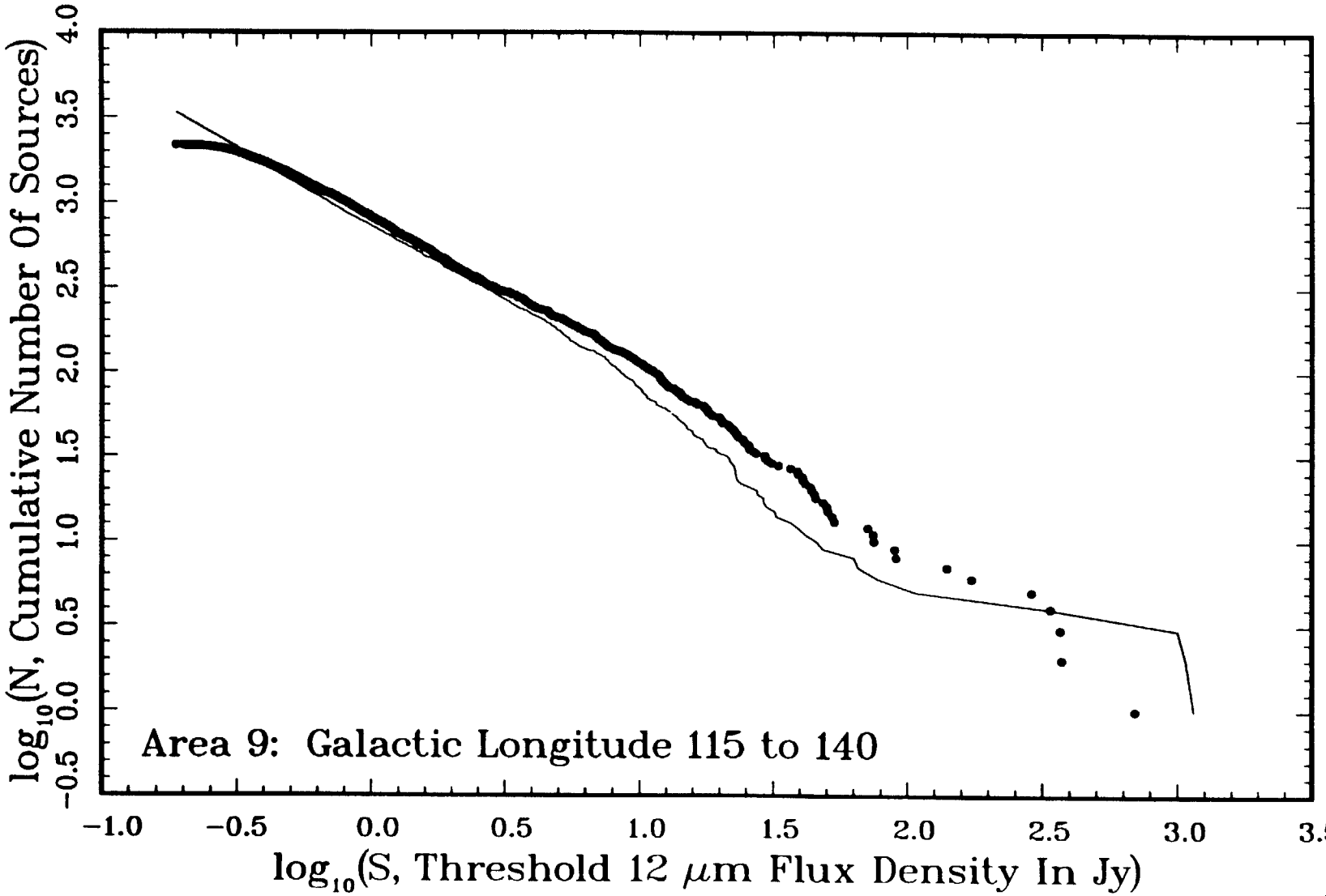
Area 9: Galactic Longitude 115 to 140
log10(N, Cumulative Number Of Sources)
log10(S, Threshold 12 μm Flux Density In Jy)
−0.5
0.0
0.5
1.0
1.5
2.0
2.5
3.0
3.5
4.0
−1.0
−0.5
0.0
0.5
1.0
1.5
2.0
2.5
3.0
3.5

Fig. 9i

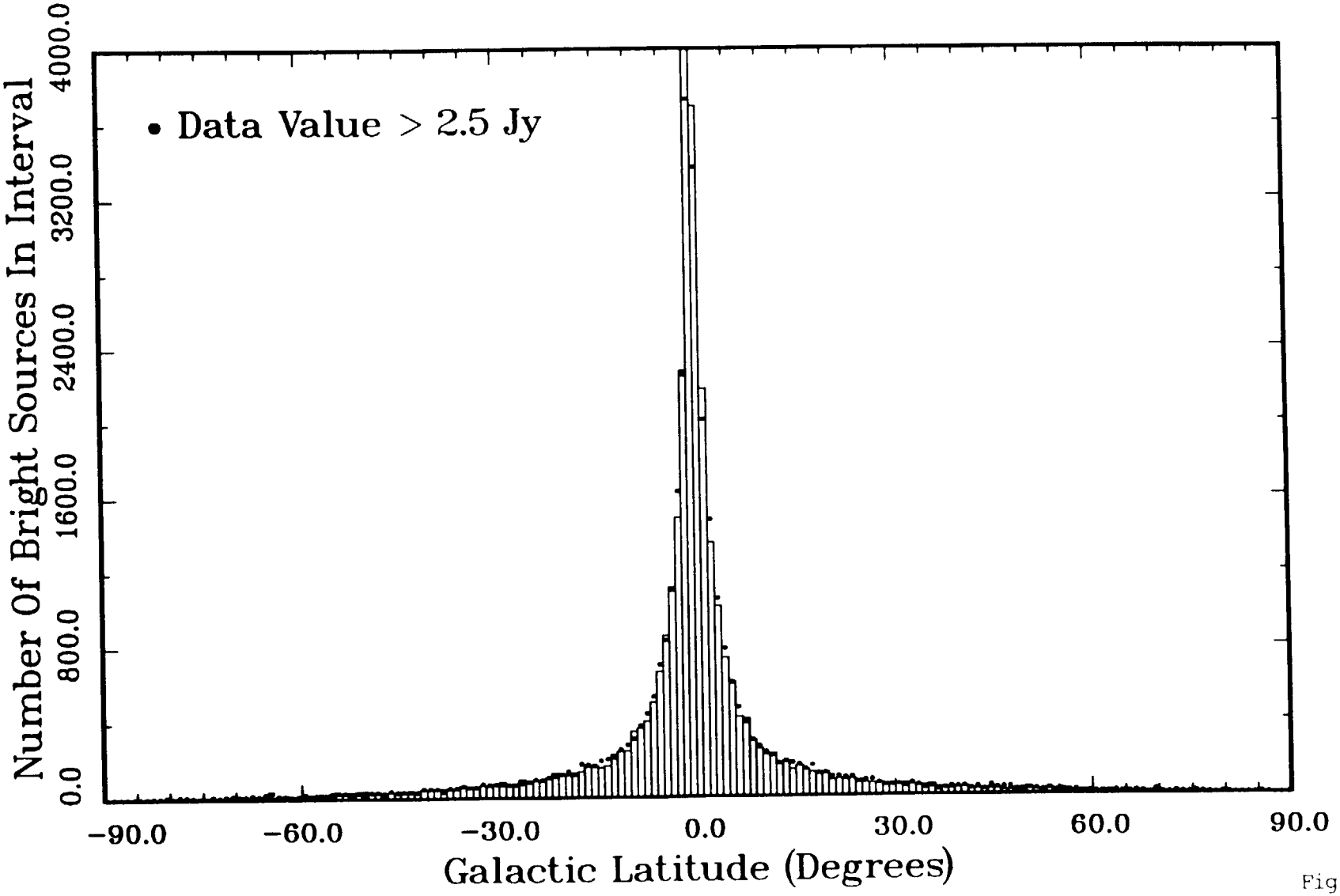
• Data Value > 2.5 Jy
Number Of Bright Sources In Interval
0.0
800.0
1600.0
2400.0
3200.0
4000.0
-90.0
-60.0
-30.0
0.0
30.0
60.0
90.0
Galactic Latitude (Degrees)

Fig. 10a

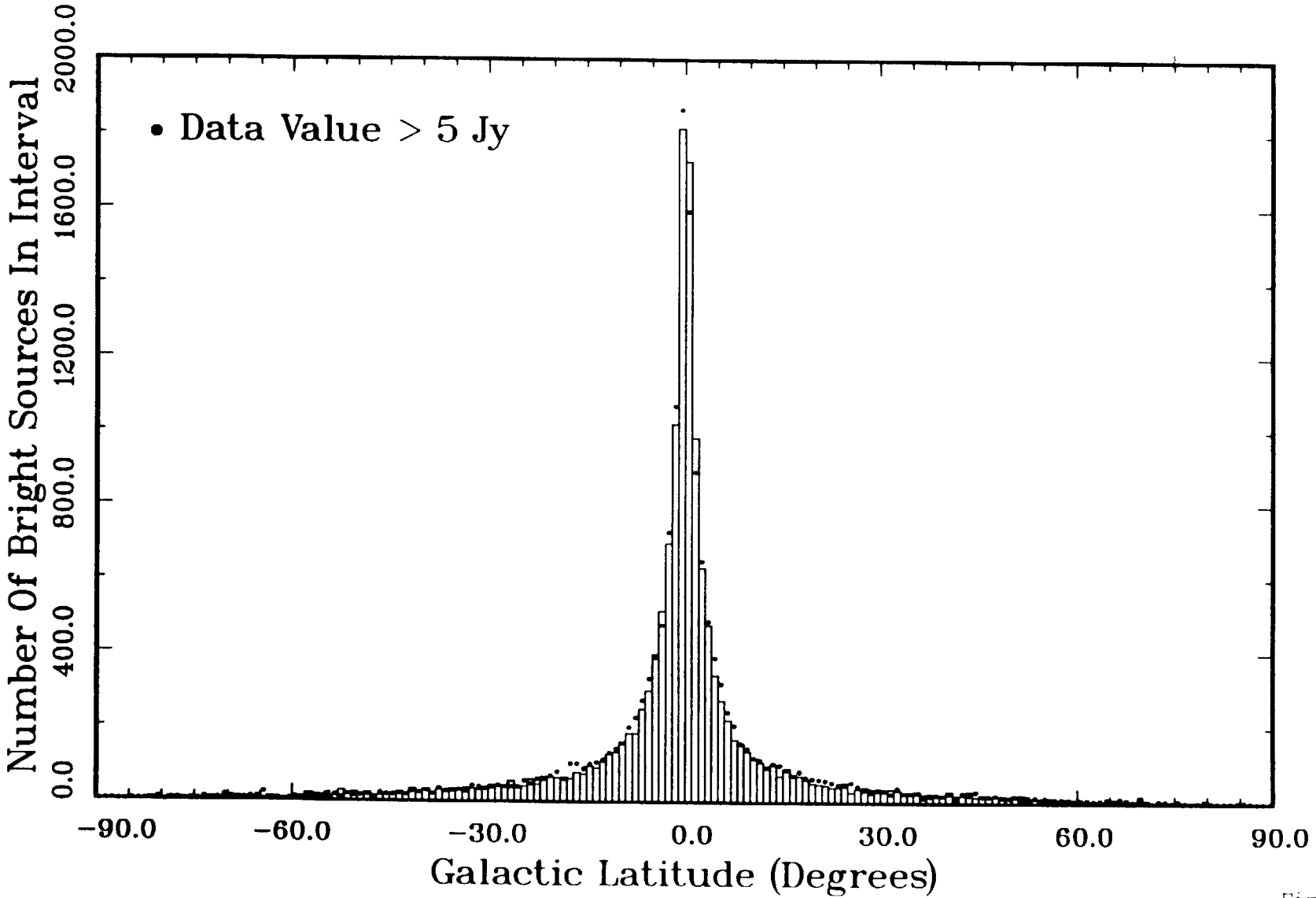
• Data Value > 5 Jy
Number Of Bright Sources In Interval
0.0
400.0
800.0
1200.0
1600.0
2000.0
−90.0
−60.0
−30.0
0.0
30.0
60.0
90.0
Galactic Latitude (Degrees)

Fig. 10b

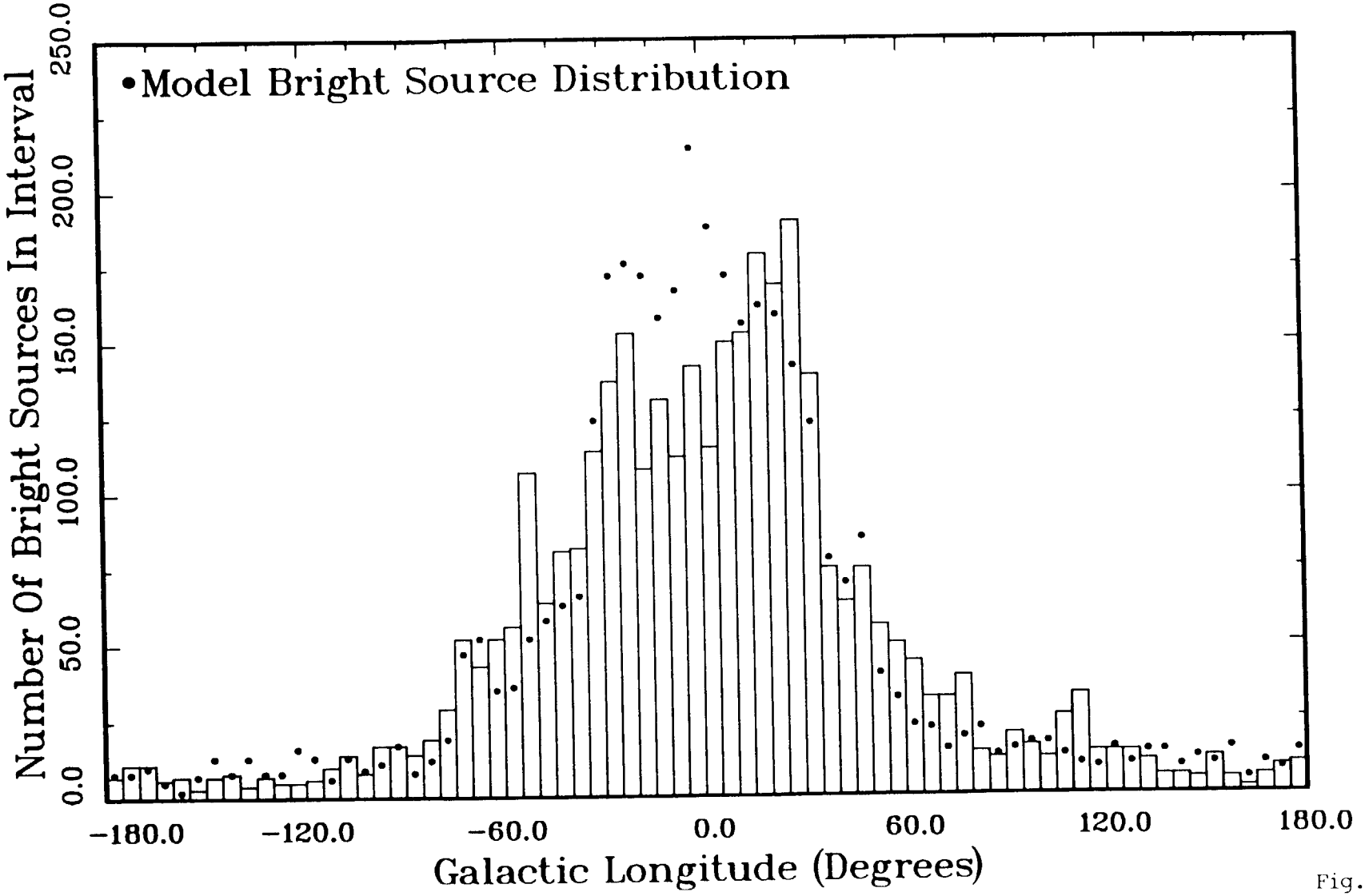
•Model Bright Source Distribution
Number Of Bright Sources In Interval
0.0
50.0
100.0
150.0
200.0
250.0
-180.0
-120.0
-60.0
0.0
60.0
120.0
180.0
Galactic Longitude (Degrees)

Fig. 11a

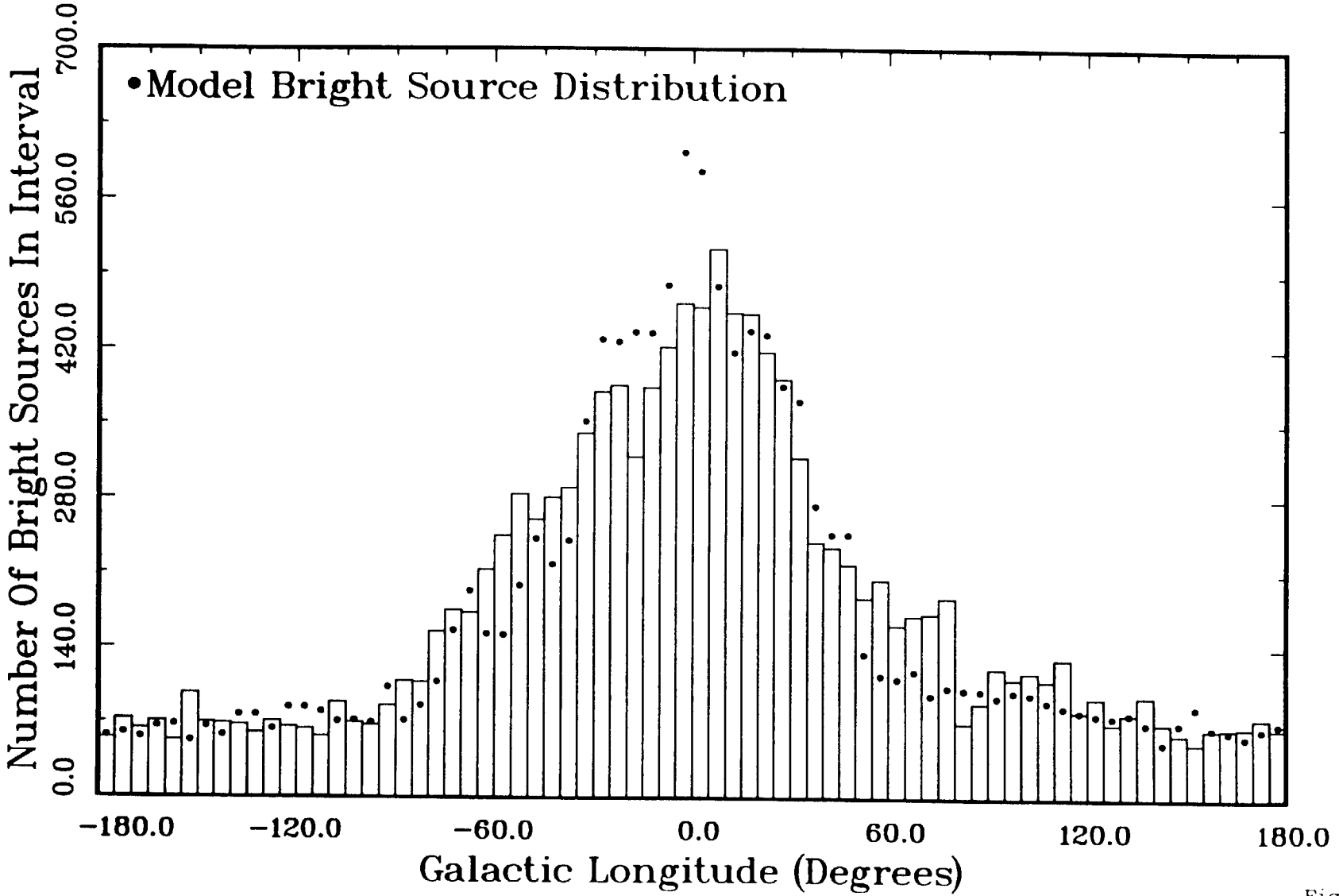
•Model Bright Source Distribution
Number Of Bright Sources In Interval
0.0
140.0
280.0
420.0
560.0
700.0
-180.0
-120.0
-60.0
0.0
60.0
120.0
180.0
Galactic Longitude (Degrees)

Fig. 11b

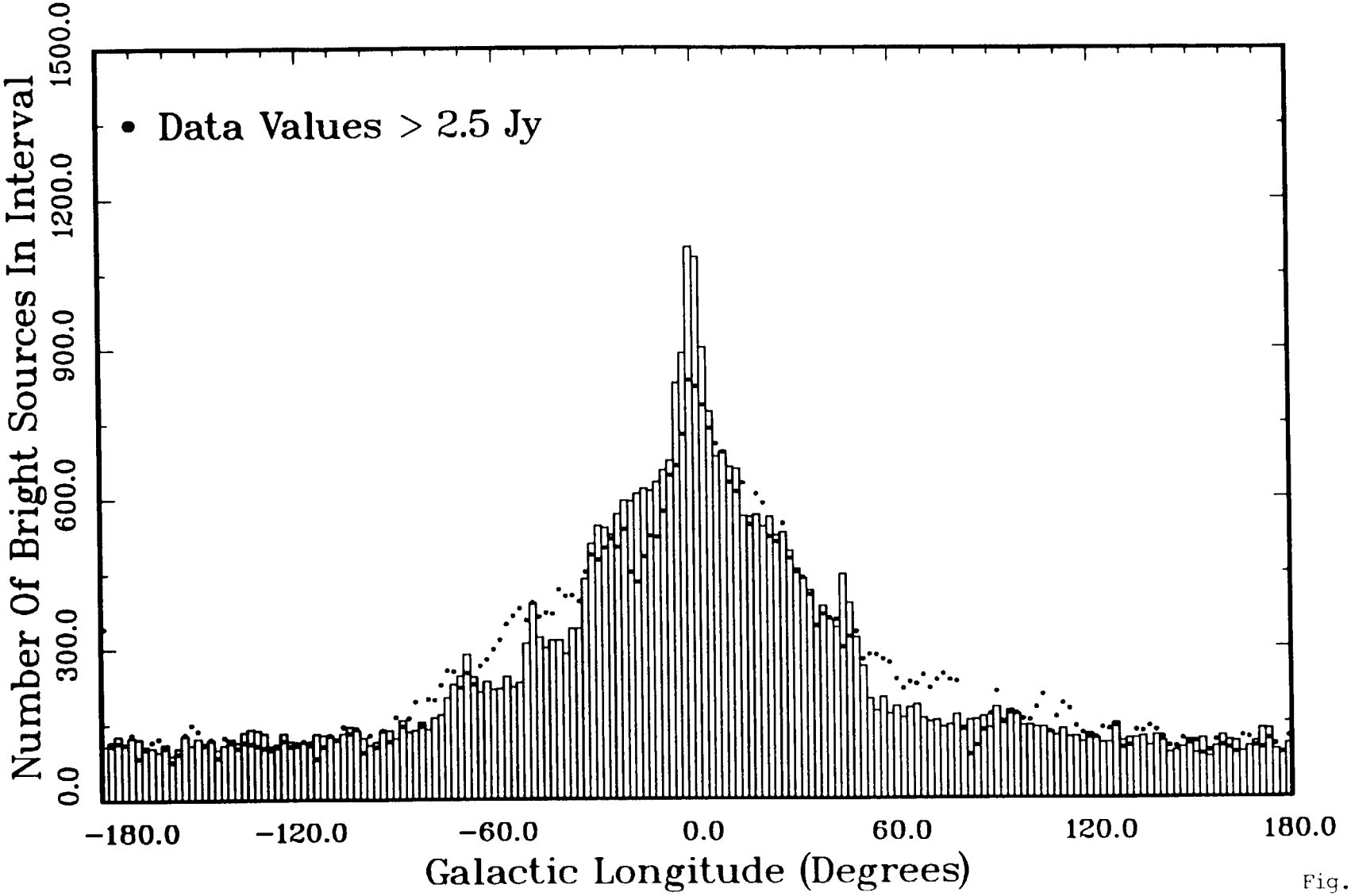
• Data Values > 2.5 Jy
Number Of Bright Sources In Interval
0.0
300.0
600.0
900.0
1200.0
1500.0
−180.0
−120.0
−60.0
0.0
60.0
120.0
180.0
Galactic Longitude (Degrees)

Fig. 11c

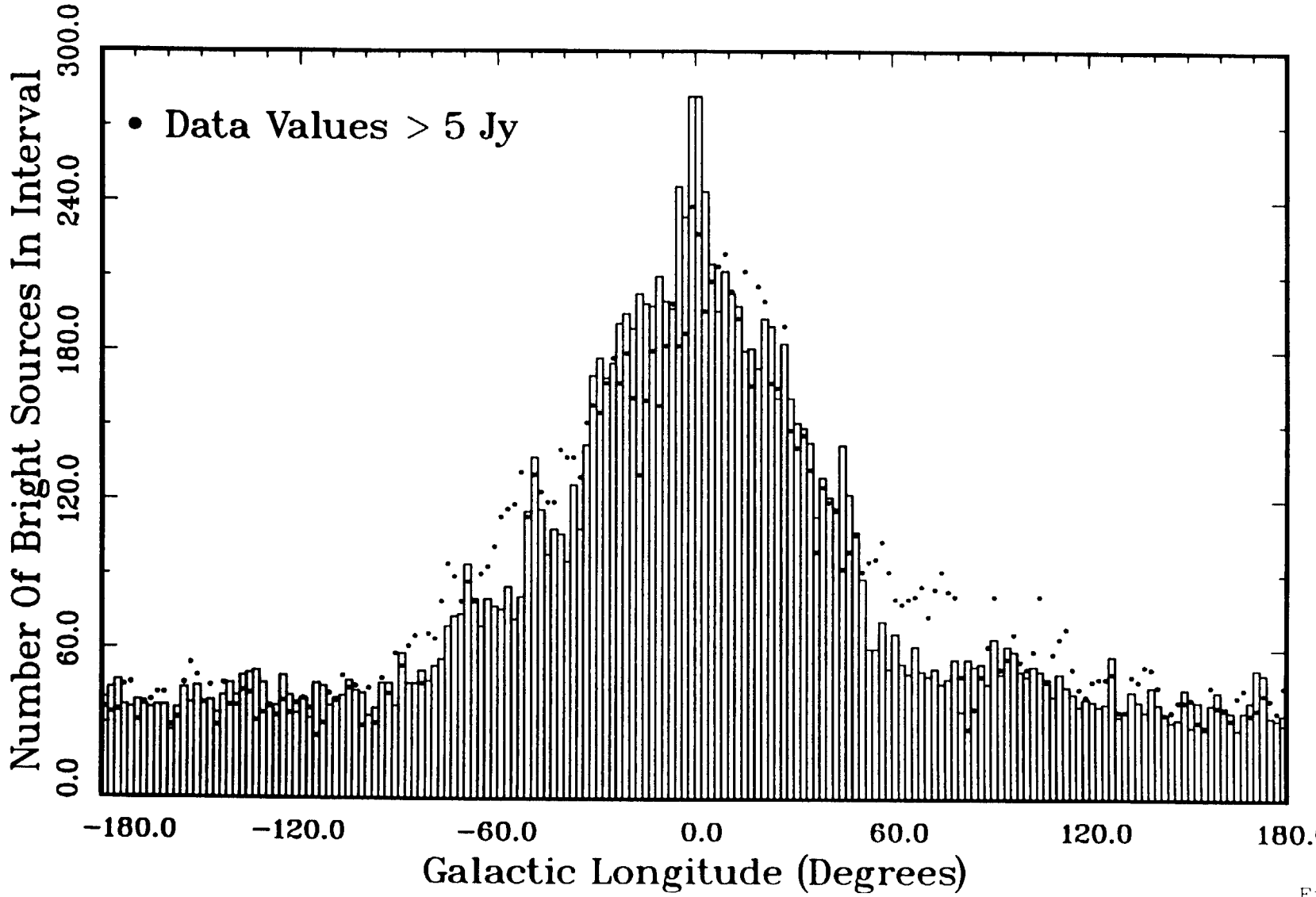
• Data Values > 5 Jy
Number Of Bright Sources In Interval
0.0
60.0
120.0
180.0
240.0
300.0
−180.0
−120.0
−60.0
0.0
60.0
120.0
180.0
Galactic Longitude (Degrees)

Fig. 11d

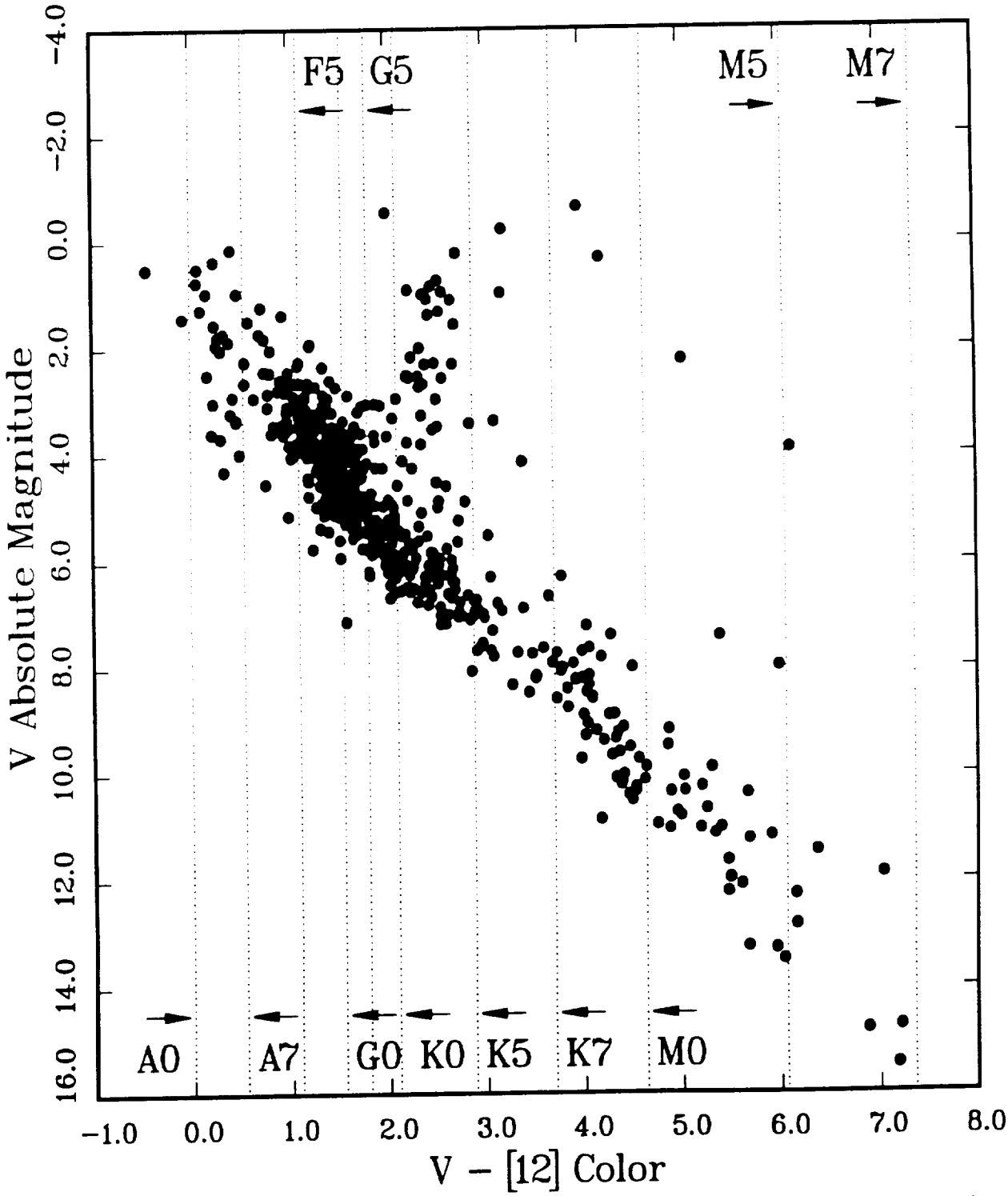
F5
G5
M5
M7
A0
A7
G0
K0
K5
K7
M0
V Absolute Magnitude
V − [12] Color
−4.0
−2.0
0.0
2.0
4.0
6.0
8.0
10.0
12.0
14.0
16.0
−1.0
0.0
1.0
2.0
3.0
4.0
5.0
6.0
7.0
8.0

Fig. 12

APPENDIX H. "A Model of the 8-25 μm Point Source Sky"

A MODEL OF THE 8–25 μm POINT SOURCE INFRARED SKY

RICHARD J. WAINSCOAT

NASA Ames Research Center and SETI Institute

MARTIN COHEN

Jamieson Science and Engineering Inc., and Radio Astronomy Laboratory, University of California, Berkeley

AND

KEVIN VOLK, HELEN J. WALKER, DEBORAH E. SCHWARTZ

NASA Ames Research Center and SETI Institute

Received: .....

TABLE OF CONTENTS

Abstract

We present a detailed model for the infrared point source sky that comprises geometrically and physically realistic representations of the galactic disk, bulge, spheroid, spiral arms (including the 'local arm'), molecular ring, and the extragalactic sky. We represent each of the distinct galactic components by up to 87 types of galactic source, each fully characterized by scale heights, space densities, and absolute magnitudes at $BVJHK$, 12, and 25 μm. Our model has been guided by a parallel Monte Carlo simulation of the Galaxy at 12 μm. The content of our galactic source table constitutes an excellent match to the 12 μm luminosity function in the simulation, as well as to the luminosity functions at V and K. We are able to produce differential and cumulative infrared source counts for any bandpass lying fully within the IRAS Low Resolution Spectrometer's range (7.7–22.7 μm) as well as for the IRAS 12 and 25 micron bands. These source counts match the IRAS observations extremely well. The model can be used to predict the character of the point source sky expected for observations from future infrared space experiments (e.g., ISO, SIRTF, LDR).

I Introduction

In 1983, the IRAS satellite surveyed the sky at wavelengths of 12, 25, 60 and 100 μm. At 12 and 25 μm, many of the points sources seen by IRAS are red giant stars with mass loss; these stars are very luminous in the mid-infrared and can therefore be seen at great distances. The extinction at these wavelengths is relatively small, so these stars are seen even at low galactic latitudes. The IRAS Point Source Catalog (1988, hereafter PSC) therefore offers a valuable tool for studying the structure of our Galaxy.

The comparison of $(\log \mathit{Number}, \log \mathit{Flux})$ from star counts with models for galactic structure has a long history. Bahcall (1986) provides a recent review of modern star count models. The models currently in use are based primarily on star counts at visible light wavelengths. These star counts are, therefore, restricted to the higher galactic latitudes where the extinction is small. Eaton, Adams, and Giles (1984), and Ruelas-Mayorga (1986) have obtained K (2.2 μm) star counts

at a few locations at low galactic latitude and compared them with models for the structure of the Galaxy.

Habing (1986,1988) and Garwood and Jones (1987) have attempted to model subsets of the IRAS star counts, but the first general attempt to model the entire sky as seen by IRAS was made by Volk *et al.* (1989). These authors used a Monte-Carlo approach to simulate the geometrical and luminosity distributions of 12 μm IRAS sources. In this paper, we describe a more versatile model which can predict source counts not only in the IRAS 12 μm passband, but also in the IRAS 25 μm passband and in any passband lying within the IRAS Low Resolution Spectrometer (LRS) range of wavelengths (7.7–22.7 μm). The predictions available from this model will clearly be of great value to the design and operation of future infrared space observatories (e.g., ISO, SIRTF, LDR). In addition to being able to predict star counts at these mid-infrared wavelengths, our model also operates at near-infrared (JHK) and visible light wavelengths (BV). These wavelengths allow self-consistency checks to be made, as well as permitting future direct tests of the model predictions.

In order to allow our model to predict source counts through any bandpass lying in the LRS wavelength range, we have made use of the IRAS LRS spectra. This necessitated the representation of galactic sources through a large source table (with each class of source having its own representative LRS spectrum), rather than using the classical luminosity function approach (e.g., Bahcall and Soneira 1984). Our method is, therefore, similar to that used by Jones *et al.* (1981).

A prerequisite for any model which represents the sky by a specific set of categories of galactic source is a complete database in which are assembled: the absolute magnitudes in a 'reference' passband; broadband colors for other 'standard' passbands relative to the reference; full spectral representations across any wavelength domain where a 'non-standard' passband will be used; space densities; and geometrical information such as scale height, radial scale length, and whether the sources are found in the disk, spheroid, bulge, arms, and/or ring. In § II.b we treat the construction of such a database for our model.

Extragalactic sources have extreme colors compared with stars. For example, the nearby galaxy NGC 253 has $V - [25] \approx 10$ (cf. an A0 star has $V - [25] = 0$). Therefore, especially at the longer of the two IRAS wavelengths that we model, 25

μm, and at the higher galactic latitudes, galaxies make an important contribution to the source counts. We have, therefore, included the prediction of galaxy counts in our model for these mid-infrared wavelengths. As we will see later, at relatively modest flux levels, not far below the IRAS threshold, galaxies actually become the dominant source at high latitudes at 25 μm. In the galactic plane, galactic sources dominate at all wavelengths and at all practical flux levels.

It is clearly important to represent the Galaxy with as much physical realism as possible. The new sources discovered by IRAS show strong color dependence on galactic latitude (Walker *et al.* 1989). These effects speak for the importance of an accurate representation of the disk, spiral arms, and bulge, in which reside almost all of the extremely red galactic objects.

In a series of papers we have explored the broadband IRAS colors of normal (Cohen *et al.* 1987) and AGB stars (Walker and Cohen 1988), and of non-stellar IRAS sources (Walker *et al.* 1989). Histograms of IRAS color indices, e.g. [12]−[25], show that there is a strong concentration of most very red IRAS sources to the galactic plane (Walker *et al.* 1989). This is suggestive of contributions from both the intermediate mass AGB population and from the traditional high-mass optical tracers of spiral structure (HII regions and reflection nebulae), all of which are very red to IRAS. These red objects become increasingly important to models of the infrared sky as the wavelength increases. Such studies of the IRAS color-color planes are crucial since they often reveal that optically defined populations may have more than one infrared representation. For example, carbon stars are found in two color-color domains depending on their visual detectability (Cohen *et al.* 1989); likewise, planetary and reflection nebulae, and "normal" galaxies occur in distinct "red" and "blue" varieties as mapped in the 12–25–60 μm color-color planes (Walker *et al.* 1989).

Once these various populations are considered, there seems no reason to conclude that IRAS detected any other abundant population, at least as indicated by the sample of sources newly discovered by IRAS that were bright enough to be well detected at 12, 25, and 60 μm (Walker *et al.* 1989). This conclusion is in part supported by ground-based optical spectroscopy of some 300 IRAS objects having optical counterparts but not associated in pre-existing catalogs (e.g., Cohen *et al.* 1989).

One might worry about the possible contributions from small extended sources to our representation of the point source infrared sky. However, Walker *et al.* (1989) have found only small color differences for individual galaxies and nebulae between the PSC and IRAS Small Scale Structure Catalog (1988) measurements, all of which are understandable in terms of either the different beam sizes inherent in the IRAS survey at 25 and 60 μm, or spatially-extended emission by PAH molecules. These slight differences do not justify the definition of different colors for members of these non-stellar populations unresolved and spatially resolved by IRAS since the emphasis of our model is on point sources. Therefore, we adopt the infrared colors ([12]−[25], [25]−[60]) of the basic populations as defined by Walker *et al.* (1989) for our purposes.

For $V-[12]$ colors we follow Cohen *et al.* (1987) for stars with standard spectral types and luminosity classes. For more exotic objects we describe below our methods for relating V to [12]. To relate the near-infrared wavelengths to one another we have relied upon the literature to provide basic photometry (and sometimes colors) for broad classes of object, as described in § II.b.

The detailed spectral characterization of our model in the mid-infrared has required extensive use of data from the Low Resolution Spectrometer (LRS). These spectra have been available to us from two sources: the IRAS LRS Atlas (1986; hereafter the Atlas), which is a collection of average spectra for 5425 sources and is the official IRAS product; and the complete LRS extracted database, which is the much larger (~170 000 spectra) database from which the Atlas was drawn.

Throughout this paper, all fluxes have been color corrected by assuming that the source is a 10 000 K blackbody. The zero-points for the magnitudes are defined by equation (VI.C.1) in the IRAS *Explanatory Supplement* (1988); the color corrections are in Table VI.C.6. We define:

$$[12] = 4.034 - 2.5\log_{10} F_\nu(12\mu\mathrm{m}) \quad (1)$$

$$[25] = 2.444 - 2.5\log_{10} F_\nu(25\mu\mathrm{m}) \quad (2)$$

$$[60] = 0.490 - 2.5\log_{10} F_\nu(60\mu\mathrm{m}) \quad (3)$$

where F_ν is from the PSC, and $[P]$ is the magnitude in passband P. In this representation, α Lyr has $[12] = -0.01$ which is consistent with the general definitions of magnitudes found in the literature. (Note that for α Lyr, $[25] = -0.16$, and

$[60] = -1.96$—these anomalous values at longer wavelengths are due to cool dust around this star.) This representation of IRAS magnitudes is identical to that used by Cohen *et al.* (1987). We define corresponding absolute magnitudes M_{12}, M_{25}, and M_{60}, which are simply the above definitions of [12], [25], and [60] for the source located at a distance of 10 pc.

II The Galaxy

II.a Galactic structure

Our treatment of Galactic structure closely follows that of Volk *et al.* (1989), who simulated the observed IRAS 12 μm structure of the Galaxy using Monte Carlo techniques. Below, we describe in detail the five geometrical components which we found were necessary to model properly the source counts in the Galaxy. Our model differs from the traditional optical star count models (e.g., Bahcall and Soneira 1980) through the necessary inclusion of the Galactic bulge and sources in the spiral arms and molecular ring. Optical star counts are only useful for $|b| \gtrsim 20^\circ$ due to extinction; our model must also work at low galactic latitudes.

We have chosen to represent galactic sources by a series of classes rather than by a luminosity function. This has the advantage of allowing much greater versatility in selecting passbands, but is computationally more cumbersome. The aggregate of all the classes that we represent in this way, expressed in terms of (Mag,log ϕ) is simply the luminosity function.

Throughout this paper, we will use a cylindrical coordinate system (R, θ, z), where R is distance from the galactic center within the plane, θ is the angular coordinate in the plane, with origin at $l = 0$ and handedness such that $\sin l \leq 0$ implies $0 \leq \theta \leq \pi$, and z is distance from the plane. We use R_0 to represent galactocentric distance and have assumed $R_0 = 8.5$ kpc.

II.a.i The exponential disk

Our treatment of the exponential disk closely follows that of Bahcall and Soneira (1980). We assume that

$$\rho(R,z,S) = \begin{cases} \rho_D(S) \exp[-(R-R_0)/h - |z|/h_z(S)] & R \leq R_{\max} \\ 0 & R > R_{\max} \end{cases} , \qquad (4)$$

where S has been used to denote spectral class, h is the radial scale length, $\rho_D(S)$ is the number density in the solar neighborhood of stars of class S, $h_z(S)$ is their scale height, and $R_{\max}$ is a truncation in the disk.

The radial exponential decline in the disks of spiral galaxies is well established in the literature (see e.g., de Vaucouleurs 1959, Freeman 1970, Kormendy 1977). Bahcall and Soneira (1980) discuss in detail a number of determinations of h, and adopted $h = 3.5$ kpc. More recent determinations of h (4.4 ± 0.3 kpc—Lewis and Freeman 1989; 5.5 ± 1.0 kpc—van der Kruit 1986) have yielded larger values. Our model is not very sensitive to the choice of h (as will be discussed later); we have adopted $h = 3.5$ kpc for consistency with the Bahcall and Soneira model. The truncation seen in the disks of external galaxies is discussed in detail by van der Kruit and Searle (1982), who find that the truncation distance has a mean and scatter of $R_{\max}/h = 4.2 \pm 0.6$. We will assume that such a truncation exists in our Galaxy also, at a distance of $R_{\max} = 15.0$ kpc.

Van der Kruit and Searle (1981a,1981b,1982) have proposed a locally isothermal disk model with vertical distribution $L(z) \propto \mathrm{sech}^2(z/z_0)$. We have chosen instead to use $L(z) \propto \exp[-|z|/h_z(S)]$. The choice of the exponential instead of the isothermal distribution is motivated by recent observations of edge-on galaxies in the near-infrared (Wainscoat, Freeman, and Hyland 1989; Wainscoat and van der Kruit 1989). At K (2.2 μm), the vertical light distribution in these galaxies is seen to persist as an exponential to very small values of z.

It is well known that the older stars in the disk have larger scale heights than the younger stars (collisions with clouds are expected to cause an increase in velocity dispersion over time). We have, therefore, assigned a scale height to each class of star in our source table (Table 2, discussed in more detail in § II.b). We have adopted scale heights ranging from $h_z = 90$ pc for the youngest stars to $h_z = 325$ pc for the oldest.

The exponential disk is the most important point source component of the Galaxy at the shorter IRAS wavelengths (12 and 25 μm) and at IRAS flux levels ($F_nu > 0.1$ Jy) everywhere in the Galaxy, except for small $|b|$, where the arms and ring components contribute, and near the galactic center, where the bulge is important.

II.a.ii The bulge

We adopt the structural bulge representation derived by Volk *et al.* (1989). This can be summarized by

$$\rho(x,S) = \rho_B(S)x^{-1.8}e^{-x^3} \quad \text{, where} \tag{5}$$

$$x = \sqrt{R^2 + k_1^2 z^2}/R_1 \tag{6}$$

is a dimensionless number, $\rho_B(S)$ is the number density of bulge stars of class S at $x^{-1.8}e^{-x^3} = 1$ (i.e. $x = 0.77338$), k_1 is the bulge axis ratio (note that we define $k_1 = a/b$, so $k_1 \geq 1.0$), and R_1 is the bulge 'radius'—note that the exponential term in equation (5) produces a rapid decline in bulge star density outside R_1. We use the values of $k_1 = 1.6$ and $R_1 = 2.0$ kpc found by Volk *et al.*

We have assumed that the bulge has a similar stellar composition to the disk, except that we have not allowed young massive stars to be present in the bulge. The bulge has low mass high-metallicity giants which attain high [12]−[25] colors yet have more modest luminosites than their higher mass disk counterparts. We do not explicitly include these stars in our model.

II.a.iii The spheroid

We have assumed that the spheroid conforms to the $R^{\frac{1}{4}}$ law (de Vaucouleurs 1959). This is a projected distribution, observed in the spheroidal components of spiral galaxies as well as in elliptical galaxies. It has the form

$$\log_{10}\frac{I(\alpha)}{I(1)} = -3.3307(\alpha^{\frac{1}{4}} - 1) \tag{7}$$

where I is the observed surface brightness, α is the dimensionless angular distance defined by

$$\alpha = \sqrt{R^2 + k_e^2 z^2}/R_e \tag{8}$$

k_e is the spheroid axis ratio, and R_e is the 'effective radius' of the spheroid—the constant in equation (7) has been chosen so that half of the total luminosity is enclosed within $\alpha = 1$.

Studies of the globular cluster system in our Galaxy (de Vaucouleurs 1977, de Vaucouleurs and Buta 1978) have shown that their distribution closely follows the de Vaucouleurs $R^{\frac{1}{4}}$ law, and that they have an effective radius of $R_e \approx R_0/3.0$. We

therefore adopt $R_e = 2.83$ kpc. We use $k_e = 1.25$ and normalize the spheroid star density to be $\rho_S = 0.002\rho_D$ in the solar neighborhood; these values are the same as used by Bahcall and Soneira (1984). We do not allow young massive stars to be present in the spheroid; due to the spheroid's relatively low metallicity, we also decrease the numbers of the redder giant stars.

As will be shown later, the spheroid is not an important component of the Galaxy anywhere at IRAS fluxes and wavelengths. In the log$N$–log$F$ plane, the spheroid stars have a steeper slope than the disk stars—this is because their distribution falls off less rapidly than the disk stars. It is only at fainter magnitudes (e.g., in deep optical star counts) that the spheroid becomes important.

II.a.iv The spiral arms

Volk *et al.* (1989) showed that a much better fit to the distribution of low latitude galactic point sources was possible when sources in the spiral arms were included. We have therefore included spiral arm sources in our model. Our spiral arm representation is derived from the data of Georgelin and Georgelin (1976)—we use a four arm logarithmic spiral

$$\theta(R) = a \log(R/R_{\rm min}) + \theta_{\rm min} \qquad (9)$$

where a is a winding constant, $R_{\rm min}$ is the inner radius and $\theta_{\rm min}$ is the angle at that inner radius. The arms are set to be 6 radians long, but are truncated at $R = R_{\rm max}$ if they attain that radius. We have used the same exponential radial and vertical distributions for the arms as for the exponential disk component, except that the arms are 750 pc wide (in R), centered on the radial locations described by equation (9). We define corresponding arm number density normalization constants $\rho_A(S)$ which are analogous to the constants $\rho_D(S)$ in equation 4. Table 1 describes the parameters for the two pairs of arms; in this table, $\theta_{\rm min}$ is in radians. Each arm pair consists of an arm and a duplicate, π radians away in θ.

The arms are assumed to consist primarily of massive young stars. They therefore represent an enhancement of this type of star over the population present in the smooth exponential disk. We do not include a corresponding enhancement in the lower mass older stars in the arms; these stars are assumed to be old enough

that they have diffused away from the spiral arms (if they were formed there) and form part of the smooth exponential disk.

In addition to the four arms described above, we found it necessary to include the types of source found in the spiral arms in the 'local arm' too. There is evidence for this feature from HI (Weaver 1989) and CO observations (e.g., Cohen *et al.* 1980), as well as in observations of high mass stars (Becker and Fenkart 1970, Blaauw 1985, Weaver 1989). This feature was required to improve the match in number of stars and slope in the $\log N$–$\log F$ relation in the region $50° \lesssim b \lesssim 150°$ for low galactic latitude. We regarded the local arm as having the same stellar composition and geometrical form as the four main arms (defined by eq. [9]), with parameters shown in Table 1. These parameters reproduce the inherent curvature of the local feature and its abrupt disappearance towards $l \approx 250°$ (Becker and Fenkart 1970). For the purposes of this paper, we regard this 'local arm' as part of the spiral arm structure.

The sources in the spiral arms are an important component of the model at low latitudes, but are unimportant at higher latitudes.

II.a.v The molecular ring

CO observations of our Galaxy (e.g., Clemens, Sanders and Scoville 1988) have shown that a 'molecular ring' is present at $R \sim 0.45 R_0$. Volk *et al.* (1989) found an increase in IRAS star counts corresponding to this position, and concluded that it was necessary to include sources located in this ring. Volk *et al.* included mainly high mass infrared-bright sources in their simulations; because of the large distance from us, IRAS could only see very bright sources in the ring. We initially adopted the same strategy, assigning to the ring the same stellar mix as we had assigned the arms. However, comparisons with the K star counts of Eaton *et al.* (1984), which are able to see much less luminous stars at the distance of the ring, suggested that the ring should also contain some of the lower mass, less luminous sources. In this sense, the 'molecular ring' could therefore be regarded as a true stellar ring; there are many examples of rings in external galaxies (e.g., Buta 1986, 1987).

The ring was assumed to have a Gaussian distribution of the form

$$\rho(R,S) = \rho_r(S) \exp\left[\frac{-(R-R_r)^2}{2\sigma_r^2}\right] \tag{10}$$

where the 'ring radius' $R_r = 0.45R_0$, and $\sigma_r = 0.064R_0$ corresponds to a half-width for the Gaussian ring of $0.15R_0$, and $\rho_r(S)$ is the density of ring stars of class S at $R = R_r$. The vertical z distribution of the ring stars was assumed to be the same as that of their disk counterparts.

II.b Source tables

We now describe in detail our source tables from which the five components of the Galaxy are composed. The basic approach that we have adopted is similar to that of Elias (1978), Jones *et al.*, (1981) and Garwood and Jones (1987), who chose to represent the luminosity function by breaking it down into stellar classes. Each class of star (or non-stellar source) is represented by an absolute magnitude in a selection of passbands of interest, a dispersion in the absolute magnitude, a number density in the solar neighborhood in the disk, a disk scale height, and a set of numbers showing the relative occurrence of that type of source in each of the five galactic components. Each class of source is assumed to have a Gaussian distribution with dispersion σ, of the form

$$N(M) \propto \exp\left[\frac{-(M-M_\lambda)^2}{2\sigma^2}\right] \tag{11}$$

where M_λ is taken from Table 2.

Below, we describe how we calculated the absolute magnitudes, number densities, dispersions and scale heights in our table. We do not consider that this table should be used as a definitive reference for absolute magnitudes and number densities of galactic sources; rather it is our best effort at estimating these quantities from the literature. Some of the quantities may have large errors.

II.b.i Stars

Table 2 lists the 87 types of galactic source that we considered. The first section of the table is very similar to that of Jones *et al.* (1981). This section of the source table contains all 'normal' stars; it consists of 33 classes of star. We have split

the F8-G2 V class defined by Jones *et al.* into two separate classes (F8 V and G0-2 V)—this was done to make the V luminosity function synthesized from the source table match the observed V luminosity function more closely. We added the 'M late V' class to represent very low mass red dwarfs, and removed the M8+ III class. This class contains evolved stars with mass loss—these stars are very important for IRAS, and we devote the second section of Table 2 to characterizing them.

We took most of the K magnitudes, number densities and magnitude dispersions for these 'normal' stars from Jones *et al.* (1981). We modified some of the numbers in order to attain better consistency with the observed V luminosity function and the faint part of the 12 μm luminosity function derived by Volk *et al.* (1989). Colors and absolute magnitudes in the shorter wavelength passbands were obtained from a variety of sources, including Blaauw (1963), Keenan (1963), Johnson (1966), other references listed by Elias (1978), and from Ruelas-Mayorga (1986). We used the $V-[12]$ and $V-[25]$ colors derived by Cohen *et al.* (1987), except for the reddest M giants, where we relaxed their condition of non-variability and found slightly redder colors. We have used scale heights which are slightly larger than the values used by Jones *et al.*. Our values are similar to those used by Bahcall and Soneira (1980).

The second section of Table 2 consists of the evolved AGB stars. These stars have mass loss, so are in varying degrees surrounded by dust. They therefore emit a large fraction of their luminosity in the mid-infrared, and warrant careful characterization in a model of the Galaxy at the shorter IRAS wavelengths. This section of the table contains O-rich and C-rich stars. The C-rich stars are further subdivided into 'optically visible' and 'optically invisible' C stars. The M_{12} and M_{25} values, the relative log ρ_0 values, and the dispersions in the table result from a detailed AGB stellar evolution model (see Appendix) for stars in the mass range 1.25–8 $M_\odot$ (only stars in the range 1.25–4 $M_\odot$ could become carbon stars). Each class in the table represents a range of $[12]-[25]$ color—e.g., the class 'AGB M 07' represents O-rich stars having $0.6 < [12]-[25] < 0.8$ and is shown in the table as having $[12]-[25] = 0.7$.

For the M stars, we used stars listed in the *General Catalog of Variable Stars* (Kukarkin *et al.* 1970, hereafter GCVS) having LRS class 2 or 3, and very red M

stars selected from the AFGL Sky Survey (Price and Walker 1976) and studied by Cohen and Kuhi (1976,1977), to define $K-[12]$, $V-K$, and $B-V$ for each range of $[12]-[25]$. The B magnitudes were taken from the *Bright Star Catalog* (Hoffleit and Jaschek 1982, hereafter BSC) and from the *Smithsonian Astrophysical Observatory Star Catalog* (1966, hereafter SAOC); the V magnitudes were taken from the BSC, the SAOC or the *Two Micron Sky Survey* (Neugebauer and Leighton 1969, hereafter TMSS); and the K magnitudes were taken from the TMSS or from Gezari, Schmitz and Mead (1987). For the $[12]-[25]$ color ranges for which no observations existed, plausible estimates were made based on trends in the observed colors. The $J-H$ and $H-K$ colors were estimated from the $V-K$ colors.

The near-infrared carbon star colors were calculated from the tabulations of Claussen *et al.* (1987). We assigned carbon stars having $K-[12] \geq 2.4$ to the 'infrared' carbon star classes, and others to the 'optical' carbon star classes. We obtained B and V colors from Stephenson's (1973) catalog, and corrected them for interstellar extinction using the A_K values from Claussen *et al.* For the carbon star classes having large values of $[12]-[25]$, shorter wavelength observations are not available; we therefore estimated colors for these stars based upon the colors at smaller $[12]-[25]$ values.

The relative space densities for the AGB stars were taken from our stellar evolution model, as were the absolute magnitudes and dispersions. The final space densities were subsequently obtained by normalizing the synthesized total 12 μm luminosity function in the magnitude range $-14 \lesssim M_{12} \lesssim -11$ to the luminosity function derived by Volk *et al.* (1989).

The third section of Table 2 contains 'ultraluminous' 12 μm sources. It was clear from our parallel Monte Carlo simulations of the Galaxy at 12 μm that very bright 12 μm sources are indeed present in the Galaxy, and that the luminosity function must extend beyond the luminosities defined by our AGB stars, to at least $M_{12} = -17$.

In order to represent these correctly we endeavored to identify individual stars that lay in this very luminous range. One obvious potential source of such objects is the set of OH/IR stars detected by IRAS for which OH phase lag or kinematic distances are available so we could determine M_{12}. We found 46 of these to be in the ultraluminous category. We then searched the literature in an effort to identify

other types of star having $M_{12} < -13$. An appreciable number of probably very bright stars were identified but estimates of their distance were judged far less secure than the kinematic distances often available through OH radio measurements (or from the known location of an object in one of the Magellanic Clouds). Objects with well-determined distances were as follows, in order of increasing absolute 12 μm brightness: Hubble-Sandage variables in the LMC (S Dor and R71); the luminous M supergiant, S Per; M hypergiants such as VX Sgr and VY CMa; the B1 hypergiant MWC 300 (Wolf and Stahl 1985); the peculiar object, η Car. All lie in the range $-18.1 \leq M_{12} \leq -13.5$.

Based upon the above findings, we populated this region by six classes of star (Xn in Table 2; classes X1E and X1A have an almost identical M_{12} but silicate emission and absorption features respectively). To attain such high 12 μm luminosities, these sources must be both of high mass (and therefore young), and shrouded by dust. We have therefore assigned them young population scale heights; they usually have very red colors. Where possible, we have assigned them near-infrared and optical colors based upon known counterparts; in other cases, the colors have been estimated. The choice of these colors is relatively unimportant because these sources are ultraluminous only at wavelengths longer than K; these sources are rare and red, so at shorter wavelengths they are a less important part of the luminosity function. The number densities of these ultraluminous sources were chosen to match the 12 μm luminosity function derived by Volk *et al.* (1989) in the magnitude range $-17 \lesssim M_{12} \lesssim -14$.

The fourth section of Table 2 represents the final stellar type that we consider—the T Tau stars. These are a young stellar population, still intimately involved in their parental molecular clouds, so we have assigned them the young disk scale height of 90 pc.

We calculated $(B-V)_0$ and M_V for T Tau stars in the Taurus-Auriga cloud using the Herbig and Bell (1988) catalog, combining their B and V magnitudes with A_V values given by Cohen and Kuhi (1979). For $(J-H)_0$ and $(H-K)_0$ we followed Rydgren, Schmelz, Zak, and Vrba (1984) and the unpublished T Tau database of Cohen, Emerson, and Beichman (1989). We similarly calculated M_{12} for the Taurus-Auriga sample discussed by Cohen *et al.* To assess their space densities we assumed that 1) all main sequence stars with masses below 3 $M_\odot$

have a T Tau phase; 2) the maximum duration of this pre-main-sequence phase is 3×10^7 yr for all stars with core mass $\leq 1.0 M_\odot$ for which the approach to the main sequence can be quite protracted (this essentially is the maximum age for known T Tau stars, for example, in NGC 2264: Cohen and Kuhi 1979); and 3) for stars above 1.0 $M_\odot$, the duration of the T Tau phase is the actual time to achieve Iben's (1965) "point 8", on the zero age main sequence. For each mass, we evaluated the space density of T Tau stars as the space density for the appropriate main sequence star multiplied by the fraction of main sequence lifetime (again from Iben 1965) represented by the duration of the T Tau phase. The sum of all relevant masses of the resulting densities yielded $\phi = 3.7 \times 10^4$ kpc^{-3} and we encapsulated all T Tau stars into a single category of celestial source.

II.b.ii Non-stellar sources

The final section of Table 2 contains galactic non-stellar sources. These are planetary nebulae, reflection nebulae, and HII regions. The HII regions were assumed to have a young population scale height, the reflection nebulae a slightly larger scale height (because they are associated with a population of less massive stars), and the planetary nebulae were assumed to have similar scale height to the giant stars from which they form.

For planetary nebulae, we conducted a literature search for associated distances determined by a wide variety of techniques (see, for example, Gathier 1984). Near-infrared photometry came from Whitelock (1985) and optical data from the reference catalogue of planetary nebulae of Acker, Marcout, and Ochsenbein (1981). The separation into red and blue planetaries (cf. Walker *et al.* 1989) is essentially achieved by defining the "blue" category as nebulae for which $1.0 < [12]-[25] < 2.7$ and $0.7 < [25] - [60] < 3.5$.

Analysis of the sets of blue and red planetary nebulae with known distances indicates that the blue nebulae are essentially all brighter than $M_{12} = -11$ and comprise $\sim$ 5% of all planetary nebulae. IRAS detected 30 planetary nebulae within 1 kpc of the sun. This is $\sim$ 40% of all known planetaries within 1 kpc (the others are too old and have faded away at IRAS wavelengths). Using this number, we derive a number density of 19 kpc^{-3} for the 250 pc scale height that we have assumed for the planetary nebulae.

For reflection nebulae, we adopted the identifications of illuminating stars and the observed values of V, $B-V$, and $U-B$ tabulated by van den Bergh (1966), Herbst (1975), and van den Bergh and Herbst (1975), along with standard values for intrinsic colors and M_V for these dominantly OBA stars (e.g., Revista Mexicana ref.). We determined distance moduli ourselves, and thence individual M_{12} values. Our color-color analyses of reflection nebulae yielded estimates for the proportions of the two differently colored populations (blue and red). The division of the 12–25–60 μm plane into these two populations of reflection nebulae is as follows: for blue reflection nebulae, $1.10 \leq [12]-[25] < 2.30$ and $[25]-[60] > 2.00$; for red nebulae, $[12]-[25] \geq 2.30$ and $[25]-[60] > 2.00$.

We determined the volume out to which our total sample of reflection nebulae was complete by estimating at what distance, D, the number of nebulae detected by IRAS within D, divided by D^2, began to decline steeply, after allowance for Poisson statistics. This technique showed that these nebulae were completely sampled out to 500 pc. We subsequently used only this volume-limited sample to derive the 12 and 25 μm mean absolute magnitudes, associated sample standard deviations, and space densities for the populations (by assuming that the illuminating stars had a scale height of 120 pc and using the proportions for red and blue nebulae described above).

We applied the same method to two samples of HII regions drawn from work by Reifenstein *et al.* (1970) and by Wilson *et al.* (1970), for which distances were available through radio recombination line velocities. We found that IRAS had sampled these completely out to 1 kpc. The resulting volume-limited complete sample provided our estimates of M_{12} and M_{25}, and of their space density with the additional assumption that the scale height for the exciting stars of these regions was 90 pc. Shorter wavelength photometry for the HII regions was taken from Gezari *et al.* (1987).

II.b.iii Synthesized luminosity functions

In order to compare our source tables with observed luminosity functions, we have used the absolute magnitudes, dispersions and number densities in Table 2 to synthesize luminosity functions in the V, K, and 12 μm passbands, using the Gaussian representation given by equation (11). These luminosity functions are

shown in Figure 1*a*–*c*.

In Figure 1*a* we compare the V luminosity function with that used by Bahcall and Soneira (1980) and with that of Allen (1973). The match is good everywhere except at the brightest V magnitudes where our luminosity function has a higher number density. Our luminosity function, however, is designed to match the entire disk, whereas the other luminosity functions represent solely the solar neighborhood. Since the sun is located in an interarm region, it is reasonable that the local luminosity function is deficient in luminous stars relative to the total luminosity function. The roll off at very faint magnitudes is due to our not considering stars later than our 'M late V' category; we also have not included white dwarfs in the model.

In Figure 1*b* we compare the K luminosity function with that used by Eaton *et al.* (1984). The two functions are essentially identical, which is not surprising since they have an almost identical origin (Jones *et al.* 1981). Nevertheless, this figure serves as a useful check on the effect of the formal inclusion into the K luminosity function of AGB stars, ultraluminous stars, T Tau stars, and non-stellar galactic sources. It is important to compare the K luminosity functions in Figure 1*b* with that derived by Mamon and Soneira (1982). Our luminosity function is not as steep in the high luminosity section as that of Mamon and Soneira. We attribute this difference to the large contribution to the K luminosity function coming from the M stars. These stars are not adequately considered in Mamon and Soneira's transformation from V to K, so their luminosity function is deficient at the brighter luminosities.

In Figure 1*c* we compare our synthesized 12 μm luminosity function with that used by Volk *et al.* (1989). The two luminosity functions match well over most of the magnitude range. Our luminosity function extends slightly beyond $M_{12} = -17$, and rolls off at the faintest magnitudes (again due to the absence of very low mass dwarfs and white dwarfs in the source table).

II.b.iv Normalization

The normalization of the five components of the Galaxy was achieved using the factors f_D, f_A, f_r, f_B, and f_S in the five columns at the right of Table 2, the adjacent column of $\log \rho_0$ values, and four additional factors listed below. The

factors listed in the table represent our attempt to break down the *total* disk luminosity function (exponential disk + spiral arms + ring) into its components. We chose to use this *total* disk luminosity function for consistency with that used by Volk *et al.* (1989). The factors f_D, f_A, and f_r (for exponential disk, spiral arms and ring respectively) sum to 1.0 in the Volk *et al.* picture of the Galaxy, in which both the arms and ring are a dominantly young stellar population. In our table, we allow the ring to contain lower mass stars so, for these stars, these three columns no longer add to unity. We have preserved the Volk *et al.* normalization of the ratio of 1:2:2 for exponential disk:arms:ring for the total population of young stars.

For the disk star normalization, the number density $\rho_D(S)$ in equation (4) is simply

$$\rho_D(S) = \rho_0(S) f_D(S) \quad . \tag{12}$$

The spiral arm star normalization is slightly more complex, because it involves an additional factor g_A. This factor is simply the ratio of the total surface area of the exponential disk to the area of the part populated by the arms, weighted by the radial exponential decline. We find $g_A = 5.0$. The spiral arm number density (cf. eq. [4], eq. [9]) is then

$$\rho_A(S) = \rho_0(S) f_A(S) g_A \quad . \tag{13}$$

Using this normalization, for example, the factors in Table 2 imply that there are, in total, twice as many high mass stars located in the arms as there are in the smooth exponential disk. The ring normalization requires the factor g_r, which is the ratio of the total surface area of the disk (weighted by the exponential decline, normalized to unit surface density in the solar neighborhood) to the total surface area of the ring (weighted by its radial decline in surface density, normalized to unit density at R_r). We find $g_r = 25$. The ring number density $\rho_r(S)$ is then

$$\rho_r(S) = \rho_0(S) f_r(S) g_r \quad . \tag{14}$$

Consequently, the factors in Table 2 imply that there are, in total, twice as many high mass stars located in the ring as there are in the smooth exponential disk. The values of the factors $f_r(S)$ shown in Table 2 are rather uncertain. The values for the high-mass, luminous stars come from Volk *et al.* (1989). The values for the

lower mass stars are a compromise between an attempt to to match the predicted K star counts from the model to the observations of Eaton *et al.* (1984), while requiring that the ring does not become an important dynamical component of the Galaxy (rotation curves for the Galaxy do not require a massive ring-like component to be present).

The bulge is normalized using the constant g_B defined as the ratio of bulge star density at $x^{-1.8}e^{-x^3} = 1$ (i.e. $x = 0.77338$) to the local solar neighborhood disk density. We used $g_B = 3.6$. The bulge number density $\rho_B(S)$ (cf. equation [5]) is then

$$\rho_B(S) = \rho_0(S) f_B(S) g_B \quad . \tag{15}$$

Finally, the spheroid normalization is given by

$$\rho_S(S) = \rho_0(S) f_S(S) g_S \tag{16}$$

where $g_S = 0.002$ and $\rho_S(S)$ is the local number density of stars of class S in the spheroid.

II.c LRS spectra

For the purposes of this model we wished to accommodate any view of the point source sky through a filter whose bandpass fitted entirely within the continuous wavelength range sampled by IRAS, namely the LRS range (7.67–22.74 μm). To this end, we required that every one of our 87 classes of galactic source be represented by an appropriate LRS spectrum.

All LRS spectra that we have used have been modified by the small calibration corection factors derived by Volk and Cohen (1989a). Their correction factors, and the smooth fit to them that we used, are shown in Figure 2.

II.c.i Stars

LRS spectra for most types of 'normal' star were available from the LRS Atlas (1986). We used the entire LRS database to supplement the number of spectra for a particular class of star when the signal-to-noise ratio in the relevant Atlas spectrum was poor or for types under-represented in the Atlas (such as cool dwarf stars). We normalized all the LRS spectra to unity, to facilitate ready combination of several

spectra to achieve an average for one source type. For our "young OB" category, we combined the spectra of HD 21389 (A0 Iae), β Ori (B8 Iae:), ζ Pup (O5 Iaf), and γ^2 Vel (WC8+O7.5e). For dwarfs later in type than M0 V, we were able to locate very few adequate LRS spectra even in the database. However, we readily determined that our actual LRS spectra for all cool dwarf stars beyond M0 V were well matched by cool (T=3500K) blackbodies. Consequently, we substituted these cool blackbody curves for the real but noisy LRS spectra, and for spectral types not represented in the LRS database, to produce a complete grid of LRS stellar spectra for 'normal' stars. These subsitutions were employed for types M0,1 V and M4,5 V; we were able to locate a suitable real spectrum for type M2 V.

In order to provide archetypical LRS spectra largely from the LRS database, it was necessary to smooth a number of the normalized spectral averages. Source categories whose averages were of sufficient quality to use directly (or which showed spectral lines making it undesirable to smooth the spectra) were: B2-3 V; M0,1,2,3,4,5,6,7 III; M3-4 I-II; K-M2 I; blue and red reflection nebulae; red planetary nebulae; and HII regions. When smoothing, we used a Gaussian of half-width # channels; this was applied to all other source categories except K4-5 V, M0-1 V, M4-5 V and M late V for which we used a 3500K blackbody.

For cool giants and AGB stars, we subdivided the sources into different categories depending on their oxygen- or carbon-richness, and on their [12]−[25] colors, binning these into 0.2 mag intervals. We assembled two sub-databases of IRAS point sources: one consisted of all sources associated either with Atlas spectra corresponding to silicate emission (LRS class 20–29), or absorption (LRS class 30–39), or optically known M stars in the GCVS; the second sub-database included only those point sources whose Atlas spectra we had already inspected and validated as having SiC emission characteristic of carbon stars (after exclusion of any silicate self-absorbed spectra—see Walker and Cohen [1988]).

We then extracted the Atlas spectra for all objects from the subset of 2958 oxygen-rich stars having $0.0 < [12]-[25] < 3.2$. These spectra were then normalized and averaged to represent AGB stars with [12]−[25] colors of 0.1, 0.3,...,3.1, where, for example, we represent stars with $1.0 < [12]-[25] \leq 1.2$ as having a single color of $[12]-[25] = 1.1$. The sizes of the samples that defined these average spectra are shown in Table 3. We averaged the LRS spectra for indices of 2.7

and 3.1 to interpolate a spectrum for [12]−[25]=2.9. We show the sequence of LRS spectra for O-rich giants in Figure 3*a*. Table 3 also shows the breakdown by [12]−[25] color of our sub-database of 802 Atlas spectra of carbon giants. No SiC emitting sources are known with redder broadband colors than 1.9; we chose to use the [12]−[25] = 1.9 spectrum to represent the LRS spectra of the carbon stars in our source table (Table 2) with [12]−[25] > 2.0. We show the sequence of LRS spectra for C-rich giants in Figure 3*b*. We used the same set of LRS spectra to represent the optically visible and the optically invisible carbon stars.

We discovered adequate LRS database spectra for 25 of the 51 objects chosen to typify the most luminous 12 μm objects in the Galaxy, then grouped all the objects according to their values of M_{12} and LRS spectral class. Figure 3*c* shows the average spectra of the 6 classes to which we assigned the 25 ultraluminous sources with acceptable LRS spectra.

Although several of the T Tau stars are represented in the LRS database, too few are available to establish the frequencies of occurrence of different LRS shapes for these stars. However, ground-based 8–13 μm spectroscopy (Cohen and Witteborn 1985) indicates that roughly 80% of the T Tau stars studied show 10 μm silicate emission features and 20% show silicate absorptions. We, therefore, chose to represent the T Tau category by the normalized LRS average spectrum of (2 × RY Tau + 2 × GW Ori + R Mon), where RY Tau and GW Ori are silicate emission T Tau stars, and R Mon is a silicate absorption T Tau star. Figure 3*d* displays the resulting LRS spectrum.

II.c.ii Galactic non-stellar objects

For nebulae, we sought LRS database spectra for every object of that particular category for which we had found an association in the PSC. In all cases we found that more than one LRS shape characterized the populations, although some of these diverse shapes corresponded to peculiar, incomplete, or noisy spectra.

HII regions presented the clearest situation with essentially one dominant LRS spectral signature and only 4 frequently occurring usable shapes; planetary nebulae had 7 different categories of usable spectrum (treated in more detail by Volk and Cohen 1989b); reflection nebulae similarly had 6 categories. We excluded all unusable (incomplete or noisy) spectra and selected one object whose LRS spec-

trum was of good quality to represent each category for every nonstellar source. We generated normalized composite LRS spectra by combining these representatives, weighted by their actual frequencies of occurrence within the LRS database, into a single LRS spectrum. We were careful only to combine spectra for objects with similar [12]−[25] indices so that normalizations at very different peak wavelengths would not bias the average LRS shape improperly. In practice, our distinctions drawn from the color-color planes, between red and blue planetaries, and red and blue reflection nebulae, were sufficient to ensure that only LRS spectra for similarly colored objects were combined. Figure 3*d*–*e* presents these LRS average spectra.

II.c.iii Use of non-standard filters

By utilizing the LRS spectra described above, our model can calculate (with a confidence level similar to that at 12 or 25 μm) expected source counts for any passband lying wholly within the IRAS LRS wavelength range of 7.67–22.74 μm. This is achieved in the following way. First, the absolute 12 μm magnitudes for each class of source (see Table 2) are used to calibrate absolutely the characteristic LRS spectrum for each class. Next, each calibrated spectrum is integrated over the bandpass of interest, resulting in a flux from each source (at a distance of 10 pc). A $\lambda F_\lambda = constant$ emission profile is used to define an effective wavelength for the bandpass, and a magnitude scale is then defined using equation (VI.C.1) in the IRAS *Explanatory Supplement* (1988). (Note that this choice of magnitude scale is solely for convenience.) Finally, the observed fluxes for each class are transformed to this new magnitude scale. Computationally, the new 'absolute magnitudes' are then handled in exactly the same way as for the normal broadband filters (e.g., [12], K) are handled. After the integration through the Galaxy and then through extragalactic space is complete, (resulting in a $[\log N, \mathrm{mag}]$ relationship), the transformation from flux to magnitude is applied in reverse to deliver the desired quantity—in-band flux—and a $[\log N, \log F]$ relationship.

II.d Interstellar extinction

Our model requires a representation of the interstellar extinction curve over the full LRS wavelength grid. This is used both to derive the interstellar extinction in any arbitrary filter in the LRS wavelength range, and to derive the interstellar extinction in the 12 μm filter used by IRAS.

Rieke and Lebofsky (1985, hereafter RL) have calculated the interstellar extinction law A_λ/A_V in the wavelength range 8–13 μm, at a resolution of $\Delta\lambda \approx 0.5\mu$m. Their determinations were based on a study of heavily extinguished luminous early-type stars and sources in the vicinity of the Galactic center. To define the extinction law in full wavelength detail, we initially extracted the LRS database spectra for VI Cyg #12, the canonical heavily reddened B5 Ia star. The chief attraction of this star was the prospect of simultaneously defining the spectral shape of the interstellar 18 μm absorption feature, which has never been investigated in detail, and the well-studied 10 μm interstellar feature (often represented by the shape of the Orion Trapezium emission spectrum [Forrest, Gillett and Stein 1975]).

We examined the average of 4 independent LRS spectra of VI Cyg #12 with varying qualities of the blue and red LRS spectral sections, but all having essentially similar spectral shapes. However, we were never able to match satisfactorily the dereddened broadband energy distribution of this star and its LRS spectrum with any blackbody, in particular with one close to 14 000 K in temperature (corresponding to spectral type B5 I). The definition of the intervening extinction using the ratio of the LRS spectrum to such a blackbody depends too critically on the accurate and simultaneous normalization of the blackbody to the dereddened broadband photometry and to the peak of the LRS data, near 8 μm. A further problem with VI Cyg #12 is its peculiarly flat energy distribution in the range 15–23 μm. No blackbody can match this shape. Indeed, it is possible that the stellar photosphere is no longer the primary source of emission at these long wavelengths—free-free emission from the stellar wind may dominate the energy distribution (Leitherer *et al.* 1984, Barlow and Cohen 1977). If so, free-free radiation may likewise contaminate the spectrum even shortward of 15 μm.

Consequently, we abandoned our effort to use this star. Instead we examined

two normalized average LRS spectra: for 401 IRAS sources having $1.05 < [12] - [25] < 1.15$ with optically thin silicate emission at 10 and 18 μm; and for the only IRAS source with $3.0 < [12] - [25] < 3.2$ having deep silicate absorptions at both 10 and 18 μm. In each case, we spline interpolated the underlying continuum between the two silicate features to remove the non-silicate contributions and compared the resulting "excess emission" and "excess absorption" profiles in the 10 μm region to that created by spline fitting the 11 calculated broadband values of A_λ/A_V of RL onto the LRS set of wavelengths and normalizing. The 10 μm "excess emission" profile was much narrower than the splined RL law, whereas the absorption data yielded a close match. We, therefore, adopted the entire normalized absorption profile defined from the source having both the silicate absorption features, to represent the silicate aspect of interstellar extinction.

Outside the 10 μm silicate band there is also extinction and we adopted a λ^{-1} law for the non-resonant extinction by these grains, scaled to correspond closely at 7.67 μm (the shortest LRS wavelength) to the RL value of $A_\lambda/A_V = 0.020$ at $\lambda = 8.0$ μm. Because this component underlies the silicate features we scaled the silicate extinction profile so that the sum of the non-silicate and silicate extinctions closely matched the actual peak value in the RL data (near 9.5 μm). The resulting extinction law appears in Figure 4.

Rigorous treatment of extinction would require that the derived extinction law be applied at every LRS wavelength for each object. Fortunately, such a detailed treatment is not necessary; the approximation $A_P = \int R_\lambda A_\lambda / \int R_\lambda$, where R_λ is the response function of passband P, is sufficient provided that the passband is not too broad. The interstellar extinction is not high enough in the mid-infrared to warrant more detailed treatment—we have, therefore, adopted this approximation in our model. In this way, we derive $A_{12}/A_V = 0.048$ for the IRAS 12 μm filter. Since the IRAS 25 μm passband lies partially outside the LRS wavelength range, we could not use this technique to derive A_{25}. We extrapolated our detailed LRS extinction law by the λ^{-1} and calculated $A_{25}/A_V \approx 0.005$.

The interstellar extinction (dust) was assumed to be located solely in the disk of the Galaxy, and to have a smooth exponential distribution, similar in form to the disk stellar distribution. This is an idealized representation; we expect that the dust has a somewhat clumpy distribution, and that it has concentrations in

the spiral arms and molecular ring—it is difficult to represent such a distribution analytically. However, the absorption is relatively low in the mid-infrared, so our simple dust distribution should be adequate. The absorption in an interval D to $D + \delta D$ was assumed to be:

$$\delta A_\lambda(R,z) = \begin{cases} A_{\lambda 0} \exp[-(R - R_0)/h_d - |z|/h_{z_d}]\delta D & R < R_{max} \\ 0 & R > R_{max} \end{cases} \quad (17)$$

where $A_{\lambda 0}$ is the absorption per unit length in the solar neighborhood, h_d is the radial scale length of the absorption, h_{z_d} in the scale height of the absorption, and D is distance along the line of sight to position (R, z). We assumed that the dust absorption in the solar neighborhood is 0.07 mag kpc^{-1} at K. This corresponds to $A_{V0} = 0.62$ mag kpc^{-1} using the interstellar extinction law determined by RL. Jones *et al.* (1981) derived a radial scale length for the extinction of 4 kpc. This value is similar to values derived for the scale length of the stars in the disk (3.5 kpc, de Vaucouleurs and Pence 1978; 4.4 kpc, Lewis and Freeman 1989; 5.5 kpc, van der Kruit 1986). We, therefore, assumed that the scale length of the absorption was the same as that of the stars, so $h_d = h$. We used a value of $h_{z_d} = 100$ pc for the extinction scale height.

For Galactic sources, the extinction calculation was carried out in parallel with the source count calculation. At each step along the line of sight, the source numbers and magnitudes were calculated, along with the extinction due to that increment in distance. The sources were assumed to be located at the mid-point of the step: half of the extra extinction was added to the total extinction to that point along the line of sight; the sources were dimmed by that 'total' extinction, then the other half of the extinction increment added to the total. When the 'edge' of the Galaxy is reached, the total Galactic absorption along that line of sight has been calculated; this was used as the extinction for the extragalactic sources. Intergalactic absorption was assumed to be neglibible.

II.e Integration through the Galaxy

The integration through the Galaxy is performed by stepping along a ray which starts at the earth and goes along the appropriate line of sight to infinity. Because they are the natural units for use in this work, we adopt galactic coordinates (l, b) as the standard input. If a large area is to be studied, or the area being studied

has a large number density gradient (e.g., near the galactic center or near the galactic plane), we arrange a grid (in $[l,b]$ coordinates) of suitably chosen, equally spaced, rays across the area, integrate along each ray, then sum their contributions (weighted by $\cos b$).

The integration along each ray is performed by regarding each ray as corresponding to a cone subtending a solid angle of 1 deg^2. (The results can be scaled to the appropriate observed area later.) The cone is split into volume elements, starting with the element $0 < D < 2$pc. The volume of the element is calculated then, for each of the five galactic components, the contribution from each class in the source table is calculated for that position and volume. These sources are assumed to be all located at the midpoint of the cone element (this assumption is valid provided that a sufficiently small step size is chosen; step size is discussed in detail below). The extinction to that point is calculated, then the magnitudes for each class of galactic source at that location calculated.

We have chosen a relatively simple method to represent the Gaussian distribution in magnitude of sources of a particular class. We approximate the Gaussian using the 5 delta functions listed in Table 4. Thus, at a particular location, stars of each class are assumed to have five different magnitudes (with appropriate number weighting). In this way, we achieve a computationally simple, yet reasonably realistic, representation of the Gaussian. (The Gaussian could be better represented by more delta functions, but a corresponding penalty in computational speed would be incurred.)

The step size that we have chosen ranges from a minimum of 2 pc to a maximum of 80 pc, and is determined from the distance, D, from the sun or from the distance, x, in equation (6). If either of these distances is less than 100 pc, the 2 pc step is used; a 4 pc step is used if $100 \leq (D \text{ or } x) < 300$ pc; 8 pc if $300 \leq (D \text{ or } x) < 700$ pc; 16 pc if $700 \leq (D \text{ or } x) < 1500$ pc; 32 pc if $1500 \leq (D \text{ or } x) < 3100$ pc; 64 pc if $3100 \leq (D \text{ or } x) < 6300$ pc; and 80 pc if $6300 \leq (D \text{ and } x)$ pc. The integration proceeds along the ray using these step sizes until a user-defined distance, $D_{\max}$, is reached. At this point, the integration through the Galaxy is complete. For our model, we have assigned $D_{\max} = 25$ kpc. For comparison with deep optical star counts, this value is probably too small and could be increased.

As the integration through the Galaxy proceeds, we collect the counts for each

class of star, in each of the 5 galactic components, into magnitude bins. We chose to use bins of 0.25 mag. Therefore, when the integration is complete, the breakdown of the star counts among each of the galactic components is available, as is the breakdown within each of the components into its constituent stellar classes. This will permit future direct spectroscopic and photometric tests of the detailed model predictions, as well as giving a clear picture of what stellar classes and galactic components are dominant. The classes and components are finally summed to yield either differential or cumulative total counts *vs.* magnitude relations, and the familiar $(\log N, \log F)$ diagrams (see § IV).

III The extragalactic sky

We now discuss the methods by which we have represented extragalactic sources in our sky model, including their colors, their separation into diverse types of galaxy, and their luminosity functions. The treatment of galaxies differed from that of galactic sources since we assumed them to have an isotropic distribution (we have ignored any effects due to individual galaxy clusters or to the supergalactic plane). Hence, there will always be the same contribution from galaxies at a given wavelength, scaled solely by the area of the sky zone chosen.

III.a Colors and luminosity functions

By their nature, nearby galaxies can subtend angles greater than the IRAS survey beamsizes, at least at 12 and 25 μm, which might influence their color distributions. Walker *et al.* (1989) have compared PSC colors of galaxies with the spatially-integrated colors from the sample of IRAS observations of large galaxies by Rice *et al.* (1988), and have found essentially no need to redefine the occupation zones for galaxies in the color-color planes. The slight differences that these authors did find were explicable in terms of the increased effective beam sizes inherent in spatially integrating the 12 and 25 μm maps of these galaxies.

From the color-color planes one can study the distribution of colors of different galaxy types. We found it convenient to divide galaxies into "normal", "Seyferts", and "quasars" based on IRAS-related studies in literature; "starburst" galaxies seem to overlap strongly with the luminosities and IRAS colors of normal galaxies

(cf. Soifer *et al.* 1987) so we combined the two. When we extracted all sources from the PSC associated with extragalactic catalogs we were able to define color-color diagrams for a sample of 11,595 galaxies.

However, we decided that such an approach had two inherent problems: 1) it would show a clear bias towards optically peculiar galaxies (for example, Seyferts) that had been catalogued as of particular interest and would thereby overestimate the true incidence of Seyferts; and 2) it would not treat IRAS upper limits correctly by addressing the color-dependent flux thresholds at 12 and 25 μm where most galaxies are not bright. We, therefore, used a 4000 km sec^{-1} volume-limited sample to assess the colors of galaxies, drawn from the larger study by Strauss and Davis (1988). This study essentially includes only the categories of normal and starburst galaxies; it does not sample high luminosity galaxies. However, it provides a clear quantitative estimate of the relative populations of "blue" (65%) and "red" (35%) normal galaxy types (cf. Walker *et al.* 1989) defined by the projection of the volume-limited sample onto the [12]$-$[25] axis. For all types, we used Gaussians to represent the color indices of galaxies in the three independent IRAS colors, with appropriate means and sigmas. In [25]$-$[60], normal galaxies show a well-defined peak which we fit by two Gaussians, preserving both the integrity and the proportions of the blue and red galaxies. There is also a weak blue component in the distribution, corresponding to the contribution from Seyferts (and quasars) in this color. We found that the area of this tail represents aproximately 4–5% of the total projected color distribution and attributed this entirely to Seyfert galaxies.

For more exotic galaxies, we follow Walker *et al.* (1989) in using the colors of Seyferts and quasars found by Miley, Neugebauer, and Soifer (1985) and Neugebauer *et al.* (1986).

Since galaxies are most easily seen by IRAS at 60 μm, we sought a luminosity function defined at 60 μm. Two groups have discussed such a function for galaxies. After correction to a common value of $H_0 = 75$ km s^{-1} Mpc^{-1}, we found little difference between the double power law of Soifer *et al.* (1987) and the smoother representation offered by Lawrence *et al.* (1986) except at the highest luminosities ($M_{60} \lesssim -40$, or $L \gtrsim 2 \times 10^{12} L_\odot$). The Lawrence *et al.* luminosity function is steeper (slope -2.5 in $[\log_{10} L, \log_{10} \rho]$) than the Soifer *et al.* luminosity function (slope -2.0). We chose to use the double power law representation of Soifer *et al.*

for the luminosity function of galaxies at 60 μm because it has a more simple analytical representation. We defined the luminosity function as

$$\rho(M_{60}) = \begin{cases} 0 & M_{60} < -44.0; \\ \rho_b 10^{0.80(M_{60}-M_b)} & -44.0 \leq M_{60} < M_b; \\ \rho_b 10^{0.32(M_{60}-M_b)} & M_b \leq M_{60} < -26.0; \\ 0 & -26.0 \leq M_{60}, \end{cases} \tag{18}$$

where $\rho_b = 7.6 \times 10^{-4}$ Mpc^{-3} mag^{-1} is the number density at the break in the double power, and $M_b = -34.43$ is the 60 μm absolute magnitude at which the break law occurs. These values differ slightly from the values given by Soifer *et al.* in the following ways. First, the luminosity function of Soifer *et al.* is defined for color corrected $F_\nu(60\mu\text{m})$ whereas we are interested in matching the observed quantity, in-band flux. We have crudely corrected for this by assuming that galaxies located in the flat part of the double power law (with $M_b \leq M_{60} < -26.0$) have $T < 32$ K and have negligible color corrections, whereas galaxies located in the steep part of the double power law (with $-44.0 \leq M_{60} < M_b$) have a color correction of 0.91 (typical for warmer galaxies with $T > 32$ K). This has the effect of producing a small shift in M_b and a corresponding small change in ρ_b. Also, our value of ρ_b has been scaled by 0.96 relative to that fitted from the Soifer *et al.* luminosity function to compensate for the somewhat lower density of galaxies in the southern sky; the Soifer *et al.* sample comes primarily from the northern sky. The magnitudes of -26.0 and -44.0 represent the faintest and brightest sources that were considered. Our absolute magnitude is related to the luminosities defined by Soifer *et al.* through $M_{60} = -9.03 - 2.5 \log_{10}(\nu L_\nu \text{ at } 60\mu\text{m, in } L_\odot)$.

It is not yet clear how the 60 μm galaxy luminosity function should be decomposed into normal/starburst galaxies, Seyferts and quasars. We have chosen the following approach. First, we assumed that for $M_{60} < -41$, all sources were quasars or had the colors of quasars, and that in the range $-41 < M_{60} < -33.5$, the quasar luminosity function had the same slope (–0.8) as the flat part of the total luminosity function, thus resulting in a fairly rapidly decreasing fraction of quasars with fainter magnitudes. Objects such as IRAS 09104+4109 (Kleinmann *et al.* 1988), have luminosities placing them in this quasar range; in spite of the fact that they are not quasars, they have similiar infrared colors to quasars (for IRAS 09104+4109, [12]–[25] = 2.49, [25]–[60] = 2.33) so are consistent with our

picture. Next, we assumed that Seyfert galaxies (or galaxies with the colors of Seyferts) exist in the magnitude range $-41 < M_{60} < -29$, and comprise a total of 4% of all galaxies at the lower luminosities, with this fraction increasing to 10% of the non-quasar population at the higher luminosities. This strategy has the merit of being consistent with the statement of Lawrence *et al.* (1986) that 'IRAS galaxies are probably 10–25 times as common as all types of Seyfert galaxy' and also predicts the correct relative proportion of galaxies with Seyfert-like colors in the volume limited sample of Strauss and Davis (1988). We attribute the remainder of the luminosity function to galaxies with the colors of normal/starburst galaxies, and to the blue/red categories of these normal/starburst galaxies in the ratio 65:35.

Having settled upon the 60 μm luminosity function and the breakdown of this function into its four constituent types, we are able to calculate the luminosity function for galaxies in other passbands. We assumed that the colors had Gaussian distributions; Table 5 lists the mean and sigmas of the [12]−[25] and [25]−[60] color distributions for our four classes of galaxy. The values in this table are the same as those derived by Walker *et al.* (1989) except that (1) the magnitude definitions in equations (1)–(3) have been used; and (2) we have now preserved the integrity of the [12]−[25] blue and red samples in the [25]−[60] color projection.

If a wavelength shorter than 60 μm was to be modeled, it was necessary first to transform the 60 μm luminosity function to 25 μm. This was achieved by first separating the four classes of galaxy, then calculating the contribution at each M_{25} from each value of M_{60}, assuming the [25]−[60] colors had the Gaussian distributions detailed in Table 5. If 25 μm was the passband for modeling, the four components of the luminosity function were summed to produce the composite 25 μm luminosity function; otherwise, the 12 μm luminosity function was calculated similarly, using the [12]−[25] colors. If 12 μm was the passband of interest, the four components were added to yield the 12 μm luminosity function for extragalactic sources. If, on the other hand, a filter in the LRS wavelength range was to be modeled, characteristic LRS spectra (see § III.b below) for the four classes of galaxy were used, in a procedure completely analogous to that described for Galactic sources in § II.c.iii, to define four separate offsets in the magnitude scale. Finally, these four offsets were separately applied to the four components of the 12

μm luminosity function, and the result regridded and summed to yield the composite M_P luminosity function for passband P. Figure 6 shows the 12 and 25 μm luminosity functions for extragalactic sources, calculated in this way; the 60 μm luminosity function is shown for comparison. We have not attempted to model the extragalactic sky at wavelengths shorter than the LRS limit of 7.7 μm.

III.b LRS spectra of galaxies

As noted above, in order to transform the luminosity function for extragalactic sources to any arbitrary filter within the LRS wavelength range, it is necessary to obtain charateristic LRS spectra for each class of extragalactic source.

The Atlas includes very few galaxies and those that are represented are peculiar (e.g., Cen A; NGC 253; M82). Therefore, we searched the LRS database for spectra of any PSC objects associated with galaxies whose 12 μm fluxes promised a usable spectrum. To supplement our sample, we also sought LRS data for the 42 starburst galaxies in the sample chosen by Jackson *et al.* (1988) for their microwave CO survey—in particular, those 9 in which CO emission was detected. Of these 42, we found LRS spectra for 4 galaxies (NGC 2146, NGC 2903, NGC 3504, and NGC 4490), all of which were detected in CO emission; only the spectrum for NGC 2146 had an adequate signal-to-noise ratio for our purposes.

We finally selected 13 galaxies for which reasonable LRS spectra were available and averaged their normalized shapes which were all very similar and obviously suggest the presence of PAH features in emission (Fig. 3*e*) (see Cohen and Volk 1989). The 12 galaxies are listed in Table 6. All these galaxies have similar [12]−[25] colors and we, therefore, adopt our LRS average as a good representation for the spectrum of galaxies with [12]−[25] $\approx$ 3.0.

Ground-based 8–13 μm spectra exist for about sixty galaxies (see the recent review by Roche 1989), selected on the basis of 10 μm brightness. Relatively few types of spectrum occur and, as for the LRS database, spectra are available exclusively for galaxies that are both infrared-bright and physically peculiar (often Seyferts) because of the probable link between active galactic nuclei, optical emission lines, and the influence of nuclear activity on IRAS brightness. The starburst galaxies studied all have very similar spectra and reveal PAH emission; Seyferts tend to have featureless spectra or show what might be weak silicate absorptions

(or possibly PAH emission again) and occasionally even weak silicate emission (Roche 1989). In spite of the absence of actual spectra, it is believed that normal galaxies should have spectra very similar to the composite we have created. In support of this belief, we note that the spatially-integrated IRAS broadband energy distribution of M31 (Walterbos 1986) is consistent with that from individual dark clouds in our Galaxy as if we saw a "typical" interstellar medium in M31. From a distance, we see the interstellar media very clearly in external galaxies and PAH molecules are probably ubiquitous in these media too.

Consequently, we have chosen to represent our 4 types of galaxy by the same LRS composite but have linearly tilted this composite by appropriate amounts to match the observed mean [12]−[25] colors for the 4 categories of galaxy. We did this by extrapolating the LRS shape slightly shortward of 7.7 μm, based on real astrophysical PAH spectra, and longward of 23 μm, essentially by a power law, then convolved this spectrum with real IRAS filter profiles at 12 and 25 μm to derive the color indices. The extrapolations were necessary to match the IRAS bandpasses as defined in the IRAS *Explanatory Supplement*.

III.c Integration of galaxies through space

Having derived a luminosity function for the passband of interest, we then integrated this luminosity function along a ray through space. The resulting count/luminosity relation was subsequently scaled to the number of square degrees in the area of interest. Our integration through space includes cosmological effects, but no evolution. We assumed that $H_0 = 75$ km s^{-1}, $\Lambda_0 = 0$ and $\Omega_0 = 1$, so $q_0 = 0.5$. The choice of cosmology only becomes important for $[60] \gtrsim 10$, (i.e., $F_\nu(60\mu\text{m}) \lesssim 0.15$ mJy); the effects of evolution (Hacking, Condon and Houck 1987) are likely to be much greater. We have chosen to ignore evolution because more work is required to confirm that any evolution is seen (as opposed to clustering) and to distinguish between the various evolutionary models proposed.

Below, we choose to use the symbol $\mathbf{z} = \Delta\lambda/\lambda_0$ to denote redshift, to distinguish it from z which we have used above for distance from the Galactic plane. The integration through space was performed using (see, e.g., Weinberg 1972)

$$dN = n_0(1+\mathbf{z})^3 dV, \qquad \text{where} \tag{19}$$

$$dV = s^2 \frac{c}{H_0} \frac{dz}{(1+z)\sqrt{1+2(q_0+1)z+(1+q_0+1.5\Omega_0)z^2+\Omega_0 z^3}} \quad (20)$$

and n_0 is the number density in the rest-frame, $s = \vartheta r_A$ is the side of the cone over which the integration is being performed, ϑ is the angular extent and r_A, the angular size distance, is

$$r_A = \frac{r_L}{(1+z)^2} \quad , \qquad \text{where} \quad (21)$$

$$r_L = \frac{cz}{H_0} \frac{2\sqrt{1+z}}{1+\sqrt{1+z}} \qquad \text{for } \Omega_0 = 1; \quad (22)$$

r_L is the luminosity distance. This integration was performed from $z = 5 \times 10^{-6}$ ($D = 20$ kpc) to $z = 5.0$, with a multiplicative step size of $dz = 0.001z$.

In Figure 7, we compare model predictions with IRAS observations for several areas of the sky. We show areas near the galactic poles, for which appropriate color criteria were used to select the galaxies from the PSC. The fits to the data are generally good, becoming somewhat worse at the shorter wavelengths; this is exactly what would be expected from consideration of the smaller detector size and the lower flux density of the galaxies at the shorter wavelengths. We also show a comparison with the bright galaxy sample of Soifer *et al.* (1988) from which the luminosity function was derived, and with the deep IRAS survey data from Hacking and Houck (1987). The deviation of the model from the data at the higher luminosities in some of the areas is due to local clustering. The north-south asymmetry mentioned above is also evident.

IV Comparison with observations and discussion

We have subdivided the whole sky into 121 zones, each containing 1000–2000 "high quality" IRAS 12 μm sources, and compared the IRAS 12 and 25 μm source counts with the model in these zones. We divided the sky into 9 lataitude zones and further subdivided each of these zones into longitude zones. We summarise below the results from this comparison, and list the zones in which there are conspicuous differences between the model prediction and the IRAS source counts at either 12 or 25 μm. Nearly all these discrepancies are in the sense of the model predicting

too few sources compared with the IRAS source counts. These deficiencies are greater at 25 μm than at 12 μm. We list the areas by their latitude zones:

$-90° < b < -60°$ Very good match (within 20%).

$-60° < b < -45°$ Very good match (within 20%).

$-45° < b < -20°$ Good match except for $275° < l < 300°$ (LMC); zone $300° < l < 330°$ is influenced by the SMC, but the fit is not poor.

$-20° < b < -4°$ Generally a good match; $165° < l < 190°$ (Taurus) shows an excess of sources of $\sim 40\%$ at 25 μm, $190° < l < 215°$ (Orion) shows an excess of sources of $\sim 40\%$ at 12 μm and $\sim 100\%$ at 25 μm, $295° < l < 305°$ shows an excess of sources of $\sim 60\%$ at 25 μm.

$-4° < b < 4°$ Generally a good match in the region $0° < l < 31°$; the region $31° < l < 40°$ shows a deficiency of $\sim 60\%$ at some magnitudes; the region $50° < l < 115°$ shows deficiencies of varying degrees, the worst two parts of which are $78° < l < 89°$ (Cygnus) which is deficient by $\sim 140\%$ at 25 μm and $100° < l < 115°$ which is deficient by $\sim 100\%$ at 25 μm; the regions $115° < l < 280°$ and $286° < l < 298°$ have better fits, though there is a tendency for the fits to be not as good at 25 μm as at 12 μm; the regions $280° < l < 286°$ (Carina) and $298° < l < 310°$ show deficiencies of $\sim 100\%$ at 25 μm; the region $310° < l < 328°$ shows smaller deficiencies; the region $328° < l < 352°$ gives an excellent fit at both 12 and 25 μm; and the region $352° < l < 360°$ gives a good fit.

$4° < b < 20°$ Generally a good match—almost all within $\sim 20\%$; $100° < l < 115°$ shows an excess of sources of $\sim 70\%$ at 25 μm.

$20° < b < 45°$ Very good match (within $\sim 20\%$).

$45° < b < 60°$ Very good match (within $\sim 20\%$).

$60° < b < 90°$ Good match

The following items are likely to contribute to the deficient predictions:

- Our representation of the spiral arms as both homogeneously populated and symmetrically distributed about the plane of the Galaxy is overly simplistic.
- There exist local influences—for example Gould's belt
- The extragalactic sky is also not homogeneous, although the effects of clustering are at a much lower level than the former two causes.

In Figure 8, we show some examples comparisons of model predictions with IRAS data. We have chosen a few directions that illustrate various aspects of the model and of the structure of the Galaxy.

In Figure 8*a,b*, we show results for a region near the south galactic pole. In this region, the only components that contribute are the disk, the spheroid, and the external galaxies. The fit is very good at both 12 and 25 μm. It is clear that the disk dominates, and that the spheroidal component is relatively unimportant. It is less important than the external galaxies. The model predicts that, at these high galactic latitudes, galaxy counts will overtake star counts at $[12] \approx 10.8$ and at $[25] \approx 5.7$.

In Figure 8*c,d*, we show the model predictions for the Hacking and Houck (1987) area. We show the fit for stars only (galaxies were suppressed in both the model and the comparison data) for 12 μm, and for all sources at 25 μm. The fits are acceptably good considering the uneven signal-to-noise ratio in the area sampled and the small number statistics involved.

In Figure 8*e,f*, we show the model predictions for a region at intermediate galactic latitude. This direction is one where the spheroid contribution is likely to be larger. It is nevertheless clear that the disk dominates. At faint [12], the external galaxies become more numerous than spheroid stars; and at faint [25], the external galaxies are more numerous than the disk stars.

In Figure 8*g,h*, we show the model predictions for a region in the plane where the disk, the ring and the arms are important. The fit is very good at both wavelengths. The spheroid and external galaxies are negligible in comparison.

In Figure 8*i,j*, we show the model predictions for a region chosen to highlight the bulge. The fit is acceptable at 12 μm and very good at 25 μm. The model predicts too many sources around $[12] = 2.0$. This is most likely because the bulge

sources which produce such a good fit at 25 μm have a larger [12]−[25] color than they are represented as having in the source table, and are thus less luminous at 12 μm.

In Figure 8*k,l*, we show the model predictions for a region in the plane where the model prediction is deficient—this zone is one of the worst cases. The deficiency is greater at 25 μm than at 12 μm, so it is likely that the 'missing' sources are young, spiral arm type sources which have $[12] - [25] > 0$.

Next, we compare the model predictions with the K star counts of Eaton *et al.* (1984). These authors studied 7 evenly spaced regions in the plane in the longitude range $0° < l < 60°$. We show comparisons for five of their regions (for $l = 10, 20, 30, 40, 50°$) in Figure 9*a–e*. These figures explain our inclusion of older stars in the ring. The extinction is larger at K than at 12 μm and therefore more important. It is of course possible that some of the inner areas studied by Eaton *et al.* correspond to 'holes' in the extinction—the model treats extinction as being uniform. Reduced extinction would mimic the increased star count behavior that we (and also Eaton *et al.*) have chosen to interpret as due to increased stellar density in the ring. The model fits are very good for $l = 40°$ and for $l = 50°$, and are acceptable for $l = 10°$ and $l = 20°$; the worst fit is for $l = 30°$. It is clear that further K star counts will provide valuable input to galactic structure models such as the model presented in this paper.

The main area in which the model has difficulty is the galactic plane. The model works very well for $|b| > 4°$. It is likely that the model deficiency in the plane can be attributed mainly to the young, spiral arm type population. Our representation of the arms is probably overly simplistic, as is our representation of the spiral arm sources through our source tables. The model does work very well for about half of the galactic plane zone; that suggests that while our spiral arm representation may not be perfect, it is a close approximation to reality.

V Conclusions

We have constructed a detailed model of the infrared point source sky. This model can operate using any arbitrary filter lying in the LRS wavelength range (7.7–22.7 μm), as well as with a selection of broadband filters. We represent the galactic

sources by means of a large source table rather than by a luminosity function. The model includes the extragalactic sky at the mid-infrared wavelengths. The model predicts cumulative or differential source counts for a range of magnitudes (or fluxes).

Five galactic components are necessary: the exponential disk, the bulge, the spiral arms, the molecular ring, and the spheroid. The spheroid is the least important component of the Galaxy at mid-infrared wavelengths. We have represented each of these components with as much physical realism as possible, by deriving as many of their parameters as possible from independent studies at other wavelengths.

The model produces a good fit for nearly all areas for the sky located at $|b| > 4°$. The model gives deficient predictions in some zones of the galactic plane. We attribute these deficiencies to local structure, inhomogeneity, and other possible inadequacies in our representation of the spiral arms.

VI Appendix—Modeling the asymptotic giant branch stars

Many of the stars observed by IRAS are asymptotic giant branch (AGB) stars: carbon stars and most of the stars with silicate dust features, which represent at least 50% of the bright 12 μm sources observed by IRAS based upon the features seen in the LRS spectra (also see Walker and Cohen 1988). These stars represent the final stage of evolution of stars of intermediate main sequence mass (from $\sim 1.25 M_{\odot}$ up to $\sim 8.0 M_{\odot}$). Such stars are relatively uncommon compared to main sequence stars and have reliable distances in only a small number of cases, particularly for carbon stars. Further, the types of AGB stars that are easily detected by IRAS are generally not easily observable at optical wavelengths. Carbon stars with thick dust shells, such as IRC+10°216, and their oxygen-rich counterparts, such as the OH/IR stars, have either very faint optical counterparts or no optical counterpart at all, but are extremely bright in the infrared and can be observed by IRAS anywhere in the Galaxy.

Under these circumstances, the absolute properties of AGB stars cannot be observationally determined, so we have attempted to derive the space densities and

absolute magnitudes for these stars from a model of the overall AGB evolution. A number of assumptions which are poorly constrained by the observations must be made in the model. In this Appendix, we describe this model and discuss the assumptions that were used to derive the properties of AGB stars observed by IRAS.

VI.a Parameters From Stellar Evolution Models

Models of AGB stellar evolution are available for a wide range of main sequence masses, but there are indications that these models are not yet good enough to be matched with observations. There is a long-standing problem in producing AGB models for carbon stars, the 'carbon star mystery', because the models uniformly predict that all carbon stars should be massive and luminous while the observations indicate that most carbon stars are of low mass. This problem with the AGB stellar models is a serious drawback in understanding general AGB evolution. Also, few of the AGB evolution models allow for mass loss, which is observed to be an important property of most of these stars. Recent models have included mass loss using the Reimers (1977) formula, but generally such models need to invoke a 'superwind' late in the evolution to adjust the final stellar mass to the desired value (see Weidemann and Koester 1983). This is an undesirable characteristic because we know of no physical mechanism to produce a superwind. Thus, while the stellar evolution models serve as a guide to the AGB evolution, at this time they should not be over-emphasized.

There are some useful results from the AGB evolution models. The model results of Boothroyd and Sackmann (1988a,b,c,d) were used as prototypes, because these models are for low masses (1.20 and 3 $M_{\odot}$), from which the bulk of carbon stars are probably derived, and because mass loss was included in the models. One well-established result of all the AGB stellar models is that, to a good approximation, the stellar luminosity is determined by the mass of the stellar core, which is almost completely de-coupled from the envelope. Boothroyd and Sackmann (1988b) give approximations to the stellar luminosity, L_*, as a function of the core mass, M_c, in the form

$$L_* = L_0(M_c - M_0)L_{\odot} \qquad (23)$$

where L_0 and M_0 are constants for various ranges of M_c. The actual luminosity is predicted to deviate from the values from the equation due to interactions within the stellar core, which produce helium shell flashes at intervals during the evolution. We assumed that the stellar luminosity was always given by equation 23 with the constants from Boothroyd and Sackmann.

The models are also important in setting the initial AGB core mass as a function of the main sequence mass. For low mass stars we used the results from Boothroyd and Sackmann (1988c) while for the highest mass AGB stars we used results from the review by Iben and Renzini (1983). Combined with equation 23, these determine the AGB luminosity evolution. The initial AGB core mass was assumed to be linear between the 1.2 and 3.0 $M_\odot$ values from Boothroyd and Sackmann and a quadratic between 3.0 and 8.0 $M_\odot$. The initial core mass for an 8 $M_\odot$ star was taken to be 1.075 $M_\odot$. There is some mass loss before the stars reach the AGB; for the low mass stars, the values from Boothroyd and Sackmann were used and, for the more massive stars, the previous mass loss was assumed to be negligible.

Stellar models also give a relation between stellar mass, luminosity, and effective temperature (Wood and Cahn 1977),

$$\log_{10}(T_*) = (101.35 - 2.5\log_{10}(L_*/L_\odot) + 0.533M_*/M_\odot)/26.423 \quad , \qquad (24)$$

whence the stellar radius, R_*, can be calculated assuming that the star is a blackbody.

The other major constraint on the AGB models is the value of the minimum supernova progenitor mass, normally denoted as $M_{\rm up}$. This determines the upper mass limit for the AGB. The value of $M_{\rm up}$ is not well determined but is generally thought to be between 5 and 8 $M_\odot$. We used $M_{\rm up} = 8M_\odot$, from Weidemann and Koester (1983).

VI.b The Mass Loss Formula

At present there is no satisfactory theory for the cause and the magnitude of stellar mass loss in AGB stars. The mass loss is critical in determining the AGB lifetime as a function of mass and is the most important factor for IRAS observations. We are forced to use empirical results because there is no basic theory predicting the

mass loss rate. The most widely used parameterization of the mass loss rate is the Reimers formula

$$\dot{M} = 4 \times 10^{-13} \eta (L_*/L_\odot)(R_*/R_\odot)/(M_*/M_\odot) \quad M_\odot \mathrm{yr}^{-1} \tag{25}$$

where the constant η is usually presumed to be in the range $\frac{1}{3} \lesssim \eta \lesssim 3$. On the basis of studies of globular cluster stars, the value for population II red giants must be near the lower limit of $\frac{1}{3}$ (see the references given by Iben and Renzini [1983]). We assume that η is a function of the stellar mass and that only low mass stars need η of order 0.4.

Observational determination of mass loss rates is notoriously difficult and absolute luminosities are also difficult to determine for stars with high mass loss rates; therefore, the $\dot{M}$ values in the literature cannot determine η. The strongest observational constraint on η is the 'initial-final mass relation' (Weidemann and Koester 1983; Weidemann 1984) which tells us how soon the star must lose its envelope and leave the AGB. The observations indicate that the final mass changes only slightly for main sequence masses between $\sim 1.25\ M_\odot$ and $\sim 3\ M_\odot$. A star of main sequence mass $M_{\rm up}$ must leave the AGB by the time the core mass reaches $1.41\ M_\odot$, or possibly sooner depending upon conditions for core stability.

For our assumed initial AGB core mass we found that $\eta = 3.0$ is required to make $M_{\rm up} = 8\ M_\odot$. We assumed that for a $1.2\ M_\odot$ star, $\eta \approx 0.4$ as determined from the globular cluster stars. At intermediate mass, η was assumed to be a quadratic function of the initial mass. A linear relation was first tried, but it was unable to reproduce the initial-final mass relation. After a series of trials we adopted a formula for η:

$$\eta(M_{\rm ms}) = -0.059 + 0.382\ M_{\rm ms} + 0.288\ (M_{\rm ms} - 1.20\ M_\odot)(8.0\ M_\odot - M_{\rm ms}) \tag{26}$$

This formula has the linear term and a quadratic term that boosts the mass loss rate for stars of $\approx 3\ M_\odot$main sequence mass. We varied the amplitude of the quadratic term until a reasonable initial-final mass relation was obtained.

The initial-final mass relation predicted from the models using these η values is shown in Figure 10. From 1.25 to $3.0\ M_\odot$ the models match the observed values from planetary nebulae central star masses (Weidemann 1984) reasonably well. The relation from white dwarf mass determinations (Weidemann and Koester

1983) is similar in form to the model curve but has somewhat lower final masses. In our models it is not possible to match the Weidemann and Koester values because the model initial AGB mass from Boothroyd and Sackmann (1988c) for a 1.2 $M_{\odot}$ star is less than the corresponding Weidemann and Koester final AGB mass.

VI.c Other Observational Constraints

There are other observations must be considered in creating an AGB model. Generally it is estimated that there are 10% as many carbon stars as oxygen-rich AGB stars, while abundance studies of planetary nebulae indicate that $\gtrsim$ 50% of planetary nebulae are carbon-rich and thus presumably had carbon star progenitors (Zuckerman and Aller 1986). If there is no change in AGB lifetime when a star becomes a carbon star, this implies that, on average, a star which becomes a carbon star spends 20% of its AGB lifetime as a carbon star.

The IRAS observations of carbon stars are also important to the model, as a test of the mass loss rates for carbon stars. For comparison with the models we used all optically identified carbon stars (Stephenson 1973) with IRAS observations at 12, 25, and 60 μm and all the IRAS objects with class 40–49 LRS spectra, excluding sources which appeared to be misclassified silicate feature sources. This resulted in a sample of 825 IRAS sources for comparison with the models.

The color-color distribution of the carbon stars is unusual compared to the silicate feature sources because there are many optically identified carbon stars with 60 μm excesses (see Fig. 11). Willems (1987) and Chan and Kwok (1988) interpret this as the result of an interruption of the stellar mass loss when the star becomes carbon-rich. However, as discussed by Claussen *et al.* (1987), this scenario for carbon star evolution does not produce the proper number of optically visible carbon stars if the mass loss is only interrupted once, because the remnant shell disperses quickly compared to the estimated mean lifetime of carbon stars. In our models we used the concept of interrupted mass loss, which gives a good fit to the colors of many carbon stars (see Chan and Kwok 1988), but assumed that mass loss was interrupted several times during the life of a carbon star, in addition to when the star first becomes carbon-rich.

VI.d Parameters Of The Models

A set of radiative transfer models for AGB stars, both oxygen-rich and carbon-rich, with dust shells of optical depths from ~0.1 to ~30 (at 9.7 or 11.3 μm depending upon the type of dust used) was run to produce a grid of model colors. Dust condensation temperatures of 1500 K, 1000 K, and 750 K were used in the models. Radiative transfer models for stars which have suffered an interruption of mass loss were provided by S.J. Chan for 12 different initial optical depths and some new, detached dust shell, radiative transfer models were run to extend the range of parameters to higher initial optical depths. These model colors were used to simulate the color evolution of AGB stars of different masses. The mass loss rate and optical depth were assumed to be related by

$$\dot{M} = (0.00602\ M_\odot\ \mathrm{yr}^{-1}\ \mathrm{pc}^{-1}\ (\mathrm{km/s})^{-1})\tau_{11.3\mu\mathrm{m}} r_0 v \quad (27)$$

$$\dot{M} = (0.00303\ M_\odot\ \mathrm{yr}^{-1}\ \mathrm{pc}^{-1}\ (\mathrm{km/s})^{-1})\tau_{9.7\mu\mathrm{m}} r_0 v \quad (28)$$

for carbon dust and silicate dust respectively (see Chan and Kwok 1988, eq. 12) where r_0 is the inner dust shell radius, v is the stellar wind velocity, $\dot{M}$ is the stellar mass loss rate, and τ is the optical depth. The r_0 value was assumed to be independent of the stellar temperature and proportional to $\sqrt{L_*}$. v was taken as 10 km s^{-1} for all the model stars.

In the models, the AGB evolution was followed by numerical integration of the mass loss as a function of time, using a predictor-corrector method, and the colors were calculated at each time step. If the mass loss was interrupted, the star was followed through the detached shell phase until the mass loss resumed. A set of 200 stars with mass distribution randomly assigned, but consistent with a Salpeter initial mass function, was used. For any star with initial mass less than 4 $M_\odot$ there was a 60% chance that the star would become a carbon star over some fraction f_1 of its AGB lifetime. f_1 was a free parameter in the models, which affected the carbon star to oxygen-rich star ratio. The transition time was chosen at random within a time period

$$t_c = f_1 t_{\mathrm{agb}}[1 - (M_{\mathrm{ms}} - 1.25\ M_\odot)/2.75\ M_\odot] \quad (29)$$

where t_{agb} is the nominal AGB lifetime for an oxygen-rich star of the same initial mass. The transition was assumed to occur later in more massive stars because a

larger amount of carbon-rich material must be dredged up from the stellar core to transform the star into a carbon star.

At the time of transition, the mass loss was assumed to cease. After a period of time without mass loss, a new stellar wind was assumed to begin at a lower mass loss rate than that given by the Reimers formula with the set η value, and to build up exponentially to the full (Reimers) mass loss rate over a set period. The models had free parameters for how long the mass loss is disrupted, how long the recovery of the mass loss rate takes, and the time between the resumption of mass loss and the next disruption. These were the major free parameters used in looking for a fit to the IRAS observations.

The IRAS carbon stars have a wide range of infrared colors, so the sensitivity of IRAS to these stars is a function of the phase of evolution. The sample was required to have a 60 μm observation so carbon stars with thick dust shells and redder colors are favored over the optical carbon stars. This is partially offset by the requirement of an LRS spectrum for the redder sources, because sources had to be relatively bright to be accepted into the published set of LRS spectra. To allow for the different conditions for acceptance into the sample for sources with different colors, the model sources were assigned weights as a function of color. For each area of the color-color diagram, the model absolute magnitudes for the three IRAS bands were compared with the sample minimum flux densities. This comparison gave an estimate of the distance to which the stars could be observed in each wavelength band. The minimum of these three distances determined the limiting distance at which the model source would be observable. This distance was used to weight the model points. For model sources whose limiting distance was < 1 kpc the weight was the square of the limiting distance. For sources that could be observed to greater distances, the weight was proportional to the distance. This weighting allows for the effects of incompleteness of the IRAS observations of distant sources near the galactic plane. Confusion for LRS sources is a more serious problem than for the PSC sources because the IRAS scan direction on the sky was also the direction of LRS spectral dispersion.

VI.e Results Of The Models

Models were run for various combinations of mass loss recovery and mass loss disruption times. The best-fit model had the following parameters:

- Silicate dust condensation temperature distribution: equally divided between 1500 K, 1000 K and 750 K
- SiC dust condensation temperature distribution: 80% with 1500 K and 20% with 750 K
- Carbon star transition occurring at random in the last 10% of the oxygen-rich AGB lifetime, for 60% of all stars up to 4.0 $M_{\odot}$
- Dust mass loss disruption time: until the shell reaches 8000 times the initial inner radius ($\sim 4 \times 10^4$ years)
- Mass loss recovery time: 1.24 times the period of no mass loss (exponential time constant 0.25 times the period of no mass loss)
- Subsequent disruption of mass loss after 1.09 times the period of no mass loss

These parameters, along with the colors from the models, gave a χ^2 fit to Figure 11 of 53, for 31 degrees of freedom, or 1.77 per bin, which is marginally acceptable. As well as calculating the weighted color distribution, the model program tabulated the relative luminosity function for the AGB sources, which was used to derive space density values by scaling to match the empirical 12 μm luminosity function determined from Monte Carlo models (Volk *et al.* 1989). Figure 12 shows a subset of the model points for comparison with Figure 11. The scatter of points near a particular color value is smaller in the models than in the actual data. The models lack the sources with $[25]-[60] < 0$. Radiative transfer models suggest that these sources could be stars with a particularly sudden increase in the mass loss rate, producing a steeper density profile in the circumstellar shell than for steady mass loss, thereby reducing the 60 μm flux density because there is comparatively little dust at low temperatures.

The carbon stars in this model end up with higher core masses than a star of the same initial mass which stays oxygen-rich, because the periods of mass loss

disruption lengthen the AGB lifetime, so the core grows larger before the envelope is exhausted. Carbon stars in this model are generally more luminous than oxygen-rich stars of the same initial mass because the transition occurs late in the AGB lifetime and the core mass can become larger than the values used in Figure 10.

The model predicts intrinsic number ratios of 1.65:1:13.52 for optically visible carbon stars, infrared bright carbon stars, and oxygen-rich AGB stars, respectively. The overall carbon star to oxygen-rich AGB star ratio is predicted to be 1:5.1. The optical carbon stars are fairly common among AGB stars but, at least with IRAS, are observed only locally.

The model also predicts that generally carbon stars should have lower mass loss rates than oxygen-rich stars of the same luminosity. This result is somewhat dependent upon the assumptions about the dust grain properties used to derive the constant in equation 28. The fundamental result is that the dust shells of carbon stars in these models are generally of lower optical depth than for an equivalent oxygen-rich star, which appears to be generally consistent with the observations. In the models the carbon stars spend roughly the same amount of time as optical carbon stars and as infrared carbon stars.

The model program tabulates the relative numbers of carbon stars and oxygen-rich stars as a function of color. These values, unweighted, are proportional to the true space density values if the models are correct. There is a question of uniqueness in the models, especially given the number of assumptions required. Where possible, the $V-[12]$ and $K-[12]$ colors were obtained from the literature while the model M_{12} values were adopted for the table of sources. The models also yield values for the magnitude dispersion, σ, as a function of color. The overall space density of AGB stars was set by scaling the contribution to the luminosity function until a match to the empirical luminosity function of Volk *et al.* (1989) was obtained.

References

Acker, A., Marcout, J., and Ochsenbein, F. 1981, *Astr. Ap. Suppl.*, **43**, 265.

Allen, C.W. 1973, *Astrophysical Quantities*, 3rd ed. (London: Athlone).

Bahcall, J.N. 1986, *Ann. Rev. Astr. Ap.*, **24**, 577.

Bahcall, J.N., and Soneira, R.M. 1980, *Ap. J. Suppl.*, **44**, 73.

Bahcall, J.N., and Soneira, R.M. 1984, *Ap. J. Suppl.*, **55**, 67.

Barlow, M.J., and Cohen, M. 1977 , *Ap. J.*, **213**, 737.

Blaauw, A. 1963, in *Basic Astronomical Data*, ed. K. Aa. Strand (Chicago: University of Chicago Press), p. 383.

Blaauw, A. 1985, in *IAU symposium No. 106, The Milky Way Galaxy*, ed. H. van Woerden, R.J. Allen, and W.B. Burton (Dordrecht: Reidel), p. 335.

Becker, W., and Fenkart, R. 1970, in *IAU symposium No. 38, The Spiral Structure of our Galaxy*, ed. W. Becker and G. Contopoulos (Dordrecht: Reidel), p. 205.

Boothroyd, A.I., and Sackmann, I.-J. 1988a, *Ap. J.*, **328**, 632.

Boothroyd, A.I., and Sackmann, I.-J. 1988b. *Ap. J.*, **328**, 641.

Boothroyd, A.I., and Sackmann, I.-J. 1988c. *Ap. J.*, **328**, 653.

Boothroyd, A.I., and Sackmann, I.-J. 1988d. *Ap. J.*, **328**, 671.

Buta, R. 1986, *Ap. J. Suppl.*, **61**, 609.

Buta, R. 1987, *Ap. J. Suppl.*, **64**, 1.

Chan, S.J., and Kwok, S. 1988, *Ap. J.*, **334**, 362.

Claussen, M.J., Kleinmann, S.G., Joyce, R.R, and Jura, M. 1987, *Ap. J. Suppl.*, **65**, 385.

Clemens, D.P., Sanders, D.B., and Scoville, N.Z. 1988, *Ap. J.*, **327**, 139.

Cohen, M., Emerson and Beichman, C.A. 1989, *Ap. J.*, in press.

Cohen, M., and Kuhi, L.V. 1976, *Pub. A.S.P.*, **88**, 535.

Cohen, M., and Kuhi, L.V. 1977, *Pub. A.S.P.*, **89**, 829.

Cohen, M., and Kuhi, L.V. 1979, *Ap. J. Suppl.*, **41**, 743.

Cohen, M., and Volk, K. 1989, in preparation.

Cohen, M., Wainscoat, R.J., Walker, H.J., Volk, K., and Schwartz, D.E. 1989, *A.J.*, in press.

Cohen, M., and Witteborn, F.C. 1985, *Ap. J.*, **294**, 345.

Cohen, M., Schwartz, D.E., Chokshi, A., and Walker, R.G. 1987, *A.J.*, **93**, 1199.

Cohen R.S., Cong, H., Dame, T.M., and Thaddeus, P. 1980, *Ap. J. (Letters)*, **239**, L53.

de Vaucouleurs, G. 1959, in *Handbuch der Physik*, **Vol. 53**, ed. S. Flügge (Berlin: Springer-Verlag), p. 311.

de Vaucouleurs, G., 1977, *A.J.*, **82**, 456.

de Vaucouleurs, G., and Buta, R.J. 1978, *A.J.*, **83**, 1383.

de Vaucouleurs, G., and Pence, W., 1978, *A.J.*, **83**, 1163.

Eaton, N., Adams, D.J., and Giles, A.B. 1984, *M.N.R.A.S.*, **208**, 241.

Elias, J.H. 1978, *Ap. J.*, **223**, 859.

Forrest, W.J., Gillett, F.C., and Stein, W.A. 1975, *Ap. J.*, **195**, 423.

Freeman, K.C. 1970, *Ap. J.*, **160**, 811.

Garwood, R., and Jones, T.J. 1987, *Pub. A.S.P.*, **99**, 453.

Gathier, R. 1984, Ph.D. thesis, Univeristy of Groningen.

Georgelin, Y.M., and Georgelin, Y.P. 1976, *Astr. Ap.*, **49**, 57.

Gezari, D.Y., Schmitz, M., and Mead, J.M. 1987, *Catalog of Infrared Observations*, NASA RP-1196.

Habing, H. 1986, in *Light on Dark Matter*, ed. F.P. Israel (Dordrecht: Reidel), p. 329.

Habing, H. 1988, *Astr. Ap.*, **200**, 40.

Hacking, P., Condon, J.J., and Houck, J.R. 1987, *Ap. J. (Letters)*, **316**, L15.

Hacking, P., and Houck, J.R. 1987, *Ap. J. Suppl.*, **63**, 311.

Herbig, G.H., and Bell, K.R. 1988, *Lick Obs. Bull.*, No. 1111.

Herbst, W. 1975, *A.J.*, **80**, 212.

Hoffleit, D., and Jaschek, C. 1982, *The Bright Star Catalogue*, 4th revised ed. (Yale University Observatory, New Haven).

Iben, I. 1965, *Ap. J.*, **141**, 993.

Iben, I. and Renzini, A. 1983, *Ann. Rev. Astr. Ap.*, **21**, 271.

IRAS Catalogs and Atlases, Vol. 1, Explanatory Supplement. 1988, ed. C.A. Beichmann, G. Neugebauer, H.J. Habing, P.E. Clegg, and T.J. Chester (Washington, DC: GPO).

IRAS Catalogs and Atlases, Vol. 2-6, The Point Source Catalog. 1988, Joint IRAS Science Working Group (Washington, DC: GPO).

IRAS Catalogs and Atlases, Vol. 7, The Small Scale Structure Catalog. 1988, ed. G. Helou, and D.W. Walker (Washington, DC: GPO).

IRAS Catalogs and Atlases, Atlas of low-resolution spectra. 1986, IRAS Science Team, *Astr. Ap. Suppl.*, **65**, 607.

Jackson, J.M., Snell, R.L., Ho, P.T.P., and Barrett A.H. 1989, *Ap. J.*, **337**, 680.

Johnson, H.L. 1966, *Ann. Rev. Astr. Ap.*, **4**, 193.

Jones, T.J., Ashley, M., Hyland, A.R., Ruelas-Mayorga, A. 1981, *M.N.R.A.S.*, **197**, 413.

Keenan, P. 1963, in *Basic Astronomical Data*, ed. K. Aa. Strand (Chicago: University of Chicago Press), p. 78.

Kleinmann, S.G., Hamilton, D., Keel, W.C., Wynn-Williams, C.G., Eales, S.A., Becklin, E.E., and Kuntz, K.D. 1988, *Ap. J.*, **328**, 161.

Kormendy, J. 1977, *Ap. J.*, **217**, 406.

Kukarkin, B.V., Kholopov, P.N., Efremov, Y.N., Kukarkina, N.P., Kurochkin, N.E., Medvedeva, G.I., Perova, N.B., Fedorovich, V.P., and Frolov, M.S. 1970, *General Catalogue of Variable Stars* (Moscow: Nauka).

Lawrence, A., Walker, D., Rowan-Robinson, M., Leech, K.J., and Penston, M.V. 1986, *M.N.R.A.S.*, **219**, 687.

Leitherer, C., Bertout, C., Stahl, O., and Wolf, B. 1984, *Astr. Ap.*, **140**, 199.

Lewis, J.R., and Freeman, K.C. 1989, *A.J.*, **97**, 139.

Mamon, G.A., and Soneira, R.M. 1982, *Ap. J.*, **255**, 181.

Miley, G.K., and Neugebauer, G., and Soifer, B.T. 1985, *Ap. J. (Letters)*, **293**, L11.

Neugebauer, G., Miley, G.K., Soifer, B.T., and Clegg, P.E. 1986, *Ap. J.*, **308**, 815.

Neugebauer, G., and Leighton, R.B. 1969, *Two Micron Sky Survey*, NASA SP-3047.

Price, S.D., and Walker, R.G. 1976, *The AFGL Four Color Infrared Sky Survey: Catalog of Observations at 4.2, 11.0, 19.8, and 27.4 Microns*, AFGL-TR-76-0208.

Reifenstein, E.C., Wilson, T.L., Burke, B.F., Mezger, P.G., and Altenhoff, W.J. 1970, *Astr. Ap.*, **4**, 357.

Reimers, D. 1977, *Astr. Ap.*, **61**, 217.

Rice, W., Lonsdale, C.J., Soifer, B.T., Neugebauer, G., Kopan, E.L., Lloyd, L.A., de Jong, T., and Habing, H.J. 1988, *Ap. J. Suppl.*, **68**, 91.

Rieke, G.H., and Lebofsky, M.J. 1985, *Ap. J.*, **288**, 618.

Roche, P.F. 1989, in *Proc. 22nd ESLAB Symposium, Infrared Spectrscopy in Astronomy*, ed. M.F. Kessler and A.Glasse, (Dordrecht: Kluwer)

Ruelas-Mayorga, R.A. 1986, Ph.D. thesis, Australian National University.

Rydgren, A.E., Schmelz, J.T., Zak, D.S., and Vrba, F.J. 1984, *Publ. USNO*, **XXV**, Part I (RSZV).

Smithsonian Astrophysical Observatory 1966, *Smithsonian Astrophysical Observatory Star Calalog*, (Washington DC: Smithsonian Institution).

Soifer, B.T., Sanders, D.B., Madore, B.F., Neugebauer, G., Danielson, G.E., Elias, J.H., Lonsdale, C.J., and Rice, W.L. 1987, *Ap. J.*, **320**, 238.

Stephenson, C.B. 1973, *Publ. Warner and Swaysey Obs.*, **1**, No. 4.

Strauss, M.A., and Davis, M. 1988, in *IAU Symposium No. 130, Large Scale Structure of the Universe*, ed. J. Adouze *et al.*, (Dordrecht: Reidel), p. 191.

van den Bergh, S. 1966, *A.J.*, **71**, 990.

van den Bergh, S., and Herbst, W. 1975, *A.J.*, **80**, 208.

van der Kruit, P.C., and Searle, L. 1981a, *Astr. Ap.*, **95**, 105.

van der Kruit, P.C., and Searle, L. 1981b, *Astr. Ap.*, **95**, 116.

van der Kruit, P.C., and Searle, L. 1982, *Astr. Ap.*, **110**, 61.

van der Kruit, P.C., 1986, *Astr. Ap.*, **157**, 230.

Volk, K., and Cohen, M. 1989a, submitted to *A.J.*

Volk, K., and Cohen, M. 1989b, in preparation.

Volk, K., Wainscoat, R.J., Walker, H.J., Schwartz, D.E., and Cohen, M. 1989, in preparation.

Wainscoat, R.J., Freeman, K.C., and Hyland, A.R. 1989, *Ap. J.*, **337**, 163.

Wainscoat, R.J., and van der Kruit, P.C. 1989, in preparation.

Walker, H.J., and Cohen, M. 1988, *A.J.*, **95**, 1801

Walker, H.J., Cohen, M., Volk, K., Wainscoat, R.J., and Schwartz, D.E. 1989, submitted to *A.J.*.

Walterbos, R.A.M. 1986, Ph.D. thesis, University of Leiden.

Weaver, H. 1989, private communication.

Weidemann, V., and Koester, D. 1983, *Astr. Ap.*, **121**, 77.

Weidemann, V. 1984, *Astr. Ap. (Letters)*, **143**, L1.

Weinberg, S. 1972, *Gravitation and Cosmology*, (New York: Wiley).

Whitelock, P.A. 1985, *M.N.R.A.S.*, **213**, 59.

Willems, F. 1987, Ph.D. thesis, University of Amsterdam.

Wilson, T.L., Mezger, P.G., Gardner, F.F, and Milne, D.K. 1970, *Astr. Ap.*, **6**, 364.

Wolf B., and Stahl, O. 1985, *Astr. Ap.*, **148**, 412.

Wood, P.R., and Cahn, J.H. 1977, *Ap. J.*, **211**, 499.

Zuckerman, B., and Aller, L.H. 1986, *Ap. J.*, **301**, 772.

TABLE 1

SPIRAL ARM PARAMETERS

Arm	a	$R_{\min}$	$\theta_{\min}$	extent
1	4.25	3.48	0.000	6.0
1′	4.25	3.48	3.141	6.0
2	4.89	4.90	2.525	6.0
2′	4.89	4.90	5.666	6.0
L	4.57	8.10	5.847	0.55

TABLE 3

NUMBERS OF LRS SPECTRA OF AGB STARS USED TO CONSTRUCT COMPOSITE LRS SPECTRA.

[12]−[25]	O-rich	C-rich
0.1	83	52
0.3	119	190
0.5	239	131
0.7	370	87
0.9	434	69
1.1	401	55
1.3	276	33
1.5	123	10
1.7	56	5
1.9	34	1
2.1	37	
2.3	27	
2.5	13	
2.7	7	
2.9	0	
3.1	1	

TABLE 2
SOURCE TABLE

Type	M_B	M_V	M_J	M_H	M_K	M_{12}	M_{25}	σ	h_z pc	log ρ_0 kpc^{-3}	disk	arms	ring	bulge	spheroid
B0,1 V	-4.08	-3.80	-3.15	-3.07	-2.93	-2.80	-3.30	0.70	90	2.90	0.2	0.4	0.4	0.0	0.0
B2,3 V	-2.23	-2.01	-1.51	-1.44	-1.33	-1.27	-1.77	0.50	90	3.83	0.2	0.4	0.4	0.0	0.0
B5 V	-1.16	-1.00	-0.65	-0.60	-0.53	-0.50	-1.00	0.50	90	4.09	0.2	0.4	0.4	0.0	0.0
B8-A0 V	0.15	0.20	0.29	0.31	0.34	0.27	0.27	0.50	110	5.33	0.4	0.3	0.3	0.0	0.0
A2-5 V	1.68	1.58	1.39	1.32	1.33	1.31	1.31	0.50	130	5.54	0.6	0.2	0.2	0.0	0.0
F0-5 V	3.37	2.94	2.15	1.90	1.87	1.99	1.99	0.50	160	6.15	0.8	0.1	0.1	0.0	0.0
F8 V	4.54	4.00	3.04	2.79	2.73	2.73	2.71	0.50	270	6.20	1.0	0.0	0.1	1.0	1.0
G0-2 V	5.16	4.55	3.49	3.21	3.15	3.23	3.21	0.50	270	6.30	1.0	0.0	0.1	1.0	1.0
G5 V	5.66	5.00	3.86	3.55	3.51	3.58	3.55	0.50	325	6.50	1.0	0.0	0.1	1.0	1.0
G8-K3 V	6.85	6.02	4.62	4.22	4.15	4.15	4.10	0.50	325	6.80	1.0	0.0	0.1	1.0	1.0
K4-5 V	8.40	7.25	5.21	4.61	4.50	4.97	4.89	0.60	325	6.85	1.0	0.0	0.1	1.0	1.0
M0-1 V	10.23	8.78	5.89	5.14	5.00	5.04	4.94	0.70	325	6.95	1.0	0.0	0.1	1.0	1.0
M2-3 V	11.46	9.92	6.41	5.69	5.50	5.82	5.70	0.80	325	7.05	1.0	0.0	0.1	1.0	1.0
M4-5 V	13.11	11.52	7.40	6.73	6.50	6.70	6.57	1.00	325	7.15	1.0	0.0	0.1	1.0	1.0
M late V	14.65	13.00	8.50	7.80	7.50	7.25	7.05	1.00	325	7.30	1.0	0.0	0.1	1.0	1.0
F8-G2 III	3.45	2.53	1.01	0.50	0.45	0.92	0.91	1.00	325	4.65	1.0	0.0	0.1	1.0	1.0
G5 III	2.92	2.00	0.48	-0.03	-0.08	0.00	-0.03	1.00	325	4.65	1.0	0.0	0.1	1.0	1.0
G8 III	2.55	1.60	0.03	-0.50	-0.56	-0.59	-0.63	0.80	270	5.20	1.0	0.0	0.1	1.0	1.0
K0,1 III	2.69	1.62	-0.14	-0.72	-0.80	-0.78	-0.83	0.70	270	5.59	1.0	0.0	0.1	1.0	1.0
K2,3 III	2.33	1.10	-0.90	-1.55	-1.66	-1.53	-1.59	0.70	270	5.23	1.0	0.0	0.1	1.0	1.0
K4,5 III	1.58	0.10	-2.44	-2.95	-3.10	-3.20	-3.28	0.70	325	4.40	1.0	0.0	0.1	1.0	1.0
M0 III	1.20	-0.35	-3.17	-3.98	-4.14	-4.30	-4.40	0.60	325	3.48	1.0	0.0	0.1	1.0	1.0
M1 III	1.08	-0.48	-3.38	-4.23	-4.40	-4.67	-4.78	0.60	325	3.13	1.0	0.0	0.1	1.0	1.0
M2 III	0.94	-0.65	-3.73	-4.58	-4.76	-5.08	-5.20	0.60	325	3.13	1.0	0.0	0.1	1.0	1.0
M3 III	0.95	-0.65	-4.16	-5.03	-5.23	-5.56	-5.68	0.60	325	3.13	1.0	0.0	0.1	1.0	1.0
M4 III	0.79	-0.80	-5.06	-5.81	-6.04	-6.28	-6.41	0.60	325	3.00	1.0	0.0	0.1	1.0	0.8
M5 III	0.71	-0.84	-5.88	-6.64	-6.90	-6.93	-7.13	0.50	325	3.00	1.0	0.0	0.1	1.0	0.6
M6 III	0.65	-0.89	-6.75	-7.60	-7.90	-8.56	-8.96	0.50	325	2.45	1.0	0.0	0.1	1.0	0.4
M7 III	0.60	-1.00	-7.70	-8.57	-8.90	-10.23	-10.83	0.50	325	2.09	1.0	0.0	0.1	1.0	0.2
YOUNG OB	-5.30	-5.14	-4.80	-4.76	-4.70	-4.64	-4.64	1.20	90	2.21	0.2	0.4	0.4	0.0	0.0
A-G I-II	-5.62	-6.05	-6.72	-6.85	-7.00	-7.29	-7.29	2.00	90	1.53	0.2	0.4	0.4	0.0	0.0
K-M2 I-II	-4.93	-6.37	-8.68	-9.30	-9.50	-10.37	-10.47	1.00	90	1.49	0.2	0.4	0.4	0.0	0.0
M3-4 I-II	-4.45	-6.09	-9.98	-10.74	-11.00	-11.50	-11.70	1.00	90	1.10	0.2	0.4	0.4	0.0	0.0
AGB M 01	2.70	1.19	-3.27	-4.05	-4.38	-4.64	-4.74	0.25	270	-0.79	1.0	0.0	0.1	1.0	1.0
AGB M 03	2.77	1.21	-3.64	-4.49	-4.85	-5.51	-5.81	0.78	270	0.44	1.0	0.0	0.1	1.0	1.0
AGB M 05	2.62	1.01	-4.11	-5.01	-5.39	-6.60	-7.10	1.21	270	1.21	1.0	0.0	0.1	1.0	1.0
AGB M 07	1.70	0.04	-5.48	-6.45	-6.86	-8.36	-9.06	1.14	270	1.42	1.0	0.0	0.1	1.0	1.0
AGB M 09	1.20	-0.52	-6.36	-7.38	-7.82	-9.69	-10.59	0.92	250	1.55	0.8	0.1	0.1	1.0	1.0
AGB M 11	1.15	-0.73	-7.05	-8.16	-8.63	-10.90	-12.00	0.80	220	1.53	0.6	0.2	0.2	1.0	0.0
AGB M 13	1.70	-0.30	-7.50	-8.76	-9.30	-12.32	-13.62	0.90	220	1.12	0.4	0.3	0.3	1.0	0.0
AGB M 15	2.39	0.29	-7.31	-8.64	-9.21	-13.32	-14.82	0.74	160	0.45	0.2	0.4	0.4	0.0	0.0
AGB M 17	3.55	1.35	-6.65	-8.05	-8.65	-13.81	-15.51	0.62	160	-0.12	0.2	0.4	0.4	0.0	0.0
AGB M 19	4.87	2.57	-5.83	-7.30	-7.93	-14.03	-15.93	0.56	110	-0.47	0.2	0.4	0.4	0.0	0.0
AGB M 21	5.72	3.32	-5.48	-7.02	-7.68	-14.18	-16.28	0.45	110	-0.89	0.2	0.4	0.4	0.0	0.0
AGB M 23	6.72	4.22	-4.98	-6.59	-7.28	-14.28	-16.58	0.43	110	-1.46	0.2	0.4	0.4	0.0	0.0
AGB M 25	7.80	5.20	-4.40	-6.08	-6.80	-14.30	-16.80	0.24	110	-1.84	0.2	0.4	0.4	0.0	0.0
AGB C 01	1.42	-1.97	-6.02	-6.88	-7.41	-8.55	-8.65	0.84	220	0.69	1.0	0.0	0.1	1.0	1.0
AGB C 03	1.55	-1.52	-6.01	-6.88	-7.41	-8.57	-8.87	0.82	220	1.06	1.0	0.0	0.1	1.0	1.0
AGB C 05	2.42	-0.86	-5.96	-6.88	-7.45	-8.79	-9.29	0.70	220	-0.39	0.8	0.1	0.1	1.0	1.0
AGB C 07	0.08	-2.03	-6.31	-7.19	-7.64	-8.67	-9.37	0.76	220	-0.90	0.8	0.1	0.1	0.0	0.0

TABLE 2—*Continued*

Type	M_B	M_V	M_J	M_H	M_K	M_{12}	M_{25}	σ	h_z pc	log ρ_0 kpc^{-3}	disk	arms	ring	bulge	spheroid
AGB C 09	-0.29	-2.40	-6.68	-7.56	-8.01	-9.04	-9.94	0.59	220	-1.02	0.8	0.1	0.1	0.0	0.0
AGB C 11	0.81	-2.19	-6.74	-7.64	-8.19	-9.19	-10.29	0.64	220	-1.32	0.8	0.1	0.1	0.0	0.0
AGB C 13	0.68	-2.32	-6.87	-7.77	-8.32	-9.32	-10.62	0.65	220	-1.20	0.8	0.1	0.1	0.0	0.0
AGB C 15	0.57	-2.43	-6.98	-7.88	-8.43	-9.43	-10.93	0.60	220	-1.66	0.6	0.2	0.2	0.0	0.0
AGB C 17	0.38	-2.62	-7.17	-8.07	-8.62	-9.62	-11.32	0.58	220	-1.95	0.6	0.2	0.2	0.0	0.0
AGB C 19	1.33	-1.67	-7.22	-8.12	-8.67	-9.77	-11.67	0.59	160	-1.34	0.4	0.3	0.3	0.0	0.0
AGB C 21	1.24	-1.76	-7.31	-8.21	-8.76	-9.86	-11.96	0.52	160	-1.85	0.4	0.3	0.3	0.0	0.0
AGB C 23	1.32	-1.68	-7.23	-8.13	-8.68	-9.78	-12.08	0.50	160	-2.15	0.4	0.3	0.3	0.0	0.0
AGB C 25	1.17	-1.83	-7.38	-8.28	-8.83	-9.93	-12.43	0.49	160	-2.39	0.2	0.4	0.4	0.0	0.0
AGB CI 01	5.98	2.17	-3.37	-4.66	-5.81	-8.92	-9.02	0.35	270	-0.85	1.0	0.0	0.1	1.0	1.0
AGB CI 03	4.21	1.51	-4.17	-5.27	-6.22	-9.12	-9.42	0.53	270	0.19	1.0	0.0	0.1	1.0	1.0
AGB CI 05	4.20	2.20	-3.14	-4.69	-6.09	-9.69	-10.19	0.65	220	0.33	0.8	0.1	0.1	1.0	1.0
AGB CI 07	2.71	-0.26	-5.57	-6.59	-7.25	-10.09	-10.79	1.06	220	0.36	0.8	0.1	0.1	0.0	0.0
AGB CI 09	1.34	-1.66	-6.97	-7.99	-8.65	-11.49	-12.39	2.90	220	0.31	0.6	0.2	0.2	0.0	0.0
AGB CI 11	1.69	-1.31	-6.61	-7.81	-8.81	-11.81	-12.91	2.21	220	0.16	0.6	0.2	0.2	0.0	0.0
AGB CI 13	1.29	-1.71	-7.01	-8.21	-9.21	-12.21	-13.51	0.93	220	-0.16	0.6	0.2	0.2	0.0	0.0
AGB CI 15	0.49	-2.51	-7.81	-9.01	-10.01	-13.01	-14.51	0.78	220	-1.00	0.4	0.3	0.3	0.0	0.0
AGB CI 17	2.34	-0.66	-5.96	-7.16	-8.16	-11.16	-12.86	1.10	220	-1.74	0.4	0.3	0.3	0.0	0.0
AGB CI 19	4.50	1.50	-3.80	-5.00	-6.00	-9.00	-10.90	0.60	220	-2.59	0.4	0.3	0.3	0.0	0.0
AGB CI 21	4.16	1.16	-4.14	-5.34	-6.34	-9.34	-11.44	0.60	220	-2.59	0.4	0.3	0.3	0.0	0.0
AGB CI 23	3.82	0.82	-4.48	-5.68	-6.68	-9.68	-11.98	0.60	160	-2.42	0.4	0.3	0.3	0.0	0.0
AGB CI 25	3.48	0.48	-4.82	-6.02	-7.02	-10.02	-12.52	0.60	160	-2.38	0.4	0.3	0.3	0.0	0.0
AGB CI 27	3.14	0.14	-5.16	-6.36	-7.36	-10.36	-13.06	0.60	160	-1.69	0.2	0.4	0.4	0.0	0.0
AGB CI 29	2.80	-0.20	-5.50	-6.70	-7.70	-10.70	-13.60	0.60	160	-1.67	0.2	0.4	0.4	0.0	0.0
AGB CI 31	2.46	-0.54	-5.84	-7.04	-8.04	-11.04	-14.14	0.60	160	-2.22	0.2	0.4	0.4	0.0	0.0
X 1E	0.49	-1.51	-6.51	-8.31	-9.71	-14.31	-15.82	0.37	90	-0.45	0.2	0.4	0.4	0.0	0.0
X 1A	9.20	7.20	2.20	-0.30	-2.80	-14.40	-16.85	0.31	90	-0.24	0.2	0.4	0.4	0.0	0.0
X 2	4.25	2.25	-2.75	-4.65	-7.15	-15.35	-17.75	0.45	90	-0.01	0.2	0.4	0.4	0.0	0.0
X 3	9.29	7.29	2.29	-0.71	-3.71	-16.31	-18.80	0.28	90	-0.70	0.2	0.4	0.4	0.0	0.0
X 4	-1.90	-3.90	-8.90	-10.20	-11.30	-16.80	-17.77	1.41	90	-0.50	0.2	0.4	0.4	0.0	0.0
X 5	-1.18	-3.18	-8.18	-10.28	-12.38	-16.98	-18.88	0.28	90	-0.85	0.2	0.4	0.4	0.0	0.0
T TAURI	7.29	6.01	2.88	2.11	1.74	-1.86	-3.81	1.40	90	4.57	1.0	0.0	0.1	0.0	0.0
PN BLUE	-2.61	-3.32	-3.98	-3.66	-4.37	-11.00	-12.96	1.10	250	-0.02	1.0	0.0	0.1	1.0	1.0
PN RED	0.04	-0.67	-1.33	-1.01	-1.72	-8.35	-12.06	1.35	250	1.26	1.0	0.0	0.1	1.0	1.0
RN BLUE	-0.50	-0.40	-0.18	-0.78	-0.10	-4.05	-5.92	1.73	120	2.15	0.2	0.4	0.4	0.0	0.0
RN RED	-0.50	-0.40	-0.18	-1.13	-0.10	-4.54	-7.65	2.31	120	2.04	0.2	0.4	0.4	0.0	0.0
H II REG	12.53	8.53	5.53	1.53	-1.47	-8.50	-12.26	2.40	90	1.63	0.2	0.4	0.4	0.0	0.0

TABLE 4

REPRESENTATION OF GAUSSIAN BY DELTA FUNCTIONS.

Magnitude range	Location	Fraction
$(-\infty, -1.5\sigma)$	-1.939σ	0.0668
$(-1.5\sigma, -0.5\sigma)$	-0.921σ	0.2417
$(-0.5\sigma, +0.5\sigma)$	0.000σ	0.3830
$(+0.5\sigma, +1.5\sigma)$	0.921σ	0.2417
$(+1.5\sigma, +\infty)$	1.939σ	0.0668

TABLE 5

IRAS COLORS OF FOUR TYPES OF GALAXY.

	[12] − [25]		[25] − [60]	
Source type	mean	sigma	mean	sigma
Blue Galaxies	2.02	0.28	4.27	0.14
Red Galaxies	2.75	0.25	3.95	0.13
Seyferts	2.75	0.35	3.30	0.32
Quasars	2.34	0.44	2.64	0.49

TABLE 6

GALAXIES WITH USABLE LRS SPECTRA.

IRAS name	Common name
00450−2936	NGC 253
02401−0013	NGC 1068
03317−3618	NGC 1365
03419+6756	IC 342
05059−3734	NGC 1808
06106+7822	NGC 2146
09517+6954	NGC 3034=M 82
10257−4338	NGC 3256
11257+5850	NGC 3690/IC 694
13025−4911	NGC 4945
13225−4245	NGC 5128=Cen A
13341−2936	NGC 5236
14092−6506	in Abell 1409−65

Figure captions

FIG. 1.—Synthesized luminosity functions. (*a*) The V luminosity function. The 'spikes' show the 87 categories of source in our model by assuming that they have no dispersion but instead are found in a magnitude range of width 0.10 mag. The dashed line is the V luminosity function used by Bahcall and Soneira (1980), with parameters detailed at the top left corner of the figure. The dots show the luminosity function given by Allen (1973). The dotted line is the composite derived from our 87 types of sources, using the M_V and σ values for each class of source given by Table 2. (*b*) As for Fig. 1*a*, for K, except that the dashed line shows the K luminosity function derived by Mamon and Soneira (1982) and the dots show the luminosity function used by Jones *et al.* (1981). (*c*) As for Fig. 1*a*, for 12 μm, except that the dashed line shows the 12 μm luminosity function used by Volk *et al.* (1989).

FIG. 2.—Fit to correction factors for LRS spectra. The points with error bars show the correction factors derived by Volk and Cohen (1989a), and the solid line shows our fit. We used a spline to fit the points in the blue part of the LRS spectral range and a quadratic for the red part. All spectra used in this paper were divided by these fitted correction factors.

FIG. 3.—Representative LRS spectra of Galactic sources. Each spectrum is in units of F_λ and has been normalized to unity at its maximum. (*a*) O-rich giants. Each spectrum has been offset from its neighbor by 0.2 and is normalized to unity. The spectra are, from top to bottom, for characteristic [12]−[25] colors of 0.1,0.3,...,3.1. (*b*) C-rich giants. Each spectrum has been offset from its neighbor by 0.2. The spectra are, from top to bottom, for characteristic [12]−[25] colors of 0.1,0.3,...,1.9. (*c*) Ultraluminous stars. Each spectrum has been offset from its neighbor by 0.2. The spectra are, from bottom to top, X3, X1A, X2, X5, X1E, X4. (*d*) T Tau stars and planetary nebulae. (*e*) HII regions, reflection nebulae, and 'blue normal' galaxies.

FIG. 4.—Interstellar extinction law. The interstellar extinction, expressed as A_λ/A_V, over the LRS spectral range.

FIG. 5.—Breakdown of galaxy types. The assumed breakdown of galaxy types into 'blue' and 'red' 'normal' galaxies (these categories include starburst galaxies), Seyferts, and quasars. The dotted line shows the double power law on the same magnitude scale.

FIG. 6.—12, 25 and 60 μm luminosity functions for galaxies. The 60 μm double power law luminosity function for galaxies of Soifer *et al.* (1987) is shown, along with the 12 and 25 μm luminosity functions for galaxies that we have derived using the breakdown into type shown in Fig. 5 and the colors shown in Table 5.

FIG. 7.—Comparison of model galaxy counts with IRAS data. (*a*) The plot shows the cumulative ($\log N$, mag) relationship for the galaxies in the large area flux limited sample of Soifer *et al.* (1987). The model prediction is shown as a solid line, and the plus signs show the 60 μm data. (*b*) As for Fig. 7*a*, but for $b > 70°$. The 12 μm data are shown by the three pointed symbols, the 25 μm data are shown by crosses and the 60 μm data are shown by plus signs. The data points come from appropriate color selection criteria which were applied to the PSC to select galaxies. A correction to the area has been applied to compensate for the gap in coverage. The lines show the model predictions for these three passbands. (*c*) As for Fig. 7*b*, but for $50° < b < 70°$. (*d*) As for Fig. 7*b*, but for $-70° < b < -50°$. (*e*) As for Fig. 7*b*, but for $b < -70°$. (*f*) As for Fig. 7*b*, except that the data points come from the deep IRAS survey of Hacking and Houck (1987). The counts in each passband have been scaled to a common area of 1.0 deg^2.

FIG. 8.—Comparison of model predictions with IRAS data. (*a*) The plot shows the cumulative ($\log N$, mag) relationship for the IRAS 12 μm bandpass, for the region $180° < l < 360°$, $-90° < b < -60°$. The solid line shows the total counts predicted, the dotted line shows the contribution from the exponential disk, the

long dash-dot line shows the spheroid, and the long dash-short dash line shows the contribution from external galaxies. The plus signs are the data points. (*b*) As for Fig. 8*a*, but for 25 μm. (*c*) As for Fig. 8*a*, but for stars only, in the Hacking and Houck (1987) area at the north ecliptic pole. (*d*) As for Fig. 8*c*, but for all sources at 25 μm. (*e*) As for Fig. 8*a*, but for the region $0° < l < 30°$, $20° < b < 45°$; the long dashed line is the spiral arm contribution, and the short dashed line is the contribution from the bulge. (*f*) As for Fig. 8*e*, but for 25 μm. (*g*) As for Fig. 8*e*, but for the region $27° < l < 31°$, $-4° < b < 4°$; the short dash-dot line represents the contribution from the ring. (*h*) As for Fig. 8*g*, but for 25 μm. (*i*) As for Fig. 8*g*, but for the region $-5° < l < 5°$, $-5 < b < -3$, specially chosen to show the bulge. (*j*) As for Fig. 8*i*, but for 25 μm. (*k*) As for Fig. 8*g*, but for the region $78° < l < 89°$, $-4° < b < 4°$; the data points have been boosted by a factor 1.68 to compensate for a hole in coverage in this area. (*l*) As for Fig. 8*k*, but for 25 μm.

FIG. 9.—Comparison of model predictions with K star counts. The model predictions are shown using the same line definitions as used in Fig. 8. The star counts and model predictions have been scaled to an area of 1.0 deg^2. (*a*) $l = 10.42°$, $b = 0.13°$. (*b*) $l = 19.93°$, $b = 0.46°$. (*c*) $l = 29.26°$, $b = 0.08°$. (*d*) $l = 39.96°$, $b = 0.07°$. (*e*) $l = 49.68°$, $b = 0.16°$.

FIG. 10.—The initial-final mass relation predicted from the AGB models (dashed curve) compared with the observational values of Weidemann (1984) for 1.2 and 3.0 $M_\odot$ from masses of central stars of planetary nebulae (solid points), and the values of Weidemann and Koester (1983) from white dwarf masses (open points). To produce the very flat final mass curve the mass loss efficiency must be increased for stars of initial masses near 3.0 $M_\odot$ as in equation 26.

FIG. 11.—The observed IRAS colors for sources associated with carbon stars in the *General Catalogue Of Cool Carbon Stars* (Stephenson 1973), the 'optical carbon stars' (open circles), and the IRAS sources with class 40–49 LRS spectra,

the 'infrared carbon stars' (filled circles). These groups are not exclusive; however the infrared carbon stars are redder in [25] – [60] than the optical carbon stars and the optical carbon stars often have 60 μm excesses.

FIG. 12.—A subset of sources from the best-fit carbon star evolution model. The points were chosen at random from the full set of calculated points for comparison with Figure 11. Each grid square was one element for the χ^2 fit.

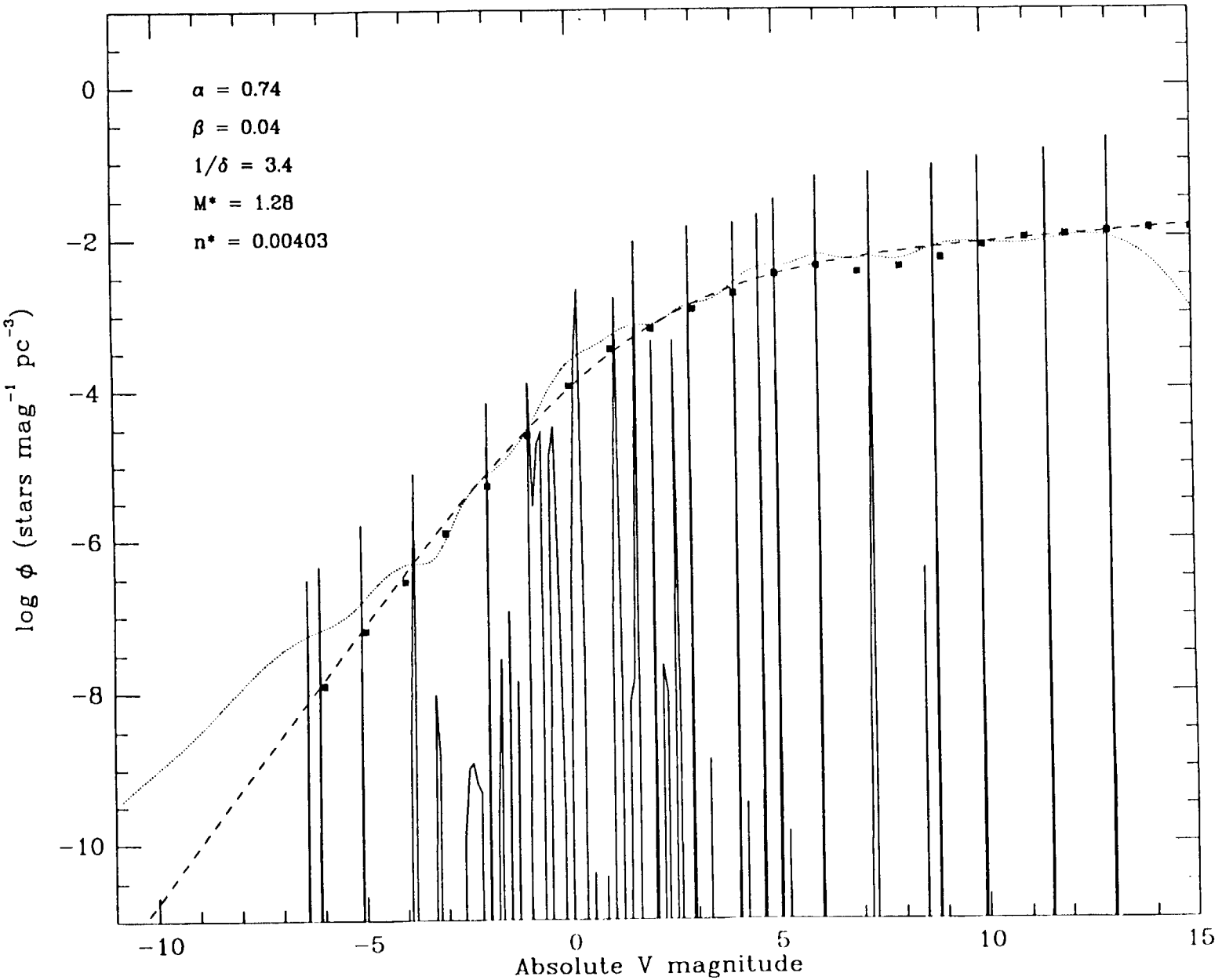
α = 0.74
β = 0.04
1/δ = 3.4
M* = 1.28
n* = 0.00403
log φ (stars mag^{-1} pc^{-3})
0
−2
−4
−6
−8
−10
−10
−5
0
5
10
15
Absolute V magnitude

Fig. 1a

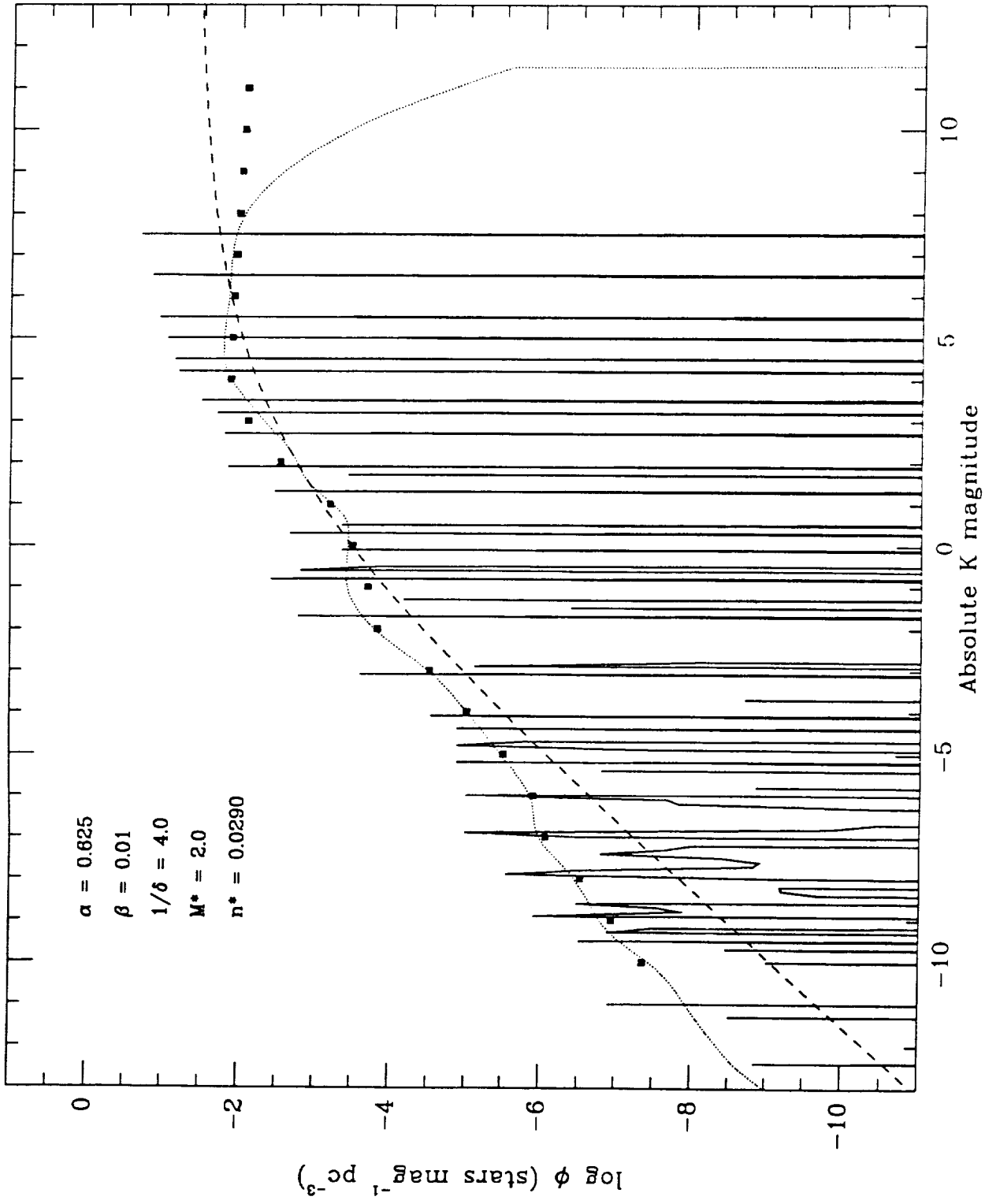
α = 0.625
β = 0.01
1/δ = 4.0
M* = 2.0
n* = 0.0290
Absolute K magnitude
log φ (stars mag⁻¹ pc⁻³)

Fig. 1b

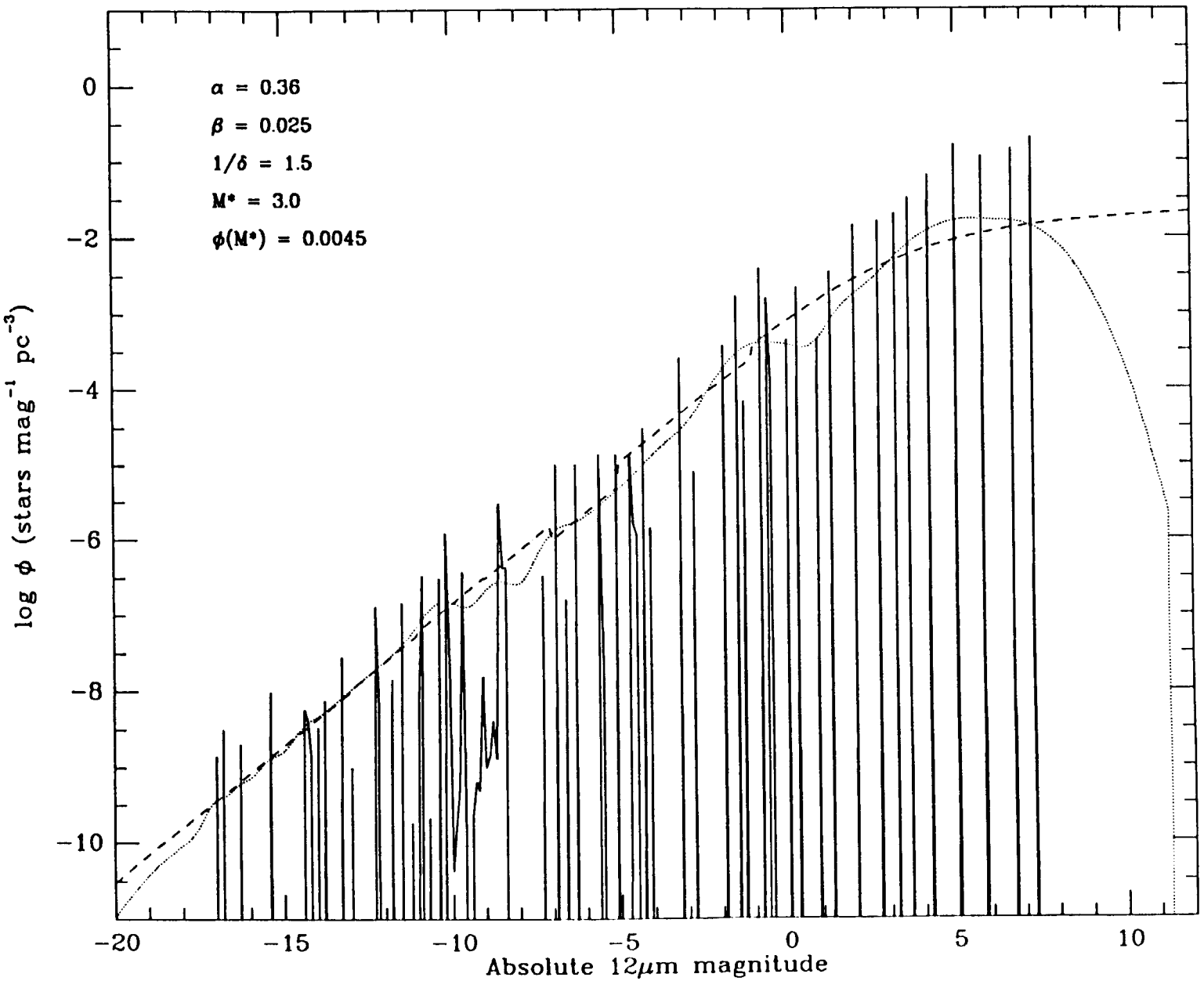
α = 0.36
β = 0.025
1/δ = 1.5
M* = 3.0
φ(M*) = 0.0045
log φ (stars mag⁻¹ pc⁻³)
0
−2
−4
−6
−8
−10
−20
−15
−10
−5
0
5
10
Absolute 12μm magnitude

Fig. 1c

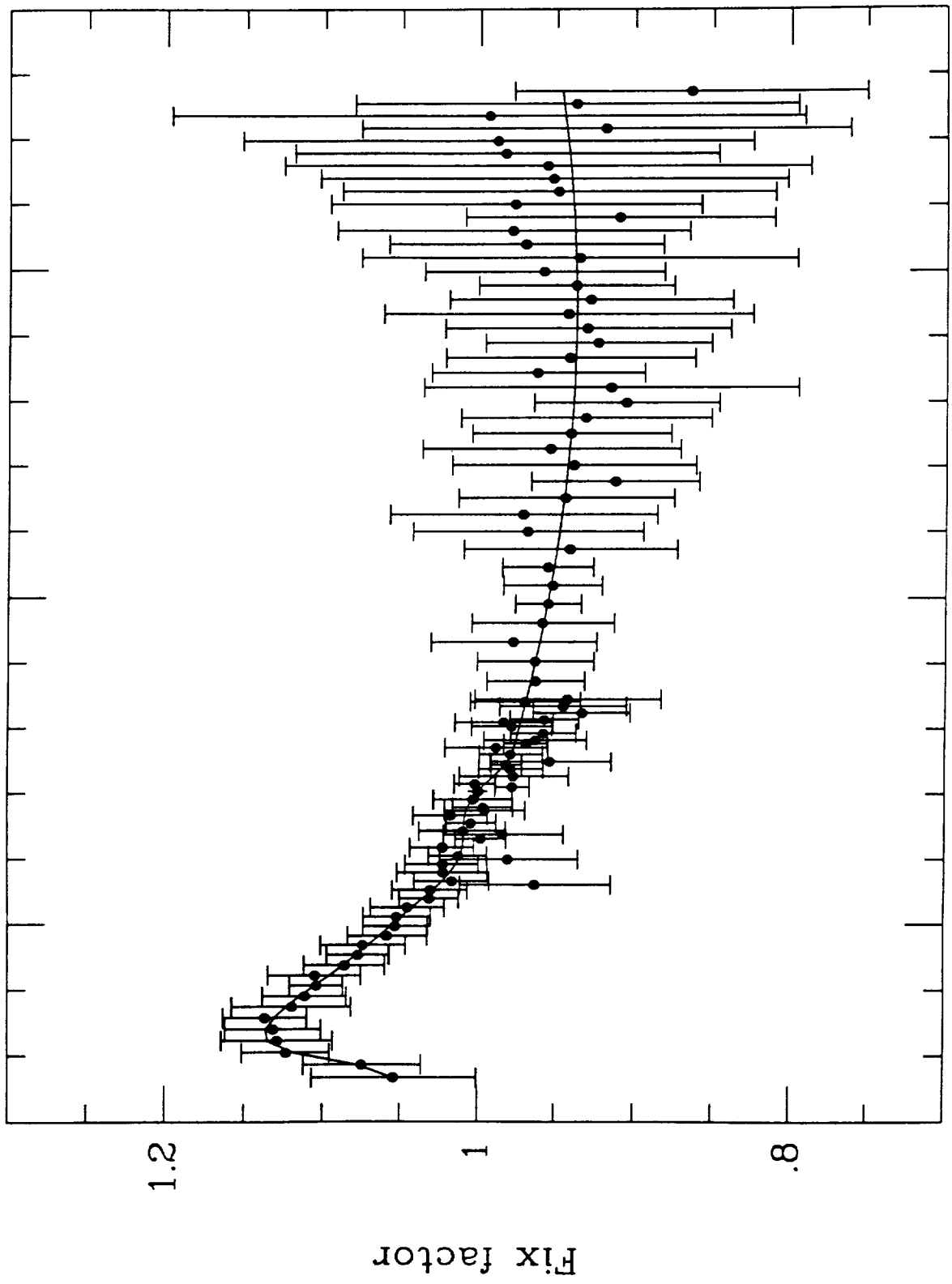

Fig. 2

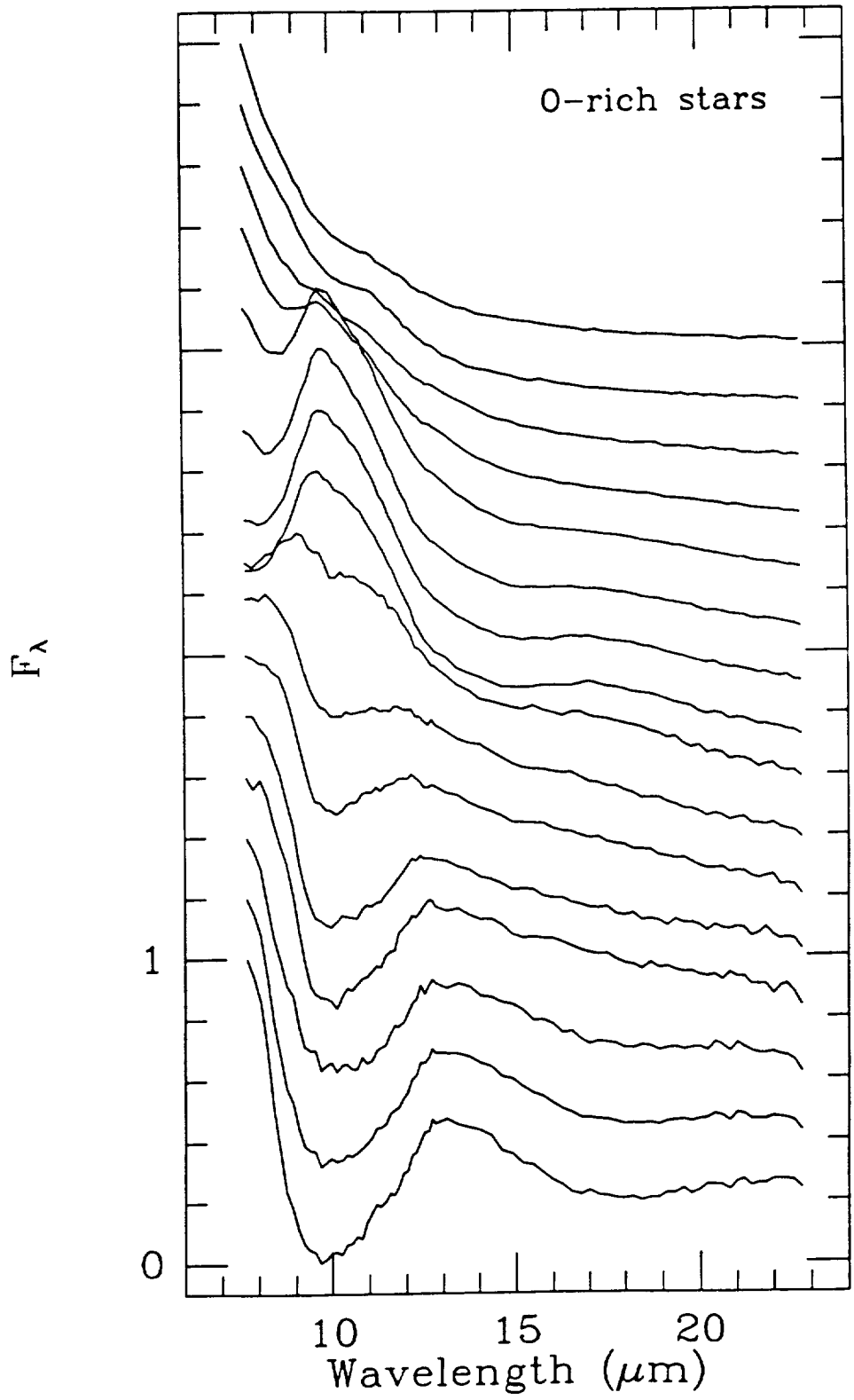

Fig. 3a

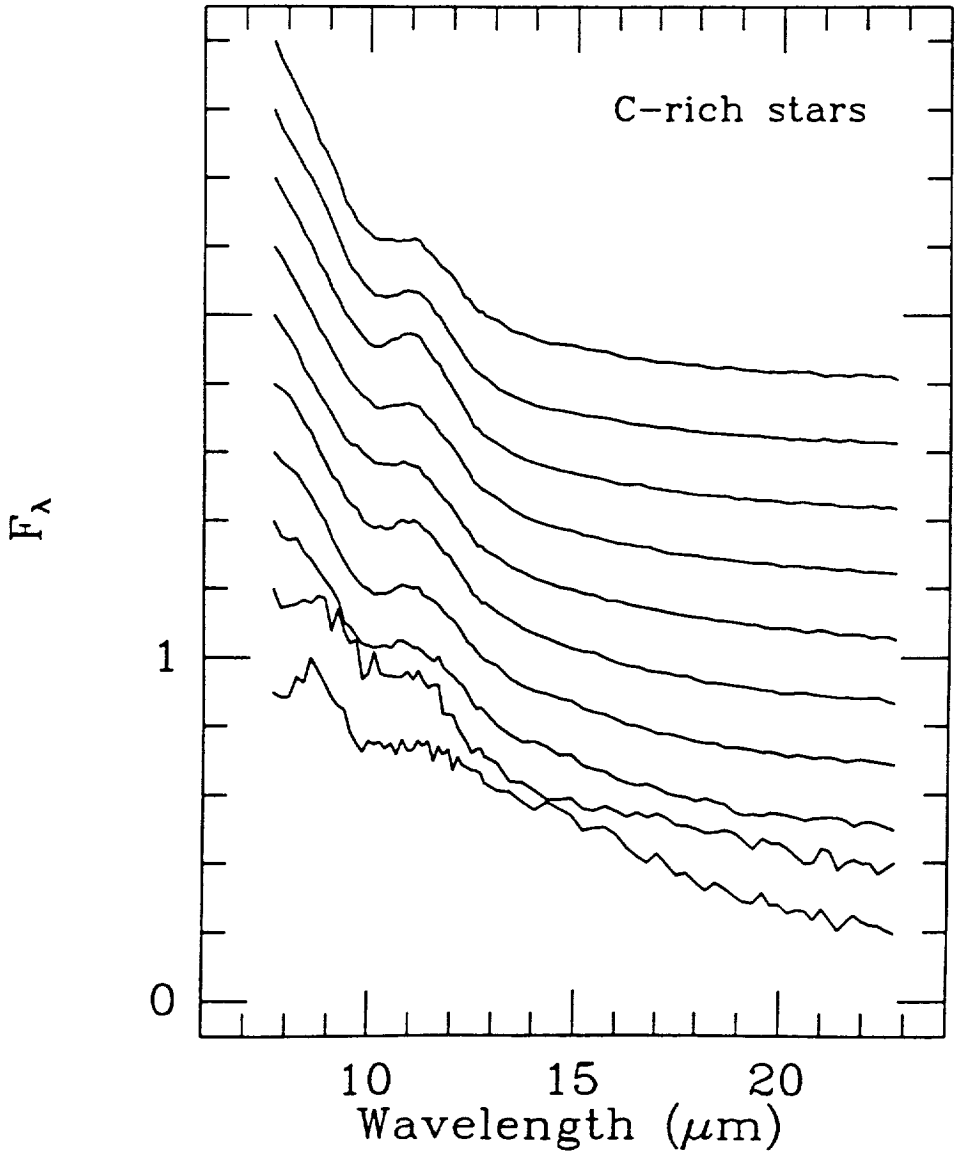

Fig. 3b

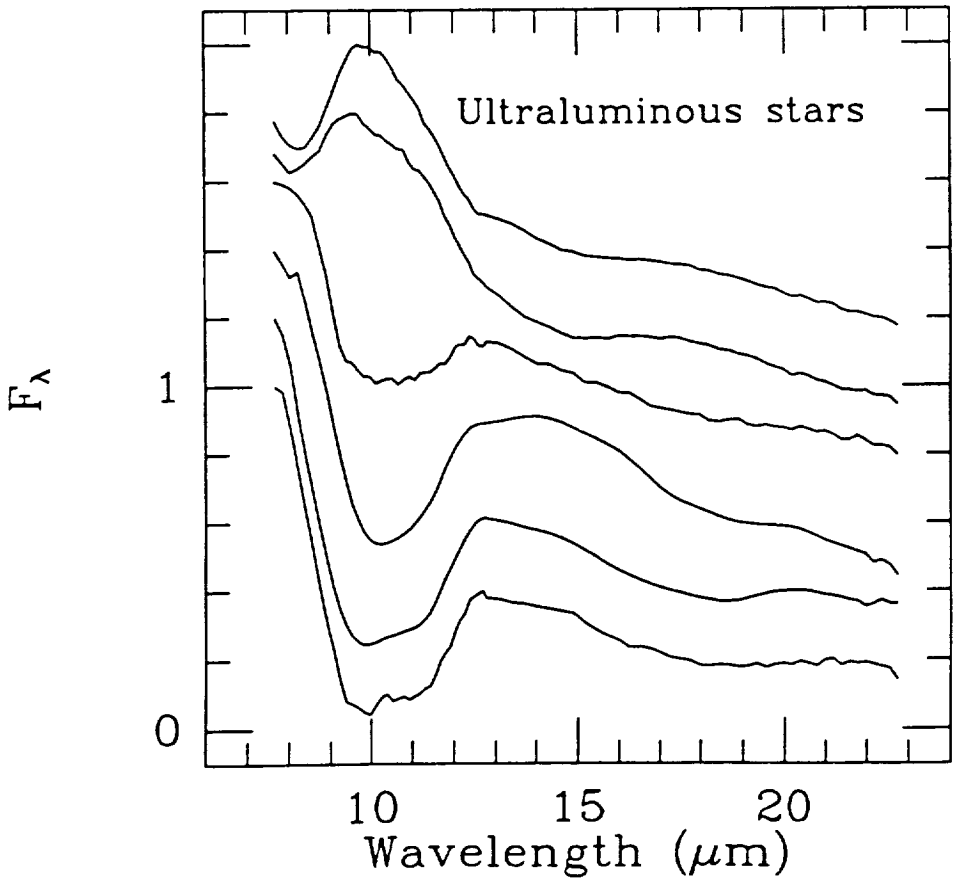

Fig. 3c

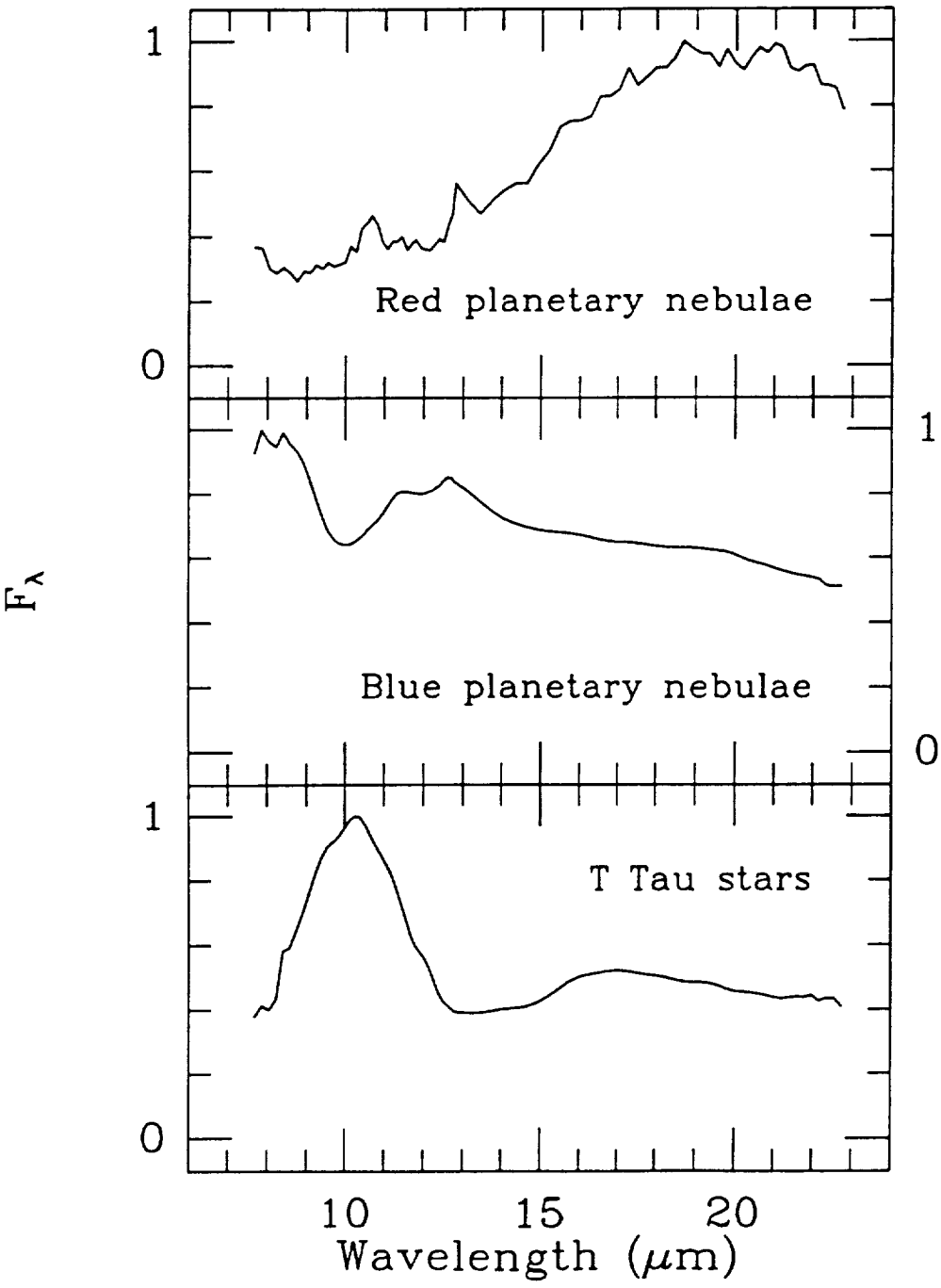
1
0
Red planetary nebulae
1
0
Blue planetary nebulae
1
0
T Tau stars
F_λ
10
15
20
Wavelength (μm)

Fig. 3d

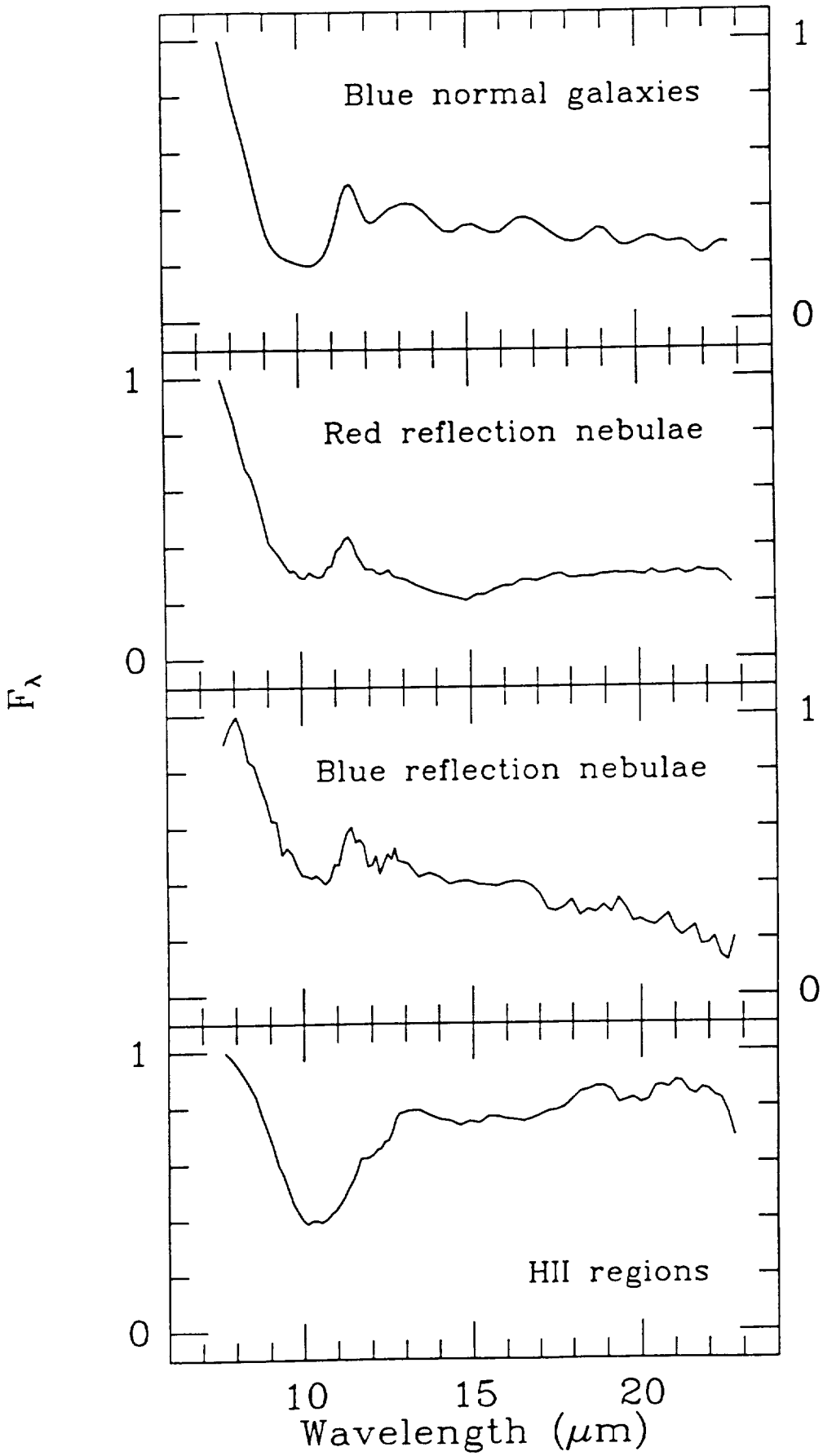
Blue normal galaxies
Red reflection nebulae
Blue reflection nebulae
HII regions
1
0
1
0
1
0
1
0
F_λ
10
15
20
Wavelength (μm)

Fig. 3e

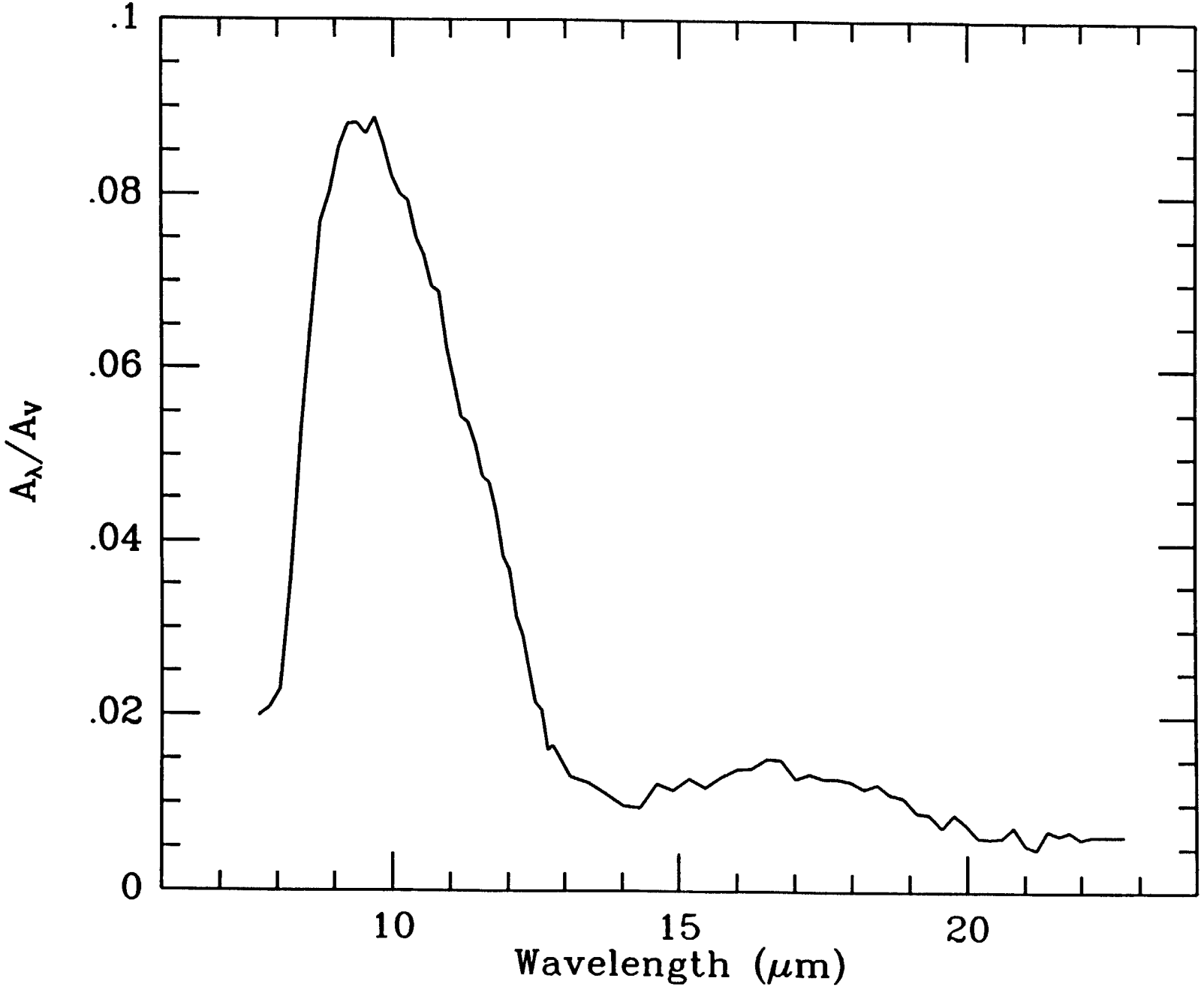

Fig. 4

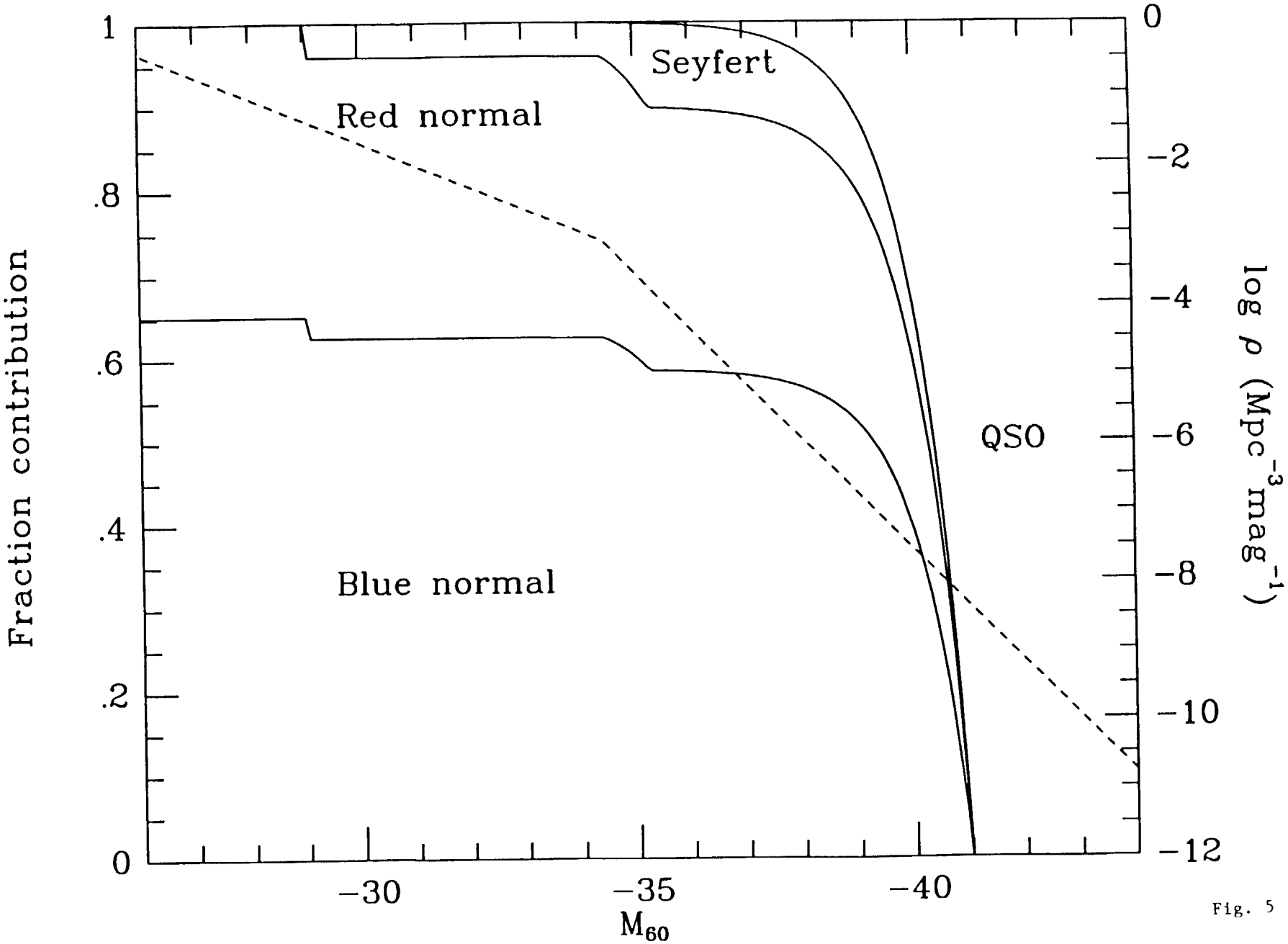
Fraction contribution
1
.8
.6
.4
.2
0
Seyfert
Red normal
Blue normal
QSO
−30
−35
−40
M_{60}
0
−2
−4
−6
−8
−10
−12
log ρ (Mpc^{-3} mag^{-1})

Fig. 5

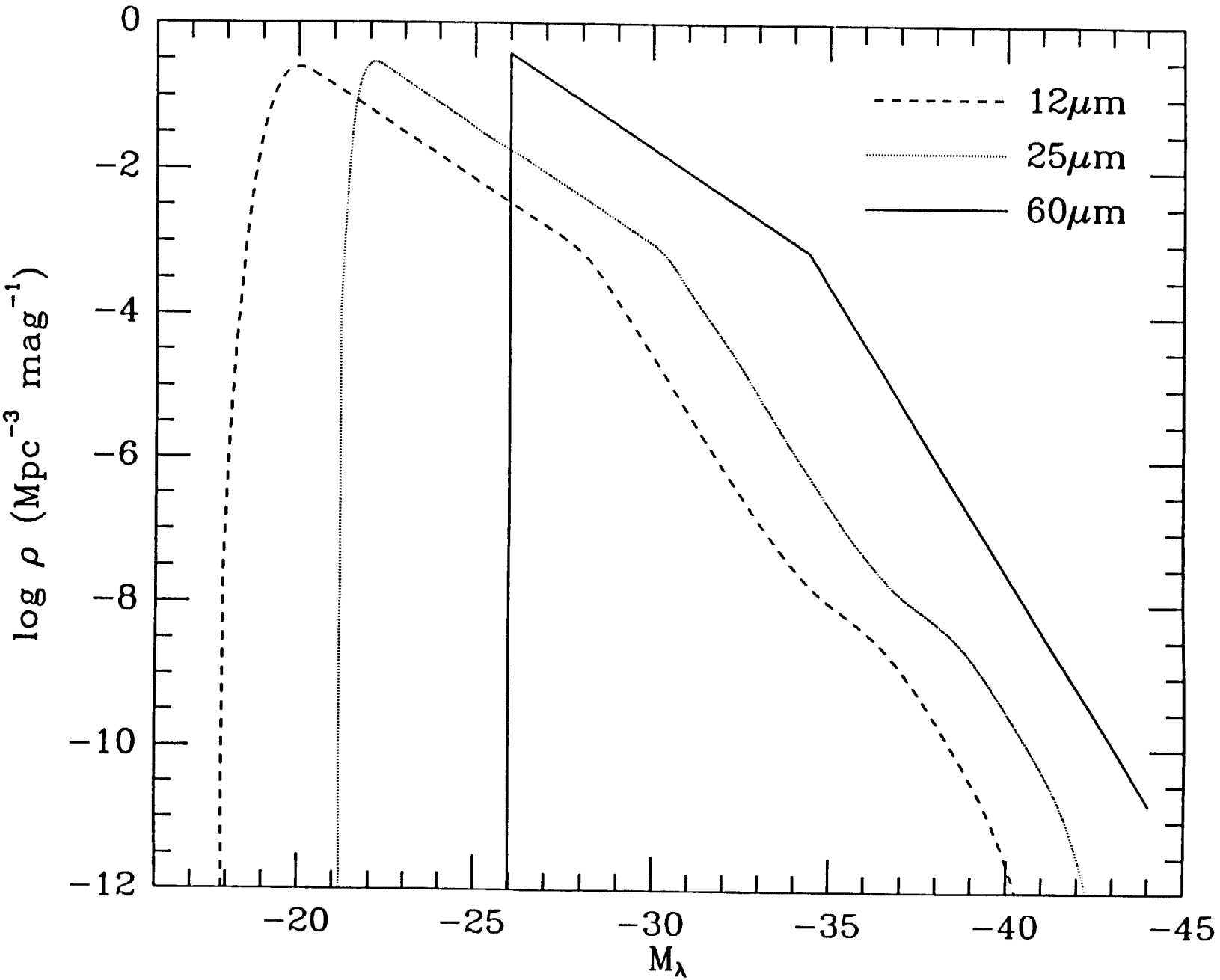
0
−2
−4
−6
−8
−10
−12
log ρ (Mpc^{-3} mag^{-1})
−20
−25
−30
−35
−40
−45
M_λ
12μm
25μm
60μm

Fig. 6

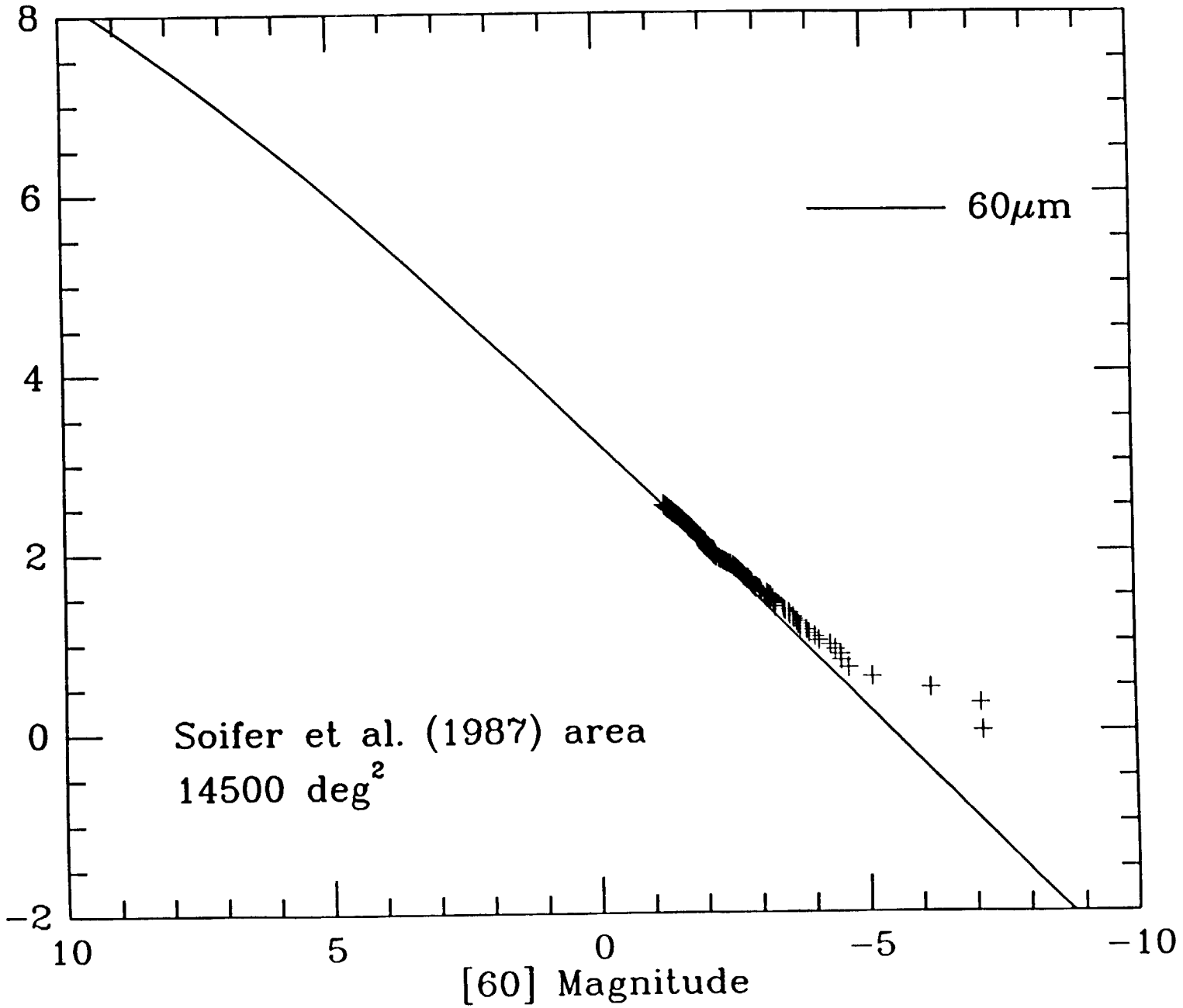
8
6
4
2
0
−2
log N
60μm
Soifer et al. (1987) area
14500 deg²
10
5
0
−5
−10
[60] Magnitude

Fig. 7a

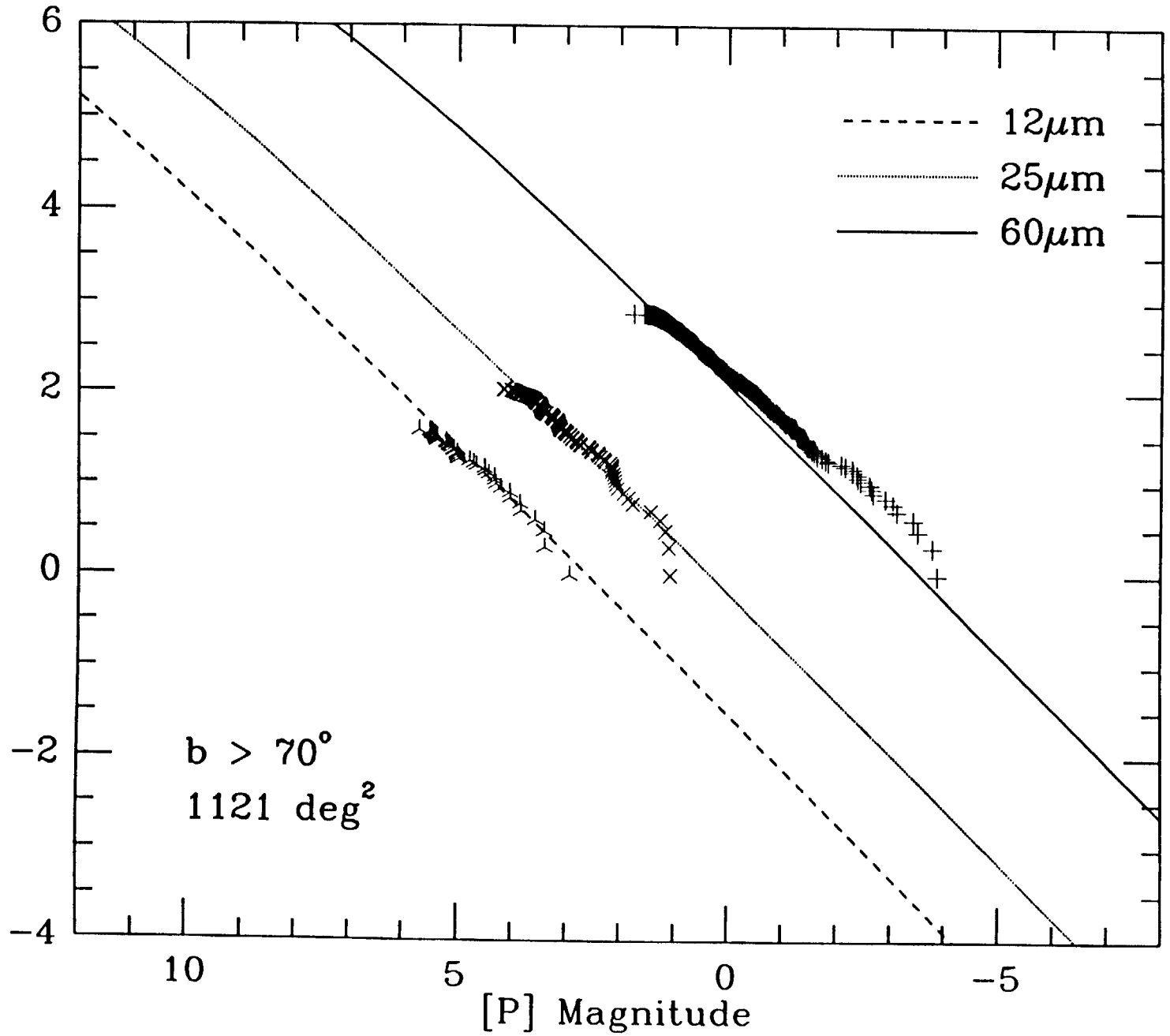
6
4
2
0
−2
−4
log N gal
10
5
0
−5
[P] Magnitude
12μm
25μm
60μm
b > 70°
1121 deg²

Fig. 7b

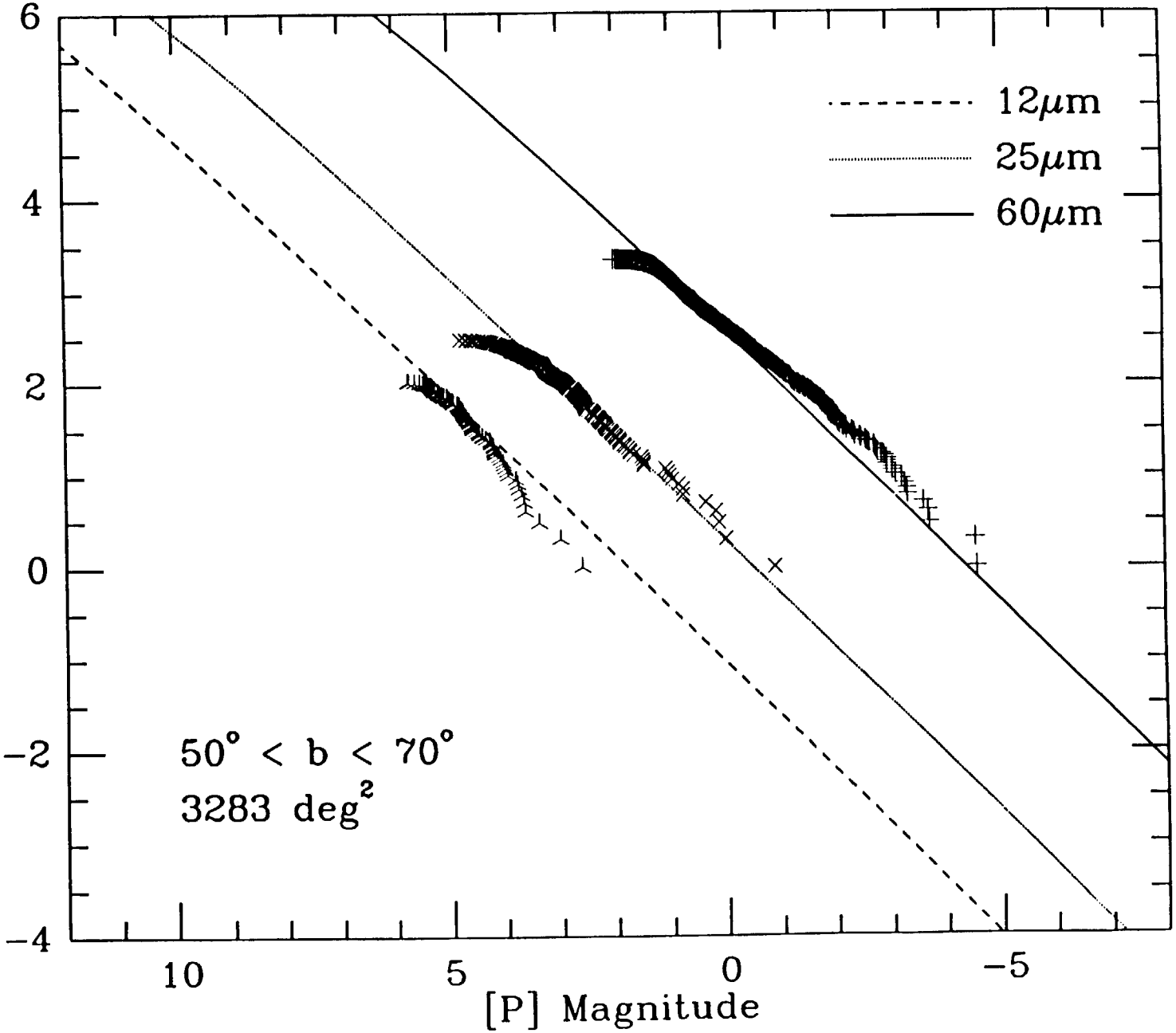
12μm
25μm
60μm
50° < b < 70°
3283 deg²
log N
[P] Magnitude
6
4
2
0
−2
−4
10
5
0
−5

Fig. 7c

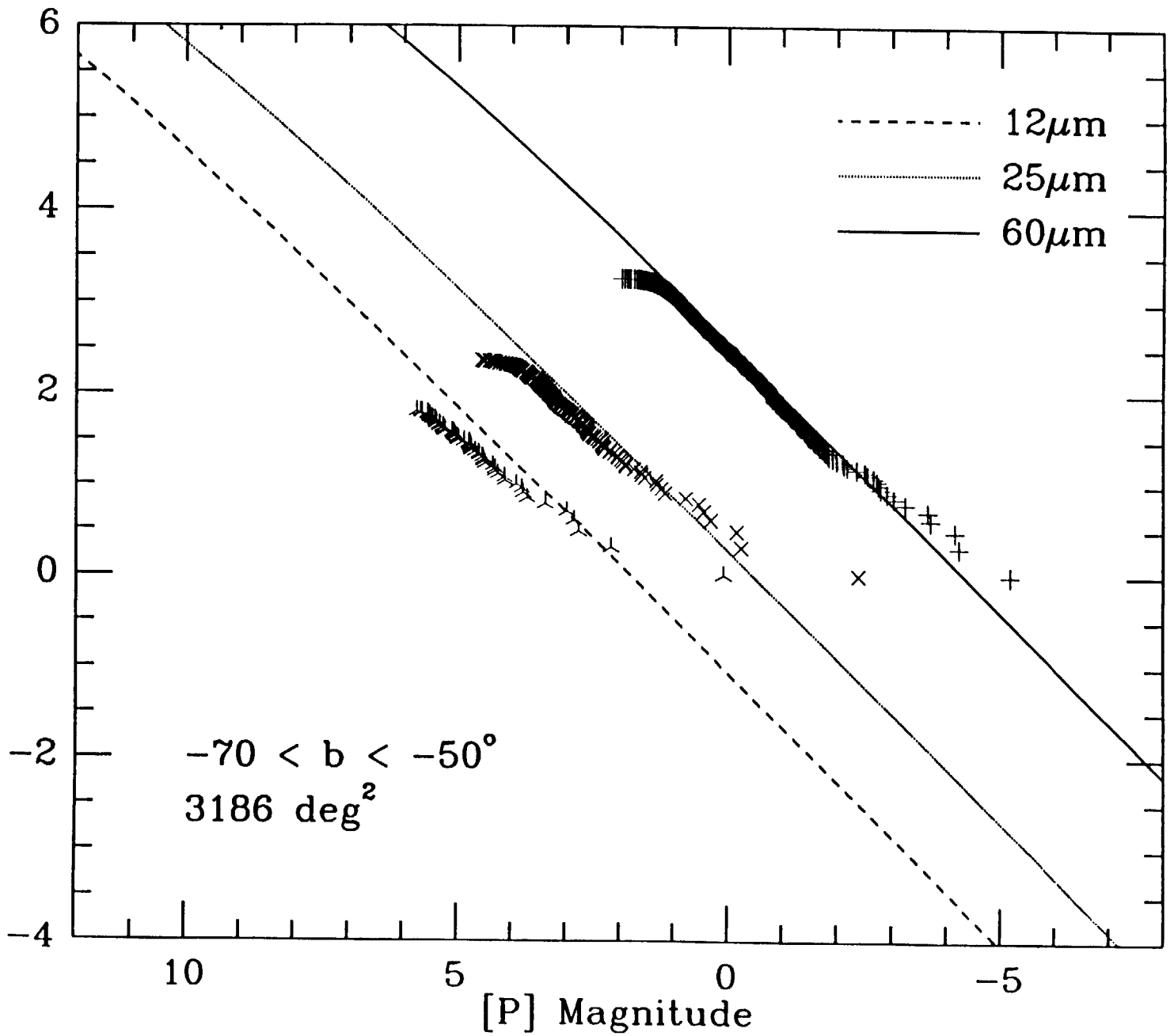
6
4
2
0
−2
−4
log N
10
5
0
−5
[P] Magnitude
12μm
25μm
60μm
−70 < b < −50°
3186 deg²

Fig. 7d

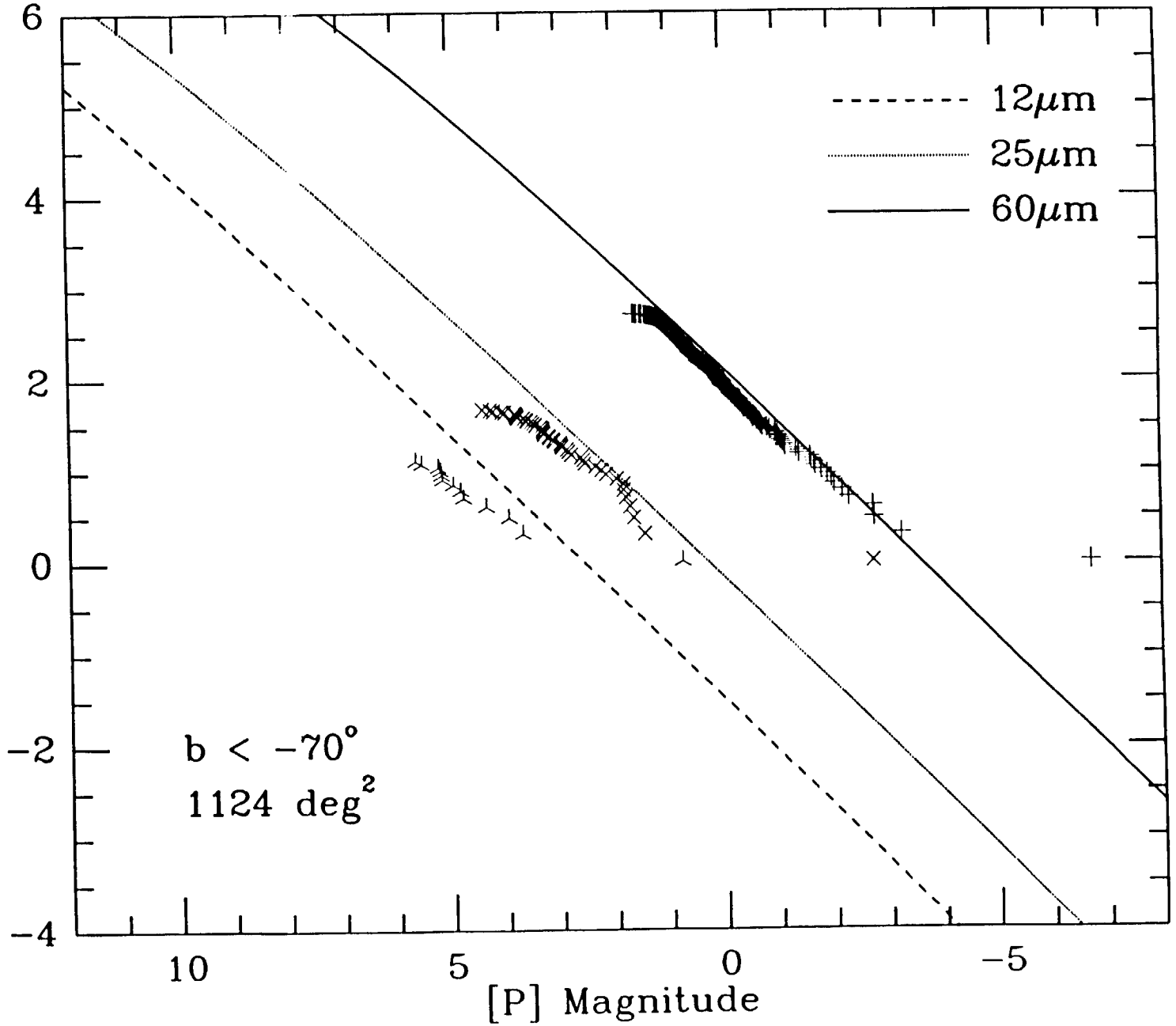

Fig. 7e

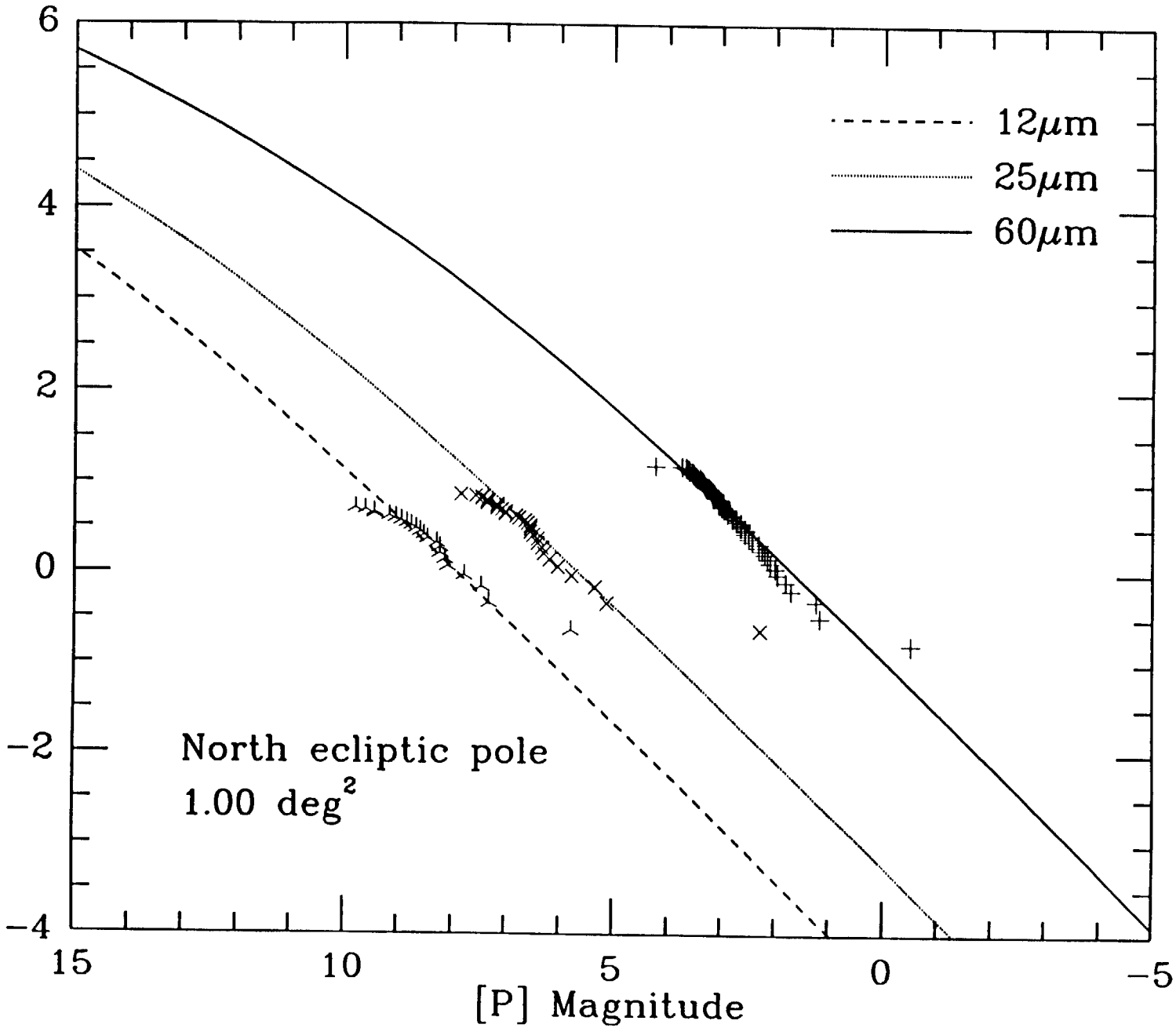
12μm
25μm
60μm
North ecliptic pole
1.00 deg²
log N
[P] Magnitude
6
4
2
0
−2
−4
15
10
5
0
−5

Fig. 7f

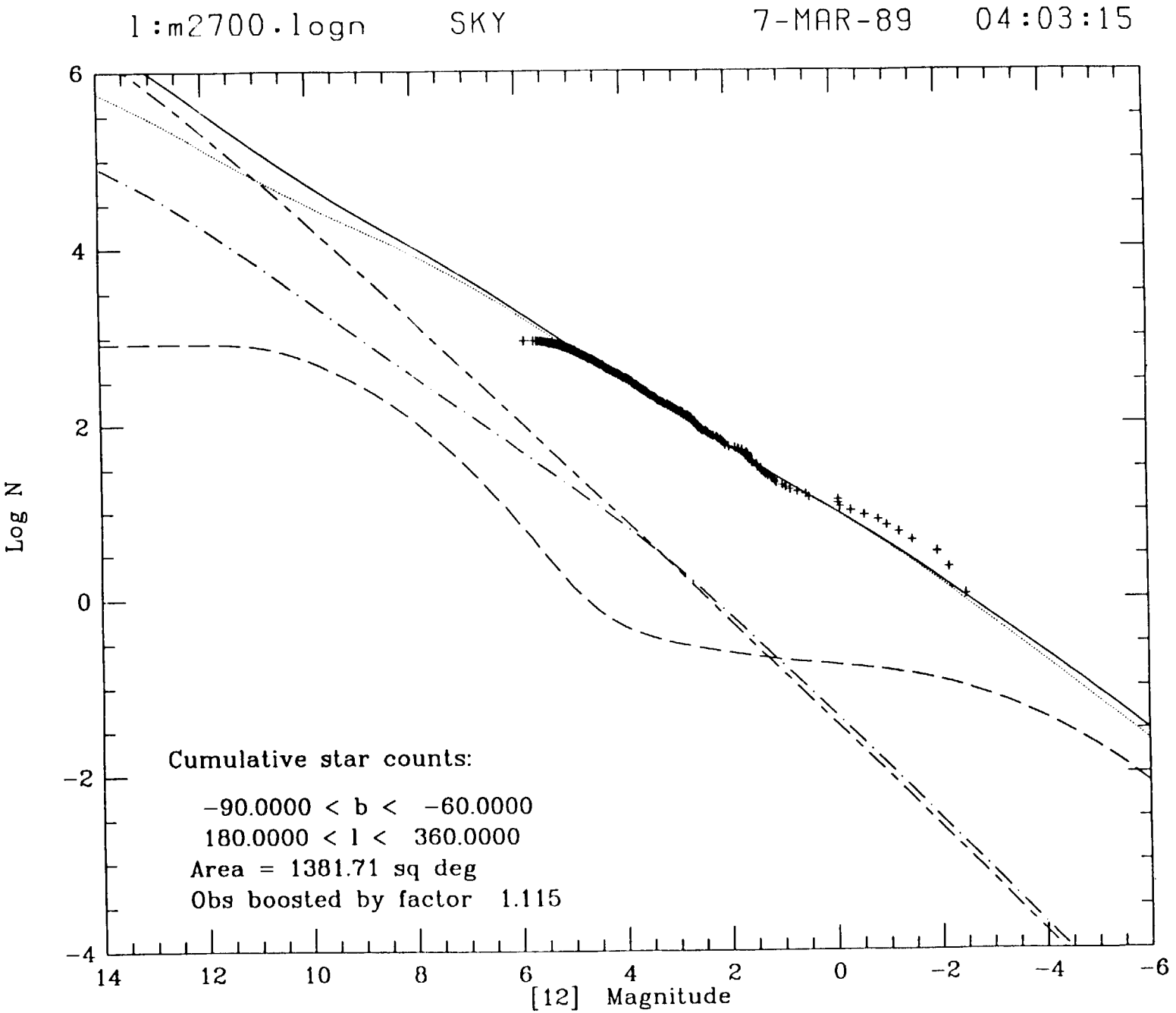
1:m2700.logn SKY 7-MAR-89 04:03:15
Log N
6
4
2
0
-2
-4
14
12
10
8
6
4
2
0
-2
-4
-6
[12] Magnitude
Cumulative star counts:
-90.0000 < b < -60.0000
180.0000 < l < 360.0000
Area = 1381.71 sq deg
Obs boosted by factor 1.115

Fig. 8a

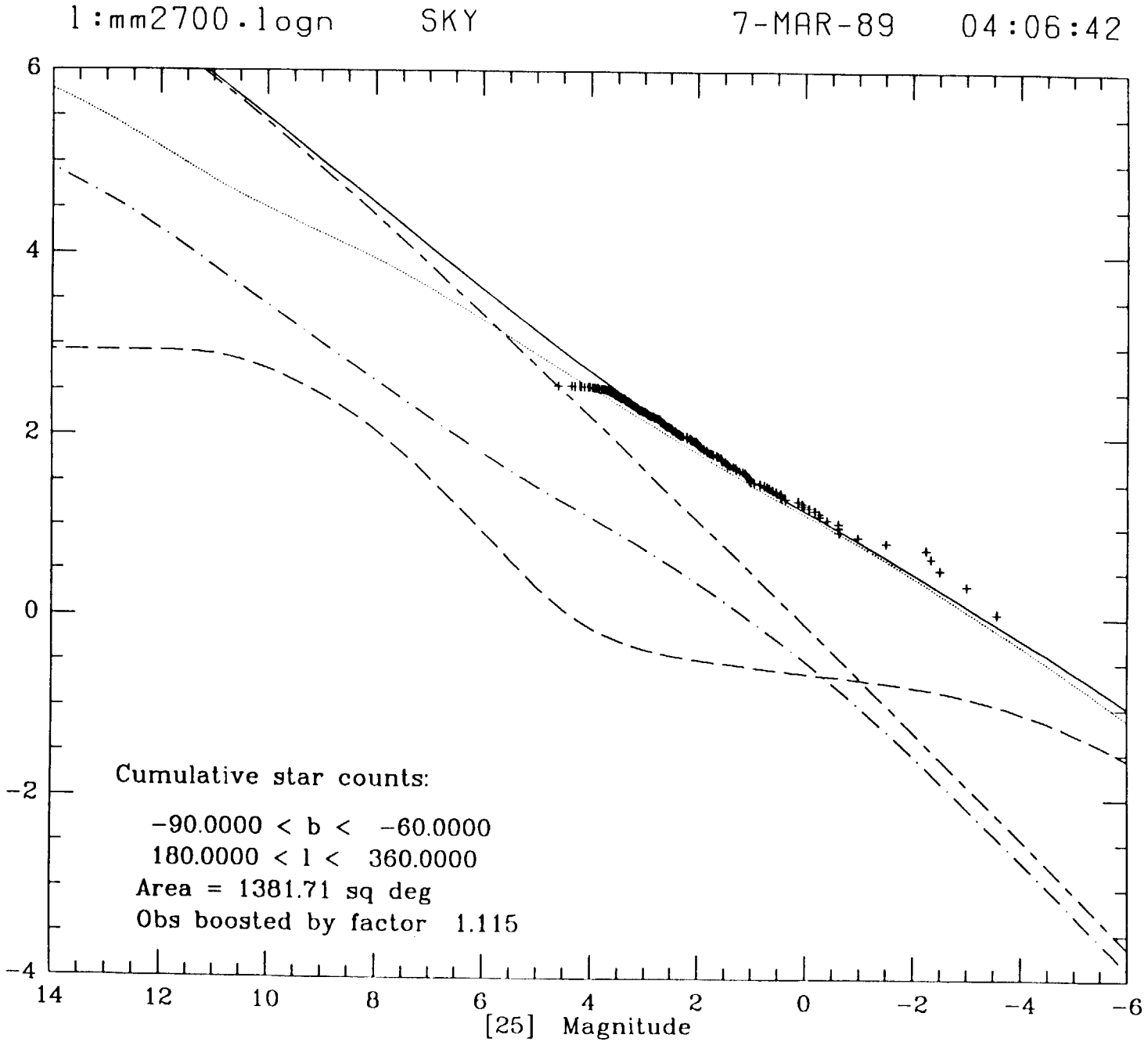
1:mm2700.logn SKY 7-MAR-89 04:06:42
Log N
6
4
2
0
-2
-4
14
12
10
8
6
4
2
0
-2
-4
-6
[25] Magnitude
Cumulative star counts:
-90.0000 < b < -60.0000
180.0000 < l < 360.0000
Area = 1381.71 sq deg
Obs boosted by factor 1.115

Fig. 8b

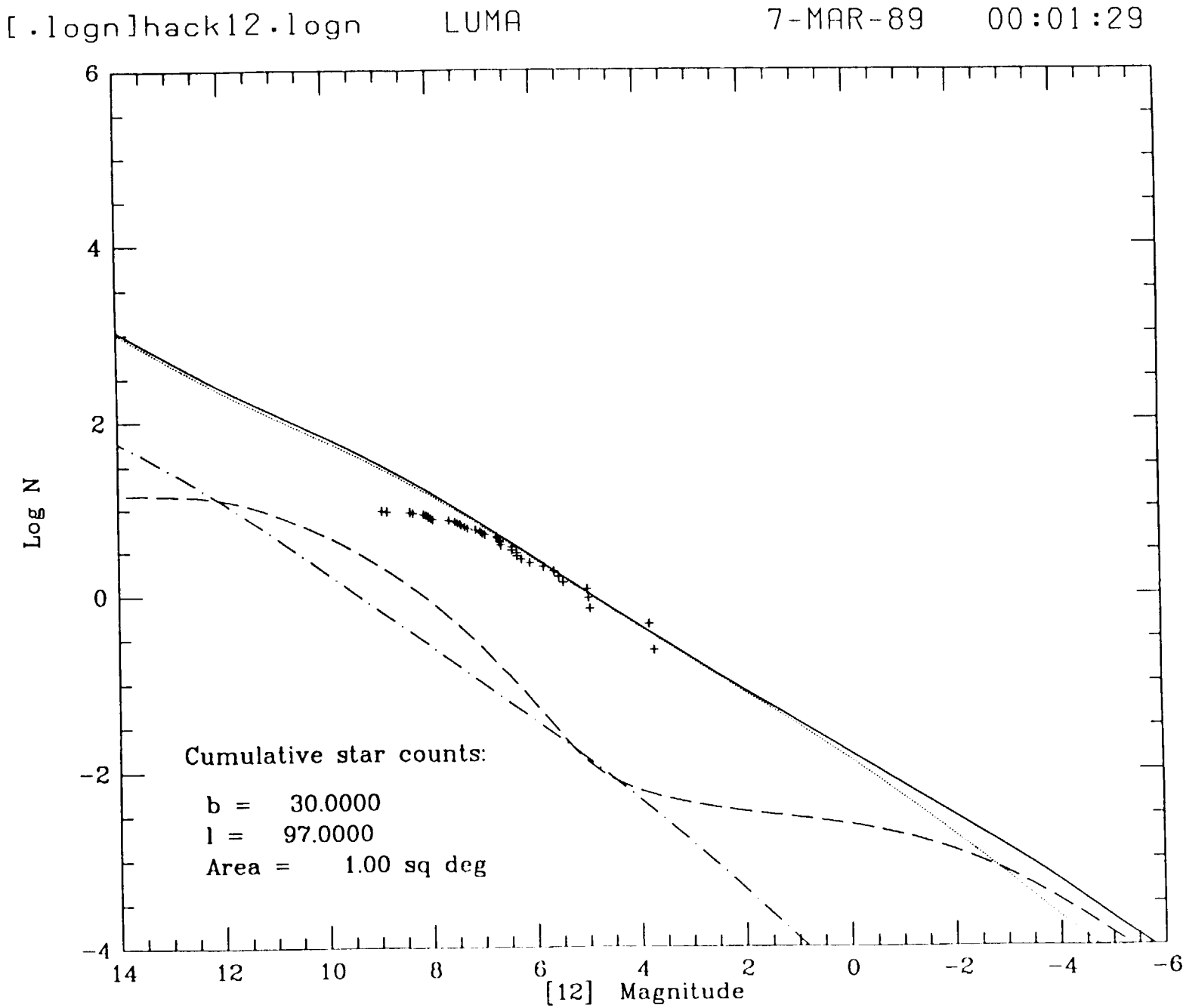
[.logn]hack12.logn LUMA 7-MAR-89 00:01:29
Log N
6
4
2
0
-2
-4
14
12
10
8
6
4
2
0
-2
-4
-6
[12] Magnitude
Cumulative star counts:
b = 30.0000
l = 97.0000
Area = 1.00 sq deg

Fig. 8c

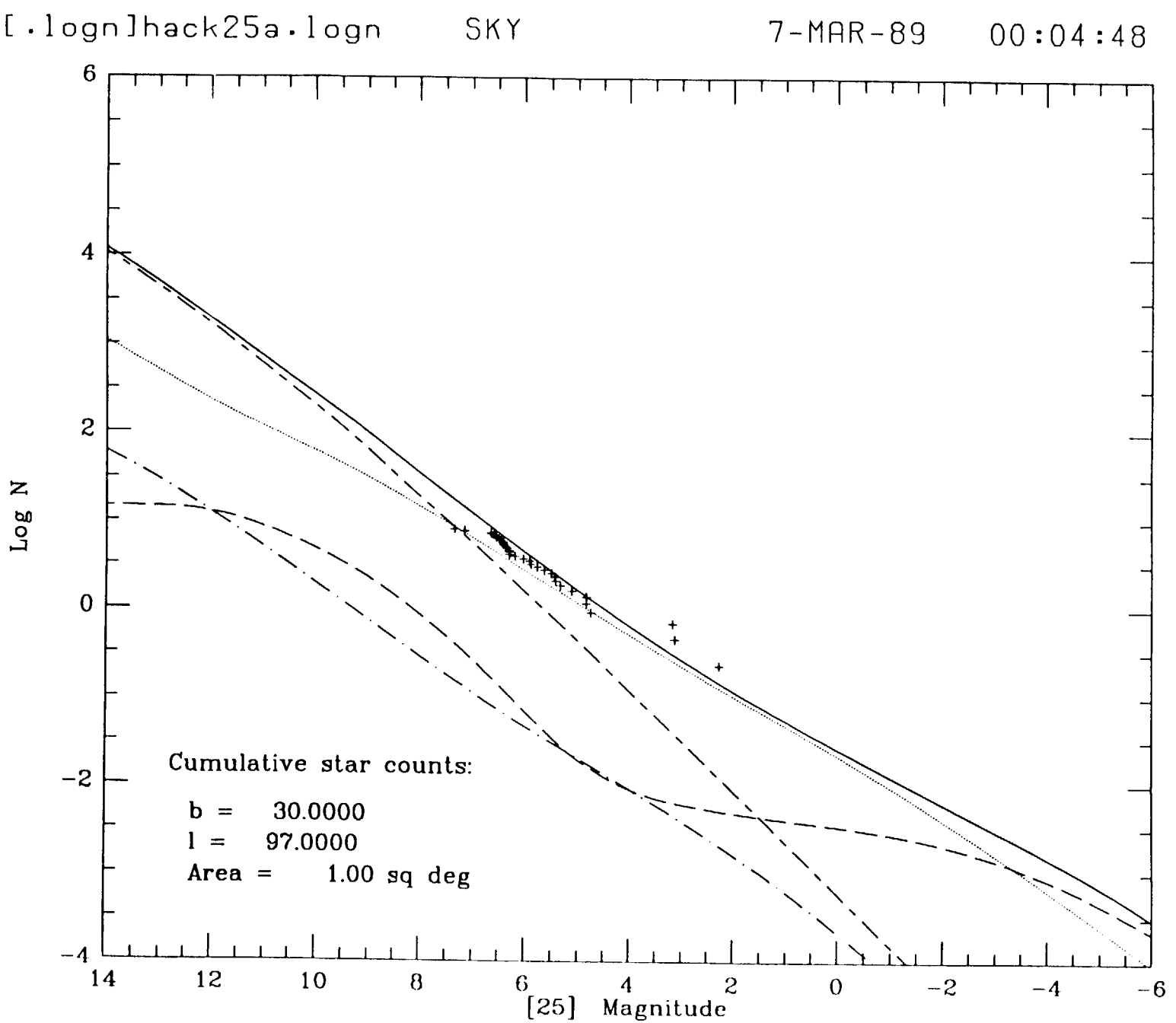
[.logn]hack25a.logn SKY 7-MAR-89 00:04:48
Log N
6
4
2
0
-2
-4
14
12
10
8
6
4
2
0
-2
-4
-6
[25] Magnitude
Cumulative star counts:
b = 30.0000
l = 97.0000
Area = 1.00 sq deg

Fig. 8d

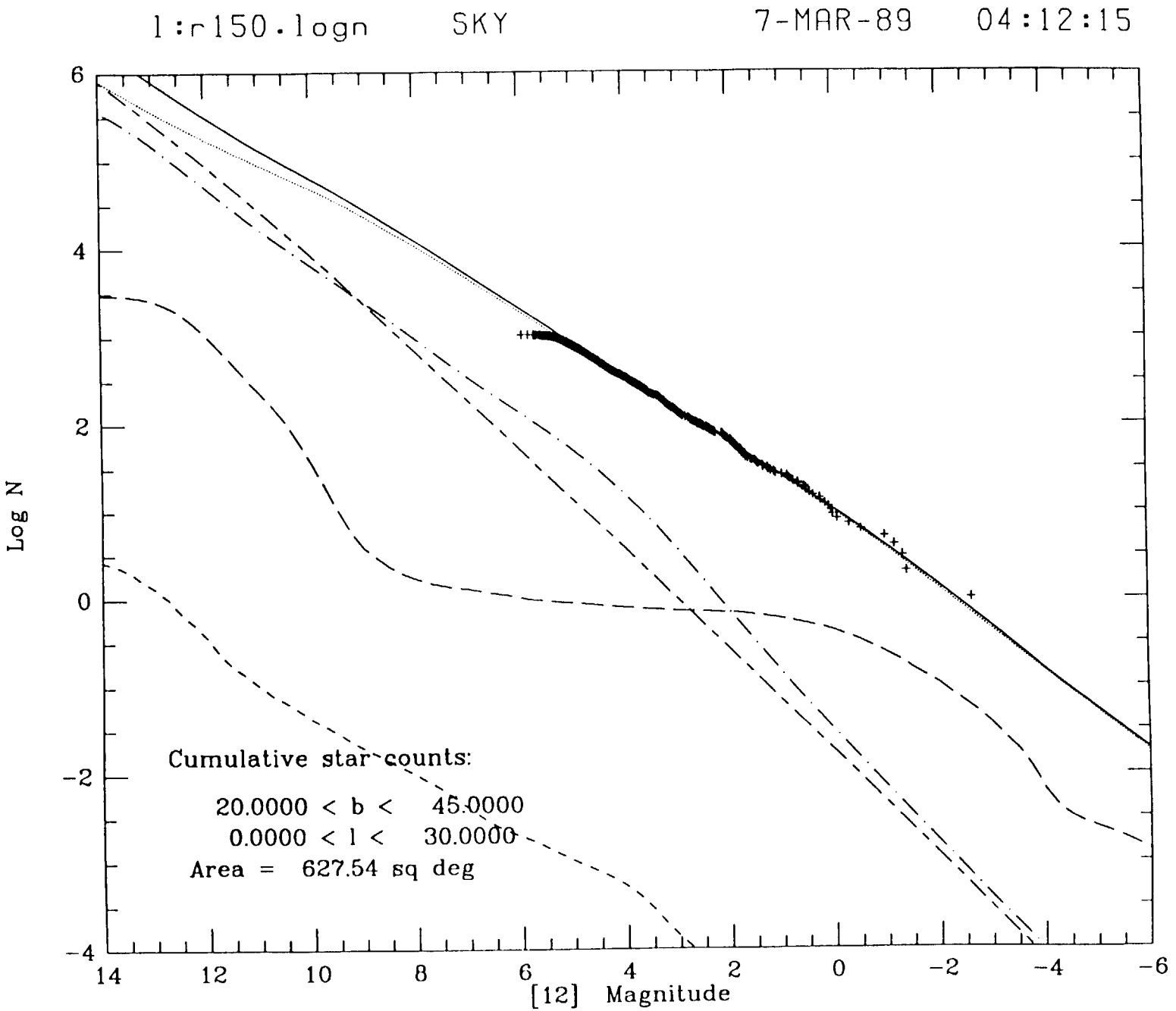
1:r150.logn SKY 7-MAR-89 04:12:15
Log N
[12] Magnitude
Cumulative star counts:
20.0000 < b < 45.0000
0.0000 < l < 30.0000
Area = 627.54 sq deg

Fig. 8e

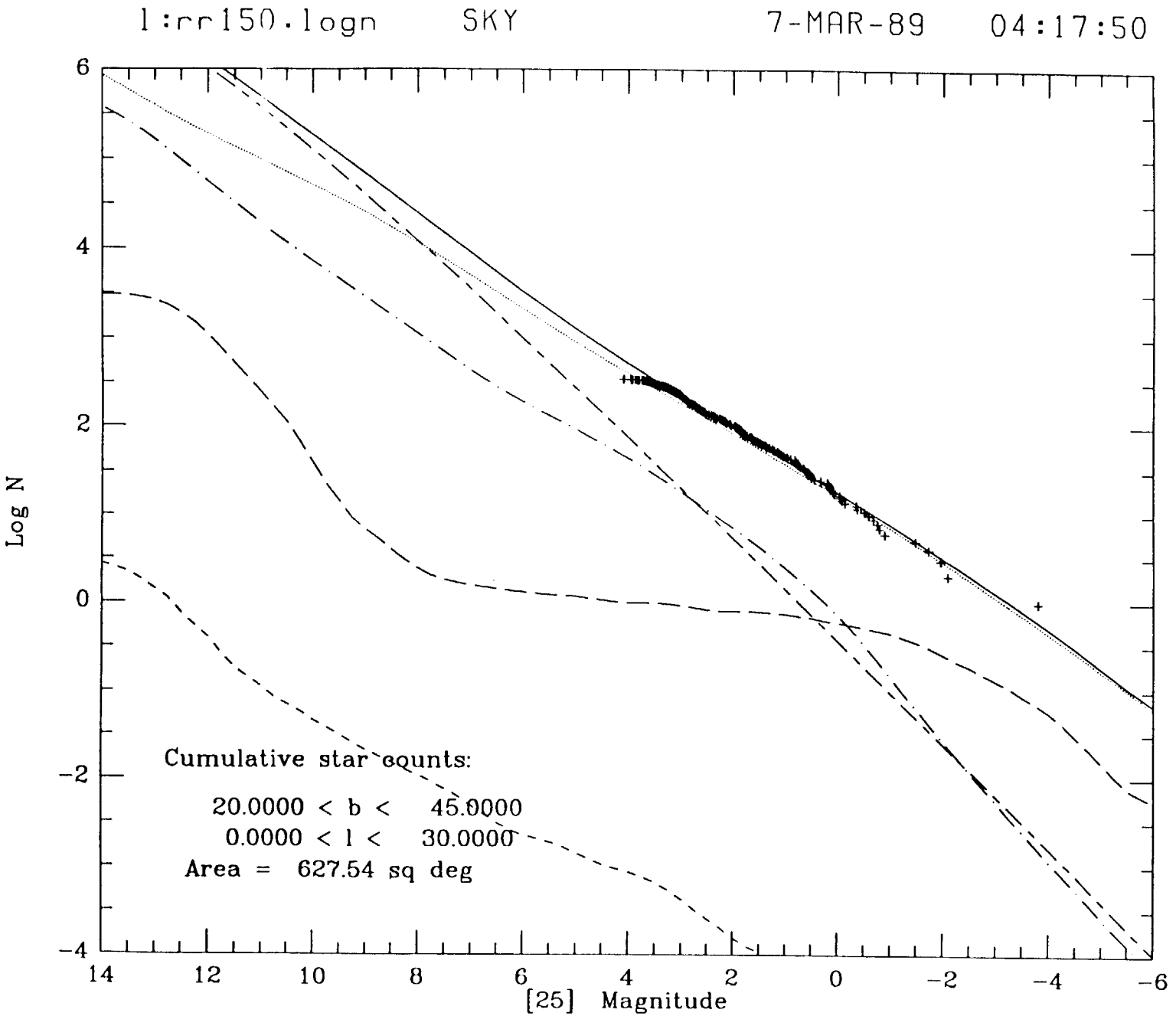
1:rr150.logn SKY 7-MAR-89 04:17:50
Log N
6
4
2
0
-2
-4
14
12
10
8
6
4
2
0
-2
-4
-6
[25] Magnitude
Cumulative star counts:
20.0000 < b < 45.0000
0.0000 < l < 30.0000
Area = 627.54 sq deg

Fig. 8f

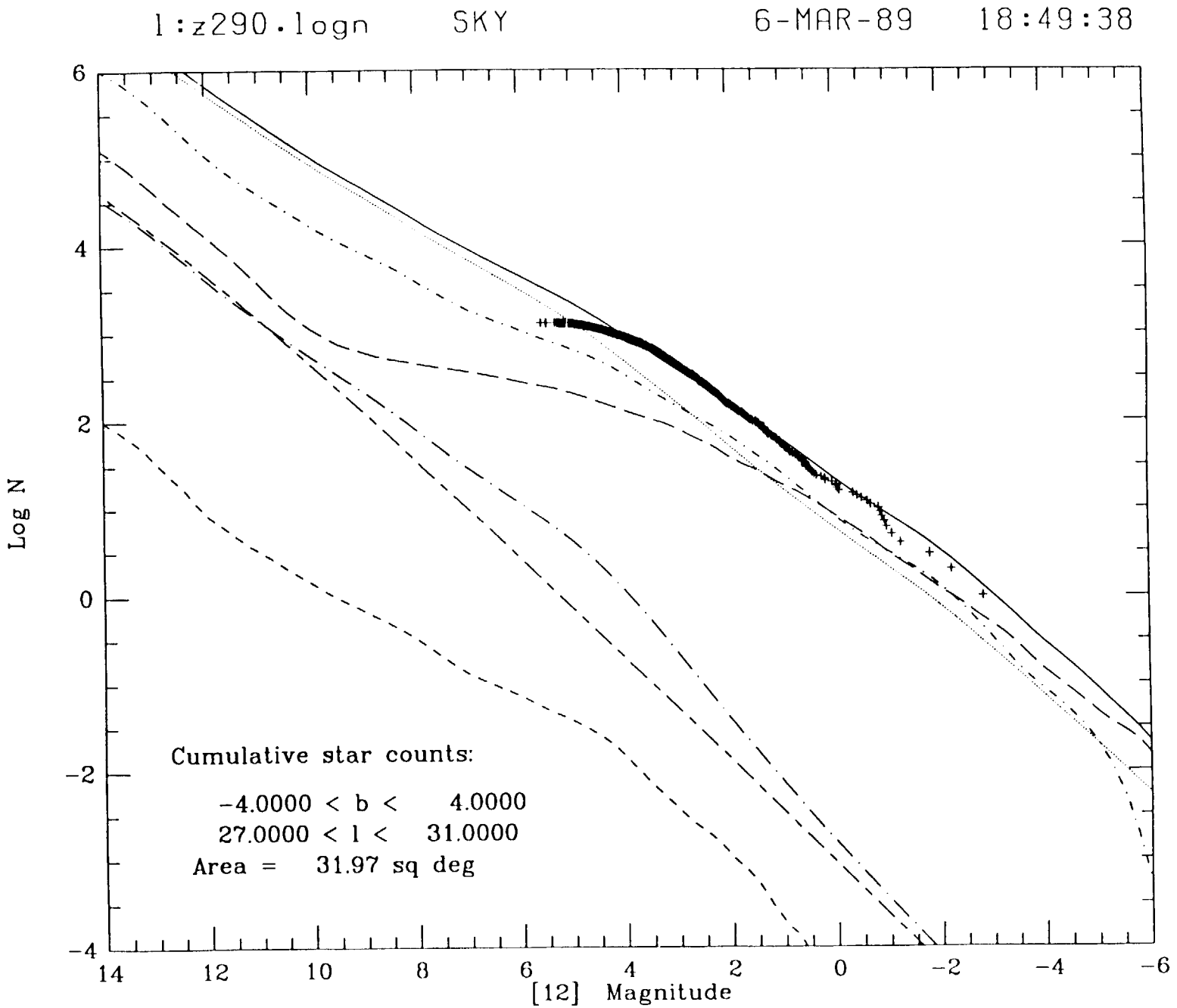
1:z290.logn SKY 6-MAR-89 18:49:38
Log N
[12] Magnitude
Cumulative star counts:
-4.0000 < b < 4.0000
27.0000 < l < 31.0000
Area = 31.97 sq deg

Fig. 8g

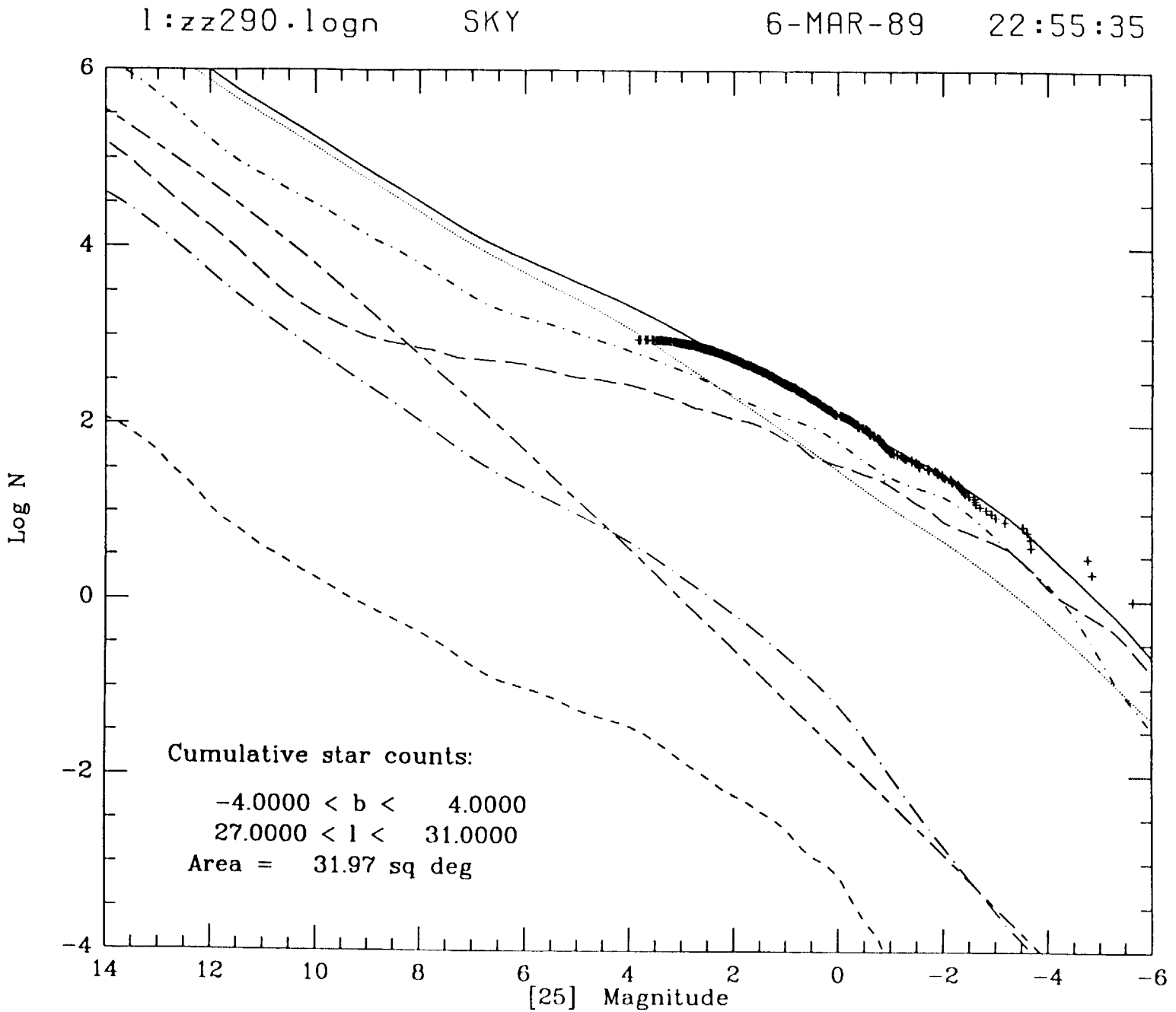
l:zz290.logn SKY 6-MAR-89 22:55:35
Log N
[25] Magnitude
Cumulative star counts:
-4.0000 < b < 4.0000
27.0000 < l < 31.0000
Area = 31.97 sq deg

Fig. 8h

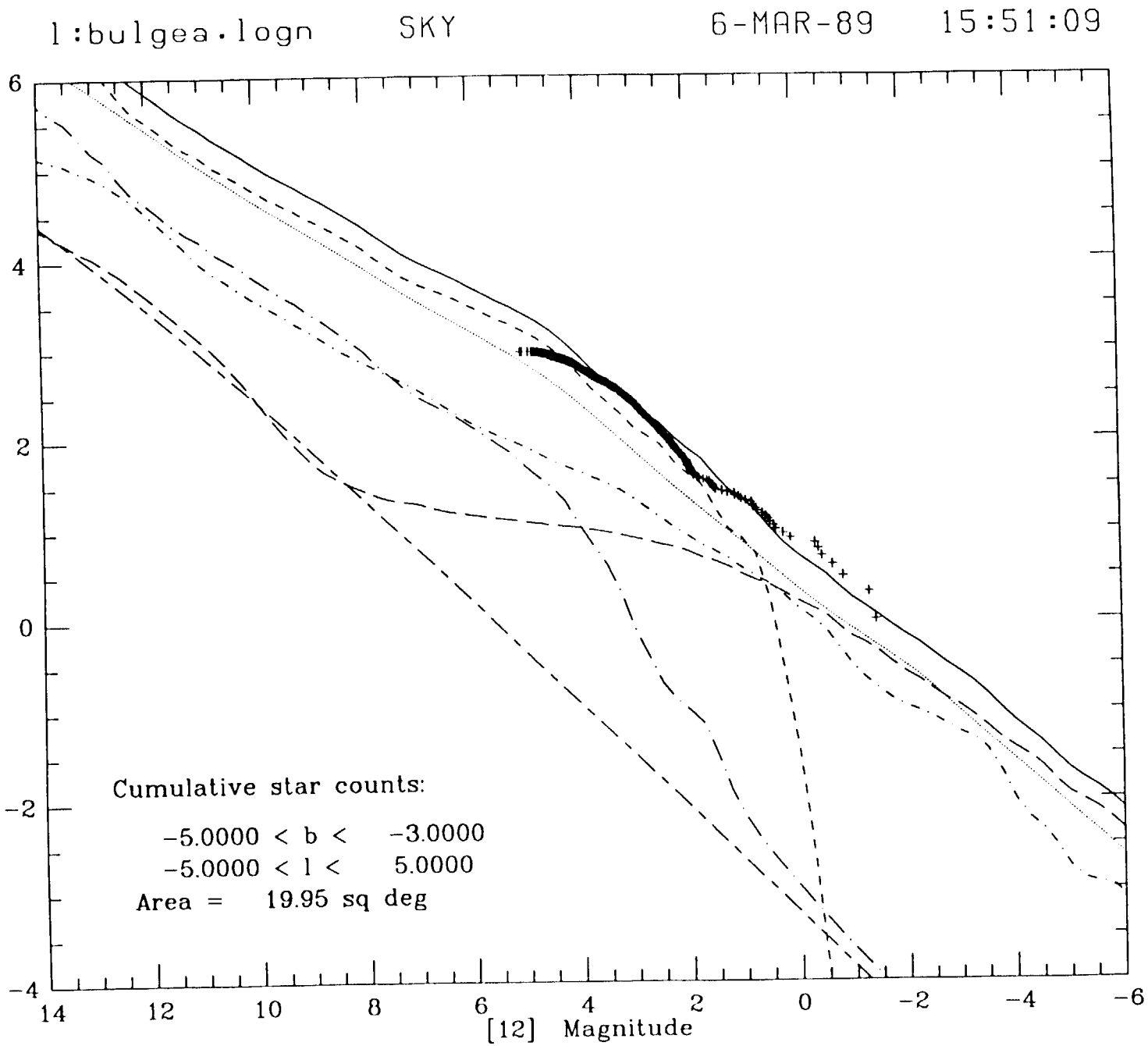
l:bulgea.logn SKY 6-MAR-89 15:51:09
Log N
[12] Magnitude
Cumulative star counts:
-5.0000 < b < -3.0000
-5.0000 < l < 5.0000
Area = 19.95 sq deg

Fig. 8i

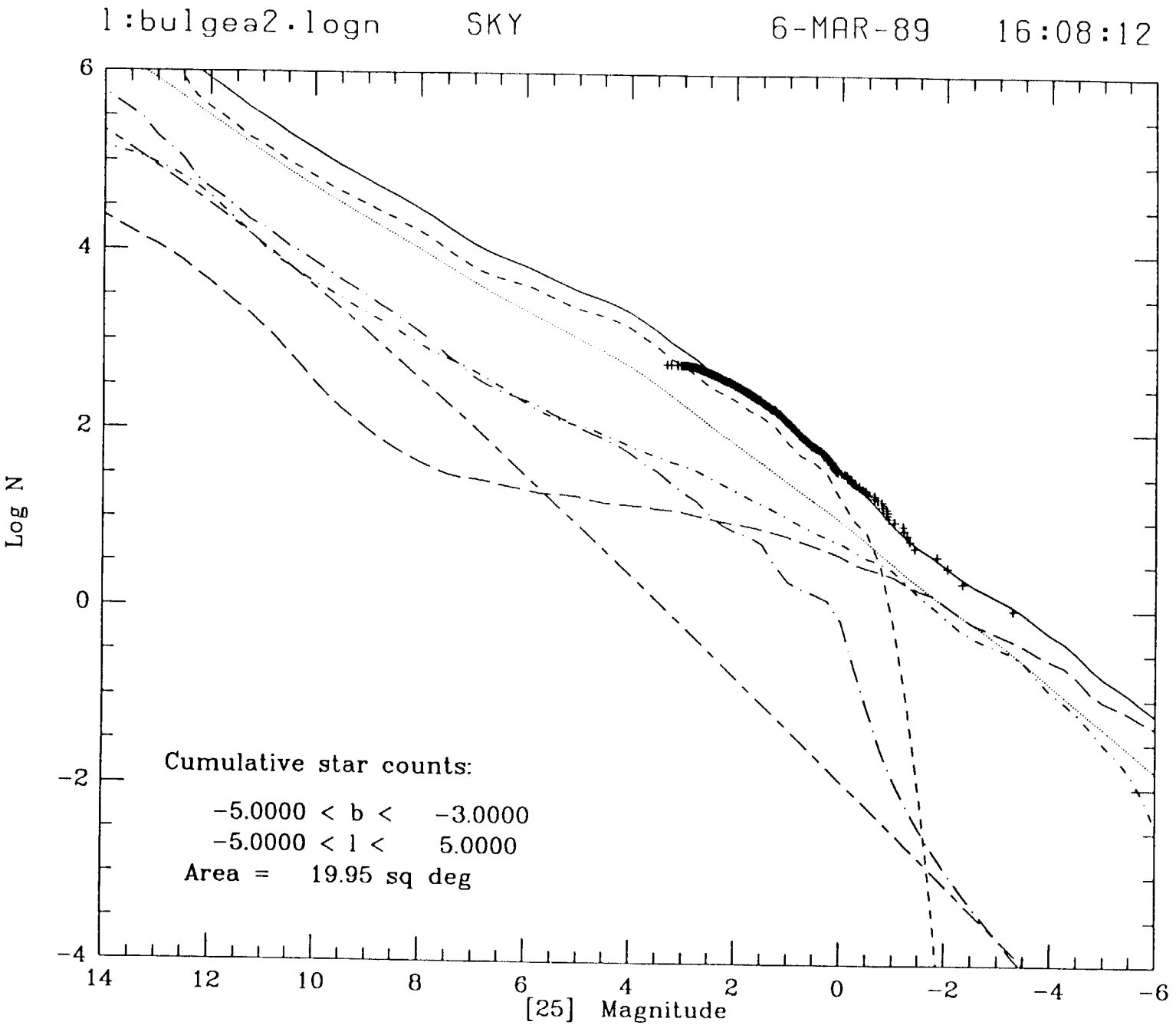
1:bulgea2.logn SKY 6-MAR-89 16:08:12
Log N gal
6
4
2
0
-2
-4
14
12
10
8
6
4
2
0
-2
-4
-6
[25] Magnitude
Cumulative star counts:
-5.0000 < b < -3.0000
-5.0000 < l < 5.0000
Area = 19.95 sq deg

Fig. 8j

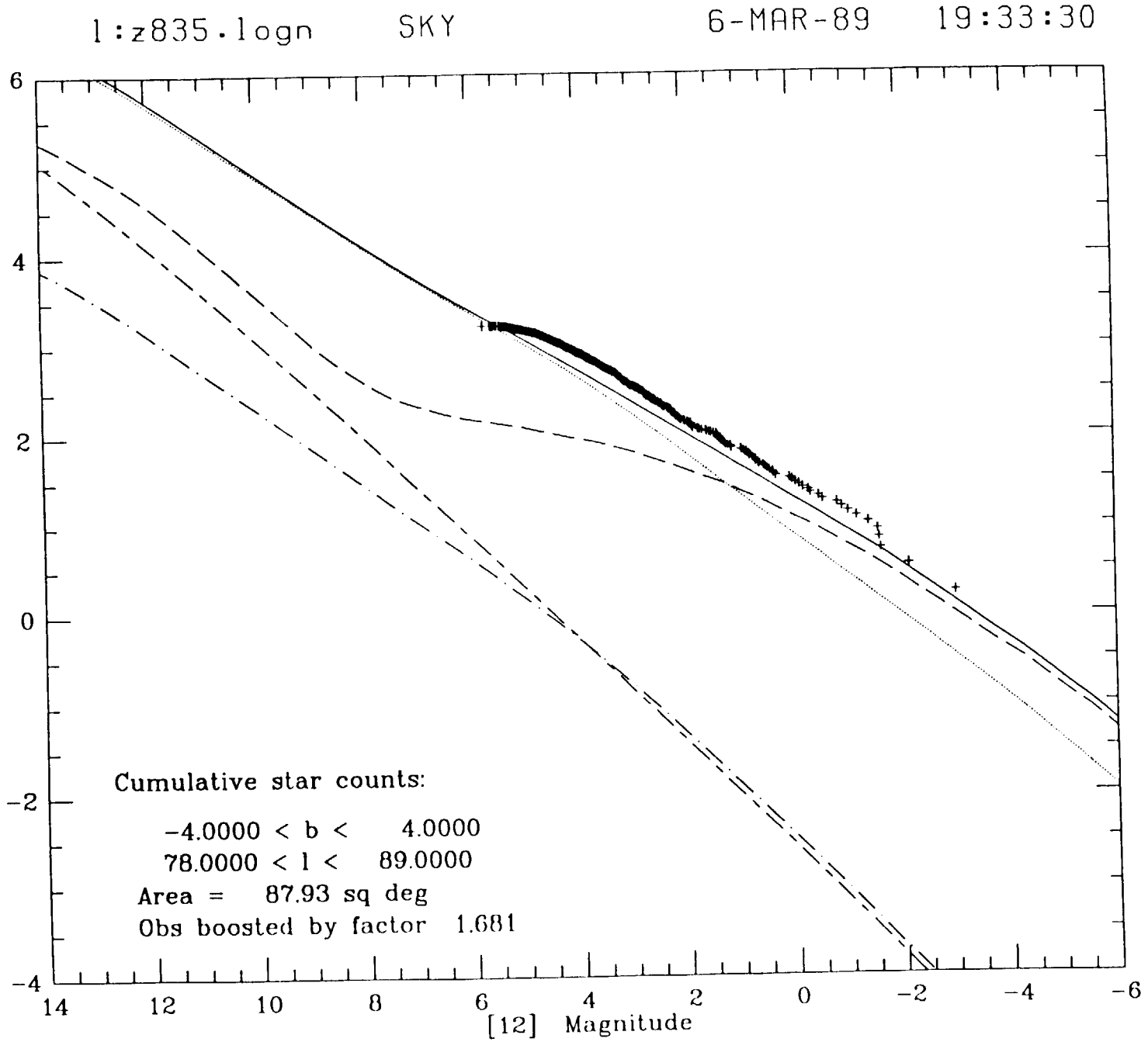
1:z835.logn SKY 6-MAR-89 19:33:30
Log N
6
4
2
0
-2
-4
14
12
10
8
6
4
2
0
-2
-4
-6
[12] Magnitude
Cumulative star counts:
-4.0000 < b < 4.0000
78.0000 < l < 89.0000
Area = 87.93 sq deg
Obs boosted by factor 1.681

Fig. 8k

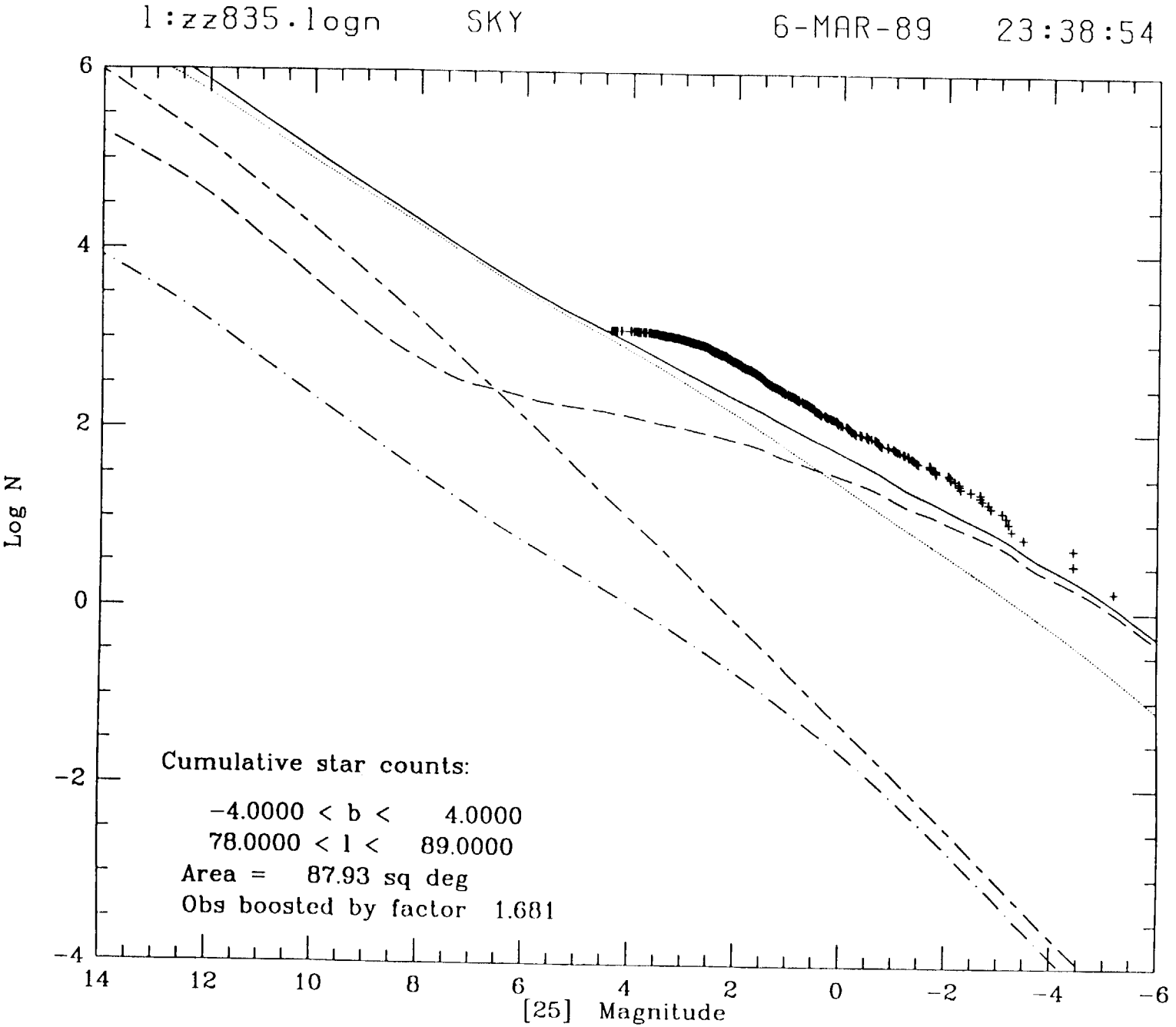
1:zz835.logn SKY 6-MAR-89 23:38:54
Log N
6
4
2
0
-2
-4
14
12
10
8
6
4
2
0
-2
-4
-6
[25] Magnitude
Cumulative star counts:
-4.0000 < b < 4.0000
78.0000 < l < 89.0000
Area = 87.93 sq deg
Obs boosted by factor 1.681

Fig. 81

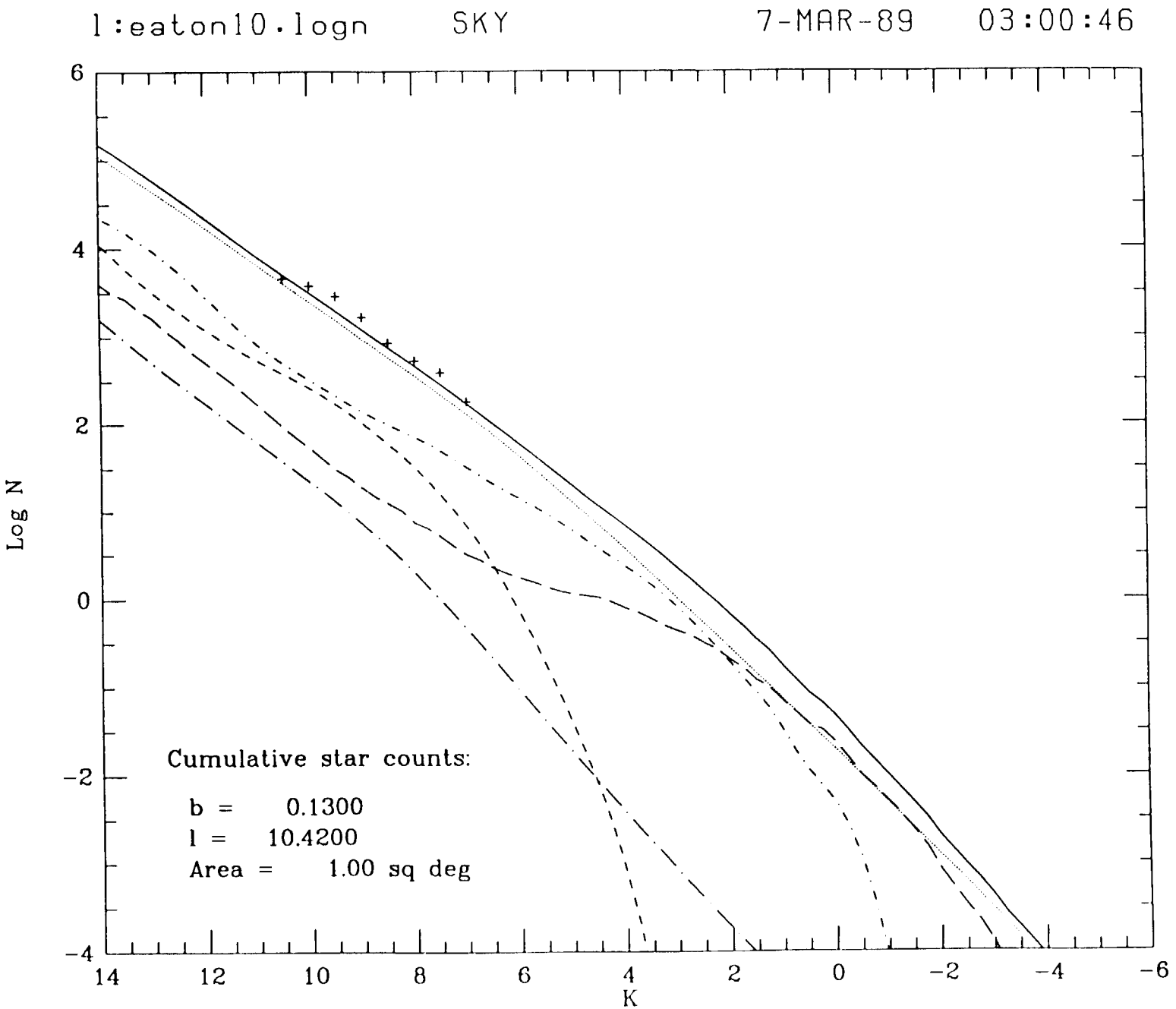
l:eaton10.logn SKY 7-MAR-89 03:00:46
Log N
K
Cumulative star counts:
b = 0.1300
l = 10.4200
Area = 1.00 sq deg

Fig. 9a

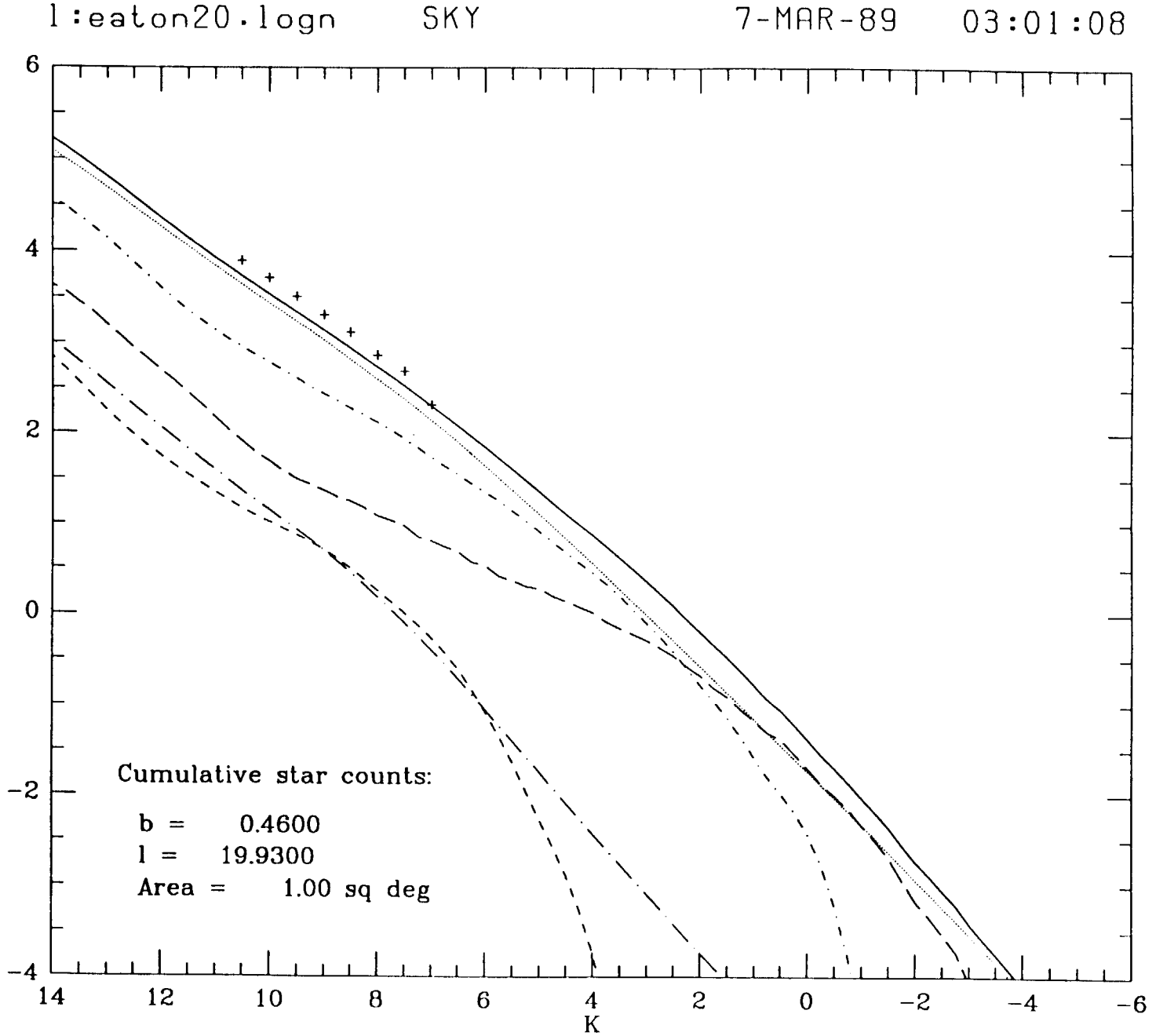
l:eaton20.logn SKY 7-MAR-89 03:01:08
6
4
2
0
-2
-4
Log N
14
12
10
8
6
4
2
0
-2
-4
-6
K
Cumulative star counts:
b = 0.4600
l = 19.9300
Area = 1.00 sq deg

Fig. 9b

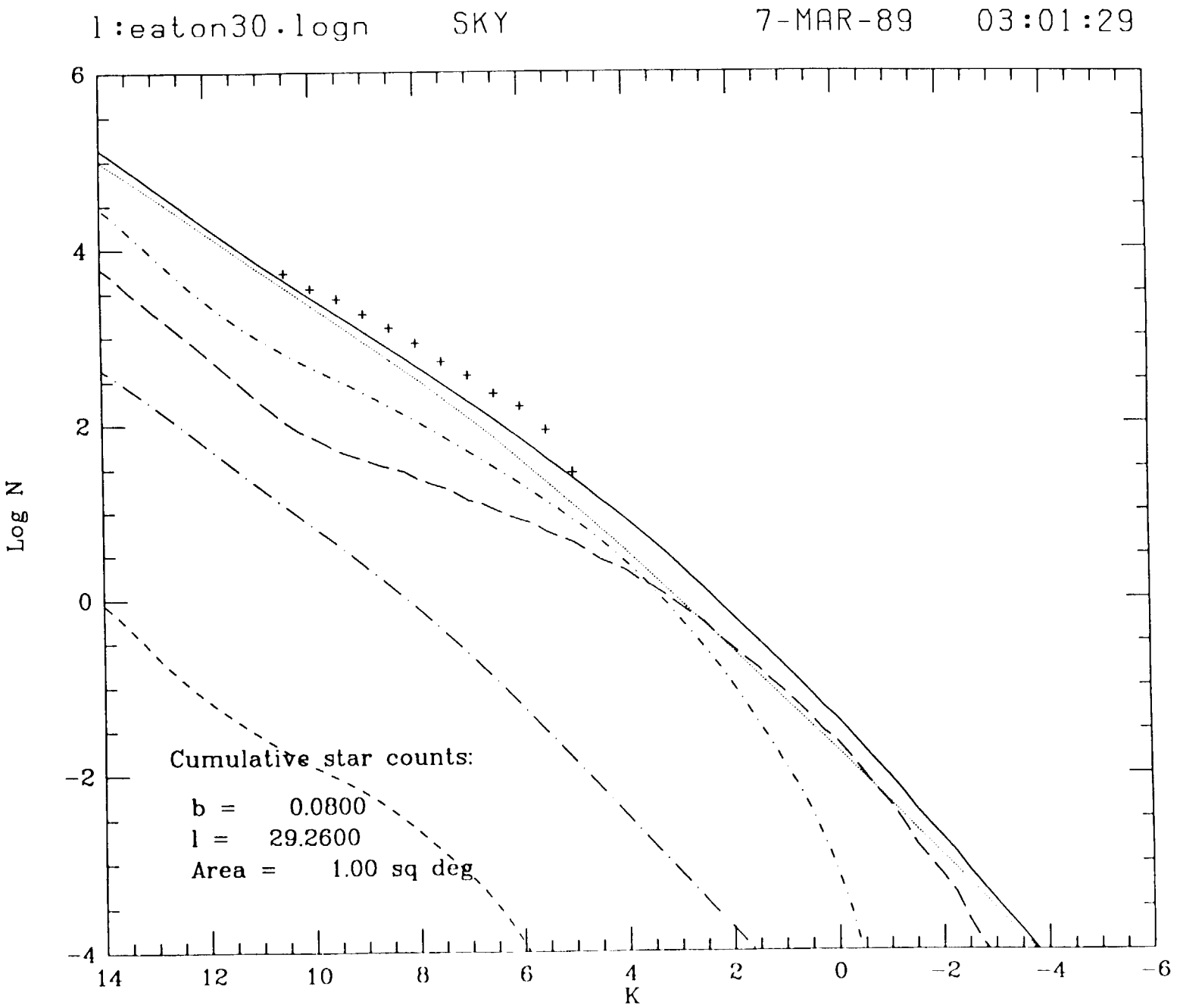
l:eaton30.logn SKY 7-MAR-89 03:01:29
Log N
K
Cumulative star counts:
b = 0.0800
l = 29.2600
Area = 1.00 sq deg
6
4
2
0
-2
-4
14
12
10
8
6
4
2
0
-2
-4
-6

Fig. 9c

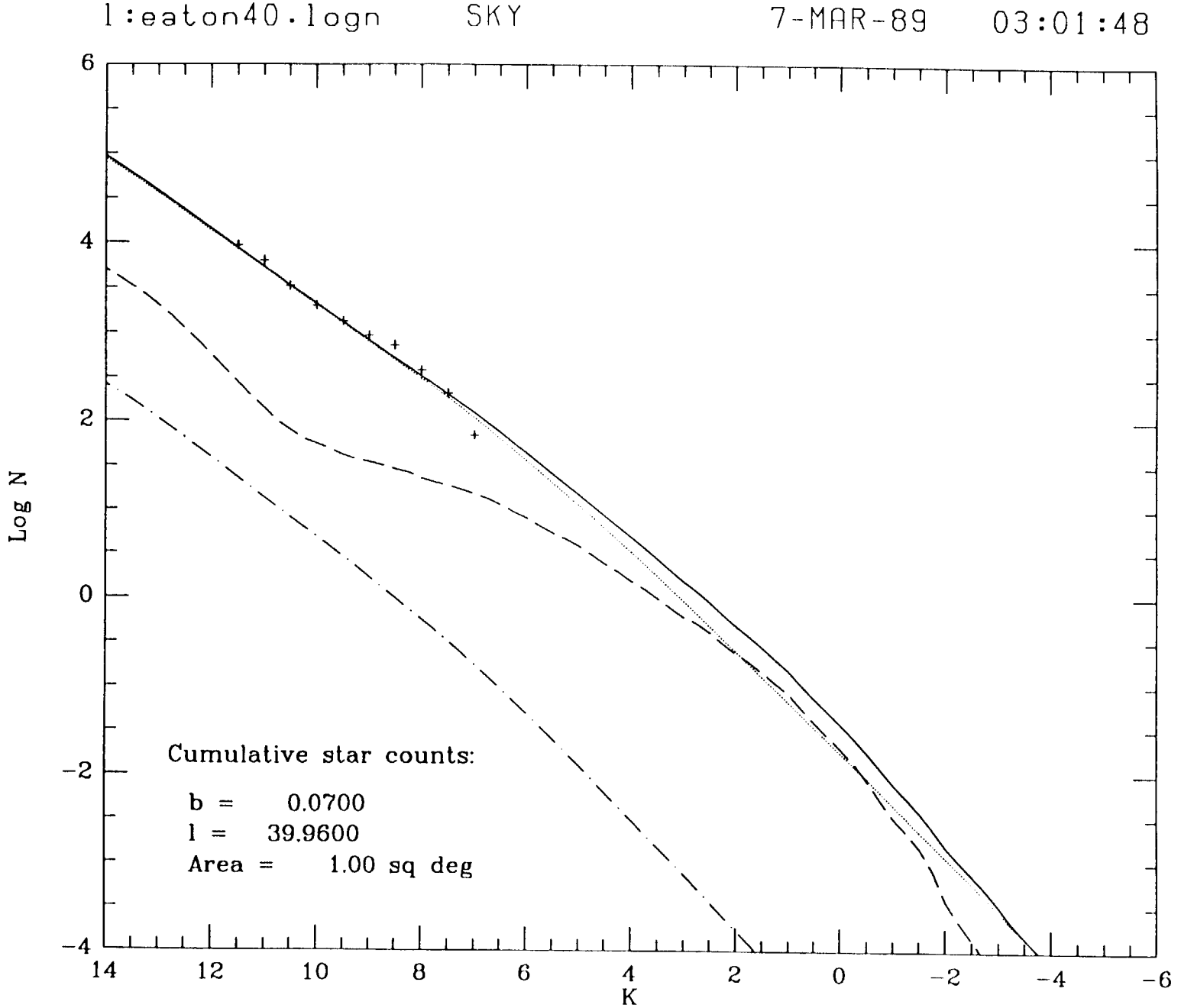
l:eaton40.logn SKY 7-MAR-89 03:01:48
Log N
K
Cumulative star counts:
b = 0.0700
l = 39.9600
Area = 1.00 sq deg

Fig. 9d

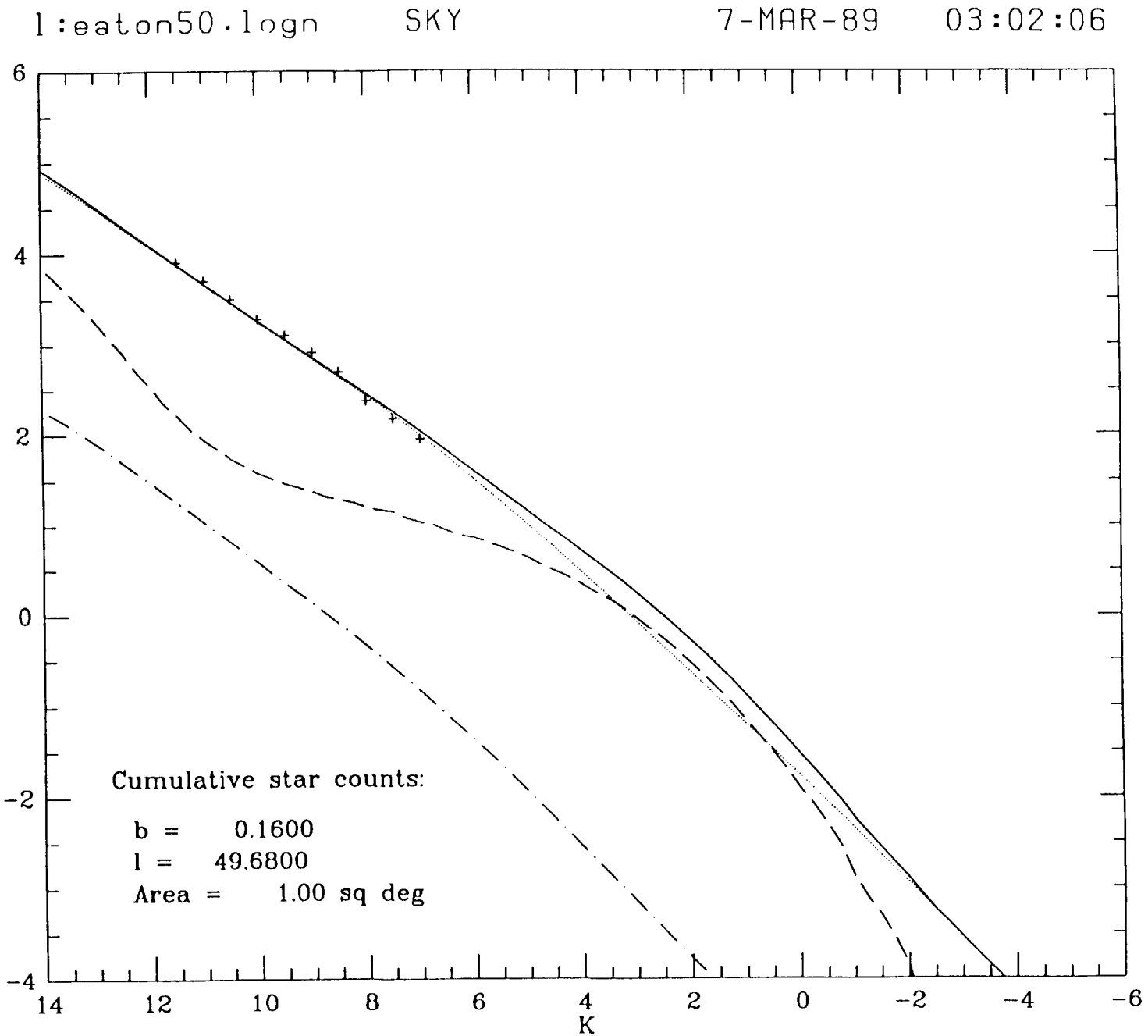
l:eaton50.logn SKY 7-MAR-89 03:02:06
Log N
K
Cumulative star counts:
b = 0.1600
l = 49.6800
Area = 1.00 sq deg
6
4
2
0
-2
-4
14
12
10
8
6
4
2
0
-2
-4
-6

Fig. 9e

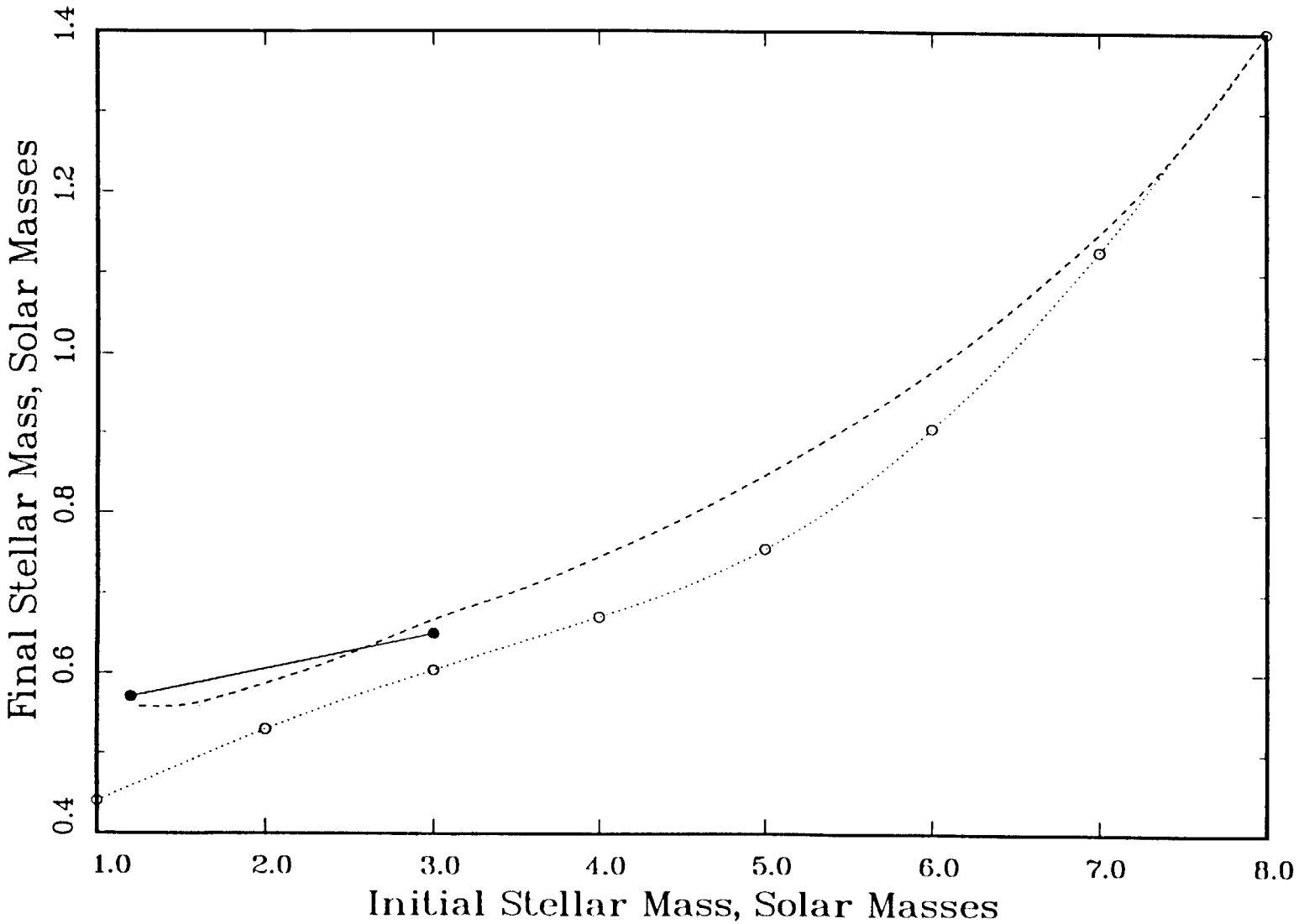
Final Stellar Mass, Solar Masses
0.4
0.6
0.8
1.0
1.2
1.4
1.0
2.0
3.0
4.0
5.0
6.0
7.0
8.0
Initial Stellar Mass, Solar Masses

Fig. 10

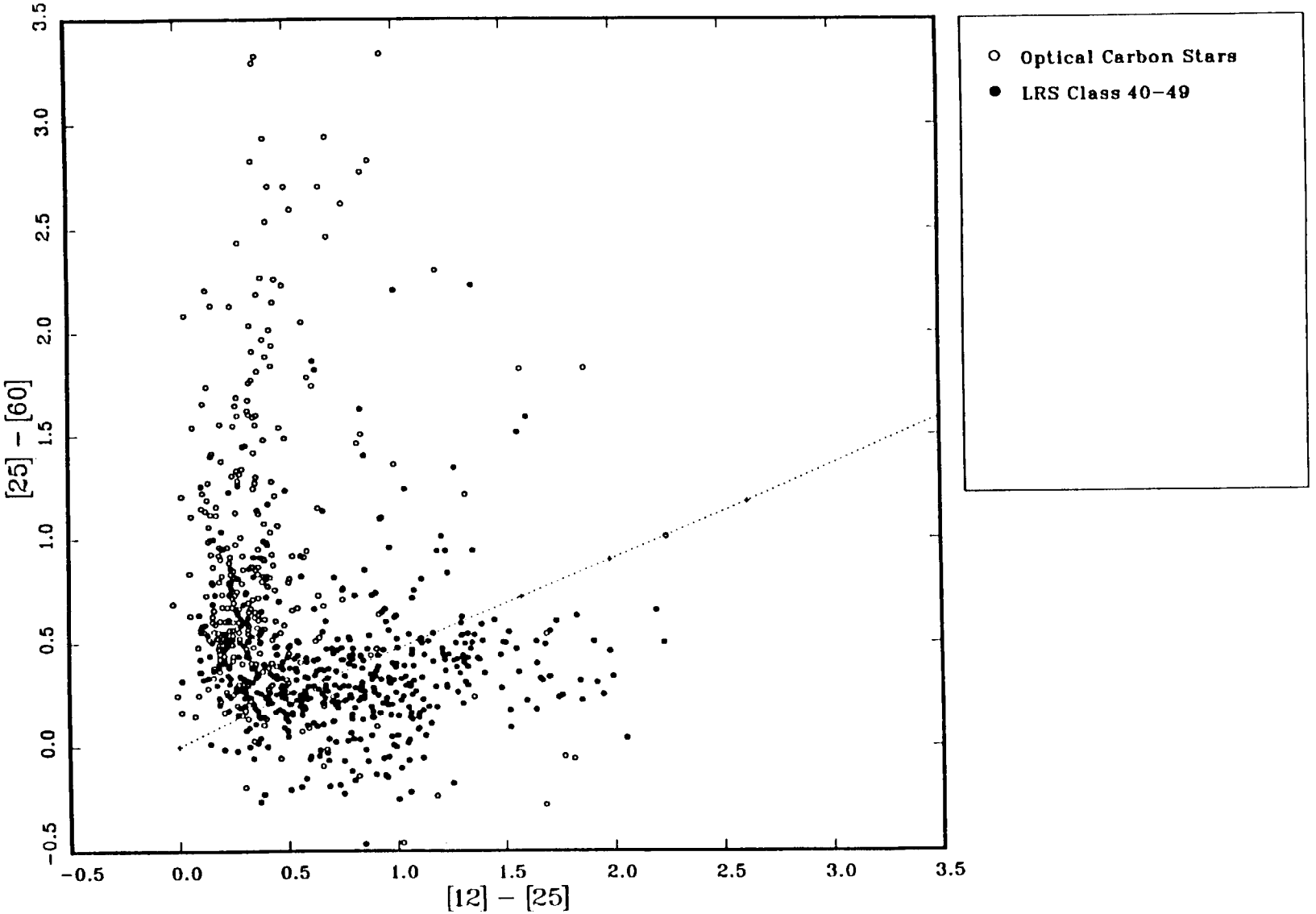
Optical Carbon Stars
LRS Class 40–49
[25] – [60]
[12] – [25]
−0.5
0.0
0.5
1.0
1.5
2.0
2.5
3.0
3.5

Fig. 11

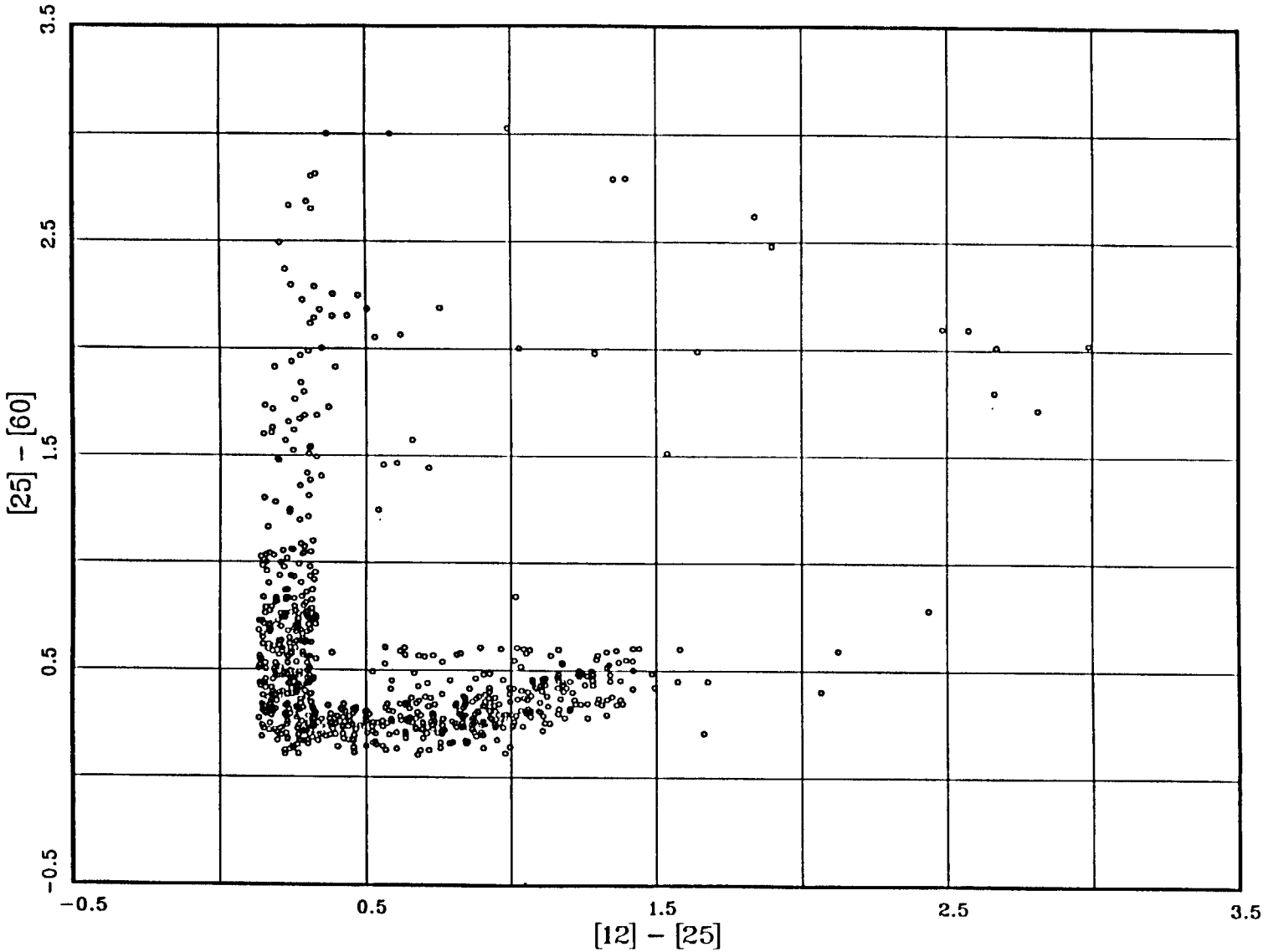

Fig. 12

APPENDIX I. "Confusion in the IRAS Point Source Catalog"

Appendix I. Confusion in the IRAS Point Source Catalog

- R.G. Walker -

1. INTRODUCTION

As an infrared telescope scans the sky, the detector baseline fluctuates due to many unresolved point sources crossing the focal plane. If these fluctuations dominate over those due to the intrinsic noise from the detectors the system is said to be confusion noise limited. Confusion noise increases the errors in estimating the position and flux density of a point source, and also reduces the completeness of source counts, because confused sources cannot be counted.

Methods for dealing with confusion noise and the resultant flux density error distributions have been developed by Scheuer (1957) and Condon (1974) in the context of radio telescope surveys. They show that the probability distributions of the fluctuations are completely specified by the normalized spatial response of the detector and the differential form of the source number density vs flux density relationship. These methods have recently been applied to analysis of a very deep IRAS survey of the ecliptic pole region by Hacking and Houck (1987).

It is the purpose of this paper to apply these techniques to the IRAS point source survey data, and determine if source confusion in the large IRAS beam is sufficient to account for the observed roll-off (incompleteness) of the IRAS point source counts near the galactic plane.

2. CONFUSION NOISE

We begin by assuming a power-law relation between the differential source counts and the flux of the following form:

$$dn/d(\log f) = k\, f^{-\alpha} \qquad (1)$$

where n is the number of sources per square degree, f is the in-band flux density in watts per square centimeter, and k and α are the intercept and slope of the distribution. Following Condon (1974) the confusion noise (baseline variance) can then be written

$$\sigma^2 = c\,[dn/d(\log f)]\, f^3\, \Omega\, /(2-\alpha) \qquad (2)$$

σ is the confusion noise in watts per square centimeter, and Ω is the effective solid angle of the field of view in square degrees, and is given by

$$\Omega = \int |g(\theta,\phi)|^{\alpha} \, d\theta \, d\phi \qquad (3)$$

with $g(\theta,\phi)$ the spatial response function normalized to unity at the peak response.

3. APPLICATION TO IRAS DATA

IRAS point sources were selected by a complex process of threshold detection and confirmation. A source was detected whenever its deflection exceeded a predetermined signal to noise ratio (SNR), usually 3.0, and its correlation with the expected shape of a point source transit exceeded 0.87. For a gaussian frequency distribution the probability of detection is given by

$$Pd = P(t-b) = (2\pi)^{-\frac{1}{2}} \int_{(t-b)}^{\infty} \exp(-y^2/2) \, dy \qquad (4)$$

where t is the threshold SNR and b is the SNR of the deflection, and is based on the total (in the RSS sense) of the confusion noise plus system noise.

Once a candidate source had been detected, confirming detections were searched for during the same focal plane transit (SCON), on later orbits (HCON), and in repeat scans made several days to weeks later (MCON). On the average a single transit could be expected to produce two detections, and a single HCON two more detections. To be entered in the IRAS point source catalog a source must have at least two HCONS, with one being a high quality HCON, that is, a minimum of six out of a possible eight detections was required (on average) to retain a source. This type of confirmation strategy may be represented by the binomial distribution

$$p(i,j) = \sum_{i=imin}^{j} Ci \; Pd^{i} \; (1-Pd)^{j-i} \qquad (5)$$

where $Ci = j!/i!(j-i)!$ is the binomial coefficient. In the case of IRAS detections typical values of i and j are i = 6 and j = 8.

Equations 2 through 5 are implemented in a FORTRAN subroutine, CONFUSE.FOR which predicts the observed differential source density distribution given the actual (or model) distribution and the telescope field of view and system noise. Gaussian statistics are assumed throughout.

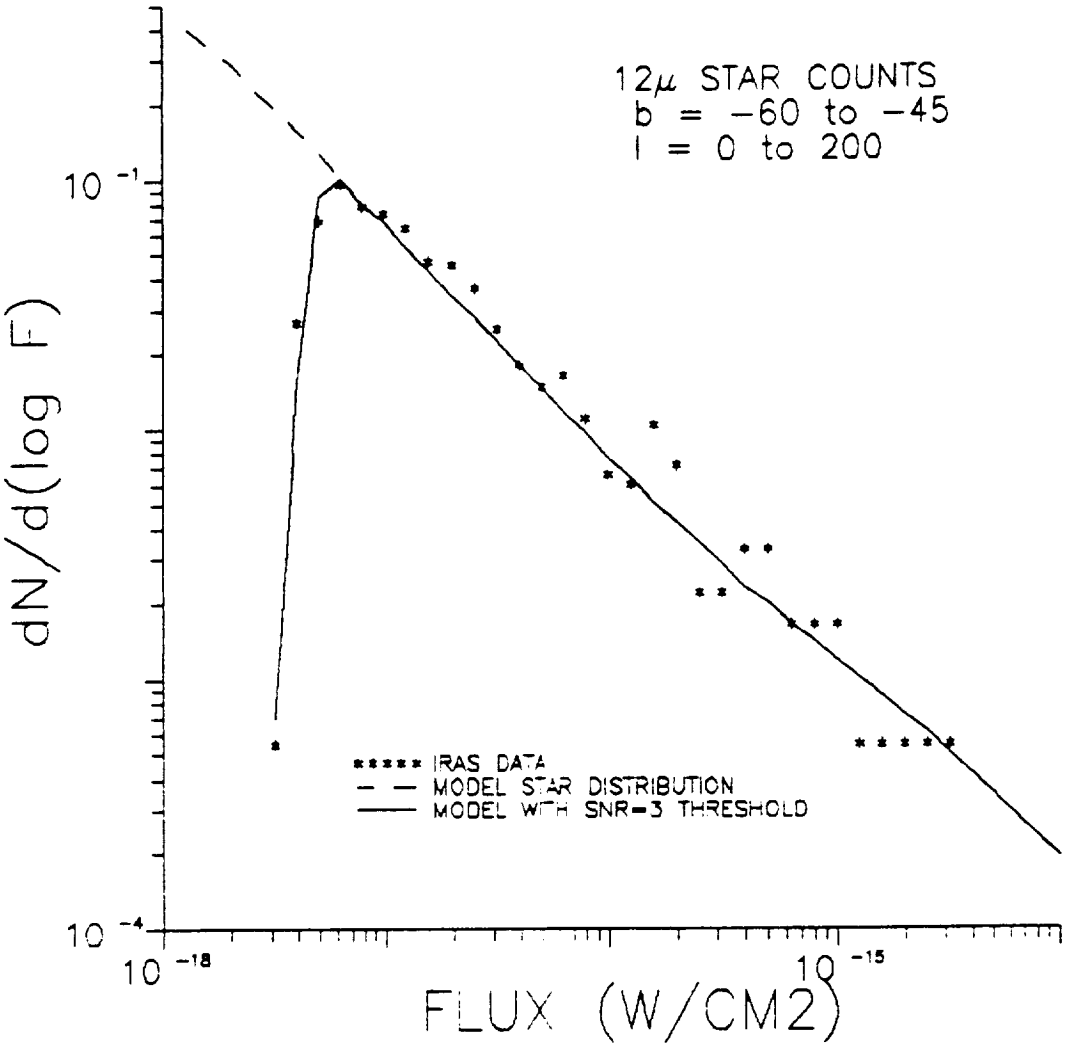

Figure 1. Point source densities at high galactic latitudes.

Equations (2) and (3) strictly apply only to a power-law source distribution. In practice it has been found that real star distributions have significant curvature. Our implementation approximates the curvature by using a "local" power-law with the slope of the real distribution determined at the flux density being considered.

We have also elected to use a constant value for the effective solid angle, that is, one which is independent of the slope of the dN, d(log f) curve. This is rigorous only for the case of unit response over the field of view. In all other cases this choice of effective solid angle yields a lower limit to the confusion noise.

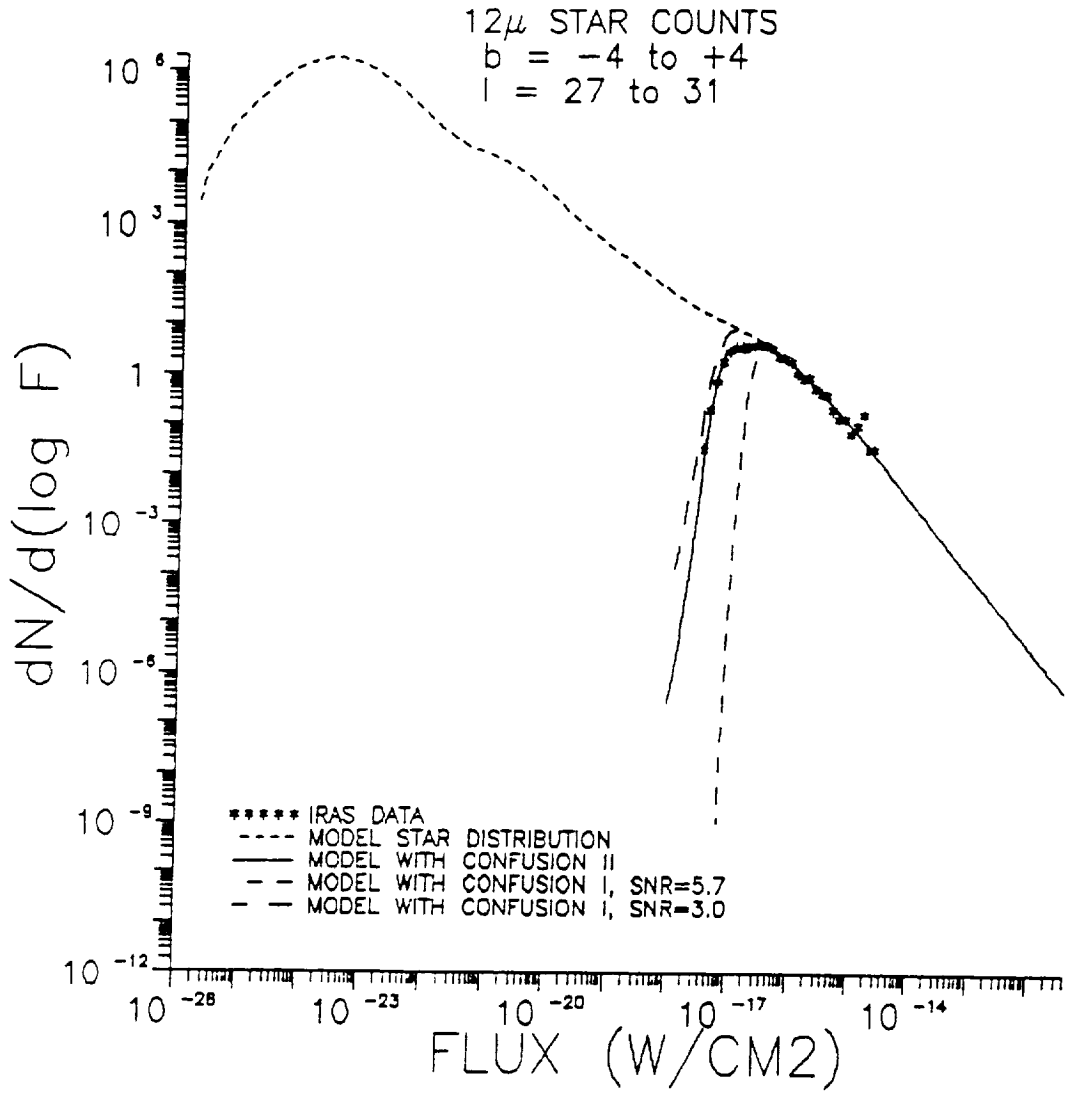

Figure 2. Point source counts in the galactic plane.

4. RESULTS

The subroutine CONFUSE.FOR has been applied to the star density distributions calculated with the ARC/JSE sky model for several different regions of the galaxy. Figure 1 shows the predicted curve plotted with the IRAS observations for a region at high galactic latitude. At the low source densities observed there is no confusion, and the abrupt cut-off is due to the system noise threshold at SNR = 3 and a confirmation strategy of at least 6 detections out of a possible 8 in this predominately 2 HCON region.

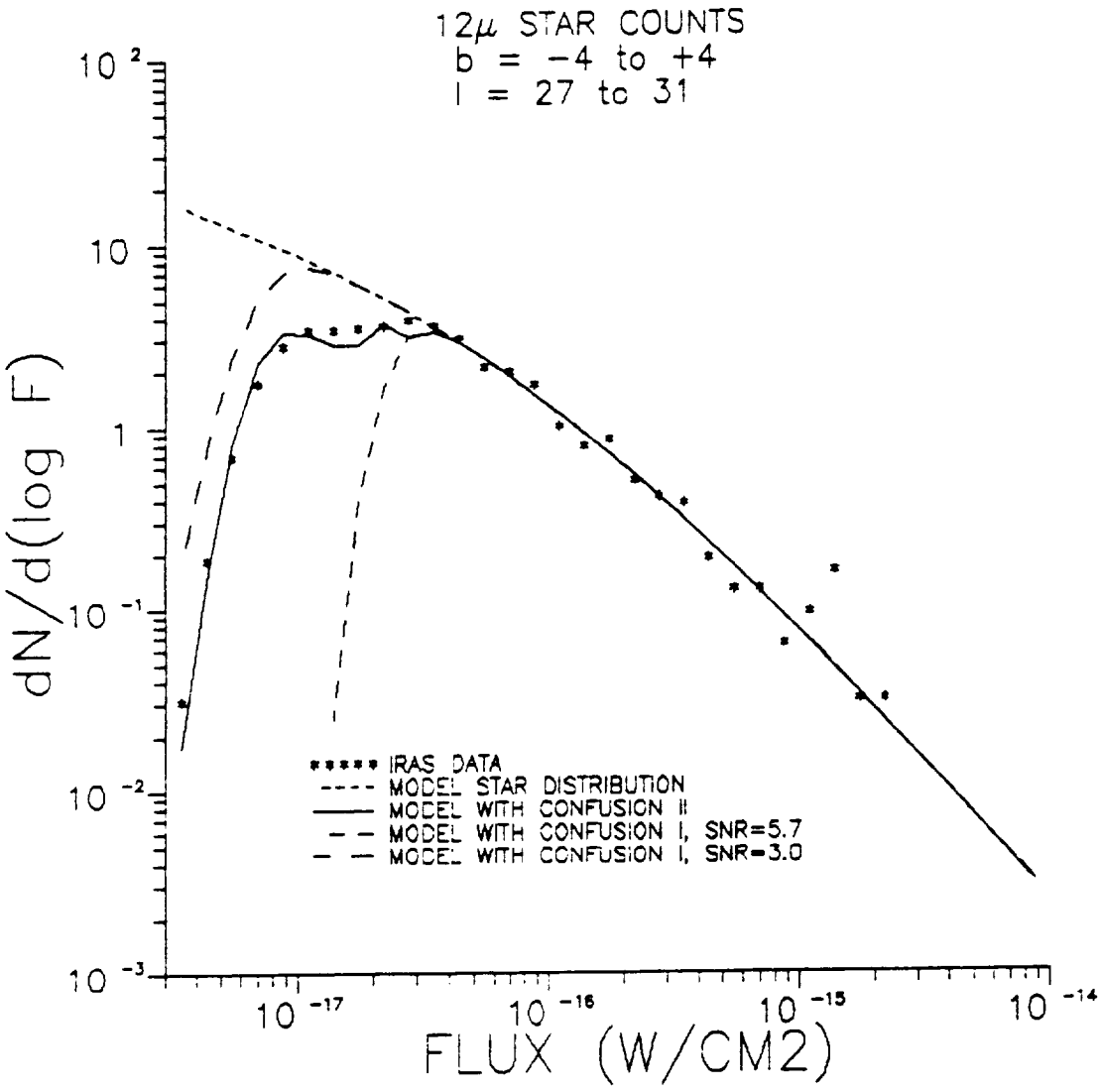

Figure 3. Point source counts in the galactic plane.

The results for a region bracketing the galactic plane where confusion noise is dominant are shown in Figures 2 and 3. Figure 2 shows that the model differential density distribution continues to grow for about -6 orders of magnitude in the flux beyond the cut-off due to the confusion threshold. Figure 3 is an enlarged view of Figure 2 showing more detail in the region of the cut-off. The confirmation strategy is 6 out of 8 for all of the plotted confusion curves. The dashed curves at SNR = 3 and SNR = 5.7 are plotted to show that no single parameter set can represent the observations. This is due to the large density gradient with galactic latitude across this region. The solid curve results from dividing the region into six latitude bands, predicting the number of sources detected at SNR = 3 in each band, and summing the results.

IRAS used special processing rules for stars that were located in confused regions. A flag was set in the PSC record for the star if it were in a confused region, and a special file of regions of high source density (HSD) was created. The IRAS criteria for "confusion" was taken to be source densities greater than or equal to 45, 45, 16, and 6 sources per square degree at 12, 25, 60, and 100 μm. These values are consistent with those calculated with equation (2) for SNR = 5 and α = 1 as shown in Table 1. The solid angles tabulated are the average of the large detectors in the IRAS array as given in the IRAS Explanatory Supplement. At SNR = 3 the confusion density limits will be $(5/3)^2$ = 2.77 times larger.

Table 1. IRAS Confusion Limits for SNR = 5 and α = 1.

BAND(μm)	Ω(sr)	Ω(sq.deg)	Density(#/sq.deg)
12	2.75E-7	9.03e-4	44.3
25	3.12e-7	1.02e-3	39.2
60	6.28e-7	2.06e-3	19.4
100	1.26e-6	4.12e-3	9.7

5. CONCLUSIONS

A simple model for confusion noise coupled with realistic threshold and confirmation criteria is sufficient to explain the behavior of the IRAS source count data. The observed abrupt roll-offs of the log n vs log f curves are a result of the noise and threshold, and are not indicative of a true decline of the galactic point source population. The criteria used by IRAS to invoke special processing in dense regions were reasonable if somewhat conservative. Thus the regions designated in the PSC as HSD regions are a valid indicator of the onset of confusion.

6. REFERENCES

Condon, J.J., Astrophys. J., **188**, pp. 279-286, 1974.

Hacking, P., and Houck, J.R., Astrophys. J. Supp. Series, **63**, pp. 311-333., 1987.

Scheuer, P.A.G., Proc. Cambridge Phil. Soc., **53**, p. 764, 1957.

APPENDIX J. "Zodiacal Emission Code"

Appendix J. Zodiacal Emission Code
- R.G. Walker and M. Schlapfer -

1. INTRODUCTION

The diffuse infrared emission from interplanetary dust grains sets the fundamental lower limit to the photon flux on infrared detectors in the 5 to 30 μm spectral region and, thus determines the ultimate sensitivity of the detection system. The earth is imbedded in the interplanetary medium and, therefore, an earth orbiting infrared sensor will observe the emission in all directions.

Prior to the IRAS observations, the surface brightness of the zodiacal emission was considered to be a slowly varying function of viewing coordinate with no components at high spatial frequencies. IRAS altered this view with the discovery of a fine structure consisting of several narrow bands of emission which run nearly continuously around the solar system (Low, et al,1984). These have been suggested to be the result of asteroid collisions in the vicinity of the Main Belt (Sykes, 1986; Gautier, et al, 1986; Dermott, et al, 1986). The intensity of the bands observed in the 1/2° x 1/2° synthesized beam of the IRAS Zodiacal History File are a few percent of the local diffuse component.

At this time there is no analytical model for the banded zodiacal structure that is sufficiently advanced to permit a predictive code to be written. There has, however, been a number of models developed in recent years which attempt to fit the observations and predict the infrared radiance of the diffuse component (Murdock and Price, 1985; Roser and Stroud, 1978; Frazier, 1987; Duel and Wolstencroft, 1988; Hong and Um, 1987; Dumont and Levasseur-Regourd, 1988; Kniessel and Giese,1986; Good, et al, 1986; Good, 1988).

Our purpose here was to produce an efficient computer code for computation of the line-of-sight diffuse zodiacal emission in the near infrared region from 5 to 30 μm. For this purpose we chose the recent model of Good (1988), which is based on the IRAS observations.

2. THE MODEL

The Good (1988) model assumed a physical model for the interplanetary dust cloud and evaluated the unknown model parameters by fitting the calculated radiance to that observed by IRAS. The models virtue is that it is defined by only a few parameters. Its disadvantages derive from the explicit incorporation of the

assumptions about the nature and distribution of the dust, and the fact that it can be computationally intensive.

Good (1988) assumes that the physical properties of the grains are spatially homogeneous. Their temperature T has a power law variation with heliocentric distance r

$$T(r) = T_o \ (R_o/r)^{\delta} \qquad (1)$$

where T_o is the temperature at $r = R^o = 1$ AU. The emissivity of the grains is assumed to be unity for wavelengths less than 37 μm. T^o and δ are both free parameters of the model. The dust density distribution is assumed to be that of a modified fan distribution

$$n(r,z) = n_o \ (R_o/r)^{\alpha} \exp \ [-\beta(|z|/r)^{\gamma}] \qquad (2)$$

where z is the height above the dust symmetry plane, and n_o is the volumetric absorption cross-section at r = 1 AU and z = 0. The orientation of the dust plane is such that the plane of symmetry is inclined an angle I with respect to the plane of the ecliptic, with the longitude of the ascending node at Ω. The constants n_o, α, β, and γ, and the angles I, Ω are also free parameters of the model. The integral radiance $N(\theta,\phi,t)$ along a line of sight at ecliptic latitude θ, ecliptic longitude ϕ, and at time t is calculated from

$$N(\theta,\phi,t) = \int_{\lambda_{min}}^{\lambda_{max}} S(\lambda) \left[\int_0^{L_{max}} n(r,z) B(\lambda,T) dL \right] d\lambda \qquad (3)$$

where $S(\lambda)$ is the normalized spectral response of the detector/filter combination, $B(\lambda,T)$ is the Planck radiation function, L is the unit vector in the direction (θ,ϕ) at time t. Positions in (r,z) are calculated from (L,θ,ϕ) taking into account the position of the Earth in its eccentric orbit at time t, and the orientation of the plane of symmetry of the dust cloud.

Table 1 gives the values of the free parameters found by Good (1988) and adopted for these calculations. These parameters are entered into the code in an initializing routine in the main calling program, where they can be easily modified as better data become available. In addition to the integral Eqn.3, Good (1988) found it necessary to include a small isotropic radiance term in each of the four IRAS bands to fit the observations. We

have found that this term is well represented in the 5 to 35 μm region by a greybody at temperature 193 K with emissivity of 6.9×10^{-8}. There is some concern that the isotropic term may be due to baseline offset errors in the IRAS calibration and not representative of the real zodiacal radiance. We include it in the code. Typical values of the offset are 4.75×10^{-12} w cm^{-2} μm^{-1} sr^{-1} at 10 μm and 6.32×10^{-12} w cm^{-2} μm^{-1} sr^{-1} at 20 μm.

Table 1. Adopted Parameters of the Model

$n_o = 1.439 \times 10^{-20}$ cm^{-1}
$= 2.154 \times 10^{-7}$ AU^{-1}
$\alpha = 1.803$
$\beta = 4.973$
$\gamma = 1.265$
$T_o = 266.2$ °K
$\delta = 0.359$
$\Omega = 68.61°$
$I = 1.73°$

To reduce computation time for sensors with large bandwidths we have opted to approximate Eqn. 3 with an integral over the effective wavelength and passband. The effective wavelength λ_e is defined by

$$\lambda_e \int S(\lambda) B(\lambda, T_m)\, d\lambda = \int \lambda S(\lambda) B(\lambda, T_m)\, d\lambda \qquad (4)$$

and the effective bandwidth $\Delta\lambda_e$ is defined by

$$\Delta\lambda_e\, B(\lambda_e, T) = \int S(\lambda) B(\lambda, T_m)\, d\lambda \qquad (5)$$

where T_m is the grain temperature at the smallest heliocentric distance of the line of sight, and the limits of the integrals are those of the spectral response $S(\lambda)$. With these approximations Eqn. 3 may be rewritten

$$N(\theta, \phi, t) = \Delta\lambda_e \int_0^{L_{max}} n(r,z) B(\lambda_e, T)\, dL \qquad (6)$$

The code approximates Eqn. 6 by three sums with different step size, for the range: $0 < L < 2$ AU, $\Delta L = 0.05$ AU,

$2 < L < 3$, $\Delta L = 0.10$,
$3 < L < 6$, $\Delta L = 0.30$, the computation is terminated at L = 6 AU.

3. RESULTS

To test the integrity of the code we calculated the in-band radiance for several IRAS scans and compared the results with those given in the IRAS Zodiacal History File. These are plotted in Figures 1 through 12. These particular scans were chosen to represent extremes of orbital position and elongation angle. In most cases the fit is quite good. The largest deviation of about 15% occurs near the ecliptic at 60.4° solar elongation in the IRAS 25 μm band. For most of the other scans the differences are much smaller, typically only a few percent. Shoulders due to the Zodiacal bands and structure due to the galactic plane are readily seen in the scans.

Figure 13 is a comparison of the model prediction at the position of maximum radiance with that of the ZIP data (Murdock and Price, 1985). The shape of the model curve is in good agreement with their data, however, the model radiance is 50% higher at 10.9 μm and 40% higher at 20.9 μm.

4. USE OF THE MODEL

The Zodiacal Emission model code is contained in a set of FORTRAN subroutines, which are to be used with a main calling program that supplies the following inputs:

a. The Julian date of the observation (JDN) - the program accepts any date after JD 244605.5

b. The Ecliptic Latitude and Longitude of the line of sight (LATITUDE,LONGITUDE) - the angles are entered in decimal degrees

c. The sensor response function (RESPONSE(wavelength,amplitude)) - this is a file or table of wavelength (μm) vs amplitude of the normalized response at that wavelength. The first and last entries must be zero response. The wavelength interval must be constant. To calculate the monochromatic radiance at wavelength λ_o the following three point response function must be entered: $(\lambda_{-1},0.0)$, $(\lambda_o,1.0)$, $(\lambda_{+1},0.0)$.

The realm of applicability of the code is restricted to the following:

a. The appropriate spectral region is from about 3 to 30 μm,

that is, the region where thermal emission from the dust is dominant. There is no provision in the code to include the component of solar radiation scattered by the grains.

b. In principal, the model applies to all solar elongations. However, the model will surely fail at elongations less than a few degrees from the Sun. This is due to modifications of the dust distribution that are not treated by the model, for example, burn-out zones in which the grains are vaporized by the solar flux.

c. The model assumes that the grain emissivity is grey with no dependence on wavelength. Thus the model will not reproduce spectral features that may be observed due to the real optical properties of the grains.

5. REFERENCES

Dermott, S.F.,,Nicholson, P.D., and Wolven, B., "The Structure of the Zodiacal Cloud Revealed by IRAS" , Asteroids, Comets, Meteorites II, ed. C-I. Lagerkvist et al,(Uppsala), p. 583, 1986

Deul, E.R., and Wolstencroft, R.D., Astron. Astrophys., **196**, 277-286, 1988

Dumont, R. and Levasseur-Regourd, A.C., Astron. Astrophys., **191**, 154-160, 1988

Gautier, T.N., Good, J.C., and Hauser, M.G., "The Geometry of the Zodiacal Dust Bands", Adv. Space Res. Vol. 6, No. 7, pp.91-94,1986

Good, J.C., Hauser, M.G., and Gautier, T.N., "IRAS Observations of the Zodiacal Background", Adv. Space Res. Vol. 6, No. 7, pp.83-86, 1986

Good, J.C., "Zodiacal Dust Cloud Modelling Using the IRAS Data", preprint (IPAC), 1988

Hong, S.S., and Um, I.K., Astrophys. J., **320**, 928-935, 1987

Frazier, E.N., in Infrared Technology XIII, I.J. Spiro, ed, Proc. SPIE, **819**, 2-6, 1987

Kniessel, B. and Giese, R.H., "The Impact of the IRAS Results on Three Dimensional Models of the Global Distribution of Interplanetary Dust", Adv. Space Res. Vol. 6, No. 7, pp.79-82, 1986

Low, F.J., et al, 1984, Astrophys. J. (Letters), 278, L19.

Meeus, J., "Astronomical Formulae for Calculators", 3rd edition,

(Willmann-Bell, Inc., Richmond, VA), 1985

Murdock, T. L., and Price, S. D., Astron.J., v90, no.2, p375,1985

Roser, S. and Staude, H.J., Astron. and Astrophys., **67**, 381, 1978

Sykes, M., Ph. D. Thesis, Univ. of Arizona, 1986

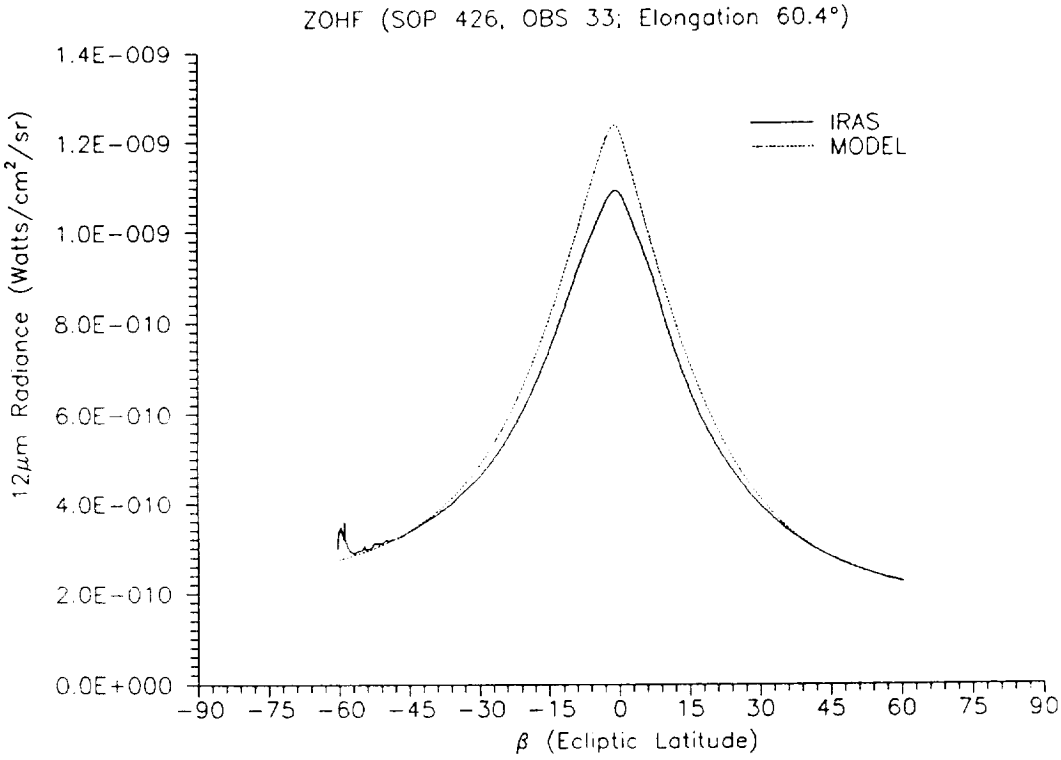

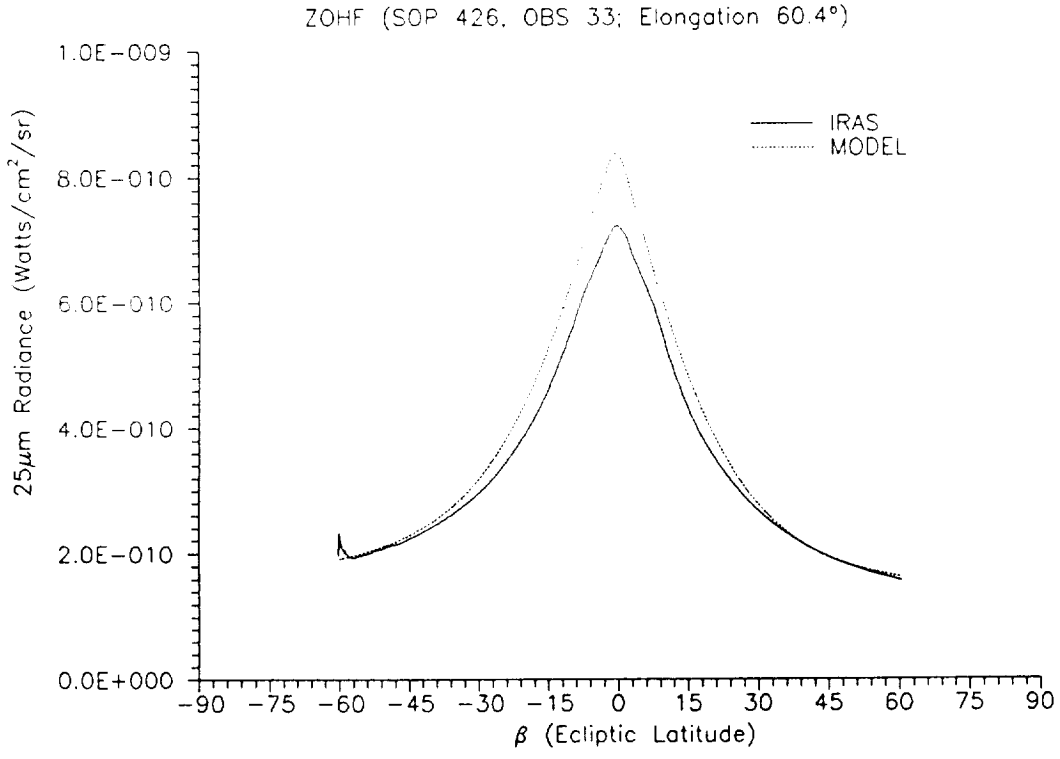

Figure 1. Comparison of model calculations with IRAS data.

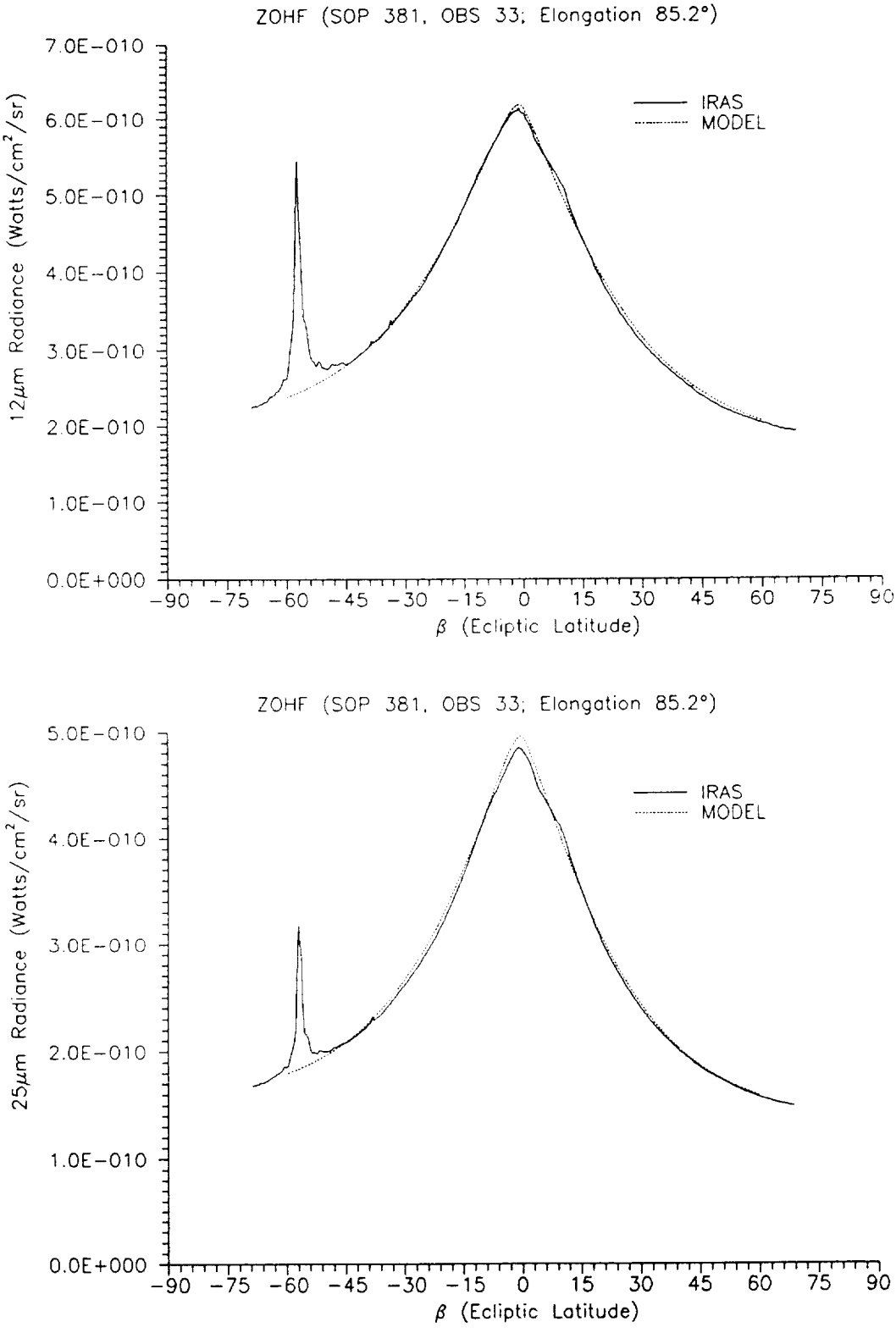

Figure 2. Comparison of model calculations with IRAS data.

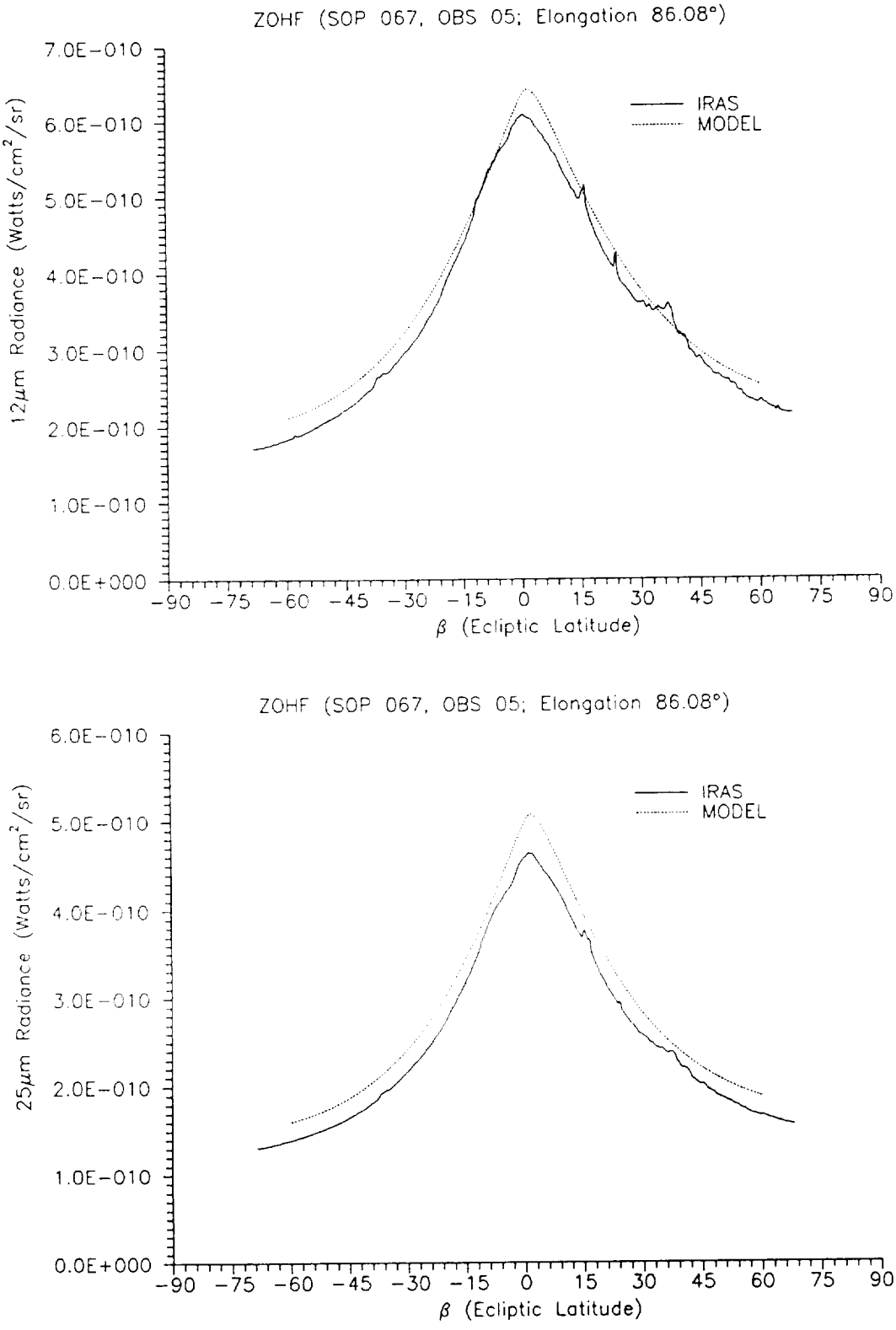

Figure 3. Comparison of model calculations with IRAS data.

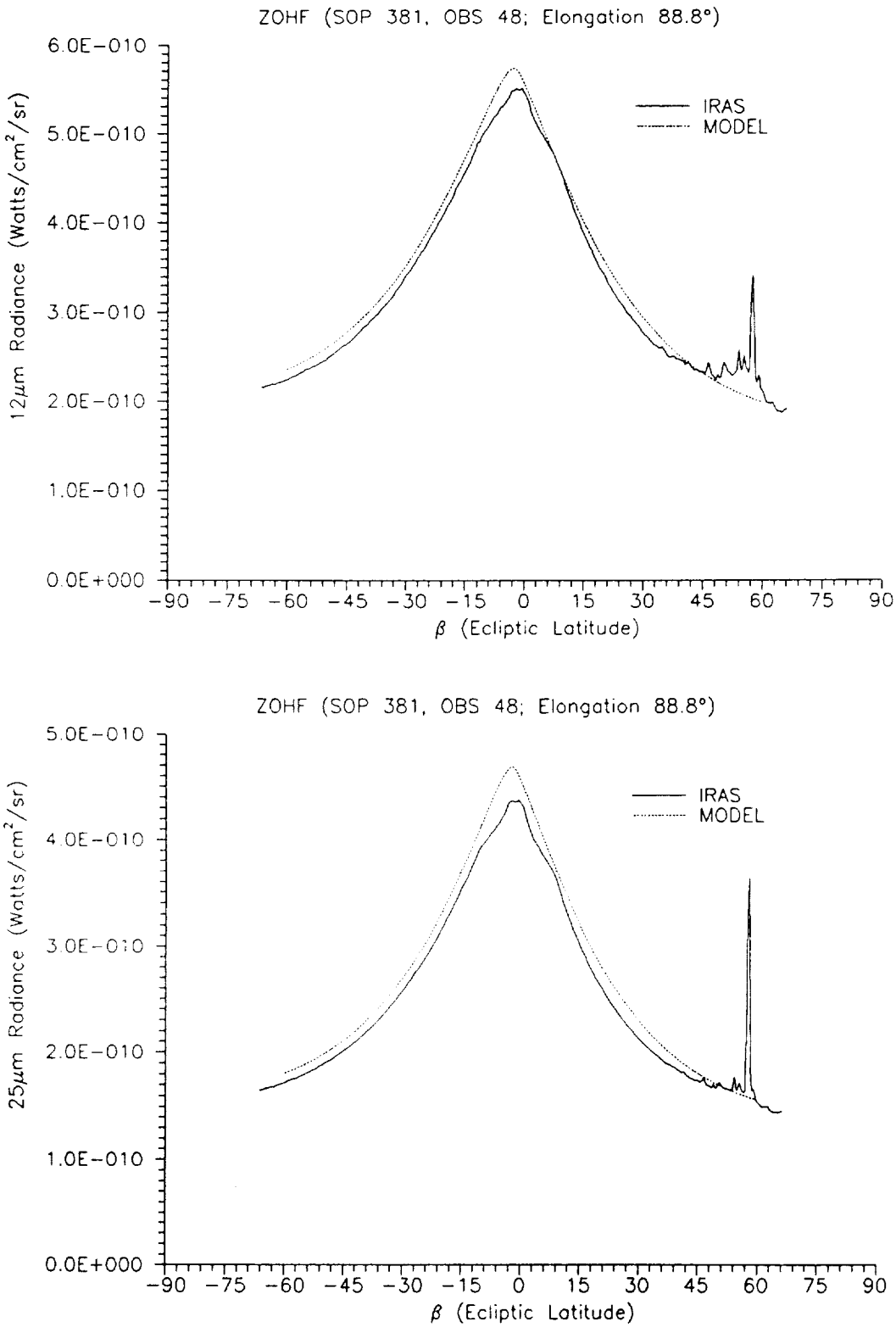

Figure 4. Comparison of model calculations with IRAS data.

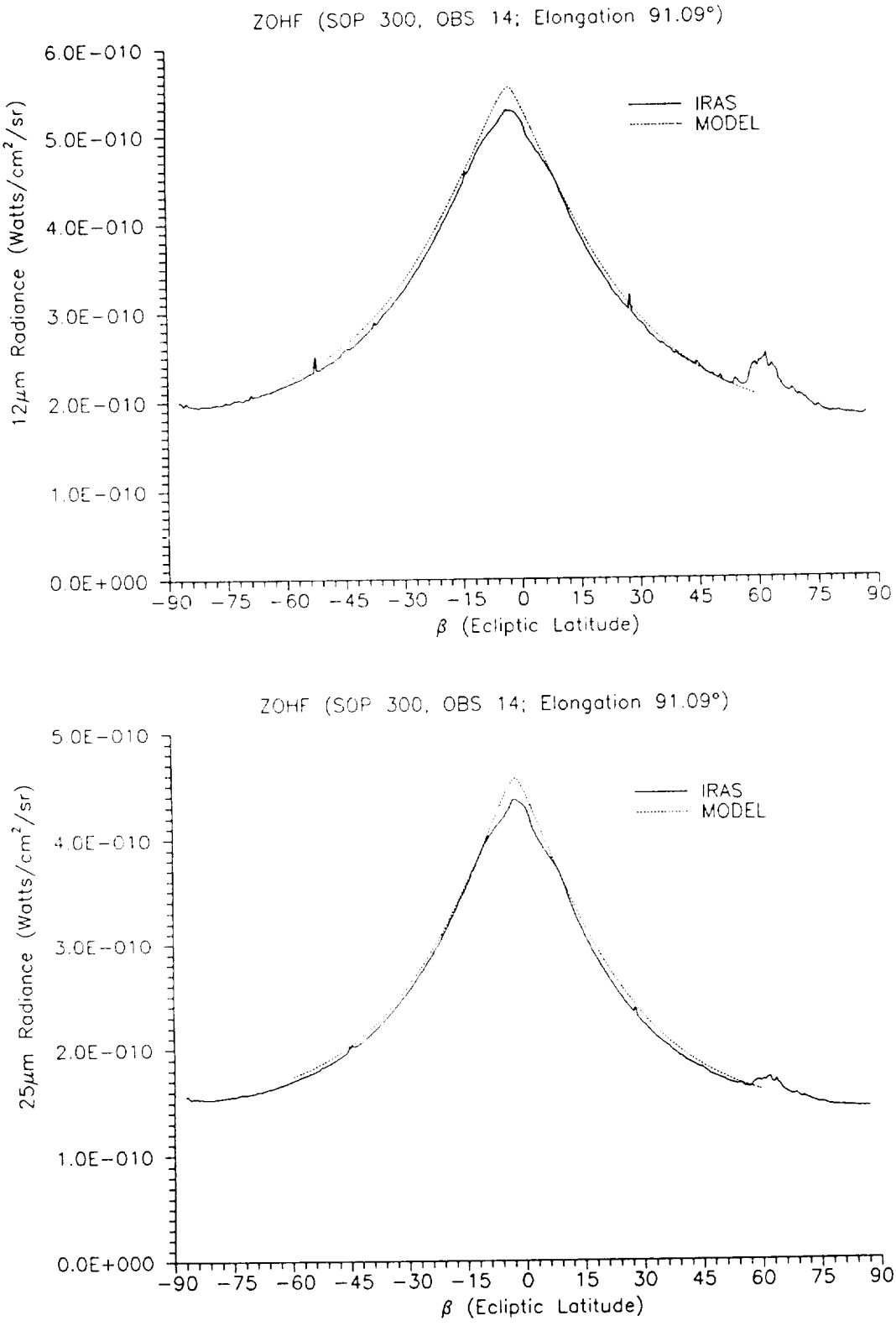

Figure 5. Comparison of model calculations with IRAS data.

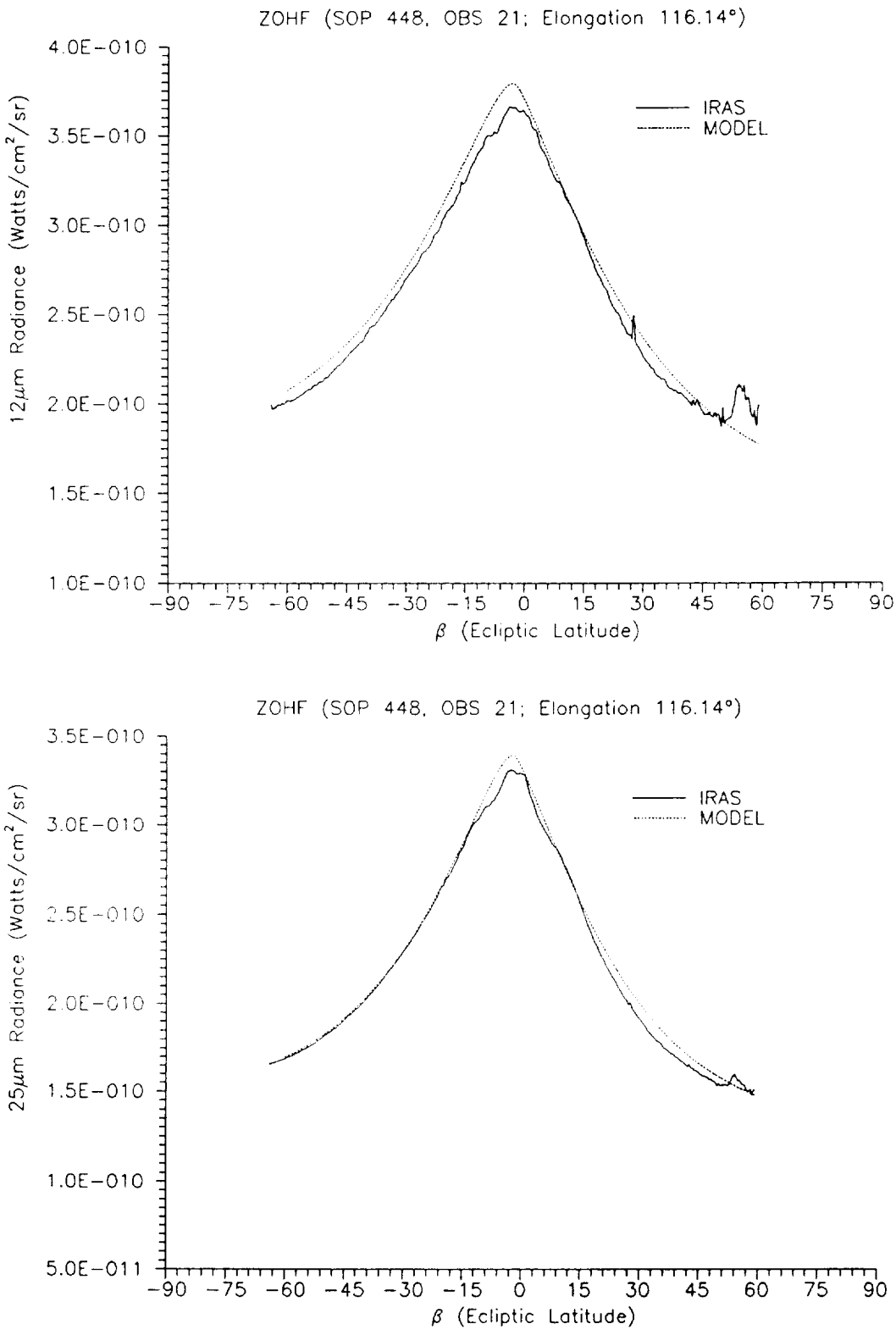

Figure 6. Comparison of model calculations with IRAS data.

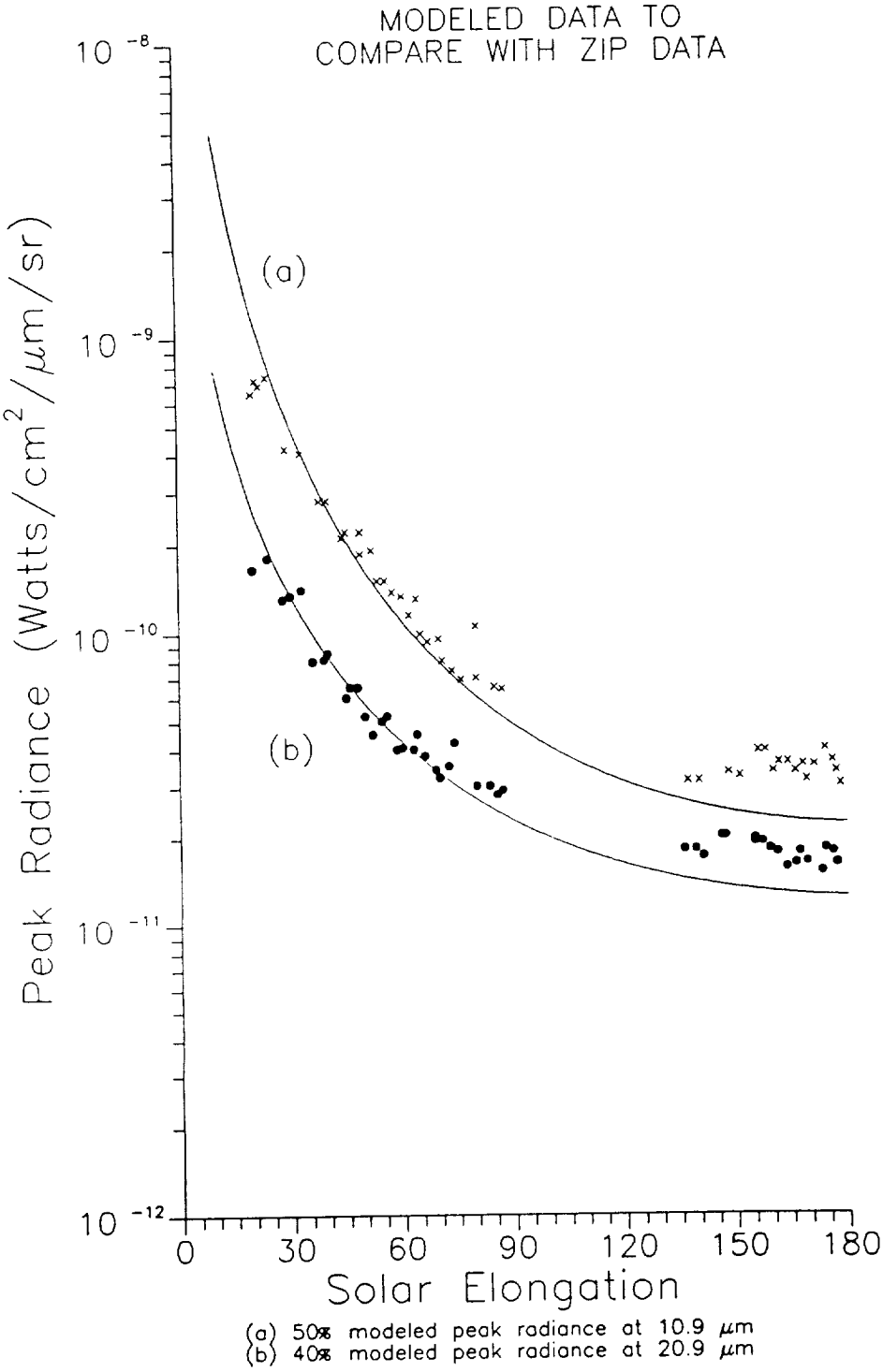

Figure 7. Comparison of model calculations with ZIP data.

APPENDIX K. "Celestial Background Structure Definition Study, Final Report, Sub-contract JSE-88-S-001"

CELESTIAL BACKGROUND STRUCTURE DEFINITION STUDY

Contract Number JSE-88-S-001

FINAL REPORT -- DUE SEPTEMBER 15, 1988

Submitted by

S. D. Kilston
E. L. Schweitzer
R. D. Sears

Reporting Period: MARCH 7 - SEPTEMBER 30

Personnel on program:

Primary:	R. D. Sears, Principal Investigator
(all 97-10)	S. D. Kilston, Staff Engineer/Astronomer
	E. L. Schweitzer, Scientist/Programmer
	K. A. Anderson, Programmer, Computer Operator
Supporting:	C. E. Smith, Laboratory Manager, 97-10
	D. E. Dorset, Contract Administrator, 90-31
	P. R. Bull, Contract Administrator, 90-31
	P. E. Dolan, Cost Controller, 25-60
	P. M. Pearson, Finance and Controls, 25-60

Overall Program Tasks:

1. Production and analysis of one-dimensional power spectral densities derived from IRAS cirrus scans provided by JS&E.

2. Detailed analysis of cirrus scans and inference of 2-D PSDs from orthogonal scans. Also, PSDs of other celestial sources, as available.

Accomplishments During Contract Performance Period:

Data from selected Infrared Astronomical Satellite (IRAS) single scan segments (each generally about 8° long), as well as interpretive software, were received from Jamieson Science & Engineering (JS&E) and translated successfully into working modules on the LMSC VAX computer system. Since the aim of the project is to characterize IR cirrus phenomenology, all other environmental and instrumental sources of confusion had to be removed from the basic data. The basic analytical scheme allowing data to be produced in formats suitable for physical interpretation is shown in Figure 1.

One of our first tasks was to develop and test the coordinate conversion software for use with the point-source-removal algorithm. An

efficient point-source-removal algorithm was constructed based on the IRAS Point Source Catalog (PSC); it minimizes effects upon the PSDs separately for each waveband, uses PSC brightness and cirrus flags as criteria, and selects PSC data corresponding to locations close to the scan path.

Next, a PSD generating program was developed using the International Mathematics and Statistics Library Fast Fourier Transform (FFT) subroutine; this program was refined until valid and in proper output format. The FFT subroutine required input data with an average ordinate of zero (on an intensity versus time graph); to accomplish this we employed a median-filter baseline-removal algorithm supplied by JS&E. Radiance PSDs were then produced for each spectral band, combining data from all unimpaired detectors in the band, properly weighted for solid angles and data variances of each detector.

As a test of the method up to this point, these PSDs from all bands were compared for three different scans in the same sky region: preliminary results showed variations, particularly for the 100 μm band. Following this, some problems were observed with the point location subroutine used with the point-source-removal algorithm: stars apparent in the intensity scan data were not being removed as desired. Since these position calculations are based partly on the solar location, a more accurate solar position subroutine was supplied by JS&E; it was translated successfully into working modules on the LMSC VAX computer system. Corrections were also made then to the Gaussian randomizing software which replaces (with an appropriately noisy baseline) the data points affected by subtracting stars. We tested the effects of the entire point-source removal algorithm, demonstrating that the randomized substitute data seemed to provide a natural intensity scan.

As all data scans (16) available at the time were analyzed for radiance PSDs, using all working detectors in a band, the point source removal effects seemed minimal. PSDs from different scans in same sky region were compared for all bands: the results still showed apparent variations, particularly in the 100 μm band. All graphs were stored in a single large notebook for ease of reference, since our understanding of each grew out of the visual intercomparisons we could make.

At this stage JS&E provided a large collection of new data scans and noise (stare-mode) runs; these tapes were successfully tested for readability and the nearly 100 readable scans provided the data set for our full-scale analysis.

The median-filter baseline-removal algorithm proved to eliminate nearly all cirrus components before the PSD calculation, so we then

tested the effects of other baseline removal algorithms. We tried different scan sub-intervals in the median filter (corresponding to low-pass filtering) to allow detection of large-scale cirrus structures, but decided that the smooth variation of the dominant zodiacal radiance over the scan paths warranted use of a simple sloping linear baseline.

The stare-mode data included in the tapes consisted of data streams collected while the sensor stared at a particular location in space (chosen to be relatively free of stars and diffuse structures). These data were analyzed to obtain PSDs of stationary system noise, translating time intervals into equivalent spatial distances corresponding to the average scan rate. All working detectors in a band (except those obviously receiving photons from a star), properly weighted for detector solid angles and data variances, were combined to derive a standard noise PSD for each spectral band, using the same type of simple sloping linear baseline as above. The different stare files were quite consistent with each other; they could therefore be combined to give a suitable average noise PSD (representing additive stationary instrumental noise) for each waveband. A second-order polynomial fit to the log-log graph of each of these average noise PSDs provided us with four noise equations to be subtracted from the PSDs made from the scan data.

At this time one of us (S. K.) prepared and presented a paper, including preliminary PSD results, at an LMSC corporate infrared research conference.

Reviewing all data to this point, we found normalization errors by checking PSD integrations versus scan variances. The data were then corrected, including proper weights for detector solid angles and data variances. We also found several peculiarities in the coordinate-calculating subroutines (supplied by JS&E) for particular field and sun positions; we made adjustments to the programs to correct all positions so that proper star removals could be effected.

Next we began producing net PSDs (all detectors of the same waveband added together for the scan) for each waveband, with the stare-mode noise subtracted. We compared noise and net scan slopes to results of Gauthier and Boulanger, finding good agreement in noise slopes, but differences in scan slopes presumably attributable to choice of fields analyzed.

At this point in the project, one of us (S.K.) attended a program review and infrared phenomenology session at the Air Force Geophysical Laboratory, presenting a report on program progress.

A new research assistant, Kevin Anderson, was trained to program and run the remaining PSD plots. He compiled the whole data set of summary net PSDs (of beyond-solar-system celestial background, but still

uncorrected for scanning instrumental effects) for each waveband and region.

At first we fit each summary net PSD with a power-law parabolic function of frequency, f :

$$\text{PSD}(f) = \log I^2(f) = \log a + b \log f + c (\log f)^2$$

Comparing net function slopes, b, to each other and to results of Gauthier and Boulanger, we found wide differences in scan slope (b) for different fields. We also found several very peculiar PSDs, each with very large curvature coefficient ($|c|$); on further examination these appeared to have the (sin f)/f behavior associated with a finite instrumental integration time affecting the PSD of a bright point source that escaped our PSC deletion scheme. We enlisted Russ Walker's help in evaluating all IRAS instrumental scanning effects (from the combination of finite slit-passage time, optical point-spread function, and high-frequency electronic filtering to remove aliasing) expected in the data, and then re-calculated deconvolved PSDs free of those instrumental effects. We also changed the calculation of PSD slope to a linear function of log f:

$$\text{PSD}(f) = \log I^2(f) = \log a + b \log f$$

We constructed summary tables of scan results, including equatorial coordinates of scan path beginnings and ends, for ease of location and comparison of scan paths, and interpretation of results. These tables and graphs of their salient features are included in the material of this report. A detailed description of the final data analysis scheme is diagrammed in Figures 2, 3 and 4.

Interpretation of Results

Two typical sets of PSDs (from scans taken near the North Celestial Pole) are displayed in Figures 5 and 6. The four spectral bands exhibit quite different PSD behavior, with the slopes generally steeper with increasing wavelength. Since the 100 μm band is well known to display the greatest evidence of IR cirrus structure (which is apparently due to very cool interstellar dust and molecular clouds), we might have expected these observed spectral band variations simply from signal-to-noise ratio differences. (We also expect any residual zodiacal noise to be greatest in the shorter spectral bands). However, it is not clear if this is the true explanation.

The 12 and 25 μm band PSDs displayed in Figures 6a and 6b are very close to horizontal, indicating perhaps that point sources (perhaps

unsubtracted stars) are still important in these scans near
Variations of PSD slope with spectral band and position are shown in Figures 7, 8 and 9 and are discussed in the next section.

This IR cirrus spatial analysis demonstrates that the PSD spatial structure analysis provides a useful parametric technique for describing the cirrus structured backgrounds. The PSDs produced for a variety of LOS directions for each of the four IRAS wavelength bands show presence of point-like (or white-noise) backgrounds in the 12 μm band, which may be attributable to zodiacal radiance (photon noise) or to unresolved IR cirrus.

CELESTIAL BACKGROUND STRUCTURE DEFINITION STUDY

Contract Number **JSE-88-S-001**

FINAL REPORT -- DUE SEPTEMBER 15, 1988

Figure Captions

Figure 1-- Overview of data processing. Sources of data are discussed in the text. Details of the data flow are contained in Figures 2, 3, and 4.

Figure 2a-- Data Flow Diagram (DFD) of the processing performed on the VAX mainframe computer system. Deliverable data files and program source codes are supplied on two 1600 bpi VAX tapes. Hard copies of two of the PSD plots after deconvolution are shown in Figures 5 and 6. Plots of the noise-less PSDs have already been delivered. Programs without a language listed were supplied by the system and were not written as part of this contract, so are not included on the tapes.

Figure 2b-- Data Flow Diagram of the processing performed on the MacIntosh personel computer. Deliverable data are are shown in Figures 7, 8, and 9. All programs listed are commercially available and were not written as part of this contract.

Figure 3-- Data Flow Diagram of the FORTRAN program CIRRUS.

Figure 4-- Data Flow Diagram of the FORTRAN program STARECIR.

Figures 5a, b, c, and d-- Plot of the PSD for each of the four bands of the data from SOP 83 OBS 11 over the range selected. PSD is after all processing was performed.

Figures 6a, b, c, and d-- Plot of the PSD for each of the four bands of the data from SOP 103 OBS 4 over the range selected. PSD is after all processing was performed.

Figures 7a, b, c, and d-- Plots of the PSD slopes for each of the four bands as a function of the absolute value of galactic latitude. Equations of linear fit are listed above each plot. Each point represents one data scan. Only those scans that had a second-order term (curvature) of less then 0.25 are listed. However, the slopes are for a first-order (linear) fit. R is the corralation coeficient.

Figures 8a, b, c, and d-- Cross plots of the PSD slopes for each of the four bands. Equations of linear fit are listed above each plot. Each point represents one data scan. Only those scans that had a second-order term (curvature) of

less then 0.25 are listed. However, the slopes are for a first-order (linear) fit. R is the corralation coeficient.

Figure 9-- Plot of the PSD slope for the 100 μm band as a function of galactic longitude. Equation of linear fit is listed above the plot. Each point represents one data scan. Only those scans that had a second-order term (curvature) of less then 0.25 are listed. However, the slopes are for a first-order (linear) fit. R is the correlation coeficient.

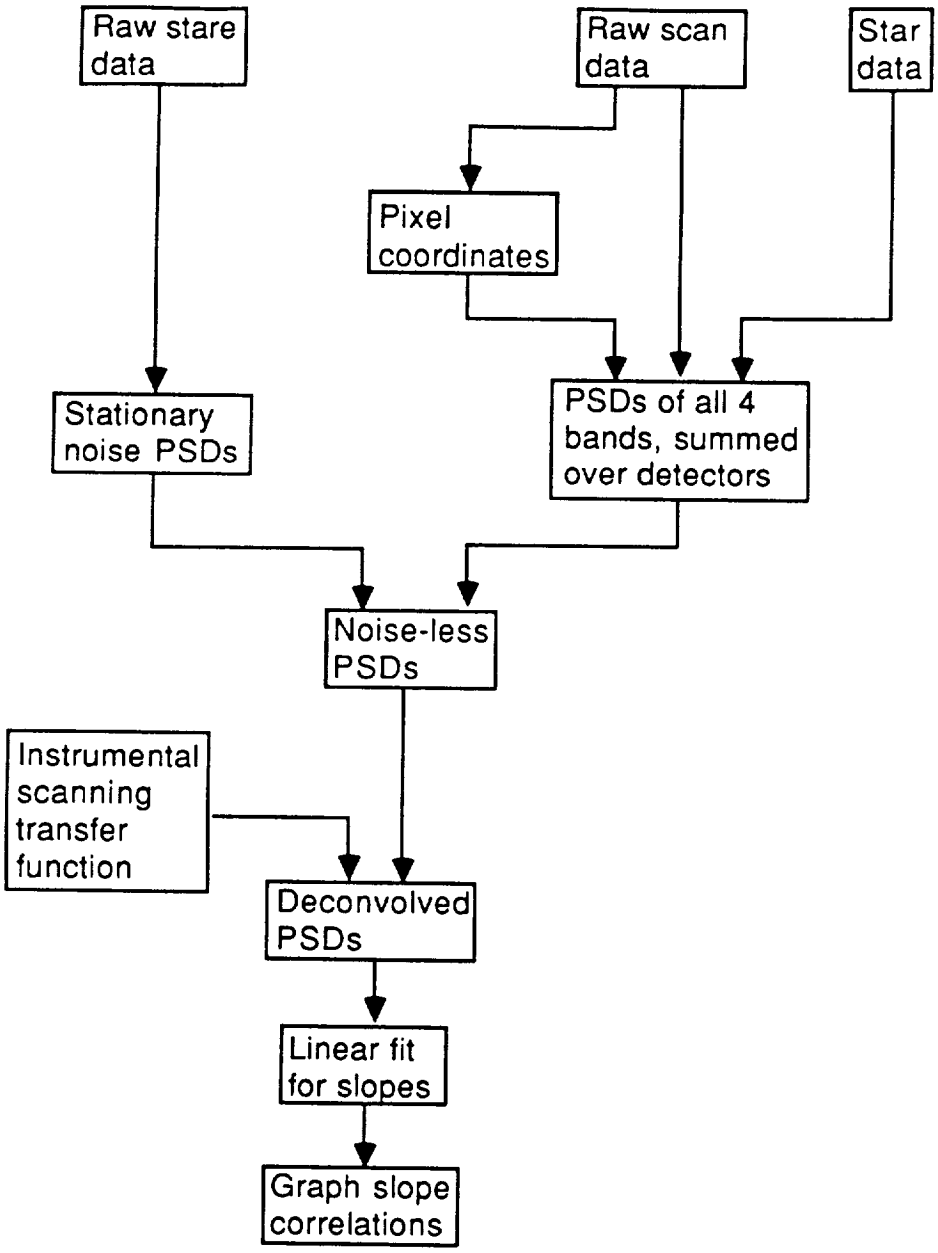
Raw stare data
Raw scan data
Star data
Pixel coordinates
Stationary noise PSDs
PSDs of all 4 bands, summed over detectors
Noise-less PSDs
Instrumental scanning transfer function
Deconvolved PSDs
Linear fit for slopes
Graph slope correlations

Figure 1

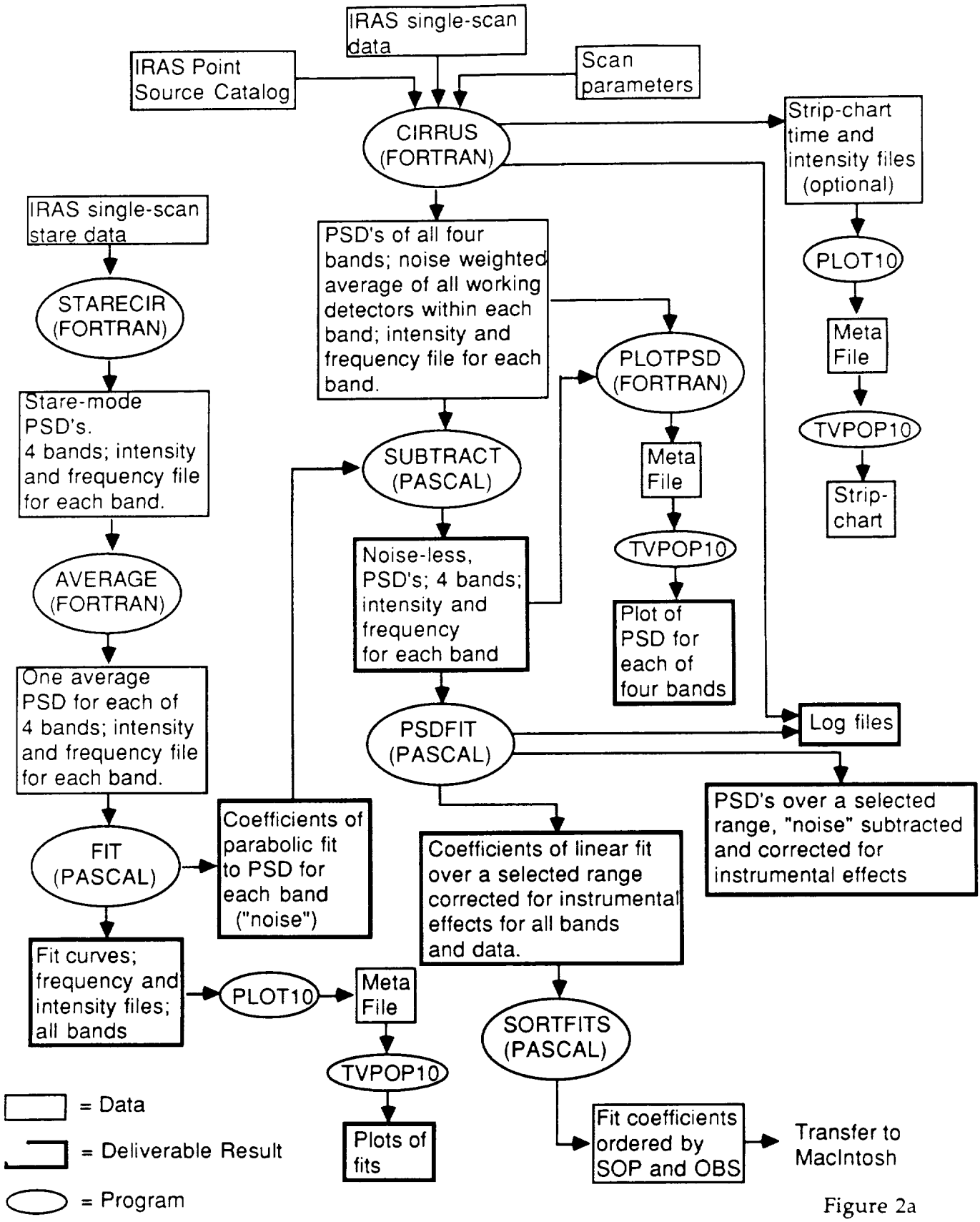
IRAS single-scan data
IRAS Point Source Catalog
Scan parameters
CIRRUS (FORTRAN)
Strip-chart time and intensity files (optional)
PLOT10
Meta File
TVPOP10
Strip-chart
IRAS single-scan stare data
STARECIR (FORTRAN)
Stare-mode PSD's. 4 bands; intensity and frequency file for each band.
AVERAGE (FORTRAN)
One average PSD for each of 4 bands; intensity and frequency file for each band.
FIT (PASCAL)
Coefficients of parabolic fit to PSD for each band ("noise")
Fit curves; frequency and intensity files; all bands
PLOT10
Meta File
TVPOP10
Plots of fits
PSD's of all four bands; noise weighted average of all working detectors within each band; intensity and frequency file for each band.
SUBTRACT (PASCAL)
Noise-less, PSD's; 4 bands; intensity and frequency for each band
PLOTPSD (FORTRAN)
Meta File
TVPOP10
Plot of PSD for each of four bands
PSDFIT (PASCAL)
Log files
PSD's over a selected range, "noise" subtracted and corrected for instrumental effects
Coefficients of linear fit over a selected range corrected for instrumental effects for all bands and data.
SORTFITS (PASCAL)
Fit coefficients ordered by SOP and OBS
Transfer to MacIntosh
= Data
= Deliverable Result
= Program

Figure 2a

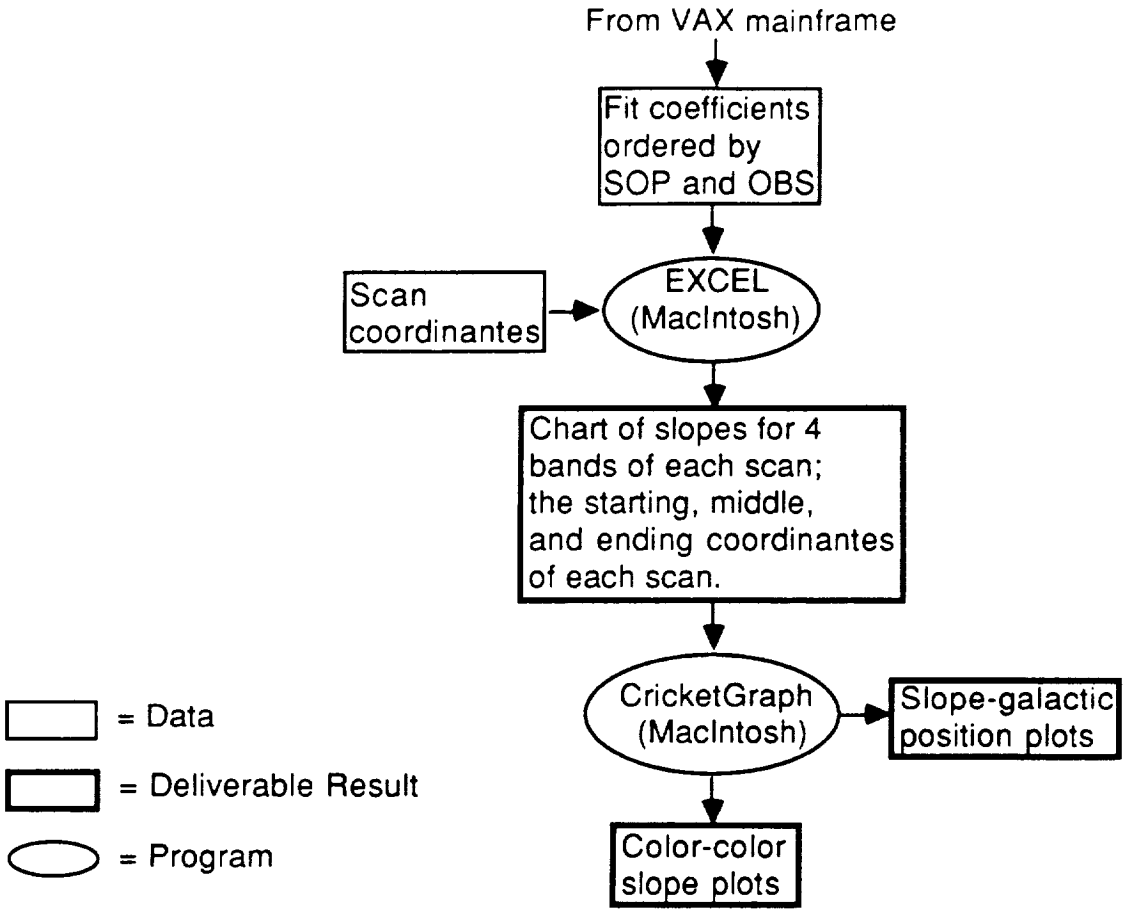
From VAX mainframe
Fit coefficients ordered by SOP and OBS
Scan coordinantes
EXCEL (MacIntosh)
Chart of slopes for 4 bands of each scan; the starting, middle, and ending coordinantes of each scan.
CricketGraph (MacIntosh)
Slope-galactic position plots
Color-color slope plots
= Data
= Deliverable Result
= Program

Figure 2b

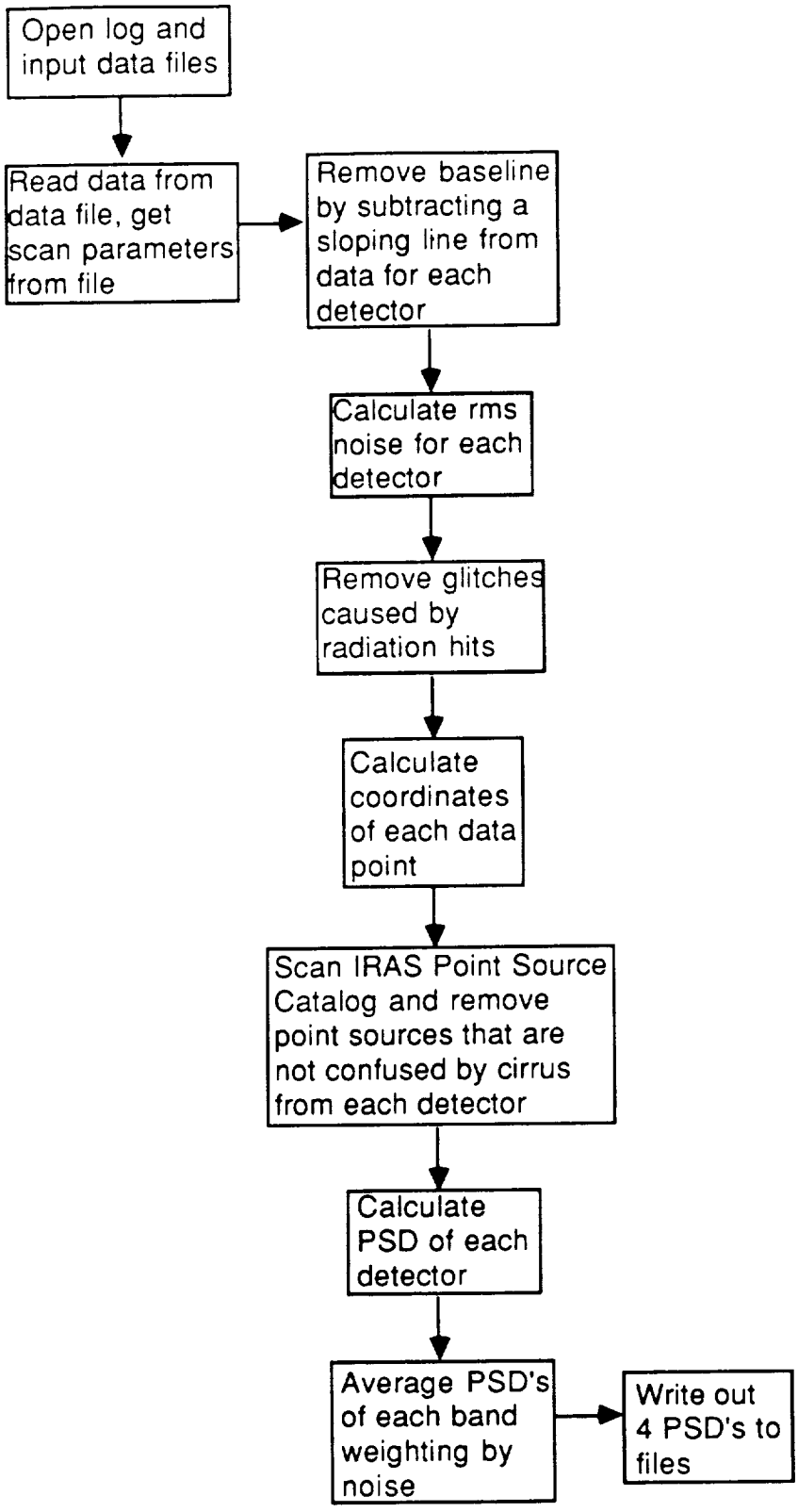
Open log and input data files
Read data from data file, get scan parameters from file
Remove baseline by subtracting a sloping line from data for each detector
Calculate rms noise for each detector
Remove glitches caused by radiation hits
Calculate coordinates of each data point
Scan IRAS Point Source Catalog and remove point sources that are not confused by cirrus from each detector
Calculate PSD of each detector
Average PSD's of each band weighting by noise
Write out 4 PSD's to files

Figure 3

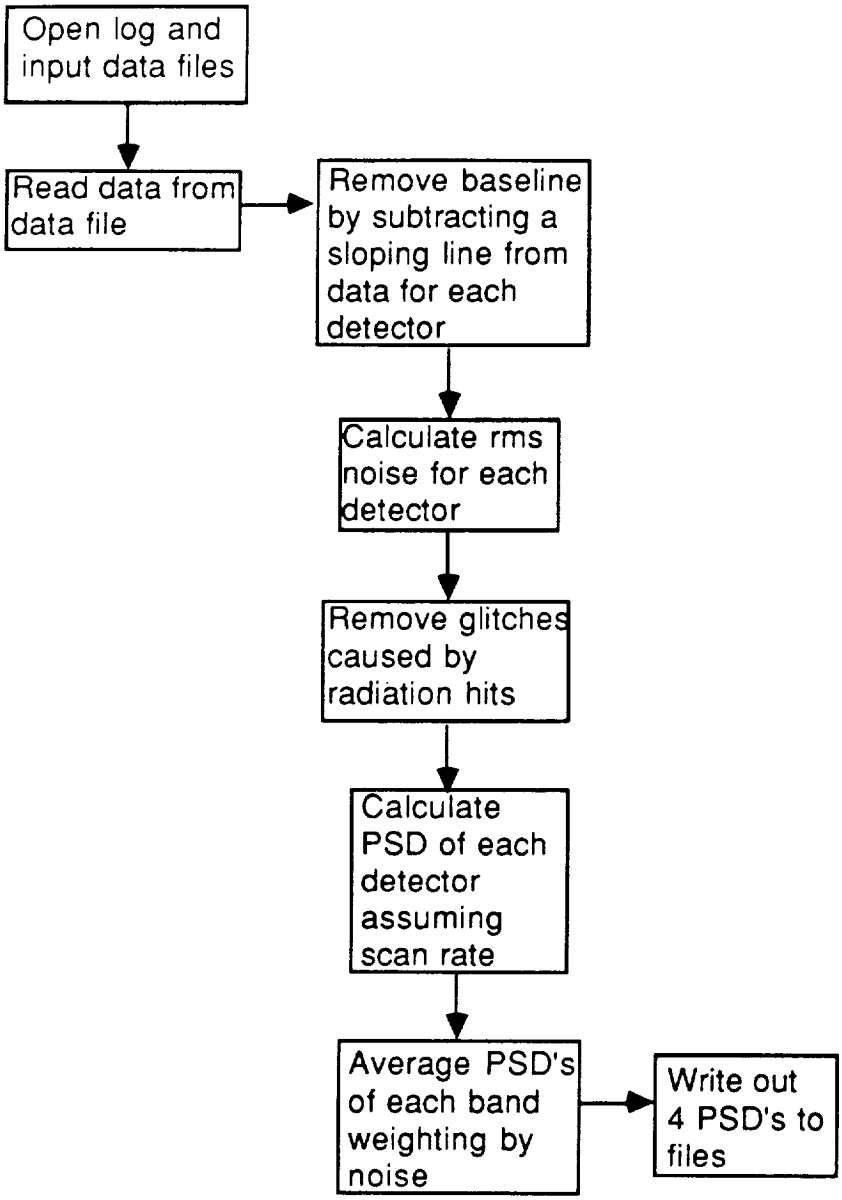
Open log and input data files
Read data from data file
Remove baseline by subtracting a sloping line from data for each detector
Calculate rms noise for each detector
Remove glitches caused by radiation hits
Calculate PSD of each detector assuming scan rate
Average PSD's of each band weighting by noise
Write out 4 PSD's to files

Figure 4

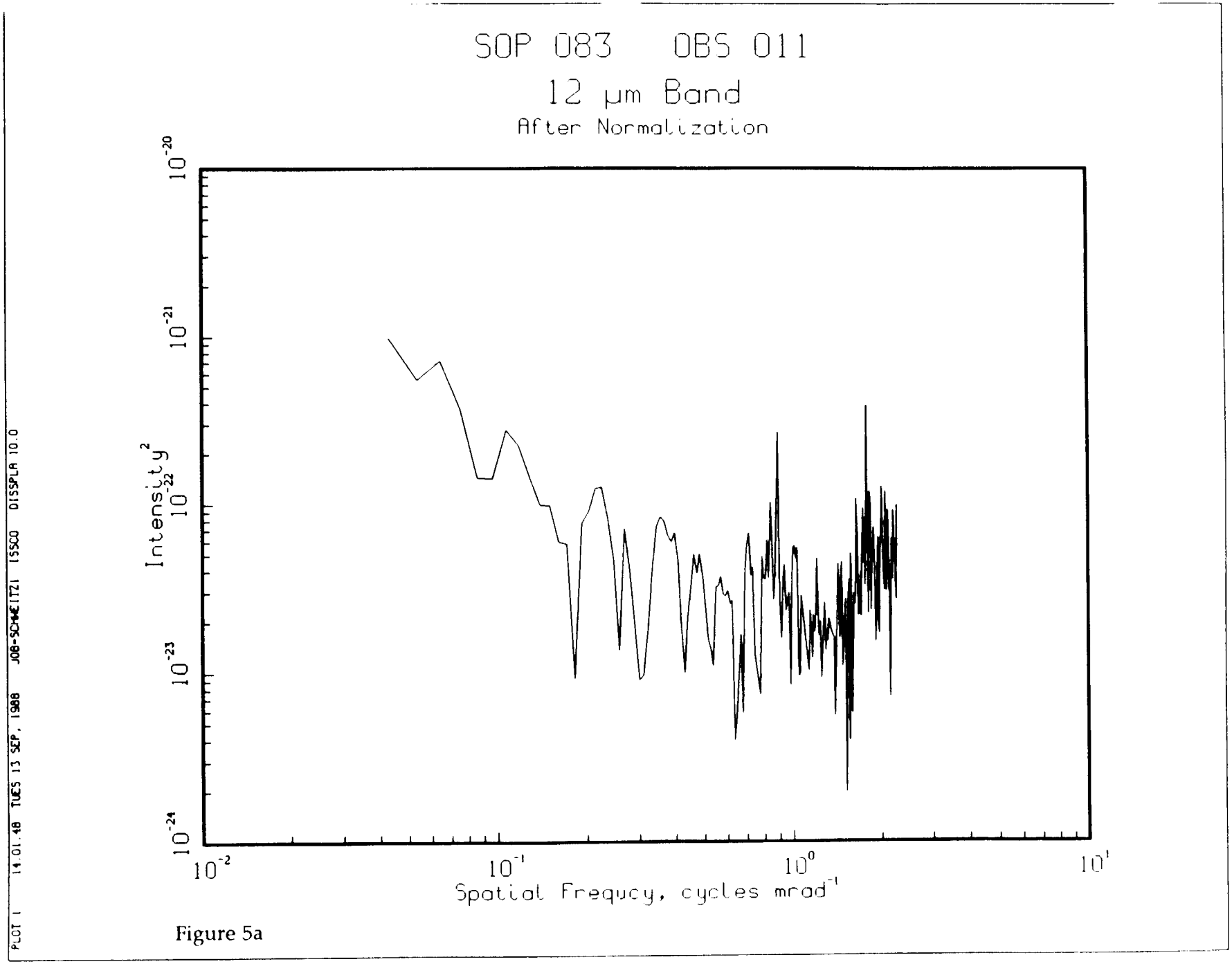
SOP 083 OBS 011
12 μm Band
After Normalization
Intensity^2
10^{-20}
10^{-21}
10^{-22}
10^{-23}
10^{-24}
10^{-2}
10^{-1}
10^{0}
10^{1}
Spatial Frequcy, cycles mrad^{-1}
PLOT 1 14.01.48 TUES 13 SEP, 1988 JOB-SCHEITZI ISSCO DISSPLA 10.0

Figure 5a

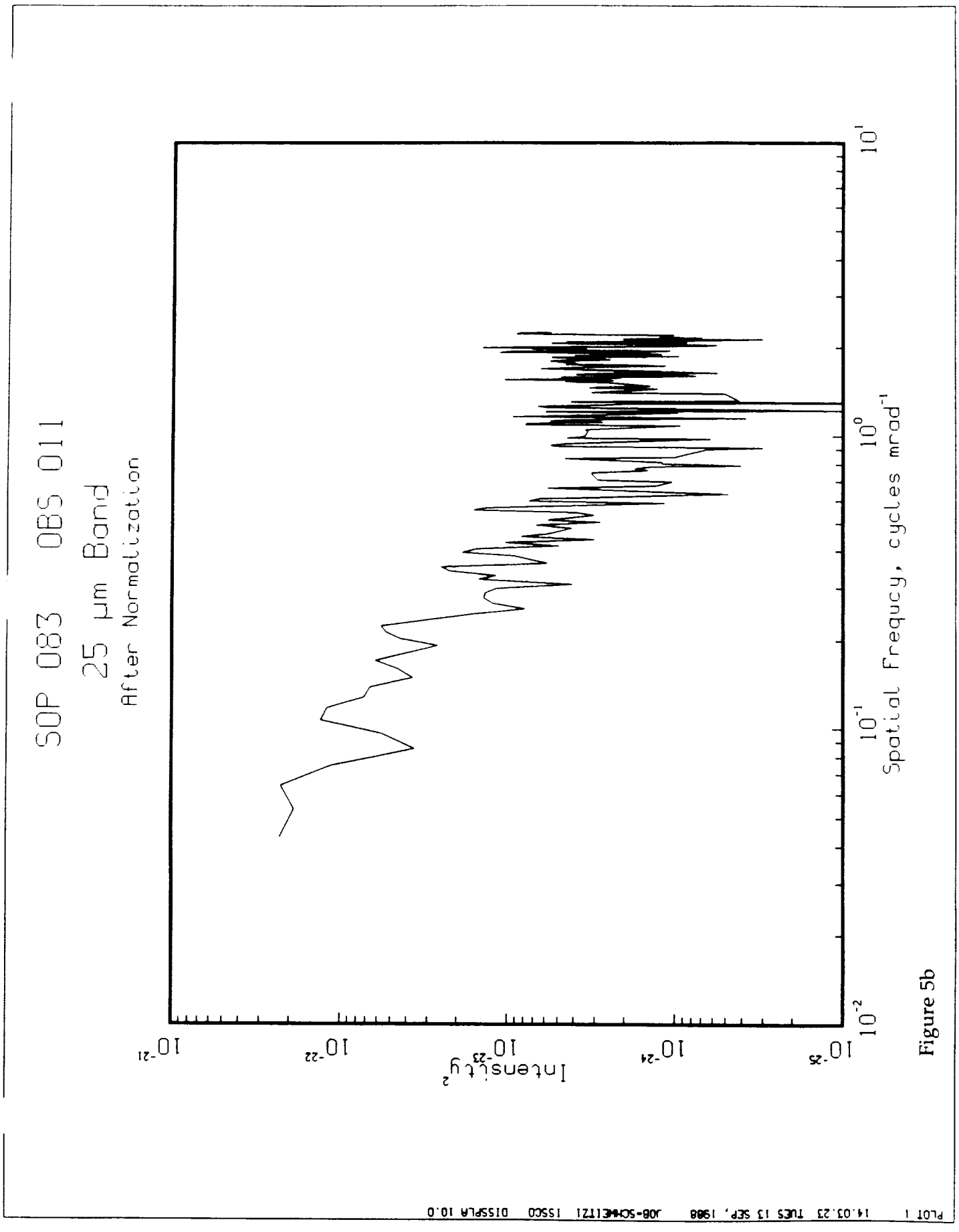
SOP 083 OBS 011
25 μm Band
After Normalization
Intensity²
Spatial Frequcy, cycles mrad⁻¹
10⁻²¹
10⁻²²
10⁻²³
10⁻²⁴
10⁻²⁵
10⁻²
10⁻¹
10⁰
10¹
PLOT 1 14:03:23 TUES 13 SEP, 1988 J08-SCHMEITZI ISSCO DISSPLA 10.0

Figure 5b

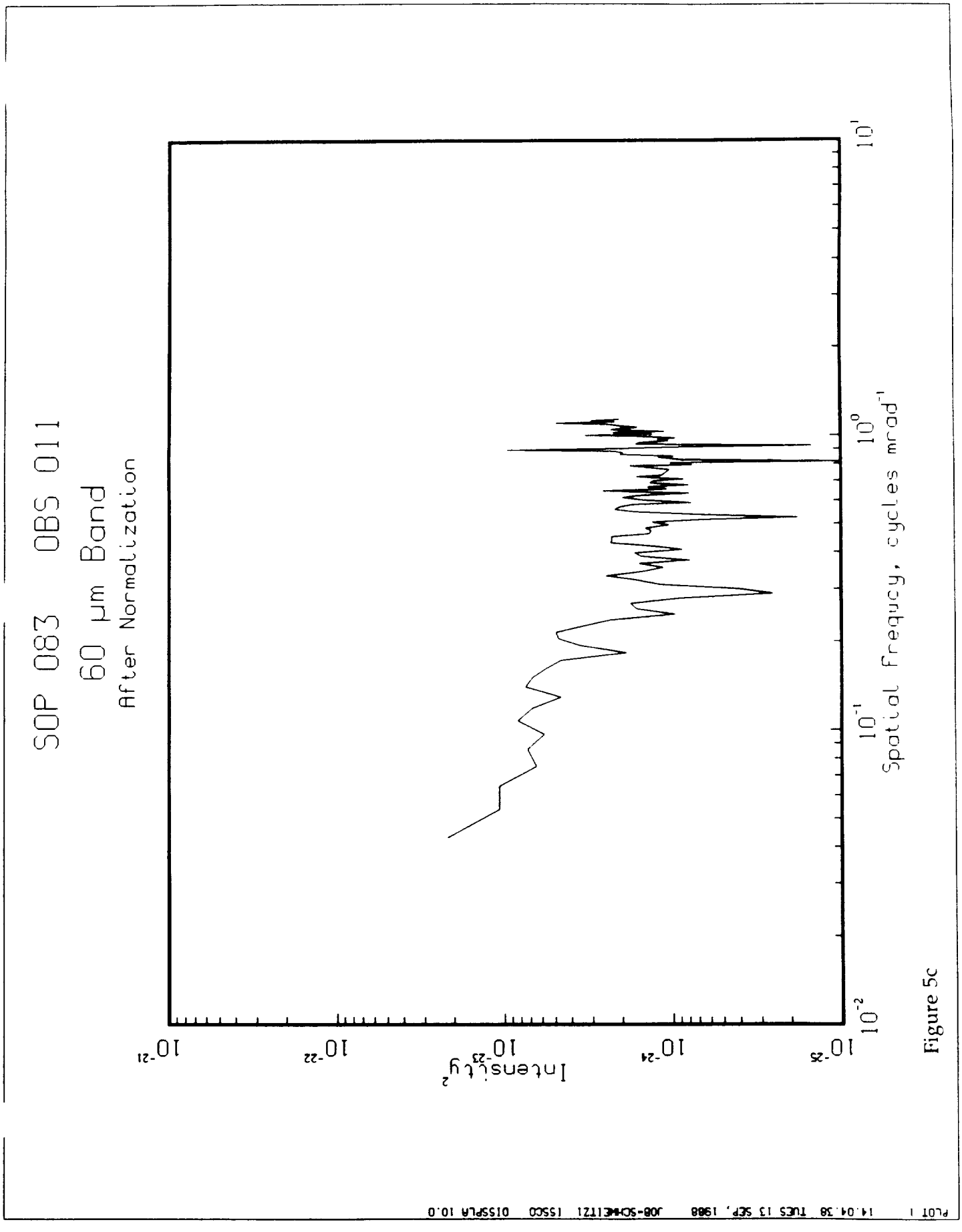
SOP 083 OBS 011
60 μm Band
After Normalization
Intensity²
10⁻²¹
10⁻²²
10⁻²³
10⁻²⁴
10⁻²⁵
10⁻²
10⁻¹
10⁰
10¹
Spatial Frequcy, cycles mrad⁻¹
PLOT 1 14:04:38 TUES 13 SEP, 1988 J08-SCHMEITZI 1550 0155PLA 10.0

Figure 5c

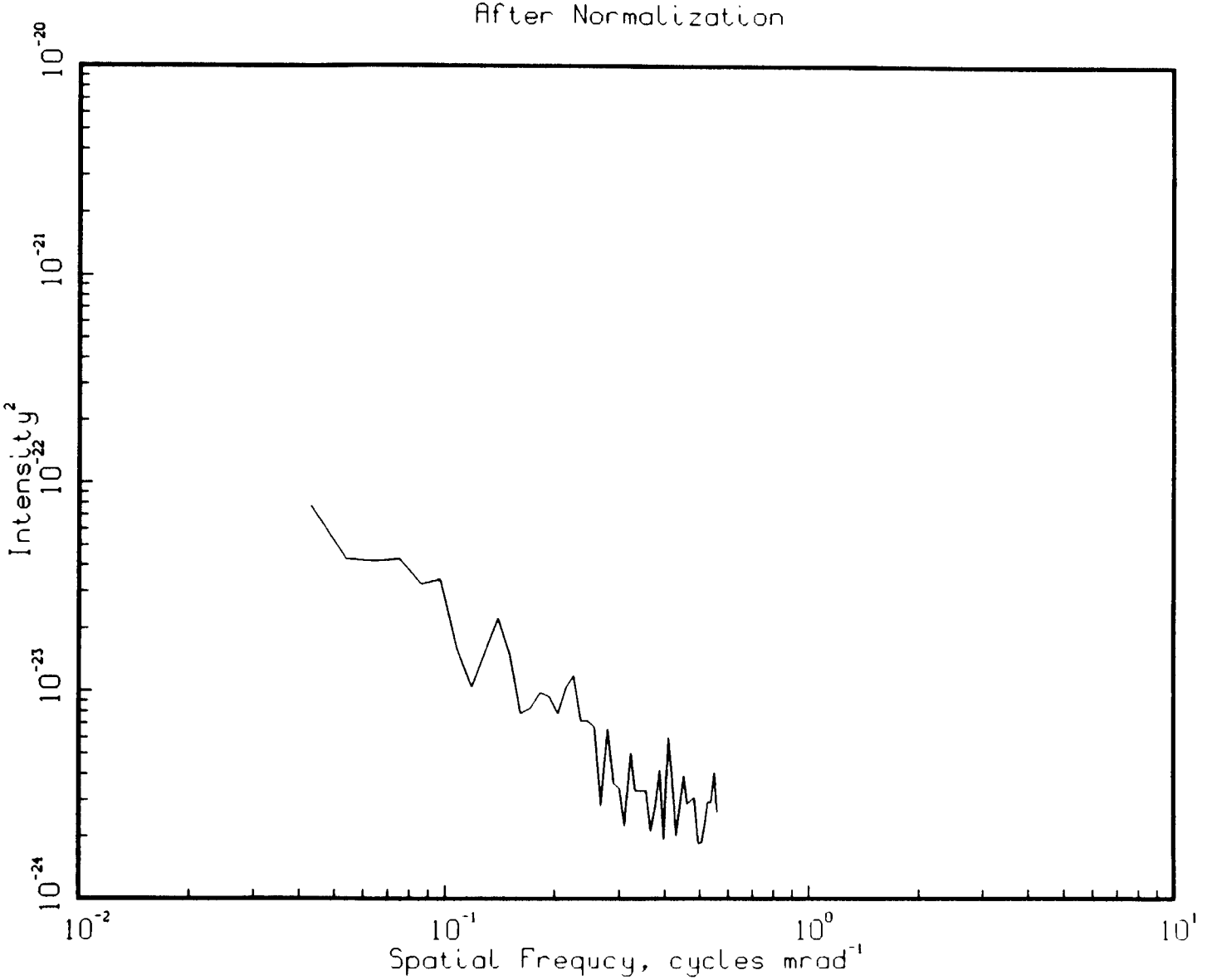

Figure 5d

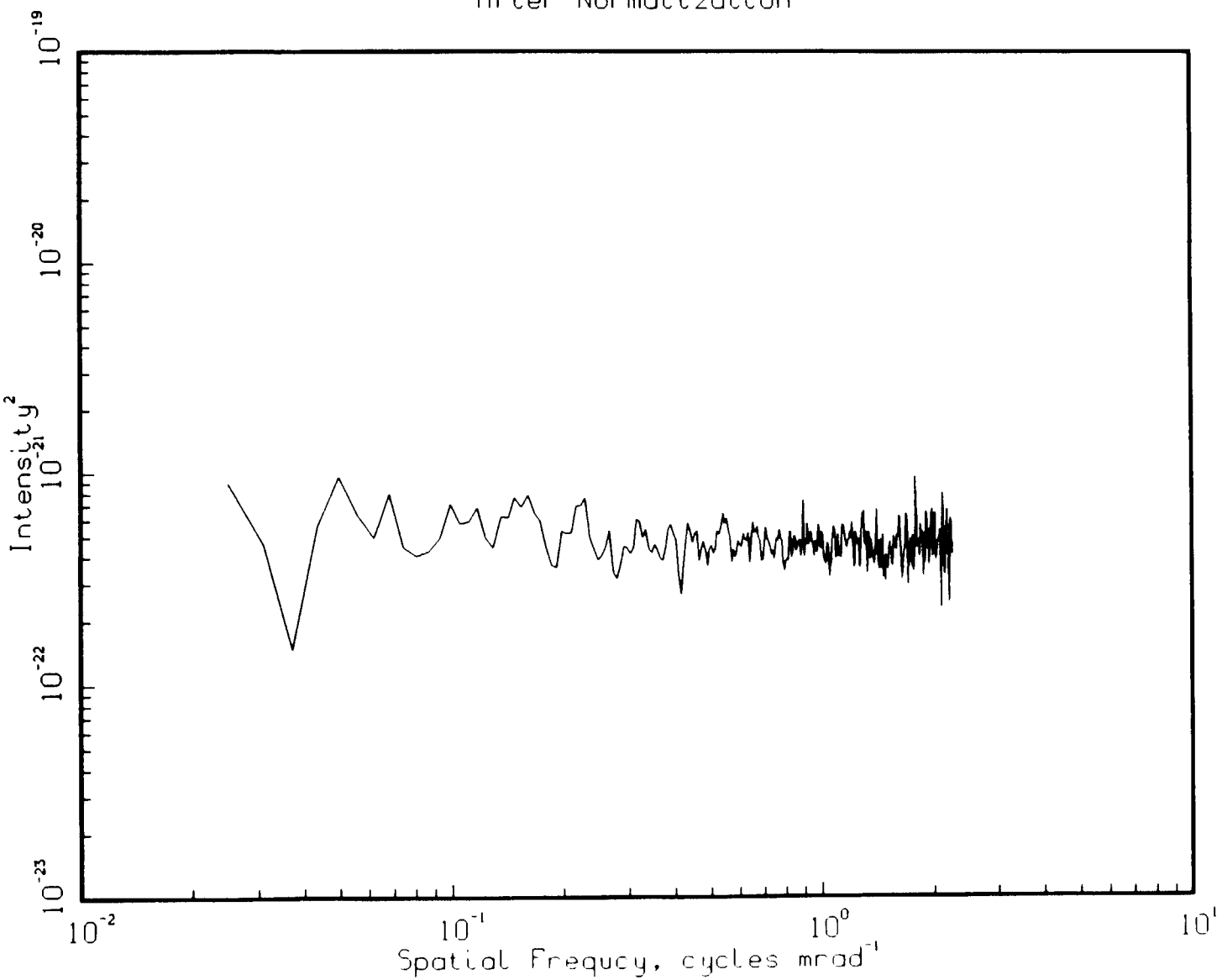
SOP 103 OBS 004
12 μm Band
After Normalization
Intensity^2
10^{-19}
10^{-20}
10^{-21}
10^{-22}
10^{-23}
10^{-2}
10^{-1}
10^{0}
10^{1}
Spatial Frequcy, cycles mrad^{-1}
PLOT 1 13.38.45 TUES 13 SEP, 1988 JOB-SCHMEITZI ISSCO DISSPLA 10.0

Figure 6a

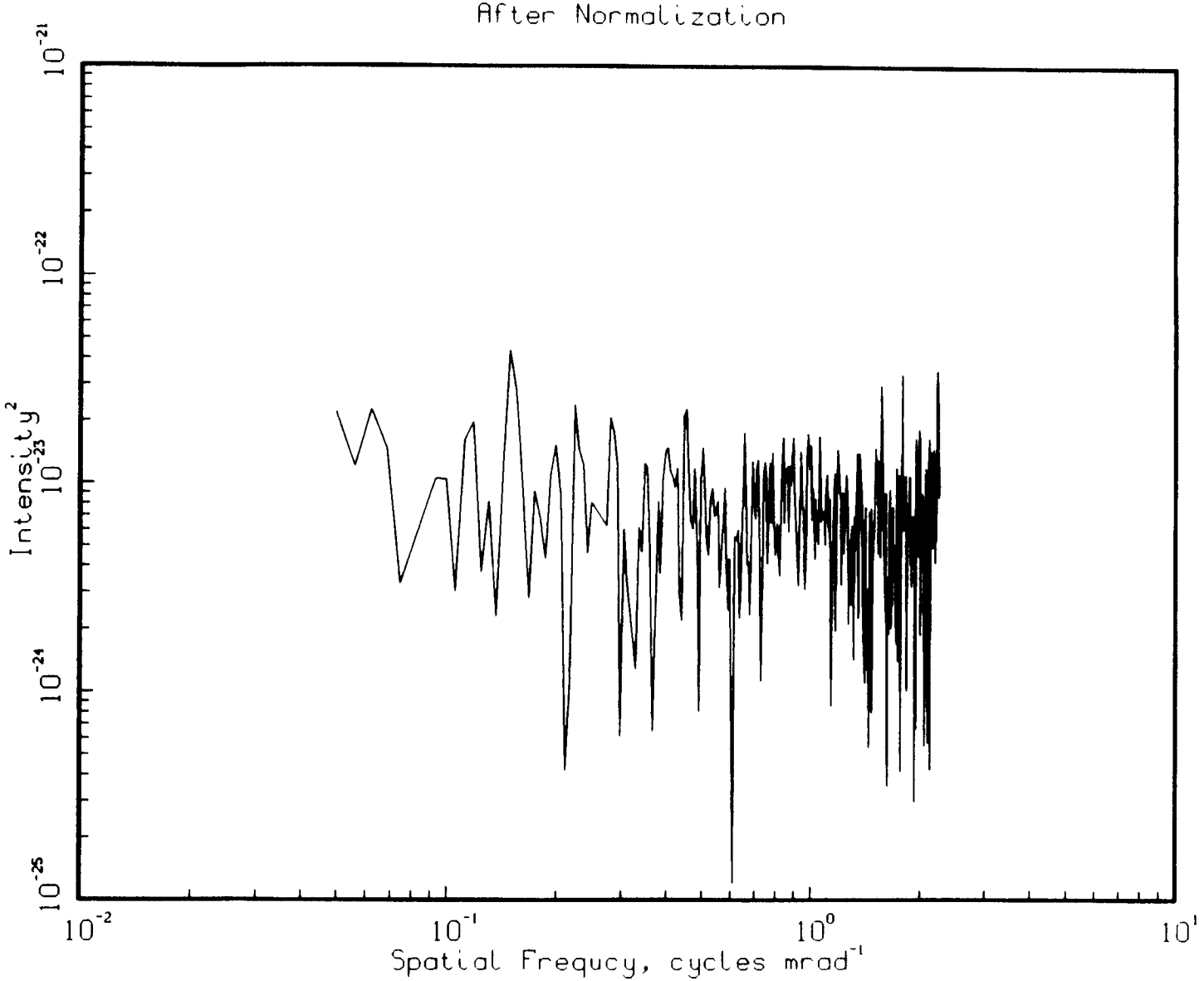
SOP 103 OBS 004
25 μm Band
After Normalization
Intensity^2
10^{-21}
10^{-22}
10^{-23}
10^{-24}
10^{-25}
10^{-2}
10^{-1}
10^{0}
10^{1}
Spatial Frequcy, cycles mrad^{-1}
PLOT 1 13.41.26 TUES 13 SEP, 1988 JOB-SCHMEITZI ISSCO DISSPLA 10.0

Figure 6b

PLOT 1 13.44.00 TUES 13 SEP, 1988 JOB-SCHWEITZI ISSCO DISSPLA 10.0

Figure 6c

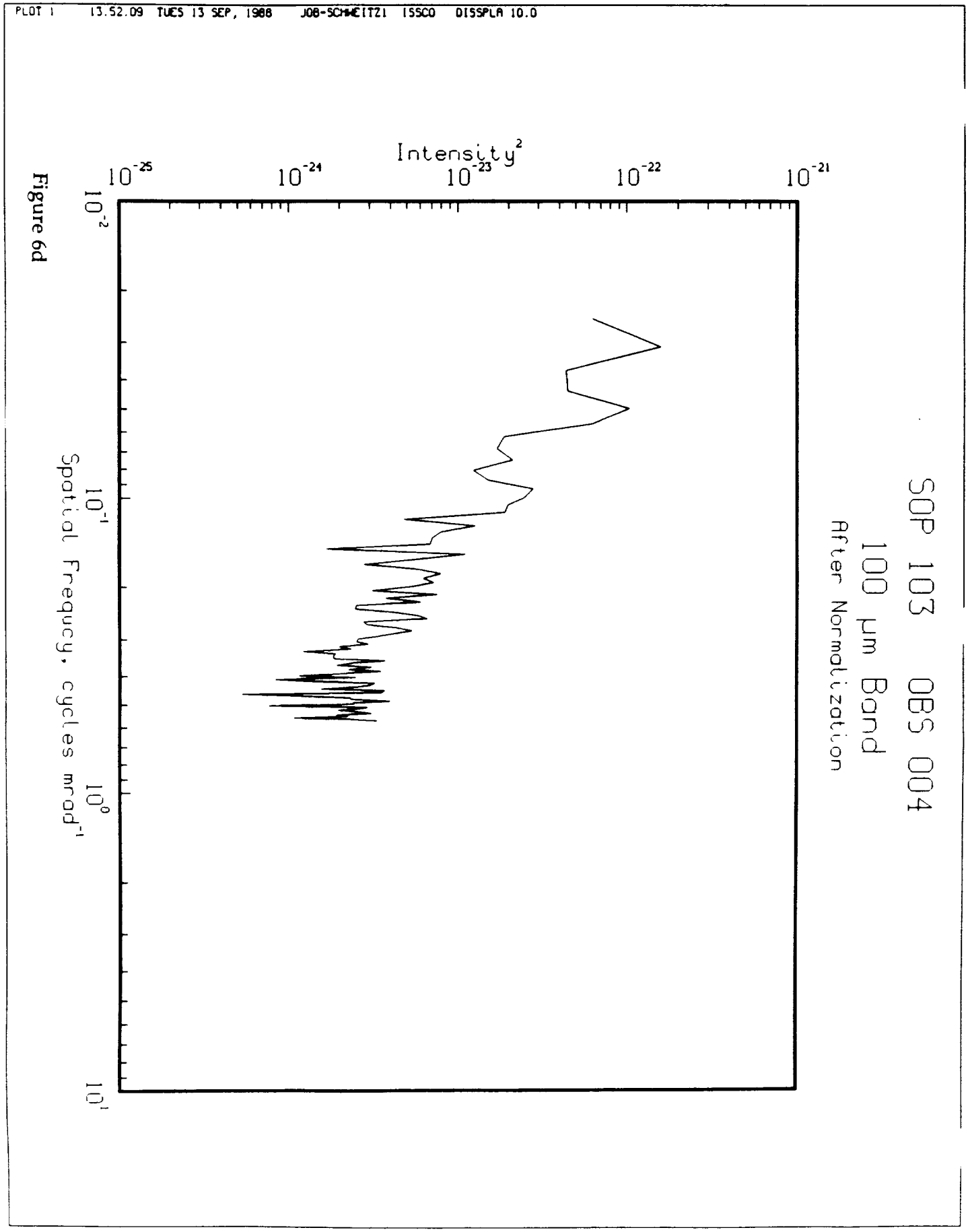
PLOT 1 13.52.09 TUES 13 SEP, 1988 JOB-SCHWEITZI ISSCO DISSPLA 10.0
Intensity^2
10^{-25}
10^{-24}
10^{-23}
10^{-22}
10^{-21}
10^{-2}
10^{-1}
10^{0}
10^{1}
Spatial Frequcy, cycles mrad^{-1}
SOP 103 OBS 004
100 μm Band
After Normalization

Figure 6d

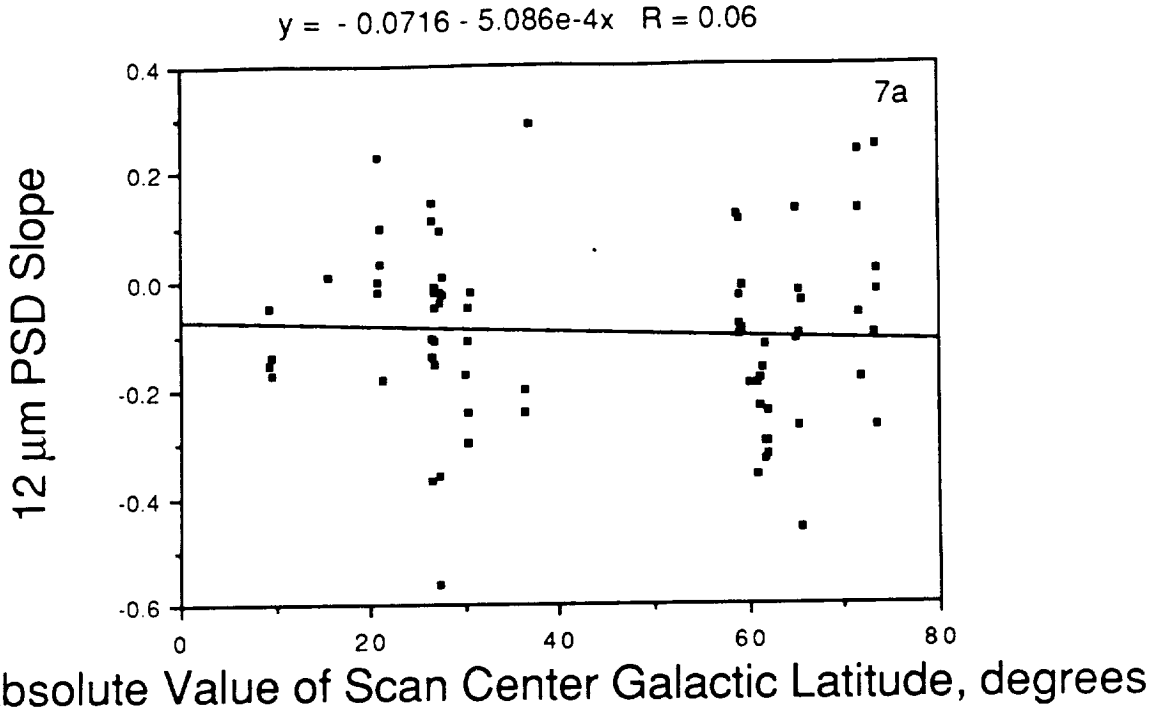
y = - 0.0716 - 5.086e-4x R = 0.06
7a
12 µm PSD Slope
0.4
0.2
0.0
-0.2
-0.4
-0.6
0
20
40
60
80
Absolute Value of Scan Center Galactic Latitude, degrees

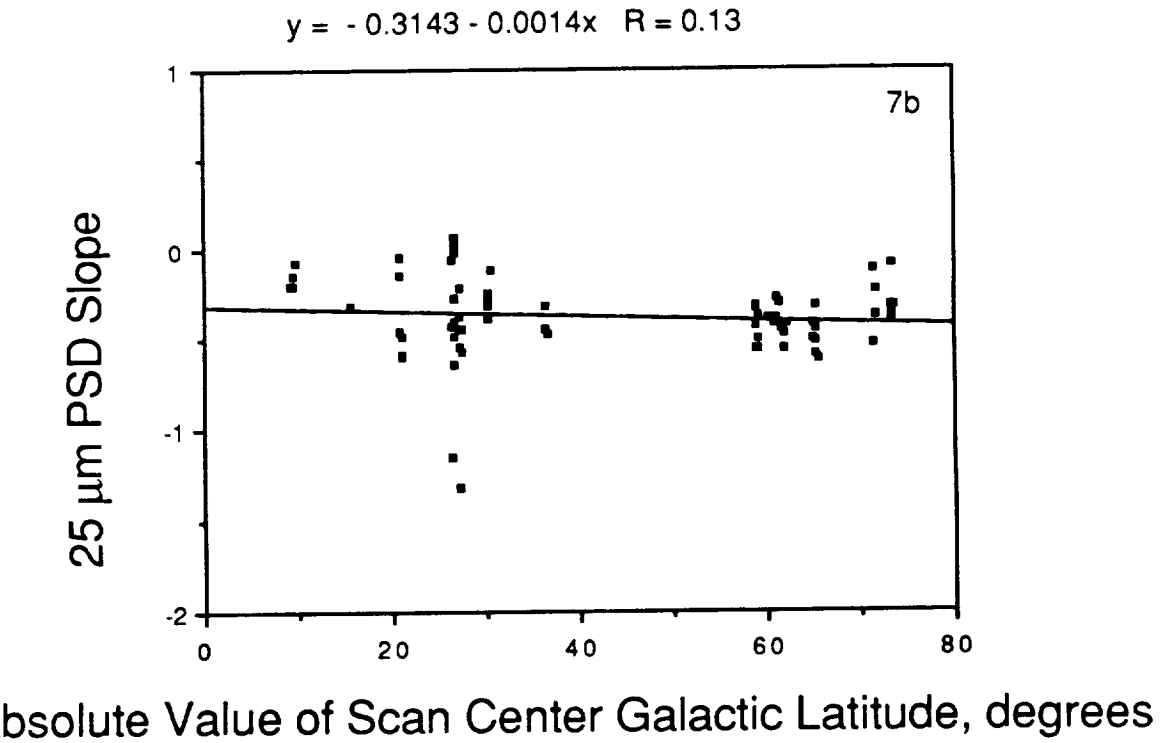
y = - 0.3143 - 0.0014x R = 0.13
7b
25 µm PSD Slope
1
0
-1
-2
0
20
40
60
80
Absolute Value of Scan Center Galactic Latitude, degrees

Figure 7

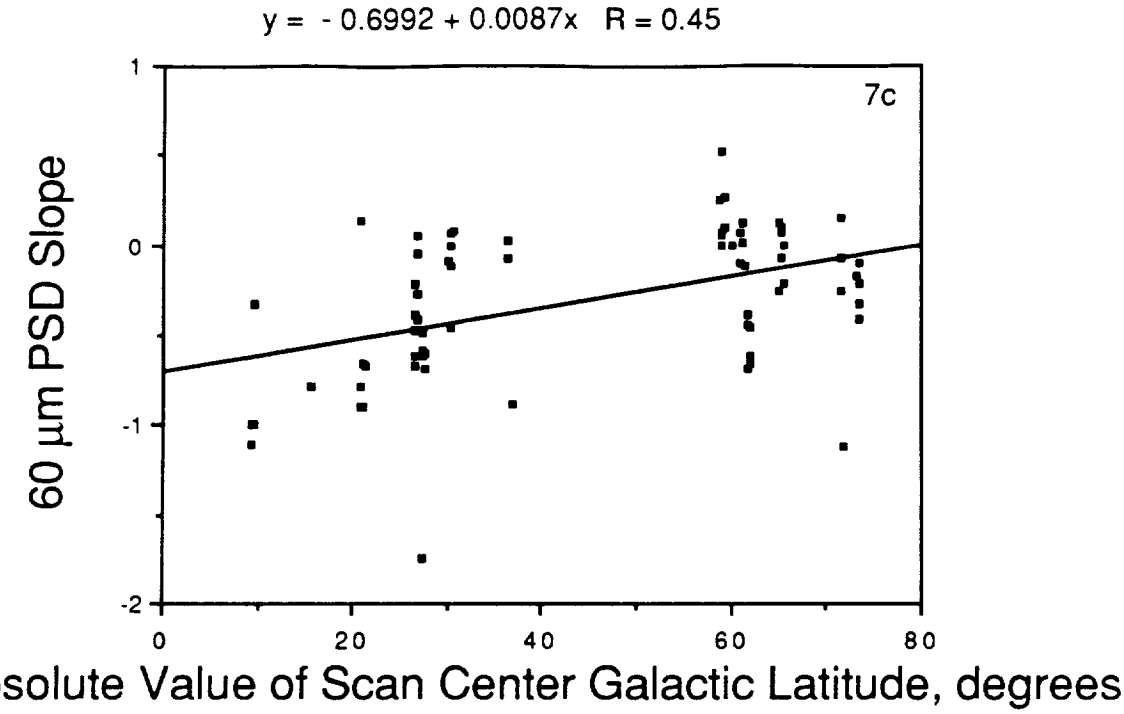
y = - 0.6992 + 0.0087x R = 0.45
7c
60 µm PSD Slope
1
0
-1
-2
0
20
40
60
80
Absolute Value of Scan Center Galactic Latitude, degrees

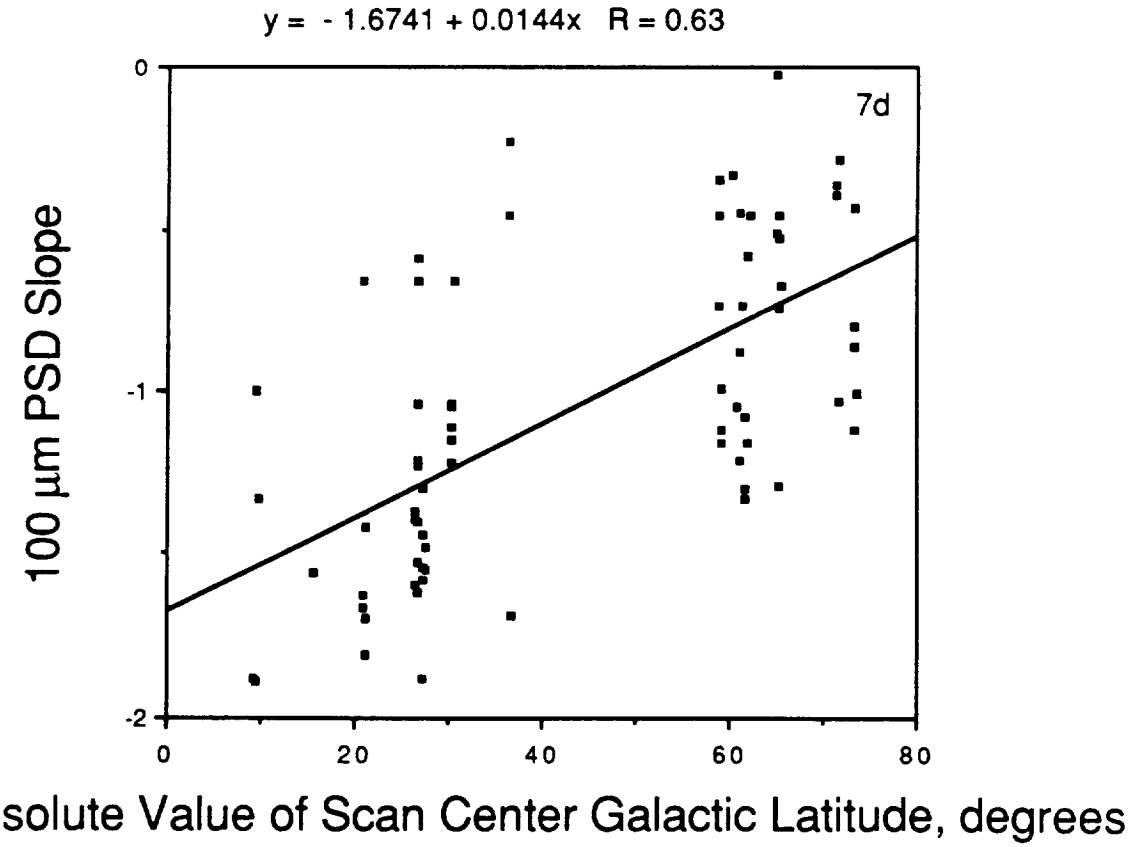
y = - 1.6741 + 0.0144x R = 0.63
7d
100 µm PSD Slope
0
-1
-2
0
20
40
60
80
Absolute Value of Scan Center Galactic Latitude, degrees

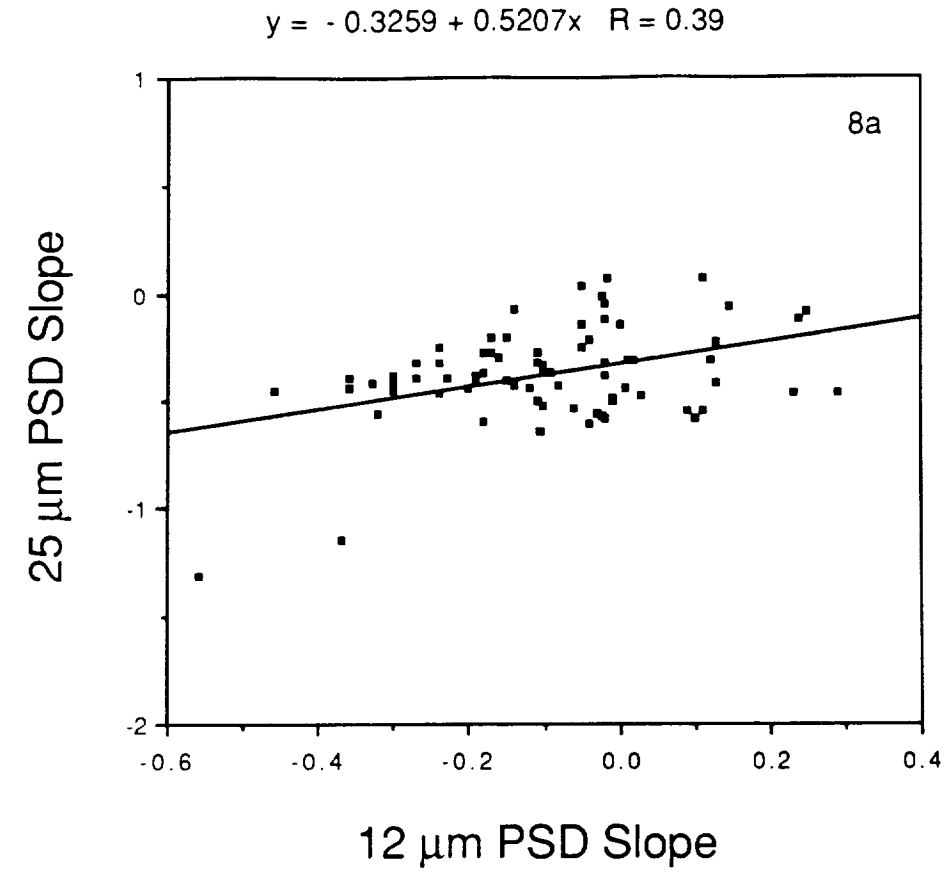
y = - 0.3259 + 0.5207x R = 0.39
8a
25 µm PSD Slope
12 µm PSD Slope
1
0
-1
-2
-0.6
-0.4
-0.2
0.0
0.2
0.4

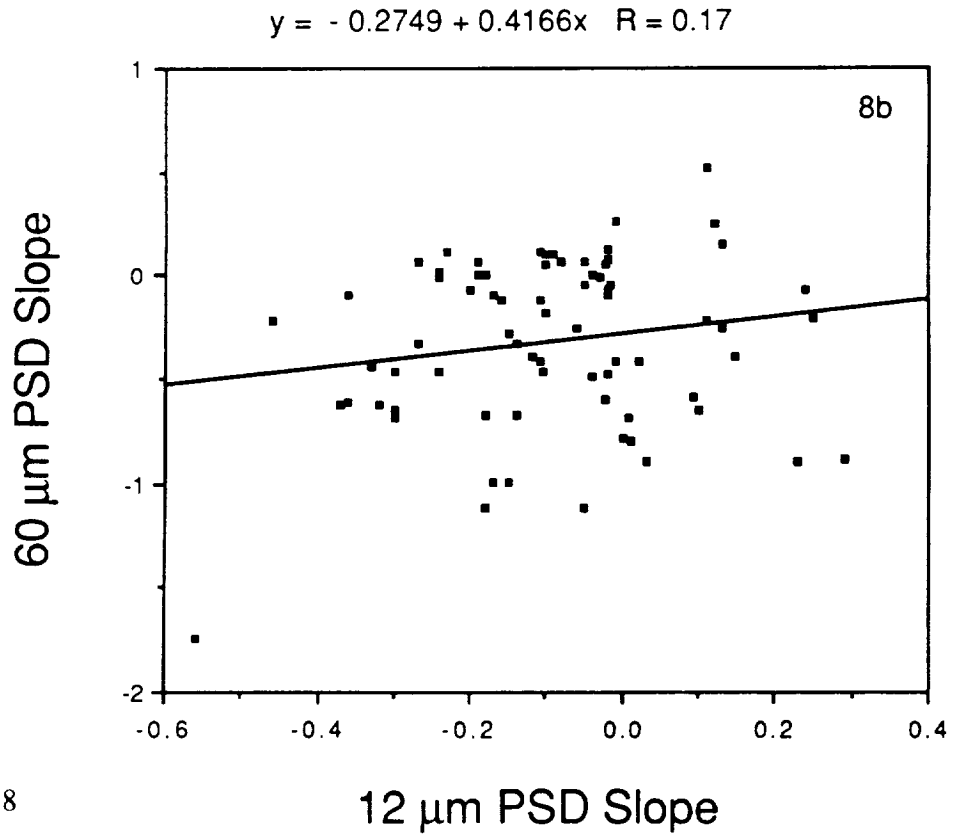
y = - 0.2749 + 0.4166x R = 0.17
8b
60 µm PSD Slope
12 µm PSD Slope
1
0
-1
-2
-0.6
-0.4
-0.2
0.0
0.2
0.4

Figure 8

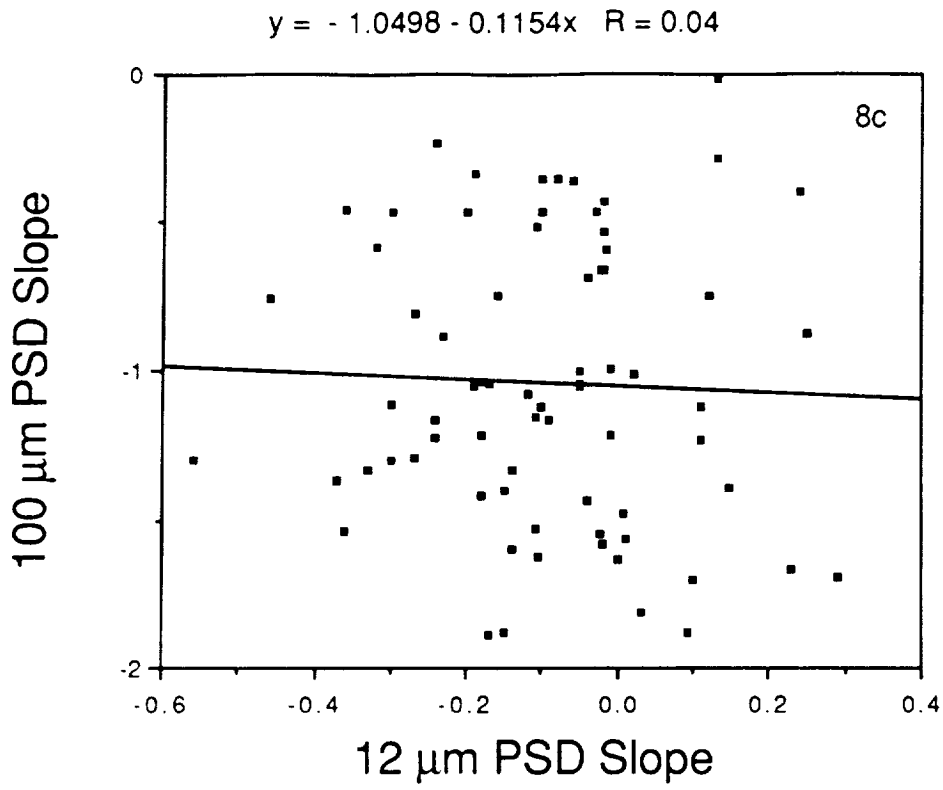
y = - 1.0498 - 0.1154x R = 0.04
8c
100 µm PSD Slope
12 µm PSD Slope
0
-1
-2
-0.6
-0.4
-0.2
0.0
0.2
0.4

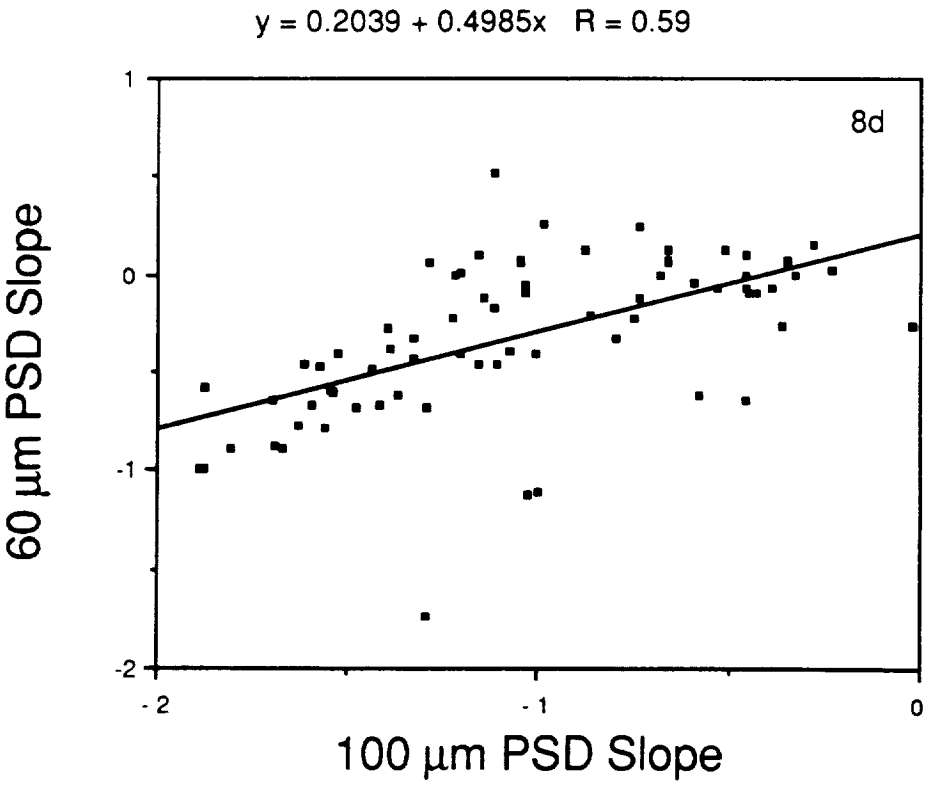
y = 0.2039 + 0.4985x R = 0.59
8d
60 µm PSD Slope
100 µm PSD Slope
1
0
-1
-2
-2
-1
0

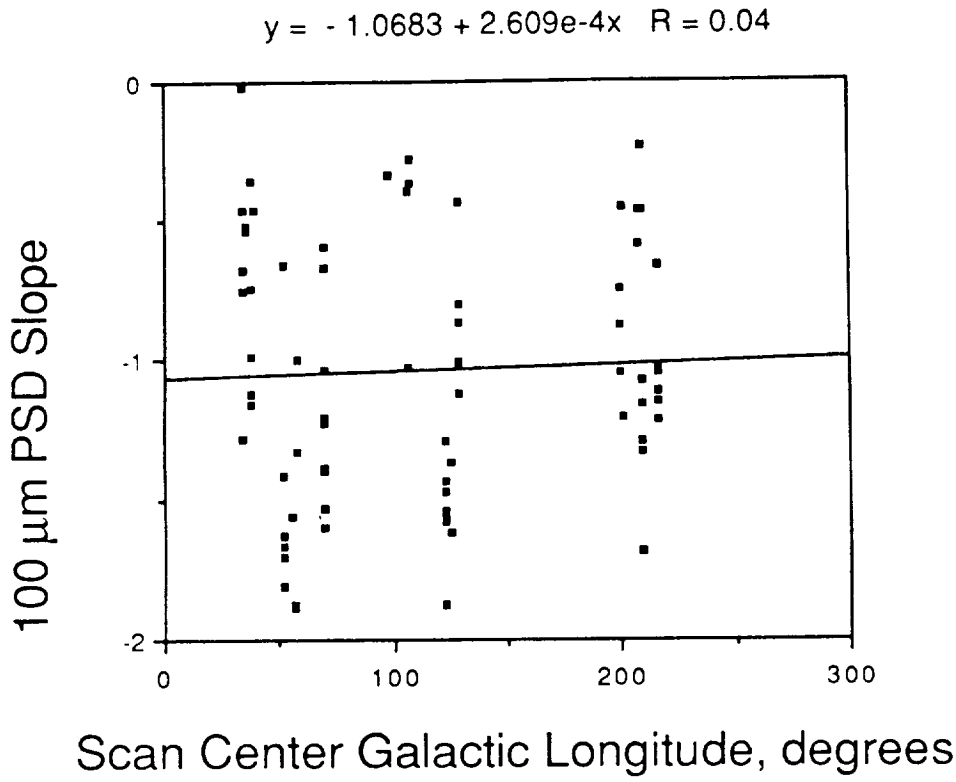
y = - 1.0683 + 2.609e-4x R = 0.04
0
-1
-2
100 µm PSD Slope
0
100
200
300
Scan Center Galactic Longitude, degrees

Figure 9

APPENDIX L. "Celestial Background Structure Analysis"

APPENDIX L. Celestial Background Structure Analysis

Introduction

The work reported in Appendix K was primarily concerned with the acquisition and processing of IRAS scans for power spectral density (PSD) analysis. Little was accomplished to relate the measured PSD's to the phenomenon being observed. It is the purpose of this paper to examine the source of the PSDs and attempt to sort out the observations and assess their significance in the context of the type of celestial source responsible.

Method

One method successfully used in astronomy to classify astronomical sources is by their colors, or in the infrared, the logarithm of the ratio of the fluxes observed in different spectral bands. To apply this technique to the PSD data we integrate the PSD over frequency to estimate the total power in the spectrum. For a spectrum that can be expressed as a power law,

$$S(f) = a\ f^{b} \tag{1}$$

then the total flux R within the bandpass of spatial frequencies 0 to f_c is given by

$$R = \int S(f)\ df = [a/(|b|+1)]\ f_c^{(b+1)} \tag{2}$$

which for the case $f_c = 1$, reduces to $R = [a/(|b|+1)]$.

To relate the infrared colors and fluxes to the composition of the regions scanned, overlays of the focal plane scan tracks were prepared to the scale of the IRAS Sky Flux Plates, and the plates examined. Table 1 contains a brief summary of the morphology pertaining to each of the PSD scans. Table 2 presents a summary of the color, flux, and slope data. To derive IRAS in-band flux ratios from the colors given in Table 2, use the following: if F12/F25 is the IRAS flux ratio and C is the tabulated color then

$$F12/F25 = 10^{C/2} \tag{3}$$

and similarly for the other colors.

Results

Fluxes and flux ratios calculated from Equation 2 are plotted in various combinations in Figures 1 through 6. These plots may be

used to discriminate classes of objects, for example, in Figure 1 sources with both log(R12/R25) and log(R25/R60) near 1 have colors of normal relatively hot stars, while those with log(R12/R25) > 1.2 and large R25/R60 ratios are probably due to reflection of star light by small particles in nebulae. The cluster of five sources near log R12 = -9.6 in Figure 4 is composed of four scans through the OB association in Lacertae and one scan in a region identified with reflection nebulae (see Table 1, fields 46,26).

Several correlations of the slope of the PSD with flux and color are shown in Figures 7, 8 and 9. The system has been deconvolved from the PSD data, therefore, a bright point source or ensemble of point sources will have a PSD with slope b = 0. Positive slopes, which may have physical meaning in some contexts, are in all cases considered here due to low SNR in the measurement and must be considered spurious. The scale of the spatial structure increases with an increasing absolute value of the negative slopes. Figure 7 shows a concentration of b value in the $0 < b < -0.04$ due to point-like sources. The five reflection nebulae at log R12 = -9.6 have b = -.08 indicating that these sources are slightly extended.

Since the infrared cirrus is dominant at 60 and 100 μm one would expect their slopes to show a good correlation. This is in fact the case as can be seen in Figure 11. Of equal interest is the cluster of 10 scans in the range $-2 < b(60) < -1$ and $-1.6 < b(100) < -.9$. These are from scans at galactic latitudes -10° and $+9^{\circ}$.

The plot of the 100 μm slope versus galactic latitude in Figure 12 shows a great deal of scatter but a decided trend for the scale of the structures to increase with decreasing galactic latitude. This is what one would expect if the cirrus was spread throughout the galactic plane rather than being exclusively a nearby phenomenon. As we view closer to the plane our line of sight passes through more cirrus. The superposition of cirrus elements merge to form larger scale structures. In addition, the higher temperature of the cirrus near the plane may be more conducive to the formation of larger turbulent elements.

The data plotted in Figures 13 and 14 are for 25 μm. The radiance of the infrared cirrus is a minimum at 25 μm and it is reasonable to expect that these data will provide information on the Zodiacal background which is dominant. In Figure 13 we plot the PSD flux as a function of ecliptic latitude for scans at high galactic latitude and away from obvious cirrus features. There is a notable increase in the flux at low latitudes in agreement with that discussed in Appendix O. The slopes of the PSD are shown in Figure 14. There is little variation with latitude with the values being scattered from about -0.28 to -0.48. Slopes in this range are indicative of small extended structures. Two sets

of scans were made in the region of the broader zodiacal bands. The set which scanned both central α bands and one of the β bands had a mean slope b = -0.35±0.9 and a flux of $(3.5\pm2)\times10^{-12}$ w cm^{-2} sr^{-1}. The other set which scanned the region between the β and γ bands was found to have a mean slope of b = -0.26±.08 and a flux of $(5.1\pm2)\times10^{-12}$ w cm^{-2} sr^{-1}. Thus there does not seem to be a significant difference in the scale of the structure observed at the two positions. The fluxes observed are somewhat higher than the 1.8×10^{-12} w cm^{-2} sr^{-1} predicted by the noise model in Appendix O.

Table 1. Morphological Description of Cirrus Fields

Field	Band(μm)	Description of Scanned Field
49017	100	1/3 Bright cirrus, field completely covered by cirrus, no bright point sources
(1)	60	same as 100um field
	25	cirrus very faint, possibly one bright point source but more likely a glitch
	12	cirrus easily seen over all the field, many point sources
83006	100	note scan is about 3/2 as long as a normal scan, scan covers brightest part of cirrus
(1)	60	bright cirrus
	25	faint cirrus, possibly faint point sources
	12	bright cirrus, many point sources
103004	100	1/4 bright cirrus, faint cirrus in rest of field, one bright point source
(1)	60	same as 100um but with two bright point sources
	25	faint cirrus obscured by zodiacal emission, several point sources
	12	cirrus in 1/2 field, many point sources
132025	100	1/3 bright cirrus, one very bright extended knot, field full of cirrus
(1)	60	same as above, possible faint point source
	25	field bright with zodiacal emission
	12	faint cirrus with several bright point sources
83011	100	same as 83006, confirming scan, slightly shorter
(1)	60	same as 100um field
	25	zodiacal stripes
	12	same as 83006
49021	100	same as 49017, confirming scan
(1)	60	same as 100um field
	25	cirrus very faint, no evidence of point sources
	12	same as 49017
103008	100	same as 103004, cirrus with bright point source, probably galaxy
(1)	60	same as 103004
	25	same as 103004, one source may be other band of 60 um source
	12	same as 103004

Table 1. Morphological Description of Cirrus Fields (continued)

Field	Band(μm)	Description of Scanned Field
49025	100	same as 49017 and 49021 but contains 4 extended bright cirrus knots not in other fields
(1)	60	same as 100um field
	25	same as 49017 etc.
	12	same as 49017 but with one very bright point source
103001	100	same as 103008 but misses the bright point source
(1)	60	same as the 100um field
	25	same as 103008
	12	same as 103008
132021	100	same as 132025 but with more of the bright cirrus knots
(1)	60	same as 132025
	25	same as 132025 but with no bright point sources
	12	same as 321025 but with no bright point sources
520005	100	good cirrus, less clumpy and fainter than in other plate 1 fields, bright galaxy near end of scan
(1)	60	same as 100um data
	25	very faint cirrus, some point sources
	12	faint cirrus, many point sources
520011	100	same as 520005 field
(1)	60	same as 100um data
	25	same as 520005 but with more bright point sources
	12	same as 520005 but with more bright point sources
333047	100	field full of diffuse cirrus with localized regions which appear like reflection nebulae or shock boundaries, some point sources
(26)	60	same as 100um with the cirrus features more well defined
	25	bright knots and shock-type structures, perhaps reflection nebulae
	12	bright structures still apparent, much like 25um field
257013 ** 295001 (38)		Plate #38 has very faint cool cirrus with much contamination by extragalactic sources. All the scans cover much the same kind of structure although two separate regions were scanned.

Table 1. Morphological Description of Cirrus Fields (continued)

Field	Description of Scanned Field
282005 299025 298020 298023 (46)	All four scans cover the same basic structure. This is a bright filament orientated along the scan direction, with a very bright structure near the southern end of the scans. This is probably the OB association in Lacertae (RA=22h30m,DEC=40d30m). Scan 299025 has much less of the filament and more of the blob at the end. All scans contain numerous bright point sources at 12 and 25 um.
153038 153043 170008 170013 539002 539009 539015 (66)	All of these scans cover the same basic structure near the galactic plane. No point sources are visible at 60 or 100um. Many point sources are in the scans at 12 and 25um. The cirrus is quite uniform with intensity increasing toward the plane.
113045 130014 130019 130024 509030 510026 509035 (65)	All of these scans cover essentially the same structure. Moderately bright cirrus at 60 and 100um that is difficult to see at 12 or 25um. A few point sources are visible in all scans, however, the cirrus clearly dominates the scene at 60 and 100um. The cirrus is quite uniform with intensity increasing toward the plane.
337018 ** 439042 (62)	All of these scans cover the same kind of structure. Faint cirrus which is very cool, seen well at 60 and 100 um, but not at all at 12 and 25um. It appears that a large number of point sources (galaxies) are seen at 60 and 100 um, in fact it would appear that the extra galactic component is dominating the PSD, i.e., flat slopes due to many point sources. It should be noted that this could be a cirrus phenomena - more small knots visible at high latitudes with lower optical thickness of the cloud, that is, the small knots do not coalesce into larger structures.

Table 1. Morphological Description of Cirrus Fields (continued)

Field	Description of Scanned Field
48014 48017 ** 525020 (42)	Scans of cool cirrus across a large loop structure. All scans cover much the same kind of structure (bright rim > faint center > bright rim), with the exception that 48014 and 48017 spend more time in faint portions. Cirrus is easily seen at 60 and 100um, but not seen at 12 and 25 microns.
237026 238024 247017 247024 584031 585067 585060 (58)	Scans along filamentary cirrus. Seen easily at 60 and 100um, but not at all at 12 and 25um, probably due to strong zodiacal emission. Many extragalactic sources seen at 60 and 100 um.
241001 240936 249043 240025 588029 588026 (58)	Scans of the same plate as above, but across a quite different region containing loop structures. Same comments apply here as above.

Note: 1. The ** symbolizes a large number of scans used but not listed to save space.
2. The numbers in parentheses are Sky Flux Plate Numbers.

Table 2. PSD data summary. C1 = C(F12/F25), C2 = C(F25/F60), C3 = C(F60/F100), F12,etc = log F12, b12,etc = 12 um slope , GLAT = galactic latitude, GLONG = galactic longitude, PN = plate number.

Scan No.	C1	C2	C3	F12	F25	F60	F100	b12	b25	b60	b100	GLAT	GLONG	PN
83011	1.21	0.38	0.23	-11.30	-11.90	-12.09	-12.21	-0.37	-1.15	-0.62	-1.38	26.42	125.46	1.00
83006	1.75	0.41	0.55	-11.01	-11.88	-12.09	-12.36	-0.11	-0.64	-0.47	-1.62	26.54	124.68	1.00
132021	0.96	0.90	0.24	-11.32	-11.80	-12.25	-12.37	-0.36	-0.44	-0.61	-1.54	27.17	122.99	1.00
103001	2.06	0.90	0.64	-10.63	-11.66	-12.11	-12.43	-0.06	-0.21	-0.38	-1.52	27.20	123.05	1.00
49017	1.16	0.63	0.73	-11.36	-11.94	-12.25	-12.62	0.09	-0.54	-0.58	-1.88	27.26	122.85	1.00
49021	0.89	0.66	0.45	-11.42	-11.86	-12.19	-12.42	-0.02	-0.38	-0.47	-1.58	27.33	123.09	1.00
520005	1.90	1.39	0.11	-10.55	-11.50	-12.19	-12.25	-0.56	-1.32	-1.74	-1.30	27.34	122.87	1.00
132025	0.34	1.16	0.31	-11.42	-11.60	-12.18	-12.33	-0.04	-0.22	-0.49	-1.45	27.36	123.12	1.00
103004	1.92	0.74	0.52	-10.68	-11.63	-12.01	-12.27	-0.04	-0.13	-0.28	-1.31	27.39	123.07	1.00
520011	2.23	0.77	0.57	-10.50	-11.61	-12.00	-12.28	-0.06	-0.15	-0.38	-1.31	27.54	122.88	1.00
49025	1.28	0.66	0.27	-11.31	-11.95	-12.28	-12.42	-0.02	-0.57	-0.60	-1.55	27.54	123.15	1.00
103008	1.07	0.76	0.21	-11.30	-11.84	-12.22	-12.33	0.01	-0.44	-0.68	-1.48	27.57	123.18	1.00
mean	1.40	0.78	0.40	-11.07	-11.76	-12.15	-12.36	-0.13	-0.52	-0.61	-1.49	27.22	123.37	1.00
std dev	0.54	0.27	0.19	0.35	0.15	0.09	0.10	0.19	0.36	0.36	0.16	0.35	0.79	
450012	0.59	1.25	0.62	-11.23	-11.53	-12.16	-12.46	-0.19	-0.38	-0.00	-0.33	-60.18	97.74	26.00
333047	1.46	1.08	0.30	-9.70	-10.43	-10.97	-11.12	-0.09	-0.25	-1.34	-1.51	2.34	100.78	26.00
269032	0.70	0.07	0.04	-11.35	-11.70	-11.73	-11.75	-0.06	-0.53	-0.26	-0.36	71.40	107.24	38.00
269036	0.65	0.61	0.20	-11.39	-11.72	-12.02	-12.12	0.24	-0.12	-0.07	-0.39	71.51	106.65	38.00
294027	0.97	0.15	0.43	-11.24	-11.72	-11.80	-12.01	0.13	-0.23	0.15	-0.28	71.62	107.11	38.00
295001	1.14	0.52	0.37	-11.33	-11.90	-12.16	-12.35	-0.18	-0.36	-1.12	-1.03	71.68	106.44	38.00
mean	0.86	0.34	0.26	-11.33	-11.76	-11.93	-12.06	0.03	-0.31	-0.33	-0.51	71.55	106.86	38.00
std dev	0.20	0.23	0.15	0.05	0.08	0.17	0.22	0.16	0.15	0.48	0.30	0.11	0.33	
257013	1.08	0.70	1.10	-11.31	-11.85	-12.20	-12.75	-0.10	-0.36	-0.18	-1.12	73.29	128.78	38.00
281021	0.85	1.10	0.73	-11.35	-11.77	-12.32	-12.69	-0.27	-0.39	-0.33	-0.80	73.38	129.25	38.00
281027	1.03	1.12	0.74	-11.15	-11.66	-12.22	-12.59	0.25	-0.09	-0.21	-0.87	73.47	128.51	38.00
289001	0.98	0.82	0.35	-11.28	-11.77	-12.18	-12.35	-0.02	-0.32	-0.10	-0.43	73.47	128.67	38.00
257019	0.81	1.11	0.74	-11.41	-11.82	-12.37	-12.74	0.02	-0.31	-0.41	-1.01	73.55	128.59	38.00
mean	0.95	0.97	0.73	-11.30	-11.77	-12.26	-12.62	-0.02	-0.29	-0.24	-0.84	73.43	128.76	38.00
std dev	0.11	0.17	0.23	0.09	0.06	0.07	0.15	0.17	0.11	0.11	0.24	0.09	0.26	

133005	1.76	0.81	0.61	-10.74	-11.61	-12.02	-12.33	-0.06	-0.10	-0.11	-0.63	26.12	68.44	42.00
143024	1.17	1.07	0.91	-10.95	-11.54	-12.07	-12.52	-0.02	-0.15	-0.24	-1.06	26.44	69.12	42.00
113041	1.89	0.41	1.12	-10.95	-11.89	-12.10	-12.66	0.15	-0.07	-0.39	-1.39	26.46	69.86	42.00
515023	1.44	0.85	0.62	-11.11	-11.83	-12.26	-12.57	0.27	-0.25	-0.49	-1.27	26.49	69.95	42.00
48017	1.20	0.96	0.68	-11.26	-11.86	-12.35	-12.68	-0.14	-0.42	-0.67	-1.60	26.52	69.97	42.00
133036	2.20	0.58	0.78	-10.85	-11.95	-12.24	-12.63	-0.15	-0.01	-0.37	-1.29	26.52	70.03	42.00
143026	1.88	0.44	0.88	-10.93	-11.87	-12.09	-12.53	-0.04	0.09	-0.21	-1.18	26.53	69.73	42.00
515018	1.06	0.39	0.90	-11.38	-11.92	-12.11	-12.56	0.10	0.07	-0.22	-1.23	26.58	69.68	42.00
525020	1.54	2.50	0.57	-10.23	-11.00	-12.25	-12.54	-0.01	0.02	-0.46	-1.27	26.59	69.76	42.00
112026	1.59	0.51	0.42	-10.91	-11.70	-11.96	-12.17	-0.02	0.07	-0.05	-0.59	26.68	70.01	42.00
113037	1.71	0.34	0.43	-10.94	-11.80	-11.97	-12.18	-0.02	-0.02	0.06	-0.66	26.69	70.00	42.00
48014	1.22	0.44	0.91	-11.36	-11.97	-12.19	-12.64	-0.15	-0.40	-0.28	-1.40	26.73	69.92	42.00
133032	1.47	0.62	0.70	-11.05	-11.79	-12.10	-12.45	-0.05	0.03	-0.05	-1.04	26.74	70.03	42.00
525014	1.14	0.40	0.70	-11.45	-12.02	-12.21	-12.57	-0.01	-0.49	-0.41	-1.21	26.77	69.69	42.00
515012	1.14	0.66	0.88	-11.41	-11.98	-12.31	-12.75	-0.11	-0.28	-0.41	-1.53	26.78	69.62	42.00
112020	1.81	0.70	0.85	-10.99	-11.89	-12.24	-12.67	0.04	-0.28	-0.38	-1.31	26.82	69.76	42.00
mean	1.51	0.73	0.75	-11.03	-11.79	-12.15	-12.53	-0.01	-0.14	-0.29	-1.17	26.59	69.72	42.00
std dev	0.33	0.50	0.18	0.30	0.24	0.11	0.16	0.11	0.19	0.18	0.29	0.17	0.40	
298020	1.62	2.75	-0.41	-9.79	-10.60	-11.97	-11.77	-0.06	-0.14	-1.24	-1.26	-11.03	95.70	45.00
282005	1.50	2.92	-0.86	-9.85	-10.60	-12.06	-11.63	-0.08	-0.13	-1.37	-1.02	-10.97	96.02	45.00
298023	1.66	2.75	-0.56	-9.71	-10.54	-11.91	-11.63	-0.07	-0.13	-1.17	-1.11	-10.96	95.92	45.00
299025	1.40	2.19	-0.20	-9.81	-10.51	-11.61	-11.51	-0.10	-0.09	-0.62	-0.85	-10.93	96.01	45.00
mean	1.55	2.65	-0.51	-9.79	-10.56	-11.89	-11.63	-0.08	-0.12	-1.10	-1.06	-10.97	95.91	45.00
std dev	0.10	0.27	0.24	0.05	0.04	0.17	0.09	0.01	0.02	0.29	0.15	0.04	0.13	
247017	1.60	1.97	0.79	-10.55	-11.35	-12.34	-12.73	0.10	-0.27	-0.34	-0.68	61.35	198.19	58.00
584031	1.96	1.29	0.85	-10.49	-11.47	-12.12	-12.54	-0.09	-0.31	0.35	-0.31	60.94	199.53	58.00
585060	0.30	1.15	1.31	-11.36	-11.51	-12.08	-12.74	-0.23	-0.39	0.12	-0.88	61.17	199.58	58.00
585067	0.25	1.14	1.14	-11.36	-11.49	-12.05	-12.62	-0.16	-0.30	-0.12	-0.74	61.36	199.86	58.00
237026	0.23	1.57	1.48	-11.37	-11.49	-12.27	-13.01	-0.19	-0.41	0.07	-1.05	60.89	200.10	58.00
247024	-0.53	2.31	1.65	-11.34	-11.07	-12.23	-13.05	-0.18	-0.27	0.01	-1.21	61.12	200.33	58.00
238024	0.01	1.42	0.69	-11.45	-11.45	-12.16	-12.51	-0.36	-0.39	-0.10	-0.45	61.00	200.66	58.00
mean	0.54	1.55	1.13	-11.13	-11.40	-12.18	-12.74	-0.16	-0.33	-0.00	-0.76	61.12	199.75	58.00
std dev	0.83	0.41	0.34	0.39	0.14	0.10	0.20	0.13	0.06	0.20	0.29	0.17	0.74	

588026	0.52	1.11	-0.30	-11.21	-11.47	-12.02	-11.87	-0.32	-0.56	-0.62	-0.57	61.88	208.16	58.00
588029	0.27	0.76	-0.10	-11.33	-11.47	-11.85	-11.80	-0.30	-0.42	-0.65	-0.46	62.10	208.35	58.00
240025	0.39	1.30	0.72	-11.26	-11.46	-12.11	-12.47	-0.12	-0.44	-0.39	-1.08	61.78	208.70	58.00
249036	0.00	1.60	0.84	-11.44	-11.44	-12.24	-12.66	-0.30	-0.45	-0.68	-1.30	61.61	208.76	58.00
241001	0.23	1.43	0.82	-11.41	-11.52	-12.24	-12.64	-0.24	-0.47	-0.46	-1.16	61.94	209.11	58.00
249043	0.35	1.52	0.92	-11.29	-11.47	-12.23	-12.69	-0.33	-0.42	-0.43	-1.33	61.77	209.16	58.00
mean	0.29	1.29	0.48	-11.32	-11.47	-12.12	-12.35	-0.27	-0.46	-0.54	-0.98	61.85	208.71	58.00
std dev	0.16	0.28	0.49	0.08	0.02	0.14	0.37	0.07	0.05	0.11	0.34	0.15	0.36	
365032	0.73	0.73	1.06	-11.55	-11.91	-12.27	-12.80	0.12	-0.31	0.25	-0.74	58.78	38.33	62.00
382039	0.91	0.73	0.53	-11.45	-11.90	-12.26	-12.53	-0.08	-0.43	0.07	-0.35	58.89	38.23	62.00
439042	0.83	0.75	0.79	-11.48	-11.89	-12.27	-12.66	-0.03	-0.56	-0.01	-0.46	58.94	38.48	62.00
381038	0.81	0.91	0.50	-11.45	-11.86	-12.31	-12.56	-0.10	-0.33	0.05	-0.35	59.01	38.19	62.00
365029	1.29	0.91	1.33	-11.27	-11.92	-12.37	-13.04	0.11	-0.55	0.52	-1.12	59.03	38.05	62.00
439035	0.81	0.90	1.20	-11.49	-11.89	-12.34	-12.94	-0.01	-0.50	0.26	-0.99	59.13	38.27	62.00
381033	0.72	0.90	1.50	-11.48	-11.84	-12.29	-13.05	-0.09	-0.37	0.10	-1.16	59.23	38.12	62.00
mean	0.87	0.83	0.99	-11.45	-11.89	-12.30	-12.80	-0.01	-0.43	0.18	-0.74	59.00	38.24	62.00
std dev	0.18	0.09	0.36	0.08	0.03	0.04	0.20	0.08	0.09	0.17	0.33	0.14	0.13	
359035	0.81	0.97	-0.16	-11.48	-11.89	-12.37	-12.29	0.13	-0.42	-0.26	-0.02	64.96	34.64	62.00
337025	0.90	0.64	0.82	-11.43	-11.88	-12.20	-12.61	-0.11	-0.50	0.12	-0.51	64.97	34.90	62.00
431013	1.96	2.01	1.42	-10.13	-11.11	-12.11	-12.82	-0.07	-0.18	-0.02	-0.61	65.04	34.85	62.00
359032	0.83	0.86	0.81	-11.41	-11.83	-12.26	-12.66	-0.10	-0.52	0.10	-0.46	65.18	34.66	62.00
337018	1.25	0.67	0.69	-11.34	-11.97	-12.30	-12.65	-0.02	-0.58	-0.07	-0.53	65.18	35.09	62.00
430052	0.91	0.83	1.61	-11.34	-11.79	-12.21	-13.01	-0.27	-0.32	0.06	-1.29	65.21	34.50	62.00
359028	0.80	0.43	1.36	-11.43	-11.83	-12.04	-12.72	-0.46	-0.45	-0.22	-0.75	65.41	34.69	62.00
430044	0.91	0.69	1.00	-11.43	-11.89	-12.23	-12.73	-0.04	-0.61		-0.68	65.42	34.41	62.00
mean	1.04	0.89	0.94	-11.25	-11.77	-12.21	-12.69	-0.12	-0.45	-0.04	-0.61	65.17	34.72	62.00
std dev	0.37	0.45	0.52	0.43	0.26	0.10	0.19	0.17	0.13	0.13	0.33	0.17	0.21	
509035	1.28	0.70	0.79	-11.27	-11.91	-12.26	-12.65	0.01	-0.31	-0.79	-1.56	15.58	55.13	65.00
113045	1.22	0.77	0.57	-11.34	-11.95	-12.33	-12.62	0.23	-0.46	-0.89	-1.67	20.78	52.45	65.00
510026	1.77	0.26	0.44	-10.94	-11.83	-11.96	-12.18	-0.02	-0.05	0.13	-0.66	20.81	52.25	65.00
130024	-0.30	2.40	0.74	-11.18	-11.04	-12.23	-12.60	-0.00	-0.14	-0.78	-1.63	20.85	52.49	65.00
130019	1.29	0.52	0.89	-11.30	-11.95	-12.21	-12.65	0.10	-0.58	-0.65	-1.70	21.02	52.35	65.00
509030	1.15	0.97	0.83	-11.34	-11.91	-12.40	-12.81	0.03	-0.48	-0.89	-1.81	21.05	52.12	65.00
130014	1.03	0.76	0.55	-11.31	-11.83	-12.21	-12.48	-0.18	-0.60	-0.67	-1.42	21.20	52.22	65.00
mean	1.03	0.95	0.67	-11.24	-11.75	-12.22	-12.56	0.03	-0.38	-0.62	-1.48	20.95	52.31	65.00
std dev	0.64	0.69	0.16	0.14	0.32	0.14	0.19	0.12	0.21	0.35	0.38	0.15	0.13	

539015	1.34	1.48	-0.30	-10.79	-11.46	-12.20	-12.05	0.09	-0.23	-1.08	-1.28	9.14	57.42	66.00
539009	0.84	1.40	0.56	-11.09	-11.51	-12.21	-12.49	-0.15	-0.20	-0.99	-1.88	9.29	57.28	66.00
153043	1.05	1.75	-0.72	-10.86	-11.39	-12.26	-11.90	-0.05	-0.15	-1.11	-1.00	9.31	57.67	66.00
170013	1.91	1.82	-0.12	-10.40	-11.35	-12.26	-12.20	-0.08	-0.32	-1.18	-1.59	9.50	57.73	66.00
539002	0.83	1.40	0.57	-11.09	-11.51	-12.21	-12.50	-0.17	-0.20	-0.99	-1.90	9.52	57.21	66.00
170008	1.49	1.99	-0.29	-10.56	-11.30	-12.30	-12.15	-0.02	-0.08	-1.23	-1.42	9.60	57.51	66.00
153038	1.05	0.31	0.82	-10.99	-11.51	-11.67	-12.08	-0.14	-0.08	-0.33	-1.33	9.64	57.77	66.00
mean	1.22	1.45	0.07	-10.83	-11.43	-12.16	-12.20	-0.07	-0.18	-0.99	-1.48	9.43	57.51	66.00
std dev	0.36	0.51	0.53	0.25	0.08	0.20	0.21	0.08	0.08	0.28	0.30	0.17	0.20	
185001	-0.16	1.49	1.95	-11.06	-10.98	-11.72	-12.70	-0.17	-0.27	-0.09	-1.04	30.14	216.06	80.00
199015	-0.11	1.54	1.60	-11.24	-11.18	-11.95	-12.75	-0.23	-0.24	-0.01	-1.22	30.19	215.98	80.00
562020	-0.06	1.90	0.79	-11.31	-11.28	-12.23	-12.62	-0.30	-0.38	-0.46	-1.11	30.21	215.97	80.00
199019	0.21	1.49	1.31	-11.20	-11.31	-12.06	-12.71	-0.11	-0.32	-0.12	-1.15	30.28	216.27	80.00
185006	0.21	1.45	1.45	-11.07	-11.18	-11.90	-12.63	-0.05	-0.25	0.06	-1.05	30.38	216.17	80.00
562026	1.78	0.25	0.44	-10.94	-11.84	-11.96	-12.18	-0.02	-0.12	0.08	-0.66	30.46	216.05	80.00
mean	0.31	1.35	1.26	-11.14	-11.29	-11.97	-12.60	-0.15	-0.26	-0.09	-1.04	30.28	216.08	80.00
std dev	0.67	0.51	0.50	0.12	0.27	0.15	0.19	0.10	0.08	0.18	0.18	0.11	0.11	
201039	0.13	1.56	0.99	-11.15	-11.21	-11.99	-12.49	-0.24	-0.32	0.02	-0.23	36.30	208.68	80.00
185028	0.27	1.55	1.09	-11.16	-11.29	-12.07	-12.62	-0.20	-0.44	-0.07	-0.46	36.37	209.01	80.00
203037	1.75	1.78	0.84	-10.34	-11.22	-12.11	-12.53	0.07	-0.32	-0.17	-0.34	36.43	208.96	80.00
564006	2.00	0.38	1.12	-10.91	-11.91	-12.10	-12.66	-0.02	-0.18	-0.39	-1.39	36.61	208.63	80.00
185033	1.68	1.49	1.18	-10.38	-11.22	-11.97	-12.56	0.14	-0.35	-0.08	-0.30	36.62	209.08	80.00
564014	1.18	0.78	0.63	-11.35	-11.94	-12.33	-12.65	0.29	-0.47	-0.88	-1.69	36.76	208.88	80.00
mean	1.17	1.26	0.97	-10.88	-11.46	-12.10	-12.59	0.01	-0.35	-0.26	-0.73	36.51	208.87	80.00
std dev	0.73	0.50	0.19	0.39	0.33	0.12	0.06	0.19	0.09	0.30	0.58	0.16	0.17	

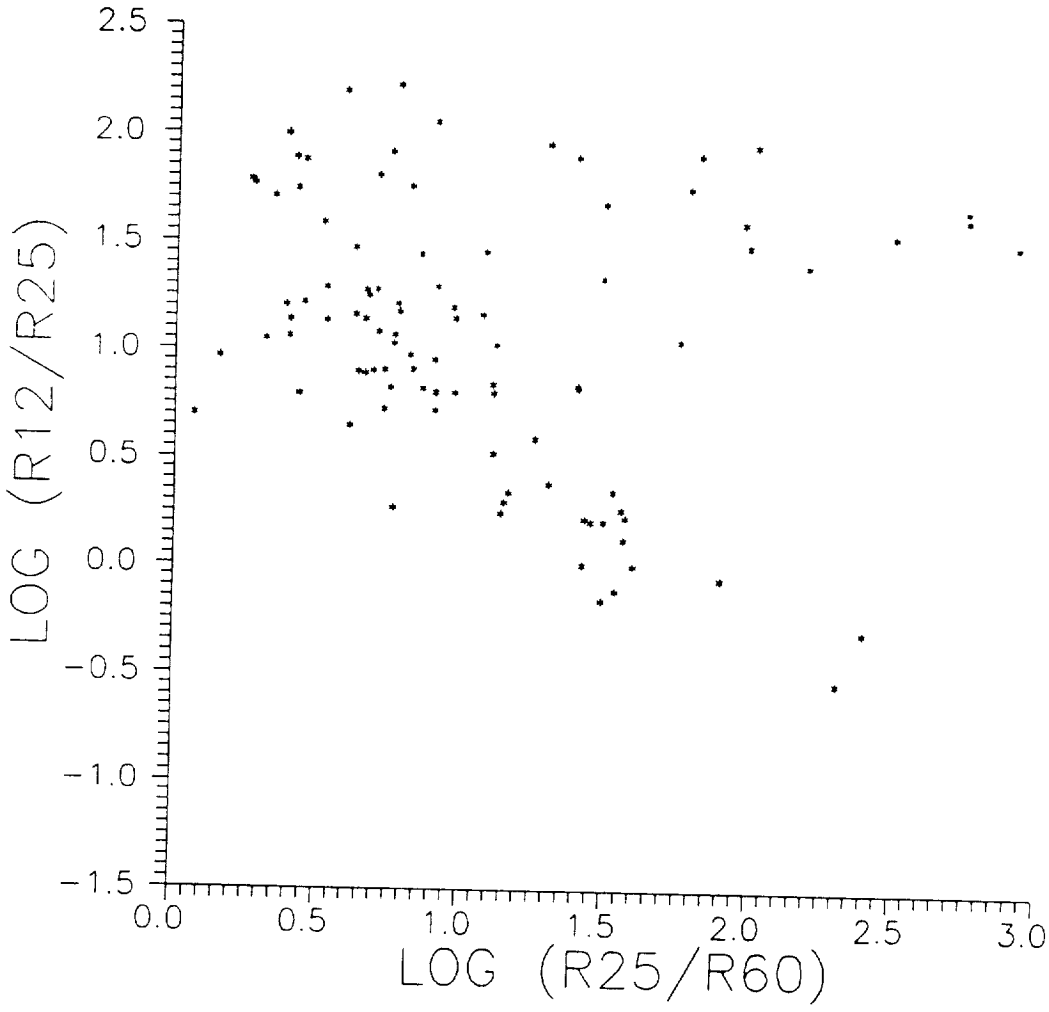

Figure 1. Color-color diagram derived from power spectral density data.

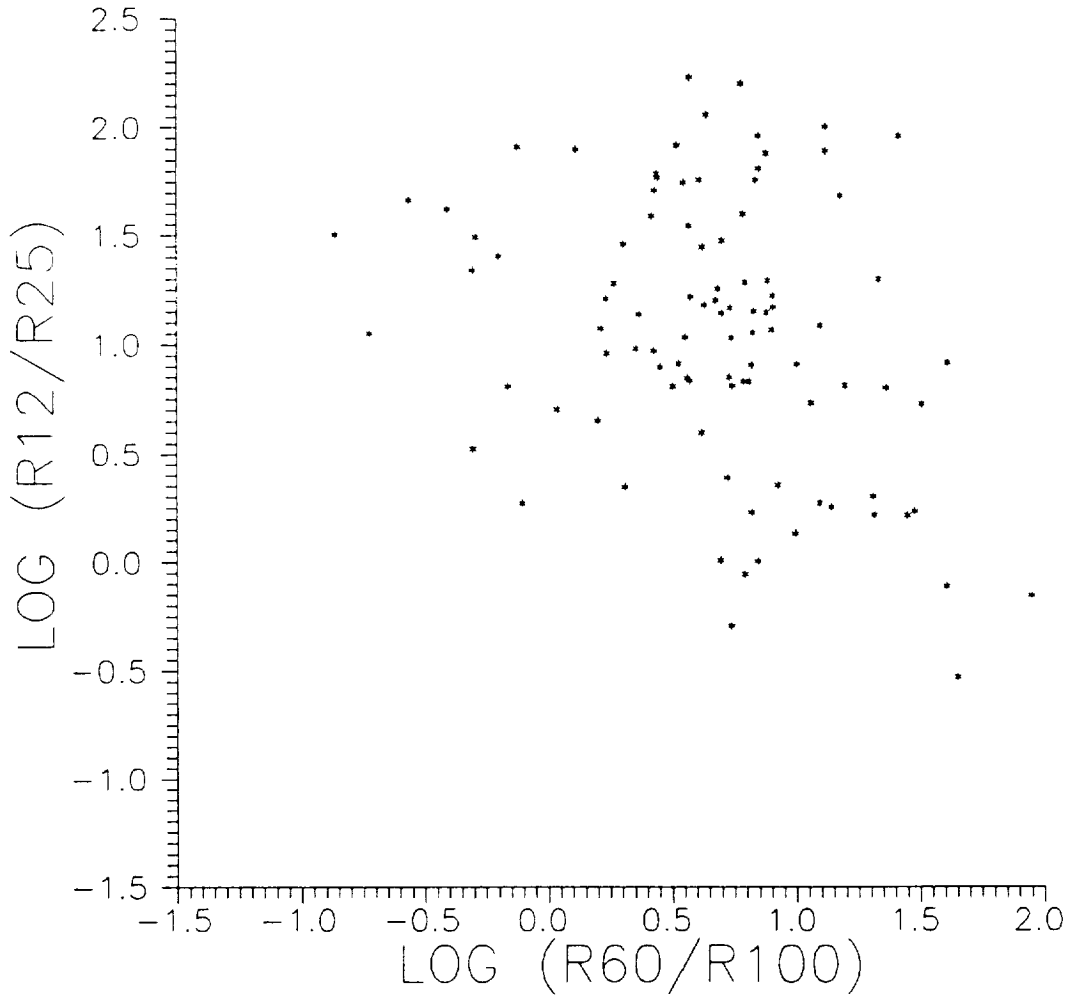

Figure 2. Color-color diagram derived from power spectral density data.

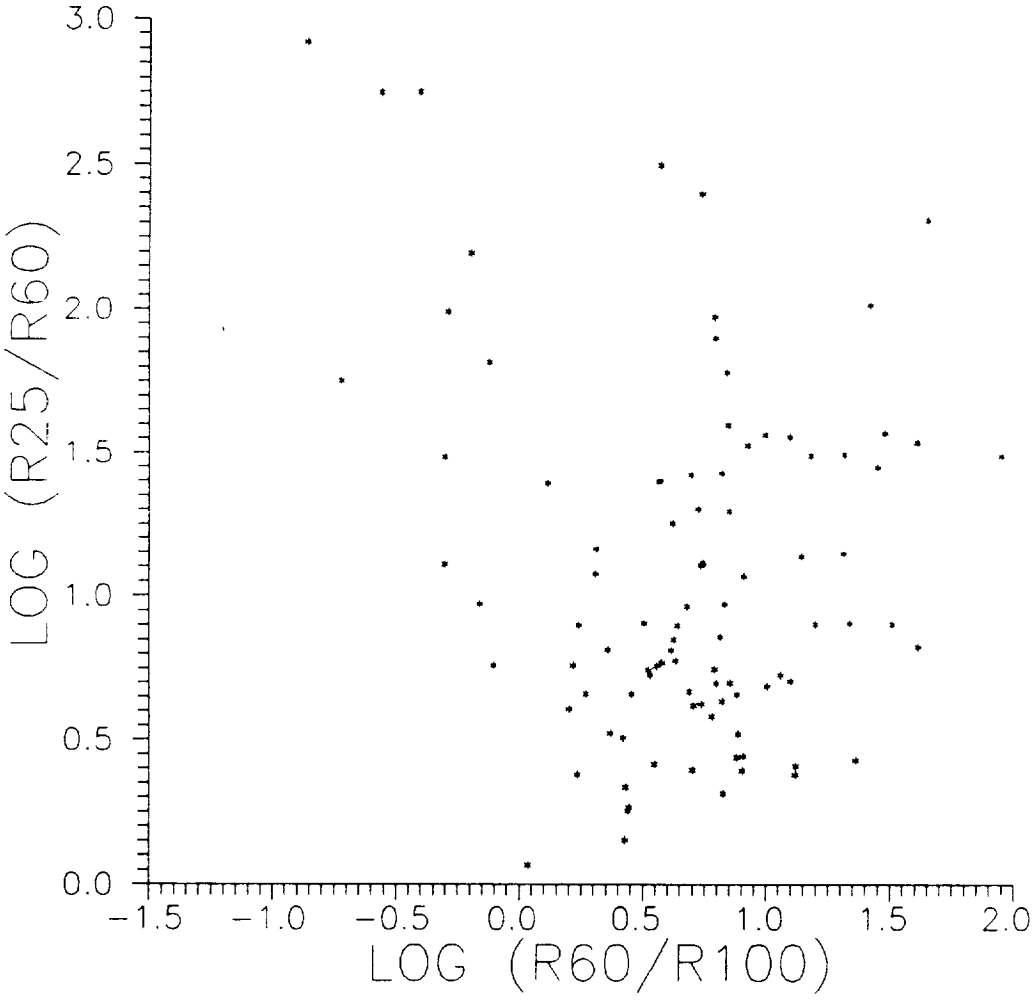

Figure 3. Color-color diagram derived from power spectral density data.

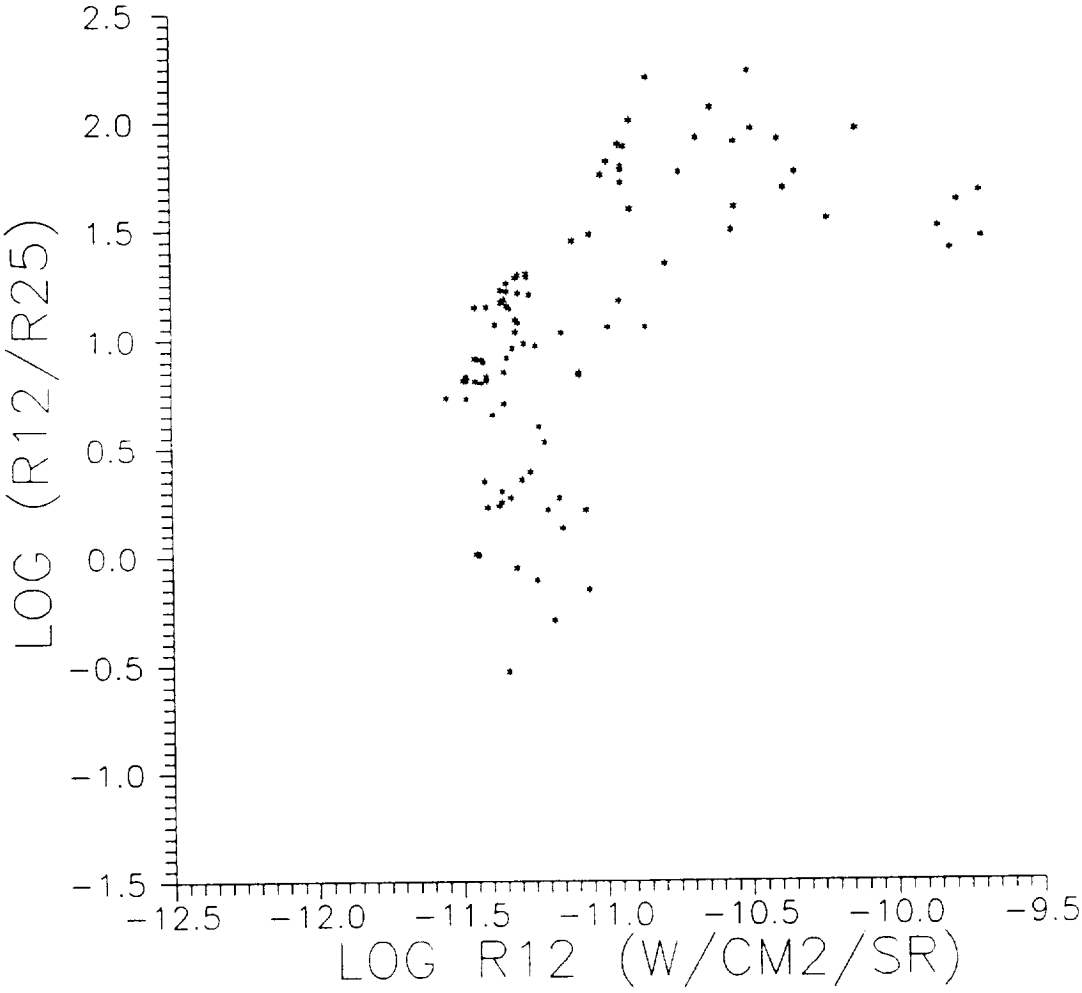

Figure 4. Color-flux diagram derived from power spectral density data.

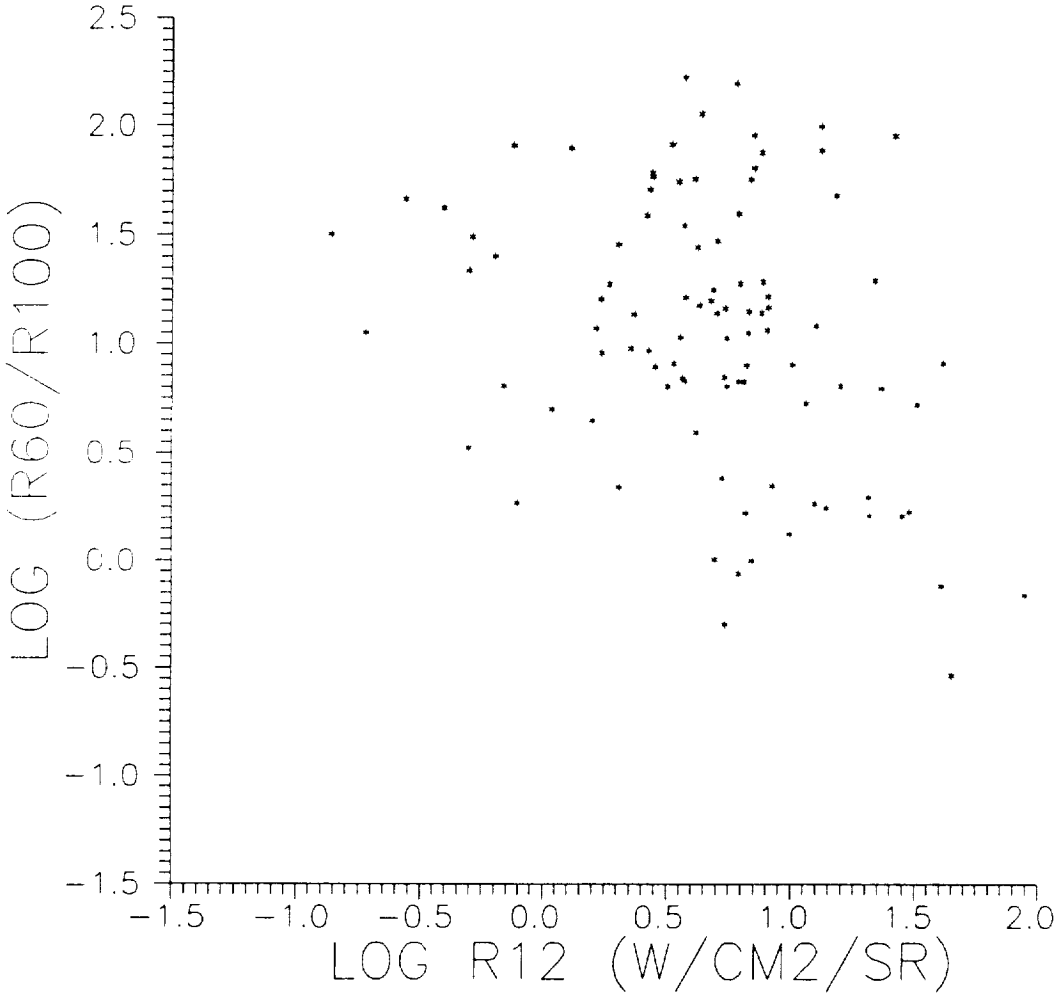

Figure 5. Color-flux diagram derived from power spectral density data.

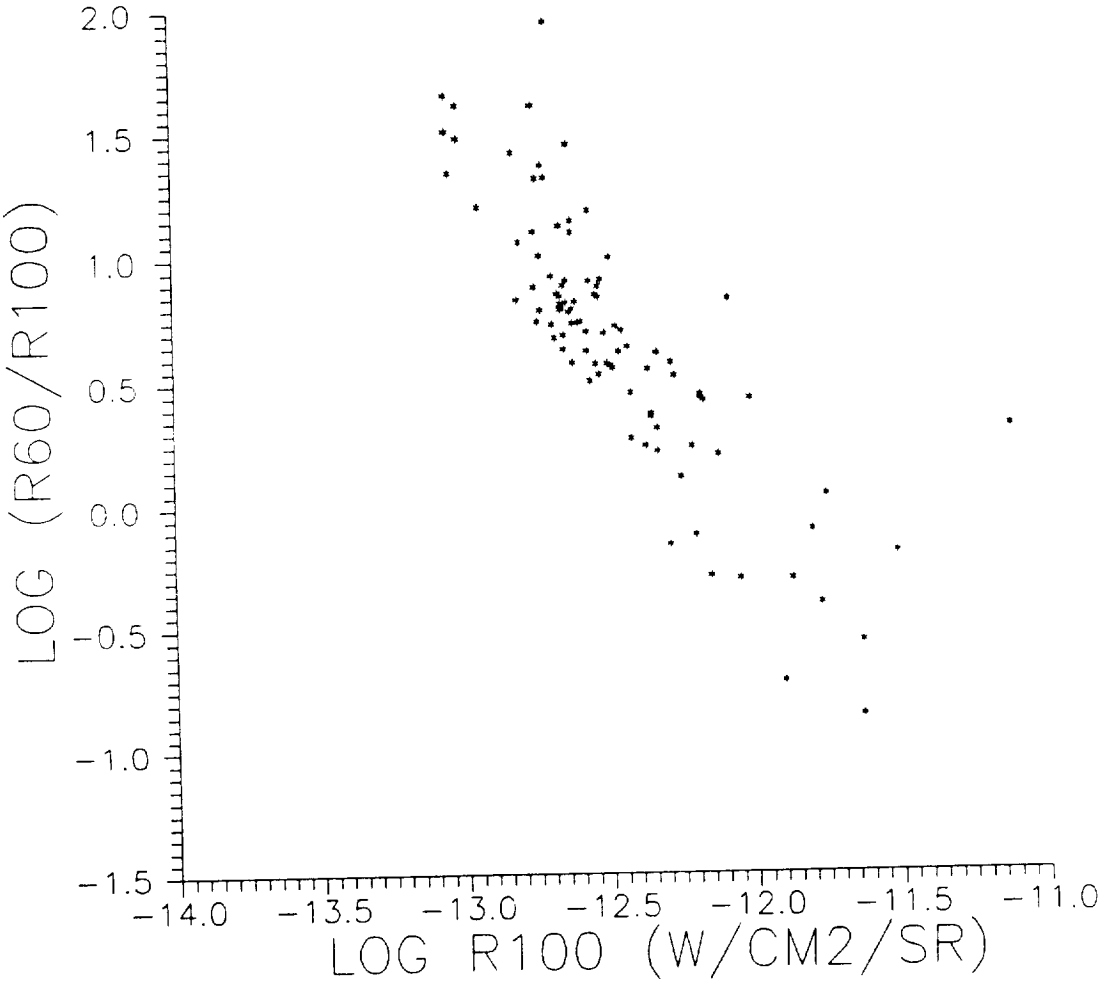

Figure 6. Color-flux diagram derived from power spectral density data.

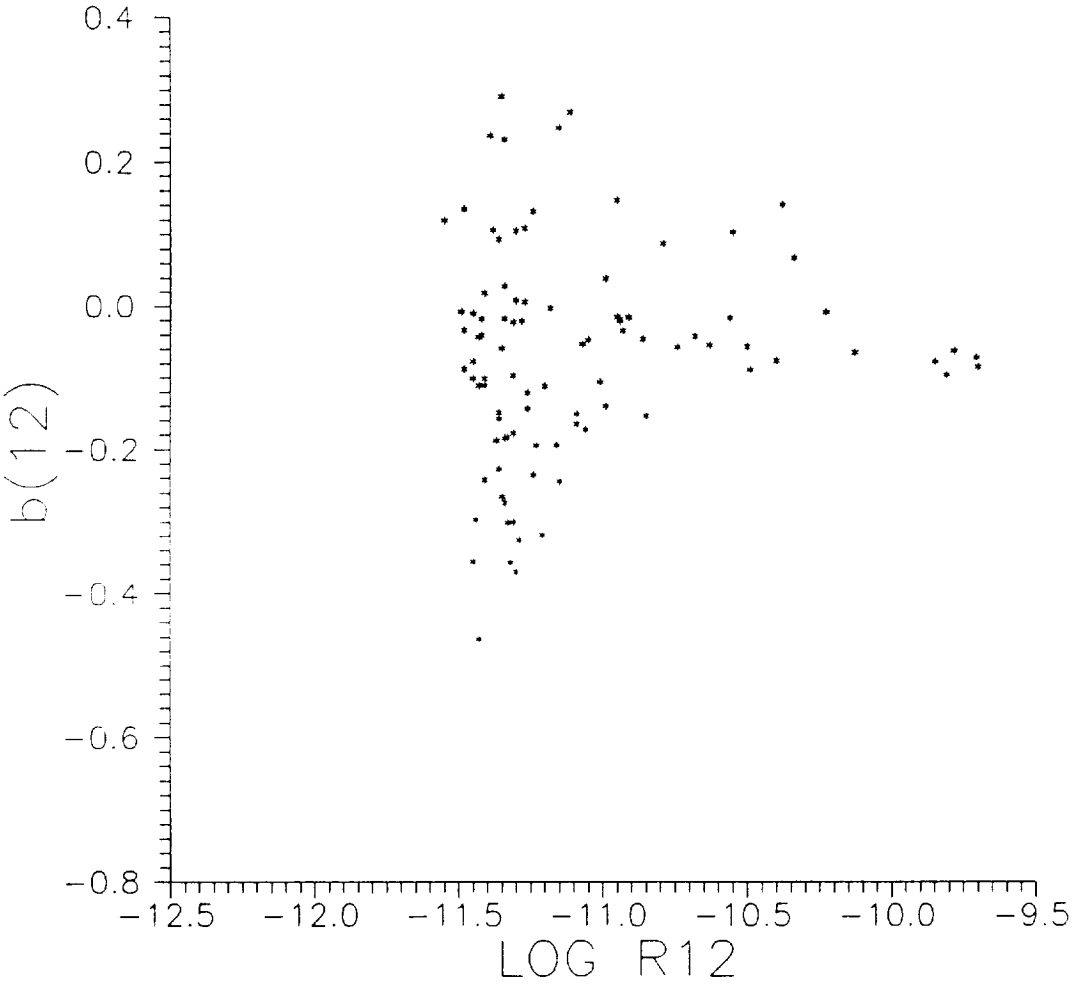

Figure 7. Correlation of the PSD slope with flux.

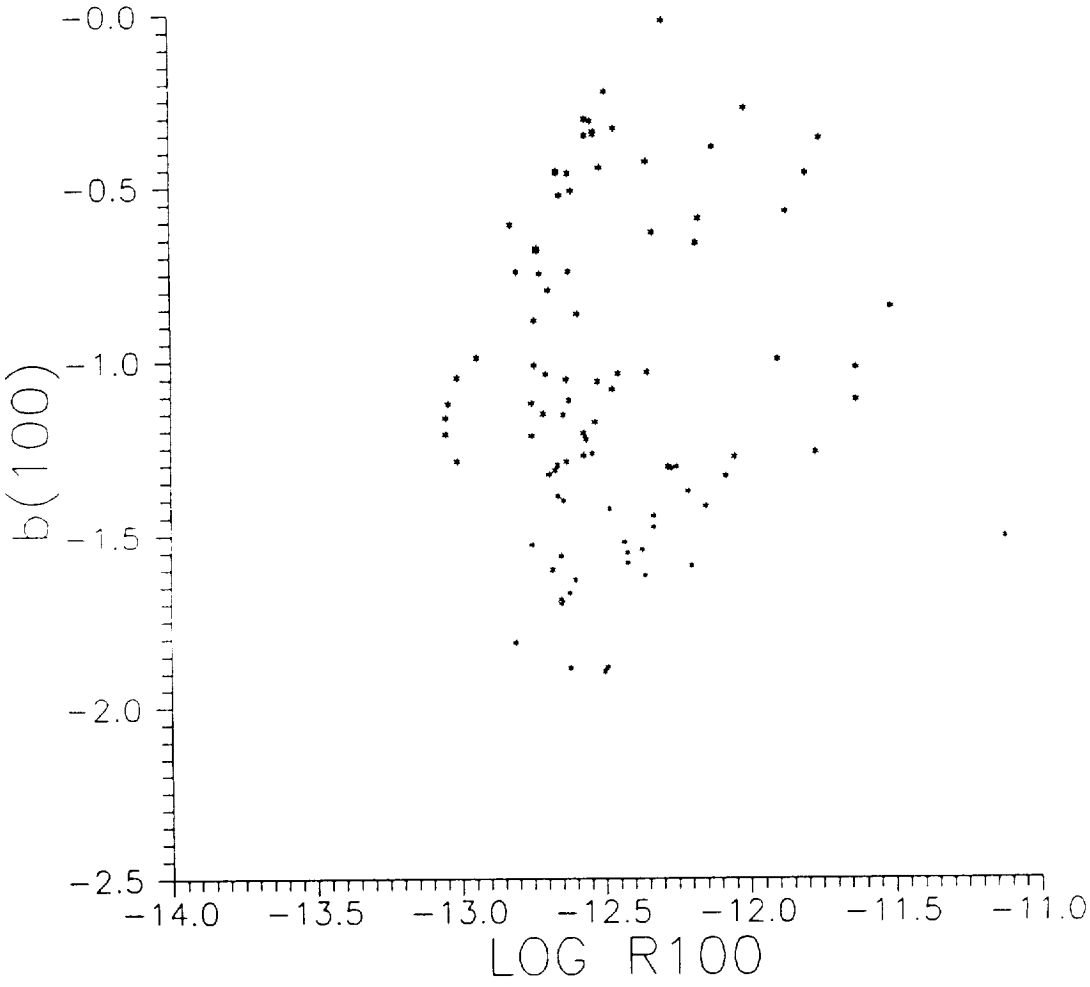

Figure 8. Correlation of the PSD slope with flux.

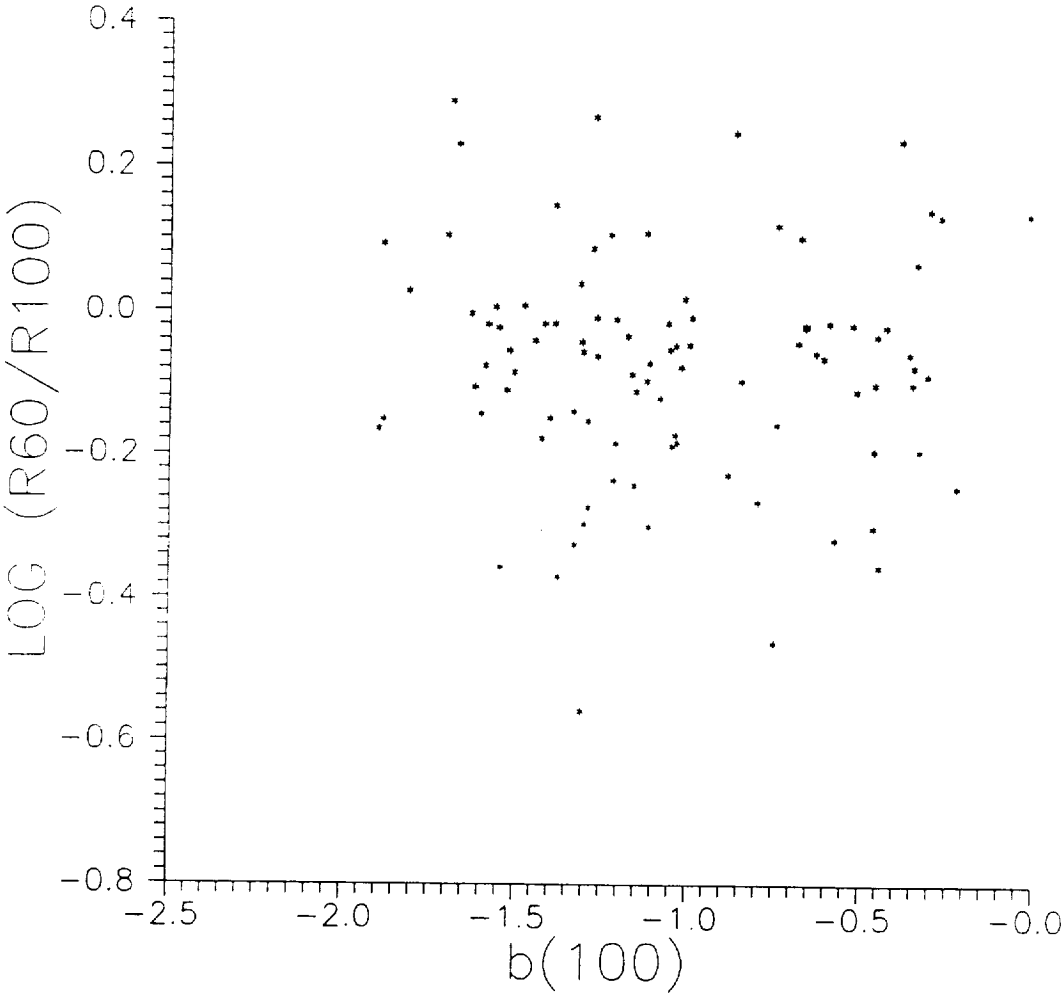

Figure 9. Correlation of the PSD slope with color.

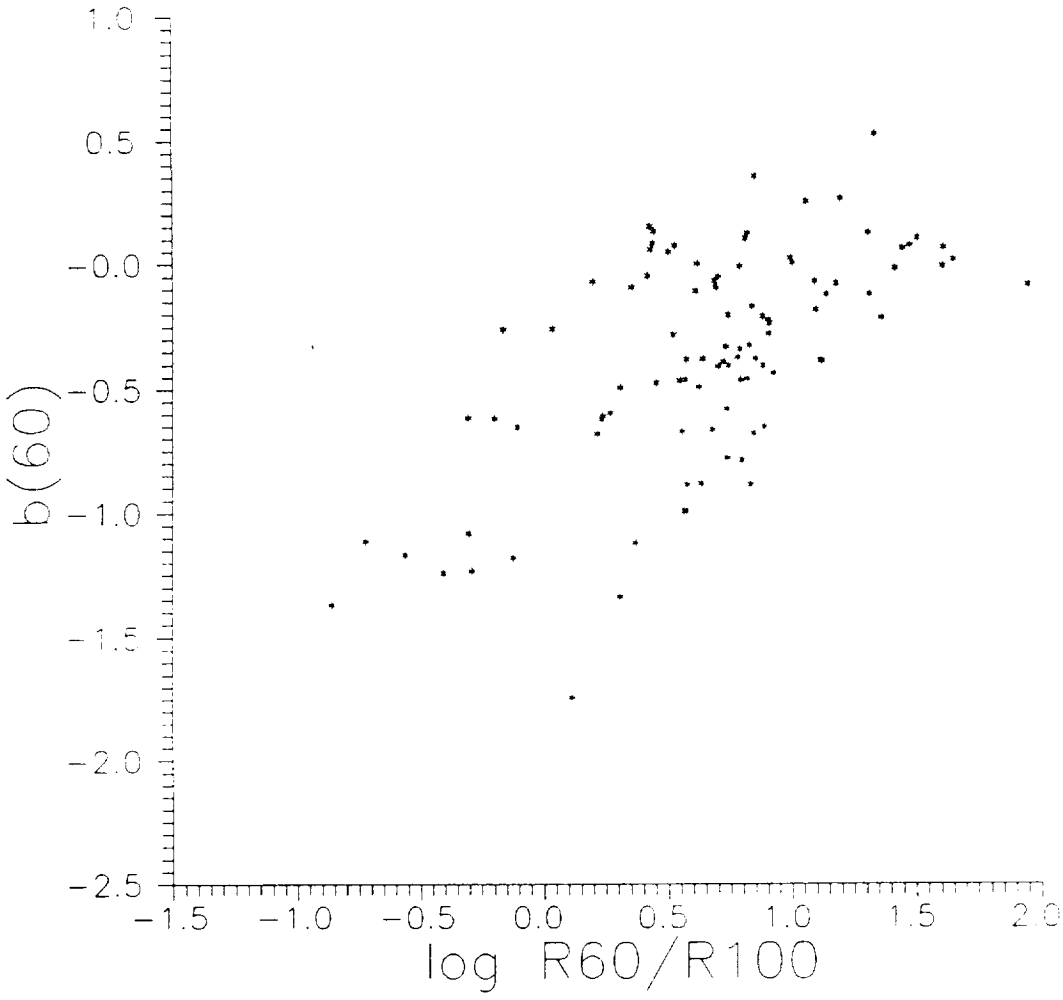

Figure 10. Correlation of the PSD slope with color.

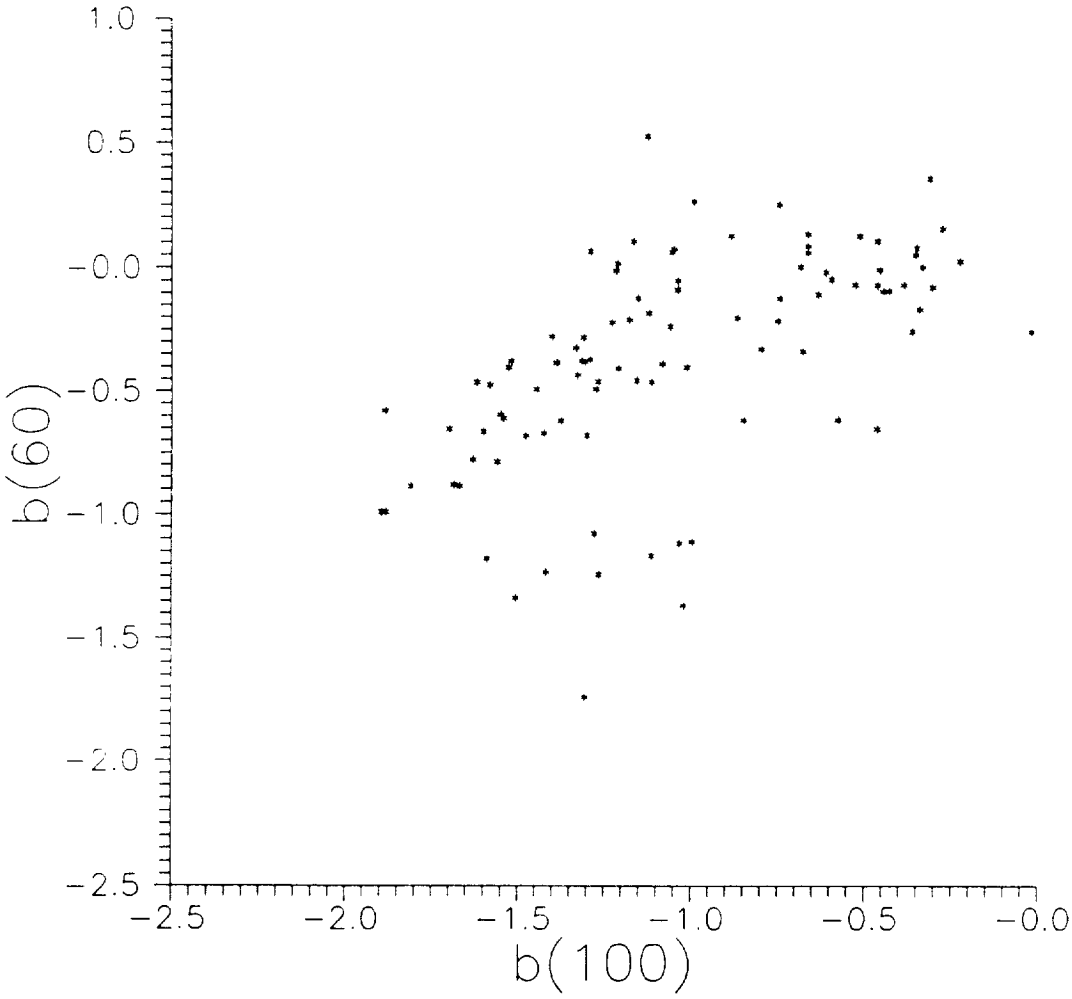

Figure 11. Correlation of the PSD 60 and 100 μm slopes.

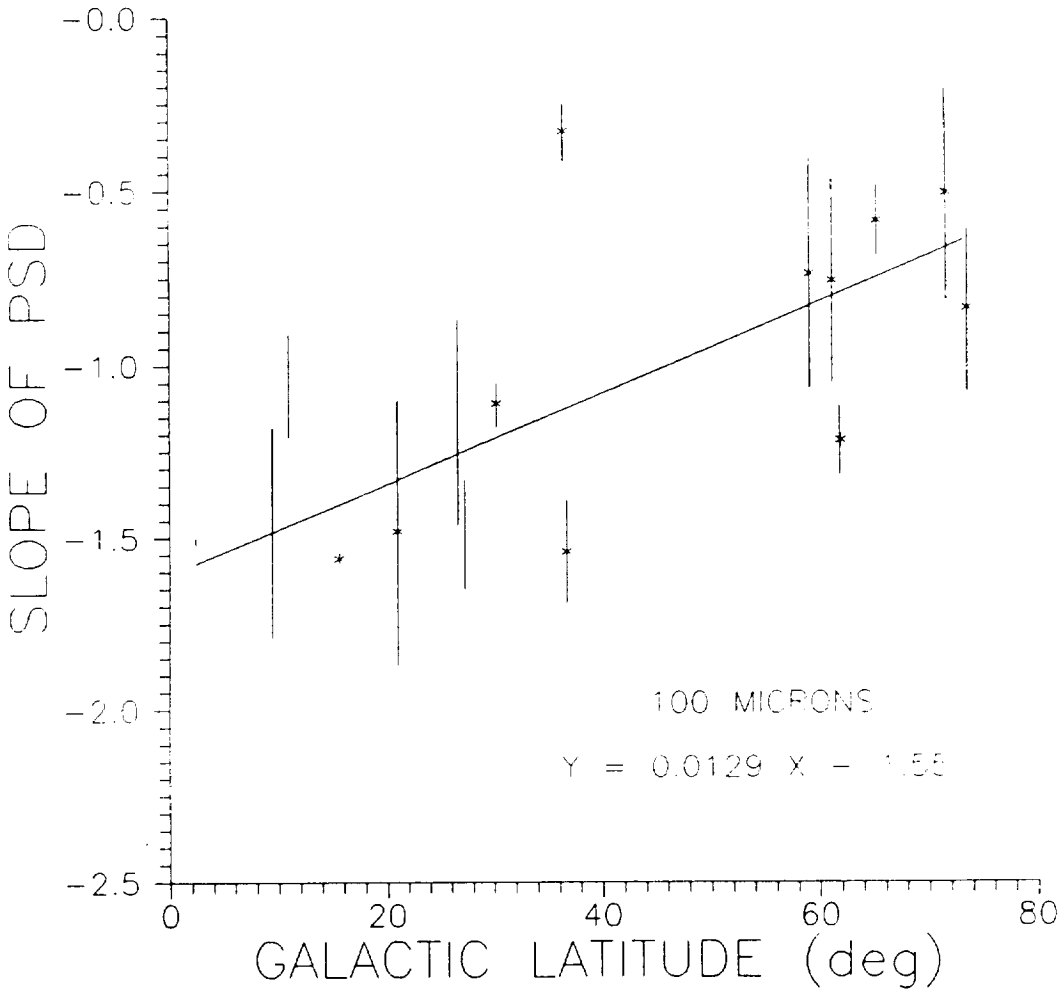

Figure 12. Variation of the 100 μm PSD slope with galactic latitude.

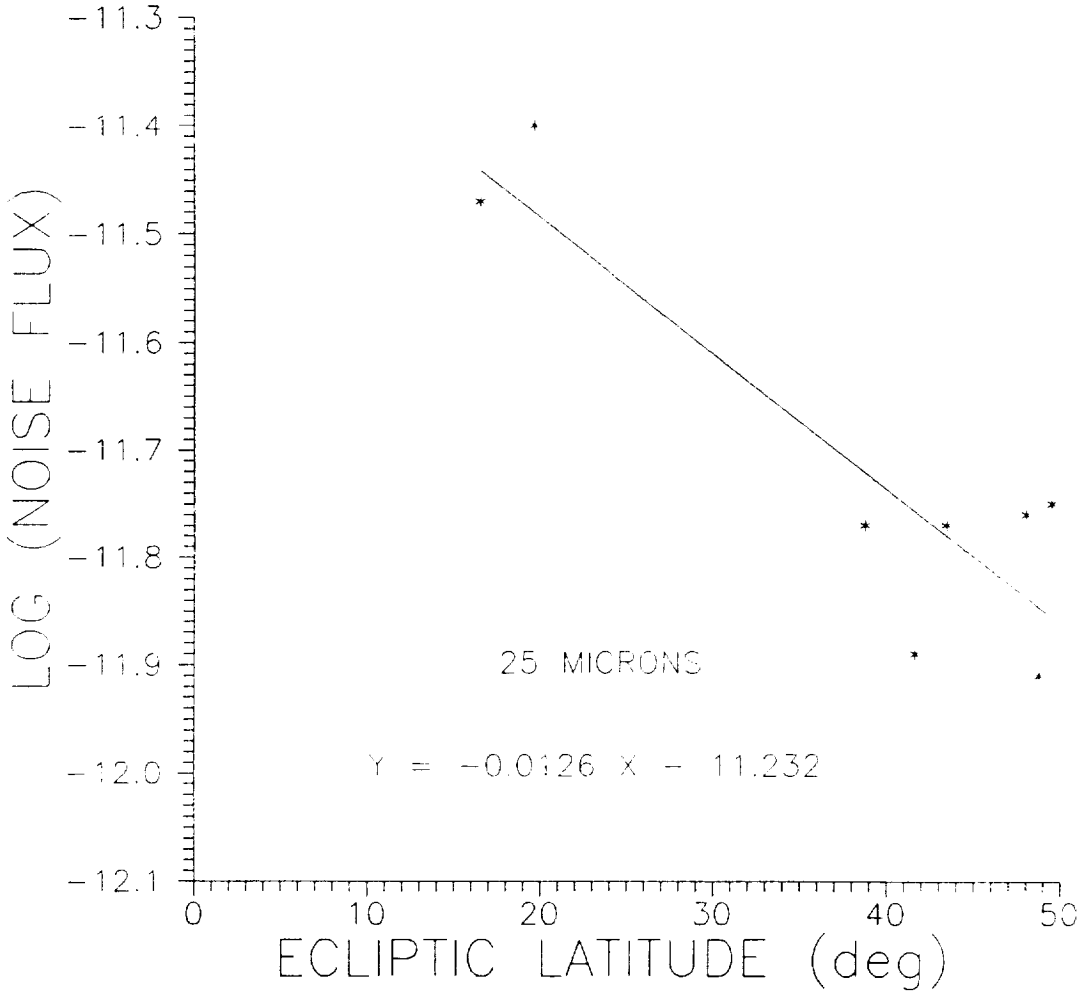

Figure 13. Correlation of the 25 μm PSD flux with ecliptic latitude.

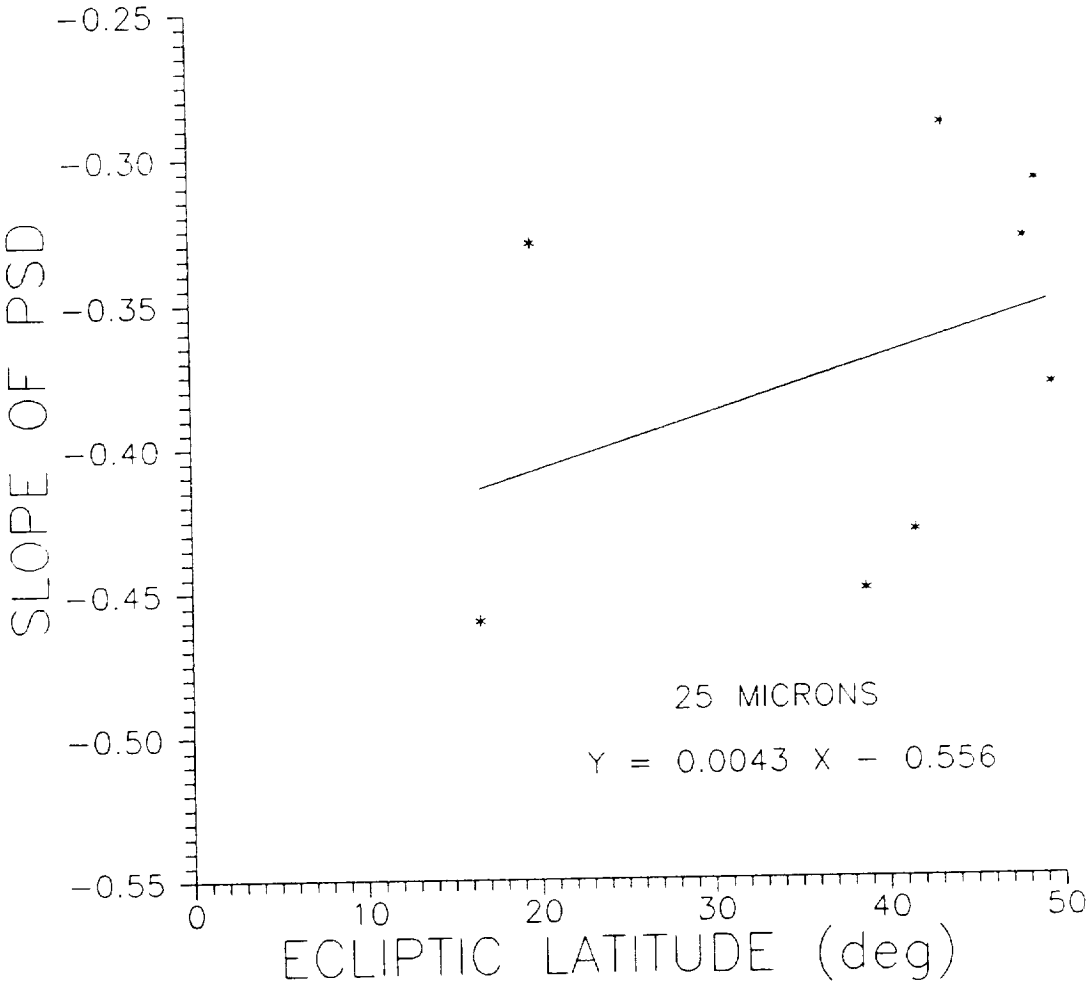

Figure 14. Variation of the 25 μm PSD slope with ecliptic latitude.

APPENDIX M. "Asteroid Model"

Appendix M. Asteroid Model
- R.G. Walker -

1. INTRODUCTION

Several thousand asteroids are known to orbit the Sun in a relatively flat belt concentrated mainly between the orbits of Jupiter and Mars. A few asteroids in highly eccentric orbits cross the orbits of the inner planets, Earth, Venus and Mercury. Physical and dynamical studies lead to the conclusion that the asteroids are a population of small bodies that were probably created and shaped by multiple collisions.

With the accomplishment of the IRAS mission, an extensive set of infrared observations of asteroids was obtained. It is our purpose to develop from that database a simple model to predict the number and density of asteroids that could be observed by a space-borne infrared sensor.

2. THE MODEL

Conceptually our model is quite simple. Given the orbital elements of the asteroid, we compute its position on the sky, its distance from the Sun and Earth, and the phase of its observation. The temperature of the surface of the asteroid is determined by its albedo, emissivity, angle of incident solar irradiance, and distance of the asteroid from the Sun. Integration of the thermal emission from the surface yields the irradiance at the Earth orbiting telescope. The incident flux is then compared with the sensor threshold to determine if the asteroid will be detected.

2.1 The Thermal Model

Infrared observations coupled with various asteroid thermal models have been used to deduce the diameters and albedos of asteroids for the past 15 years or so. These models assume an idealized spherical asteroid whose surface elements are in instantaneous thermal equilibrium with the solar insolation. In reality this is never true, but given the large uncertainties in the observations and our knowledge of the properties of the surface, this assumption is acceptable for typical asteroids. IRAS adopted a "Standard Thermal Model" for reduction and analysis of their measurements. For consistency with the vast bulk of thermal data obtained by IRAS we will also adopt their model. The IRAS standard thermal model has been described in detail by Lebofsky, et al (1978) and Matson (1986), and we will present only a brief sketch here.

For a spherical asteroid the balance between the absorbed incident flux and the emitted thermal radiation is

$$\pi R^2 \ (1-A) \ S_o = \beta \epsilon \sigma R^2 \int_{-\pi}^{\pi} \int_{-\pi/2}^{\pi/2} T^4(\theta,\phi) \ \cos\phi \ d\phi \ d\theta \qquad (1)$$

where R is the radius of the asteroid, A is the bolometric Bond albedo, ϵ is the surface emissivity, S_o is the incident solar flux, σ is the Boltzman radiation constant, and $T(\theta,\phi)$ is the surface temperature at longitude θ and latitude ϕ. The normalization constant β is called the "beaming factor" and represents the departure of the emission at zero phase from that of a uniformly radiating sphere. Only the sunlit hemisphere contributes to the radiation, that is T = 0 on the dark side.

In the case of a perfect sphere the surface temperature distribution is given by

$$T(\theta,\phi) = T_s \cos^m\theta \ \cos^m\phi = T_s \cos^m \psi \qquad (2)$$

where T_s is the temperature at the subsolar point, and ψ is the angle between the local surface normal and the incident solar flux. The subsolar point temperature can be derived from Eqn. 1

$$T_s = 395.57 \left[\frac{1 - A}{\beta \ \epsilon} \right]^{1/4} \rho^{-1/2} \qquad (3)$$

where ρ is the heliocentric distance of the asteroid. In the IRAS standard model m = 0.25, β = 0.756, ϵ = 0.9, and A = q pv where q is the phase integral and pv is the photovisual geometric albedo. The phase integral and pv are related as follows: $0.0 \leq pv \leq 0.1$, q = 0.393; $0.1 < pv \leq 0.38$, q = 0.461; pv > 0.38, q = 0.564.

The spectral irradiance F_λ received at the telescope is found by summing the irradiance from each of N rings over the surface of the asteroid observed at geocentric distance Δ,

$$F_\lambda = K \ \Sigma \ \sin(2\psi) \ [\ e^{c/\lambda T} - 1 \ ]^{-1} \qquad (4)$$

with c = 14388 and the constant K given by

$$K = 1.6719 \times 10^{-12} \epsilon R^2 \sin(\pi/2N)\ \lambda^{-5} \Delta^{-2} \qquad (5)$$

The irradiance is then corrected for the phase angle of the observation. For this we have adopted the IRAS value of the phase coefficient of 0.01 magnitudes/degree.

The current implementation of the code uses N = 10. Integration of the flux over the sensor spectral response $\Psi(\lambda)$ is performed by calculating an effective wavelength and bandwidth for the sensor for a blackbody at the IRAS 12 to 25 μm color temperature of the asteroid, that is $T_c = 0.92\ T_s$. The effective wavelength λ_e is defined by

$$\lambda_e \int \Psi(\lambda) B(\lambda, T_c)\ d\lambda = \int \lambda \Psi(\lambda) B(\lambda, T_c)\ d\lambda \qquad (6)$$

and the effective bandwidth $\Delta\lambda_e$ is defined by

$$\Delta\lambda_e\ B(\lambda_e, T_c) = \int \Psi(\lambda) B(\lambda, T_c)\ d\lambda \qquad (7)$$

The limits of the integrals are those of the spectral response function $\Psi(\lambda)$.

2.2 The Dynamical Model

Our approach to computing the positions of the asteroids follows the standard procedure given by Meeus(1985). Calculation of the coordinates of the Sun on the Julian date of the observation is based on Newcomb's method (1895). We use osculating orbital elements for the asteroids as prepared for the IRAS program, and solve Kepler's equation by iteration. The orbit calculation gives the Ecliptic Latitude and Longitude of the asteroid, its distance from the Sun and Earth, and the phase angle of the observation.

Good orbital elements are available for about 3000 numbered asteroids, however, to extrapolate to faint, as yet undetected, pseudo-asteroids we require a suitable set of orbital elements, as well as, physical and optical properties. To obtain bogus orbital elements for our pseudo-asteroids we rely heavily on the review of asteroid dynamics by Scholl (1987), and the assumption that the orbital elements of the pseudo-asteroids will have essentially the same distribution as the orbital elements of the known asteroids.

For each pseudo-asteroid we select each orbital element by random

number generation from a representative set of distributions. We characterize the distributions of the orbital elements as follows:

a. The time of perihelion passage is uniformly random in the interval JD 2415588 to JD 2450132 for the epoch of the osculation of the IRAS elements (JD 2445440.5). This time window is from the measured distribution in the IRAS orbital element database.

b. The argument of perihelion is uniformly random in the range 0° to 360°. Also from the measured distribution in the IRAS database of orbital elements.

c. The orbital inclination i is Gaussian random in the absolute value of sin(i), with zero mean and full width at half peak σ = 0.4 (from Scholl, 1987).

d. The longitude of the ascending node is uniformly random in the range 0° to 360°, as determined from the IRAS database.

e. The eccentricity of the orbit is Gaussian random in absolute value with mean = 0.14 and full width at half peak σ = 0.18 (from Scholl, 1987).

f. The perihelion distance is Gaussian random with mean = 2.8 and full width at half peak σ = 0.59 (Scholl, 1987). The analysis of Scholl (1987) clearly shows that the distribution is bimodal with a minimum near 2.2 AU. We have chosen to distribute the pseudo-asteroids symmetrically about the second peak at 2.8 AU. This choice can be rationalized by the argument that the discovery circumstances favor nearby asteroids, thus undiscovered asteroids should be biased toward orbits with larger perihelion distances.

2.3 The Number vs Diameter Relationship

To extrapolate the number-diameter distribution of the asteroids to small diameters, it was assumed that the observed relationship is complete to about d = 24 km (see Figure 1). At smaller diameters the distribution is assumed to follow a power law with slope determined by a least squares fit to the linear part of the curve in the region d = 24 to d= 100 km. This yields the following expression for the diameter d as a function of the cumulative number n

$$d = 10^{[(5.2486-\log(n-1246)/1.4]} \qquad (8)$$

Equation 8 is applicable only in the region where d < 24 km. The implementation of Eqn. 8 in the computer code somewhat over-estimates the number of asteroids with diameters in the range of 10 to 24 km, since the code first considers all the numbered asteroids before extrapolating from 24 km to smaller diameters.

Equation 8 is also used to select the number of asteroids to be considered as potential detections. This is based on the minimum diameter detectible at the system threshold. For this estimate we assume pv = 0.04, ρ = 2 AU, and Δ = 1 AU in order to insure the completeness of the sample.

3. THE DATABASE

3.1 DIAMETERS AND ALBEDOS

The extensive Asteroid Data Analysis System (ADAS) database of numbered asteroids is our basic source of infrared properties of asteroids.

As a part of the daily processing of IRAS data, all detections of sources with temperatures in the range 30K to 450K were written to special files for later analysis. These files contain possibly the largest and most complete survey of asteroids and comets ever performed.

The first product to be released from the ADAS processing is a catalog of IRAS detections with positional associations with the numbered asteroids and known comets. These are in general the brightest of the asteroid and comet distribution, and the best set of data on the infrared signatures of these small solar system bodies. The part of that database which is pertinent to this study is the tabulation of the deduced albedos, and diameters for 1790 asteroids. There are 3318 numbered asteroids for which we have orbital elements. We have extended the number of diameters and albedos from the 1790 measured by IRAS by adding 91 diameters and albedos from the TRIAD (Morrison and Zellner, 1979; Bowell,et al, 1979) database. In several instances where diameters d were available, the albedos were calculated from the absolute magnitude B(1,0) by

$$pv = 10^{[6.496 - 0.4\ B(1,0) - 2\ LOG\ d]} \qquad (9)$$

We also added 1437 albedos and diameters assuming pv = 0.04 and calculating the diameter from the absolute magnitude H(1,0) tabulated in the IRAS file.

$$d = 10^{[3.82257 - 0.2\ H(1,0)]} \qquad (10)$$

The augmented data file, PV-DIAM.DAT, is included on the program disk. A plot of the number of asteroids with diameters greater than d in the data file is given in Figure 1. The lower curve is the original IRAS data. The upper curve is the augmented IRAS data.

3.1 ORBITAL ELEMENTS

The orbital elements for 3318 numbered asteroids are contained in

the file ASTEL600.DAT on the program disk. This is the file of osculating orbital elements for the epoch JD 2445440.5 created for the IRAS project by B. Marsden, D. Bender, and E. Bowell (Matson, et al, 1987). Although the epoch is 1983, the year of the IRAS mission, these data should provide sufficient accuracy for most statistical or system related studies. A current update of these orbital elements to the present epoch can be obtained from the Minor Planet Center, Smithsonian Astrophysical Observatory, in Cambridge, Massachusetts.

4. RESULTS

The results of a typical model run are plotted in Figures 2 and 3. The symbols give a coarse measure of the irradiance of the asteroid, a factor of ten from one symbol to the next in order of decreasing intensity @, X, O, *, +, the faintest range extending from the system threshold to 10x the system threshold. The date of the plot is JD 2445415.5. The threshold is at IRAS SNR = 3, 1.938×10^{-18} W/cm2, in the 25 μm band. Figure 2 is a plot of all the numbered asteroids detected, a total of 2495 out of 3318. Figure 2 plots the pseudo-asteroids detected, a total of 559. The total number of asteroids considered was 20106. The run time on a 80386/87, 20 MHz computer was 8 minutes.

The detections in Figure 2 are spread more or less uniformly in longitude, while those in Figure 3 are concentrated around longitude 180°. This is a threshold effect to be expected since on this date, the Vernal Equinox, the Earth is at longitude 180°. The faint population of detected asteroids will be distributed about the positions of minimum separation between the asteroids and Earth. The brighter population of larger asteroids can be detected at all longitudes.

5. REFERENCES

Bowell, E., Gehrels, T., and Zellner, B., in Asteroids, ed. T. Gehrels (Univ. of Arizona Press, Tucson), pp 1108-1129, 1979

Morrison, D., and Zellner, B., in Asteroids, ed. T. Gehrels (Univ. of Arizona Press, Tucson), pp 1090-1097, 1979

Matson, D.L., Veeder, G.J., Tedesco, E.F., Lebofsky, L.A., and Walker, R.G., "IRAS Survey of Asteroids", Advances in Space Research, vol.6, no.7, p.47, 1987.

Lebofsky, L.A., Veeder, G.J., Lebofsky, M.J., and Matson, D.L., Icarus, **35**, 336, 1978

Matson, D.L., "Infrared Astronomical Satellite Asteroid and Comet Survey", preprint version No.1, October, 1986

Meeus, J., "Astronomical Formulae for Calculators", 3rd edition, (Willmann-Bell, Inc., Richmond, VA), 1985

Newcomb, "Tables of the Sun", A.P.A.E., **6**, 1895

Scholl, H., "Dynamics of Asteroids" in The Evolution of Small Bodies in the Solar System, (North Holland Physics Publishing, Amsterdam), p 53-78, 1987

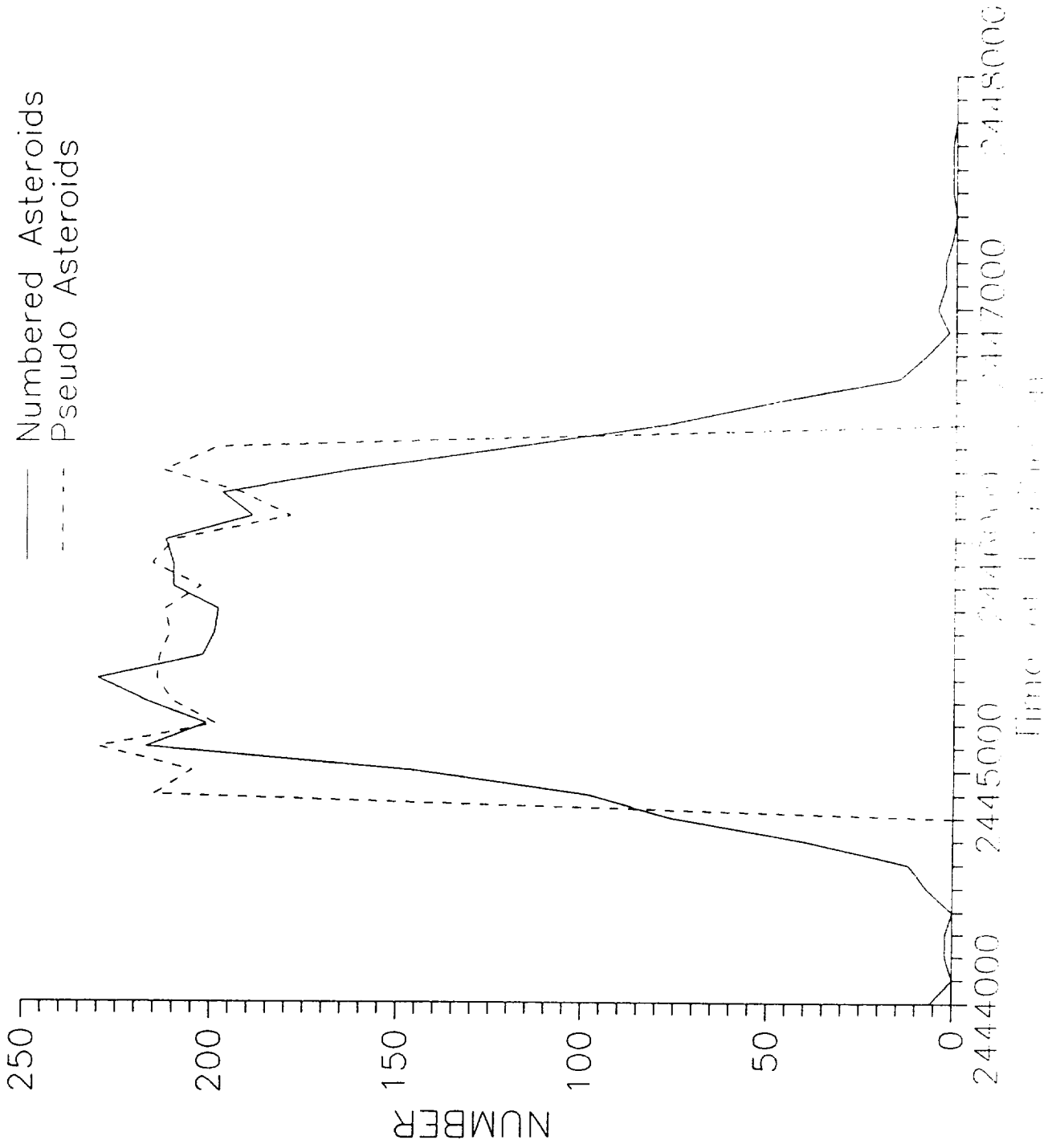

Figure 1. Frequency of Perihelion Passage Time (Julian Day).

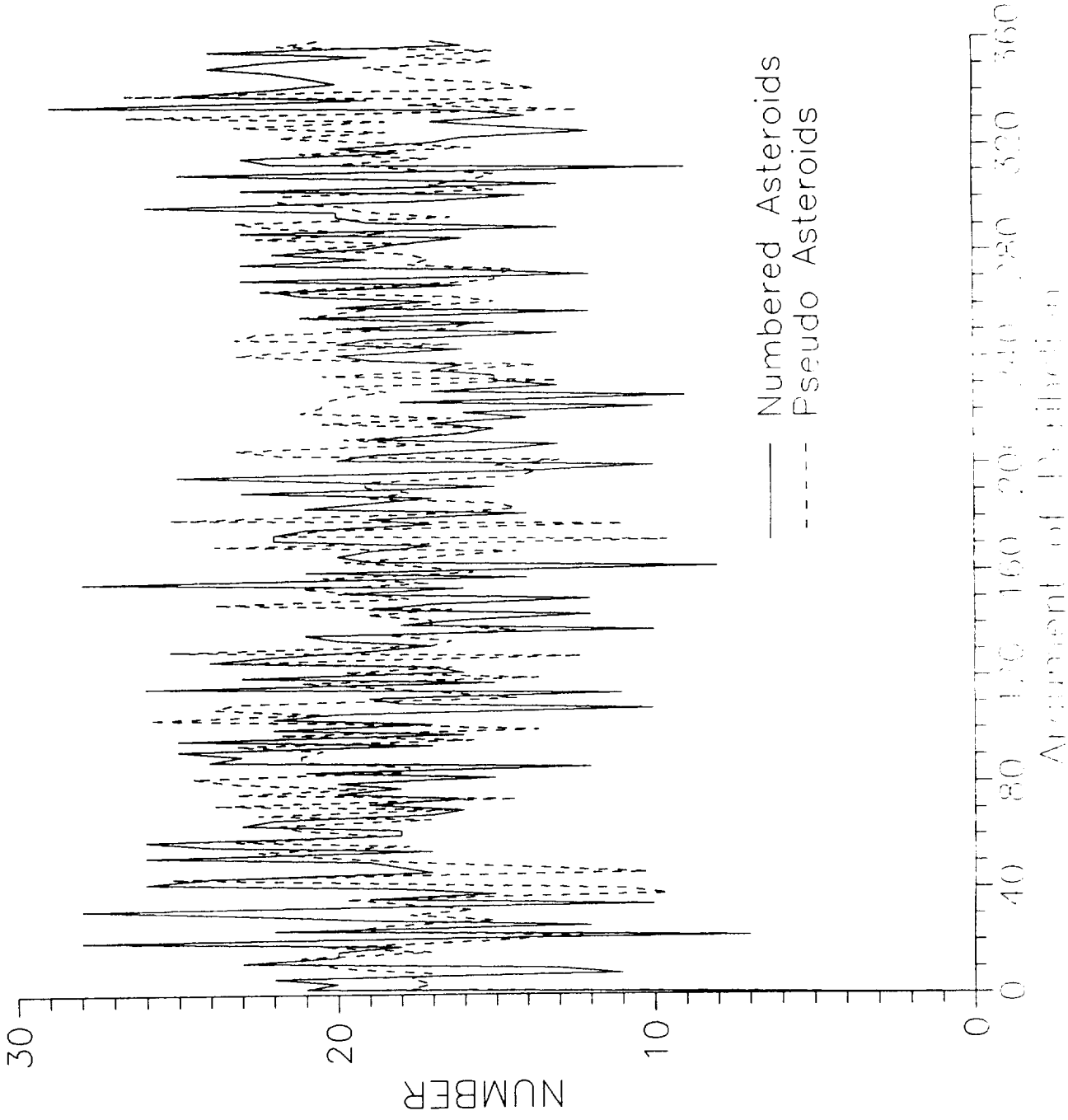

Figure 2. Frequency of the Argument of Perihelion (degrees).

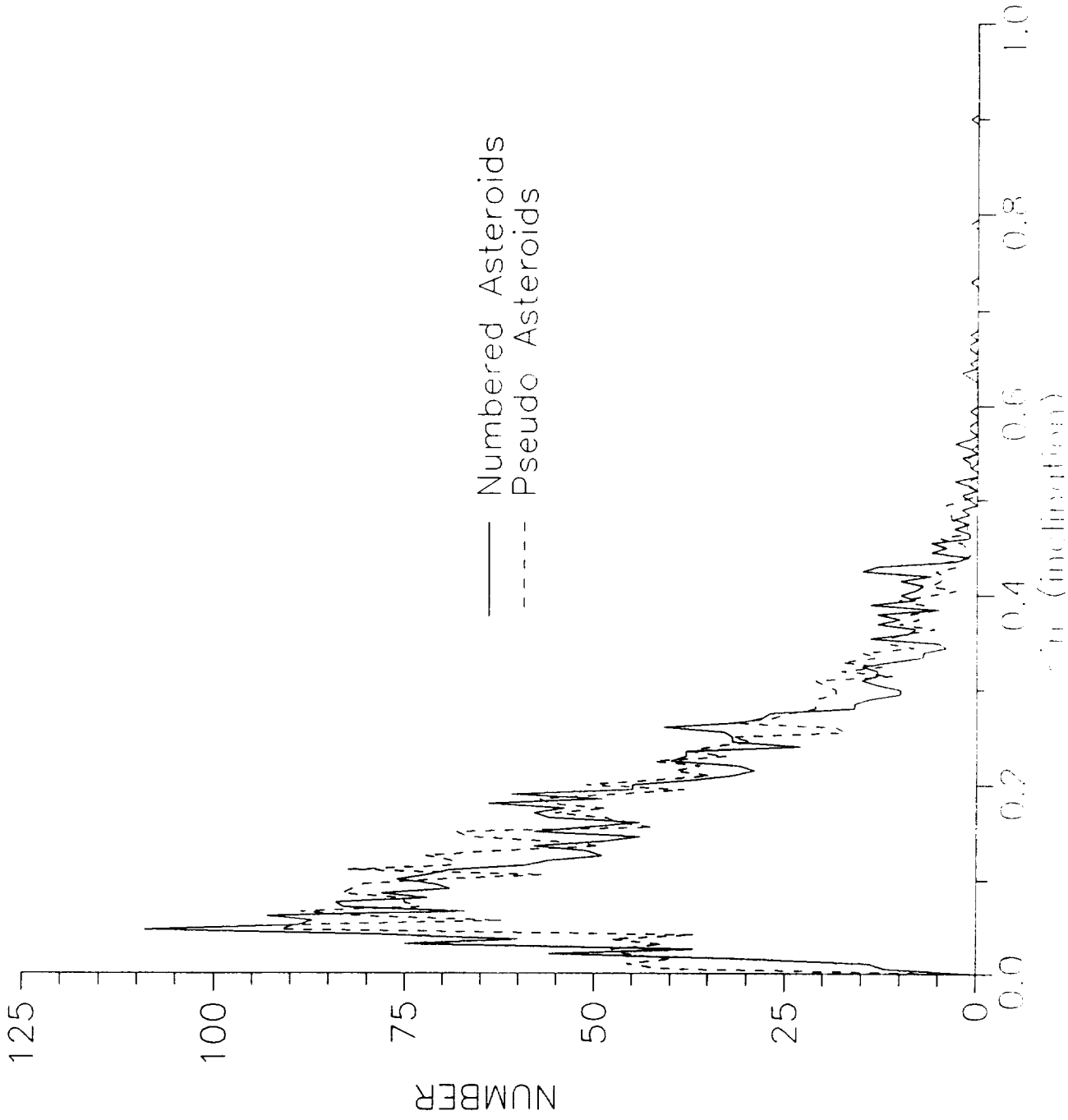

Figure 3. Frequency of the sine of the orbital inclination.

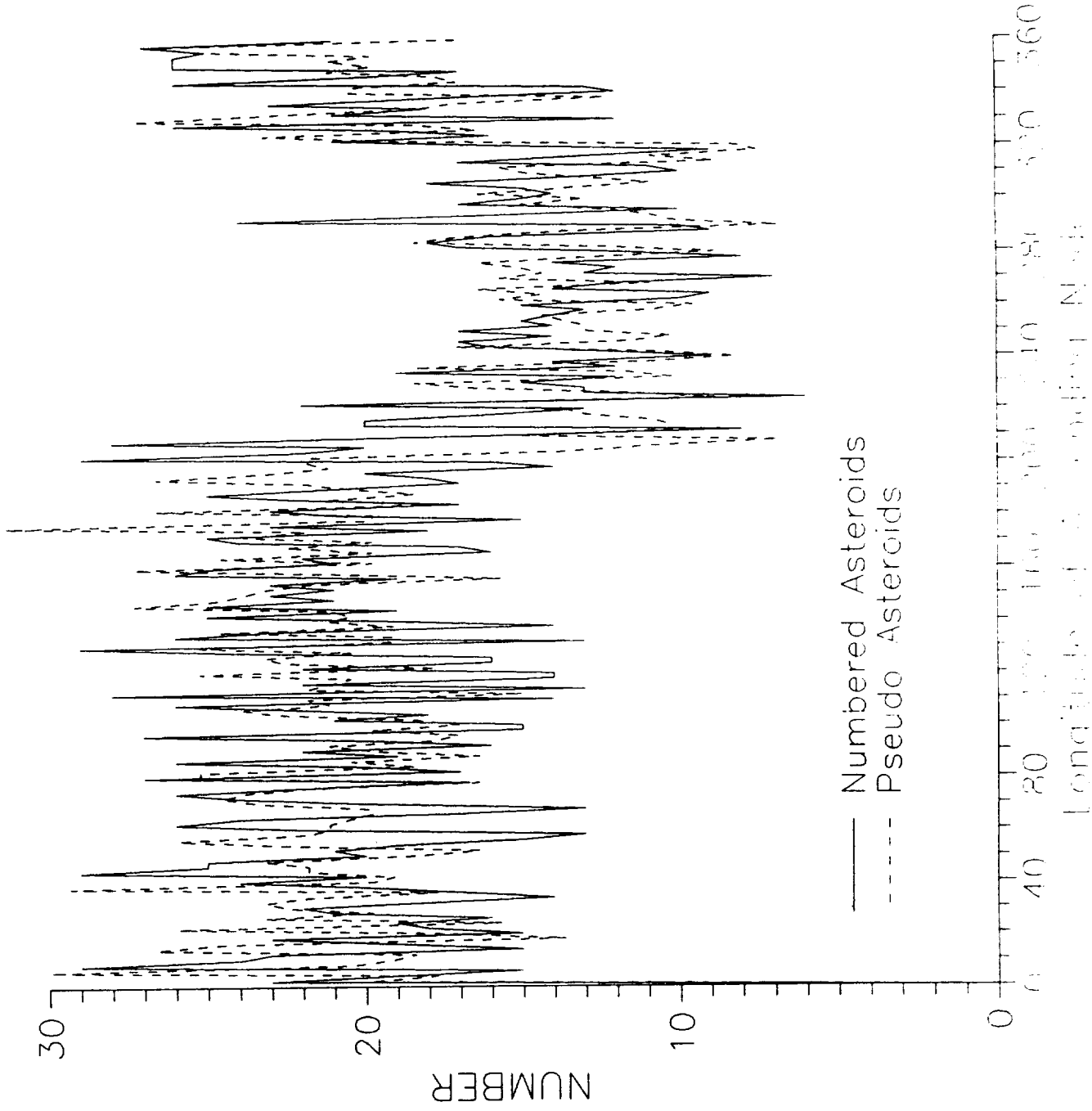

Figure 4. Frequency of the Longitude of the Ascending Node (degrees).

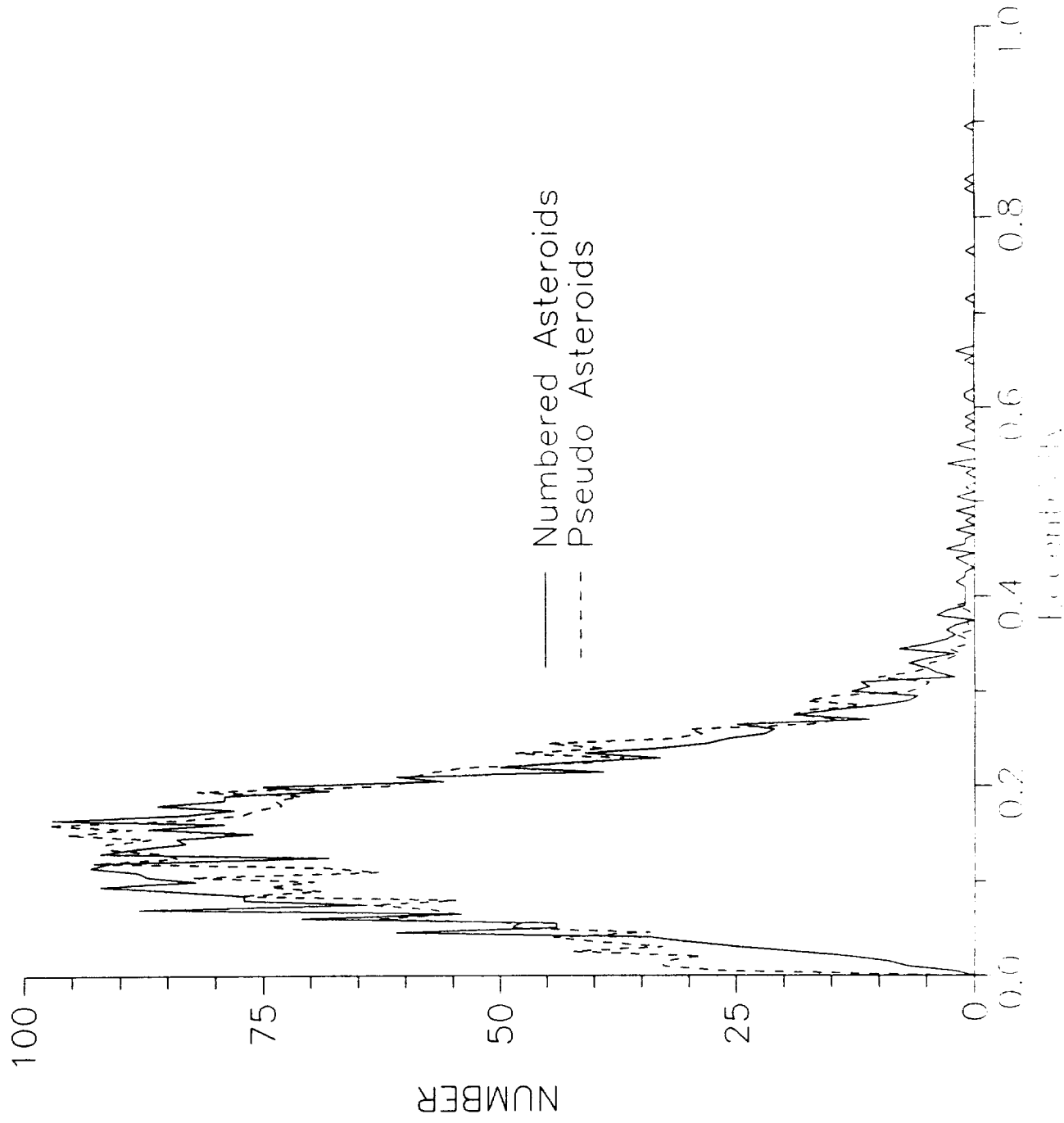

Figure 5. Frequency of the orbital Eccentricity.

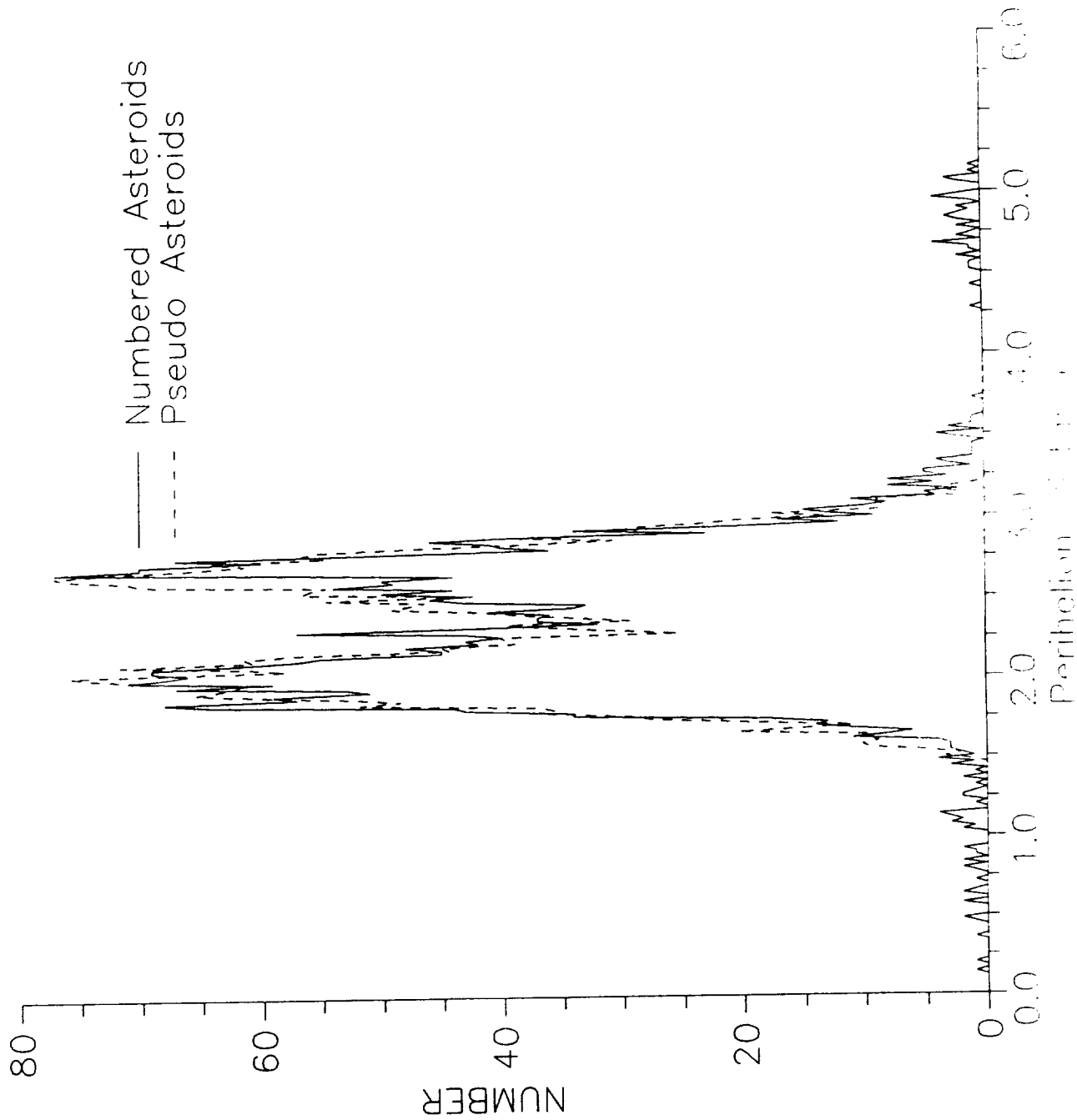

Figure 6. Frequency of Perhelion Distance (AU).

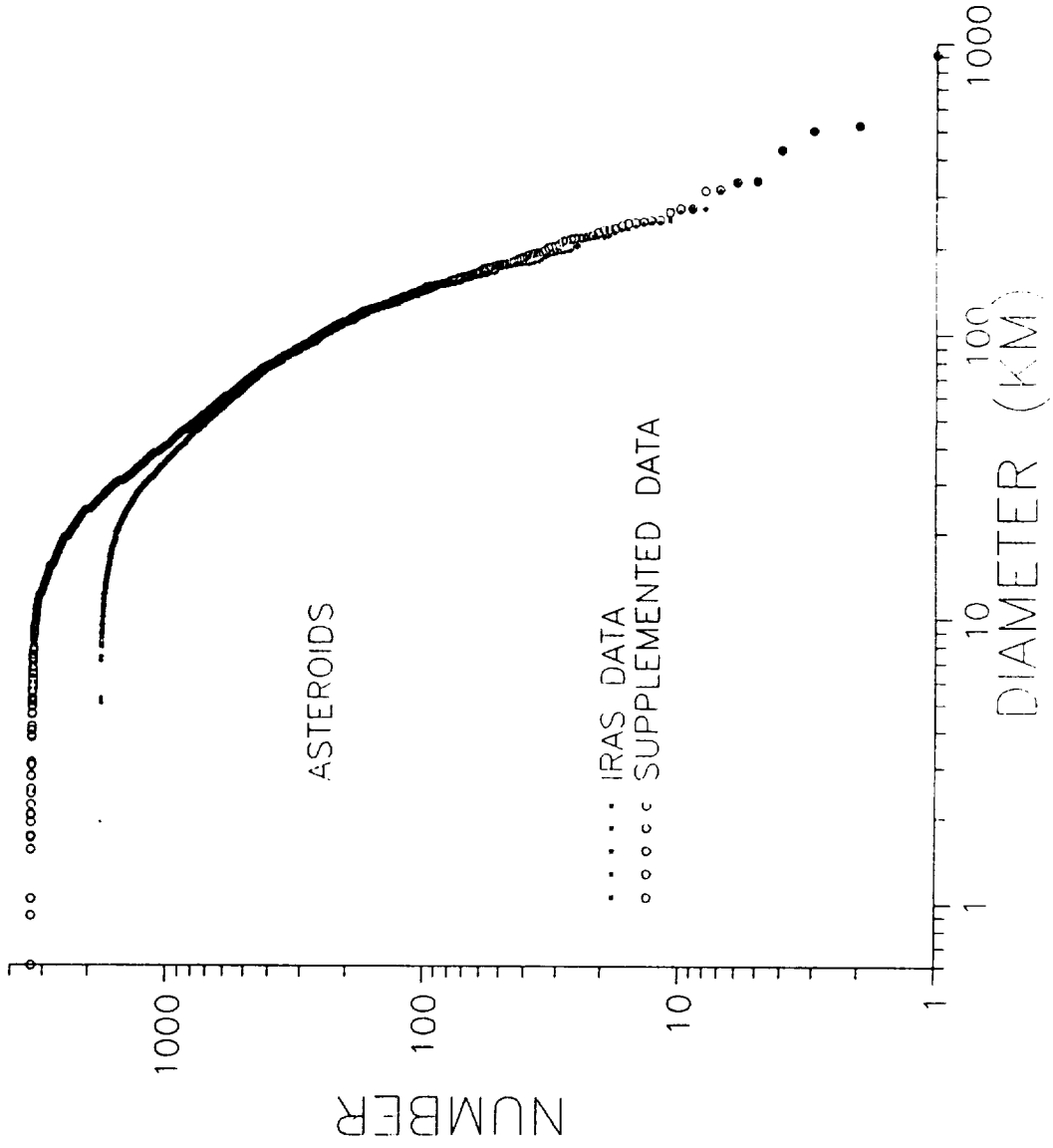

Figure 7. The number of asteroids versus diameter.

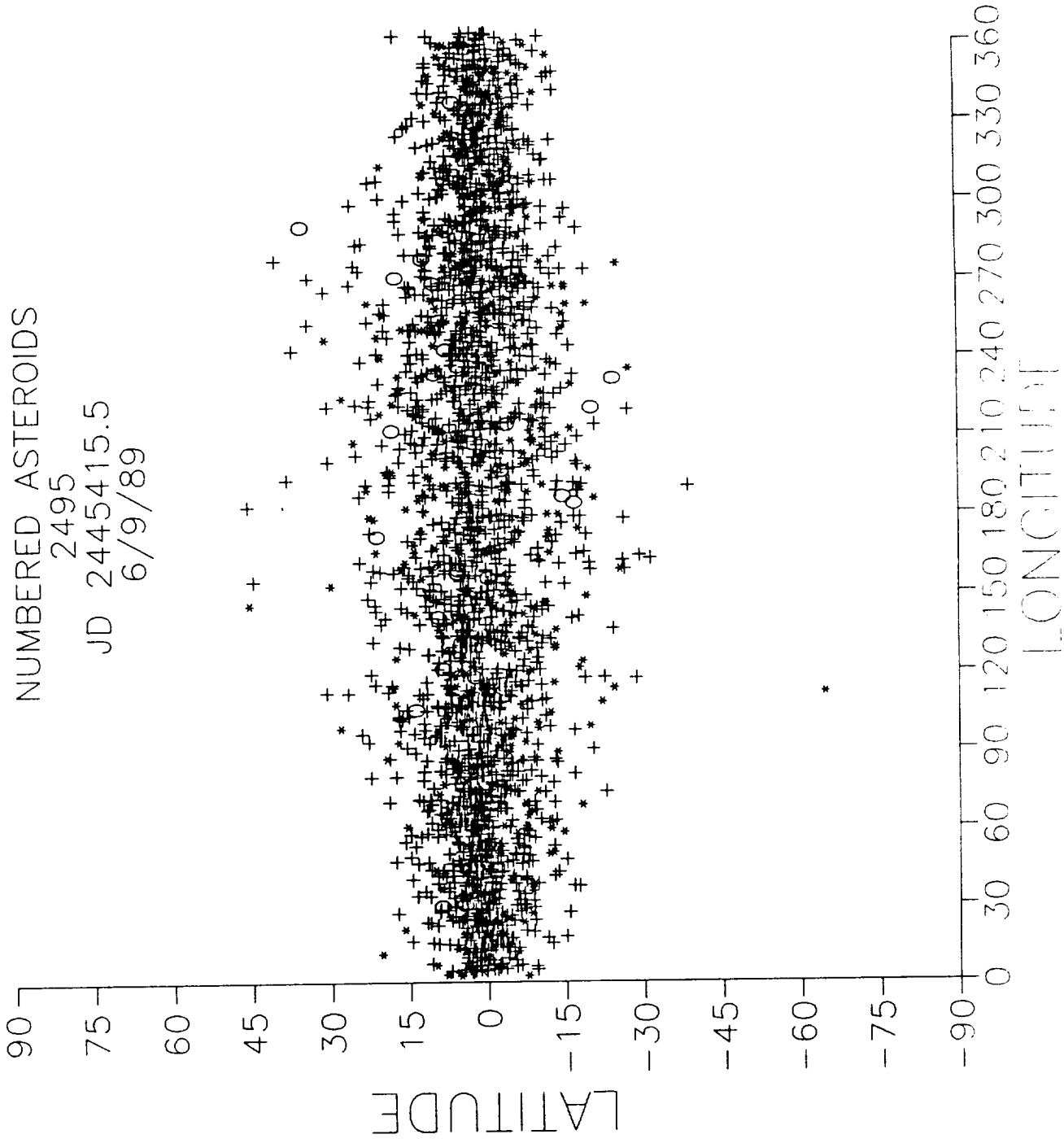

Figure 8. The distribution of predicted numbered asteroids.

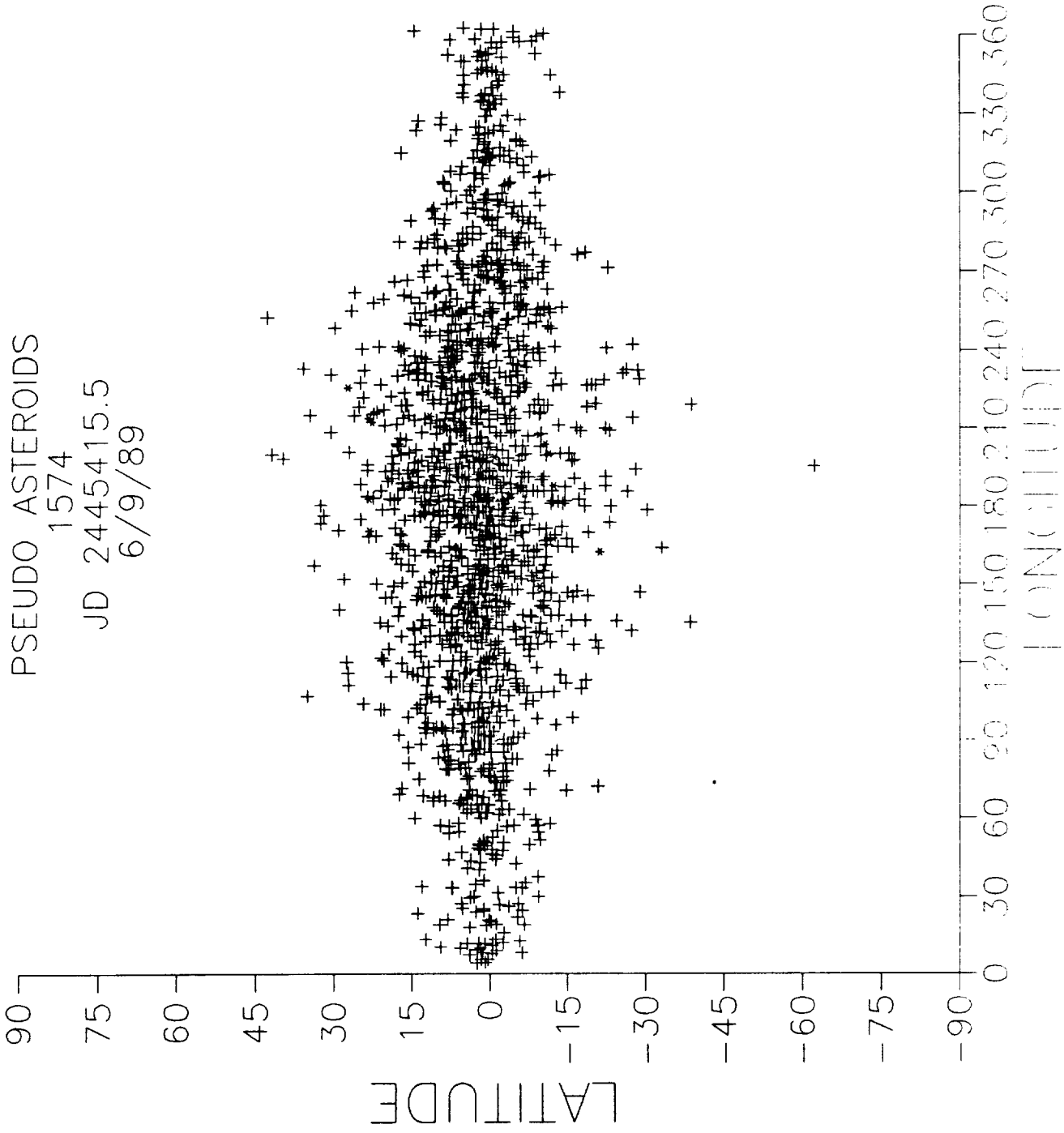

Figure 9. The distribution of predicted psuedo-asteriods.

APPENDIX N. "Comets and Debris Streams"

Appendix N. Comets and Debris Streams

Introduction

Studies of cometary dust can yield information not only about comets themselves but also about interplanetary dust and possibly about pre-solar interstellar dust. The IRAS observations of cometary dust coma represent a quantum jump in the available infrared observations of these objects.

The large field of view and high sensitivity of the IRAS detectors made the IRAS sensor particularly suitable to detect the faint diffuse thermal emission from cometary dust. As a consequence IRAS discovered seven new comets and recovered five previously known comets. These data are summarized by Walker, et al (1986) and the point source photometry presented in some detail in the IRAS Asteroid and Comet Catalog (Matson, et al, 1986).

Infrared images of Comets IRAS-Araki-Alcock, Kopff, and Tempel 2 reconstructed from IRAS observations have been published (Walker, et al, 1983; Walker and Aumann, 1988; Walker and Campins, 1988). These attest to the complex nature of thermal emission from comets, and the difficulties encountered when interpreting the observations in terms of the physical phenomena. In particular, the point source photometry of these extended objects.

One of the most significant discoveries made by IRAS was that some periodic comets are accompanied by narrow trails of debris that both lead and follow the comet in its orbit. These trail particles may be the precursors of meteor streams, and may populate the entire orbit. The recent trail study of Sykes and Dow (1989) associates debris trails with eight periodic comets and has detected an additional large number of trails with no apparent associations. While the apparition of a comet may be infrequent, debris trails offer a potential large number of encounters.

Comets

The nucleus is where all the activity of a comet originates; however, most of the information about a comet comes from studies of its coma. This is because the direct observation of the nuclear surface of a comet using earth-based telescopes is extremely difficult. Therefore, the structure and composition of the nucleus must be inferred based mostly on our knowledge of the solids and gasses in the coma. Studies of cometary dust can yield information not only on the comet nucleus but also about interplanetary dust and very possibly about pre-solar interstellar dust. Comets are believed to be the main source of

interplanetary dust particles (e.g., Brownlee, 1978). There is also growing evidence that at least some of the cometary dust is well-preserved interstellar dust incorporated into the comet during accretion in the early solar nebula (Greenberg, 1986).

Preliminary studies carried out on a small fraction of the IRAS comet data have already revealed remarkable discoveries in the comets observed, such as the presence of extensive tails not observable at visible wavelengths (e.g., Walker and Rowan-Robinson, 1984; Walker et al., 1984,). Dust production rates have been estimated from IRAS point source photometry (Walker and Aumann, 1984), and the morphology of the comet is now being revealed through high resolution infrared comet images are now being produced from the IRAS data (Walker and Aumann, 1989; Walker and Campins, 1988). The process through which comets contribute to the interplanetary dust cloud is becoming clearer with the discovery and study of comet dust trails in the IRAS observations (Davies, et al, 1984; Sykes et al., 1986).

IRAS observations of comets include photometry, spectroscopy, and multiple wavelength imagery. However, the large beam of the IRAS detector array, which was well suited to detect faint extended emissions of cometary origin, has produced a large data set that is complex to analyze. Although some preliminary results of the IRAS comet photometry have been published, definitive analysis must explicitly account for the convolution of the emission source with the non-uniform spatial response of the detector array.

An overriding concern during the design of the IRAS focal plane array and in the subsequent production of the point source catalog was the high reliability of the cataloged sources. The entire system was optimized for the detection of point sources at the expense of degraded performance on complex extended objects. Even so, the large instantaneous fields of view of the detectors were well suited to the detection and measurement of low level extended thermal emission from cometary dust.

The bulk of the observations were performed in the survey mode which systematically mapped the sky with a series of overlapping and confirming scans. A near real time analysis of these data led to the IRAS discovery of six comets and one possibly inactive comet nucleus, the recovery of five periodic comets, and the discovery of a debris trail associated with comet P/Tempel 2. Post mission analysis of survey detections of potential solar system objects was accomplished with the Asteroid Data Analysis System (ADAS), and a preliminary comet catalog of highly reliable detections of 23 previously known comets was published. These data showed that the observed 12 to 25 micron flux density ratios in the coma were consistent with small particles hotter than the local blackbody temperature at that heliocentric distance. However, the flux density ratios Jy25:Jy60, and Jy60:Jy100

suggested that we were observing emission from a significant population of larger, and therefore cooler grains. Interpretation of these data is complex. The flux densities were derived from the response of the IRAS point source data filter which high passes the data, suppressing the response to low spatial frequencies, and thereby underestimating the total flux. The situation is further aggravated by the variation with wavelength of the size of the instantaneous field of view. IRAS spent about 1/3 of its total observing time making observations at enhanced sensitivity and spatial resolution toward objects selected for their particular astronomical interest. Comets were among the targets chosen for these additional observations (AOs). The typical AO maps a small region (1.0 x 0.5 degree) centered on the target with a number of repetitive scans, each offset by a small increment (0.4 arc min) in the cross scan direction. Maps of inertial sources can be spatially coadded to further improve sensitivity. A total of 57 AOs were performed on 19 comets during the mission. Dust production rates and grain characteristics have been derived from analysis of the coma of several of these comets using images produced by the standard AO processing system. Although these data offer a significant improvement in signal to noise ratio, the gridding process degraded the spatial resolution.

The IRAS comet data can provide information relating to the distribution of dust in the coma and tail. The realization of this must wait upon the production of high resolution images.

Debris Trails

The discovery of comet dust trails in the IRAS data (Eaton, et al, 1984; Davies et al, 1984; Green et al, 1985; Sykes et al. 1986a) has added a new dimension to the infrared study of comets. Cometary dust trails are narrow sources of infrared emission that have apparent lengths between a few degrees and several tens of degrees and widths of arcminutes or less Sykes et al., 1986a; Sykes et al. 1986b). Of the many dust trails identified to date in the now completed Major Trail Survey (Sykes and Dow, 1988), eight are definitely associated with known comets and all of these are short-period comets as shown in Table 1.

This debris is thought to be composed primarily of millimeter or centimeter sized particles; otherwise radiation pressure would quickly disperse them into a faint, unrecognizable infrared background. However, the existence of very small particles cannot be ruled out because the ratio of radiation pressure forces to gravitational forces becomes very small for the 10-100 A diameter-sized grains presently known to exist in several parts of the galaxy (Burns, 1987).

Table 1. Comets With Known Debris Trails

COMET	SEMI-MAJOR AXIS	INCLINATION
P/Encke	2.21 au	11.9 deg.
P/Tempel 2	3.03	12.4
P/Tempel 1	3.11	10.5
P/Pons-Winnecke	3.44	22.3
P/Kopff	3.45	4.7
P/Churyumov-Gerasimenko	3.52	7.1
P/Gunn	3.59	10.3
P/Schwassmann-Wachmann 1	6.04	9.4

The distribution of the remaining trails clusters around low ecliptic latitudes which suggest that these too might be associated with short-period comets. Although other classes of objects such as long-period comets, asteroids with comet-like orbits, and meteor streams have been examined by Sykes and Dow (1989) for possible association with the dust trails, none have been found.

During the IRAS mission, the longest and brightest dust trail observed was that of P/Tempel 2. Analysis of the IRAS observations of this trail showed it to consist of large particles, submillimeter and larger, with a possible excess of particles larger than several millimeters over that expected from a single power-law distribution (Sykes et al., 1986b). Further analysis showed these particles to have a bolometric Bond albedo of about 5% (Sykes, 1987), equivalent to the surface of Comet Halley as observed by Giotto (Keller et al., 1986), and Vega (Sagdeev et al., 1986) spacecraft.

To date the only trail for which extensive analysis is available is that of P/Tempel 2. Debris trail emissions are usually faint. The brightest trail detections of Tempel 2 were typically at a signal to noise ratio (SNR) of about 3. Due to the linear nature of the trail, it is possible to trade spatial resolution along the trail for enhanced SNR and an improved measurement of trail width. This leads to the concept of averaging the trail radiance along the length of the trail, say for one focal plane width (10 to 13 full sized detectors, depending on the spectral band), to reduce the uncertainties of the flux estimate, while maintaining the in-scan resolution inherent in the array. Additional enhancements may be obtained by coadding multiple trail crossings. The software package to perform this was developed under another NASA program, and has been applied to the debris trail of P/Tempel 2.

The 12 and 25 μm radiance at the peak of the trail profile is plotted in Figures 1 and 2 versus perihelion passage time for the debris particle. Two sets of data are shown. Each set was

scanned in 10 days by IRAS. The two sets are also separated in time by 10 days. The one sigma error bars represent about ±10% uncertainty. As can be seen, the radiance of the trail decreases away from the comet, and the agreement between the two sets of results is quite satisfactory. All the data plotted are trailing the comet.

Figure 3 shows the gaussian trail width derived for the same two data sets. The error bars represent about ±6% uncertainty in the width measurement. As with the radiance data, the two sets agree quite well. The trail width is observed to increase with distance from the comet. Modulations of the width, which exceed that due to the uncertainties are also apparent along the trail. These are possibly related to Tempel 2's outburst history over several orbits.

The optical depth at the center of the trail (determined from the 12 and 25 μm color temperature) is plotted in Figure 4. A comparison with Figure 3 reveals that the optical depth is anti-correlated with the trail width. That is, the optical depth decreases with increasing trail width. The product of the trail width and peak radiance is proportional to the total number of radiating particles. Plots of this quantity are shown in Figures 5 and 6. In combination with the optical depth we estimate the total mass of radiating grains to be 4×10^8 kilograms if spread completely around the orbit.

The color temperature of the emitting grains found from the ratio of the radiances at 12 and 25 μm is plotted if Figure 7 against the heliocentric distance of the trail particle. Also plotted is the locus of temperatures for a small black particle in equilibrium with the solar radiation at that distance. Although the scatter in the data is quite large, it is significant that the bulk of the estimates of the grain temperature are systematically hotter than the equilibrium blackbody. If the Bond albedo of the grains is 0.05 then the required mean emissivity in the infrared is 0.85.

Fortunately, and entirely by accident, a single IRAS additional observation (AO) scheduled to observe the coma of Tempel 2 missed the target and was performed on the Tempel 2 debris trail at 1.5 days of perihelion passage behind the comet permitting an independent estimate of the trail width. We have deconvolved the detector response function from the debris trail in this AO grid by means of the Richardson-Lucy algorithm at IPAC. Table 2 shows a comparison of the trail width and radiance derived by these two independent means. The radiance profile of the trail, when corrected for faint background stars, is well represented by a gaussian.

Table 2. Comparison of Derived Trail Parameters

PARAMETER (TS/RL)	TRAIL SOFTWARE	R-L ALGORITHM	RATIO
Width(km)	37985	36758	1.033
Radiance(W/M2/sr)			
12um	2.05E-7	1.97E-7	1.041
25um	1.71E-7	1.62E-7	1.056
60um	2.52E-8	2.72E-8	0.926

Conclusions

A wealth of new information concerning the infrared phenomenology of comets and their associated debris trails has been obtained by the IRAS satellite. These data are in only the beginning stages of reduction and analysis, and much work must be accomplished in the future to fully exploit this valuable resource.

Existing analysis programs are just beginning to give some insight into the complex nature of comet dust production and distribution of the grains around the nucleus, in the tail, and into the extensive debris trail. It would be premature at this time to attempt to develop a model for cometary emission in the infrared.

References

Brownlee, D.E. (1979). Rev. Geophys. Space Phys. **17**, 1735.
Burns, J.A., (1987), in "Evolution of Small Bodies in the Solar System", (North Holland, Amsterdam), p 252-276.
Campins, H. and Hanner, M.S. (1982). In Comets, ed. L.L. Wilkening, U. of Arizona Press, Tucson, p. 341.
Campins, H., (1988), private communication.
Davies, J.K., Green, S.F., Stewart, B.C., Meadows, A.J., and Aumann, H.H. (1984), Nature, v. **309**, n. 5967, pp. 315-319.
Eaton, N., Davies, J.K.,and Green, S.F., (1984), Mon. Not. R. Astron. Soc. **211**, pp 15-19.
Fanale, F.P., and Salvail,J.R., (1984), Icarus **60**, pp 476-511.
Green, S.F., Davies, J.K., Eaton, N., Stewart, B.C., Meadows, A.J., ICARUS, **64**, pp 517-527, 1985.
Greenberg, J.M. (1982). In Comets, ed. L.L. Wilkening, U. of Arizona Press, Tucson, p. 131.
Greenberg, J.M. (1986). ESA SP-249, p. 47.
Hanner, M.S. (1980). In Solid Paricles in the Solar System, eds. I. Halliday and B. McIntosh (Dordrecht: D. Reidel) p. 223.
Knacke, R.F. (1987). Sky and Tel. **73**, 246.

Press, W.H., Flannery, B.P., Teukolsky, S.A., Vetterling, W.T., (1986), "Numerical Recipes", Cambridge Univ. Press, p 521
Sekanina, Z., (1979), Icarus **37**, p 420-442.
Sykes, M.V., Lebofsky, L.A., Hunten, D.M. and Low, F.J. 1986a Science, **232**, 1115-1117
Sykes, M.V., Hunten, D.M. and Low, F.J. 1986b Adv. Space Res., **6**, 67-78
Sykes, M.V. and Dow, R., (1988) in preparation
Sykes, M.V., (1988a) In "Comets to Cosmology II",A. Lawerence, ed., Springer-Verlag, p 66.
Walker, R.G., Aumann, H.H., Davis, J., Green, S., DeJong, T., Houck, J.R.and Soifer, B.T. (1984). Ap. J. Lett. L11.
Walker, R.G. and Rowan-Robinson (1984), M., Bull. Am. Astron. Soc., 6, n 2
Walker, R.G., Matson, D.L., and Veeder, G.J., (1987), "IRAS Observations of Comets", Advances in Space Research, Vol.6, no.7, p.57.
Walker, R.G., and Aumann, H.H., (1989) "IRAS Comet Observations The Continuing Saga", to be published in Advances in Space Research.
Walker, R.G. and Campins, H., (1988), "IRAS Observations of Comet Tempel 2", poster paper, DPS Meeting of AAS, Austin, TX.
Walker, R.G., "Infrared Astronomical Satellite Asteroid and Comet Survey", Chap.3, (ed: D.L. Matson), October, 1986.

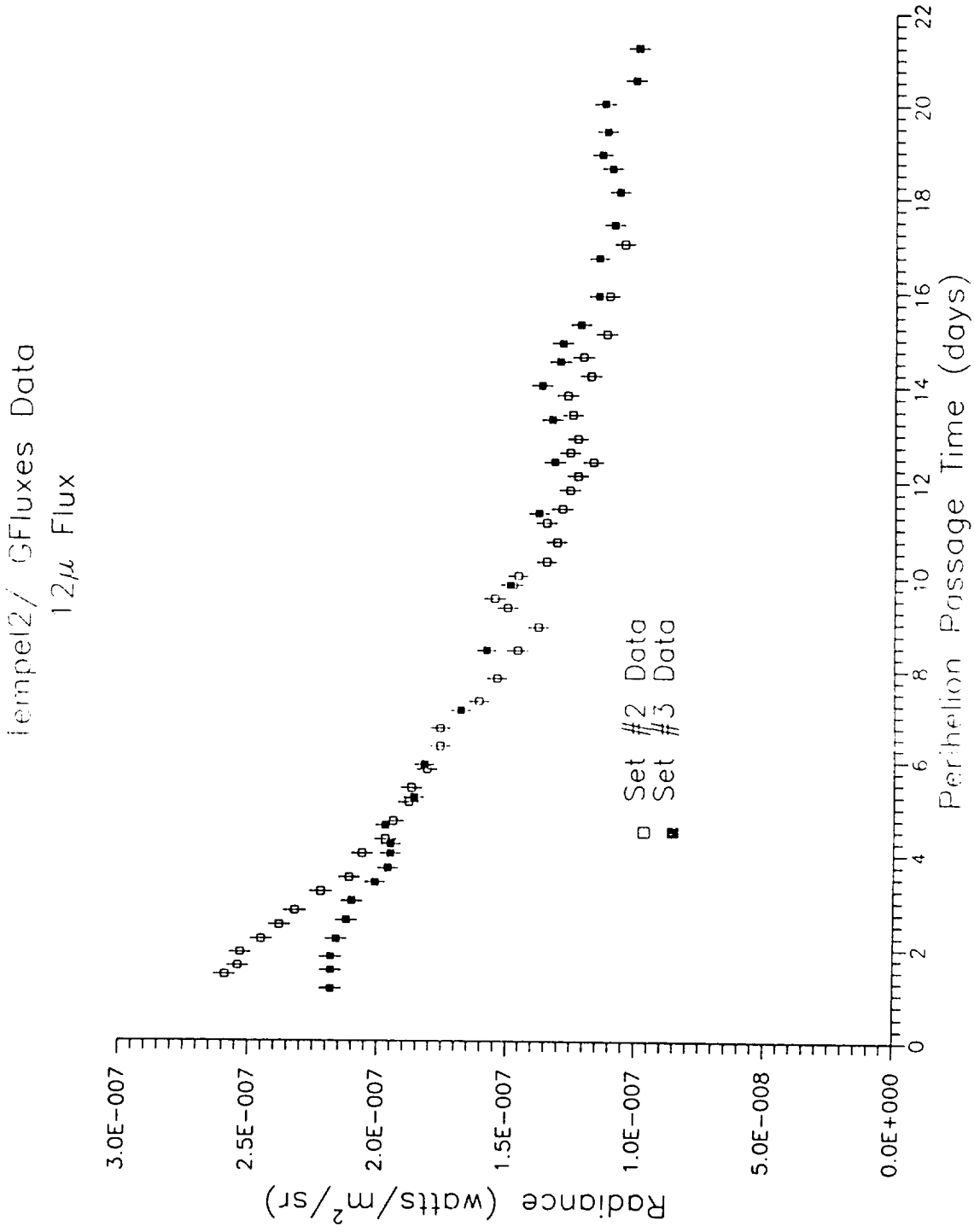

Figure 1. Peak Radiance at 12 μm.

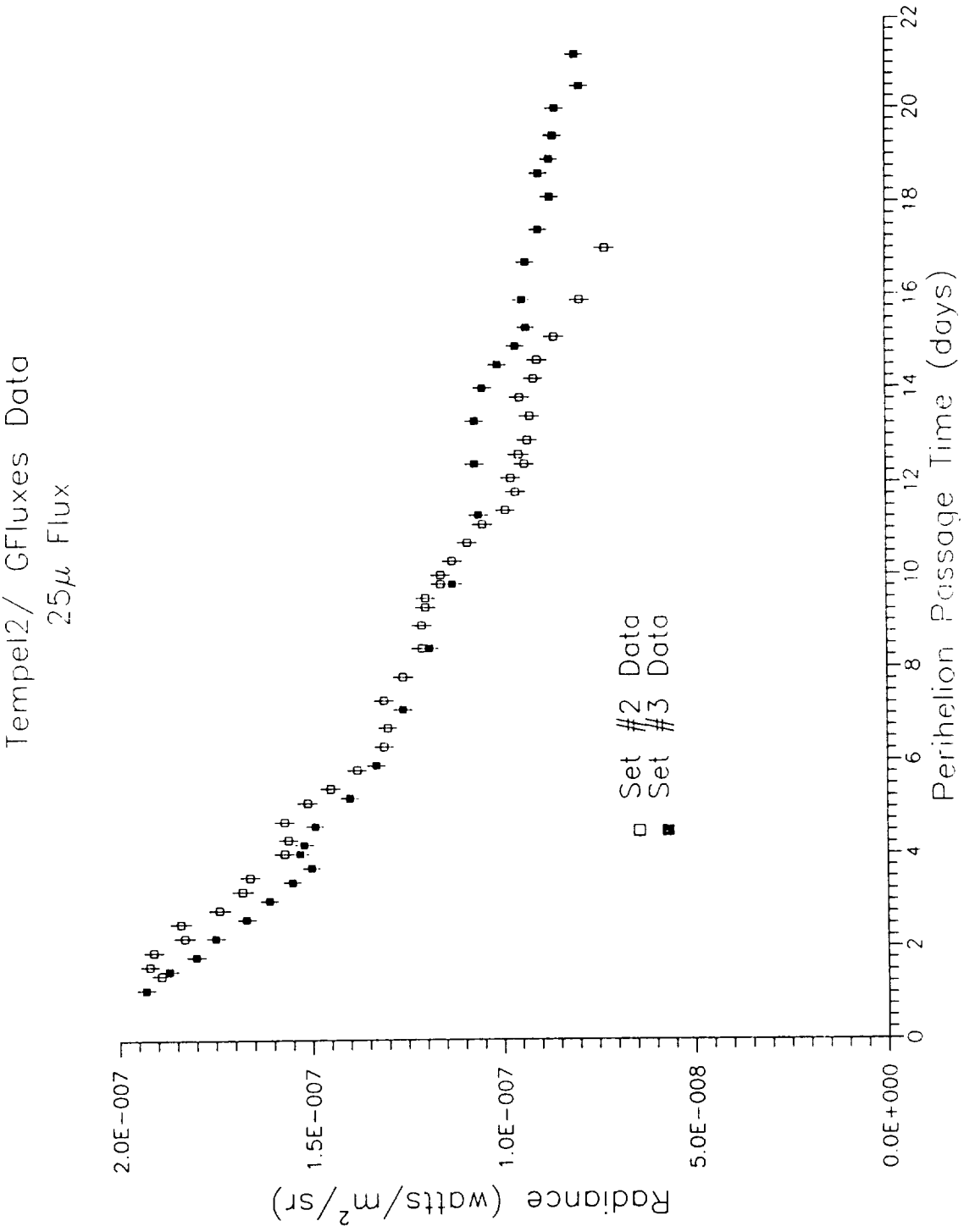

Figure 2. Peak Radiance at 25 μm.

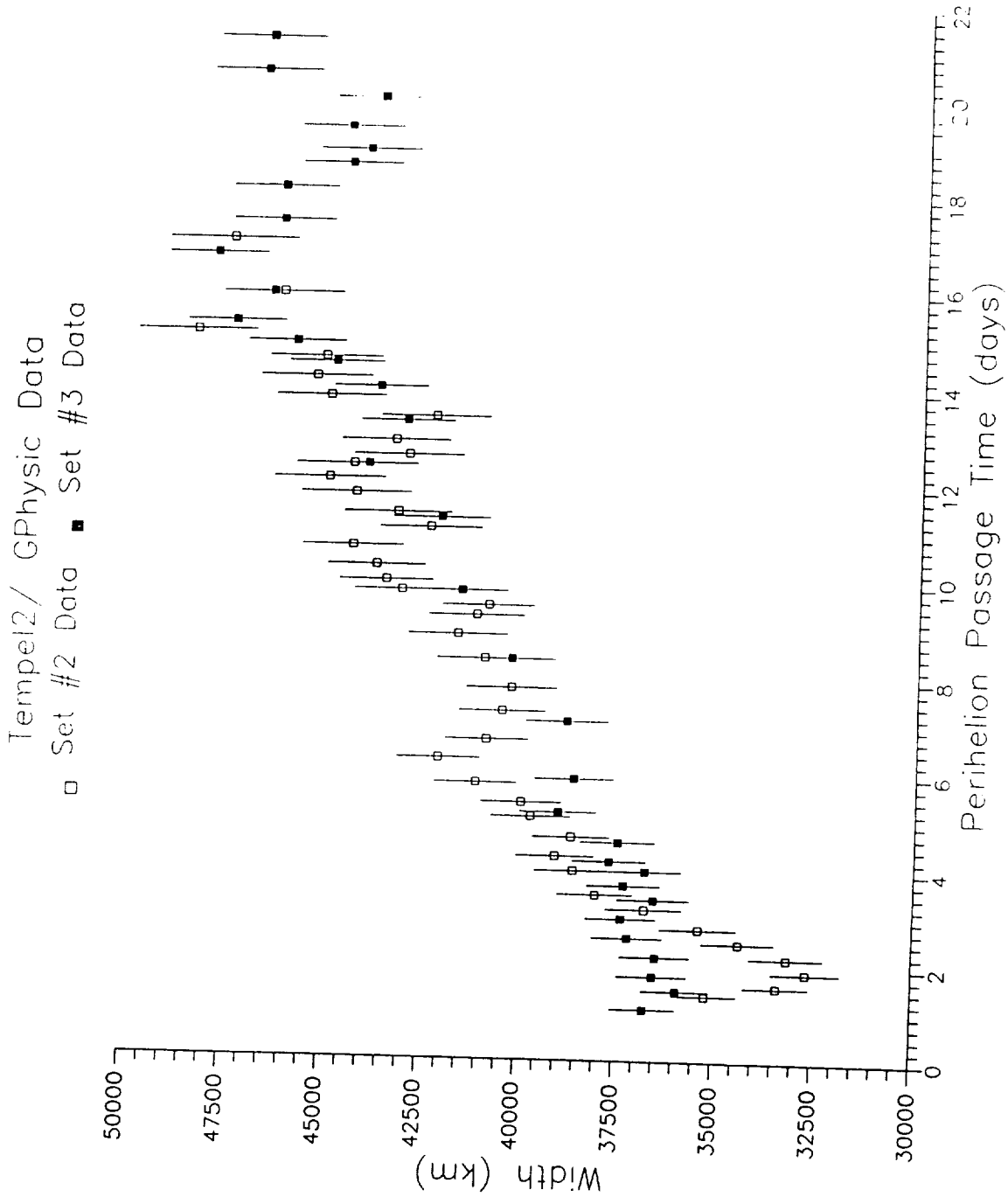

Figure 3. Trail Width versus Perihelion Passage Time.

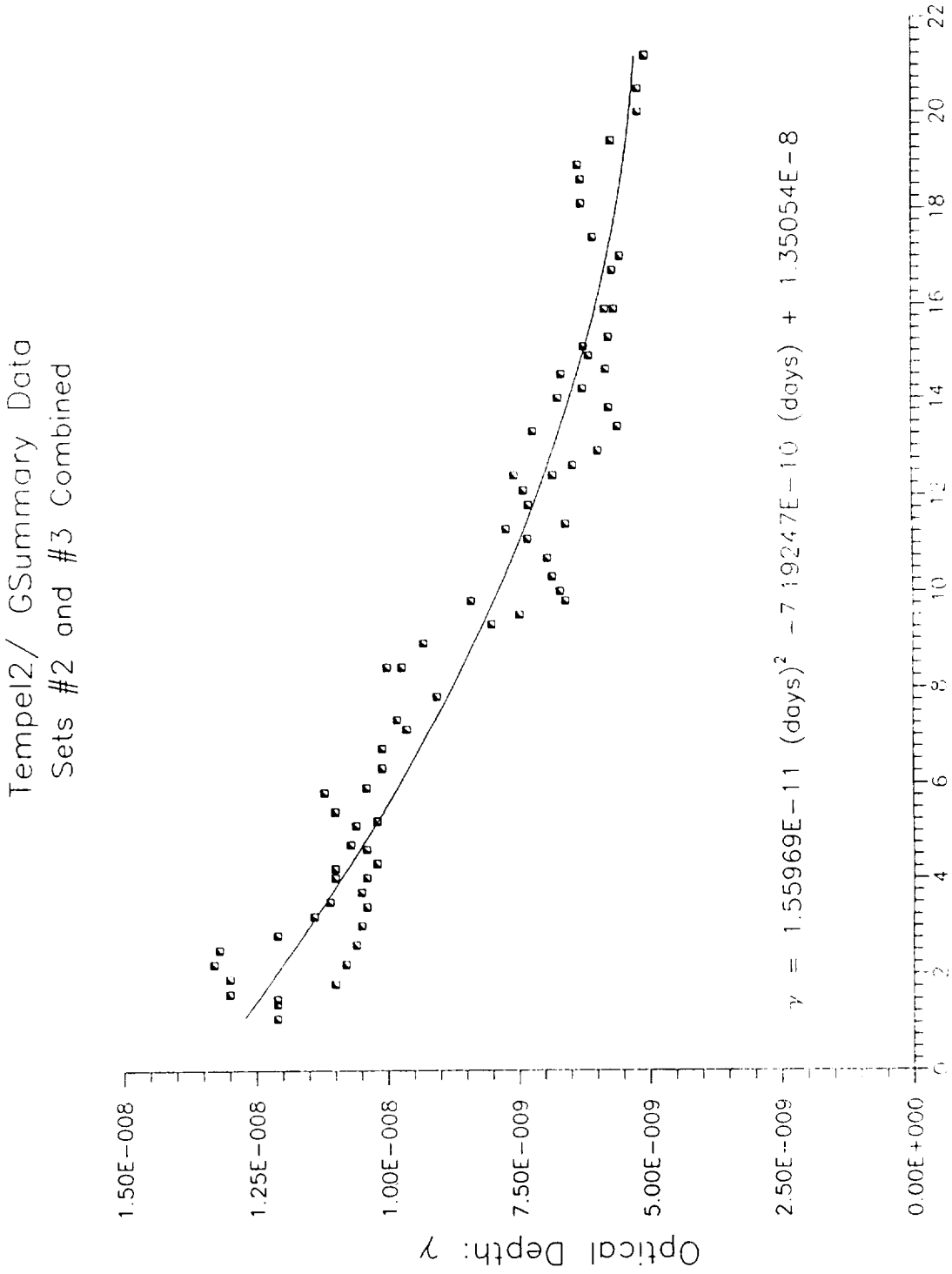

Figure 4. Optical depth at the center of the trail.

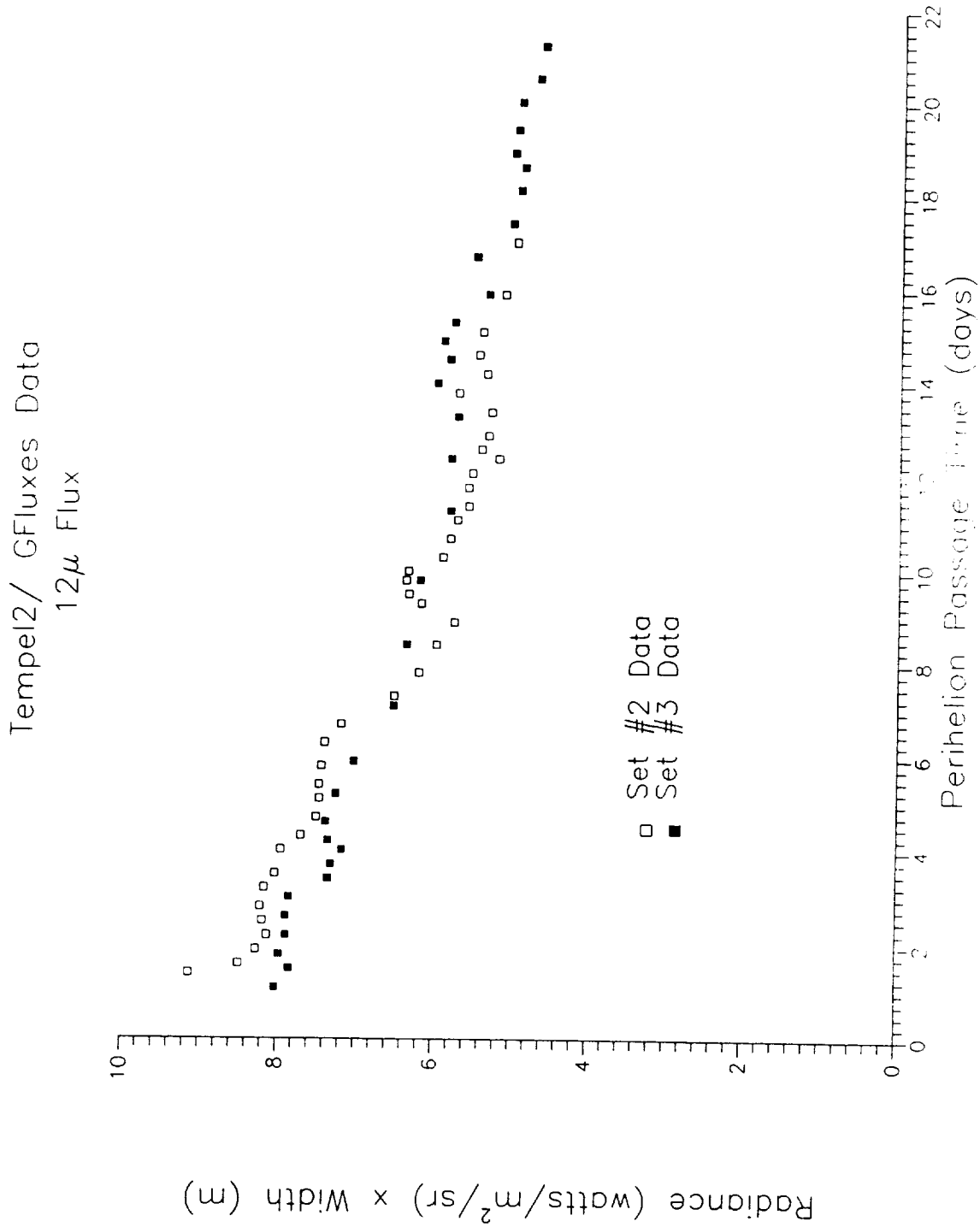

Figure 5. Integrated radiance of the Trail at 12 μm.

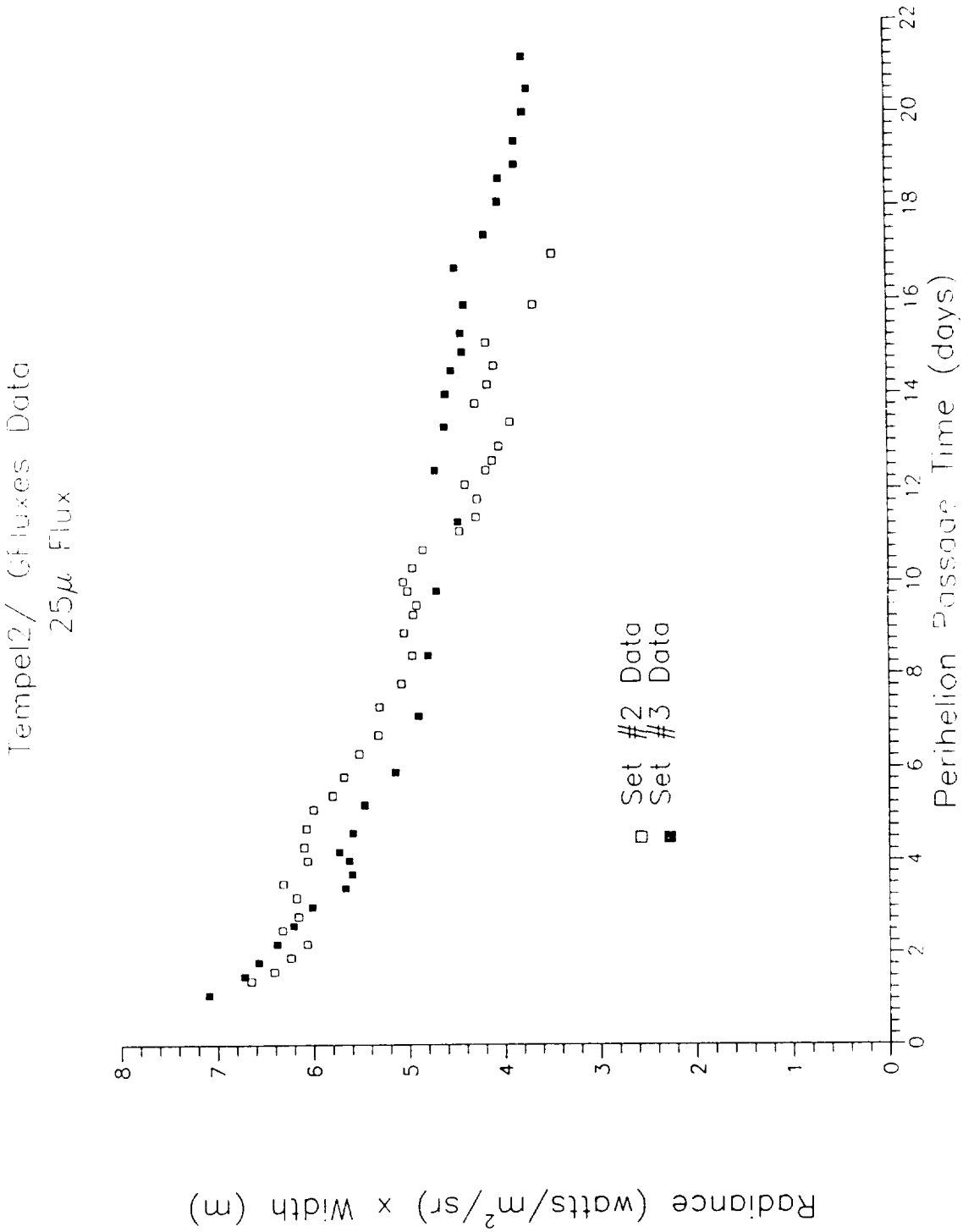

Figure 6. Integrated radiance of the Trail at 25 μm.

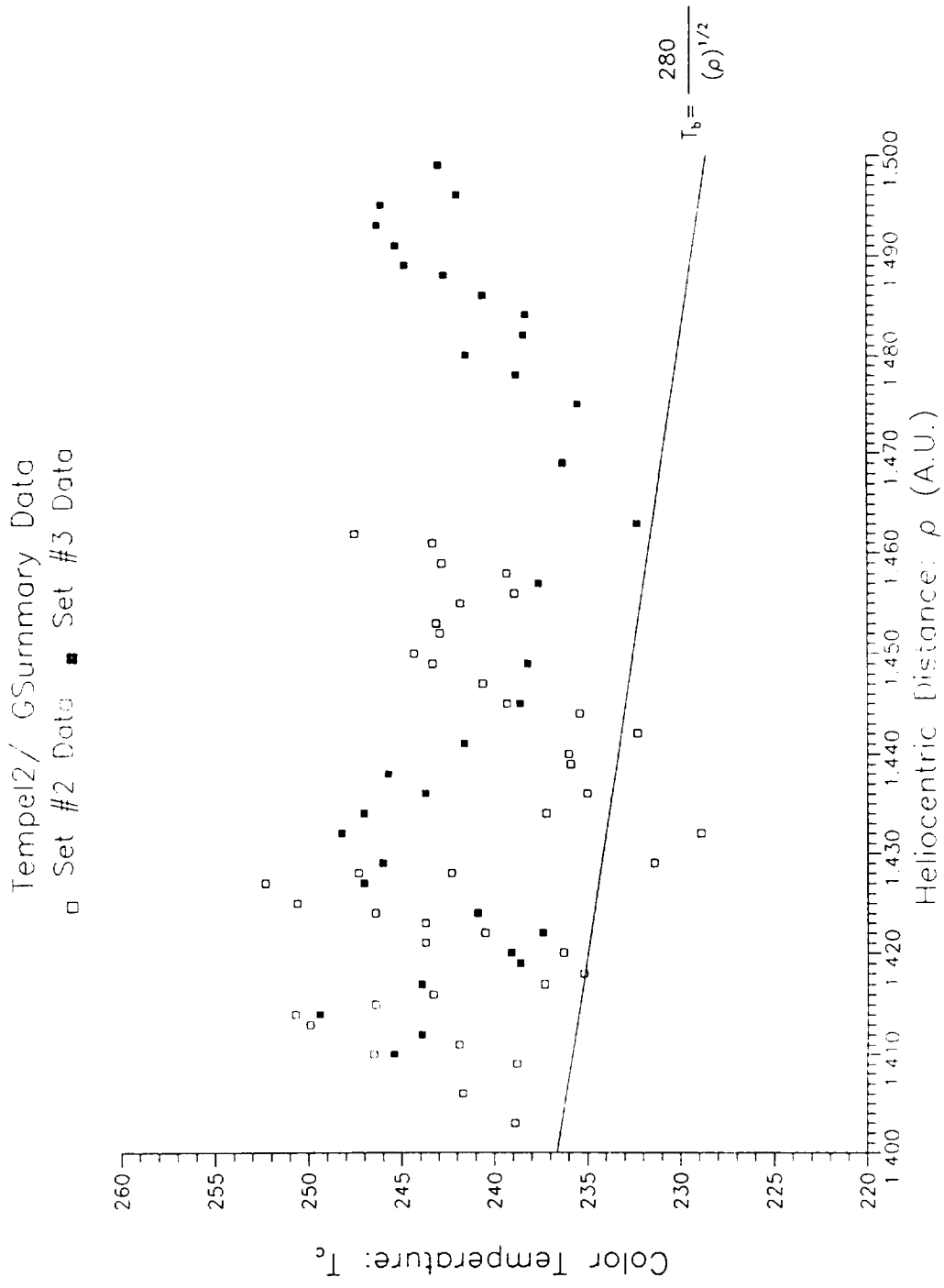

Figure 7. The 12 to 25 μm color temperature of the trail particles.

APPENDIX O. "The 25 μM Single HCONS"

APPENDIX O. The 25 Micron Single HCONs

Russell G. Walker

Introduction

The IRAS sky survey produced a large number of "point sources" that were detected only in the 25 μm band. The presence of the vast majority of these was not confirmed on repeated scans of the sky. This leads one to infer that the detections were either spurious, or of objects with variable brightness and/or celestial coordinate. The purpose of this study is to examine these data, discuss some of the possibilities which have been suggested to explain their origin, and develop the arguments supporting a "most-likely" interpretation of the observations.

Background

The IRAS telescope, focal plane, and mission strategy were designed to produce a reliable and complete infrared survey of the entire sky to a definable limiting flux (Beichman,et al, 1988). To achieve a high degree of reliability the sky was observed at intervals of seconds, hours, and weeks, and the resulting data stream examined for confirming detections. This process of repeated confirmation provided a means to discriminate, among other things, slowly moving distant astronomical objects from more rapidly moving nearby solar system objects, and was used by Davies, et al (1985) as the basis for a near real time search for earth crossing asteroids.

Seconds confirmation (SCON) was accomplished by observing the source during its transit of the focal plane with redundant detectors located in a row separated by a few seconds of transit time. Hours confirmation (HCON) involved repeating the observations with time separations ranging from 100 minutes to 36 hours, usually on consecutive orbits. The final stage of confirmation, weeks confirmation (MCON), searched for HCON observations of the same sources with time separations varying from about a week to six months.

The IRAS 25 micron band is unique to the IRAS focal plane array in that it has two dead adjacent detectors and one very noisy detector. A consequence of this is that it is not possible to get true seconds confirmation of a faint point source in about 45% of the area mapped during a single scan. Sources which failed SCON due to failed or noisy detectors were carried forward to the HCON processor, where this information was used in the HCON decision. This increased the completeness of the survey at the expense of decreasing the reliability of the 25 micron detections, a fact that must be borne in mind constantly when evaluating these data.

The Phenomenon

A number of observers have commented, both in and out of the literature, on the large number of detections IRAS made in the 25 μm band. The following is a brief summary of these comments:

1. The IRAS Fast Moving Objects Survey

Davies et al (1984) and Green et al (1985) reported that during their search for earth-crossing asteroids their efforts to detect sources with apparent motions greater than about 5 arcmin/hr were hampered by large numbers of SCON detections made only in the IRAS 25 μm band. These "sources" were detected at a rate of "a few to several hundred" per day, most were at or near the detection threshold of SNR = 7, and were concentrated toward the ecliptic. The signals appeared as noise on the strip charts and were attributed to the zodiacal background.

2. IRAS Point Source Data Processing

Approximately 100,000 to 200,000 detections per day passed the signal to noise and correlation coefficient thresholds set in the IRAS point source processor (Beichman et al, p. VII-1, 1988). One third of the total were in the 25 μm band. This was the largest fraction in one band, with one fourth in each of the bands at 12 μm and 100μm and about one sixth at 60 μm.

The influence of the large numbers of 25 μm detections also became evident during the tests to find an optimum position threshold to be used to seconds confirm a detected source (Beichman, et al, p. VII-32, 1988)). The expected plateau indicating the range of optimal thresholds was found for 12, 60 and 100 μm bands, however, although the number of confirmations rolled off with increasing threshold, a plateau was never reached in the 25 μm band. An attempt at that time to identify the spatial distribution of the excess events was not conclusive.

3. Comet and Asteroid Processing

The IRAS Asteroid Data Analysis System (ADAS) reduced and analyzed the detections of sources with asteroid colors (infrared flux ratios) that had been extracted and written to special files during the daily processing of the survey data for point sources (Matson, 1986). Since a faint asteroid could be detected at 25 μm only, all of these detections were retained. The final database contains more than 2.5 million detections, the vast majority with only a detection at 25 μm. These sources have been discussed by Veeder (1987). He finds 35,618 detections at 25 μm only that are true SCONs (no alibis) with correlation coefficient greater than 0.93. This may be compared to 5488 sightings with detections at 12 and 25 um, and 2687 sightings with detections at 25 and 60 microns. A detection at 25 μm was

required for each candidate asteroid, thus there are no detections at only 12, 60, or 100 μm in this sample.

A histogram of the number of 25 μm only detections per square degree versus ecliptic latitude clearly shows a strong concentration toward the ecliptic for detections with flux less than 1.8 Jy. The brighter sources appear more randomly distributed on the sky. A plot of the amplitude of the detections versus ecliptic latitude shows that the minimum detectible fluxes near the ecliptic plane are about twice as bright as those detected near the ecliptic poles.

4. The IRAS Faint Source Survey

Fifty-two plates from the IRAS Faint Source Survey, each covering 43.5 square degree of the sky have been examined for 25 μm only detections. In the 2263 square degrees studied the mean density of sources detected only in the 25 μm band is 2.5 sources per square degree. This varies with ecliptic latitude from about 0.7 sources per square degree for a field centered on +87.4° latitude to 4.7 sources per square degree at latitude -0.4 degrees. This strong latitude dependence is also evident in the mean 1 sigma noise calculated for each plate. The noise is about a factor of five higher in the ecliptic than at the poles. This is in contrast to the noise at 60 μm which is relatively constant over the sky, and that at 100 μm which varies with galactic latitude. The noise at 12 μm mimics that at 25 um, although with much reduced amplitude, the ratio of ecliptic noise to that at the pole being about a factor of two.

Plots of log N versus Log F for different plates all show a straight line portion at low fluxes. The typical slope is -7. A plot of log N for all the 25 μm only detections versus log SNR closely fits a straight line of slope -6.23 for SNR in the range 4 to 6, with a gradual roll-off in the number of sources in the SNR range from 4 to 3.

Potential Mechanisms

It is of interest to speculate on a number of mechanisms that might be responsible for the observed phenomena. It is particularly important to determine if the subject detections are the result of instrumental artifacts and/or processing anomalies. The following is a list of potential mechanisms that have been suggested:

1. High Energy Radiation

The IRAS photoconductors were sensitive detectors of energetic radiation received from cosmic rays, and from protons, electrons, and gamma rays during passages through the South Atlantic Anomaly

and Van Allen belts. The signal processing electronics included nuclear pulse circumvention circuitry to prevent saturation of the electronics by large energetic events. These circuits performed quite well, but remnants of the "deglitched" radiation hits are present in the data stream and can masquerade as point source detections. The noise level of a 25 μm detector typically increased a factor of two during passage through the horns of the Van Allen belts due to many electron induced pulses that were too small in amplitude to trigger the deglitcher (Beichman et al, 1988).

2. Excess Detector Noise

The noise of a background limited photoconductor is proportional to the square root of the number of incident photons. This kind of noise behavior cannot explain the 25 μm only detections. However, it has been noted that many Si photoconductors exhibit a number of anomalous effects, including spontaneous spiking, when operated in low backgrounds (Young and Low, 1985, Boggess et al, 1979). The occurrence of spiking depends on detector temperature, bias, background, and previous illumination. The spikes are typically very fast pulses similar to those produced by radiation hits, and will be treated by the deglitcher in the same manner as the energetic events, leaving remnants of large spikes to be detected as point sources.

3. Lag of the IRAS Noise Estimator

The IRAS median noise estimator is described by Beichman et al (1988, p. V-10). The method used to continually update the noise estimate for each detector caused the noise level used to threshold source extractions to lag about 25 arc min behind the detection. In regions with steep source density gradients, such as the galactic plane, there is also a steep gradient in the amplitude of the noise. Hence the noise is underestimated in regions of increasing source density and overestimated in regions with decreasing density. This caused too many sources to be extracted in regions of increasing density, and too few in regions of decreasing density. This gave rise to an effect known as the galactic plane shadow, and was most prominent at 100 μm (Beichman, et al, 1988, pg.VIII-11). The gradients associated with the ecliptic plane crossings are less than those encountered in galactic plane crossings, and one would expect the effect to be much less.

4. Processing Errors

As noted above the IRAS 25 micron band has two dead adjacent detectors and one very noisy detector eliminating the possibility of SCON in about 45% of the area mapped during a single scan. Sources which failed SCON due to failed or noisy detectors were carried forward to the HCON processor, where this information was

used in the HCON decision. This led to failures to band-merge creating 25 μm only sources, and allowed HCONs with weak radiation hits and radiation hit remnants. These are PSC processing problems and do not exist in the FSS data.

5. Zodiacal Bands

One of the remarkable discoveries made by IRAS was bands of zodiacal dust which run nearly continuously around the solar system (Low et al, 1984). These bands appear in pairs and are attributed to individual collisional events occurring in the asteroid belt (Gautier et al, 1984, Hauser et al, 1985, Gautier et al, 1986, Dermott et al, 1984a,1984b, Dermott et al 1985, Dermott et al, 1986, Sykes et al, 1984, Sykes et al, 1985). A dynamical model has been developed by Sykes (1986) which shows how band pairs are formed out of the debris from asteroid collisions, and evolve sufficient surface area to be detected by IRAS. His models predict that IRAS should have seen an additional 30 band pairs in the Sky Flux Plates. Recent results from examination of an improved higher resolution IRAS Zodiacal History file show many of the predicted bands, and cause one to speculate that perhaps a major part of the infrared zodiacal radiance is due to a superposition of large number of faint dust bands (Sykes, 1987). If this were the case then it is possible that the emission from the composite of dust bands varies with sufficiently high spatial frequencies to be detected by IRAS in the point source filter.

6. Comet Debris Trails

The IRAS survey detected extensive trails of debris in the orbits of periodic comets (Eaton et al, 1984, Davies et al, 1984, Green et al, 1985, Sykes et al ,1986a, Sykes et al, 1986b). These trails appear to consist of submillimeter and larger particles emitted from the comet nucleus at low velocities. They appear both in front of and behind the orbital position of the comet, and are observed to extend several degrees in mean anomaly. Of the approximately 100 dust trails identified to date in the now completed Major Trail Survey (Sykes and Dow, 1988), eight are definitely associated with known comets and all of these are short-period comets. The distribution of the remaining trails clusters around low ecliptic latitudes which suggest that these too might be associated with short-period comets. As in the case of the zodiacal bands, it is possible that the emission from the debris trails varies with sufficiently high spatial frequency to be detected by IRAS as a point source. This, of course, is the way the debris trail of Tempel 2 was first detected (Davies et al, 1984). During the period from 10 to 17 July, 1983 the fast moving object program detected about 50 low SNR detections at 25 μm only. The trail was similarly detected again during the MCON scans on 21 to 27 July and again on 9 August.

7. Near Earth Objects

Although the ecliptic plane with its zodiacal emission is well defined in the 25 μm only detections, there is a significant density of detections at high ecliptic latitudes. If these are of solar system origin they must be due to objects in high inclination orbits or to objects relatively near to the earth. The following is a list of the types of object that might satisfy these requirements:

a. Earth-Moon "Trojans" - Kordylevsky (see Alfven and Arrhenius, 1976) first reported observations of faint clouds of small bodies in the region of the Earth-Moon Lagrangian points. The observation was verified by Roach (1975) from a spacecraft in transit to the Moon. However, there is still much skepticism as to the existence of such particles. Particles librating about the Earth-Moon Lagrangian points would be expected to be hotter than those in the asteroid belt. These bodies will fail to HCON due to their large apparent motions.

b. Earth-Sun "Trojans" - Stable orbits also exist at the 60 degree positions (L4 and L5) of the Earth-Sun and in the anti-sun direction (L1). It has been suggested that the gegenschein is due to reflected sunlight from a swarm of particles concentrated near L1. L1 was not directly observable by IRAS due to viewing constraints. L4 and L5 were at the extreme limit of the IRAS sun limit and little or no time was spent at that elongation. The bodies trapped at L4 and L5 are expected to be librating in horseshoe orbits with periods of a few thousand years. These orbits carry them high above the ecliptic and into IRAS' view. Particles at low ecliptic latitudes will fail to HCON, and all will fail to MCON due to their large apparent motions. These bodies would also be expected to be hotter than those in the asteroid belt.

c. Earth-crossing Asteroids

The expected flux of Earth-crossing asteroids is insufficient to produce the large number of observed 25 μm detections. Helin and Shoemaker (1979) estimate that there are 400 to 1000 Apollos, 1000 to 2000 Amors, and about 100 Atens with $V(1,0) < 18$ mag. Based on the IRAS sensitivity for detecting fast moving objects Green et al (1985) estimate that IRAS should observe 5 to 15 earth-crossing asteroids, a number consistent with their experience.

d. Earth Rings

Of the nine planets, four are known to have rings or halos of small particles, presumable meter size or less. At the present no evidence exists for a ring or halo of particles dynamically bound to earth.

e. Meteoritic Flux

The meteoritic flux near the earth could be a source of some of the 25 μm detections. If we assume that the temperature of a near earth particle is 280 K, IRAS could detect a single 50 μm particle in the 25 μm band at a distance of 28 km with a signal to noise ratio of 3. Using the near earth flux of meteorites given by Allen (1976) one can estimate that the density of detectable meteorites would be on the order of 0.1 per square degree. This is probably an upper limit since the transit time for most meteorites will be quite short due to their velocities relative to the spacecraft. The signature is similar to that of a radiation event.

f. Artificial Earth Satellites

IRAS detections of the orbital debris from earth orbiting satellites has been studied by Anz-Meador et al (1986). Their initial results indicate that the IRAS detection rate of 48 events per day for orbital debris was a factor of 3.7 higher than predicted by the Johnson Space Center Debris Models. They note that all of the detected events had correlation coefficients in the range of 0.5 to 0.87.

The Data

The source of the data to be discussed here is the IRAS Working Survey Data Base (WSDB) which contains all the HCON detections made during the survey. We confine our analysis to those sources detected only in the 25 μm band and which have only a single HCON. There are 56,320 sources of this type in the WSDB. These are plotted in Figure VII.Ap.18 of the Explanatory Supplement (Beichman et al, p. VII-57, 1988), where the band of source concentration along the ecliptic is easily seen.

The plot of the log (Number of sources brighter than F) versus log (Flux) in Figure 1 can be approximated over most of its range by two straight line segments; one for fluxes > 2 Jy with a slope of about -1, and the other at fluxes < 2 Jy with slope of about -4. The maximum flux measured is 70 Jy, and the minimum 0.25 Jy.

A histogram of the number of sources/square degree in each 2 degree bin of ecliptic latitude shows a general flat distribution of sources with significant concentration (1.25 times the base level) toward the ecliptic. If one requires that at least 3 out of the 4 detections that make up each HCON be true detections (FSTAT=7), that is, allowing no more than one alibi/HCON due to a dead or noisy detector, this number shrinks to 30,000, the base level decreases, the galactic plane sources near $\pm$ 60° are

resolved, and the concentration to the ecliptic is enhanced (1.58 times the base level). Applying a correlation coefficient threshold (CC>0.94) to remove most of the remnants from high energy radiation hits (and, unfortunately, some real sources as well) reduces the total number to 11738 and increases the contrast of the concentration to the ecliptic.[1] These data are summarized in Table 1 where FSTAT=4 means all detections with FSTAT $\leq$ 4 and FSTAT=7 means only those data with FSTAT=7 (See Beichman, et al, pg. V-33, 1988 for details of the IRAS quality indicator FSTAT). Application of these criteria greatly reduces the number of the isotropic population of spurious detections due to random events, such as radiation hits and spontaneous spiking. The remaining sources, comprise a much more reliable, if less complete data set. The final column in Table 1 gives the source density at the peak of the distribution above the baseline density. Data in the range 0.93 < CC < .99 show the peak source density remaining nearly constant at 0.18 sources per square degree in each CC interval while the baseline density is decreasing by almost a factor of three.

Table 1. Summary of 25 μm only Single HCONs in the WSDB as a function of the selection criteria applied.

FSTAT	CORR. COEFF.	NUMBER	BASELINE	PEAK	(P-B)/B	P-B
4	.87-1.0	56320	0.80	1.80	1.25	1.00
7	.87-1.0	30000	0.47	1.23	1.58	0.76
7	.87-.92	11872	0.20	0.420	1.07	0.22
7	.93-.94	6390	0.095	0.274	1.88	0.179
7	.95-.96	6147	0.079	0.255	2.59	0.184
7	.97-.98	4532	0.034	0.218	5.12	0.184
7	.99-1.0	1059	0.0039	0.057	13.00	0.053

NOTES: 1. Galactic plane is clearly seen in all FSTAT=7, CC>.94.
2. Galactic plane is not seen in FSTAT=4 data for any CC.
3. All FSTAT=4 has increasing density for Latitudes > 60 degrees.
4. Baseline and Peak are in HCONS per square degree.

[1]It should be noted that the signature of a radiation hit or spike (or deglitched remnant) is characterized by a rapid rise and slow decay. The correlation of this signature with that of a point source is in general less than 0.94, a fact that may be used to reduce the number of such spurious detections in the data set.

The number of HCONS in a 1 degree bin of ecliptic latitude having FSTAT=7 and CC>.94 is histogrammed in Figure 2. It has a roughly gaussian shape (FWHM=43°) with a superimposed strong peak within ±3° of the ecliptic and shoulders extending to about ±12° latitude. The positions of these features agree well with those of the zodiacal bands discovered by IRAS (Low, et al, 1984) which surround the solar system at a mean distance of about 2.5 AU in the asteroid belt (Low et al, 1984, Gautier et al, 1984, Hauser et al, 1985, Gautier et al, 1986). The number of detections observed in these bands is consistent with the number of daughter asteroids with diameters in the range from 11 km to 19 km predicted with a simple model for the collisional products from the break-up of the parent asteroids in the Eos, Themis, and Koronos families (Walker, 1985). The peaks at ±60° latitude are due to structure in the galactic plane.

Some Special Properties of the Data Set

The WSDB sources are constrained by the HCON process to apparent motions of less than about 0.8 arcmin/hr in ecliptic longitude and 0.36 arcmin/hr in latitude. This means that if the sources are in orbit about the sun they must be at heliocentric distances greater than about 1.6 AU to be hours confirmed. The minimum time between successive HCONS was about three days, but more frequently in the range of seven to fourteen days. There was no case during the IRAS survey in which a numbered asteroid was weeks confirmed. The above constraints would limit MCONs to bodies orbiting at distances greater than about 35 AU.

Detection at 25 μm and not at 12 μm or 60 μm constrains the range of temperatures of these bodies if the emission is of thermal origin. In Figure 3 the temperature of a blackbody is confined to the region between the upper and lower solid curves. The upper curve is defined by the 12 μm detection threshold for a survey completeness of 95% (Beichman, et al, pg. XII-19, 1988). This is equivalent to a 90% probability of detecting the source at least 3 times out of a possible 4 chances. The lower curve is similarly defined by the 60 μm threshold for 95% completeness. The two curves intersect at a blackbody temperature of about 210 K and a 25 μm flux of 1.26 Jy. The likelihood is, therefore, very small that sources brighter than about 1.26 Jy are thermal. The lower dashed curve is for small grains at the indicated temperature but with the spectral emissivity proposed by Good (1988) to fit the thermal emission from the zodiacal dust cloud, that is, ϵ(lambda) = 1.0 for lambda < 38 μm, and ϵ(lambda) = 1.0/lambda for lambda > 38 μm. In this case the two curves intersect at about 200 K and 1.6 Jy.

Figure 4 gives the range of heliocentric distances possible for small spherical blackbodies in equilibrium with the Sun while radiating over 4π steradians. The two curves follow directly

from the values in Figure 3 and intersect at about 2 AU. Bodies which radiate primarily from their sunlit side, such as asteroids, would achieve the same temperatures at somewhat larger distances from the Sun.

The Origins of the 25 μm Single HCONS

At this point we confine our analysis of the 25 μm single HCONS to the subset of observations defined by FSTAT=7 and correlation coefficient ≥ 0.94. This choice of correlation coefficient effectively eliminates spurious HCONs due to spikes, high energy radiation, and nearby Earth orbital debris. The choice of FSTAT=7 removes HCONs that might have been created by the special processing rules applied to the 25 μm data to compensate for adjacent dead or noisy detectors.

From the data of Figure 2 and Table 1 we find that for this subset of data there is a net (above the background) of approximately 6500 HCONs within 30 degrees of the ecliptic, a background component of 4800 HCONs, and an excess of 420 HCONs associated with the galactic plane in two zones near ecliptic latitudes ± 60°. Complex extended structures, principally dust in HII regions, in and near the galactic plane produce the observed HCONS in this region. We estimate that an additional 350 HCONS of similar origin are present in the data within 30 degrees of the ecliptic. Thus our goal is to develop an explanation for a minimum of 6150 HCONS strongly associated with the ecliptic, and a more or less isotropic background of 4800 HCONS.

A. Creation of False Sources

Beichman, et al (pg. VIII-8, 1988) have analyzed the 12 μm detections in a 7 HCON, 70 square degree area of the sky to deduce completeness and reliability parameters for the IRAS point source survey (Mini Survey). The mean value of the probability P_q, per unit area of the sky, that a false source in the flux range 0.25 to 1.58 Jy was created on a single HCON was found to be 0.029±0.017 per square degree per HCON. This value is assumed to apply to 25 μm detections as well. The IRAS sky coverage was 96% at 2 HCONS, 72% with 3 HCONS, and 15% with more than 3 HCONS, from this we estimate that a total of 3336 ± 1955 HCONS were created. This is sufficient to account for the isotropic background HCONS. The probability P_w that these sources would MCON is just the product of the density probability times the effective area for weeks confirmation, $A_e \approx 30"x90"$. $P_w=A_e x P_q = 6x10^{-6}$, and therefore we would not expect any of these sources to MCON.

B. Near Earth Objects

As discussed above, near Earth objects, such as Earth orbiting satellites, and meteorites will have low correlation coefficients due to their rapid transit of the focal plane. The high apparent angular rates of these, as well as the more exotic Earth librating bodies, would preclude them forming an HCON provided the space density of sources was low enough that chance positional coincidences were unlikely. If P(N,M) is the probability of detecting a source N times out of M chances, then the probability $P_A(N,M)$ of detecting a source N out of M times in the area A is $P_A(N,M) = \delta A P(N,M)$ where δ is the density of sources (sources per square degree).

To HCON with FSTAT=7 a source must be detected at least 3 out of 4 times. For this case $P_A(3,4)=\delta A\{P(3,4)+P(4,4)\}$. Turning again to the Mini Survey results we find that if the probability of failing to detect a real source is 0.911, then $P_A(3,4)=1.46\times10^{-7}\delta$. There are 2×10^8 HCON areas on the celestial sphere in which IRAS detected 4800 HCONS. Since the sky was observed an average of 2.86 times, $P_A(3,4)=(4800+6150)/(2.86\times2\times10^8)$, and the resulting mean source density is 130 sources/square degree. If isotropic, this requires a nearby swarm of 5.3×10^6 point sources detectible by IRAS.

C. Asteroids

If the sources detected in the zodiacal bands can be attributed to small asteroids, one is tempted to suggest that the remainder of the detections might also be due to a population of small asteroids. Fortunately, there is a test for this hypothesis. IRAS was constrained to scan the sky between 60° and 120° of Solar elongation. The geocentric distance Δ to an asteroid at heliocentric distance 2.7 AU is 3.0118 AU at 62.5° elongation and 2.0884 AU at 117.5°, a ratio of 1.44 in the distance and a factor of 2 in $1/\Delta^2$. If the detected objects are unresolved point sources in the asteroid belt and their size distribution is homogeneous in longitude, a greater number should be detected at 120° than at 60° elongation due to their closer proximity to Earth and their lower apparent angular velocities which makes confirmation more likely. One would also expect to find the brighter objects at elongation 120°.

The number-flux distributions for the 25 μm single HCON sources from 50 scans in the solar elongation interval 60° to 65° and 50 scans in the interval 115° to 120° are compared in Figure 3. All scans are from the third HCON, and the data plotted are restricted to ecliptic latitudes ±30°. These curves show the antithesis of what was expected for point sources. We therefore conclude that the bulk of the 25 μm single HCONS cannot be due to small main belt asteroids.

A striking feature of Figure 5 is the gradual roll-off of the source counts starting at about 0.56 Jy in the $\epsilon=60^{\circ}$ curve. There is no corresponding effect in the $\epsilon=120^{\circ}$ data. This is a threshold effect as can be seen by a comparison of the data plotted in Figures 6a and 6b. These are plots of the amplitude of the HCONS versus the ecliptic latitude of their detection. The data in Figure 6a ($\epsilon=120^{\circ}$) show a minimum detected flux of about 0.25 Jy, which is independent of the latitude. In Figure 6b ($\epsilon=60^{\circ}$) the minimum detected flux is a strong function of the latitude of the detection, increasing from 0.25 Jy at $\pm$ 30° latitude to about 0.56 Jy at the ecliptic plane. A source was detected in the IRAS survey if its flux exceeded a threshold at constant signal to noise ratio = 3. The increasing threshold shown in Figure 6b must be due to an increase in the noise near the ecliptic. This phenomenon was first noted by Veeder (in Matson, 1986) during the processing of detections for the IRAS Asteroid and Comet Survey. Only the 25 μm data shows this effect in the point source survey data. It has since been noted in the IRAS Faint Source Survey at both 12 and 25 microns (Moshir, et al, 1989).

We have attempted to represent the IRAS 25 μm threshold by assuming that the noise is composed of a constant system noise σ_s, photon noise σ_p which is proportional to the square root of the background flux, and an excess noise σ_n which is proportional to the background flux. The total noise is then

$$\sigma_T = [\sigma_s^2+\sigma_p^2+\sigma_n^2]^{1/2} \qquad (1)$$

and the threshold flux F_{25} is then given by

$$F_{25} = 3(a+bR+cR^2)^{1/2} \qquad (2)$$

where $a = \sigma_s$, $\sigma_p = (bR)^{1/2}$, $\sigma_n = c^{1/2}R$, and R is the 25 μm Zodiacal flux.

The constants a and b were evaluated from four sets of stare-mode observations made by IRAS near the ecliptic pole. The constant c was found from a least squares fit to the residuals of the threshold flux. The values are $a = 2.056\times10^{-3}$, $b = 2.340\times10^{-4}$, and $c = 6.31\times10^{-6}$. The results are plotted in Figure 7. The dashed line is the threshold model without the excess noise term. It is clear from the figure that an additional noise term which is proportional to the background is essential to produce an adequate to the observations. Since this term is not present in the stare-mode data, it is appropriately called scan noise. Its rms value is 2.5×10^{-3} $\langle Jy\rangle^{1/2}/Jy$. To examine the general applicability of the threshold model we show it overlaid in on the data of Veeder (1986) in Figure 8. To produce the threshold

overlay we assumed that all of the scans were made at solar elongation 90°, and calculated the Zodiacal background flux using Good's (1988) zodiacal radiance model. The agreement is considered satisfactory. Points falling below the threshold are from scans at elongations greater than 90°.

A significant scan noise component at 25 μm requires some form of structure or clutter related to the zodiacal background, and leads one to consider the consequences of extended structures in the Zodiacal emission.

D. Extended Structures in the Zodiacal Emission

If point sources are not responsible for the observed HCONS, perhaps extended emissions, similar to the brighter dust bands previously identified in the IRAS data, are the source of the detections. To investigate this possibility we estimate the response of the IRAS point source filter to narrow extended structures. This is shown in Figure 9. The quantity plotted is the response $\phi(\sigma)$ of the point source filter to an extended band of radiance (with gaussian radiance profile of full width σ in the IRAS scan direction and constant radiance in the IRAS cross scan direction) relative to the response to a point source of the same strength. The cross scan extent of the source is at least as great as the detector length (4.65 arc min). $\phi(\sigma)$ is the integral of the convolution of the gaussian source $I(\sigma)$ with the telescope point spread function $\beta(t)$, detector width w/t, detector time constant, electronics low pass filter F(t), and the IRAS zero sum digital detection filter $\Phi(\delta)$. In the frequency domain

$$\phi(\sigma) = \int_0^\infty [I(\sigma)\beta(f)\Omega(w)F(f)\Phi(\delta)]^2\,df \quad \int_0^\infty [I(0)\beta(f)\Omega(w)F(f)\Phi(\delta)]^2 df \tag{3}$$

where

$$I(\sigma) = I_0\sigma\ \exp[-\pi(f\sigma/\omega)^2] = FT\{I_0\ \exp(-\pi x^2/\sigma^2)\} \tag{4}$$

$$\beta(a) = \exp[-\pi(f\sigma_d/\omega)^2] \tag{5}$$

$$\Omega(w) = \sin[\pi fw/\omega]/(\pi fw/\omega) \tag{6}$$

$$F(f) = 1/[1 + 0.414(f/f_c)^2] \tag{7}$$

$$\Phi(\delta) = \cos(\pi f/16)+\cos(3\pi f/16)-\cos(5\pi f/16)-\cos(7\pi f/16) \tag{8}$$

ω = scan rate = 3.85 arc min/ sec
σ_d = gaussian width of the diffraction blur = 0.4167'
w = detector in-scan width = 0.76'
f = frequency (Hz), f_c = filter cutoff frequency = 6 Hz
x = apparent angular distance from the peak of the band

We have assumed the response of the detectors is independent of frequency in the range defined by the cut-off of the electronics low pass filter. This is clearly incorrect since the ratio of the response to a point source crossing the detector at the survey rate to that of a d.c. (20 second stare) observation is 0.82 (Beichman, et al, pg. IV-9, 1988). This will lead to an underestimate of the response to a 77 arc min wide source of about 18%. The error will be much smaller for sources of a few arc min width.

The curve of Figure 9 shows a slow roll-off in response for source widths less than the detector width, and rapidly decreasing response for sources wider than a few detector widths. For sources wider than 3 arc minutes the response decreases as the power law

$$\phi(\sigma) = 1.283\ \sigma^{-2.469}. \tag{9}$$

Consider now a distribution of grains in a zodiacal band at a distance Δ with column density uniform along the length L of the band and falling off as a gaussian of width W in the direction normal to the band. The number N of particles in the band is then

$$N = N_0 L \int_{-\infty}^{+\infty} \exp[-(x/W)^2\ dx = N_0 W L \tag{10}$$

The flux received at the telescope is

$$F = (1/\Delta)^2 \int N Q_a A_p S_\lambda B(\lambda,T)\ d\lambda \tag{11}$$

where the temperature of the particle $T = T(r)$, the absorption efficiency $Q_a = Q_a(r)$, the area of the particle $A_p = \pi r^2$, S_λ is the spectral response of the sensor, and $B(\lambda,T)$ is the blackbody radiation function at wavelength λ. The observed point source flux $F_p = \phi(\sigma)F$. Defining the radiance I_o at the peak particle density

$$I_o = N_o \int Q_a A_p S_\lambda B(\lambda,T)\ d\lambda \tag{12}$$

and recognizing that the apparent angular width of the band $\sigma = W/\Delta$ and the angular length seen by the detector is $\theta = L/\Delta$, we

may write the point source flux as

$$F_p = \phi(\sigma) I_o WL/\Delta^2 = \phi(\sigma) I_o \sigma\theta. \quad (13)$$

For observations made at different distances Δ_1 and Δ_2 the observed flux ratio will be proportional to the ratio of the system response function and inversely proportional to the distance from the band, that is

$$F_{p1}/F_{p2} = \phi(\sigma_1)\Delta_2/\phi(\sigma_2)\Delta_1. \quad (14)$$

Equation 14 is the effective gain of the system due to the change of the apparent angular width of the band. If the cumulative source-flux distribution N_h is given by a power law

$$N_h = \beta F_p^{-\alpha} \quad (15)$$

then the ratio of the number of sources counted to the same flux limit at the two distances will be

$$N_{h1}/N_{h2} = [F_{p1}/F_{p2}]^\alpha = [\phi(\sigma_1)\Delta_2/\phi(\sigma_2)\Delta_1]^\alpha \quad (16)$$

Since the distance to asteroid belt is greater when viewed at ϵ=60° than at ϵ=120°, the apparent width of the band will be smaller at 60° and Equations 14 and 16 predict a larger number of detections at 60° than at 120° in accordance with the what was observed (see Figure 5).

Equation 16 implies that if we shift the ϵ=120° source count data plotted in Figure 5 vertically to match the ϵ=60° counts we can solve for the required system gain. If we know or assume a heliocentric distance for the bands we can then derive the implied ratio of system responses. Equation 3 can then be solved for the width of the band. Figure 10 shows the result of multiplying the counts at ϵ=120° by a factor of 6.5. The two distributions coincide quite well for F > 0.56 Jy, the point at which the ϵ=60° counts diverge due to the varying noise threshold. A least squares fit to the source counts for F > 0.65 Jy yields a slope of 4.34±0.12; similarly a slope of 3.22±0.02 fits the flux range 0.30 < F < 0.65 Jy. Table 2 lists the widths derived assuming various heliocentric distances for the measured slopes of the bright and faint ends of the distribution. An entry "ns" indicates that there is no solution possible consistent with the derived system gain.

The selection requirement that CC ≥ 0.94 for these data constrains the range of gaussian widths that can be included to less than about 2 arc min, in general, with only a very small probability of including features as large as 3.5 arc min. For this reason it seems likely that the origin of the fainter sources is within about 2 AU of the Sun, while that of the brighter ones may extend to about 2.5 AU. If these detections are associated with

the debris from asteroid collisions, as has been the case with the broader zodiacal bands, we would associate them with the inner belt families Nysa, Flora, and, perhaps, asteroids in the narrow Hungaria and Phocaea regions. The Floras with mean heliocentric distance 2.29 AU are the most numerous and complex asteroid family with as many as 15 sub-families identified. The Floras include about 10% of all the number asteroids and have a mean proper inclination of about 6°. The Nysa family at 2.45 AU is rather inconspicuous among the numbered asteroids, but was found to be the most numerous in the Palomar-Leyden Survey. This was due largely to their low proper inclination of 3° which was favorable for their discovery. The Hungarias in the region from 1.8 to 2.0 AU and the Phocaeas at 2.37 AU are small in number but have large proper inclinations of about 22°.

Table 2. Derived widths of the zodiacal fine structure bands.

ρ(AU)	σ(arc min) F>0.65Jy	σ(arc min) 0.3<F<0.65
1.6	1.05	1.27
1.8	1.25	1.62
2.0	1.45	1.98
2.2	1.67	2.61
2.4	1.90	3.90
2.6	2.20	ns
2.8	2.65	ns
3.0	3.30	ns

Some indication of the band structure should be evident in the data. Small scale structure would be lost in the data of Figure 2 due to the smearing and overlapping of bands observed at different times. These data will have to be separated into subsets by time, HCON, and elongation range in order to reveal the expected structure. The number of detections from the 3rd HCON set shown in Figure 5 were histogrammed and are plotted in Figure 11 for $60^\circ \leq \epsilon \leq 65^\circ$ and $115^\circ \leq \epsilon \leq 120^\circ$. The source counts are the number in a 1° ecliptic latitude bin. This bin size was chosen to accommodate the 4% latitude scale factor due to the change of parallax across the 5° elongation band. The statistical significance of the counts in any particular bin is small ($\sqrt{n}$) and any identification of bands or band pairs somewhat suspect. Nevertheless some symmetries are apparent, and based on these we have very tentatively identified the band pairs given in Tables 3 and 4.

Table 3. Band pairs tentatively identified in the ϵ=60° data.

Band Pair	β_1(deg)	β_2(deg)	β_{mid}(deg)	n_1	n_2
60-1	-3	0	-1.5	17	21
60-2	-5	+3	-1.0	24	26
60-3	-7.5	+4.5	-1.5	16	16
60-4	-10.5	+7.5	-1.5	17	18
60-5	-13.5	+11.0	-1.25	41	22
60-6	-18.5	+14.5	-2.0	12	12
60.7	-20.5	+16.5	-2.0	8	9
60-8	-24	+20.5	-1.75	15	19

Table 4. Band pairs tentatively identified in the ϵ=120° data.

Band Pair	β_1(deg)	β_2(deg)	β_{mid}(deg)	n_1	n_2
120-1	0	-	-	28	-
120-2	-3	+3	0	21	10
120-3	-6.5	+6.5	0	9	10
120-4	-8.5	-	-	9	-
120-5	-12.5	+11.5	-.5	11	9

If we were to associate band 120-3 with 60-2 the derived parallax would argue for ρ = 2.1 AU. Similarly, if we associate 120-2 with 60-1 and 120-5 with 60-3 these bands would be at ρ = 1.7 AU.

Let us adopt σ = 2' and place the bands at ρ = 2.2 AU. The black grain temperature is 189 K. From Equations 10-13 we then derive some of the properties of the bands. These are listed in Table 5. The area of a typical band is calculated from $A_B = 2\pi\rho\sigma\tau$ (assuming that the band is continuous around the sky) and the total mass of a typical band from $M_T = 8\pi dr_p\tau\rho W_\zeta$ where we have assumed Q_e = 1, the grain density d = 1.0 gm/cm^3, and the radius of the grains r_p = 10 microns. The range of values given reflects the range of point source flux measured rather than limits on the quantity shown.

In comparison to the previously discovered dust bands, these are much narrower, 2' as compared to several degrees, located in the inner part of the asteroid belt rather than near the central

region, and contain much less emitting material, 10^{17} cm^2 versus 10^{19} cm^2.

The debris trail of Tempel 2 was observed to have a width of 35,000 km and an optical depth of 1.3×10^{-8}. This yields a total radiating area of 1.2×10^{16} cm^2, a factor of 5 to 25 less than the bands considered here. We cannot rule out the possibility that comet debris trails might be responsible for the observed HCONs, however, we have searched the orbits of 94 periodic comets for positional coincidences with these detections at the time of the HCONs with null results.

Table 5. Characteristics of a Zodiacal fine structure band.

Peak radiance:	$I_0 = 1.8 \times 10^6$ to 8.5×10^6 Jy/sr
Optical depth:	$\tau = N_o Q_s A_p = 1.4 \times 10^{-8}$ to 6.5×10^{-8}
Width :	$\sigma = 215000$ km
Band area :	$A_B = 6 \times 10^{16}$ to 3×10^{17} cm^2
Mass of band :	$M_T = 2 \times 10^9$ to 1×10^{10} kg

Conclusions

We conclude a large fraction of the high quality 25 μm single HCONs are detections of extended structures in the Zodiacal emission. The scale of these features is on the order of 2 arc minutes in ecliptic latitude and may extend from a few arcminutes to 360 degrees in longitude. These features are most likely detections of debris from collisions of asteroids in the inner belt region, possibly related to the Flora family.

The rms scan noise generated by these features is about 3.4×10^5 Jy/sr (1.6×10^{-13} watts cm^{-2} μm^{-1} sr^{-1}) at 25 μm for spatial frequencies within the IRAS passband. This is about 0.3% of the zodiacal radiance at $\beta = 0^\circ$, $\epsilon = 60^\circ$.

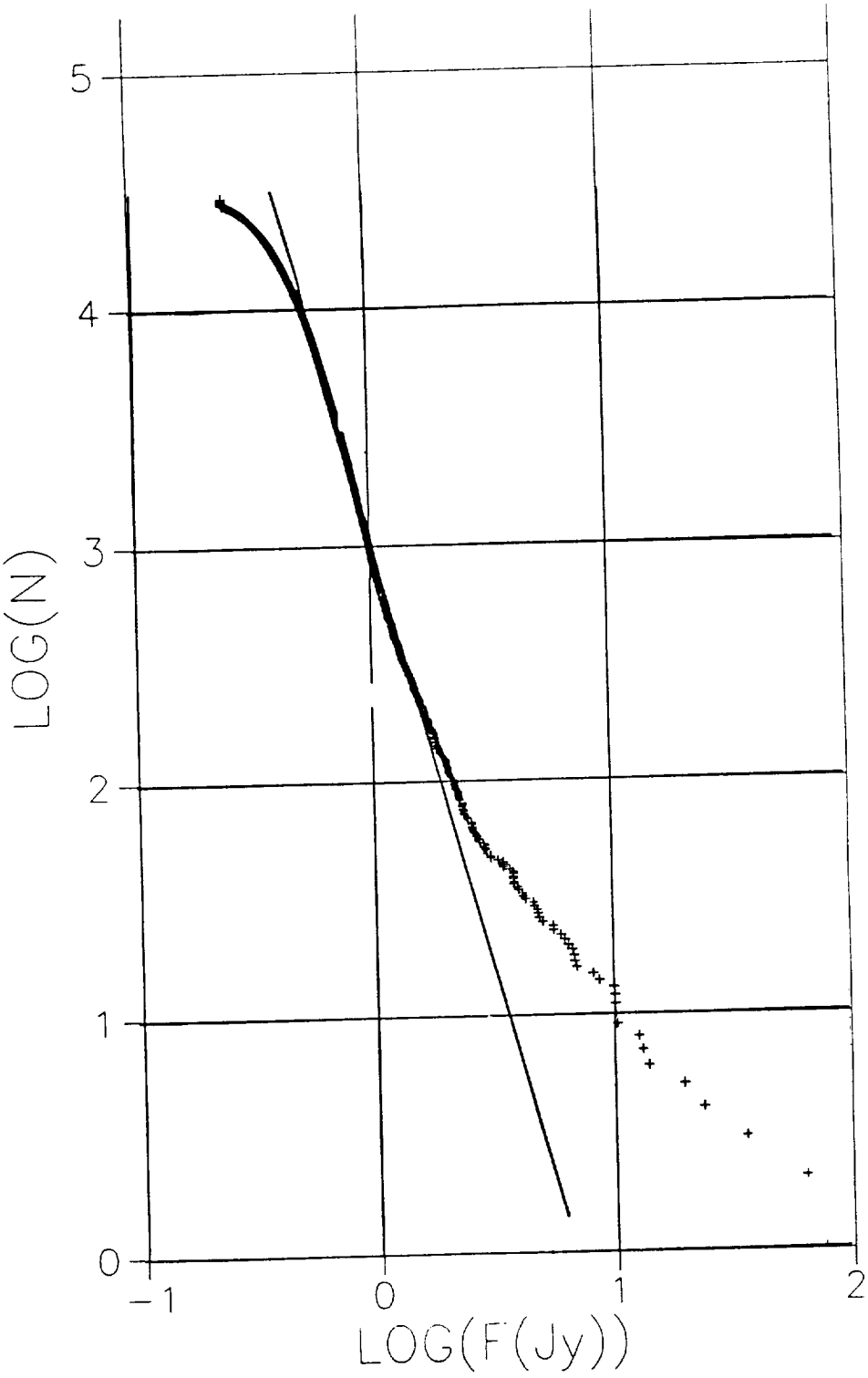

Figure 1. The number of sources brighter than a given flux threshold for the single HCON sample of Figure 2.

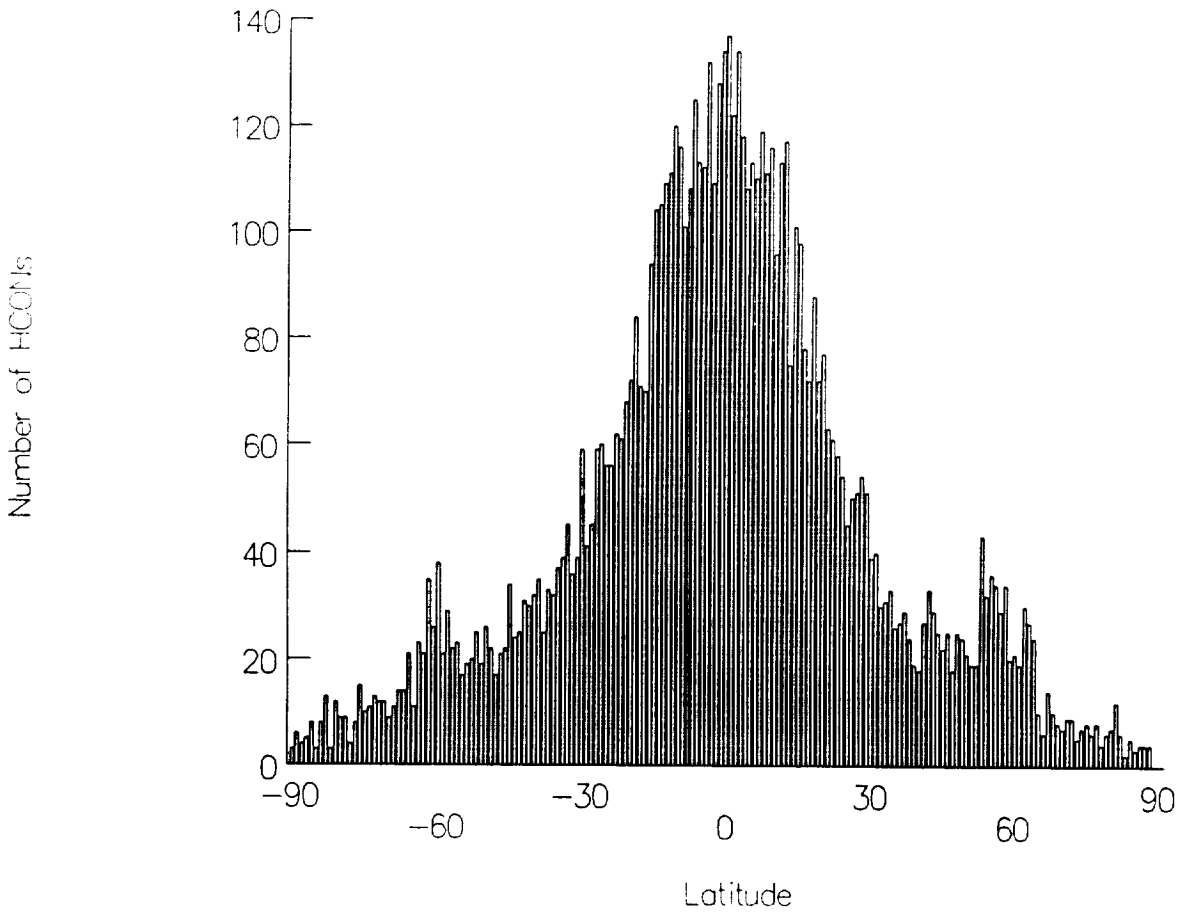

Figure 2. WSDB single HCON sources with correlation coefficient > 0.94 and at least 3 out of 4 seconds true detections.

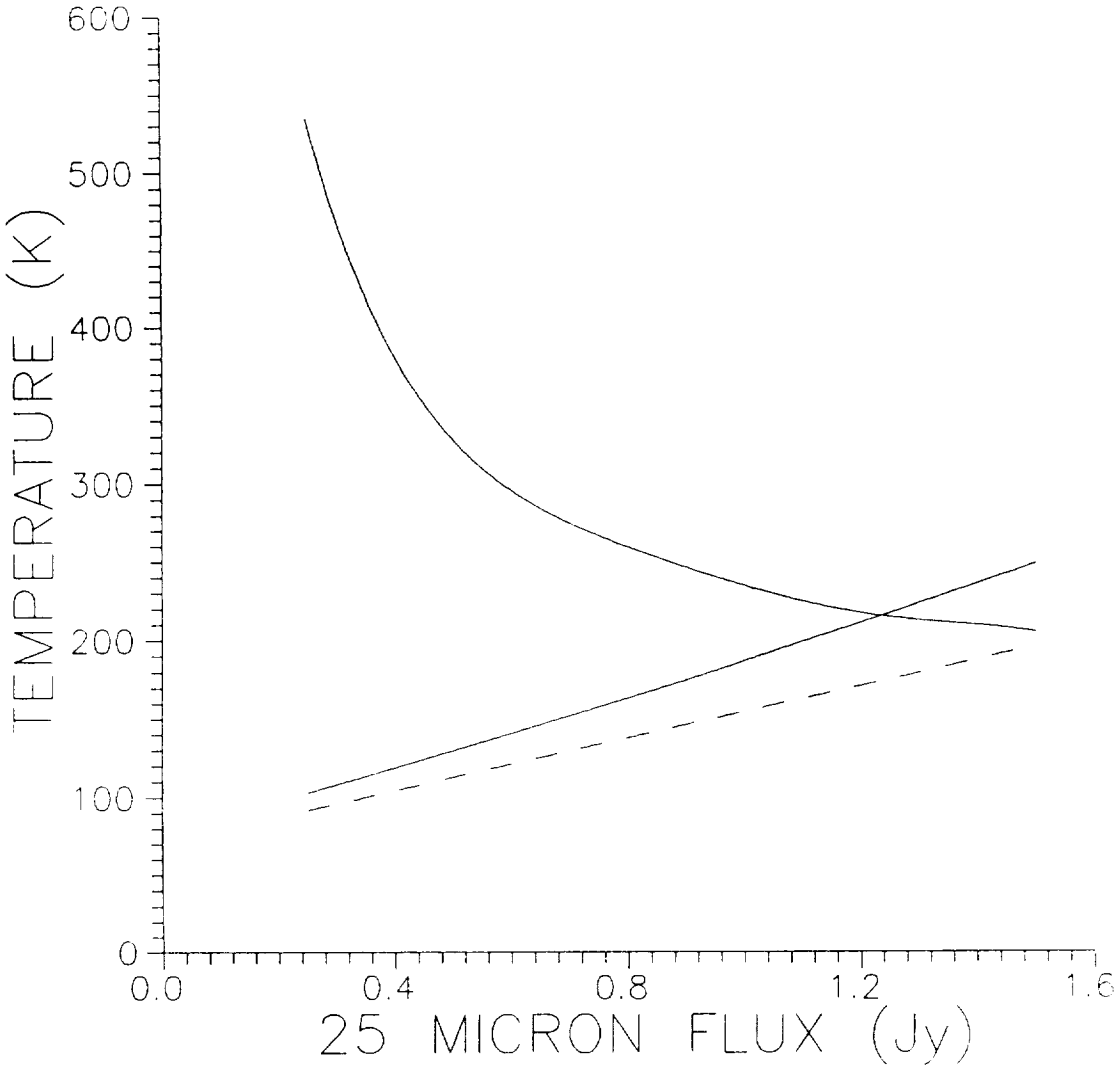

Figure 3. Range of temperatures implied by detection of thermal radiation only in the IRAS 25 μm band as a function of the measured 25 μm flux.

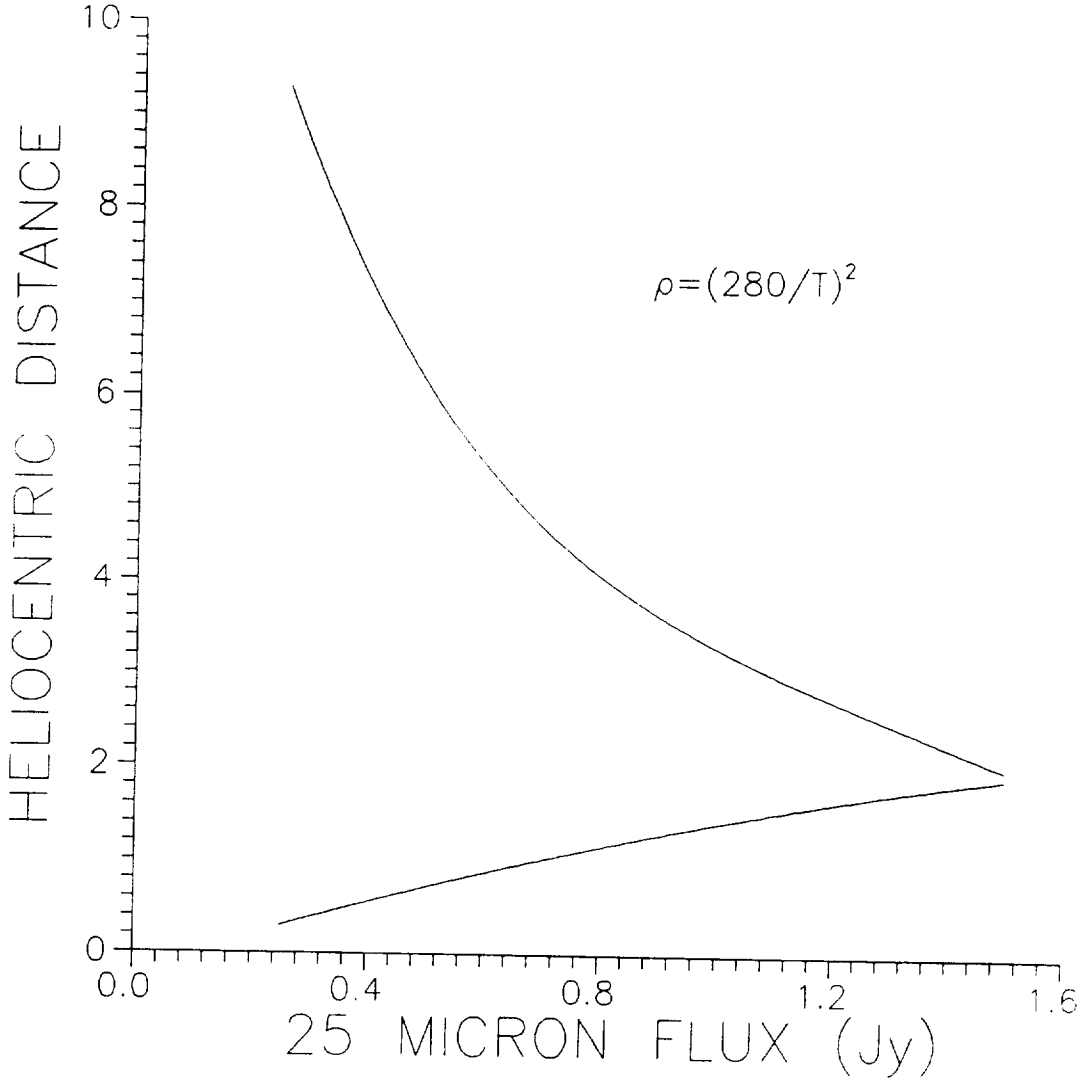

Figure 4. Range of heliocentric distances for blackbody thermal sources detected only in the IRAS 25 μm band as a function of the measured 25 μm flux.

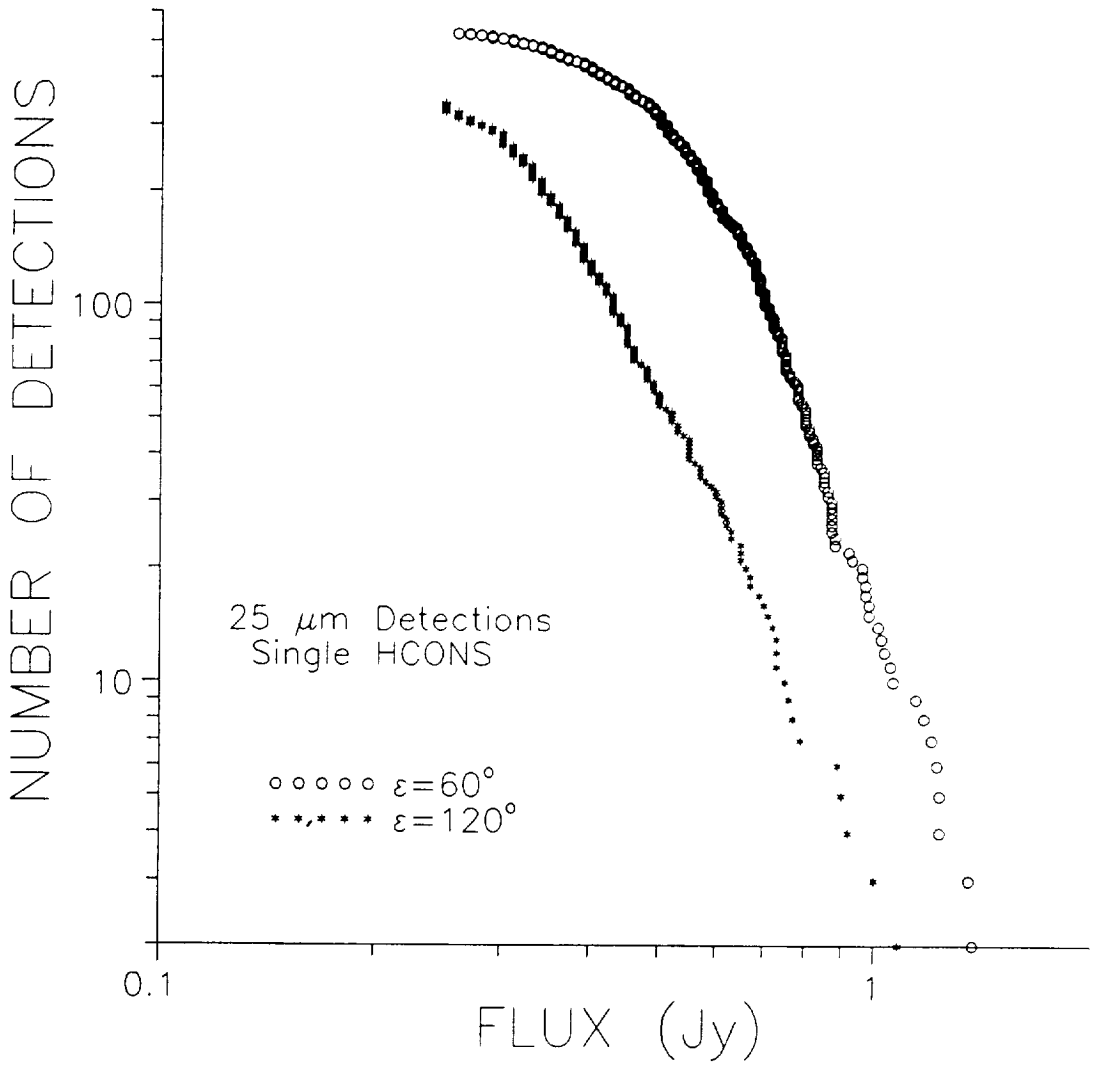

Figure 5. Comparison of log N, log F curves for HCON 3 survey scans.

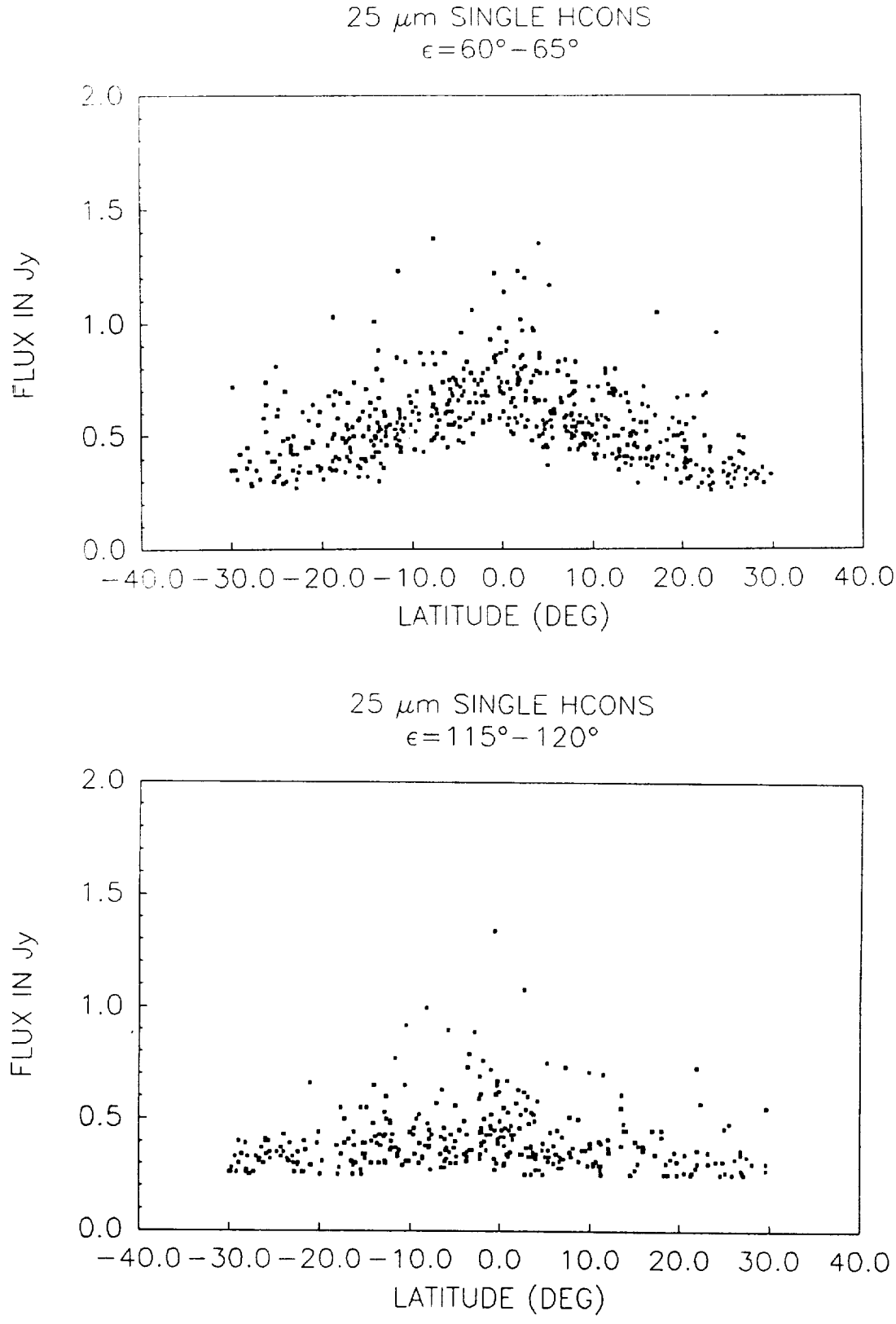

Figure 6 a,b. Amplitude of the 25 μm single HCONS versus ecliptic latitude. The data are from 100 scans during the 3rd HCON survey: a. 50 scans at solar elongations $115^{\circ}<\epsilon<120^{\circ}$, and b. 50 scans with $65^{\circ}<\epsilon<60^{\circ}$.

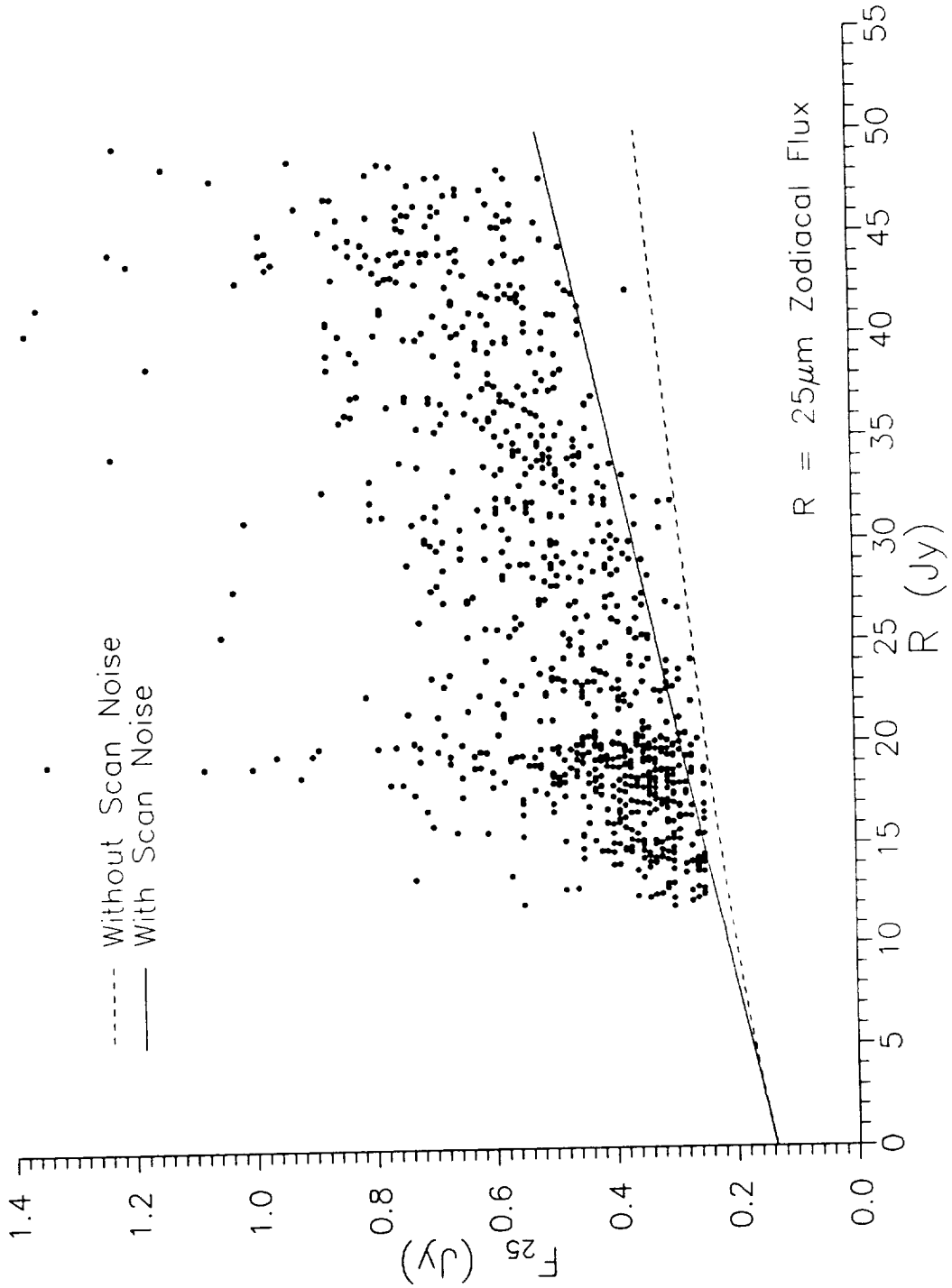

Figure 7. Threshold model from stare-mode observations with and without a scan noise component.

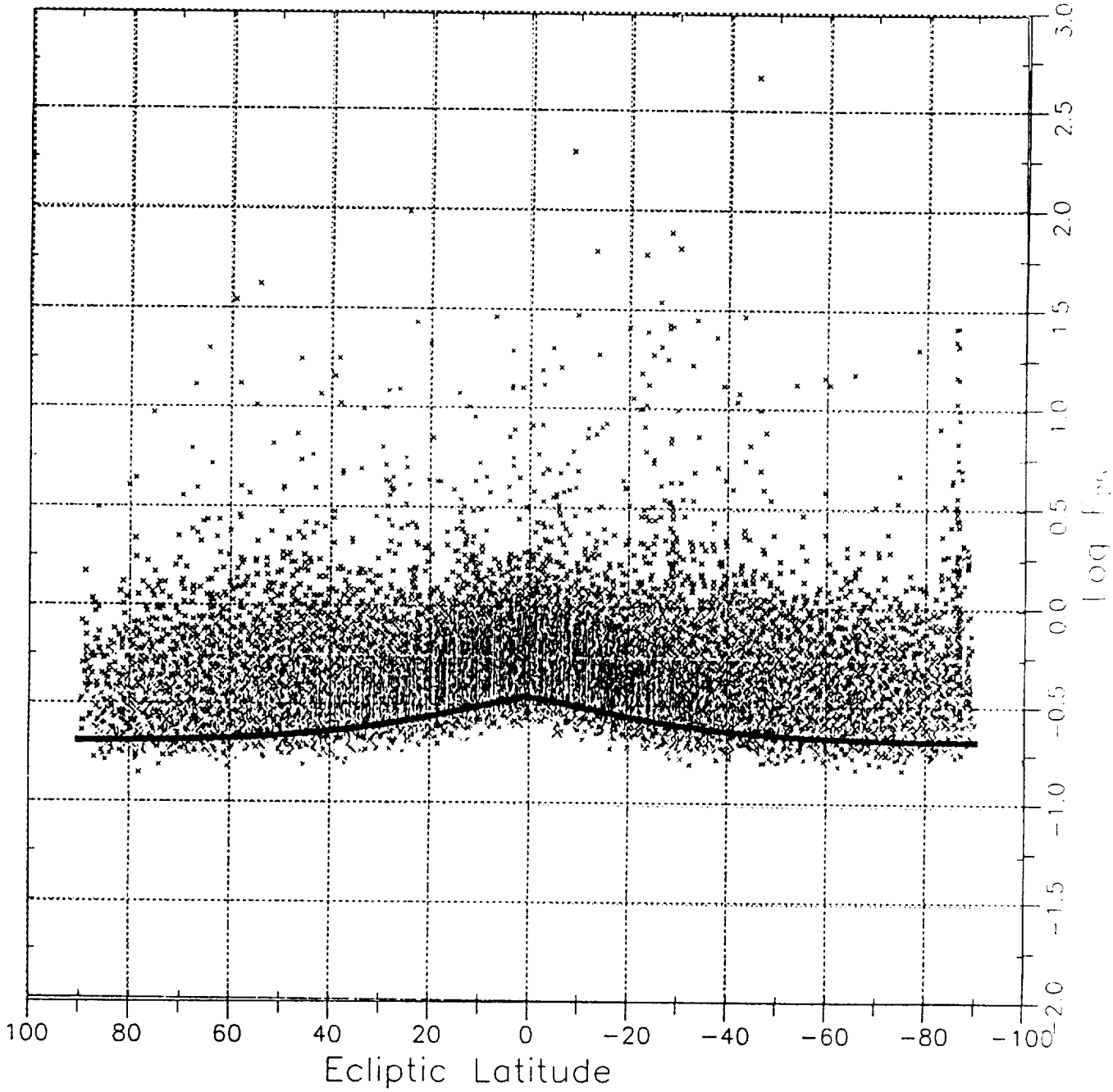

Figure 8. Threshold model plotted on the data of Veeder (1986). The logarithms of the fluxes of 35618 high quality 25 μm detections from the asteroid and comet data processing are plotted versus ecliptic latitude. All sources within 5° of the galactic plane have been excluded.

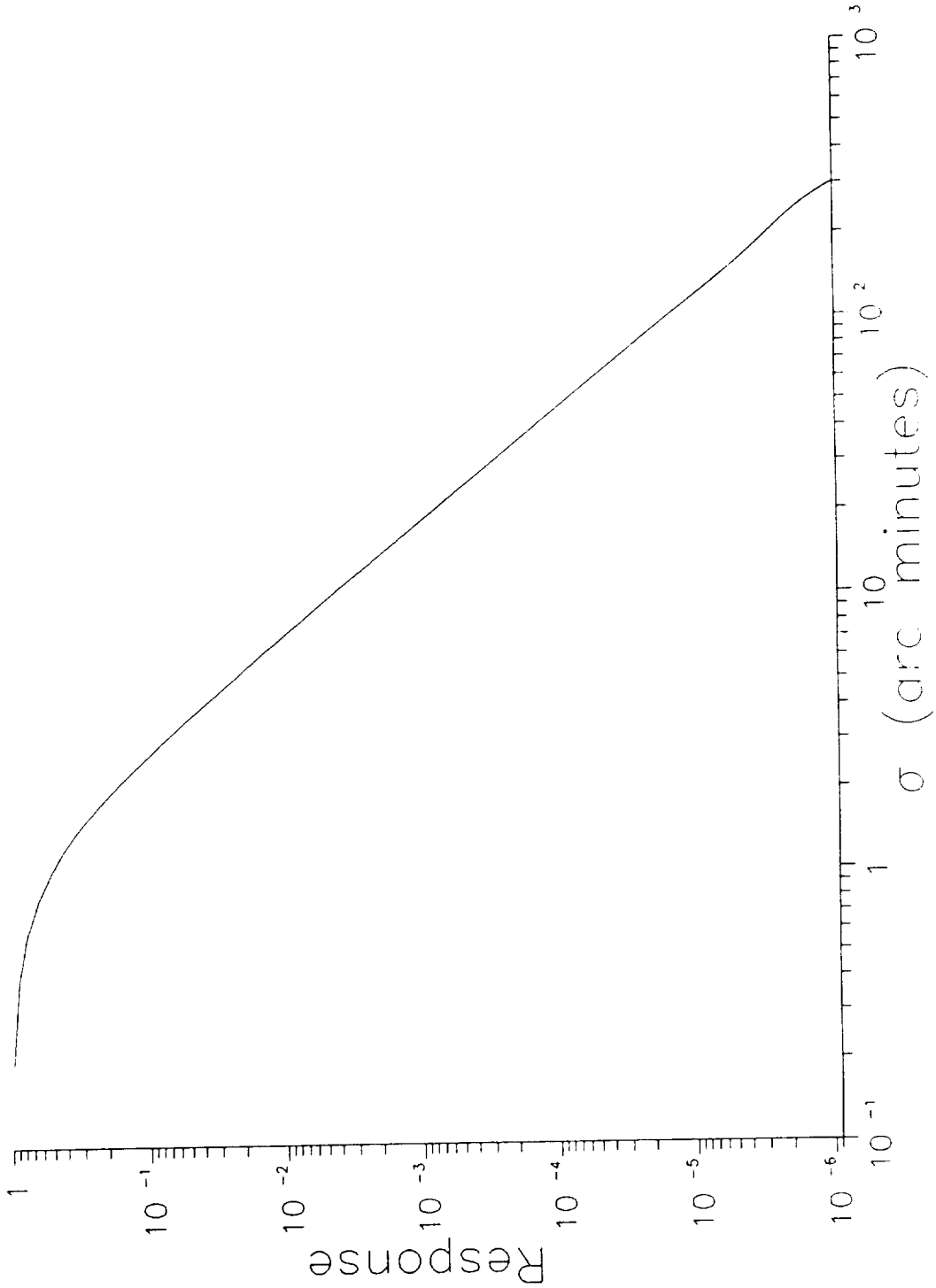

Figure 9. Response of the IRAS point source filter to narrow gaussian sources.

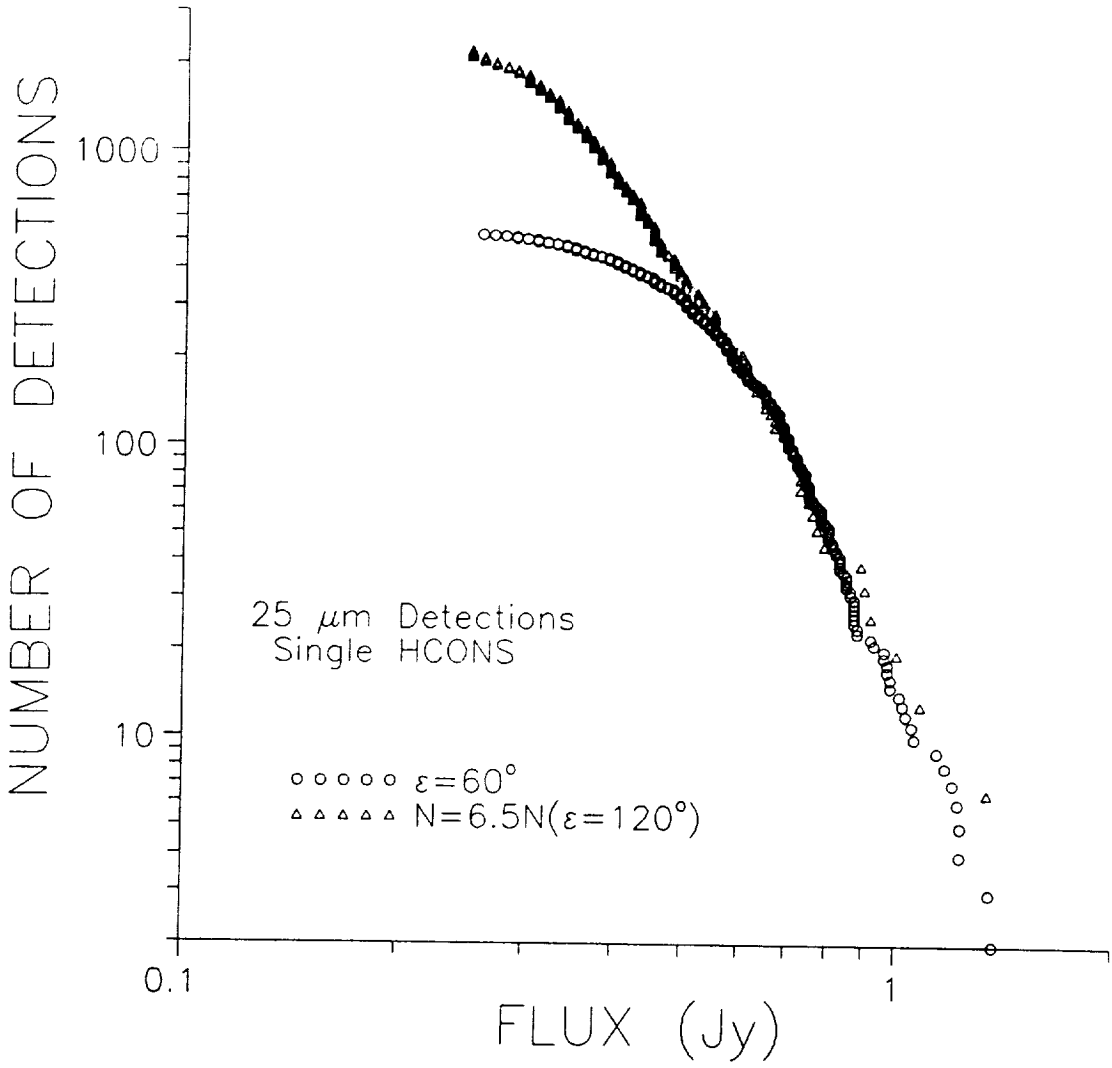

Figure 10. A replot of the Figure 5 data with the $\epsilon = 120°$ curve shifted along the Number of Detections axis by a factor of 6.5.

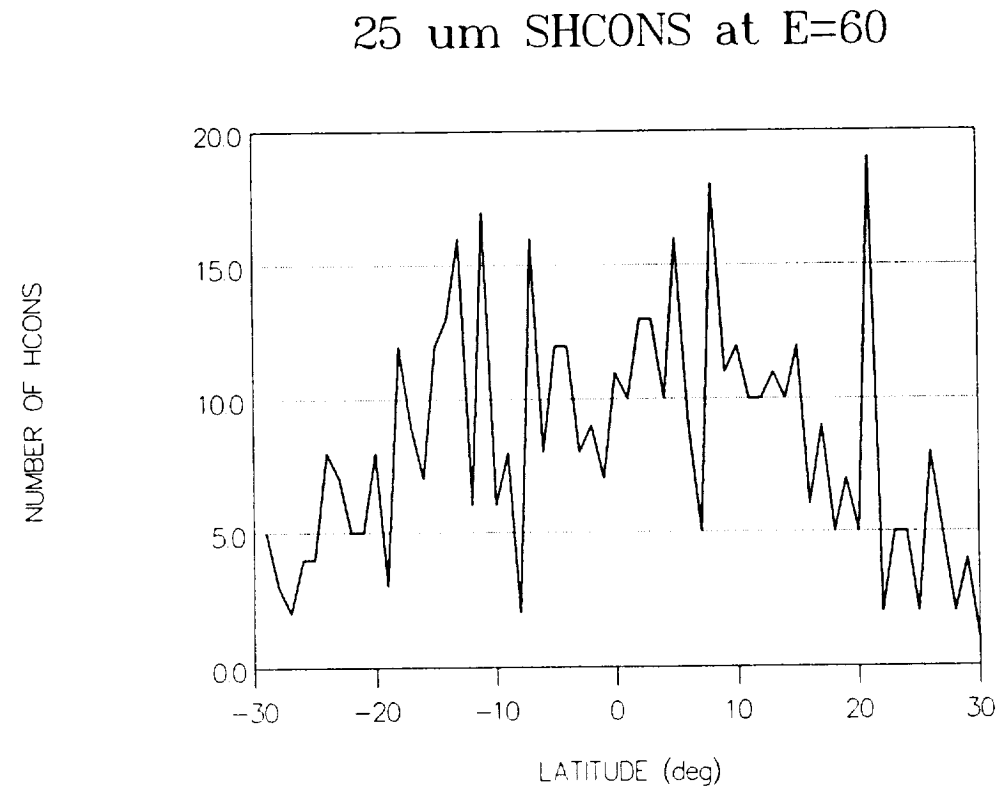

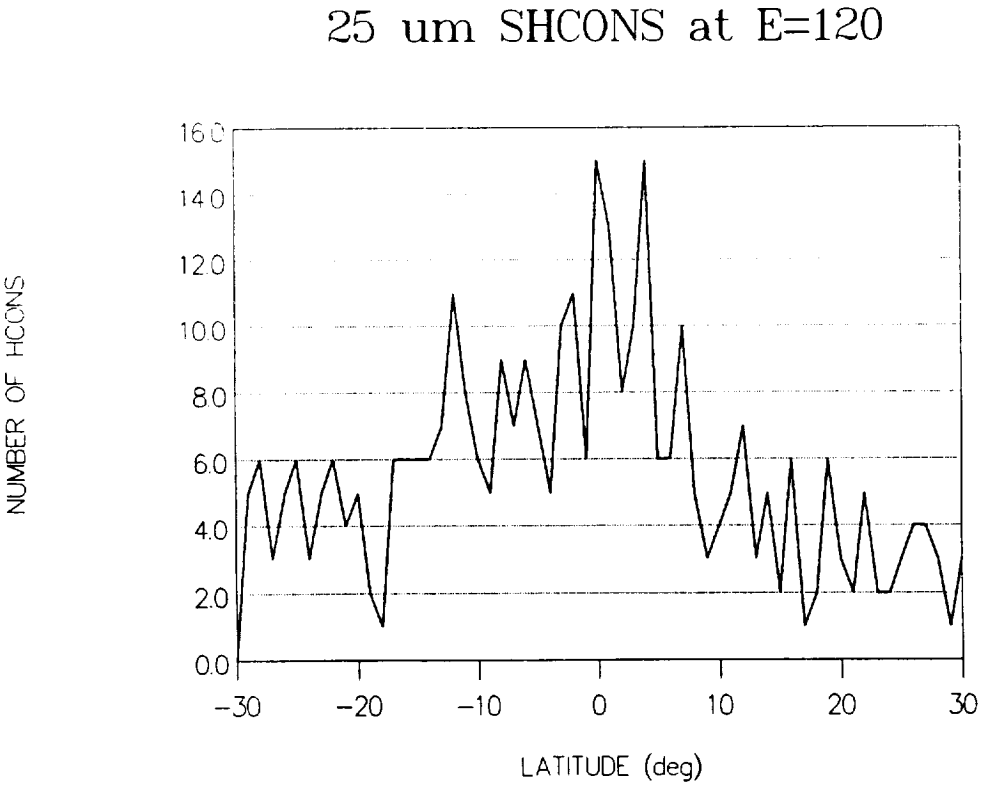

Figure 11. The latitude distribution of source counts. Sources are counted in bands of 1 degree of latitude.

References

Alfven, H. and Arrhenius, G.,"Evolution of the Solar System",NASA SP-345,1976.
Allen, C.W., "Astrophysical Quantities", 3rd edition, The Athlone Press, 1976.
Anz-Meador, P.D., Oro, D.M., Kessler, D.J., and Pitts, D.E., "Analysis of IRAS Data for Orbital Debris", Adv. Space Res., Vol. 6, no. 7, pp. 139-144, 1986.
Beichman, C.A., Neugebauer, G., Habing, H.J., Clegg, P.E., and Chester, T.J., "IRAS Explanatory Supplement", NASA RP-1190, 1988.
Boggess, N.W., Greenberg, L.T., Hauser, M.G., Houck, J.R., Low, F.J., McCreight, C.R., Rank, D.M., Richards, P.L., and Weiss, R., "Infrared Recievers for Low Background Astronomy", NASA TM 78598, June, 1979.
Davies, J.K., Green, S.F., Stewart, B.C., Meadows, A.J., and Aumann, H.H., "The IRAS Fast-Moving Object Search", Nature,vol.309, No.5967, pp.315-319, May,1984.
Dermott, S.F., Nicholson, P.D., Burns, J.A., and Houck, J.R., "Origin of the Solar System Dust Bands Discovered by IRAS", Nature, vol. 312, 505, 1984.
Dermott, S.F., Nicholson, and P.D., Burns, J.A., "A Dynamical Model for the IRAS Solar System Dust Bands", Bull. of the Am. Astron.Soc., vol. 16,689, 1984.
Dermott, S.F., Nicholson, P.D., Burns, J.A., and Houck, J.R., "An Analysis of IRAS Solar System Dust Bands", in Properties and Interactions of Interplanetary Dust, ed. R.H. Giese and P.Lamy, D.Reidel, Dordrecht, Boston, 1985.
Dermott, S.F., Nicholson, and Wolven, R., "Preliminary analysis of the IRAS Solar System Dust Data",in Asteroids, Comets, Meteors II,ed.C.T.Lagerkvist, R.A. Lindblad, R.Lundstedt,H. Rickman, Uppsala University Press, Sweeden,1986.
Gautier, T.N. and Boulanger, F., "A Study of the Small Scale Structure in the Infrared Cirrus", reprint, poster paper at Third International IRAS Conference, London, July, 1987.
Gautier, T.N., Hauser, M.G., and Low, F.J., Parallax Measurements of the Zodiacal Dust Bands with the IRAS Survey", Bull. Am. Astron. Soc., vol. 16, p. 442, 1984
Gautier, T.N., Good, J.C., and Hauser, M.G., "The Geometry of the Zodiacal Dust Bands", Adv. Space Res. vol. 6, no. 7, pp. 91-94, 1986.
Green, S.F., Davies, J.K., Eaton, N., Stewart, B.C., and Meadows, A.J., "Detection of Fast-Moving Asteroids and Comets by IRAS", ICARUS, vol 64, pp 517-527, 1985.
Hauser, M.G., Gautier, T.N., Good, J., and Low, F.J., "IRAS Observations of Interplanetary Dust", in Properties and Interactions of Interplanetary Dust, ed. R.H. Giese and P.Lamy, D.Reidel, Dordrecht, Boston, 1985.
Helin, E.F. and Shoemaker, E.M., "Palomar Planet-crossing Asteroid Survey", Icarus, vol. 40, 321-328, 1979.
Matson, D.L., "Infrared Astronomical Satellite Asteroid and Comet

Survey", JPL D-3698, October, 1986.
Low, F.J. et al, "Infrared Cirrus: New Components of the Extended Infrared Emission", Astrophys. J., vol.278 , L19-L22, 1984.
Roach, J.R., "Counterglow from the Earth-Moon Libration Points", Planet. Space Sci. vol. 23, 173, 1975.
Sykes, M.V. and Dow, R., (1988) in preparation
Sykes, M.V., Greenberg, R., and Hunten, D.M., "Formation of the Zodiacal Dust Bands in the Asteroid Belt", Bull. Am. Astron. Soc., vol. 16, p. 690, 1984
Sykes, M.V. and Greenberg, R., "The Production of the IRAS Zodiacal Dust Bands by Single Collisions Between Asteroids", Pub. Astron. Soc. of the Pacific, vol. 97, 904, 1985.
Sykes, M.V., Lebofsky, L.A., Hunten, D.M., and Low, F.J., "The Discovery of Dust Trails in the Orbits of Periodic Comets". Science,vol.232,1115-1117,1986.
Sykes, M.V., Hunten, D.M., and Low, F.J., "Preliminary Analysis of Cometary Dust Trails", Adv. Space Res. vol. 6, no. 7, pp. 67-778, 1986.
Sykes, M.V., "Iras Observations of Asteroid Dust Bands and Cometary Dust Trails", Ph.D. Dissertation, University of Arizona, 1986.
Sykes, M.V., private communication, 1987.
Veeder, G.J., in "Infrared Astronomical Satellite Asteroid and Comet Survey", Chap. 4, "Probable Asteroids", in preparation for version 2, private communication, 1987.
Walker, R.G., "IRAS Observations of Comets and Asteroids", invited paper at the 97th Meeting of the Astronomical Society of the Pacific, June, 1985.
Young, E.T. and Low, F.J., "Tests of Low Background Photoconductors", preprint of paper presented at ARC IR Detector Workshop, 1985.

NASA
National Aeronautics and Space Administration

Report Documentation Page

1. Report No.	2. Government Accession No.	3. Recipient's Catalog No.
NASA CR-177526		

4. Title and Subtitle
An Infrared Sky Model Based on the IRAS Point Source Data

5. Report Date
February 1990

6. Performing Organization Code

7. Author(s)
Martin Cohen, Russell Walker,* Richard Wainscoat, Kevin Volk, Helen Walker, and Deborah Schwartz**

8. Performing Organization Report No.

10. Work Unit No.
188-41-53

9. Performing Organization Name and Address
*Jamieson Science and Engineering, Inc.
Scotts Valley, CA 95066
**SETI Institute, Los Altos, California

11. Contract or Grant No.
NAS2-12515 (DHC)

13. Type of Report and Period Covered
Contractor Report

12. Sponsoring Agency Name and Address
National Aeronautics and Space Administration
Washington, DC 20546-0001

14. Sponsoring Agency Code

15. Supplementary Notes
Point of Contact: David Goorvitch, Ames Research Center, MS 245-6, Moffett Field, CA 94035-1000
(415) 604-5502 or FTS 464-5502

16. Abstract

We present a detailed model for the infrared point source sky that comprises geometrically and physically realistic representations of the galactic disk, bulge, spheroid, spiral arms (including the "local arm"), molecular ring, and the extragalactic sky. We represent each of the distinct galactic components by up to 87 types of galactic source, each fully characterized by scale heights, space densities, and absolute magnitudes at BVJHK, 12, and 25 μm. Our model has been guided by a parallel Monte Carlo simulation of the Galaxy at 12 μm. The content of our galactic source table constitutes an excellent match to the 12 μm luminosity function in the simulation, as well as the luminosity functions at V and K. We are to produce differential and cumulative infrared source counts for and bandpass lying fully within the IRAS Low Resolution Spectrometer's range (7.7-22.7 μm) as well as for IRAS 12 and 25 μm bands. These source counts match the IRAS observations extremely well. In addition, models are given for predicting the density of asteroids to be observed, and the diffuse background radiance of the Zodiacal cloud. The model can be used to predict the character of the point source sky expected for observations from future infrared space experiments (e.g., ISO, SIRTF, LDR).

17. Key Words (Suggested by Author(s))	18. Distribution Statement
Astronomy, Infrared, Sky model, Infrared observations, Infrared sources	Unclassified-Unlimited Subject Category - 89

19. Security Classif. (of this report)	20. Security Classif. (of this page)	21. No. of Pages	22. Price
Unclassified	Unclassified	592	A025

NASA FORM 1626 OCT 86

For sale by the National Technical Information Service, Springfield, Virginia 22161